UNIVERSITÀ DEGLI STUDI DI PADOVA

UNIVERSITÀ DEGLI STUDI DI PADOVA

Head Office: Università degli Studi di Padova
Department of Industrial Engineering

PH.D. COURSE IN: INDUSTRIAL ENGINEERING
CURRICULUM: CHEMICAL AND ENVIRONMENTAL ENGINEERING
SERIES: XXX

Microstructural Characterization of CaO-based Sorbents During CO_2 Capture and Sorbent Regeneration

Thesis written with the financial contribution of Fondazione Cariparo

Coordinator: Prof. Matteo Strumendo
Supervisor: Prof. Matteo Strumendo

Ph.D. student: Alberto Benedetti

Foreword

This dissertation is submitted for the degree of Doctor of Philosophy in Chemical and Environmental Engineering at the University of Padua.
The author wants to acknowledge the financial contribution of "Fondazione Cariparo" who supported the three years PhD course scholarship.

The research described herein was carried out under the supervision of prof. Matteo Strumendo to whom the author is extremely grateful.
Part of this work was performed at the Industrial Engineering Department facilities and laboratories at the University of Padua and in collaboration with prof. Alessandro Martucci (Department of Industrial Engineering, University of Padova), prof. Gabriella Salviulo and Dr. Federico Zorzi (Department of Geoscience, University of Padova).
Another part of the research activities has been carried out at the Department of Physics at the Illinois Institute of Technology (IIT), Chicago, IL (USA), during six months research stay under the supervision of prof. Carlo U. Segre. During this period, novelty and original experimental campaigns were performed at the Advanced Photon Source (APS), a research facility of the Argonne National Laboratory, Argonne, IL (USA). The author wants to acknowledge "Fondazione Ing. Aldo Gini" for the financial support provided during this period abroad.

This work is to the best of my knowledge original, except where acknowledgements and references are made to previous works.
Part of this work has been presented (or is planned to be submitted) in the following international publications:

Benedetti A., Strumendo M. (2015). *Application of a random pore model with distributed pore closure to the carbonation reaction.* Chemical Engineering Transactions, vol. 43, pp. 1153–1158. DOI: 10.3303/CET1543193.

Benedetti A., Modesti M., Strumendo M. (2015). *CFD analysis of the CaO-CO_2 reaction in a thermo-gravimetric apparatus.* Chemical Engineering Transactions, vol. 43, pp. 1039–1044. DOI: 10.3303/CET1543174.

Benedetti A., Ilavsky J., Segre C., Strumendo M. (2017). *Analysis of textural properties of CaO-based CO_2 sorbents by ex-situ USAXS.* Submitted to the Chemical Engineering Journal.

Benedetti A., Ilavsky J., Segre C., Strumendo M. (2017). *Micro-textural characterization and reaction kinetics during the $CaCO_3$ thermal decomposition and sintering by in-situ time-resolved synchrotron-based USAXS, SAXS and WAXS measurements.* To be submitted within 2017.

Padova, October 31st 2017

Alberto Benedetti

UNIVERSITÀ DEGLI STUDI DI PADOVA

Abstract

Department of Industrial Engineering

Microstructural Characterization of CaO-based Sorbents During CO_2 Capture and Sorbent Regeneration

by Alberto Benedetti

This work of thesis deals with the micro-textural properties characterization of calcium oxide as CO_2 capture solid sorbent, that strongly influence the carbonation reaction step performances. The investigation of the sorbent micro-structure was carried out by means of both in-situ and ex-situ techniques, varying the precursor ($CaCO_3$) activation conditions and sintering effects on the final sorbent pore network.
X-ray diffraction and N_2-adsorption techniques were used to identify correlations between the sorbent micro-textural properties and the average sorbent crystallite size, by considering completely calcined calcium carbonate samples under vacuum conditions and varying the high temperature (800–900 °C) heating step period.
With the aim to investigate the high temperature and time dependent phenomena, as pore generation, sintering processes and pore closure, in-situ X-ray small angle scattering techniques were carried out for the first time to investigate the sorbent micro-structure evolution during calcite decomposition and the CaO carbonation reaction.
Firstly, preliminary ex-situ measurements were performed at the Advanced Photon Source facilities of the Argonne National Laboratory to test the X-ray small angle scattering technique capabilities to investigate high porous samples, such as completely calcined $CaCO_3$ and partially carbonated CaO-based sorbents, and successful results were obtained, providing a detailed quantitative description of the sorbent micro-structure.
Therefore, for the first time in-situ time-resolved X-ray small angle scattering tests were carried out to investigate the sorbent micro-textural properties generation during the $CaCO_3$ calcination reaction and their evolution during the CaO carbonation reaction. Two different sets of experiments were considered, by performing $CaCO_3$ calcination reactions below 800 °C in pure nitrogen and at high temperatures (800 °C and 900°C) in presence of CO_2 (from 1 % up to 50 % in balance with N_2) in the reaction atmosphere. Afterwards, CaO carbonation tests were performed at 550 °C with 0.5 % of CO_2 in balance with N_2. Because of the non-catalytic gas-solid nature of the CaO carbonation reaction, a modified random pore model was proposed in order to represent both the reaction kinetics and the sorbent micro-structure evolution over the reaction. In addition, a computation fluid dynamic study on a thermo-gravimetric analyzer was performed to quantify the external mass transfer effects on the kinetics of the CaO carbonation reaction.

Riassunto

Le continue emissioni di gas serra (GHGs) a partire dalla seconda metà del XIX secolo hanno progressivamente modificato la composizione chimica dell'atmosfera terrestre determinando il fenomeno del surriscaldamento globale (Solomon, 2007). L'aumento della temperatura media, il restringimento dei ghiacciai perenni e l'innalzamento del livello dei mari sono dirette conseguenze dei cambiamenti climatici, inequivocabilmente dimostrati dai dettagliati rapporti tecnici da parte del Intergovernamental Panel on Climate Change (Stocker, 2013; IPCC, 2014).
La causa principale di questi cambiamenti climatici è da attribuire all'emissione incontrollata dei GHGs nell'atmosfera terrestre, il più rilevante dei quali è l'anidride carbonica (Metz et al., 2005; Solomon, 2007). Infatti, le principali fonti di emissione di quest'ultima sono associate alle "grandi fonti di emissioni stazionarie" che utilizzano i combustibili fossili come fonte di energia termica, come le centrali elettriche, i cementifici, le raffinerie, le acciaierie e le industrie del settore petrolchimico (Blamey et al., 2010; Dean et al., 2011; Solomon, 2007). Tuttavia, negli ultimi anni si è assistito ad una progressiva sensibilizzazione da parte del settore industriale in materia ambientale e la comunità scientifica è concorde nel riconoscere l'esigenza di attuare concrete strategie di mitigazione per ridurre le emissioni di CO_2 e, quindi, gli effetti dei cambiamenti climatici (Metz et al., 2005; Solomon, 2007; Stocker, 2013). La cattura e lo stoccaggio dell'anidride carbonica (CCS) è una delle strategie di mitigazione proposte dalla comunità scientifica e rappresenta un insieme di tecnologie orientate alla separazione della CO_2 da correnti gassose, per essere successivamente trasportata e stoccata in opportuni giacimenti (Metz et al., 2005). Queste tecnologie prevedono d'integrare gli esistenti impianti a maggiori emissioni di CO_2 in modo da ridurre il loro impatto ambientale, cercando di contenerne i costi aggiuntivi associati (Metz et al., 2005; Blamey et al., 2010; Dean et al., 2011; Fennel e Anthony, 2015).
La cattura dell'anidride carbonica tramite sorbenti solidi a base di metalli alcalino-terrosi è una promettente tecnologia che potrebbe soppiantare i tradizionali impianti di assorbimento e stripping basati sulle alcanolammine, processi energeticamente ed economicamente dispendiosi che presentano importanti criticità, tra cui la termo-labilità e la corrosività dei composti assorbenti (Blamey et al., 2010; Dean et al., 2011; Fennel e Anthony, 2015).
Tra i vari sorbenti solidi, l'ossido di calcio è uno dei più promettenti materiali di origine naturale caratterizzato da un'elevata capacità assorbente nei confronti della CO_2, $0.78\,\mathrm{g(CO_2)\,g(CaO)^{-1}}$, da un basso costo e da un'ampia disponibilità in natura del suo precursore, il carbonato di calcio, e da una marcata reattività nei confronti della CO_2 (Feng, An e Tan, 2007; Biasin et al., 2015). Nello specifico i processi di cattura della CO_2 e di rigenerazione del sorbente sono basati sulla reversibilità delle reazioni di carbonatazione del CaO e calcinazione del $CaCO_3$, nei quali il sorbente ossido di calcio è ripetutamente riciclato tra il carbonatatore e il calcinatore (Shimizu et al., 1999).
Entrambe le fasi sono basate su reazioni di tipo gas-solido non catalitico, nelle quali la micro-struttura del reagente solido cambia ed evolve durante la reazione influenzando la cinetica di reazione stessa (Barker, 1973; Bhatia e Perlmutter, 1983a). Nello specifico, le prestazioni complessive della reazione di carbonatazione del CaO sono definite dalla velocità di reazione e dalla massima capacità assorbente di CO_2, fortemente influenzate dalle proprietà micro-strutturali iniziali del sorbente (Bhatia e Perlmutter, 1983a; Biasin et al., 2015; Sun et al., 2007). Queste proprietà sono: la porosità interna, la superficie specifica, il raggio medio (determinate dalla distribuzione dei raggi dei pori) e la dimensione media delle cristalliti (Abanades e Alvarez, 2003; Alvarez e Abanades, 2005; Sun et al., 2007; Zhu, Wu e Wang, 2011). Inoltre, la cinetica di carbonatazione del CaO presenta due diversi regimi di reazione: il primo, veloce, controllato dalla reazione stessa, seguito da

un secondo regime più lento, che segue una cinetica controllata dalla diffusione della CO_2 nel prodotto solido di reazione (Barker, 1973; Bhatia e Perlmutter, 1983a; Grasa et al., 2009). In aggiunta, il passaggio tra i due regimi avviene in maniera brusca, a causa di una radicale modifica della struttura interna del sorbente solido. Questo cambiamento è spesso associato alla chiusura dei pori (Bhatia e Perlmutter, 1983a; Sun et al., 2008a), a causa dei diversi volumi molari tra il CaO ($16.9\,cm^3\,mol^{-1}$) e il $CaCO_3$ ($36.9\,cm^3\,mol^{-1}$), il cui rapporto è circa 2.2. La massima conversione del CaO teorica, invece, è strettamente legata alla porosità iniziale del sorbente, la cui evoluzione segue un andamento lineare in funzione della conversione di CaO (Bhatia e Perlmutter, 1981). Alla luce di queste considerazioni, la micro-struttura iniziale del CaO gioca un ruolo essenziale sulle prestazioni del sorbente in fase di cattura della CO_2 e, per queste ragioni, la caratterizzazione delle proprietà micro-strutturali iniziali del sorbente è un passaggio necessario ed essenziale.
La matrice porosa dell'ossido di calcio è generata durante la precedente fase di calcinazione del $CaCO_3$ condotta ad alta temperatura ($700 \div 900\,°C$), nella quale il carbonato di calcio non poroso si decompone in CaO e CO_2 (Barker, 1973; Bhatia e Perlmutter, 1983a; Borgwardt, 1989b; Glasson, 1958; Rodriguez-Navarro et al., 2009; Zhu, Wu e Wang, 2011). Il rilascio di CO_2 e il diverso volume molare tra il carbonato di calcio e l'ossido di calcio concorrono a generare la micro-struttura finale del sorbente, la quale è fortemente influenzata dalle condizioni operative alla quale viene condotta la decomposizione, ovvero la dimensione media delle particelle del precursore, la temperatura e la pressione, la composizione dell'atmosfera di reazione e il tempo di residenza in temperatura (Borgwardt, 1985; Fuertes et al., 1991; Ewing, Beruto e Searcy, 1979; Borgwardt, 1989a; García-Labiano et al., 2002; Borgwardt, 1989b). Tuttavia, queste condizioni operative non influenzano solamente la fase di calcinazione, poiché le alte temperature favoriscono i fenomeni di sintering che vanno a modificare la micro-struttura del sorbente fin dai primi istanti di reazione (Borgwardt, 1989b; Zhu, Wu e Wang, 2011; Maya, Chejne e Bhatia, 2017b). In generale, gli effetti di questi fenomeni sulla micro-struttura del sorbente causano una perdita di porosità e superficie specifica, associata ad un aumento del raggio medio dei pori (Borgwardt, 1989b; Fuertes et al., 1991) e della dimensione media delle cristalliti (Zhu, Wu e Wang, 2011).

Ad oggi, sono pochi i lavori in letteratura incentrati sullo studio della generazione della micro-struttura del sorbente e della sua evoluzione durante le reazioni di calcinazione del $CaCO_3$ e di carbonatazione del CaO, nella quale la micro-struttura viene consumata fino ad occludersi. In aggiunta, la relazione tra la dimensione delle cristalliti del sorbente e le sue proprietà strutturali (come la superficie specifica e la porosità) è tuttora sconosciuta e lo studio di questi fenomeni è ancora in corso.
In generale, le proprietà strutturali del CaO vengono comunemente studiate per mezzo delle tradizionali tecniche analitiche di tipo ex-situ, come l'adsorbimento con azoto, il porosimetro a mercurio e la diffrazione ai raggi X (Glasson, 1958; Barker, 1973; Ewing, Beruto e Searcy, 1979; Borgwardt, 1989b; Sun et al., 2007) and XRD (Rodriguez-Navarro et al., 2009; Zhu, Wu e Wang, 2011). Tuttavia, queste metodologie di caratterizzazione soffrono di due importanti limitazioni: l'analisi della micro-struttura del sorbente a condizioni operative di gran lunga diverse da quelle a cui è stata generata (ad es. 77 K per l'adsorbimento con N_2) e l'elevato rischio di contaminazione del campione quando viene esposto alle condizioni atmosferiche, dove il più frequente tra questi è l'idratazione ad idrossido di calcio. Inoltre, altre importanti limitazioni sono associate a modelli termodinamici approssimati sui quali i metodi di analisi come il BJH trovano fondamento (Lastoskie, Gubbins e Quirke, 1993); la pressione massima di Hg raggiungibile (che definisce il raggio dei pori minimo esplorabile) dal porosimetro a mercurio (Lowell, 2004; Washburn, 1921); la complessa micro-struttura dei sorbenti che potrebbe limitare la penetrazione del gas all'interno della matrice porosa (Nguyen e Bhatia, 2012).
Tutti questi vantaggi contribuiscono ad aumentare la variabilità del dato inerente alla

struttura interna del sorbente e a limitarne il campo di applicabilità.

Questo progetto di ricerca è inizialmente partito con lo scopo d'individuare una possibile relazione tra le proprietà strutturali del sorbente (come porosità e superficie specifica) e la rispettiva dimensione media delle cristalliti, accoppiando tre diverse tecniche sperimentali: la produzione del sorbente con l'analisi termo-gravimetrica, l'adsorbimento con azoto e la diffrazione ai raggi X. Il sorbente è quindi stato generato in vuoto (al di sotto di 0.01 bar) esplorando due diverse temperature di calcinazione (800 °C e 900 °C), variando il tempo di permanenza del sorbente stesso ad alte temperature in modo da permettere ai fenomeni di sintering di modificarne le proprietà micro-strutturali. Nello specifico, le calcinazioni in vuoto hanno permesso di minimizzare gli effetti del sintering durante la fase di decompostone termica del carbonato in modo da incentivare la rimozione della CO_2 stagnante dall'ambiente di reazione, in quanto l'anidride carbonica svolge un'azione catalitica nei confronti del sintering (Beruto, Barco e Searcy, 1984; Borgwardt, 1989a; Maya, Chejne e Bhatia, 2017b). Infatti, brevi tempi di permanenza (40 min a 800 °C e 50 min a 900 °C) hanno permesso di ottenere sorbenti con elevate proprietà micro-strutturali, ovvero elevate superfici specifiche (rispettivamente $50.4\,m^2\,g^{-1}$ e $20.7\,m^2\,g^{-1}$) e porosità (0.506 e 0.454), associate a contenute dimensioni medie delle cristalliti (40 nm e 50 nm). Al contrario tempi di permanenza più elevati portano a dimensioni delle cristalliti oltre i 100 nm e superfici specifiche al di sotto dei $20\,m^2\,g^{-1}$. In particolare, è stato osservato che a ridotte dimensioni delle cristalliti sono associate porosità e superfici specifiche elevate, viceversa, all'aumentare della dimensione media delle cristalliti sia la porosità del sorbente e, in particolar modo, la sua superficie specifica vengono drasticamente ridotte. Più precisamente, sono state individuate delle correlazioni di proporzionalità inversa tra queste proprietà indipendentemente dalla temperatura alla quale queste sono state generate. Infine, le immagini al SEM hanno permesso di osservare una micro-struttura del sorbente caratterizzata da pori a forma di fessure e cricche (nello specifico per campioni calcinati a 800 °C in vuoto per 40 min), al contrario delle comuni immagini proposte in letteratura dove la micro-struttura è caratterizzata da pori a forma cilindrica e/o da un sorbente formato da una collezione di micro-granuli.
Il principale svantaggio delle tradizionali tecniche ex-situ, come l'adsorbimento con N_2 o il porosimetro a mercurio, sta nella difficoltà di studiare quei fenomeni che concorrono a definire la struttura finale del sorbente e che avvengono ad alta temperatura e in funzione del tempo, come la generazione della porosità, i fenomeni di sintering e la chiusura dei pori.

Una tecnica più moderna e che può ovviare queste importanti limitazioni è quella basata sullo Small Angle Scattering (SAS) ai raggi X, che, al contrario delle tecniche basate sulla penetrazione di gas/vapori, è un'analisi non invasiva e non distruttiva, perché basata sulla radiazione X. Questa è in grado di fornire informazioni dettagliate sulla micro-struttura di campioni porosi fornendo informazioni sia di tipo qualitativo che quantitativo. Nello specifico, la tecnica di SAS fornisce per ogni popolazione di pori la loro superficie specifica, la porosità, il radius of gyration (o raggio di girazione legato al raggio medio dei pori indipendentemente dalla loro morfologia), il numero di pori per unità di massa e la distribuzione dei raggi dei pori.
Malgrado la tecnica di SAS sia già stata applicata all'analisi di campioni porosi particellari (Spalla, Lyonnard e Testard, 2003; Chavez Panduro et al., 2012), questa non è mai stata utilizzata per caratterizzare materiali ad elevata porosità come il sorbente ossido di calcio. Per questo motivo, la tecnica di SAS è stata inizialmente utilizzata per la *prima volta* in assoluto per analizzare campioni sia calcinati che parzialmente carbonatati di ossido di calcio con lo scopo di testare le capacità di quest'analisi nel caratterizzare materiali di questo calibro. Per fare ciò, i campioni sono stati inizialmente prodotti in TGA e, successivamente, analizzati attraverso la tecnica SAS secondo un approccio *ex-situ*. Le analisi sono state

condotte al Advanced Photon Source (APS), un sincrotrone di terza generazione parte del Argonne National Laboratory (IL, USA).
Le analisi ex-situ di SAS sono state effettuate su campioni di particolare interesse, ovvero su carbonato di calcio completamente calcinato in vuoto (al di sotto di 0.01 bar) considerando sia brevi che lunghi tempi di permanenza, esplorando due temperature di fine calcinazione: 800 °C e 900 °C. Inoltre, con lo scopo di studiare l'effetto della carbonatazione sulla micro-struttura del sorbente, il campione calcinato a 800 °C per 40 min (caratterizzato da proprietà strutturali elevate) è stato successivamente carbonatato a 650 °C con 10 % di CO_2 fermando la reazione a diversi gradi conversione del CaO.
L'analisi delle curve di intensità di scattering di questi campioni ha fornito una descrizione dettagliata della loro micro-struttura, confermando che la tecnica di SAS può essere applicata con successo nello studio di questi materiali. Nello specifico, i risultati del fitting attraverso il modello "Unified fit" (Beaucage, 1995) hanno confermato la bimodalità della micro-struttura dell'ossido di calcio poroso, caratterizzato, quindi, da due distinte popolazioni di pori che trovano posizione una nella regione dei micro-pori e l'altra in quella dei meso-pori. Inoltre, le superfici specifiche e i raggi medi dei pori risultato essere in ottimo accordo sia con i valori ottenuti dall'analisi delle curve di SAS, sia con quelli misurati tramite la tecnica di adsorbimento con azoto accoppiata al metodo BJH.
Benché la popolazione di micro-pori sia caratterizzata da una porosità ($0.01 \div 0.02$) significativamente più piccola rispetto a quella dei meso-pori ($0.21 \div 0.42$), la sua superficie risulta essere confrontabile con quella associata alla popolazione di meso-pori. Questa elevata superficie specifica è sicuramente dovuta all'elevato rapporto tra superficie e volume dei pori e, in gran parte, dal considerevole numero di pori per unità di massa (circa $10^{17}\,g^{-1}$) rispetto alla meso-popolazione che presenta un valore più basso di almeno un ordine di grandezza ($10^{16}\,g^{-1}$).
Considerando il campione parzialmente calcinato, le sue proprietà micro-strutturali (se opportunamente riscalate sul volume/massa reagiti) risultano essere significativamente simili a quelle del corrispondente materiale completamente calcinato. Questo risultato suggerisce come la micro-struttura nascente dell'ossido di calcio (800 °C in vuoto) sia quasi del tutto analoga a quella della calcite completamente reagita.
Con l'obiettivo di quantificare la forma dei pori, sono stati introdotti i fattori di sfericità (Wadell, 1935) per stimare la deviazione della loro morfologia da quella sferica. Durante la calcinazione la sfericità di entrambe le popolazioni aumenta progressivamente fino a tendere a uno in prossimità di fine reazione, malgrado i loro valori iniziali siano rispettivamente 0.8 per i micro-pori e 0.7 per i meso-pori.
Il fattore di struttura utilizzato nel fitting delle curve di scattering fornisce la cosiddetta "distanza di correlazione" (Beaucage et al., 1995) relativa alla popolazione dei meso-pori, ovvero una stima della distanza media dei meso-pori, il cui valore è di circa 45 nm per il caso di campioni poco sinterizzati. Tuttavia, all'aumentare del tempo di permanenza del campione ad alta temperatura, la distanza di correlazione dei meso-pori aumenta fino a 81 nm (720 min di riscaldamento fino a 800 °C) e 96 min (dopo 120 min di riscaldamento fino a 900 °C), suggerendo un meccanismo di sintering principalmente associato a fenomeni di coalescenza tra pori.
L'analisi dei profili di scattering inerenti ai campioni carbonatati (a 650 °C con il 10 % di CO_2) ha suggerito un drammatico cambiamento delle proprietà micro-strutturali del sorbente oltre il punto di transizione, al di là del quale la maggior parte dei pori sono occlusi dal prodotto solido $CaCO_3$. Inoltre la superficie specifica riscalata per unità di ossido di calcio non reagito è circa costante almeno durante tutto il regime cinetico, il cui valore è molto simile a quello iniziale del sorbente non reagito. Inaspettatamente, all'avanzare della reazione di carbonatazione, il radius of gyration di entrambe le popolazioni manifesta un

andamento crescente con la conversione, specialmente in prossimità del punto di transizione. Questo comportamento del tutto inatteso potrebbe essere dovuto al restringimento della meso-porosità che via via si trasferisce nella popolazioni dei micro-pori.
La maggior parte della conversione del CaO sembra quindi essere associata quasi prevalentemente al consumo della meso-porosità, il cui valore è significativamente maggiore rispetto a quello dei micro-pori. D'altro canto, l'elevata superficie specifica di quest'ultima suggerisce un ruolo chiave della micro-porosità durante il regime cinetico controllato dalla reazione, malgrado il suo alquanto modesto valore di porosità.
Infine, l'effetto globale della reazione di carbonatazione sulla sfericità dei pori è associato ad una decrescita dei fattori di sfericità di entrambe le popolazioni, fino ad un valore finale di 0.55 per i micro-pori e di 0.3 per i meso-pori, la cui distanza di correlazione rimane all'incirca costante ($38 \div 45$ nm) durante la reazione.

Le misure USAXS, SAXS, WAXS tramite l'approccio *in-situ* hanno permesso di ottenere sia informazioni sull'evoluzione della micro-struttura del sorbente sia della cinetica di reazione durante le reazioni di calcinazione e di carbonatazione.
Per quanto riguarda le prove SAS in situ sulla reazione di calcinazione del $CaCO_3$, dai profili di conversione nel tempo è stata stimata un'energia di attivazione pari a $44.5\,\mathrm{kcal\,mol^{-1}}$, in eccellente accordo con quella stimata da Borgwardt (1985), ovvero $48\,\mathrm{kcal\,mol^{-1}}$.
Durante i primi stadi della reazione di calcinazione, la micro-struttura del CaO sembra essere caratterizzata da una sola popolazione di pori, il cui raggio medio aumenta progressivamente nel tempo fino a raggiungere il punto in cui la micro-struttura sembra dividersi in due diverse popolazioni: quella dei micro e quella dei meso-pori. Da questo punto in poi, il radius of gyration della micro-popolazione decade bruscamente per assestarsi ad un valore circa costante (20 Å) durante tutta la reazione e il periodo di sintering, mentre quello dei meso-pori continua la propria crescita fino al raggiungimento di un massimo per poi assestarsi ad un valore asintotico. Malgrado il radius of gyration della micro-popolazione sia circa constate in quasi tutte le prove, quello associato alla meso-popolazione cambia sensibilmente a seconda delle condizioni operative di calcinazione, posizionandosi tra 83 Å e 102 Å quando gli effetti del sintering sulla micro-struttura sono trascurabili, per crescere fino a 520 Å quando la temperatura e la presenza di CO_2 favoriscono i fenomeni di sintering.
Per quanto riguarda i campioni calcinati al di sotto di 800 °C e in puro N_2, questi hanno permesso di ottenere importanti superfici specifiche rispetto a quelli calcinati ad alta temperatura e in presenza di CO_2. Nello specifico la calcinazione a 650 °C in azoto ha condotto a campioni con una superficie specifica pari a $128.7\,\mathrm{m^2\,g^{-1}}$, del tutto concorde con quella ottenuta da Ewing, Beruto e Searcy (1979) attraverso una calcinazioni di monocristalli di $CaCO_3$ sempre a 650 °C ma in vuoto, ovvero $127\,\mathrm{m^2\,g^{-1}}$.
Oltre ai meccanismi di sintering, altri fenomeni associati alle alte temperature hanno luogo durante la reazione di calcinazione. Questi sono stati associati all'interazione tra la CO_2 e il metastabile ossido di calcio appena prodotto, che vanno a generare comportamenti del tutto inattesi, come il profilo non lineare della porosità nascente in funzione della conversione del $CaCO_3$, il quale devia della linearità durante tutto il decorso della decomposizione, per poi tendere a valori prossimi a quelli teorici (54 %) negli ultimi istanti di reazione. L'evoluzione del numero di pori per unità di massa durante la reazione suggerisce la presenza di due importanti fenomeni: la generazione di pori, che si manifesta con un profilo crescente del numero di pori specifico e che sembra controllare i primi istanti di reazione, e il loro consumo a partire dalla seconda metà della reazione, che si traduce con una decrescita della densità del numero di pori e che prosegue anche durante il periodo di puro sintering.
Infine, la distanza di correlazione associata ai meso-pori è circa costante durante la reazione e il periodo di sintering per i campioni calcinati in puro azoto al di sotto di 800 °C, ovvero

250÷350 Å, ed aumenta fino a 3000 Å a temperature maggiori (800 °C e 900 °C) e in presenza di CO_2 nell'ambiente di reazione, ovvero quando le condizioni operative favoriscono i fenomeni di sintering.

I risultati inerenti alle misure di SAS durante le reazioni di carbonatazione a 550 °C con 0.4 % di CO_2, hanno confermato un aumento del radius of gyration della meso-popolazione fino al raggiungimento di un valore asintotico e, in alcuni casi, fino alla generazione di una terza meso-popolazione in corrispondenza del punto di transizione, ad eccezione dei campioni molto sinterizzati per i quali l'andamento del raggio dei meso-pori manifesta un aumento decisamente modesto, quasi costante. Questo fenomeno è stato associato al progressivo consumo dei pori di minori dimensioni, che spostano la distribuzione dei raggi dei pori verso valori via via maggiori, fino a dare origine a fenomeni di segregazione, dove una modesta frazione di pori (sotto il 5 % in volume) rimane non reagita e, molto probabilmente, localizzata all'interno della particella di sorbente stessa, in quanto la generazione di prodotto solido non-poroso preclude la diffusione della CO_2 negli strati più interni del sorbente.

I campioni calcinati in puro N_2 sotto 800 °C, esibiscono un andamento della superficie specifica per unità di massa lineare in funzione della conversione del CaO, che devia sensibilmente dalla linearità quando vengono carbonatati campioni di CaO molto sinterizzati.

Inoltre, il confronto tra le proprietà micro-strutturali iniziali del sorbente con quelle misurate in corrispondenza del punto di transizione, suggerisce come la micro-struttura interna del CaO sia maggiormente sfruttata quando il sorbente è poco sinterizzato. Infatti, ai campioni calcinati sotto i 800 °C in azoto si associa una relativa riduzione di porosità di circa 70÷79 %, associata ad una riduzione relativa di superficie specifica e numero di pori specifico di 66÷80 % e 60÷87 % rispettivamente. Questi valori decrescono sensibilmente, ad esempio, per i campioni calcinati a 900 °C con un tenore di CO_2 compreso tra 10 % e 50 %, ovvero 2÷18 % per la porosità e 4÷26 % per quanto riguarda la superficie specifica, anche se in alcuni casi la riduzione del numero di pori per unità di massa rimane comunque elevata, contenuta quindi in un intervallo di valori più elevato: tra 8 % e 60 %. Questi risultati confermano come micro-strutture fortemente sinterizzate siano meno reattive nei confronti della carbonatazione rispetto a quelle ottenute in condizioni tali da minimizzare gli effetti dei fenomeni di sintering.

Il confronto tra la massima velocità di reazione (localizzata nel regime controllato dalla cinetica) e il radius of gyration dei meso-pori iniziale ha condotto una correlazione negativa tra queste due grandezze, mentre un andamento lineare (crescente) ben definito è emerso considerando la derivata massima della conversione in funzione della superficie specifica dei campioni non carbonatati. Altre due interessanti correlazioni positive sono emerse considerando la massima velocità di reazione in funzione della porosità e del numero di pori per unità di massa iniziali.

Infine, anche la conversione in corrispondenza del punto di transizione sembra essere influenzata sia dal raggio iniziale dei meso-pori che dalla superficie iniziale della matrice porosa, manifestando una correlazione negativa nel primo caso e positiva nel secondo. Queste correlazioni suggeriscono come ad elevate proprietà micro-strutturali del sorbente iniziale siano associate maggiori velocità di reazione e conversioni al punto di transizione.

Contents

List of Figures

List of Tables

List of Abbreviations

BET	**B**runauer-**E**mmett **T**eller (method)
BJH	**B**arrett **J**oyner **H**alenda (method)
CFBs	**C**irculating **F**luidied **B**eds
CCS	**C**arbon **C**apture **S**torage (**S**equetration)
CS	**C**rystallite **S**ize
FWHM	**F**ull **W**idth at **H**alf **M**aximum
GHGs	**G**reen **H**ouse **G**ases
GM	**G**rain **M**odel
IPCC	**I**ntergovernmental **P**anel on **C**limate **C**hange
LFD	**L**arge **F**ield **D**etector
LOI	**L**oss **O**n **I**gnition
NUMOL	**N**umerical **M**etod **o**f **L**ines
ODE	**O**rdinary **D**ifferential **E**quation
PSD	**P**ore **S**ize **D**istribution
RPM	**R**andom **P**ore **M**odel
RT	**R**eaction **T**ime
SAS	**S**mall **A**ngle **S**cattering
SAXS	**S**mall **A**ngle **X**-ray **S**cattering
SEM	**S**canning **E**lectron **M**icroscope
ST	**S**intering **T**ime
TGA	**T**hermo-**G**ravimetric **A**nalyzer
USAXS	**U**ltra **S**mall **A**ngle **X**-ray **S**cattering
WAXS	**W**ide **A**ngle **X**-ray **S**cattering
XRF	**X**-**R**ay **F**luorescence

Physical Constants

Avogadro constant	$N_A = 6.022 \times 10^{23}\,\mathrm{mol}^{-1}$
Boltzmann constant	$k_B = 1.381 \times 10^{-23}\,\mathrm{J\,K}^{-1}$
Elementary charge	$e = 1.602 \times 10^{-19}\,\mathrm{C}$
Electron mass	$m_e = 9.109 \times 10^{-31}\,\mathrm{kg}$
Permeability of vacuum	$\mu_0 = (\epsilon\, c_0^2)^{-1} = 4\pi \times 10^{-7}\,\mathrm{N\,A}^{-2}$
Permittivity of vacuum	$\epsilon_0 = 8.854 \times 10^{-12}\,\mathrm{F\,m}^{-1}$
Planck constant	$h = 6.626 \times 10^{-34}\,\mathrm{J\,s}$
Reduced Plank constant	$\hbar = (h/2\pi) = 1.055 \times 10^{-34}\,\mathrm{J\,s}$
Speed of Light	$c_0 = 2.9978 \times 10^{8}\,\mathrm{m\,s}^{-1}$
Thomson scattering length	$r_0 = 2.818 \times 10^{-15}\,\mathrm{m}$
Universal (ideal) gas law constant	$R = 8.314\,\mathrm{Pa\,m}^3\,\mathrm{mol}^{-1}\,\mathrm{K}^{-1}$

Nomenclature

Chapters 1 and 2

A_i	cross-sectional adsorbate area	cm
C	BET method constant	–
C_i	molar concentration of specie i	$\mathrm{mol\,m^{-3}}$
C_p°	standard specific heat capacity at constant pressure	$\mathrm{J\,mol^{-1}\,K^{-1}}$
$d_{\max}$	maximum scatterer size	Å
K	Scherrer equation scale factor	–
K_{eq}	equilibrium constant	bar
m	sample mass	g
M_i	molecular weight of specie i	$\mathrm{g\,mol^{-1}}$
p_i	partial pressure of specie i	bar
P	pressure	bar
P_0	saturation pressure	bar
P_r	reduced pressure	–
$q_{\min}$	minimum scattering vector	$\mathrm{Å^{-1}}$
r	pore radius	Å
R	universal gas constant	$\mathrm{m^3\,Pa\,mol^{-1}\,K^{-1}}$
s	straight line slope of BET method	–
S	total adsorbed surface area	cm
S_m	specific surface area per unit of sample mass	$\mathrm{m^2\,g^{-1}}$
t	pre-condensation film thickness	Å
T	absolute temperature	K
V_m	molar volume	$\mathrm{m^3\,mol^{-1}}$
w_i	weight fraction of specie i	–
W	probing gas adsorbed weight	g
W_m	weight adsorbed in a monolayer	g
X_i	conversion of specie i	–
Z_i	molar volumes ratio	–

Greek Letters

β	line broadening at FWHM	–
γ	surface tension	$\mathrm{J^2\,m^{-1}}$
ΔG_f°	standard Gibb's energy of formation	$\mathrm{kJ\,mol^{-1}}$
ΔH_f°	standard enthalpy of formation	$\mathrm{kJ\,mol^{-1}}$
ΔH_r°	standard reaction enthalpy	$\mathrm{kJ\,mol^{-1}}$
ε	porosity	–
λ	X-ray wavelength	Å
θ	angular peak positions	rad
ρ_s	skeleton density	$\mathrm{g\,cm^{-3}}$

Subscripts

0	refers to initial state or conditions
eq	refers to equilibrium conditions

(g)	gas phase	
(s)	solid phase	

Superscripts

MB	moving reaction surface	
sup	particle surface	

Chapter 3

G	crystallite size	Å
k_{CS}	grain growth kinetic constant	$\mathrm{nm^n min^{-1}}$
k_p	porosity reduction kinetic constant	–
k_S	German and Munir model kinetic constant	$\mathrm{min^{-1}}$
n	crystallite growth kinetic exponent	–
P_r	reduced pressure	–
$\langle R_v \rangle$	average pore radius (on volume basis)	Å
S_m	specific surface area per unit of sample mass	$\mathrm{m^2\,g^{-1}}$
t	time	min
X_i	conversion of specie i	–

Greek Letters

γ	German and Munir model exponent	–
ε	porosity	–

Subscripts

0	refers to initial state or conditions	

Chapters 4, 5, 6 and 7

a_x	electron acceleration over x axis	$\mathrm{m\,s^{-2}}$
A	scattering amplitude	$\mathrm{cm^2\,cm^{-3}}$
A^*	complex conjugate scattering amplitude	$\mathrm{cm^2\,cm^{-3}}$
A_0	illuminated area	$\mathrm{cm^2}$
b_i	scattering length of one atom i	–
$B_{bkg,m}$	scattering background constant per unit of mass	$\mathrm{cm^2\,g^{-1}}$
$B_{bkg,v}$	scattering background constant per unit of volume	$\mathrm{cm^2\,cm^{-3}}$
B_i	constant prefactor of power law scattering profile of level i	$\mathrm{cm^2\,g^{-1}}$
e_s	sample thickness	cm
e_{solid}	solid phase sample thickness	cm
E	electric field amplitude	$\mathrm{N\,C^{-1}}$
f	atomic form factor	–
f_1	atomic form factor real part	–
f_2	atomic form factor imaginary part	–
$f_i(R)$	normalized numeral distribution of level i	$\mathrm{Å^{-1}}$
$f_m(R)$	numeral distribution per unit of mass	$\mathrm{g^{-1}\,Å^{-1}}$
$f_{m,i}(R)$	numeral distribution of level$i$ per unit of mass	$\mathrm{g^{-1}\,Å^{-1}}$
$f_v(R)$	volume distribution per unit of volume	$\mathrm{Å^{-1}}$
$f_{v,i}(R)$	volume distribution of level$i$ per unit of volume	$\mathrm{Å^{-1}}$
$F(q)$	relative scattering amplitude	–
$F^*(q)$	complex conjugate relative scattering amplitude	–
G_i	Guinier exponential prefactor of level i	$\mathrm{cm^2\,g^{-1}}$
I	intensity	a.u.
$\mathbf{k}$	wavevector	$\mathrm{Å^{-1}}$

k_c	calcination reaction kinetics	$\mathrm{m\,s^{-1}}$
m_i	median of the log-normal distribution	Å
M_i	molecular weight of specie i	$\mathrm{g\,mol^{-1}}$
M_{mix}	molecular weight of a mixture	$\mathrm{g\,mol^{-1}}$
M_{molec}	molecular weight of a molecule	$\mathrm{g\,mol^{-1}}$
N	scatterers number	–
N_m	pore number density	$\mathrm{g^{-1}}$
$N_{m,i}$	pore number density of level i	$\mathrm{g^{-1}}$
P	polrization factor	–
$P(q)$	particle form factor	–
P_i	power law exponent	–
q	scattering vector	$\mathrm{Å^{-1}}$
Q	Porod invariant per unit of volume	$\mathrm{cm^{-4}}$
Q_v	Porod invariant per unit of volume	$\mathrm{cm^{-4}}$
Q_m	Porod invariant per unit of mass	$\mathrm{cm\,g^{-1}}$
$Q_{m,i}$	Porod invariant per unit of mass of level i	$\mathrm{cm\,g^{-1}}$
r	vector position between to scatterers	m
R	pore radius	Å
R_g	radius of gyration	Å
$R_{g,i}$	radius of gyration of level i	Å
R_{HS}	hard-sphere radius	Å
$\langle R_v \rangle$	average pore radius (on volume basis)	Å
$\langle R_{v,i} \rangle$	average pore radius (on volume basis) of level i	Å
$R_{\mathrm{sph},i}$	spherical pore radius of i-th population	Å
sld	scattering length density	$\mathrm{cm^{-2}}$
$R_{S/V,i}$	surface-to-volume ratio of i-th population	$\mathrm{cm^{-1}}$
sld_i	scattering length density of specie i	$\mathrm{cm^{-2}}$
sld_{mix}	scattering length density of a mixture	$\mathrm{cm^{-2}}$
sld_{molec}	scattering length density of a molecule	$\mathrm{cm^{-2}}$
S	surface	$\mathrm{m^2}$
S_m	specific surface area per unit of sample mass	$\mathrm{m^2\,g^{-1}}$
$S_{m,i}$	spec. surf. area per unit of sample mass of i-th population	$\mathrm{m^2\,g^{-1}}$
$S_{m,\mathrm{CaO}}$	specific surface area per unit of CaO mass	$\mathrm{m^2\,g^{-1}}$
$S(q)$	structure factor	–
$S_i(q)$	structure factor of level i	–
S_V	spec. surf. area per unit of volume	$\mathrm{m^{-1}}$
$S_{V,i}$	specific surface area per unit of volume of i-th population	$\mathrm{m^{-1}}$
t	time	min
T	transmission coefficient	–
V	volume	$\mathrm{cm^3}$
V_{sample}	sample volume	$\mathrm{cm^3}$
w_i	weight fraction of specie i	–
X_i	conversion of specie i	–
z	sample thickness	cm

Greek Letters

$\Delta\rho_e^2$	scattering contrast	$\mathrm{cm^{-4}}$
ε	porosity	–
ε_i	porosity of level i	–
ζ	correlation distance	Å
ζ_i	correlation distance of level i	Å

η	hard sphere volume fraction	–
θ	scattering angle	rad
κ	packing factor	–
κ_i	packing factor of level i	–
λ	wavelength	Å
μ	linear adsorption coefficient	cm^{-1}
μ_i	linear adsorption coefficient of specie i	cm^{-1}
μ_{mix}	linear adsorption coefficient of a mixture	cm^{-1}
μ_{molec}	linear adsorption coefficient of a molecule	cm^{-1}
Ξ	polarisation angle	rad
ϕ_v	scatterers volume fraction	–
Φ	beam flux	$\mathrm{cm}^{-2}\,\mathrm{s}^{-1}$
ρ_{at}	atomic density	cm^{-3}
$\rho_e(r)$	electron charge distribution	$\mathrm{cm}^{-3}\,\mathrm{Å}^{-1}$
$\bar{\rho}_e$	average electron charge distribution	cm^{-3}
ρ_i	skeleton density of specie i	$\mathrm{g\,cm}^{-3}$
ρ_{mix}	density of a mixture	$\mathrm{g\,cm}^{-3}$
ρ_{molec}	skeleton density of a molecule	$\mathrm{g\,cm}^{-3}$
ρ_{solid}	skeleton density of solid phase	$\mathrm{g\,cm}^{-3}$
σ	microscopic scattering cross section	cm^2
σ_a	absorption cross section	cm^2
σ_i	standard deviation of level i	–
Σ	macroscopic cross section	$\mathrm{cm}^2\,\mathrm{cm}^{-3}$
Σ_m	macroscopic cross section per unit of mass	$\mathrm{cm}^2\,\mathrm{g}^{-1}$
$\Sigma_{m,i}$	macroscopic cross section per unit of mass of level i	$\mathrm{cm}^2\,\mathrm{g}^{-1}$
Σ_v	macroscopic cross section per unit of volume	$\mathrm{cm}^2\,\mathrm{cm}^{-3}$
τ_{kin}	kinetic time constant	min
Ψ_i	sphericity factor	–
ψ	dimensionless structural factor	–
ω	angular frequency	$\mathrm{rad\,s}^{-1}$
Ω	solid angle	sr

Subscripts

1	refers to micro-pore population
2	refers to meso-pore population
0	refers to incident incoming property or to an initial state
e	refers to one electron
in	refers to incident (electric) field
rad	refers to radiated (electric) field
M	refers to medium
s	refers to scatterer

Superscripts

$\hat{\cdot}$	refers to unit vector
0	refers to initial conditions

Chapter 8

$C_{\mathrm{CO_2}}$	molar concentration of $\mathrm{CO_2}$	$\mathrm{mol\,m}^{-3}$
$C^*_{\mathrm{CO_2}}$	molar concentration of $\mathrm{CO_2}$ when $p_{\mathrm{CO_2}} = 10\,\mathrm{kPa}$	$\mathrm{mol\,m}^{-3}$
d	diameter	m
k_0	zeroth order intrinsic rate constant	$\mathrm{mol\,m}^{-2}\,\mathrm{s}^{-1}$

k'_0	zeroth order intrinsic rate constant	s^{-1}
k'_1	first order intrinsic rate constant	$\mathrm{m}^3\,\mathrm{s}^{-1}\,\mathrm{mol}^{-1}$
M_i	molecular weight of specie i	$\mathrm{g\,mol}^{-1}$
Re_i	Reynolds number of specie i	–
S_0	specific surface area	$\mathrm{m\,g}^{-1}$
t	time	s
$\bar{v}_F$	furnace gas velocity	$\mathrm{m\,s}^{-1}$
$\bar{v}_{RGT}$	reactive tube gas velocity	$\mathrm{m\,s}^{-1}$
$\dot{V}_0$	normal gas flowrate	$\mathrm{Nm}^3\,\mathrm{min}^{-1}$
$\dot{V}$	effective gas flowrate	$\mathrm{m}^3\,\mathrm{s}^{-1}$
X	calcium oxide conversion	–

Greek Letters

μ_i	viscosity of specie i	Pa s
ρ_i	density of specie i	$\mathrm{g\,cm}^{-3}$

Chapter 9

C_{CO_2}	molar concentration of CO_2	$\mathrm{mol\,m}^{-3}$
D_{pl}	product layer diffusivity	$\mathrm{m\,s}^{-1}$
$E_{a,D}$	product layer diffusivity activation energy	$\mathrm{kJ\,mol}^{-1}$
$k_s^{(0)}$	zeroth order rate constant	$\mathrm{m\,s}^{-1}$
$k_s^{(1)}$	first order rate constant	$\mathrm{m}^4/\mathrm{mol/s}$
$l(r_0)$	differential length size distribution	$\mathrm{m\,m}^{-3}$
M_0	mean pore radius	Å
M_i	molecular weight of specie i	$\mathrm{g\,mol}^{-1}$
p_i	partial pressure of specie i	bar
r	pore radius	Å
r_0	initial pore radius	Å
r_p	surface pore radius	Å
r_s	surface reaction radius	Å
R	universal gas constant	$\mathrm{m}^3\,\mathrm{Pa\,mol}^{-1}\,\mathrm{K}^{-1}$
S_p	pore surface per unit of volume	m^{-1}
$S_{p,0}$	initial pore surface per unit of volume	m^{-1}
t	time	s
T	absolute temperature	K
X	CaO conversion	–
Z_{carb}	molar volumes ratio involved in CaO carbonation	–

Greek Letters

ε_0	initial porosity	–
$\varepsilon_{\mathrm{diff}}(r_0)$	differential pore size distribution	$\mathrm{Å}^{-1}$
μ_{N_0}	mean value of the normal distribution	–
ρ_i	density of specie i	$\mathrm{g\,cm}^{-3}$
ρ_s	skeleton density of CaO	$\mathrm{g\,cm}^{-3}$
σ_{N_0}	standard deviation of the normal distribution	–

Subscripts

eq.	refers to equilibrium conditions
bulk	refers to bulk conditions

Superscripts

p	refers to pore surface

s	refers to reaction surface	
$*$	refers to reduced properties	

Appendix A

a_i	activity coefficient of specie i	–
$c_{p,i}$	specific heat capacity of specie i	$\mathrm{J\,K^{-1}\,mol^{-1}}$
f_i	fugacity of specie i in mixture	bar
f_i^{pure}	fugacity of specie i (pure)	bar
$K_{\mathrm{eq.}}$	equilibrium constant	–
p_i	partial pressure of specie i	bar
P	pressure	bar
R	universal gas constant	$\mathrm{m^3\,Pa\,mol^{-1}\,K^{-1}}$
S_i	entropy of specie i	$\mathrm{J\,K^{-1}\,mol^{-1}}$
T	absolute temperature	K
$\mathbf{x_i}$	molar fraction vector of a mixture	–
y_i	molar fraction of specie i	–

Greek Letters

μ_i	chemical potential	$\mathrm{J\,mol^{-1}}$
ν_i	stoichiometric coefficient of specie i	–

Subscripts

eq.	refers to equilibrium conditions
f	refers to properties values of formation

Superscripts

0	refers to standard conditions

Appendix B

M_i	molecular weight of specie i	$\mathrm{g\,mol^{-1}}$
n_i	mole number of specie i	mol
V_{pores}	pore volume	$\mathrm{m^3}$
V_{solid}	solid phase volume	$\mathrm{m^3}$
X_i	conversion of specie i	–
Z_i	molar volumes ratio	–

Greek Letters

ε	porosity	–
ξ	extent of reaction	mol
ρ	density of specie i	$\mathrm{g\,cm^{-3}}$

Subscripts

calc	refers to $CaCO_3$ calcination reaction
calc	refers to CaO carbonation reaction

Superscripts

0	refers to initial conditions
$\hat{\cdot}$	refers to properties expressed per unit of mass
$\tilde{\cdot}$	refers to molar properties

Appendix C

E	electric field amplitude	$\mathrm{N\,C^{-1}}$
f	frequency	$\mathrm{s^{-1}}$

H	magnetic field aplitude	T
$\mathbf{k}$	wavevector	Å^{-1}
$\mathbf{r}$	position vector	m
t	time	s
T	period	s
v	velocity	$\text{m}\,\text{s}^{-1}$
z	z-axis position	m

Greek Letters

$\mathcal{E}$	X-ray wave energy	keV
$\hat{\varepsilon}$	polarization unit vector	–
λ	wavelength	Å
ω	angular frequency	$\text{rad}\,\text{s}^{-1}$

Subscripts

0	refers to initial conditions

Introduction

The increase of the anthropogenic carbon dioxide emissions in the atmosphere (IPCC, 2014) has largely contributed to the global warming. Nowadays, the Carbon Capture and Storage (CCS) technologies are essential and necessary for the mitigation of the climate change effects (Metz et al., 2005). Specifically, the CO_2 sequestration with Ca-based solid sorbents is an attractive and promising technology among the CCS processes, because potentially more efficient and less energy intensive respect to the traditional amines-based scrubbing processes (Blamey et al., 2010).
Calcium oxide is one of the most promising natural materials because of its high sorption capacity for CO_2, $0.78\,g(CO_2)\,g(CaO)^{-1}$, its low cost and naturally abundant precursor ($CaCO_3$) and its high reaction kinetics (Feng, An, and Tan, 2007; Biasin et al., 2015). Specifically, this technology is based on the reversibility of the CaO carbonation and $CaCO_3$ calcination reactions, where calcium oxide sorbent is repeatedly cycled between two reactors: the carbonator and the calciner respectively. This process is commonly named as "Ca-looping cycle" applied to post combustion CO_2-capture processes (Shimizu et al., 1999).

Both the calcination and the carbonation steps are based on non-catalytic gas-solid reactions (Barker, 1973; Bhatia and Perlmutter, 1983a), where the solid reactant microstructure changes and evolves during the reaction influencing the reaction kinetics itself. The reaction rate and the maximum CO_2-uptake (Bhatia and Perlmutter, 1983a; Biasin et al., 2015; Sun et al., 2007) define the carbonation reaction performances, that strongly depend on the initial sorbent micro-textural properties. These properties are the sorbent porosity, the specific surface area, the mean pore radius (that are completely determined by the sorbent pore size distribution), and the sorbent crystallite size (Abanades and Alvarez, 2003; Alvarez and Abanades, 2005; Sun et al., 2007; Zhu, Wu, and Wang, 2011). More specifically, the CaO carbonation kinetics shows a quite complex conversion over time profile that depends on these sorbent micro-textural properties: a fast chemically controlled step is followed by a slow product-layer diffusion controlled one (Barker, 1973; Bhatia and Perlmutter, 1983a). The transition between these two regimes occurs sharply due to a radical change of the sorbent internal micro-structure. Literature contributors ascribed this transition to the sorbent pore closure (Bhatia and Perlmutter, 1983a; Sun et al., 2008a), because of the different molar volumes between the solid reactant and the $CaCO_3$ product layer, whose ratio is about 2.2. Moreover, the maximum CO_2-capture capacity is theoretically related to initial sorbent porosity, whose evolution over the CaO conversion is linear (Bhatia and Perlmutter, 1981). For these reasons, a detailed characterization of the initial sorbent is an essential step to correctly predict the carbonation reaction performances during the CO_2-capture step.

The CaO pore network is generated during the high temperature ($700 \div 900\,°C$) activation step (Barker, 1973; Bhatia and Perlmutter, 1983a; Borgwardt, 1989b; Glasson, 1958; Rodriguez-Navarro et al., 2009; Zhu, Wu, and Wang, 2011) where non-porous calcium carbonate decomposes to calcium oxide and carbon dioxide. The CO_2 release and the different molar volume between the calcium carbonate and calcium oxide contribute to generate the sorbent internal pore matrix and the final sorbent micro-textural properties are strongly influenced by the reaction conditions, namely: the precursor particle size

(Borgwardt, 1985; Fuertes et al., 1991), the calcination reaction temperature and pressure (Ewing, Beruto, and Searcy, 1979), the reactor atmosphere composition (Borgwardt, 1989a; García-Labiano et al., 2002) and the sorbent residence time (Borgwardt, 1989a; Borgwardt, 1989b; Fuertes et al., 1991). In addition to these operative conditions, sintering phenomena contribute to modify the sorbent micro-textural properties (Borgwardt, 1989b; Zhu, Wu, and Wang, 2011; Maya, Chejne, and Bhatia, 2017b). Specifically, due to the high temperature conditions of the calcination reaction, sintering processes affect the sorbent micro-textural properties reducing the particle porosity and the specific surface area and increasing the mean pore radius (Borgwardt, 1989b; Fuertes et al., 1991) and the sorbent crystallite size (Zhu, Wu, and Wang, 2011).

Thus far, only few contributors in literature have debated the sorbent micro-textural property generation and evolution during the $CaCO_3$ calcination reaction (Ewing, Beruto, and Searcy, 1979; Powell and Searcy, 1982; Beruto, Barco, and Searcy, 1983), as well as during the CO_2-capture step (Sun et al., 2008b; Biasin, Segre, and Strumendo, 2015), and the investigation of these phenomena is still open. Additionally, the relationship between the sorbent crystallite size and sorbent pore textural properties during the CaO sintering has never been investigated.

The micro-textural properties of CaO based sorbents for CO_2 capture have been widely investigated by means of the traditional *ex-situ* techniques, namely gas-adsorption, mercury porosimetry (Glasson, 1958; Barker, 1973; Ewing, Beruto, and Searcy, 1979; Borgwardt, 1989b; Sun et al., 2007) and XRD (Rodriguez-Navarro et al., 2009; Zhu, Wu, and Wang, 2011). Because of their ex-situ nature, these techniques are affected by two important limitations: (1) the sorbent properties are analyzed at fairly different operative conditions (i.e. 77 K for the N_2 adsorption) respect to the high temperature process conditions; (2) samples are exposed to ambient conditions, leading to undesirable contaminations (sorbent hydration). In addition, gas-adsorption is based on approximated thermodynamic models (the Kelvin equation in the BJH approach), mercury porosimetry is limited by the highest achievable pressure (Lowell, 2004), that defines the minimum measurable pore size (Washburn, 1921) and the gas-probing accessibility may be limited by the complex and disordered internal pore structure (Nguyen and Bhatia, 2012).

Because of the intrinsic relationship between the CO_2 sorption/desorption reaction kinetics and the CaO sorbent internal micro-structure, the overall *goal* of the work performed in this PhD project is to investigate the sorbent micro-structural properties generation and evolution during the calcite decomposition and their influence on the kinetics of the CaO carbonation reaction, varying the $CaCO_3$ calcination conditions and accounting for the high temperature and time dependent processes, such as pore generation, sintering and pore closure.

Firstly, with the aim to investigate the mutual relationships among the sorbent microstructural properties during the precursor calcination, N_2-adsorption and XRD techniques were used to characterize Ca-based sorbents obtained by means of in-vacuum thermal decompositions in a thermo-gravimetric analyzer, varying the furnace temperature and the duration of the heating step at high temperature.
Afterwards, Small-Angle Scattering was considered as an alternative technique to analyze the sorbent microstructure. Instead of the traditional ex-situ techniques, the X-ray Small-Angle Scattering (SAS) is a non-destructive and non-invasive characterization analysis capable to avoid the aforementioned drawbacks of the ex-situ techniques. A very relevant advantage of X-Ray SAS is that it can be used *both* ex-situ and in-situ. SAS can provide both qualitative and quantitative information about the micro-textural properties and morphology of the material in-homogeneities, namely pores in the case of porous materials. Specifically, the material porosity, specific surface area and mean pore radius, as well as pore size distributions (PSDs) can be estimated (Chavez Panduro et al., 2012; Lee, 2004).

However, while X-Ray SAS was already used to analyze porous materials (Chavez Panduro et al., 2012; Spalla, Lyonnard, and Testard, 2003), it was never used thus far to characterize CaO based CO_2 sorbents.

Therefore, ex-situ Synchrotron Radiation (SR) SAS techniques were applied to the investigation of highly porous CaO sorbents, in order to verify whether such approach could provide quantitatively correct values of the sorbent micro-textural properties. Afterwards, SR X-ray SAS *in-situ* time-resolved measurements were carried out by using a capillary flow cell wherein the samples were placed, without the need of extracting the material samples from the reactor and avoiding the experimental issues associated with the sample contamination/hydration when exposed to the ambient conditions, with the goal of investigating the micro-textural property evolution during the high temperature $CaCO_3$ decomposition and sintering, and during the CaO carbonation. Therefore, time and temperature dependent phenomena were investigated at different reaction conditions (gas composition, temperature), namely the micro-structure evolution during the calcite thermal activation and sintering and during the CaO carbonation reaction.

Finally, during this PhD project modelling work was carried as well on the CaO carbonation. Specifically, the thermo-gravimetric analysis (TGA) has become a well-established method to investigate the reaction rates during the sorbent regeneration and the CO_2-capture steps. However, TGA measurements can be affected by the external mass transfer (Schulze et al., 2017), that can potentially reduce: (1) the CO_2 removal near the sorbent particles during the $CaCO_3$ decomposition favoring the internal micro-structure sintering; (2) the CO_2 supply during the CaO carbonation leading to measurements of apparent reaction kinetics, instead of intrinsic reaction rates. Therefore, in this work, a CFD study on a thermo-gravimetric analyzer was performed with the goal of verifying and quantifying the external mass transfer limitations on the CaO carbonation.
Lastly, a structural kinetic model based on the random pore model (Bhatia, 1985) was proposed and applied in order to predict both the whole reaction kinetics and the sorbent micro-structure evolution during the CaO carbonation, and the numerical results were compared with TGA and BET measurements.

The first part of this PhD project introduces calcium oxide as a CO_2 capture solid sorbent among the CCS technologies. Specifically, Chapter 1 deals with the climate change effects due to the global warming generated by the anthropogenic GHGs emissions in the atmosphere since the second half of the XIX century. This chapter summarizes the scientific and unequivocal evidences of the climate changes widely discussed by Solomon (2007), Stocker (2013), and IPCC (2014). Afterwards, the climate change causes are summarized and the CCS technologies are introduced and presented as possible mitigation strategies, focusing the attention on the carbon dioxide capture with solid sorbents.

Chapter 2 introduces the fundamental aspects of calcium oxide as solid sorbent for the CO_2 capture. Specifically, the $CaCO_3$ calcination and CaO carbonation reactions are described as CO_2 capture and sorbent regeneration steps, and the thermodynamics of these two reversible reactions is discussed. In addition, the experimental setups for the sorbent production and characterization and for the CO_2 capture reaction kinetics investigation used in this work of thesis are introduced and described.

The second part of this work of thesis is focused on the calcium oxide micro-structural properties characterization by means of ex-situ techniques. Specifically, Chapter 3 deals with the investigation of a possible relationship between the CaO sorbent micro-textural properties and its crystallite size by means of N_2-adsorption and XRD characterization techniques.
In order to provide the fundamental basis of the X-ray small angle scattering, Chapter 4

introduces the essential concepts of this topic, in terms of scattering cross section, form and structure factors and fitting models used to analyze the scattering intensity profiles. Afterwards, Chapter 5 deals with the results of ex-situ X-ray synchrotron-based small angle scattering measurements on completely (and partially) calcined and carbonated sorbents, produced in a thermo-gravimetric apparatus and then tested at the Advanced Photon Source (APS) at the Argonne National Laboratory (Argonne, Illinois).

The third part of this work of thesis provides the main results on the *in-situ* X-ray small angle scattering measurements performed at the APS facility during the $CaCO_3$ thermal decomposition and the CaO carbonation reaction. Chapter 6 deals with the results of the in-situ SAS measurements during the $CaCO_3$ calcination reaction exploring different operative conditions in terms of final heating temperature, atmosphere composition (CO_2/N_2) and heating step duration. Afterwards, Chapter 7 shows the results of the in-situ sorbent micro-structure characterization during the CaO carbonation reaction performed at 550 °C with 0.4 % of CO_2 in balance with N_2 with the aim to investigate the sorbent micro-structure influence on the CaO carbonation reaction kinetics.

Last part of this thesis proposes two modeling approaches concerning the investigation of the CaO carbonation reaction kinetics. Specifically, in Chapter 8 a computational fluid dynamic study on a horizontal thermo-gravimetric analyzer is presented and discussed in order to quantify the influence of external mass transfer when a fast chemical reaction kinetics is investigated, as that of the CaO carbonation reaction. Lastly, in Chapter 9 a modified random pore model is applied to the CaO carbonation reaction with the aim to describe both the reaction kinetics and the sorbent micro-textural properties evolution during the CO_2 capture step.

Part I

CaO as Solid Sorbent: a CCS Technology

Chapter 1

The CCS Technology: a Mitigation Strategy to the Global Warming

The Working Group I contribution to the Fifth Assessment Report of the Intergovernmental Panel on Climate Change (IPCC) provides a comprehensive assessment of the physical science basis of climate change Stocker (2013). This work puts a focus on those elements that are relevant to understand past, document current and project future climate change of the planet. The Special Report of the Working Group III of IPCC on Carbon dioxide Capture and Storage (CCS) has been developed in response to an invitation of the United Nations Framework Convention on Climate Change (UNFCCC) at its seventh Conference of Parties (COP7) in 2001. The results of this workshop were a first assessment of literature on CO_2 capture and storage, in the field of mitigation technologies for climate change. The attention is then focused on carbon dioxide capture technologies, specifically on calcium carbonate looping cycle.

1.1 Climate change

> *Warming of the climate system is unequivocal, and since the 1950s, many of the observed changes are unprecedented over decades to millennia. The atmosphere and ocean have warmed, the amounts of snow and ice have diminished, sea level has risen, and the concentrations of greenhouse gases have increased Stocker (2013).*

Human activities are continuing to affect the Earth's energy budget by changing the emissions and resulting atmospheric concentrations of important gases and aerosols and by changing land surface properties. The evidences of climate change derives from observations of the atmosphere, land, oceans and cryosphere. Unequivocal evidence from in-situ observations and ice core records shows that the atmospheric concentrations of important greenhouse gases (GHGs) such as carbon dioxide (CO_2), methane (CH_4), and nitrous oxide (N_2O) have increased over the last few centuries.

Observations of the climate system are based on direct measurements and remote sensing from satellites and other platforms. Global-scale observations from the instrumental era began in the mid-19^{th} century for temperature and other variables, with more comprehensive and diverse sets of observations available starting from 1950s. Paleo-climate reconstructions extend some records back hundreds to millions of years. Together, they provide a comprehensive view of the variability and long-term changes in the atmosphere, the ocean, the cryosphere, and the land surface.

Global mean surface air temperatures over land and oceans have increased over the last 100 years. Temperature measurements in the oceans show a continuing increase in the heat content. Observations from satellites and in situ measurements show a trend of significant reductions in the mass balance of most land ice masses and in Arctic sea ice. The

increasing of CO_2 concentrations in oceans is having a significant effect on the chemistry of sea water.

1.1.1 Atmosphere

> *Each of the last three decades has been successively warmer at the Earth's surface than any preceding decade since 1850. In the Northern Hemisphere, 1983-2012 was likely the warmest 30-year period of the last 1400 years Stocker (2013).*

The globally averaged combined land and ocean surface temperature data as calculated by a linear trend, show a warming of 0.85 °C, over the period 1880 to 2012. The total increase between the average of the 1850-1900 period and the 2003-2012 period is 0.78 °C (Fig. 1.1a). For the longest period for which calculation of regional trends is sufficiently complete (1901 to 2012), almost the entire globe has experienced surface warming, as shown in Fig. 1.1b.
Confidence in precipitation change averaged over global land areas since 1901 is low prior to 1951 and medium afterwards. Averaged over the mid-latitude land areas of the Northern Hemisphere, precipitation has increased since 1901 as reported in Fig. 1.2. Changes in many extreme weather and climate events have been observed since about 1950. It is very likely that the number of cold days and nights has decreased and the number of warm days and nights has increased on the global scale. The frequency of heat waves has increased in large parts of Europe, Asia and Australia. There are likely more land regions where the number of heavy precipitation events has increased than where it has decreased. The frequency or intensity of heavy precipitation events has likely increased in North America and Europe.

1.1.2 Ocean

> *Ocean warming dominates the increase in energy stored in the climate system, accounting for more than 90 % of the energy accumulated between 1971 and 2010. It is virtually certain that the upper ocean (0÷700 m) warmed from 1971 to 2010 Stocker, 2013.*

On a global scale, the ocean warming is largest near the surface, and the upper 75 m warmed by 0.11 °C per decade over the period 1971 to 2010 and it is likely that it has warmed from the 1870s to 1971. There is less certainty in changes prior to 1971 because of relatively sparse sampling in earlier time periods.
It is likely that the ocean warmed between 700 ÷ 2000 m from 1957 to 2009, based on 5-year averages. The ocean warmed from 3000 m to the bottom from 1992 to 2005, instead no significant trends in global average temperature were observed between 2000 and 3000 m depth from circa 1992 to 2005. Below 3000 m depth, the largest warming is observed in the Southern Ocean (Fig. 1.3).

1.1.3 Cryosphere

> *Over the last two decades, the Greenland and Antarctic ice sheets have been losing mass, glaciers have continued to shrink almost worldwide, and Arctic sea ice and Northern Hemisphere spring snow cover have continued to decrease in extent Stocker, 2013.*

The average rate of ice loss from glaciers around the world, excluding glaciers on the periphery of the ice sheets, was very likely 226 $\mathrm{Gt\,yr^{-1}}$ over the period 1971 to 2009, and

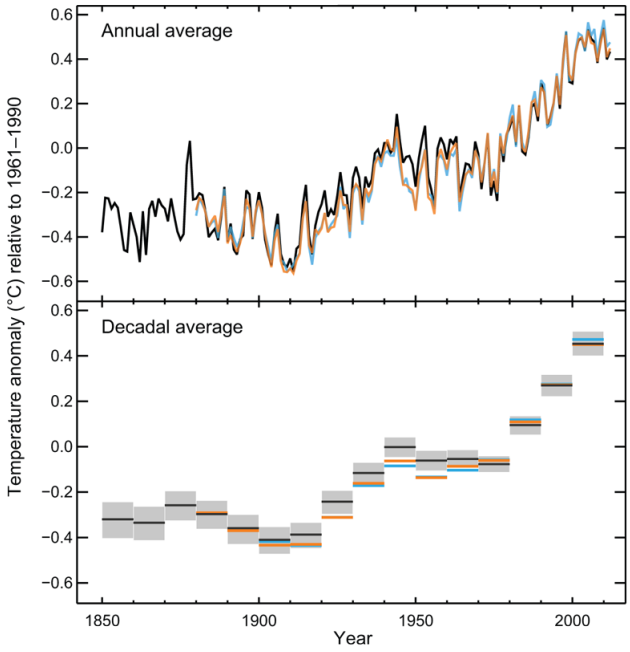

(a) *Observed globally averaged combined land and ocean surface temperature anomaly 1850-2012.*

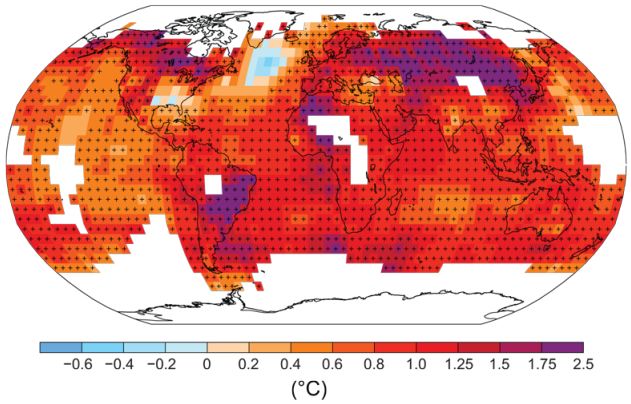

(b) *Observed change in surface temperature 1901-2012.*

Figure 1.1: (a) Observed global mean combined land and ocean surface temperature anomalies, from 1850 to 2012. Top panel: annual mean values. Bottom panel: decade mean values including the estimate of uncertainty. Anomalies are relative to the mean of 1961-1990. (b) Map of the observed surface temperature change from 1901 to 2012, according to Stocker (2013).

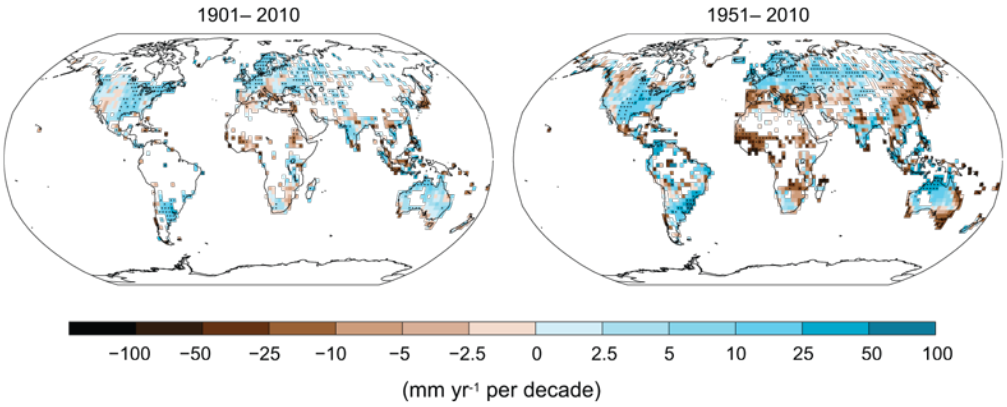

Figure 1.2: Maps of observed precipitation change from 1901 to 2010 and from 1951 to 2010, according to Stocker (2013).

very likely 275 Gt yr^{-1} over the period 1993 to 2009.
The average rate of ice loss from the Greenland ice sheet has very likely substantially increased from 34 Gt yr^{-1} over the period 1992 to 2001 to 215 Gt yr^{-1} over the period 2002 to 2011.
The average rate of ice loss from the Antarctic ice sheet has likely increased from 30 Gt yr^{-1} over the period 1992-2001 to 147 Gt yr^{-1} over the period 2002 to 2011 (Fig. 1.4).
The annual mean Arctic sea ice extent decreased over the period 1979 to 2012 with a rate that was very likely in the range 3.5 to 4.1 % per decade (range of 0.45 to 0.51 million km^2 per decade), and very likely in the range 9.4 to 13.6 % per decade (range of 0.73 to 1.07 million km^2 per decade) for the summer sea ice minimum (perennial sea ice). There is medium confidence from reconstructions that over the past three decade, Arctic summer sea ice retreat was unprecedented and sea surface temperatures were anomalously high in at least the last 1450 years.

1.1.4 Sea levels

> *The rate of sea level rise since the mid-19th century has been larger than the mean rate during the previous two millennia. Over the period 1901 to 2010, global mean sea level rose by* 0.19 m *Stocker, 2013.*

Sea level data indicate a transition in the late 19th to the early 20th century from relatively low mean rates of rise over the previous two millennia to higher rates of rise. It is likely that the rate of global mean sea level rise has continued to increase since the early 20th century.
It is very likely that the mean rate of global averaged sea level rise was 1.7 mm yr^{-1} between 1901 and 2010, 2.0 mm yr^{-1} between 1971 and 2010, and 3.2 mm yr^{-1} between 1993 and 2010. Tide-gauge and satellite altimeter data are consistent regarding the higher rate of the latter period.
Since the early 1970s, glacier mass loss and ocean thermal expansion from warming together explain about 75 % of the observed global mean sea level rise. Over the period 1993 to 2010, global mean sea level rise is, with high confidence, consistent with the sum of the observed contributions from ocean thermal expansion due to warming (1.1 mm yr^{-1}), from changes in glaciers (0.76 mm yr^{-1}), Greenland ice sheet (0.33 mm yr^{-1}), Antarctic ice sheet (0.27 mm yr^{-1}), and land water storage (0.38 mm yr^{-1}). The sum of these contributions is 2.8 mm yr^{-1}.

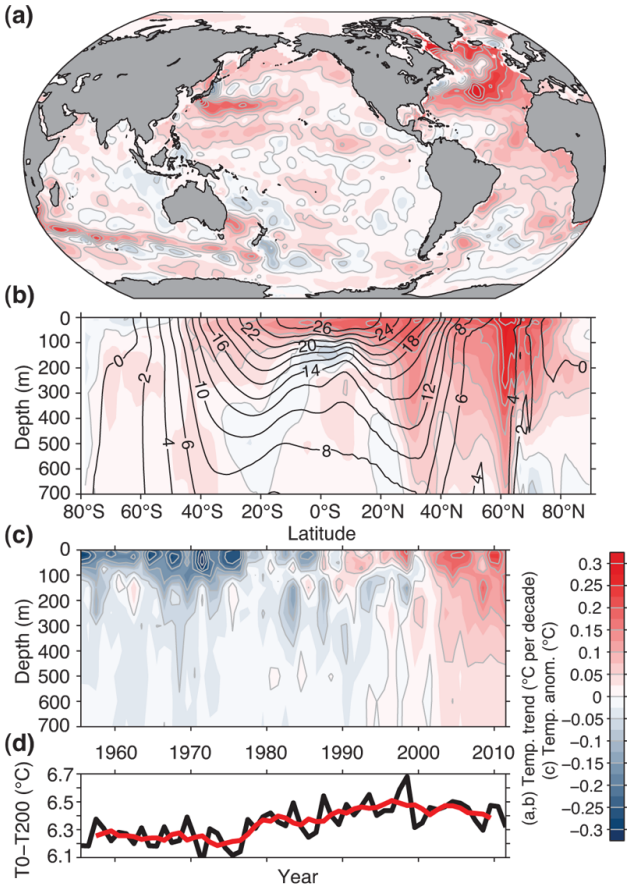

Figure 1.3: (a) Depth-averaged 0 to 700 m temperature trend for 1971–2010. (b) Zonally averaged temperature trends for 1971–2010 with zonally averaged mean temperature overplotted (black contours in degrees Celsius). (c) Globally averaged temperature anomaly relative to the 1971-2010 mean. (d) Globally averaged temperature difference between the ocean surface and 200 m depth (black: annual values, red: 5-year running mean). Source: Stocker (2013).

1.2 Causes of change

Human activities have changed and continue to change the Earth's surface and atmospheric composition. Some of these changes have a direct or indirect impact on the energy balance of the Earth and are thus drivers of climate change. Radiative forcing is a measure of the influence that a factor has in altering the balance of incoming and outgoing energy in the Earth-atmosphere system and it is expressed in $\mathrm{W\,m^{-2}}$. If RF is positive it leads to warming and, on the contrary, if RF is negative, it leads to a cooling. Human activities result in emissions of four principal greenhouse gases (GHG): carbon dioxide (CO_2), methane (CH_4), nitrous oxide (N_2O) and the halocarbons (a group of gases containing fluorine, chlorine and bromine). These gases accumulate in the atmosphere, causing concentrations to increase with time. The climate change responses are different for each GHG, because of their different warming influence on the global climate system due to their diverse radiative properties and lifetimes in the atmosphere. In order to compare the different influences, these may be expressed through a common metric based on the radiative forcing of carbon dioxide: the CO_2 equivalent emission[1].

[1]It is the amount of CO_2 emission that would cause the same time-integrated radiative forcing, over a given time horizon, as an emitted amount of a long-lived GHG or a mixture of GHGs.

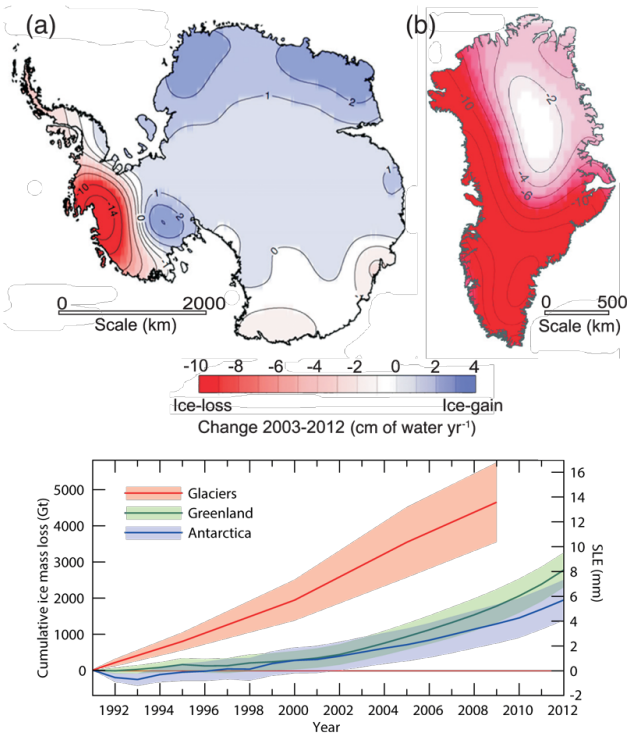

Figure 1.4: (Top) Distribution of ice loss determined from Gravity Recovery and Climate Experiment (GRACE) time-variable gravity for (a) Antarctica and (b) Greenland, shown in centimeters of water per year for the period 2003-2012. (Bottom) The assessment of the total loss of ice from glaciers and ice sheets in terms of mass (Gt) and sea level equivalent (mm) from 1992. The contribution from glaciers excludes those on the periphery of the ice sheets. Source: Stocker (2013).

Global GHG emissions have grown since pre-industrial times, with an increase of 70 % between 1970 and 2004. Carbon dioxide is the most important anthropogenic GHG because it is the most emitted anthropogenic GHG. Its annual emissions have grown between 1970 and 2004 by about 80 %, from 21 to 38 Gt, and represented 77 % of total anthropogenic GHG emissions in 2004, as shown in Fig. 1.5. The rate of growth of CO_2-eq emissions was much higher during the recent 10-year period of 1995-2004 (0.92 Gt of CO_2-eq per year) than during the previous period of 1970-1994 (0.43 Gt of CO_2-eq per year). Prior to the Industrial Era, that began in 1750, the concentration of atmospheric CO_2 fluctuated roughly between 180 ppm and 290 ppm for at least 2.1 Myr (Fig. 1.6) according to Solomon (2007). Between 1750 and 2011, the combustion of fossil fuels (coal, gas, oil and gas flaring) and the production of cement have released 375 ± 30 Pg ($1\,\text{Pg} = 1 \times 10^{15}$ g) of carbon dioxide to the atmosphere. Land use change activities, mainly deforestation, has released an additional 180 ± 80 Pg. This carbon released by human activities is called anthropogenic carbon.

Of the 555 ± 85 Pg of anthropogenic carbon emitted to the atmosphere from fossil fuel, cement and land use change, less than half have accumulated in the atmosphere (240 ± 10 Pg). The remaining anthropogenic carbon has been absorbed by the ocean and in terrestrial ecosystems, named "carbon sinks" (Fig. 1.7). The power and industry sectors combined dominate the current global CO_2 emissions, accounting for about 60 % of total CO_2 emitted. Carbon dioxide emissions in these sectors are generated by boilers and furnaces burning fossil fuels and are typically emitted from large exhaust stacks. These stacks can be described as large stationary sources, to distinguish them from mobile sources such as

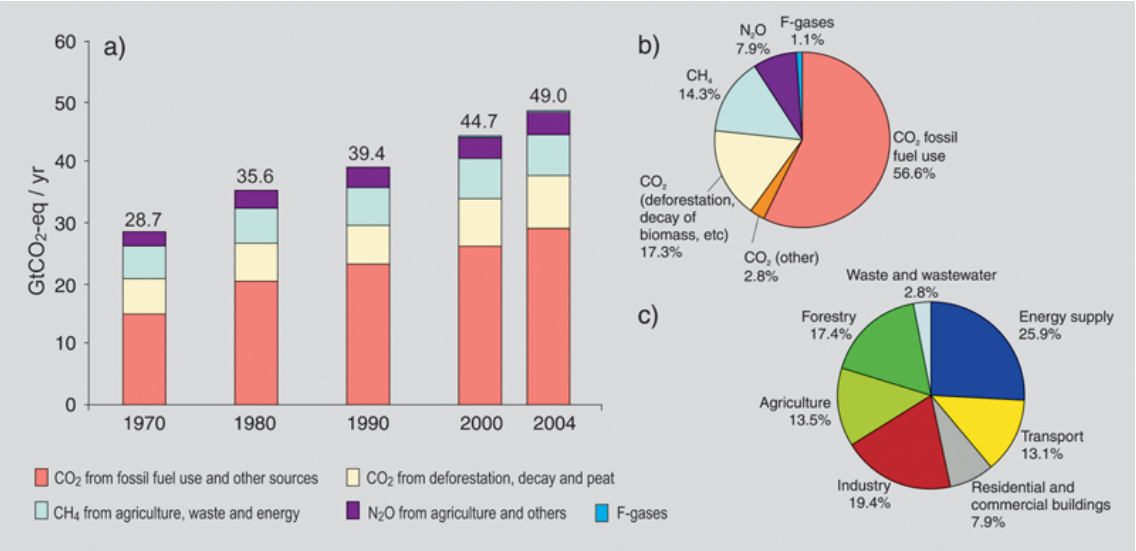

Figure 1.5: (a) Global annual emissions of anthropogenic GHGs from 1970 to 2004. (b) Share of different anthropogenic GHGs in total emissions in 2004 in terms of CO_2-eq. (c) Share of different sectors in total anthropogenic GHG emissions in 2004 in terms of CO_2-eq. Source: Solomon (2007).

those in the transport sector and from smaller stationary sources such as small heating boilers used in the residential sector. These last CO_2 emissions that account for the residential, commercial, transportation and agriculture sectors are not considered by Solomon (2007).

The emission sources considered include all large stationary sources (larger than 0.1 Mton of CO_2 per year) involving fossil fuel and biomass. These sources are present in three main areas: fuel combustion, industrial processes and natural-gas processing. The largest CO_2 emissions by far result from the oxidation of carbon when fossil fuels are burned. These emissions are associated with fossil fuel combustion in power plants, oil refineries and large industrial facilities (Tab. 1.1). The top 25 % of all large stationary CO_2 emission sources, listed in Tab. 1.2, account for over 85 % of the cumulative emissions from these types of sources. There are 330 sources with individual emissions above 10 MtonCO_2 per year. Of their cumulative emissions, 78 % come from power plants, 20 % from gas processing and the remainder from iron and steel plants.

Carbon dioxide not related to combustion is emitted from a variety of industrial production processes which transform materials chemically, physically or biologically. Such processes include: the use of fuels as feedstocks in petrochemical processes; the use of carbon as a reducing agent in the commercial production of metals from ores; the thermal decomposition (calcination) of limestone and dolomite in cement or lime production; the fermentation of biomass.

1.3 Carbon dioxide capture and storage

Carbon dioxide capture and storage (CCS) is a range of technologies that consisting of the separation of CO_2 from industrial and energy-related sources, transport to a storage location and long-term isolation from the atmosphere. It is considered as one of the options for reducing atmospheric emissions of CO_2 from human activities. CCS has the potential to reduce overall mitigation costs and increase flexibility in achieving greenhouse gas emission reductions.

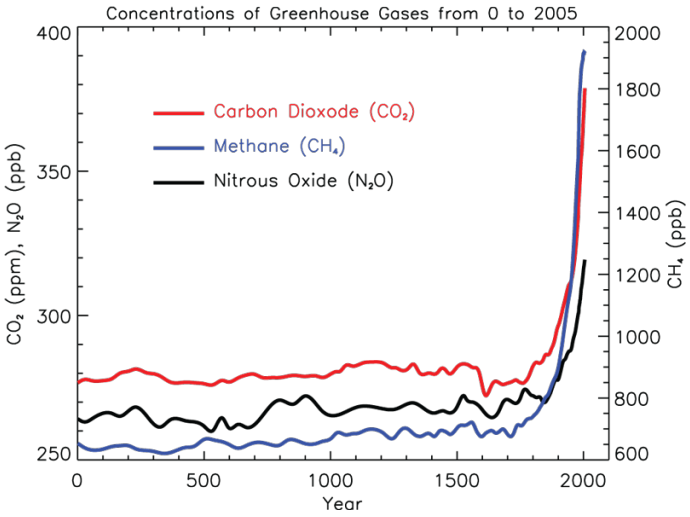

Figure 1.6: Atmospheric concentrations of important long-lived greenhouse gases over the last 2000 years. Increases since about 1750 are attributed to human activities in the industrial era (Solomon, 2007).

The CCS involves the use of different technologies, first to collect and concentrate the CO_2 produced in industrial and energy related sources, to transport it to a suitable storage location, and then to store it away from the atmosphere for a long period of time. Thus, CCS would allow fossil fuels to be used with low emissions of greenhouse gases. Application of CCS to biomass energy sources could result in the net removal of CO_2 from the atmosphere (often referred to as "negative emissions") by capturing and storing the atmospheric carbon dioxide taken up by the biomass.

The three main components of the CCS are: capture, transport and storage processes. The capture step involves separating CO_2 from other gaseous products. For fuel-burning processes such as those in power plants, separation technologies can be used to capture CO_2 after combustion or to decarbonize the fuel before combustion. The transport step may be required to carry captured CO_2 to a suitable storage site located at a distance from the CO_2 source. To facilitate both transport and storage, the captured CO_2 gas is typically compressed to a high density phase at the capture facility. Potential storage methods include injection into underground geological formations, injection into the deep ocean, or industrial fixation in inorganic carbonates. Some industrial processes also might utilize and store small amounts of captured CO_2 in manufactured products.

1.3.1 CO_2 capture technologies

Depending on the process, there are three main approaches to capture the CO_2 generated from a primary fossil fuel (coal, natural gas or oil), biomass, or mixtures of these fuels: post-combustion systems, pre-combustion systems and oxyfuel combustion systems, Fig. 1.8.

Post-combustion systems separate CO_2 from the flue gases produced by the combustion of the primary fuel with air. These systems normally use a liquid solvent to capture the fraction of CO_2 (typically $3 \div 15\,\%$ by volume) present in a flue gas stream in which the main constituent is nitrogen (from air). For a modern pulverized coal power plant or a natural gas combined cycle power plant, current post-combustion capture systems typically employ organic solvents such as monoethanolamine (MEA), according to Dean et al. (2011).

In pre-combustion systems process the primary fuel is fed in a reactor with steam and

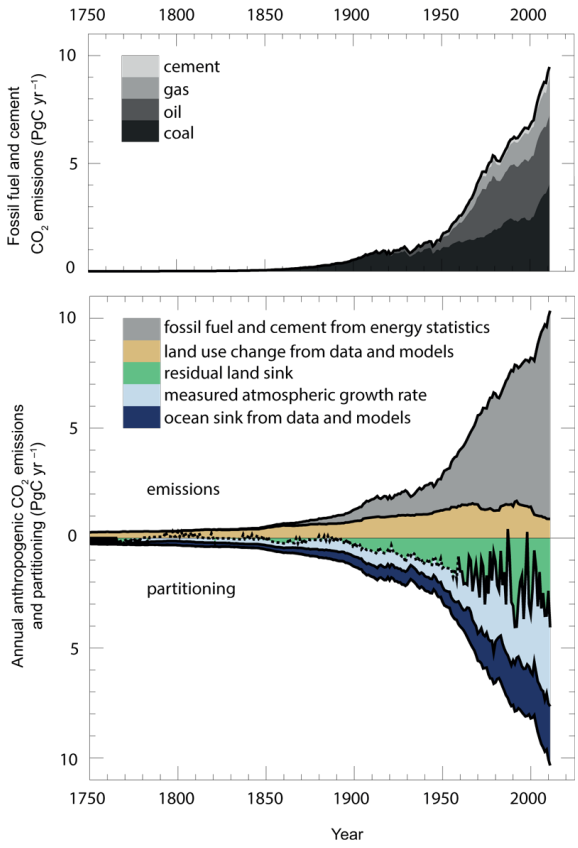

Figure 1.7: Annual anthropogenic CO2 emissions and their partitioning among the atmosphere, land and ocean ($\mathrm{Pg\,yr^{-1}}$) from 1750 to 2011. (Top) Fossil fuel and cement CO_2 emissions by category. (Bottom) Fossil fuel and cement CO_2 emissions as above. CO_2 emissions from net land use change, mainly deforestation, are based on land cover change data and estimated for 1750-1850. Source: Stocker, 2013.

air or oxygen and converted into syn-gas. Then hydrogen, together with CO_2, is produced by reacting the carbon monoxide with steam in a second reactor ("shift reactor"). The resulting mixture of H_2 and CO_2 can then be separated into a CO_2 gas stream, and a stream of hydrogen. If the CO_2 is captured, hydrogen is a carbon-free energy carrier that can be combusted to generate power and/or heat. Although the initial fuel conversion steps are more elaborate and costly than in post-combustion systems, the high concentrations of CO_2 produced by the shift reactor and the high pressures often encountered in these applications are more favourable for CO_2 separation. Pre-combustion would be used at power plants that employ integrated gasification combined cycle technology.

Oxyfuel combustion systems use oxygen instead of air for combustion of the primary fuel to produce a flue gas that is mainly water vapour and CO_2. This results in a flue gas with high CO_2 concentrations (larger than 80 % by volume). The water vapor is then removed by cooling and compressing the gas stream. Oxyfuel combustion requires the upstream separation of oxygen from air, with a purity of $95 \div 99$ % oxygen assumed in most current designs. Further treatment of the flue gas may be needed to remove air pollutants and non-condensed gases (such as nitrogen) from the flue gas before the CO_2 is sent to storage.

Table 1.1: Profile by process or industrial activity of worldwide large stationary CO_2 sources with emissions of more than 0.1 $MtCO_2$ per year. Source: Metz et al., 2005.

Process	Number of sources	Emissions $[MtCO_2\,yr^{-1}]$
Fossil fuels		
Power	4942	10539
Cement production	1175	932
Refineries	638	798
Iron and steel industry	269	646
Petrochemical industry	470	379
Oil and gas processing	NA	50
Other sources	90	33
Biomass		
Bioethanol and bioenergy	303	91
Total	7887	13466

1.3.2 Types of CO_2 capture processes

As shown in Fig. 1.9, the capturing technologies to obtain the CO_2 separation are: separation by sorbents or solvents, membranes separation and cryogenic distillation.

The separation with with sorbents/solvents is achieved by passing the CO_2-rich gas in intimate contact with a liquid absorbent or solid sorbent that is capable of capturing the CO_2. In the general case the sorbent loaded with the captured CO_2 is transported to a different vessel, where it releases the CO_2 (sorbent regeneration) after being heated or after a pressure decrease. Regenerated sorbent is sent back to the capture step establishing a cyclic process. A make-up flow of fresh sorbent is always required to compensate for the natural decay of activity and sorbent losses. One common problem of these CO_2 capture systems is that the flow of sorbent between the vessels is large because it has to match the large flow of CO_2 being processed in the power plant. Therefore, equipment sizes and the energy required for sorbent regeneration are large and tend to translate into an important efficiency penalty and added cost (Metz et al., 2005).

Membranes are specially manufactured materials that allow the selective permeation of a gas through them. The selectivity of the membrane to different gases is intimately related to the nature of the material, but the flow of gas through the membrane is usually driven by the pressure difference across the membrane. Therefore, high-pressure streams are usually preferred for membrane separation. Although membrane separation finds many current commercial applications in industry they have not yet been applied for the large scale and demanding conditions in terms of reliability and low-cost required for CO_2 capture systems, according to Metz et al. (2005).

Distillation of a liquefied gas stream and refrigerated separation requires a gas that can be made liquid by a series of compression, cooling and expansion steps. Once in liquid form, the components of the gas can be separated in a distillation column. It can be used to separate impurities from relatively high purity CO_2 streams, for example, from oxy-fuel combustion and for CO_2 removal from natural gas or synthesis gas that has undergone a shift conversion of CO to CO_2.

Table 1.2: Profile of worldwide large CO_2 stationary sources emitting more than 0.1 Mton CO_2 per year. Source: Metz et al., 2005.

Process	CO_2 concentration in gas stream % by vol.	Number of sources	Emissions ($MtonCO_2\,yr^{-1}$)	% of total CO_2 emissions	Cumulative total CO_2 emissions (%)	Average emissions per source ($MtonCO_2\,yr^{-1}$)
Power - CO_2 from fossil fuels						
Coal	12 to 15	2025	7984	59.69	59.69	3.94
Natural gas	3	985	759	5.68	65.37	0.77
Natural gas	7 to 10	743	752	5.62	70.99	1.01
Fuel oil	8	515	654	4.89	75.88	1.27
Fuel oil	3	593	326	2.43	78.31	0.55
Other fuels	NA	79	61	0.45	78.77	0.77
Hydrogen	NA	2	3	0.02	78.79	1.27
Natural-gas sweetening	NA	NA	50	0.37	79.16	
Cement production						
Combined	20	1175	932	6.97	86.13	0.79
Refineries	3 to 13	638	798	5.97	92.09	1.25
Iron and steel industry						
Integrated steel mills	15	180	630	4.71	96.81	3.50
Other processes	NA	89	16	0.12	96.92	0.17
Petrochemical industry						
Ethylene	12	240	258	1.93	98.85	1.08
Ammonia: process	100	194	113	0.84	99.70	0.58
Ammonia: fuel combustion	8	19	5	0.04	99.73	0.26
Ethylene oxide	100	17	3	0.02	99.75	0.15
CO_2 from biomass						
Bioenergy	3 to 8	213	73			0.34
Fermentation	100	90	17.6			0.2

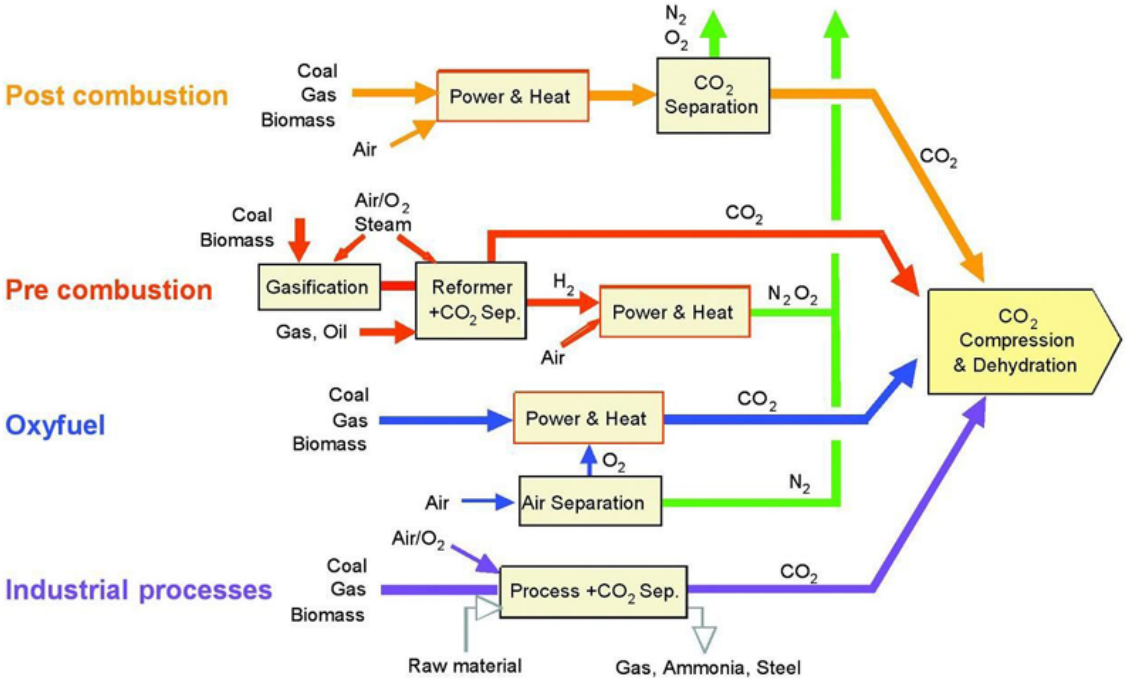

Figure 1.8: CO_2 capture systems. Source: Metz et al., 2005.

1.3.3 Transport

Except when plants are located directly above a geological storage site, captured CO_2 must be transported from the point of capture to a storage site. Gaseous CO_2 is typically compressed to a pressure above 8 MPa in order to avoid two-phase flow regimes and increase the density of the CO_2, thereby making it easier and less costly to transport. CO_2 can also be transported as a liquid in ships, road or rail tankers that carry CO_2 in insulated tanks at a temperature well below ambient, and at much lower pressures. Pipeline transport operate in the "dense phase" mode (supercritical phase), at ambient temperature and high pressure. In most of these pipelines, the flow is driven by compressors at the upstream end, although some pipelines have intermediate compressor stations.

In some situations or locations, transport of CO_2 by ship may be economically more attractive, particularly when the CO_2 has to be moved over large distances or overseas. Carbon dioxide can be transported by ship in the same way of liquefied petroleum gases (typically at 0.7 MPa).

Road and rail tankers also are technically feasible options, transporting CO_2 at a temperature of $-20\,°C$ and at 2 MPa pressure (Metz et al., 2005).

1.3.4 Storage

Carbon dioxide storage consists of three main storage technologies: geological storage, ocean storage and mineral sequestration.

Underground accumulation of carbon dioxide is a geological phenomenon, with natural trapping of CO_2 in underground reservoirs. While there are differences between natural accumulations and engineered storage, injecting CO_2 into deep geological formations at carefully selected sites can store it underground for long periods of time: it is considered likely that 99 % or more of the injected CO_2 will be retained for 1000 years. Depleted oil and gas reservoirs, possibly coal formations and particularly saline formations, can be used for the aim. To geologically store CO_2, it must first be compressed, usually to a dense

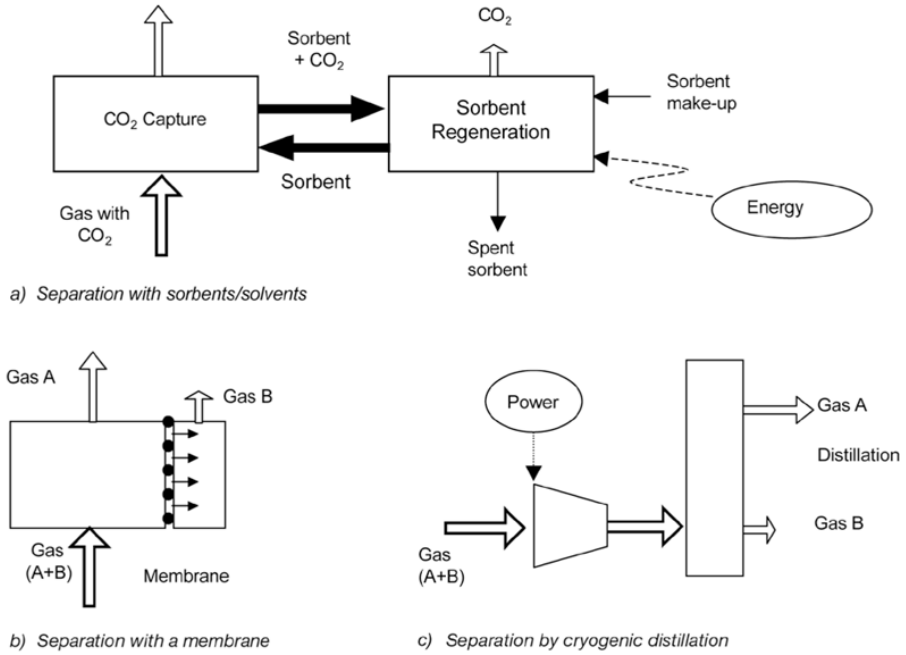

Figure 1.9: Schemes of the main separation processes relevant for CO_2 capture: (a) separation with sorbents or solvents, (b) separation with membrane, (c) separation by cryogenic distillation. Source: Metz et al. (2005).

fluid state known as "supercritical". Depending on the rate that temperature increases with depth (the geothermal gradient), the density of CO_2 increases with depth, until at about 800 m or higher, where the injected CO_2 is in a dense supercritical state. Carbon dioxide can remain trapped underground by virtue of a number of mechanisms, such as: trapping below an impermeable, confining layer (caprock); retention as an immobile phase trapped in the pore spaces of the storage formation; dissolution in-situ formation fluids; adsorption onto organic matter in coal and shale. Additionally, it may be trapped by reacting with the minerals in the storage formation and caprock to produce carbonate minerals.

Further, captured CO_2 could be injected into the ocean at great depth, where most of it would remain isolated from the atmosphere for centuries. CO_2 can be placed on a ship, injected directly into the ocean, or deposited on the sea floor. CO_2 loaded on ships could either be dispersed from a towed pipe or transported to fixed platforms feeding a CO_2 lake on the sea floor. Such CO_2 lakes must be deeper than 3 km where CO_2 is denser than sea water. Numerical models of the ocean indicate that placing CO_2 in the deep ocean would isolate most of the CO_2 from the atmosphere for several centuries, but over longer times the ocean and atmosphere would equilibrate.

Putting CO_2 directly into the deep ocean means that the chemical environment of the deep ocean would be altered immediately and change in ocean chemistry would be greater proximate to the release location. For ocean storage of CO_2, issues remain regarding environmental consequences, public acceptance, implications of existing laws, safeguards and practices that would need to be developed, and gaps in current understanding of ocean CO_2 storage.

Mineral carbonation is based on the reaction of CO_2 with metal oxides producing insoluble carbonates, calcium and magnesium are retained to be the most attractive metals. Mineral carbonation refers to the fixation of CO_2 using alkaline and alkaline-earth oxides, such as magnesium oxide (MgO) and calcium oxide (CaO), which are present in naturally occurring silicate rocks. Chemical reactions between these materials and CO_2 produces

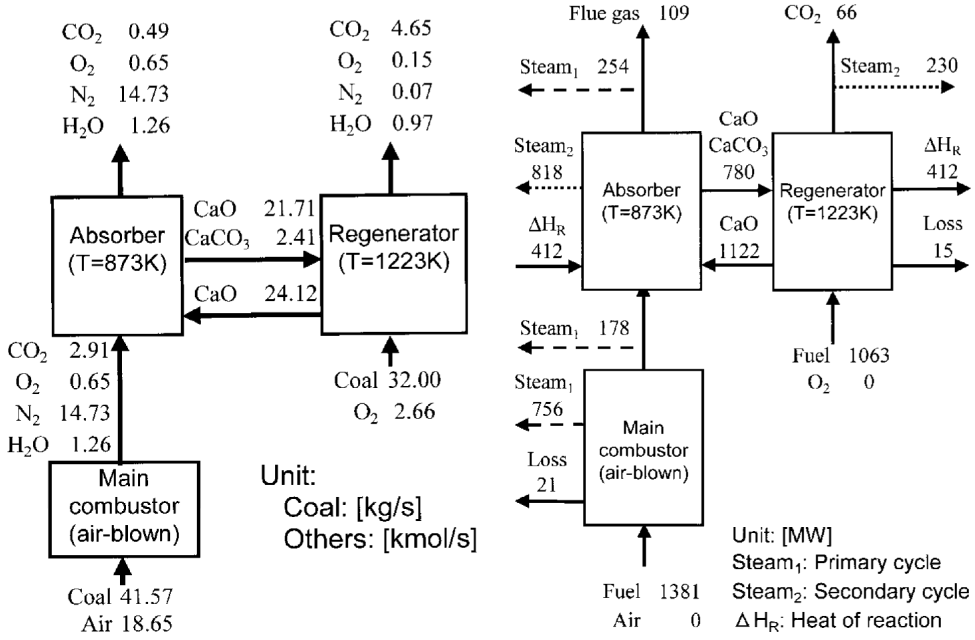

(a) *Material balance.* **(b)** *Heat balance.*

Figure 1.10: Proposed carbon oxide looping cycle process by Shimizu et al. (1999).

compounds such as magnesium carbonate ($MgCO_3$) and calcium carbonate ($CaCO_3$, commonly known as limestone). This process produces silica and carbonates that are stable over long time scales and can therefore be disposed of in areas such as silicate mines, or re-used for construction purposes.
Industrial uses of CO_2 include chemical and biological processes where CO_2 is a reactant, such as those used in urea and methanol production, as well as various technological applications that use CO_2 directly, for example in the horticulture industry, refrigeration, food packaging, welding, beverages and fire extinguishers.

1.4 CO_2 capture with calcium oxide as solid sorbent: state of the art

Emerging problems with CCS include the financial cost and energy penalty associated with the CO_2 capture step, i.e. the collection of a pure stream of CO_2 for sequestration. Currently, a technology close to market for this step is post-combustion "scrubbing" of flue gases using amine-based sorbents, such as monoethanolamine (MEA). However, there are several problems associated with this technology, such as degradation of sorbents at higher temperatures, reactions with compounds present in the flue gas such as oxygen ($\sim 2\,\mathrm{vol}\,\%$) and sulphur dioxide, and costs. Additional drawbacks of this technology are due to the corrosive nature of MEA and its degradation products, which limits the wt.% of MEA in a typical power plant (Dean et al., 2011).

The 2$^{\mathrm{nd}}$ generation CO_2 sequestration technologies with alkaline earth metal-based sorbents is potentially more efficient if compared with the traditional scrubbing with amines-based solvents (Blamey et al., 2010; MacKenzie et al., 2007). For this reason, the integration of the Ca-looping process into several industrial activities has been proposed in literature, starting from Shimizu et al. (1999), who suggested two coupled fluidized bed reactors using calcium oxide as solid sorbent. Afterwards, several Ca-looping applications for the CO_2 capture have been proposed, namely: the CO_2 sequestration from flue gases

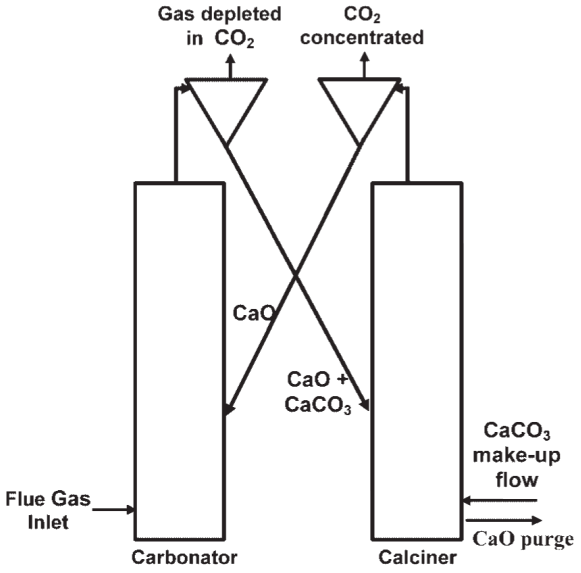

Figure 1.11: Schematics of the carbonation-calcination loop Grasa et al., 2009.

in power generation and cement manufacture plants (Dean et al., 2011); the in-situ CO_2 capture in gasification processes for the hydrogen production from biomass (Florin and Harris, 2008); the in-situ CO_2 capture in the sorption enhanced methane steam reforming (Dean et al., 2011; Harrison, 2008) and in the sorption enhanced water gas shift (Muller et al., 2009; Ramkumar and Fan, 2010)

Among natural solid sorbents, a promising material is calcium oxide, because of its high theoretical sorption capacity, namely $0.78\,g(CO_2)\,g(CaO)^{-1}$, its fast reaction kinetics and its precursor abundance ($CaCO_3$) in nature (Dean et al., 2011; Blamey et al., 2010; Shimizu et al., 1999). Specifically, the CO_2 capture and regeneration steps are based on the reversibility of the CaO carbonation reaction and the $CaCO_3$ calcination one. Both the reactions are non-catalytic gas-solid reactions where the solid reactant undergoes to a micro-structure evolution as the reaction progresses.

The CaO-based looping cycle for the CO_2 sequestration was originally proposed by Shimizu et al. (1999) and uses CaO as a regenerable sorbent to capture CO_2 from combustion flue gases, as shown in Fig. 1.10. Both pre-combustion and post-combustion applications of the calcium looping cycle follow similar principles, in that a calcium oxide sorbent is repeatedly cycled between two reactors, as shown in Figs. 1.11 and 1.12. In one vessel (the carbonator) carbonation of CaO occurs, stripping the flue gas of its CO_2. The $CaCO_3$ formed is then fed to another vessel where calcination occurs (the calciner) and the CaO formed is passed back to the carbonator leaving a pure stream of CO_2 suitable for sequestration. This cycle is continued and spent (unreactive) sorbent is continuously replaced by fresh (reactive) sorbent. The carbonation can either occur in-situ (i.e. within the gasifier/combustor) or ex-situ (i.e. on the product gases), with the former resulting in a reduction in plant complexity at the expense of a higher rate of degradation of sorbent due to contact with ash, sulphur and other impurities in the fuel burned. Heat from the exothermic carbonation of lime can be used to run a steam cycle, making up for some of the energy losses. The conditions in the calciner must be a compromise between the increased rate of reaction obtained at higher temperatures and the reduced rate of degradation of sorbent at lower temperatures. The conditions in the carbonator must strike a balance between the increased equilibrium conversion obtained at lower temperatures and the increased rate of reaction at higher temperatures.

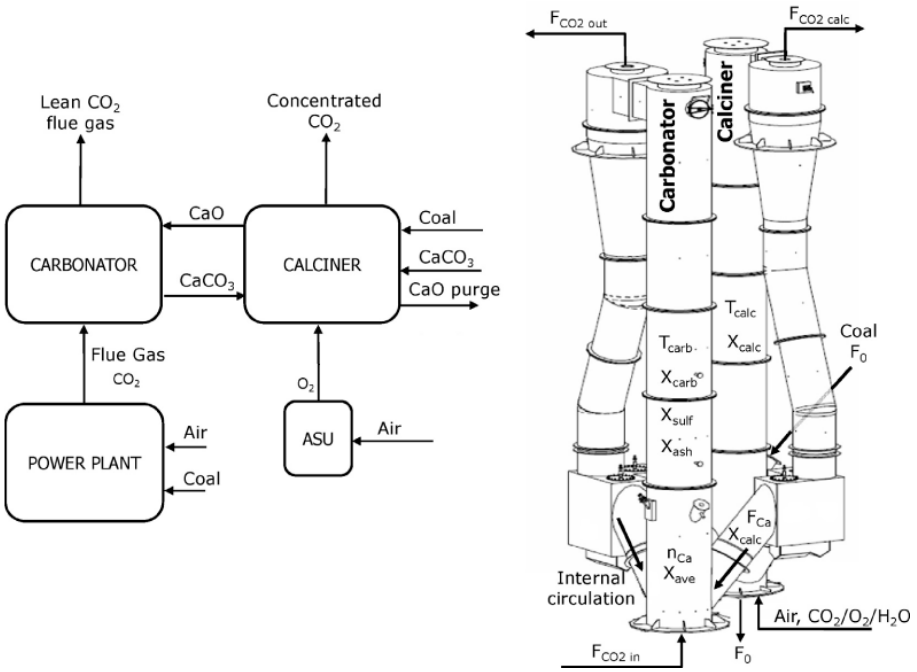

Figure 1.12: General scheme of a power plant incorporating a Ca-looping system consisting in dual interconnected circulating fluidized bed reactors for calcium oxide looping cycle (Arias et al., 2013).

According to Blamey et al. (2010), Dean et al. (2011), Fennel and Anthony (2015), and Florin and Harris (2008) the main relevant drawbacks of CaO performances can be listed as follow

1. CaO loses its CO_2 capture capacity after a number of carbonation and calcination cycles because of the high temperature sintering processes (Abanades and Alvarez, 2003; Sun et al., 2007);

2. the completely calcined precursor can undergo significant attrition in a fluidized bed (Fennell et al., 2007);

3. limestone at high temperature may be deactivated because of competitive side reactions with water vapor and sulfur dioxide (Blamey et al., 2010; Stanmore and Gilot, 2005).

However, sintering is the most widely recognized cause of this sorbent shortcoming (Stanmore and Gilot, 2005; Dean et al., 2011; Blamey et al., 2010; Florin and Harris, 2008; Sun et al., 2007). In fact, because of the reversibility of the CaO carbonation reaction, the material can be completely regenerated with a second calcination step and another capture step can be performed. However, after few cycles of capture and regeneration the sorbent performances radically decay, reducing the sorbent sorption capacity (Abanades and Alvarez, 2003; Barker, 1973; Grasa et al., 2009; Grasa and Abanades, 2006). The reasons of such behavior are ascribed to the high temperature calcination reaction conditions, that favor sintering mechanisms (Alvarez, Carlos Abanades, and Abanades, 2005; Sun et al., 2007; Zhu, Wu, and Wang, 2011), especially if the calcination is performed into an atmosphere with carbon dioxide (Borgwardt, 1989b). Specifically, sintering processes affect the sorbent structural properties, by reducing the material porosity and specific surface area (Borgwardt, 1989b; Sun et al., 2007; Zhu, Wu, and Wang, 2011), and increasing its the mean pore radius and average crystallite size (Fuertes et al., 1991; Zhu, Wu, and

Wang, 2011). Sintering modifies the sorbent PSD reducing the amount of small pores increasing the larger one, leading to a loss in specific surface area and porosity, as reported by Sun et al. (2007) and Zhu, Wu, and Wang (2011). A similar observation was reported by Abanades and Alvarez (2003) who noticed the increasing of large pores and a parallel decay of the smaller ones using SEM analysis.

During the high temperature calcite ($CaCO_3$) decomposition, the reaction operative conditions (in terms of temperature, pressure, residence time and atmosphere composition) do not influenced only the calcination reaction kinetics. In fact, during the $CaCO_3$ decomposition the calcination reaction and the high temperature sintering mechanisms are simultaneous phenomena that contribute to establish the final sorbent micro-structure (Borgwardt, 1989b; Ewing, Beruto, and Searcy, 1979; Borgwardt, 1989a; Sun et al., 2007). Therefore, sintering processes are undesired phenomena that should be minimized during the thermal activation because they irreversibly decrease the sorbent performance during the CO_2 capture step in terms of reaction kinetics and maximum CO_2 capture uptake.

For these reasons, sintering effects on the CaO micro-structure during the precursor activation and regeneration step are one of the main topics of this research project. In fact, sintering refers to a collection of high temperature processes that are difficult to investigate especially during the calcite decomposition, where sintering, pore generation and CO_2 interaction with the nascent pore structure are simultaneous phenomena. In addition, the interaction mechanisms between sintering phenomena and pore generation during the $CaCO_3$ activation are still poorly studied or unknown.

On the other hand, the design of the carbonator requires a fundamental understanding of the carbonation reaction rates of the CaO particles that are fed to the carbonator from the calciner. High reaction rates between the CO_2 in the flue gas and the sorbent particles are necessary to design absorbers of a reasonable size. Fresh calcined lime is known to be a very reactive solid in the carbonation reaction. However, the average sorbent particle must undergo many carbonation-calcination cycles as a result of which sorbent capture capacity decreases rapidly. After a fast chemically controlled initial reaction stage, a second slower reaction stage controlled by the diffusion in the product layer ($CaCO_3$) takes place. It has also been observed that the transition between the fast and slow regimes takes place quite suddenly at a given level of conversion, and that this level of conversion decreases as the number of carbonation/calcination cycles increases (Grasa et al., 2009).

Since carbonation reaction does not present a trivial kinetics, in order to estimate the carbonator size a deep understanding on the kinetics of the carbonation reaction is needed. Several models have been proposed to describe the carbonation kinetics between CaO and CO_2. These models can be classified into several types: apparent models (Lee, 2004), shrinking core models (Szekely and Evans, 1971), random pore models (RPM) (Bhatia and Perlmutter, 1980; Bhatia, S.K. and Perlmutter, 1981; Bhatia and Perlmutter, 1981; Bhatia and Perlmutter, 1983a; Bhatia and Perlmutter, 1983b; Bhatia, 1985; Sotirchos and Yu, 1985; Grasa et al., 2009) and grain models (GM) (Yu et al., 2012; Liu et al., 2012; Sotirchos and Yu, 1988). RPM and GM are especially relevant for the study of the carbonation reaction. The RPM model correlates the carbonation rate with the internal pore structure, while the GM model assumes that the sorbent is composed of small grains that are dispersed in gas, and each grain is converted according to the shrinking core model.

Chapter 2

Calcium Oxide as a CO_2-capture Solid Sorbent

The carbonation and calcination reactions of alkaline earth metal based CO_2 sorbents is a potential and attractive technology to reduce the anthropogenic carbon dioxide emissions, as a mitigation strategy to reduce the climate change effects. Among the CO_2 capture materials, calcium oxide is one of the most promising solid sorbents, where its precursor is the non-porous calcium carbonate. This chapter presents the main features of the $CaCO_3$ calcination and CaO carbonation reaction in terms of thermodynamics conditions, sorbent micro-textural properties generation and evolution, sintering mechanisms and pore closure during the CO_2 capture step. In addition, the material sorbent precursor properties and the different characterization techniques for the reaction kinetics and the sorbent micro-structure investigation will be presented.

2.1 Introduction

Among the Ca-based solid sorbents for the CO_2 capture, calcium oxide is the most promising candidate to be applied for the high temperature sequestration processes (Shimizu et al., 1999). Specifically, CaO is one of the most interesting *natural* material because of its high reactive sorption capacity for CO_2, $0.78\,\mathrm{g(CO_2)\,g(CaO)^{-1}}$, its low cost and abundance precursor ($CaCO_3$) in nature (Feng, An, and Tan, 2007) and its high reaction kinetics (Biasin et al., 2015). Specifically, the CaO looping cycle is based on the reversibility of the carbonation and calcination reactions (Dean et al., 2011; Blamey et al., 2010; Shimizu et al., 1999),

$$\mathrm{CaO}_{(s)} + \mathrm{CO}_{2(g)} = \mathrm{CaCO}_{3(s)} \qquad \Delta H_r^\circ = -178\,\mathrm{kJ\,mol^{-1}}, \tag{2.1}$$

where the calcium oxide sorbent is repeatedly cycled between two reactors (the carbonator and the calciner respectively), as formally presented for the first time by Shimizu et al. (1999) for post-combustion CO_2-capture applications. Both the calcination and the carbonation steps are based on non-catalytic gas solid reactions (Barker, 1973; Bhatia and Perlmutter, 1983a), where the solid reactant undergoes to a micro-textural evolution of its internal structure during the reaction influencing the reaction kinetics itself.
The carbonation reaction performances strongly depends on the initial sorbent micro-textural properties, namely the reaction kinetics and the maximum CO_2 uptake (Bhatia and Perlmutter, 1983a; Biasin et al., 2015; Sun et al., 2007). These properties are the sorbent porosity, specific surface area and mean pore radius, that are completely determined by the sorbent pore size distribution (PSD) generated during the previous thermal activation step (Barker, 1973; Bhatia and Perlmutter, 1983a; Borgwardt, 1989b; Rodriguez-Navarro et al., 2009; Beruto, Barco, and Searcy, 1983; Glasson, 1958).

Table 2.1: Chemical, physical and thermodynamic proprieties of calcium oxide, carbon dioxide and calcium carbonate from Haynes, 2014. All proprieties are estimated at 25 °C and 1 bar.

Property	CaO (s)	CO_2 (g)	$CaCO_3$ (s)
IUPAC name	calcium oxide	carbon dioxide	calcium carbonate
CAS number	1305-78-8	124-38-9	471-34-1
Appearance	white/pale yellow powder	colorless gas	white powder
M_i $\left[\mathrm{g\,mol^{-1}}\right]$	56.077	44.01	100.087
ρ_s $\left[\mathrm{g\,cm^{-3}}\right]$	3.34	-	2.71
MP[1] [°C]	2898	-78.5	1330
ΔH_f° $\left[\mathrm{kJ\,mol^{-1}}\right]$	-634.9	-393.5	-1207.6
ΔG_f° $\left[\mathrm{kJ\,mol^{-1}}\right]$	-603.3	-394.4	-1129.1
S° $\left[\mathrm{J\,mol^{-1}\,K^{-1}}\right]$	38.1	213.8	91.7
Cp° $\left[\mathrm{J\,mol^{-1}\,K^{-1}}\right]$	42	37.1	83.5

2.2 Thermodynamics of the calcination and carbonation reactions

The carbonation (calcination) reaction is an equilibrium reaction that can be represented by means of the chemical relationship in Eq. (2.1). Accordingly, the carbonation reaction is exothermic, while the backward step (the calcination reaction) is endothermic. Both the reactions are heterogeneous where a solid reactant, a solid product and a gas specie (reactant or product) are involved.
Thermodynamics can predict the best operative conditions at which the gas-solid reactions between CaO and CO_2 and the $CaCO_3$ thermal decomposition take place. Specifically, when heterogeneous reaction are considered, the chemical reaction equilibrium is usually performed following the approach described in Appendix A, namely

$$K_{\mathrm{eq}}(T) = p_{\mathrm{CO_2,\,eq.}}, \tag{2.2}$$

where $K_{\mathrm{eq}}(T)$ is the equilibrium constant associated with Eq. (2.1), T is the absolute temperature (in K) and $p_{\mathrm{CO_2,\,eq.}}$ is the equilibrium partial pressure of carbon dioxide expressed in bar. Therefore, using the thermodynamics coefficients (enthalpies and entropies standard of formation and gas heat capacities) of Knacke, Kubaschewski, and Hesselmann (1991), the predicted equilibrium partial pressure over temperature is showed in Fig. 2.1. Accordingly, calcium carbonate decomposes to form CaO and CO_2 when the carbon dioxide partial pressure is lower than the equilibrium partial pressure; on the contrary, calcium oxide reacts with carbon dioxide to form calcium carbonate when the CO_2 partial pressure is greater than that of the equilibrium.
Several literature contributors investigated the equilibrium conditions of Eq. (2.1), namely the equilibrium partial pressure ($p_{\mathrm{CO_2},\,eq.}$) over temperature, such as Baker (1962), Criado (1977), Morales (1978) and Criado et al. (1995). Instead, others contributors proposed other equilibrium models to predict the CO_2 equilibrium partial pressure, like García-Labiano et al. (2002), who used the thermochemical data of Barin (1993), and Silcox, Kramlich, and Pershing (1989). In these works the equilibrium vapor pressure of CO_2 was calculated as a function of the system temperature, according to Eq. (2.2). Specifically, in

[1] melting point.

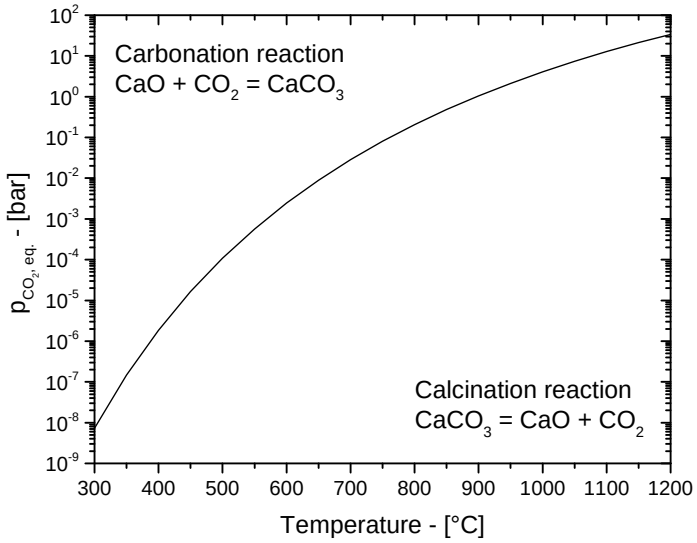

Figure 2.1: The equilibrium partial pressure of CO_2 of the carbonation and calcination reactions. Thermodynamics coefficients refers to Knacke, Kubaschewski, and Hesselmann (1991).

order to compare the different CO_2 partial pressure over temperature models (of these different contributors), a linear relationship can be obtained by plotting $\log\left(p_{CO_2,\,eq}\right)$ against $10^3/T$, as showed in Fig. 2.2. Such profiles are in good agreement between each others especially at high temperatures, namely above 1000 K. Conversely, at low temperatures these equilibrium models become less accurate, as showed in Fig. 2.2. However, Fig. 2.2 suggests a good agreement between models roughly for temperatures above 1000 K. Additionally, a useful equilibrium estimation is the reaction temperature at which the CO_2 equilibrium partial pressure becomes 1 atm, namely 898 °C using the thermochemical properties of Knacke, Kubaschewski, and Hesselmann (1991); 895 °C using the thermochemical data of Barin (1993); 897 °C according to the model proposed by Silcox, Kramlich, and Pershing (1989); 900 °C for the case of Baker (1962) equilibrium equation; 903 °C using the proposed equilibrium relationship of Criado (1977). Such temperatures clearly indicate that CO_2 equilibrium partial pressure is approximately equal to the atmospheric pressure at about 900 °C and, precisely, in a temperature range of about $895 \div 903$ °C. Clearly, this result suggests that above 900 °C the carbonation reaction cannot be performed at pressures below 1 atm because of the chemical equilibrium that shifts the reaction of Eq. (2.1) towards to the reactants. Only the increase of the reactor total pressure can re-establish the favorable condition for the carbonation reaction, although such operative conditions are not of interest from an industrial point of view.

2.3 The calcium carbonate thermal activation: the calcination reaction

The CaO micro-textural properties are generated during the high temperature ($700 \div 900$ °C) activation step where the non-porous calcium carbonate decomposes to calcium oxide and carbon dioxide according to the stoichiometry of Eq. (2.1) (Abanades and Alvarez, 2003; Sun et al., 2007; Zhu, Wu, and Wang, 2011). The CO_2 release and the different molar volume between the calcium carbonate and calcium oxide contributes to generate the sorbent internal pore matrix (Barker, 1973), as shown in Fig. 2.3. According

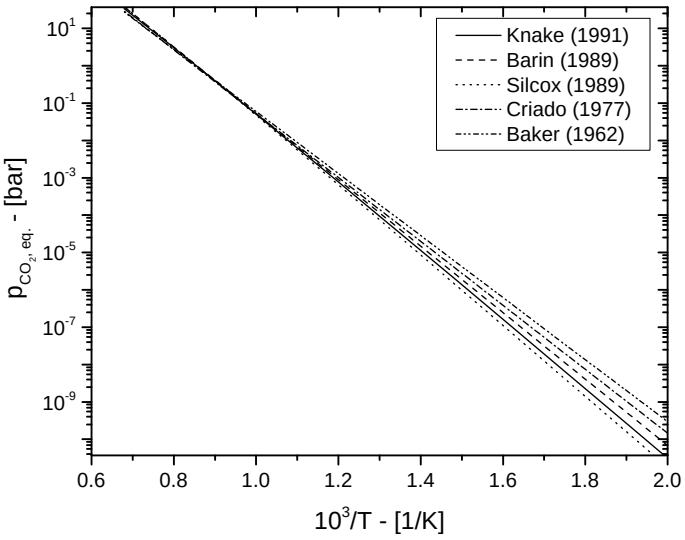

Figure 2.2: Comparison of the CO_2 equilibrium partial pressure proposed by different literature contributors: Knacke, Kubaschewski, and Hesselmann (1991), Barin (1993), Silcox, Kramlich, and Pershing (1989), Criado (1977) and Baker (1962).

to García-Labiano et al. (2002), the porosity evolution profile during the calcite decomposition should be linear over the calcination reaction conversion (in agreement with the non-catalytic nature of the $CaCO_3$ carbonation reaction):

$$\varepsilon = \varepsilon_0^{\mathrm{CaCO_3}} + (1 - Z_{\mathrm{calc}})(1 - \varepsilon_0^{\mathrm{CaCO_3}})\, X_{\mathrm{CaCO_3}} \tag{2.3}$$

where, according to Bhatia and Perlmutter (1980), the Z_i parameter is defined as

$$Z_i = \frac{\text{molar volume of the solid phase after the reaction } i}{\text{molar volume of the solid phase before the reaction } i}. \tag{2.4}$$

For the case of the $CaCO_3$ calcination reaction, Z_{calc} is the calcium oxide over the calcium carbonate molar volume, that is 0.455, according to the CaO and $CaCO_3$ properties listed in Tab. 2.1 and the demonstration of this parameter refers to Appendix B. In Eq. (2.3) $\varepsilon_0^{\mathrm{CaCO_3}}$ is the initial (eventual) porosity of the unreacted $CaCO_3$. By assuming an initial sorbent precursor ($CaCO_3$) porosity equal to zero, Eq. (2.3) predicts the well-known CaO final theoretical porosity of 0.545. The theoretical linear trend proposed by Eq. (2.3) was observed only by Beruto, Barco, and Searcy (1983) during the calcite decomposition at 686 °C under vacuum conditions. Because of the non-catalytic gas-solid nature of the calcination reaction, the final sorbent micro-textural properties are strongly influenced by the reaction conditions, namely the precursor particle size Borgwardt, Roache, and Bruce (1986) and Fuertes et al. (1991), the calcination reaction temperature and pressure (Ewing, Beruto, and Searcy, 1979), the reactor atmosphere composition (Borgwardt, 1989b; Borgwardt, 1989a) and the sorbent residence time (Borgwardt, 1989b). However, these operative conditions do not influenced only the calcination reaction kinetics. In fact, during the CaO decomposition the calcination reaction and the high temperature sintering mechanisms are simultaneous phenomena that contribute to establish the final sorbent micro-structure (Borgwardt, 1989b; Ewing, Beruto, and Searcy, 1979; Borgwardt, 1989a; Sun et al., 2007), as schematically represented in Fig. 2.3. Due to the high temperature conditions of the calcination reaction, sintering processes affect the sorbent micro-textural

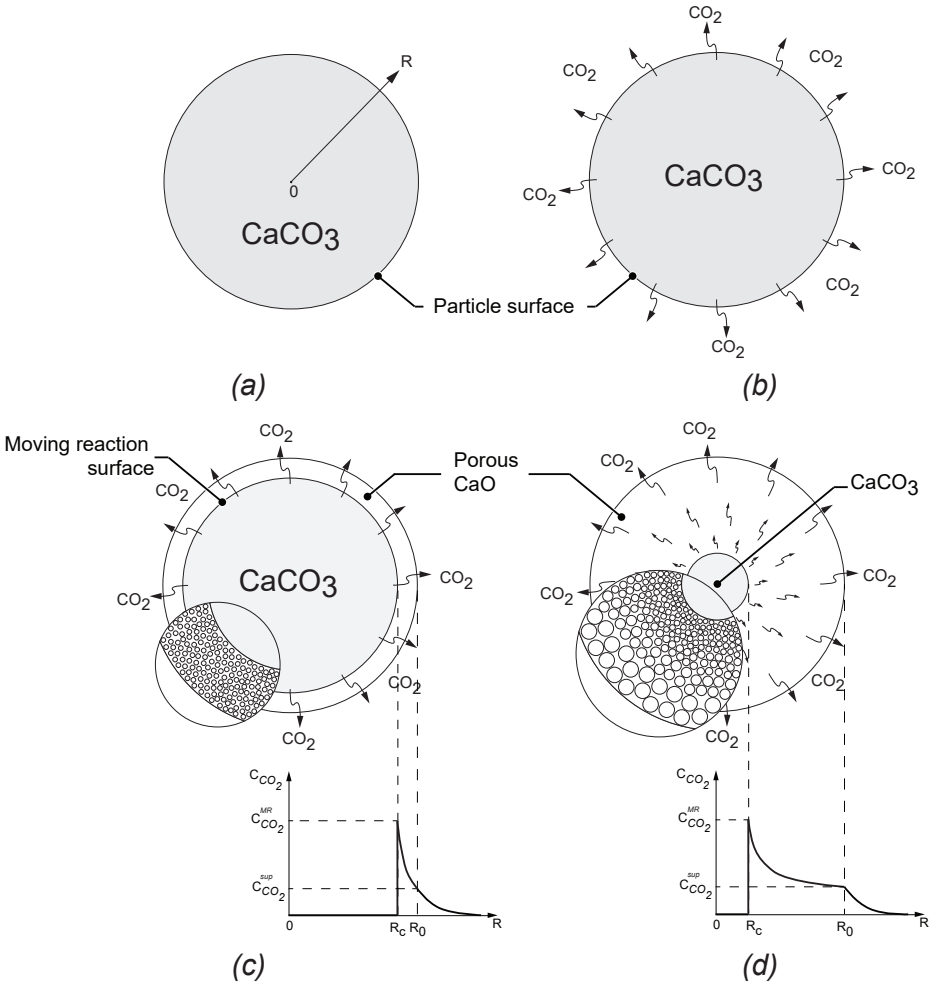

Figure 2.3: Schematic representation of thermal decomposition steps of a non-porous $CaCO_3$ particle (a), where the CO_2 release (b) and the different molar volume between $CaCO_3$ and CaO generate the sorbent micro-structure (c). Sintering phenomena affects the final sorbent micro-structure and are accelerated by the presence of CO_2 (d). For the sake of clarity, pores are ideally represented as circles, $C^{MR}_{CO_2}$ is the CO_2 concentration at the moving reaction surface and $C^{sup}_{CO_2}$ is the CO_2 concentration at the particle surface.

properties reducing the particle porosity and the specific surface area and increasing the mean pore radius (Benedetti et al., 2017; Fuertes et al., 1991; Borgwardt, 1989a; Maya, Chejne, and Bhatia, 2017a; Zhu, Wu, and Wang, 2011). Therefore, sintering processes are undesired phenomena that should be minimized during the thermal activation because they irreversibly decrease the sorbent performance during the CO_2 capture step.
Sintering refers to a collection of high temperature processes that are difficult to investigate especially during the calcite decomposition. For these reasons, the interaction mechanisms between sintering phenomena and pore generation during the $CaCO_3$ activation are still poorly studied or unknown.

2.4 Sintering processes during the calcination reaction

According to Coble (1961a), Coble (1961b), and Borgwardt (1989b) sintering process is conceptually divided into four different stages

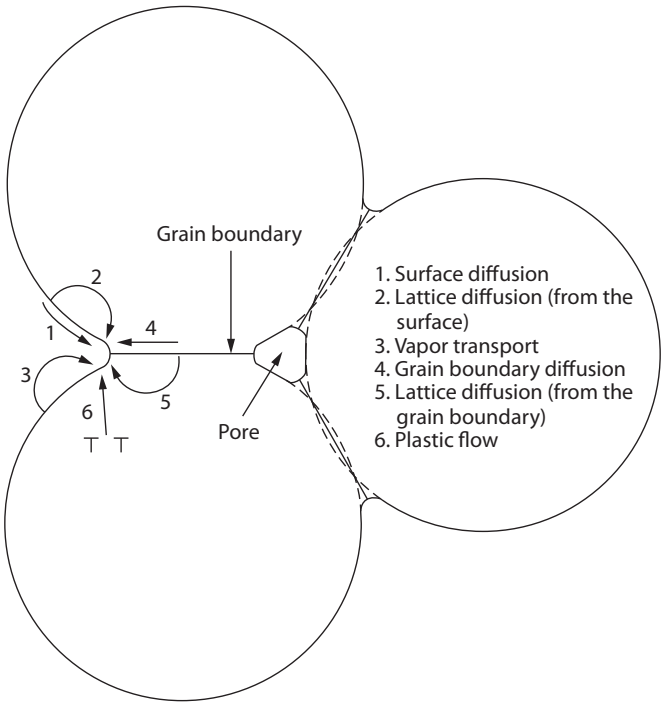

Figure 2.4: Six distinct mechanisms can contribute to the sintering of a consolidated mass of crystalline particles: (1) surface diffusion, (2) lattice diffusion from the surface, (3) vapor transport, (4) grain boundary diffusion, (5) lattice diffusion from the grain boundary, and (6) plastic flow. Only mechanisms 4-–6 lead to densification, but all cause the necks to grow and so influence the rate of densification. Source Rahaman (2007).

1. *the induction period:* in this step contact formation phenomena occur because of weak atomic forces at particle contacts hold the particles together prior to sintering. During this step, the surface area is reduced and an increase in mean pore size is observed, without an appreciable change of porosity the total porosity.

2. *the initial stage:* is associated to the neck growth between the contact points produced during the previous step. Neck growth occurs though mechanisms of diffusion, vapor transport, plastic flow, or viscous flow (Fig. 2.4). The large initial differences in surface curvature are removed in this stage, in this step shrinkage (or densification) processes begin simultaneously with neck growth;

3. *the intermediate stage:* where the neighbor growing necks start to interact between each other starting the processes of pore coarsening and enlargement. Pore phase is still continuous and densification is assumed to occur by means of pores shrinkage reducing their cross-section. In addition, pore may become unstable generationg isolated pores. The intermediate stage normally covers the major part of the sintering process;

4. *the final stage:* pores become isolated at the grain corners and may disappear. This step is mostly characterized by pore closure phenomena.

Specifically, according to (Borgwardt, 1989b) during the calcium oxide induction period its porosity is almost constant over time. Zheng and Reed (1989) and Falamaki, Afarani, and Aghaie (2004) showed that sintering of small aggregated leads to an increase of the mean pore radius related with a disappear of smaller pores size. The following steps,

namely the intermediate and final stages, are characterized by pore shrinkage and grain growth. Specifically, in the intermediate stage of sintering pores can be described as an interconnected matrix of cylinders that degenerate to isolated pores and, in this stage, the majority of porosity is loss (De Jonghe and Rahaman, 2003). This point is the transition to the final sintering stage where pores can be approximated with spheres and the overall of the material porosity is lost (De Jonghe and Rahaman, 2003). The common driving force of these sintering stages is the reduction of the surface energy associated with the solid surface (Nicholson, 1965; Suk-Joong L.Kang, 2005), that generates the material transport and, thus, sintering mechanisms. Solid state sintering phenomena in polycrystalline materials (as for the case of calcium oxide used in this research project) are considerably more complex than those controlled by other different mechanisms, such as viscous or liquid phase sintering processes, because of the availability of several matter transport paths and the presence of grain boundaries (Rahaman, 2007). The transport of matter in solid-state sintering can occur by at least six different paths, which define the high temperature mechanisms of sintering, as schematically shows in Fig. 2.4. More specifically, these material transport mechanisms are (Suk-Joong L.Kang, 2005; Rahaman, 2007; German, 2014):

1. surface diffusion;
2. lattice diffusion from surface;
3. vapor transport (evaporation/condensation and solid-state gas diffusion);
4. grain boundary diffusion;
5. lattice diffusion from the grain boundary;
6. plastic/viscous flow.

Usually, more than one of these mechanisms may operate during a sintering regime, making the sintering analysis difficult. In addition, only certain mechanisms lead to the sample shrinkage or densification. Therefore, the aforementioned processes are divided into densifying and non-densyfying mechanisms. Surface diffusion, lattice diffusion from the particle surfaces to the neck, and vapor transport lead to neck growth without densification phenomena and are referred to as non-densifying mechanisms (Rahaman, 2007). On the other hand, grain boundary diffusion and lattice diffusion from the grain boundary to the pore are the most important densifying mechanisms in polycrystalline ceramics. Diffusion from the grain boundary to the pore permits neck growth as well as densification (German, 2014). Plastic flow by dislocation motion also leads to neck growth and densification, but is more common in the sintering of metal powders (Rahaman, 2007).
According to Rahaman (2007), the most important consequence of grain boundaries is the occurrence of grain growth and pore growth during sintering, a process normally referred to as *coarsening*. Coarsening process provides an alternative route by which the free energy of the powder system can be reduced, so it reduces the driving force for densification. The interplay between the two processes, sometimes referred to as a competition between sintering (densification) and coarsening (grain growth), according to Rahaman (2007).

2.5 The calcium oxide carbonation reaction

The carbonation reaction kinetics shows a quite complex conversion over time profile that depends on these sorbent micro-textural properties: a fast chemical kinetic controlled step is followed by a slow product-layer diffusion controlled one (Barker, 1973). The transition between these two regimes occurs sharply due to a radical change of the sorbent

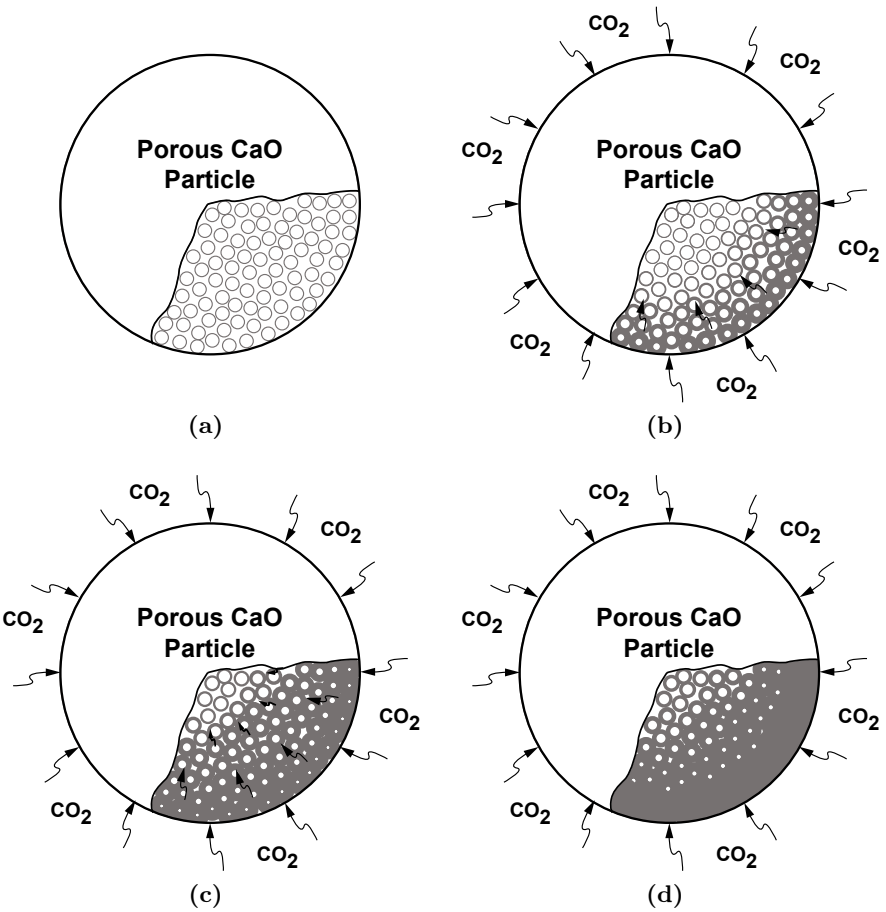

Figure 2.5: Schematic representation of the sorbent micro-structure evolution during the CaO carbonation reaction at different steps: before the reaction (a); during the early stages when the reaction kinetics is the controlling regime (b); nearly before (c) and after (d) the transition point where the sorbent micro-structure is plugged.

internal micro-structure. Bhatia and Perlmutter (1983a) and Sun et al. (2008a) associated this transition to the sorbent small pore closure. Specifically, pore closure occurs because of the different molar volumes between the solid reactant and the $CaCO_3$ product layer and the CO_2-capture uptake is theoretically related to the sorbent porosity ε according to Bhatia, S.K. and Perlmutter (1981)

$$\varepsilon = \varepsilon_0 - (Z_{\text{carb}} - 1)\,(1 - \varepsilon_0)\; X_{\text{CaO}}, \tag{2.5}$$

where ε is the initial sorbent porosity, X_{CaO} is the CaO carbonation reaction conversion and Z_{carb} is the ratio between the carbonate and the calcium oxide molar volume, according to Eq. (2.4). For the case of the CaO carbonation reaction, Z_{carb} is about 2.2, according to the CaO and $CaCO_3$ properties listed in Tab. 2.1. By assuming a zero porosity value when the carbonation reaction stops, Eq. (2.5) predicts the maximum CaO conversion value during the CO_2-capture step (Sun et al., 2007) or, vice versa, it can be used to estimate the effective initial sorbent porosity exploited by the carbonation reaction when the maximum CaO conversion is known (Biasin et al., 2015). Moreover, several literature contributors applied structural kinetics models (like random pore model) in order to accurately describe the conversion over time profile of the carbonation reaction (Benedetti and Strumendo, 2015; Sun et al., 2008a) and a detailed characterization of the initial sorbent is an essential

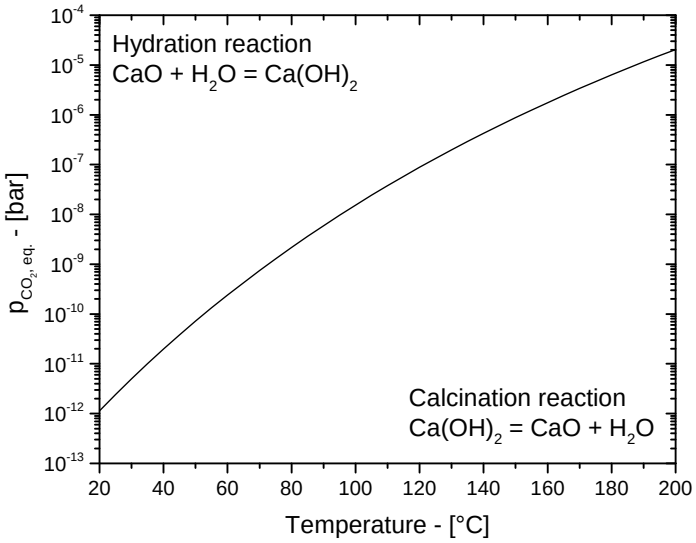

Figure 2.6: The equilibrium partial pressure of H_2O fror the hydration of the CaO in a low temperature range (below 200 °C).

step to correctly predict both the reaction kinetics and the textural sorbent evolution during the reaction.

2.6 The problem of sorbent hydration

As previously mentioned, calcium oxide as solid sorbent is produced at high temperature reaction conditions. During the calcination reaction, the reaction atmosphere is composed by an inert gaseous specie, usually nitrogen, argon or helium (Borgwardt, 1985). Additionally, mixtures of CO_2 in balance with an inert specie are used to investigate the CO_2 catalytic sintering effects on the CaO micro-structure (Borgwardt, 1989a; Beruto, Barco, and Searcy, 1984). However, once the sorbent is cooled down and unload from the experimental apparatus (like a TGA or a muffle), the air moisture starts to hydrate the new formed sorbent. Specifically, water reacts with calcium oxide to give calcium hydroxide (portlandite), according to the following stoichiometry,

$$\mathrm{CaO}_{(s)} + \mathrm{H_2O}_{(g)} = \mathrm{Ca(OH)}_{2(s)} \qquad \Delta H_r^\circ = -108.5\,\mathrm{kJ\,mol^{-1}}. \tag{2.6}$$

Moreover, the CaO hydration at room temperature is promoted by the water equilibrium partial pressure, that is extremely low at 20 °C, namely 1.135×10^{-12} bar, as showed in Fig. 2.6. This considerable low value suggests that room temperature and atmospheric conditions are favorable thermodynamic conditions to shift the CaO hydration reaction towards to the product, according to Eq. (2.6). More specifically, by assuming a relative humidity of air in the range between 60 % and 80 %, the associated H_2O partial pressures[2] are about 1.4×10^{-2} bar and 1.8×10^{-2} bar. These values are significantly greater than the equilibrium partial pressure and favour the CaO hydration reaction.
Despite the favorable thermodynamic conditions at room temperature and atmospheric

[2] According to McCabe, Smith, and Harriott (2005), the relative humidity is defined as the ratio of the partial pressure of the vapor to the vapor pressure of the liquid at the gas temperature. Usually, it is expressed on a percentage basis. Therefore, the associated vapor partial pressure is obtained if the saturation pressure of water is known, and, in this case, is 2.337×10^3 Pa at 20 °C (Smith, Van Ness, and Abbott, 2005).

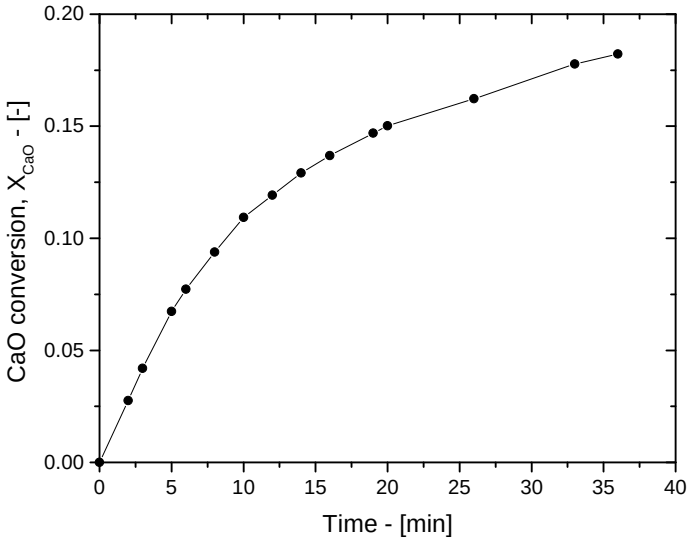

Figure 2.7: CaO conversion profile over time during the sorbent hydration at room temperature and atmospheric pressure.

pressure, the hydration reaction kinetics should be low because of the low temperature. On the contrary, the hydration reaction kinetics at room temperature is considerable, as showed by the CaO conversion over time profile in Fig. 2.7. This profile was obtained by measuring the CaO weight change with an analytical balance leaving the fresh CaO at ambient conditions for several minutes. Surprisingly, the hydration reaction kinetics is significant at ambient conditions and almost 20 % of fresh CaO hydrated to calcium hydroxide in roughly 40 min. This high reaction rate is probably due to two main factors:

- significant favorable reaction conditions in terms of $p_{H_2O} \gg p_{H_2O,\,eq.}$;
- the high CaO internal specific surface area, that favors the reaction rate because of the heterogeneous nature of the calcium oxide hydration.

The CaO hydration (and, thus, contamination) at ambient conditions is a significant experimental issue that arises when samples are unloaded from the reactor and exposed to moisture, namely during the unloading from the reactor and during the ex-situ characterization techniques, such as SEM, XRD and gas adsorption analysis.
In order to avoid the sorbent hydration, a suitable storing system is necessary, especially if the storing period is considerable, namely from few minutes up to hours. In this work, fresh CaO was stored under an inert atmosphere of nitrogen at 1 atm using borosilicate glass vials in which the powder material is loaded. Fig. 2.8 shows the main steps of the sealing procedure, that can be summarized as follow:

1. fresh calcium oxide is unloaded from the reaction system (like a TGA apparatus) and then loaded into a vial (Fig. 2.8a);
2. nitrogen is flowed in order to purge the sealing pipes, while a heating shrinking tube is used to connect the vial to the sealing system (Fig. 2.8b);
3. once the vial is linked to the sealing pipe, nitrogen is still flowing in order to avoid any air back-flow (Fig. 2.8c);
4. when the nitrogen valve is closed, vacuum is generated for about 1 h (Fig. 2.8d);

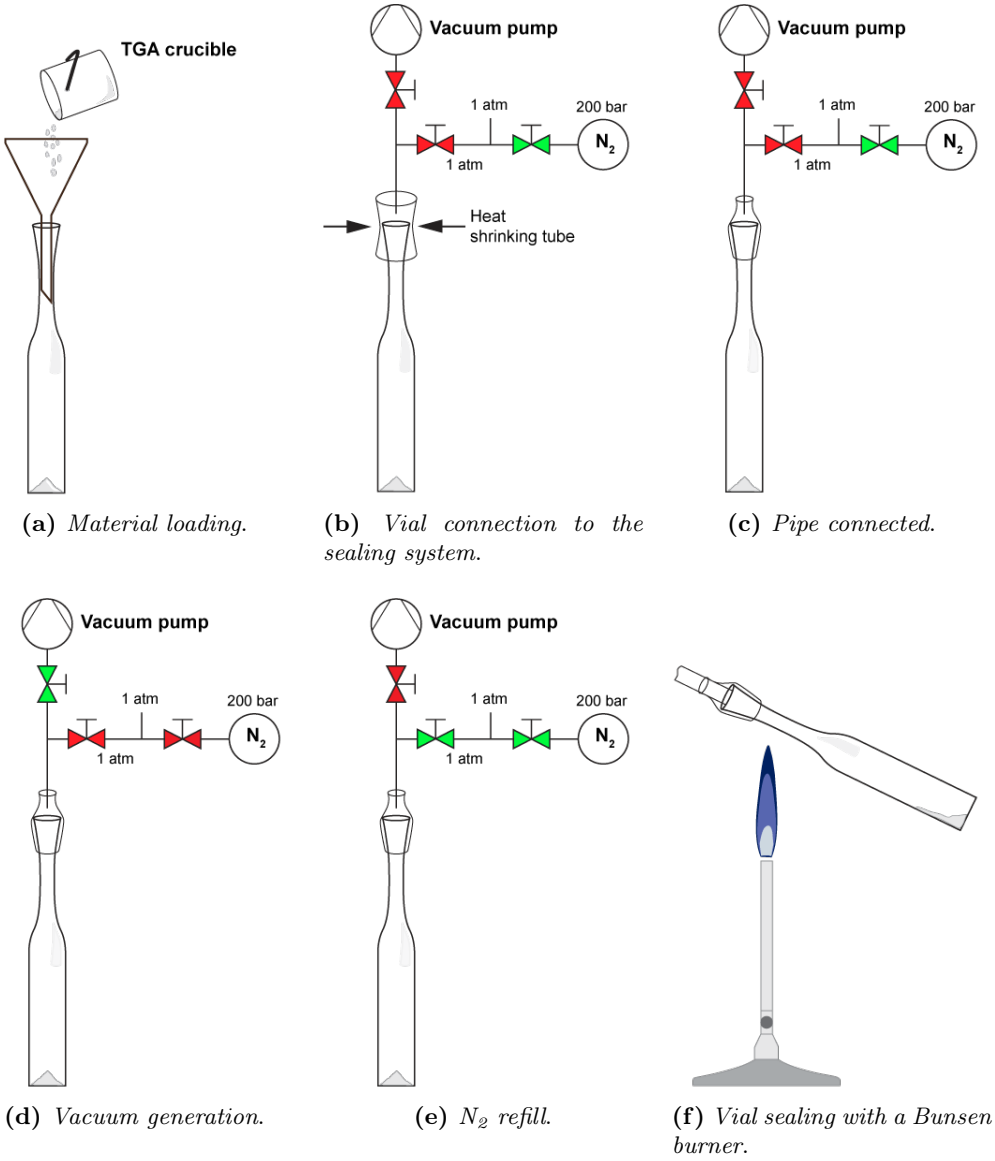

(a) *Material loading.*

(b) *Vial connection to the sealing system.*

(c) *Pipe connected.*

(d) *Vacuum generation.*

(e) *N_2 refill.*

(f) *Vial sealing with a Bunsen burner.*

Figure 2.8: Sealing system steps to store calcium oxide under an inert atmosphere in vials.

5. the vial is refilled with N_2 and a three-ways connection between the nitrogen-line valves maintains the vial at atmospheric pressure (Fig. 2.8e);

6. the vial is finally sealed with a Bunsen burner by melting its neck (Fig. 2.8f).

The sealing system depicted in Fig. 2.8 allowed the material storing under nitrogen atmosphere for several days before the characterization analysis, preventing any external contamination. The powder can be easily unloaded from the vial by breaking the sealed neck. In this way, each sample is exposed to the atmospheric conditions only when it is unloaded from the calcination reactor and from the vial for the characterization analysis. However, such steps are fast enough to minimize the sorbent hydration (less than $3 \div 3$ min).

Table 2.2: XRF spectrometry analysis of the commercial calcium carbonate by AppliChem (marble granular A6297). Data are expressed in terms of mass fractions (% by wt.) of the element oxide. LOI (loss on ignition) stands for the volatile matter.

SiO_2	TiO_2	Al_2O_3	Fe_2O_3	MnO	MgO	CaO	Na_2O	K_2O	P_2O_5	LOI
0.14	0.01	0.1	0.07	0.01	0.05	60.22	0.01	0.01	0.03	38.85

2.7 Material precursor: the powder-based calcium carbonate

Commercial calcium carbonate by AppliChem (marble granular A6297) was used as calcium oxide solid sorbent precursor. Because this material was obtained from marble granular, the XRF spectrometry analysis listed in Tab. 2.2 reveals the presence of several contaminants. These data are conveniently expressed in terms of weight fraction percentage of the element oxide and represent the 99.05 % of the material composition. The rest of the other chemical species, about 0.5 %, consists of several different elements like, S, Sc, V, Cr, Co, Ni, Cu, Zn, Ga, Rb, Sr, Y, etc.
Although the original particle size distribution of the material was wide (varying from few microns up to 300 µm), the $CaCO_3$ powder was sieved and the 150÷160 µm fraction in particle diameter was used. Such particle size was chosen for two reasons: it allows to reduce or neglect the intra-particle diffusion effects during the carbonation reaction and ensures a good compactness within the capillary used for the smallangle scattering measurements.
Despite the powder material was sieved, each single particle of CaO_3 is covered by fine particles having a mean diameter lower than 10 µm, as shown in Figs. 2.9a and 2.9a. This fine powder is likely linked to the calcium carbonate surface by van der Waals's forces. These weak interactions can be easily annulled by means of a solvent, like water.
The SEM surface details of $CaCO_3$ showed in Figs. 2.9c and 2.9d suggest a non-porous and dense structure, at least down to 10 µm.

2.8 Reaction kinetics and sorbent characterization: ex-situ and in-situ techniques

Thus far, the sorbent CO_2-capture performances in terms of reaction kinetics and maximum CO_2 capture capacity have widely been investigated by means of the thermogravimetric analysis, through which the reactant conversion over time can be obtained. The sorbent micro-structure characterization is usually performed by means of *ex-situ* techniques: N_2-adsorption and mercury porosimetry techniques for the determination of the sorbent micro-textural properties, namely the porosity, the specific surface area, the mean pore radius and the material pore size distribution (PSD); X-ray powder diffraction technique (XRD) for the sample composition (in case of partially calcined or carbonated samples and to check the material hydration degree) and for the crystallite size estimation. In this work, N_2-adsorption technique was used for the sorbent micro-texture characterization as an intrusion technique.
However, one of the main drawbacks of the ex-situ techniques is associated to their incapability to investigate the *high temperature-* and *time-dependent* phenomena that occurs during the calcite thermal decomposition and during the CaO carbonation reaction, such as pore generation, sintering mechanisms and pore closure. Instead of using these traditional techniques a more modern and promising approach to investigate the non-catalytic gas-solid reactions is based on the small angle X-ray scattering, that is a radiation-based

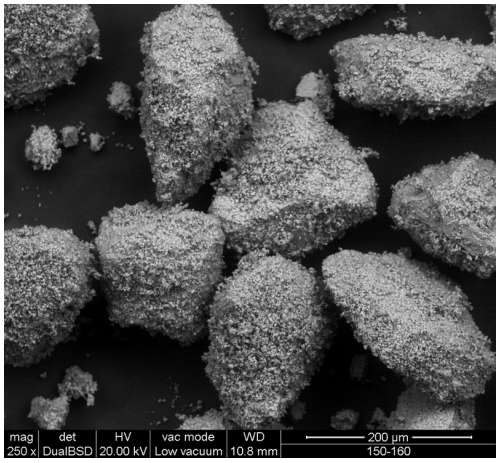

(a) *Calcite particles.*

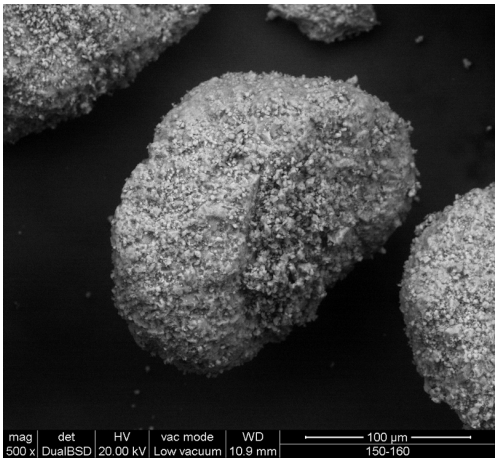

(b) *Detail of a single limestone particle.*

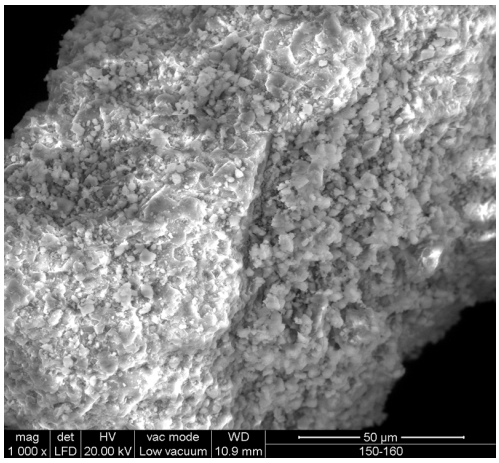

(c) *Particle detail with Large Field Detector (LFD).*

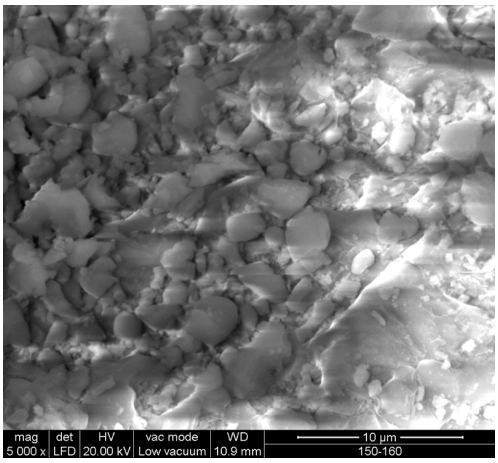

(d) *Surface detail.*

Figure 2.9: SEM images of limestone with mean particle diameter of $150 \div 160\,\mu m$.

technique (Fig. 2.10). The main advantage of this approach is that to be used *in-situ*, namely at the same operative conditions of the aforementioned phenomena, in terms of temperature, pressure and atmosphere composition, without the need to expose the material to ambient condition and, thus, avoiding the potential hydration issues.

2.8.1 The thermo-gravimetric analysis

The thermo-gravimetric analysis (TGA) is an analytical technique commonly used to determine the thermal stability of a material and its fraction of volatile components by monitoring its weight change during a specific heat treatment. Furthermore, this technique has been widely used for the investigation of the gas-solid reactions (Schulze et al., 2017; Szekely and Evans, 1970). Specifically, both the $CaCO_3$ calcination and the CaO carbonation reactions have been extensively investigated by means of the thermo-gravimetric analysis (Barker, 1973; Bhatia and Perlmutter, 1983a; Khinast et al., 1996; Kyaw et al., 1998; Grasa et al., 2008; Sun et al., 2008b; Rodriguez-Navarro et al., 2009; Alonso et al., 2014; Schulze et al., 2017).
A thermo-gravimetric analyzer is an experimental apparatus composed by several components, that allows to monitor and control the sample weight evolution and the reaction

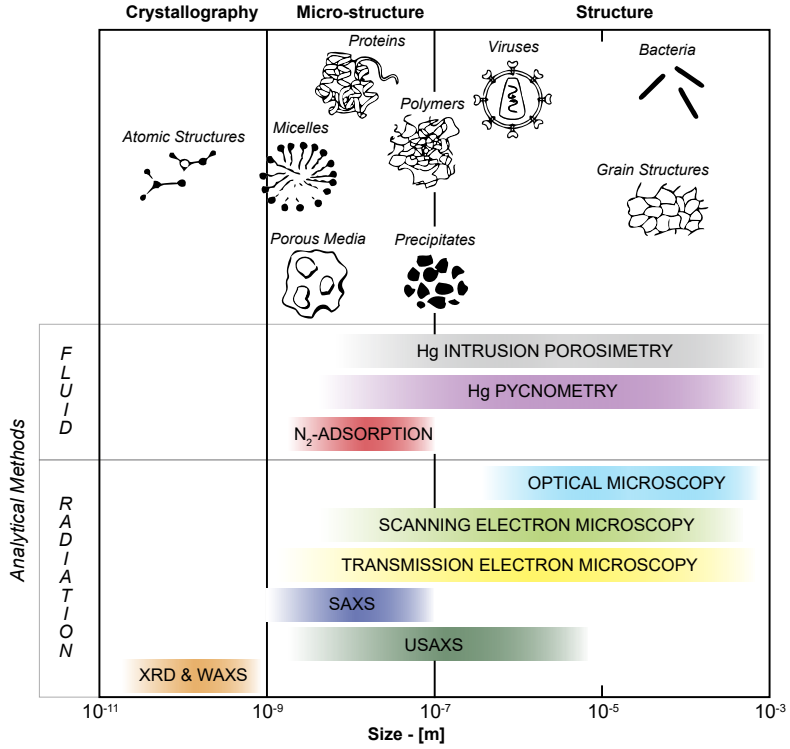

Figure 2.10: Measurable length scales of fluid-based and radiation-based characterization techniques(Brumberger, 1994).

conditions. In particular, these components are

- a *balance*: that monitors the sample weight change evolution;
- a *furnace*: though suitable heating elements, it allows to control the sample temperature over time;
- a *crucible*: where samples are placed;
- a *gas-dosing system*: that feeds one or more gaseous species into the reactor furnace;
- a *recording system* for monitoring the sample weight change and the furnace operative conditions.

Additionally, the "pressurized thermo-gravimetric analyzers" are capable to operate under vacuum or high pressure conditions in contrast with the "atmospheric thermo-gravimetric analyzers" that can operate only at atmospheric pressures. In the former case, a suitable ancillary inert gas is used to control the reaction pressure, as argon.
Usually, during a typical TGA run one or more operative conditions are varied in order to test the sampling materials, such as temperature, pressure and flow-rate and gas-composition. All these operative conditions may give rise to buoyancy effects on the sample mass evolution profile and apparent weight changes may arise if these effects are not correctly accounted for. For this reason, each sample-run weight change profile is conveniently subtracted by its own blank-run apparent weight change profile.
From thermo-gravimetric data, the reactant conversions during the $CaCO_3$ calcination and CaO the carbonation reactions were calculated using the following equations:

$$X_{\mathrm{CaCO_3}} = \frac{m_{0,\,\mathrm{calc}} - m_{\mathrm{calc}}(t)}{m_{0,\,\mathrm{calc}}} \frac{M_{\mathrm{CaCO_3}}}{M_{\mathrm{CO_2}}}, \tag{2.7}$$

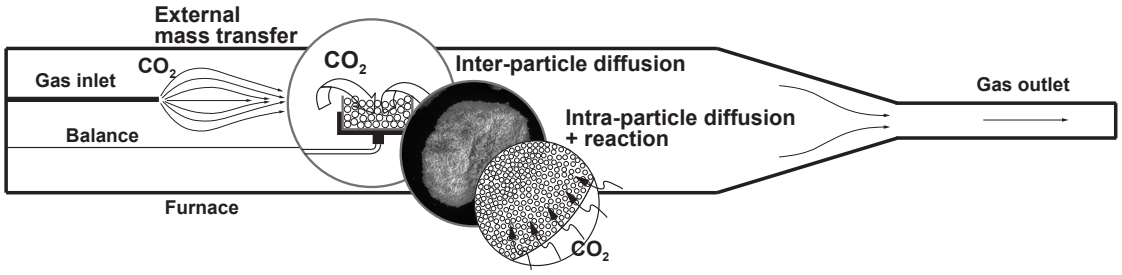

Figure 2.11: Schematic representation of the different mass transfer limitations that sequentially occurs during a typical TGA apparatus (e.g. an horizontal thermo-gravimetric analyzer) at different scales.

and

$$X_{\mathrm{CaO}} = \frac{m_{\mathrm{carb}}(t) - m_{0,\,\mathrm{carb}}}{m_{0,\,\mathrm{carb}}} \frac{M_{\mathrm{CaO}}}{M_{\mathrm{CO_2}}}, \tag{2.8}$$

where $m_{\mathrm{calc}}(t)$ and $m_{\mathrm{carb}}(t)$ are the sample mass over time during the calcination and carbonation reactions, $m_{0,\,\mathrm{calc}}(t)$ and $m_{0,\,\mathrm{carb}}(t)$ are the sample mass at the beginning of calcination and of carbonation ($CaCO_3$ starting material and completely calcined CaO, respectively), $M_{\mathrm{CaCO_3}}$, M_{CaO} and $M_{\mathrm{CO_2}}$ are respectively the $CaCO_3$, CaO and CO_2 molecular weights Tab. 2.1.

Physical limitations in TGA tests: the intrinsic kinetics problem

Many different phenomena occur during TGA tests and each one of them has its own rate. Such phenomena may verify simultaneously or one after the other depending of the operative conditions. With the aim to determinate kinetic parameters of the carbonation reaction, physical limitations should be reduced. This can be achieved when all other processes are faster than the chemical reaction, so that they can be neglected ("kinetic controlled regime").
Typically, TGA tests measure an apparent kinetic rate which is the combination of the rates of several phenomena. This may lead to measure kinetic parameters that are affected by heat and mass transfer resistances. The problem to estimate the intrinsic kinetic rate is extensively discussed in the scientific literature in a several contributions such as Bhatia and Perlmutter, 1983a, Abanades and Alvarez, 2003, Alvarez, Carlos Abanades, and Abanades, 2005, Sun et al., 2008b, and Grasa et al., 2009.
When the TGA furnace has reached isothermal conditions, the gas flow rate is switched from inert gas to carbon dioxide. In this precisely instant several physical limitations start as represented in Fig. 2.11, specifically such resistances are due to:

1. *external diffusion*: the reactant gas employs a certain time to reach the crucible positions from the outlet of the reactive gas tube and this can be regarded as a delay related to the gas flow rate. When the front arrives to the crucible, mass transport of carbon dioxide occurs from the bulk flow to the sample surface, adding another time delay to the process;

2. *inter-particle diffusion*: the reactant gas must diffuse within the sample through molecular diffusion from the particle layer surface down to the bottom of the crucibles. A concentration profile is established inside the sample;

3. *intra-particle diffusion*: the carbon dioxide diffuses inside the pore network of each particle realizing a concentration profile inside the solid particles;

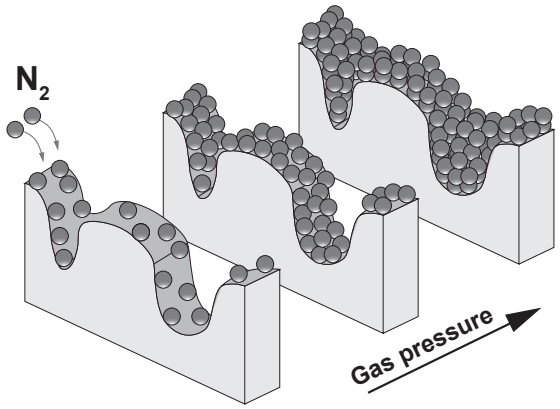

Figure 2.12: Schematic representation of a N_2-adsorption test where the gas probing molecules are adsorbed at the pore surface in terms of layers as the relative total pressure increases.

4. *product layer diffusion*: during the early stages the reaction takes place inside the pore surface and this fast kinetic regime occurs until a thick product layer is generated. Afterwards, the reactant gas must be adsorbed on the product layer surface and diffuse inside the solid matrix reaching the unreacted calcium oxide where reaction occurs. This last stage becomes the slower one when a critical product layer is reached and changes the process regime in the product diffusion controlled one.

Several strategies have been developed in order to eliminate the mass transfer resistances that affect the intrinsic kinetic measurements. The first one consists to increase the gas flow rate up to reduce the external diffusion, but it cannot be completely eliminated because the TGA only works in laminar conditions. Further, high flow rates influence balance measurements giving noisy responses. For this reason crucibles with short height should be preferred. However, crucible height can not be too low because the gas flow rate may drift the sample particle causing instrument degradation.
Particle layer resistance increases with the sample thickness and the particle packing. Low sample mass means low particle layer thickness. If the sample mass is small enough, a mono-layer can be generated. This can be considered as an ideal situation because of the difficulty to obtain an homogeneous layer.
Intra-particle limitation is due to the molecular diffusion of the reactant gas inside the particle pores. Larger particle diameters produce steep concentration profiles that may become the controlling step with low particle porosity or high particle tortuosity.

2.8.2 The gas adsorption analysis

According to IUPAC nomenclature (Renner, 2007) pores are classified on the basis of their internal pore diameter[3] (assuming cylindrical shape pores) dividing pores in three main categories:

1. *micro-pore*: pore of internal diameter less than 2 nm;
2. *meso-pore*: pore of internal diameter between 2 and 50 nm;
3. *macro-pore*: pore of internal diameter greater than 50 nm.

[3]For slit pore the diameter corresponds to the distance between opposite walls.

In this work, the investigation of the sorbent internal micro-structure by means of N_2-adsorption was performed by means of the Autosorb iQ-MP, Quantachrome Instruments® apparatus, using the BET (Brunauer, Emmett, and Teller, 1938) and the BJH (Barrett, Joyner, and Halenda, 1951) methods.

The BET method

The BET method is still the most popular approach for the calculation of the specific surface area from gas-adsorption data (Lowell, 2004). This model takes into account interactions of molecules in the first adsorbed layer with subsequent layers. The determination of surface areas from the BET theory (Brunauer, Emmett, and Teller, 1938) is obtained though the application of the BET equation (Lowell, 2004)

$$\frac{1}{W\ (P_r - 1)} = \frac{1}{W_m\, C} + \frac{C-1}{W_m\, C} P_r, \tag{2.9}$$

where W is the weight of the probing gas adsorbed, P_r is the relative density, defined as P/P_0 where P_0 is the gas saturation pressure, W_m is the weight adsorbed in a completed monolayer and C is a constant. A plot of $1/W\ (P_r - 1)$ vs P_r (usually in the P_r range of $0.05 \div 0.35$) provides a straight line, whose slope s and intercept i are respectively

$$s = \frac{C-1}{W_m\, C}, \tag{2.10}$$

$$i = \frac{1}{W_m\, C}. \tag{2.11}$$

whose solutions are

$$W_m = \frac{1}{s+i}, \tag{2.12}$$

$$C = \frac{s}{i} + 1, \tag{2.13}$$

and the total surface area is calculated as

$$S = \frac{W_m\, N_A\, A_i}{M_i}, \tag{2.14}$$

where N_A is the Avogadro's number, A_i is the cross-sectional adsorbate area and M_i is the adsorbate molecular weight. The specific surface area per unit of sample mass S_m can be determined by dividing S by the sample weight.
The validity o f the BET method was checked and evaluated (Gregg and Sing, 1983) and it is generally accepted that the monolayer capacity predicted by the BET equation is probably correct (Lowell, 2004).

The BJH method

The BJH method can be considered as the most popular method for mesopores size analysis (Lowell, 2004). This model aims to estimate the total pore volume and the sample PSD by analyzing the desorption profile of the adsorbate volume versus the gas relative pressure. This is based on the well-known Kelvin equation that relates the equilibrium vapor pressure of a curved surface, such as that of a liquid in a capillary or pore (P), to the equilibrium pressure of the same liquid on a planar surface (P_0). For a cylindrical pore

the Kelvin equation is given by

$$\ln\left(\frac{P}{P_0}\right) = \ln\left(P_r\right) = \frac{2\,\gamma\,V_m}{r\,RT} \tag{2.15}$$

where γ is the surface tension of the liquid, V_m is the molar volume of the condensed liquid contained in a narrow pore of radius r, R is the universal gas constant and T is the temperature. However, according to Lastoskie, Gubbins, and Quirke (1993) the Kelvin equation is derived from classical thermodynamics and assumes that surface tension can be defined and that the gas phase is ideal. Although this equation is accurate in the limit of large pores (where P approaches P_0), its accuracy decays when applied to narrow pores; in particular, the equation does not take into account the thickness of the layers formed on the porous surface prior to condensation, as schematically represented in Fig. 2.12. The BJH methods attempts to account for the film growth by coupling the Kelvin equation with a standard isotherm, or "t-curve", to describe the thickness of the pre-condensation film on the pore walls (Harkins and Jura, 1944; Halsey, 1948; Lippens, Linsen, and Boer, 1964; Lippens, Linsen, and Boer de, 1964). In this work, the Lippens, Linsen, and Boer de (1964) thickness equation was used:

$$t = \left[\frac{13.99}{0.034 - \log_{10}\left(P_r\right)}\right]^{\frac{1}{2}}, \tag{2.16}$$

where t is in Å. However, for micro-pores, which have widths on the order of just a few molecular diameters, this approach is incorrect (Lastoskie, Gubbins, and Quirke, 1993). Adsorption is enhanced in narrow pores due to increased interactions between adsorbed films on opposing walls and also because of stronger solid-fluid attractive forces resulting from the overlap of the wall potentials. Therefore, adsorption models based upon the Kelvin equation and the standard isotherm overestimate the pressures at which film wetting and capillary condensation occur. Consequently, PSD methods using Kelvin-type adsorption models underestimate the sizes of the pores present in the sorbent.
Several different attempts have been made in order to modify the Kelvin equation by introducing correction parameters (Evans and Marconi, 1985). Nonetheless, the modified Kelvin equation suffers the same defects as the original Kelvin equation when applied to narrow pore sizes, where film interactions are significant(Lastoskie, Gubbins, and Quirke, 1993). For this reason, in this work the original Kelvin equation was used to implement the BJH approach.
Therefore, because of the different intrinsic thermodynamics limitations of this approach, the BJH method is incapable to accurately describe the micro-pore region, where the fluid-solid interaction become stronger.

2.8.3 The XRD analysis

Ex-situ X-ray powder diffraction tests was carried out through a laboratory-scale 2θ diffractometer (X'Pert Powder by Panalytical®) using a Cu Kα radiation (1.5405 Å wavelength). In this work XRD analysis provided two main different information about the CaO sorbent properties: the average crystallite size (CS) and the sorbent hydration (if any) in terms of $Ca(OH)_2$ weight fraction. A schematic representation of the finite-size crytallites is shown in Fig. 2.13
Bragg's equation gives the position of delta-function Bragg peaks by assuming an infinite bunch of lattice planes. Finite size crystallites give rise to Bragg peaks of finite width (Dinnebier and Billinge, 2008). This size broadening is described by the Scherrer equation:

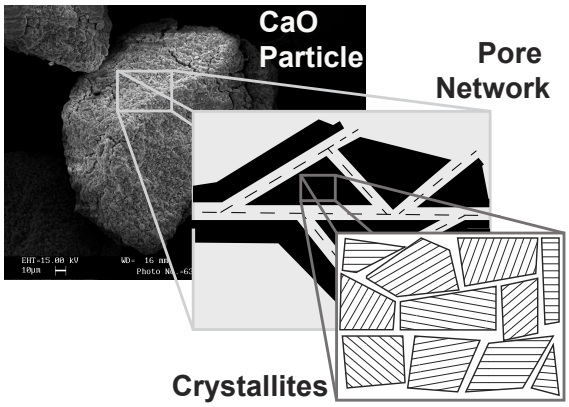

Figure 2.13: Schematic representation of finite size crystallites in a porous CaO particle.

$$CS = \frac{K\,\lambda}{\beta\,\cos(\theta)}, \tag{2.17}$$

where K is a scale factor (that is 0.89 for perfect spheres) and generally depends on the crystallite shape but is always close to unity, λ is the X-ray wavelength, β is the line broadening at half of the maximum intensity (FWHM) of a characteristic hkl reflection (in radians) and θ the peak position in terms of θ radians (i.e. half of the diffraction angle).

2.8.4 *Ex-situ* and *in-situ* USAXS, SAXS and WAXS analysis

In this work of thesis, Ultra Small Angle X-ray Scattering (USAXS), Small Angle X-ray Scattering (SAXS) and Wide Angle X-ray Scattering (WAXS) techniques were used to characterize the CaO based sorbent by means of *ex-situ* and *in-situ* approaches. These techniques are non-destructive and non-invasive (in contrast with the N_2-adsorption) analysis, based on the X-ray radiation. Fig. 2.14 a typical experiment layout to determine the SAS from large-scale structure. Firstly, the monochromatic X-ray beam impinges on the sample, after a series of apertures are used to control its angular divergence. The scattered beam is measured and recorded by a detector (in Fig. 2.14 a two-dimensional detector), which provides the scattering intensity profile. The natural variable of the scattering intensity is the scattering vector $\mathbf{q}$, that is related to the scatterer (pores in this work) dimensions d.
In this work, small angle scattering (SAS) experiments were performed at the Advanced Photon Source, that is a 3$^{\text{rd}}$ generation synchrotron-radiation light source and it is part of the Argonne National Laboratory facilities (Argonne, Illinois).
Ex-situ experiments were tested at the 9-ID-B,C beam-line with a beam energy of 18 keV while in-situ experiments were performed at 24 keV by loading the probing materials into capillaries.
Specifically, *in-situ* tests were performed by means of a flow-cell/furnace (Chupas et al., 2008) designed for conducting in-situ synchrotron-based studies of materials under non-ambient conditions. The flow-cell/furnace is based on a capillary sample geometry, where about 5 mg of sorbent precursor (powder $CaCO_3$) were loaded, that filled $3 \div 5$ mm of the capillary. Each sample was mounted on the flow cell. Both calcination and carbonation reactions were carried out flowing N_2/CO_2 mixtures through the sample. Pure nitrogen flows were fed from a N_2 gas cylinder (whose pressure was conveniently reduced at 1 atm), while CO_2/N_2 mixture were prepared and fed through a syringe pump (Teledyne Isco 1000D Syringe Pump). The temperature during each experiment was controlled by means

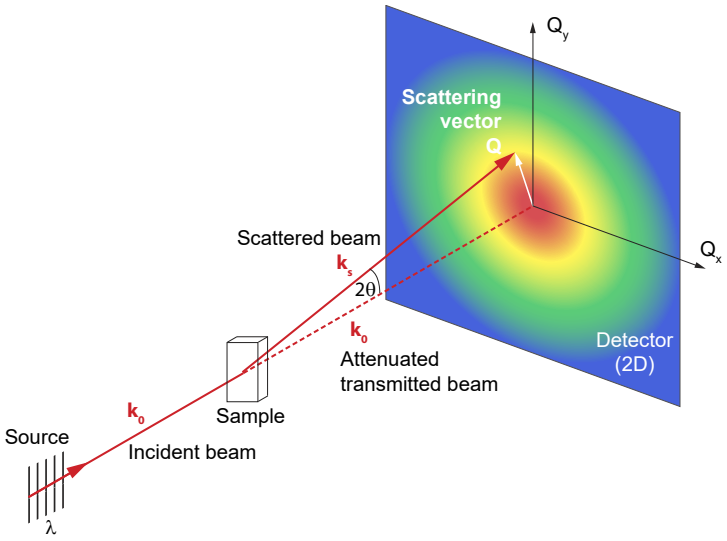

Figure 2.14: Schematic layout of a small-angle X-ray scattering experiment.

of a K-type thermocouple, placed within the capillary in contact with the powder.
According to (Glatter and Kratky, 1982), the resolution of a SAS experiments is associated with the lowest **q** value that a detector is capable to provide, namely

$$d_{\max} \approx \frac{2\pi}{|q_{\min}|}, \tag{2.18}$$

where $d_{\max}$ is the maximum scatterer size that can be explored. According to the instrumentation performances of the 9-ID-B,C beam-line (Ilavsky et al., 2009), $d_{\max} \approx 2\pi/1 \times 10^{-4}\,\text{Å}^{-1}$, namely up to a theoretical value of 6 µm. This value is significant higher if compared with the N_2-adsorption maximum probing pore size, that is about 0.4 µm (Lowell, 2004).
Finally, WAXS data provided the CaO and $CaCO_3$ diffraction peaks during the $CaCO_3$ thermal decomposition and during the CaO carbonation reaction. The data analysis provided the material weight fractions by means of the Rietveld profile method or by means of the ratio between the experimental $CaCO_3$ peaks areas of pure calcite and those of the partially calcined sorbent during the calcination reactions. Vice-versa for the case of the CaO carbonation reaction, namely

$$X_{\mathrm{CaCO_3}} = \frac{1 - w_{\mathrm{CaCO_3}}}{1 - w_{\mathrm{CaCO_3}} + w_{\mathrm{CaCO_3}} \dfrac{M_{\mathrm{CaO}}}{M_{\mathrm{CaCO_3}}}}, \tag{2.19}$$

and

$$X_{\mathrm{CaO}} = \frac{1 - w_{\mathrm{CaO}}}{1 - w_{\mathrm{CaO}} + w_{\mathrm{CaO}} \dfrac{M_{\mathrm{CaCO_3}}}{M_{\mathrm{CaO}}}}, \tag{2.20}$$

where $w_{\mathrm{CaCO_3}}$ and w_{CaO} are the calcium carbonate and calcium oxide weight fractions respectively .

Part II

Ex-situ Characterization Techniques

Chapter 3

Influence of the CaO Crystallite Size on the Sorbent Micro-textural Properties

Several literature contributors have investigated the CaO sorbent micro-textural properties effects on the CaO carbonation reaction performances and several structural kinetics models (like random pore and grain models) have been proposed to describe the CaO carbonation reaction kinetics and the micro-structure evolution during the reaction (Bhatia and Perlmutter, 1983a; Sun et al., 2008b; Sun et al., 2008a; Grasa et al., 2009; Benedetti and Strumendo, 2015). However, only few contributions have been focused on the CaO crystallite size effects on the CaO micro-textural properties and, thus, on the CaO carbonation reaction performances (Zhu, Wu, and Wang, 2011; Biasin et al., 2015; Biasin, Segre, and Strumendo, 2015). For this reason, this chapter is focused on the investigation of a possible relationship between the CaO sorbent textural properties (specific surface area and particle porosity) and its crystallite size. An experimental campaign was performed in order to generate different CaO micro-structure configurations by means of $CaCO_3$ non-isothermal thermal decompositions under vacuum conditions at 800 °C and 900 °C varing the heating step duration. Different analytical techniques were coupled in order to investigate the sorbent micro-structure, namely N_2-adsorption, XRD and SEM images.

3.1 Introduction

During the high temperature CaO sorbent precursor activation, the calcite decomposition into calcium oxide and carbon dioxide determines the generation of the final sorbent micro-structure in terms of particle porosity, specific surface area, mean pore radius and crystallite size CS (Glasson, 1958; Ewing, Beruto, and Searcy, 1979; Borgwardt, 1989b; Sun et al., 2007; Zhu, Wu, and Wang, 2011).
Due to the high temperature conditions of the $CaCO_3$ calcination reaction, the pore generation process is not the only phenomenon that occurs during the calcite decomposition. Actually, sintering processes affects the micro-structure of nascent CaO (Borgwardt, 1989b) by reducing the sorbent internal porosity and specific surface area (Borgwardt, 1989b) and increasing the mean pore radius (Fuertes et al., 1991) and the average crystallite size (Zhu, Wu, and Wang, 2011). Additionally, sintering phenomena are accelerated by the presence of CO_2 in the reactor atmosphere (Borgwardt, 1989a; Fuertes et al., 1991), acting as a sintering catalyst, according to Ewing, Beruto, and Searcy (1979), Beruto, Barco, and Searcy (1984), Borgwardt (1989a), and Maya, Chejne, and Bhatia (2017b).
Because of the non-catalytic nature of the CaO carbonation reaction, the sorbent micro-structural properties reduction leads to a decrease of the CO_2 capture step performances (Sun et al., 2007) in terms of reaction rate and maximum CO_2 capture capacity.

Zhu, Wu, and Wang (2011) investigated the crystallite growth kinetics of nano CaO derived from $CaCO_3$ under different calcination reaction conditions (temperature and residence time). Specifically the sorbent specific surface area reduction profiles were explained as a combination of grain growth processes and the sorbent pore size distribution evolution due to sintering mechanisms
Recently, Biasin et al. (2015) investigated the CaO carbonation reaction performances by means of in-situ X-ray synchrotron-based powder diffraction experiments showing that the CaO conversion over time profiles are dependent on the CaO crystallite size. Specifically, a linear relationship between the initial sorbent crystallite size and the carbonation reaction final conversion was identified. According to Eq. (2.5), the final CaO conversion reaction is associated with the sorbent porosity exploited by the carbonation reaction, namely by the $CaCO_3$ product layer. Therefore, a linear (and negative) relationship between the sorbent crystallite size and its porosity was observed, such that the lower the sorbent CS the higher the initial particle porosity (and thus the maximum CO_2 uptake). In order to explain the inversely proportionality between the sorbent CS and its maximum CaO conversion, Biasin et al. (2015) hypothesized that small CaO crystallites are characterized by high crystallite boundary length per unit of internal specific surface area and the active surface area depends on the initial CaO crystallite size. In this way, a smaller crystallite size may indicate a large active surface area and, consequently, a high conversion rate during the CaO carbonation reaction.
The main goal of this work is to investigate a possible relationship between the sorbent micro-textural properties (particle porosity and specific surface area) and its crystallite size, in order to verify the hypothesis of Biasin et al. (2015). More specifically, an experimental campaign was performed by producing calcium oxide solid sorbents by in-vacuum and non-isothermal calcination reaction conditions and exploring two different final reaction temperature, namely 800 °C and 900 °C. The duration of the heating step was varied in order to generate different micro-structural properties on the final CaO sorbents, allowing the sintering phenomena to change and evolve the CaO internal pore matrix. This was done by coupling different analytical techniques, namely the N_2-adsorption for the porosity, the specific surface area and the mean pore radius estimation (and the whole pore size distribution), the X-ray diffraction technique for the crystallite size determination and SEM images to qualitatively check the sorbent pore network.

3.2 Experimental details

In this experimental campaign the commercial calcium carbonate by AppliChem was used as sorbent precursor and the details of this material refer to § 2.7.

3.2.1 Sample preparation

CaO sorbents were prepared by means of complete calcium carbonate thermal decomposition performed under vacuum conditions using a thermo-gravimetric analyzer (Dyn-THERM MP-ST). Even though isothermal tests allowed an accurate control of the reaction temperature, the main drawback of such procedure was the high residence time of the CO_2 inside the reactor, causing the calcination to occur in an atmosphere of N_2 and stagnant CO_2. For these reasons non-isothermal decompositions of about 100 mg of $CaCO_3$ were performed under vacuum conditions (less than 0.01 bar) in order to promote the CO_2 removal from the reactor and to minimize the CO_2 effects on the reaction and sintering steps, using a heating rate of 50 °C min^{-1}. The duration of the heating step was varied from a minimum of 40 min up to 720 min in order to generate different sample pore structures.
Once the high temperature step was complete, the reactor atmosphere was restored with

Table 3.1: Micro-structural properties for 800 °C calcined samples in vacuum.

Time [min]	CS [nm]	$\langle R_v \rangle$ [Å]	S_m [$m^2\,g^{-1}$]	ε [−]
40	34.9	132	50.4	0.507
180	60.7	171	31.8	0.483
550	90.0	204	20.3	0.468
720	88.2	172	20.7	0.453

Table 3.2: Micro-structural properties for 900 °C calcined samples in vacuum.

Time [min]	CS [nm]	$\langle R_v \rangle$ [Å]	S_m [$m^2\,g^{-1}$]	ε [−]
50	44.1	126	41.0	0.484
80	49.3	141	35.0	0.464
120	52.7	-	-	-
180	119.7	-	-	-

1.3 bar of nitrogen. In this way, each sample was slowly cooled down (4 h) under an inert atmosphere by holding an inlet gas flowrate of 100 $Nm^3\,min^{-1}$ of N_2 in order to avoid any sort of contamination by the remaining stagnant carbon dioxide in the furnace atmosphere. When the material reached the room temperature, each sample was stored in sealed vials with an inert atmosphere of nitrogen before the characterization analysis, in order to prevent any contamination because of the sorbent exposure at ambient conditions (e.g sorbent hydration to form $Ca(OH)_2$). The details of the storing method refer to § 2.6.

3.2.2 Characterization techniques

Each sample was split into two fractions: one for the XRD and the second one for the N_2-adsorption analysis.
One was tested by means of the X-ray diffraction technique in order to obtain the respective diffraction profile. Measurements were carried out with a standard laboratory-scale Panalytical® (model X'Pert Powder) diffractometer. An X-ray radiation with a Cu K_α wavelength, λ, of about 1.5405 Å was used and the instrumental set-up contribution was taken into account using LaB_6 as reference material. Specifically, the X-ray diffraction patters were used to estimated the sorbent average crystallite size by means of the Debye-Scherrer equation, Eq. (2.17). In addition, the XRD analysis was used to check the material contamination,verifying the presence of additional phases in the diffraction pattern, especially for the case of calcium hydroxide.
The second sample fraction of each test was analyzed by means of the N_2-adsorption technique in order to estimate the sorbent micro-textural properties. Specifically, the BET (Brunauer, Emmett, and Teller, 1938) and the BJH (Barrett, Joyner, and Halenda, 1951) methods were used to estimate the material specific surface area (S_m) and the pore size distribution (PSD) respectively. In addition, the former method provides the sorbent internal porosity (ε) and mean pore radius ($\langle R_v \rangle$).

3.3 Results and discussion

TGA was used to thermally activate the sorbent precursor $CaCO_3$ under vacuum conditions. Fig. 3.1 shows two typical $CaCO_3$ conversion (X_{CaCO_3}) over time profiles during the thermal decomposition to calcium oxide, where the furnace temperature was increased up to 800 °C and 900 °C from room temperature. Specifically, Fig. 3.1a shows the details of a non-isothermal calcination reaction in vacuum up to 800 °C for 40 min, where the calcium carbonate conversion derivative over time is particularly useful to determine the beginning of the decomposition and, thus, the temperature at which the decomposition occurs. More specifically, for calcined samples up to 800 °C the $CaCO_3$ thermal decomposition initiated at about 20 min from the beginning of the furnace heating when the reactor temperature is roughly 610 °C. In these conditions, the calcium carbonate decomposition is complete nearly the end of the heating step, namely after about 40 min, when the reaction temperature is at 800 °C, meaning that 20 min are required to achieve the $CaCO_3$ complete conversion. On the other hand, Fig. 3.1bshows the calcium carbonate thermal decomposition in vacuum when the final calcination temperature was set at 900 °C. In this case, the starting and the complete decomposition time (since the beginning of the heating step) and temperature values are roughly 20 min at 680 °C and 32 min at 840 °C respectively. For this case the $CaCO_3$ calcination reaction took about 12 min to occur. This decomposition time difference is ascribed to the temperature controller that imposed a different local temperature ramp depending on the final set-point. In addition, the temperature ramps profile are characterized by two different slopes as can be noted in Figs. 3.1a and 3.1b. Specifically, when the final temperature is 800 °C the average heating rate is about 22 °C min^{-1}, where 45 °C min^{-1} is the local heating ramp in the first part of the temperature profile and decreases down to 13 °C min^{-1} during the last part of the heating step. For those samples where the final calcination temperature was 900 °C, the overall heating rate was slightly higher that the previous one, namely 24 °C min^{-1}, with local temperature slopes again higher than those of the 800 °C test: 50 °C min^{-1} and 15 °C min^{-1}.

The XRD analysis of samples calcined at minimum heating time of 40 min at 800 °C and 50 min at 900 °C revealed a sorbent crystallite size of 34.9 nm and 44.1 nm, as listed in Tabs. 3.1 and 3.2 respectively. By prolonging the heating step time, the CS at a fixed temperature increases up to high values as shown in Fig. 3.2. Specifically, an increase of about twice the initial size was observed at 180 min, that reached about 2.5 times the starting value when long residence time were considered, namely an additional residence time of 680 min (Fig. 3.2a). As expected, if temperature is increase up to 900 °C, only 190 min are necessary to increase the initial CS of more than 2.5 times and precisely of 2.7 times.

3.3.1 Crystallite size growth kinetics analysis

In order to investigate the crystallite growth kinetics, the following grain growth model for solid state sintering was considered, according to Brook (1976), Rahaman (2007), and Zhu, Wu, and Wang (2011):

$$G^n(t) - G_0^n = k_{CS}\, t \tag{3.1}$$

where G is the grain size, G_0 is the initial grain size at time $t = 0$, k_{CS} is a constant and n the kinetic exponent. This model assumes spherical isolated grains that migrate at the interface of large grain as sintering time progresses and larger grains increases in size during the heating step. Additionally, the exponent n value ranges between 2 and 4, depending on the controlling sintering mechanism (Brook, 1976) and in many ceramics the most common value of the exponent is 3 (Rahaman, 2007). Finally, the kinetic constant

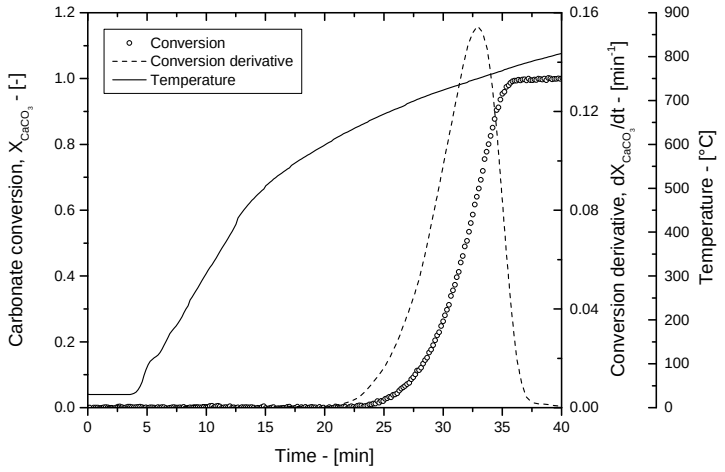

(a) 800 °C, 40 min.

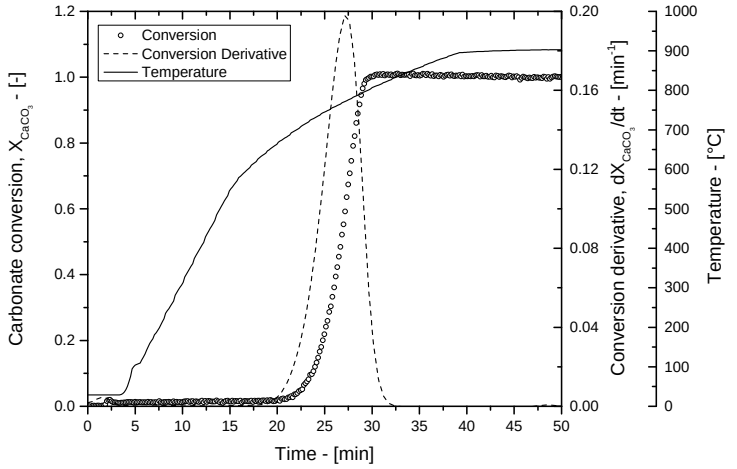

(b) 900 °C, 50 min.

Figure 3.1: $CaCO_3$ conversion profiles during non-isothermal calcinations under vacuum conditions (below 0.01 bar), with heating rate of 50 °C min^{-1} up to the final temperature (800 °C or 900 °C).

k_{CS} follows an Arrhenius-type equation (Zhu, Wu, and Wang, 2011), meaning that the temperature effect on the crystallite growth rate is exponential.
By performing a non-linear fitting of the model in Eq. (3.1) on the experimental data, the exponent value and the kinetic constants were obtained and the model profiles are represented in Fig. 3.2a and 3.2b by solid lines. More specifically, an exponent value of about 3 was obtained, suggesting that the crystallite growth is controlled by a lattice diffusion sintering mechanisms (diffusion from the grain boundary to the pore), according to (Brook, 1976; Rahaman, 2007). This is in agreement with the result of Borgwardt (1989b), who estimated the same sintering mechanism from the CaO specific surface area profile reduction. Opposite to this result, Zhu, Wu, and Wang (2011) estimated an exponent value of 2 by means of nano $CaCO_3$ decomposition. This value suggests a grain boundary controlled sintering mechanism.

As sintering processes progress, the crystallite size growth is not the only effect on the final sorbent micro-structure. Indeed, the sorbent micro-textural properties are strongly affected by sintering, namely the sorbent porosity, specific surface area and mean pore

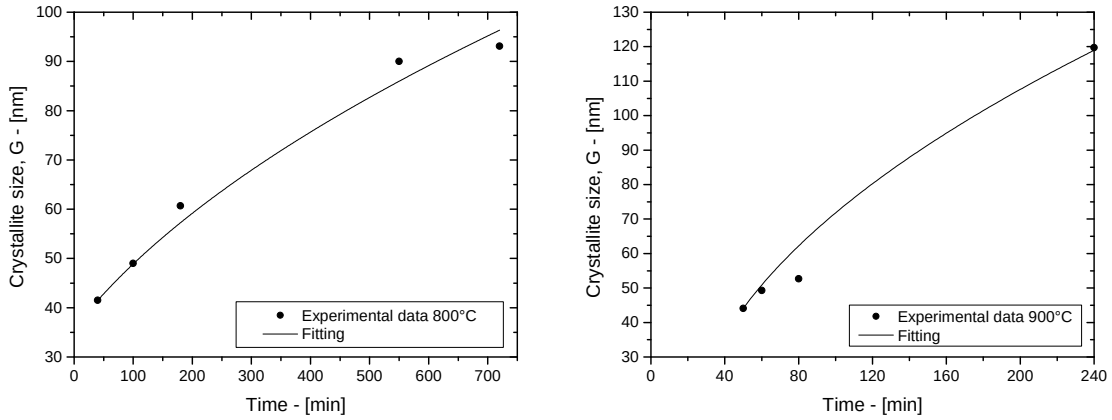

(a) 800 °C. **(b)** 900 °C.

Figure 3.2: Crytallite size evolution over time. Solid lines refers to the fitting results using the growth model in Eq. (3.1).

radius. These properties were estimated by means of the nitrogen adsorption technique (BET/BJH methods) and are listed in Tabs. 3.1 and 3.2. Particularly, the estimated specific surface area and porosity profiles over the sintering time are shown in Figs. 3.3a and 3.3b respectively. Unfortunately, according to Tab. 3.2, the micro-textural properties at 120 min and 180 min were not available. For this reason, the 900 °C samples will not considered in the textural properties sintering models. It is interesting to observe that at 800 °C sintering mechanisms almost halved the initial specific surface area after an additional time of 680 min. On the other hand, the sorbent porosity shows a decrease of about 11 % during the same sintering period.

3.3.2 Sorbent porosity and specific surface area evolution

The German and Munir model (German and Munir, 1976) represents the decreasing of the sorbent specific surface area by means of mechanisms of inter-particle neck growth in the solid phase. Specifically, the kinetic equation for the surface reduction is expresses as

$$\frac{(S_m - S_{m,0})^{\gamma}}{S_{m,0}} = k_S\, t \tag{3.2}$$

$S_{m,0}$ is the initial specific surface area, γ is the exponent and k_S an Arrhenius-like constant. This model was fitted on the 800 °C BET results (Tab. 3.1) obtaining a model exponent equal to 3.14. According to German and Munir (1976), such value suggests a sintering mechanism due to grain boundary diffusion and the model prediction is represented in Fig. 3.3a as a solid line.
The results associated with the exponents of Eq. 3.1 and Eq. 3.2 indicate that multiple sintering mechanisms, namely grain boundary diffusion and lattice diffusion, could be simultaneously relevant during the intermediate stage of sintering. The occurrence of more than one phenomenon during sintering is frequent in polycrystalline ceramics, where grain boundary diffusion and lattice diffusion from the grain boundary to the pore are the most important densifying mechanisms (Rahaman, 2007)
Coble model (Coble, 1961b) describes the porosity over time reduction using a logarithmic

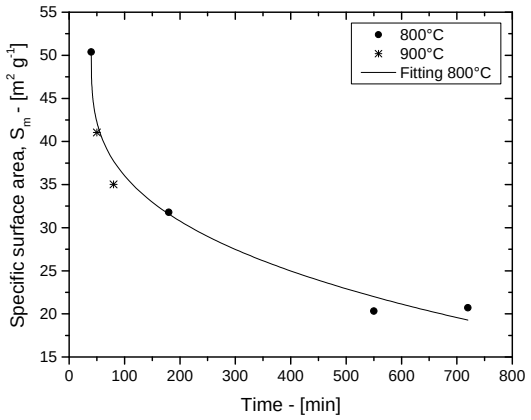

(a) *Specific surface area evolution over time.*

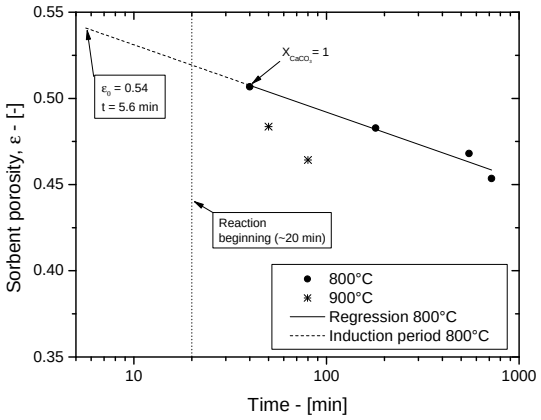

(b) *Sorbent porosity evolution over time.*

Figure 3.3: Specific surface area and porosity evolution over time. Solid lines represent the fitting results by means of the German and Munir model for the specific surface area reduction (German and Munir, 1976); the porosity profile was fitted by means of Coble's model (Coble, 1961b).

law and accounts for the transport of matter by diffusion and grain growth:

$$\varepsilon - \varepsilon_0 = k_p \ln\left(\frac{t}{t_i}\right) \tag{3.3}$$

where ε_0 and t_i are the porosity and time when particle shrinkage begins (Borgwardt, 1989b), and k_p is the porosity reduction kinetic constant that depends on the physical constant of solid-state diffusion (Coble, 1961b). More specifically, Eq. 3.3 is capable to provide the sorbent induction period by extrapolating ε to the theoretical porosity, namely at the instant when sorbent has an internal porosity of 0.545 (i.e. the maximum theoretical porosity that a CaO sorbent can achieve if decomposed from $CaCO_3$). Additionally, the induction period t_i distinguishes between the initial stage and the intermediate one (§ 2.4). Coble model was fitted on the 800 °C porosity values an the result is shown in Fig. 3.3b as a slid line. However, this model predicts that the decomposing $CaCO_3$ assumes the theoretical porosity value only after about 5 min of heating, that is clearly an unreal estimation because the $CaCO_3$ decomposition initiates after 20 min of heating as shown in Fig. 3.1a. Indeed, this result suggests lower porosity values from the theoretical ones of nascent CaO probably because other different process may accelerate the pore sintering (like the CO_2 release by the calcination reaction or a local stagnant CO_2 despite the vacuum conditions).

According to Sing et al. (1985) type IV isotherms are typical for mesoporous materials, as shown by the N_2-adsorption isotherm of a completely decomposed $CaCO_3$ at 800 °C for 40 min represented in Fig. 3.4. The most characteristic feature of the type IV isotherm is the hysteresis loop, which is associated with the pore condensation phenomena. The limiting uptake over a range of high P_r results in a plateau of the isotherm, which indicates complete pore filling (Lowell, 2004). The initial part of the type IV can be attributed to monolayer-multilayer adsorption as IV (i.e., with hysteresis loop), as reported elsewhere by (Beruto et al., 1980; Rodriguez-Navarro et al., 2009).

In this work, the number of sampling points were increased up to at least 250 experimental samplings during the desorption isotherm (those used in the BJH method). This large number of experimental points allowed a detailed estimation of the sorbent PSD, as shown in Fig. 3.5. Fig. 3.5a shows the sorbent pore size distributions at different times of the

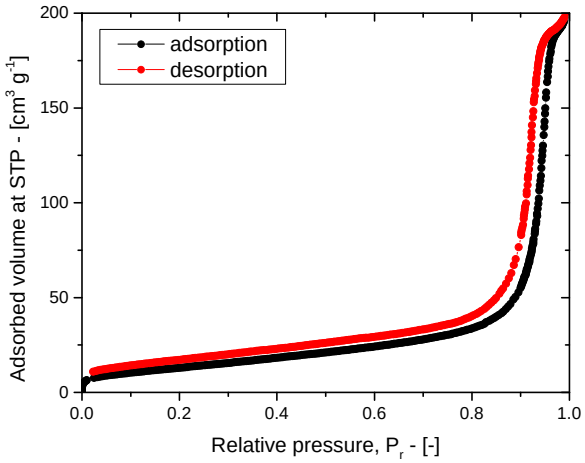

Figure 3.4: N_2-adsorption isotherm of a completely calcined sample up to 800 °C for 40 min in vacuum.

heating step. Specifically the initial PSD (obtained after the end of the calcination reaction) seems to be characterized by two different pore populations: a meso-pore population roughly placed at 100 Å and a second micro-pore population, located nearly of a pore radius of about 20 Å. However, as previously mentioned, the BJH approach is incapable to correctly represent the micro-pore region of a porous material and it is worth noting that the nitrogen adsorption lower pore size limit roughly correspond to the boundary value between the micro-pores and meso-pores at 20 Å (Sing et al., 1985), according to (Lastoskie, Gubbins, and Quirke, 1993; Seaton, Walton, and Quirke, 1989; Lowell, 2004).
Despite this limitation, as the heating time progresses at 800 °C, the meso-pore population is shifted in the direction of the high pore radii (Fig. 3.5a), as confirmed by the increase of the average pore radius in Tab. 3.1 with time: from 152 Å after 40 min of heating up to 204 Å at 550 min. Interestingly, the micro-pore population seems to be quite constant over sintering time, whose effect is in decreasing the micro-pore volume, as suggested by the initial branch of the PSD, that is decreases but not shifted, as can be appreciated in Fig. 3.5a.
A similar behavior is observed for the case of the 900 °C samples, where 30 min are sufficient to shift the mean pore radius from 126 Å to 141 Å and leaving the particle porosity almost unchanged 3.5b.

3.3.3 Micro-textural properties related to CaO crystallite size

By considering the data in Tab. 3.1 and 3.2, it was observed that the higher the CaO CS the lower the sorbent specific surface area and porosity. Specifically, Fig. 3.6a shows a well defined linear relationship between the sorbent CS and its specific surface area. Precisely, a linear correlations was identified, namely

$$S_m = -0.501\,G + 64.2\,\mathrm{m^2\,g^{-1}}, \tag{3.4}$$

for the specific surface area values. On the other hand, solid line in Fig. 3.6b highlights a correlation between the sorbent porosity and its CS, namely

$$\varepsilon = -0.785\,G + 0.516. \tag{3.5}$$

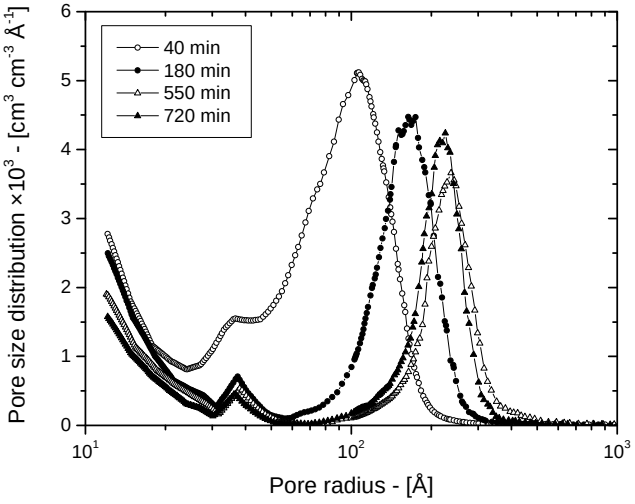

(a) 800 °C.

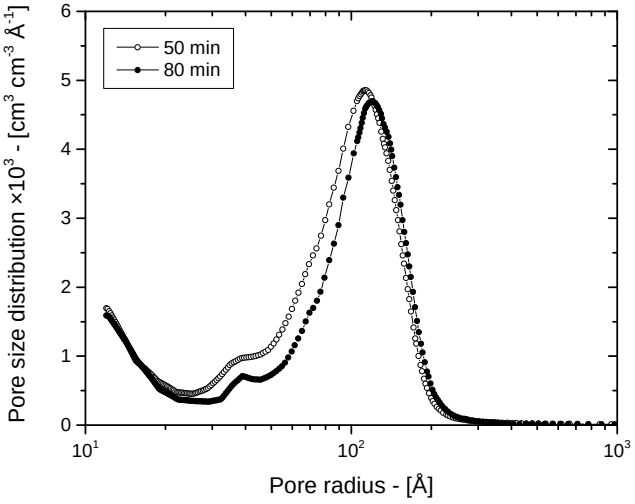

(b) 900 °C.

Figure 3.5: Evolution of the sorbent PSD over time.

Interestingly, these correlations seem to be independent from the reactor temperature (both the 800 °C and 900 °C data were considered). The Pearson correlation coefficients are -0.98 and -0.78 respectively, suggesting the goodness of the linear and negative correlations especially for the former case.
The trends emerging in Figs. 3.6a and 3.6b suggest that sorbent sample with a smaller crystallite size are also characterized by a higher specific surface area and porosity. This is in good agreement with the results of Biasin et al. (2015), who also observed a linear and negative correlation between the sorbent CS and its particle porosity in completely calcined samples at different calcination reaction temperatures ($700 \div 900$ °C) in N_2.

Finally, a significant results of this experimental campaign is liked to the SEM images in Fig. 3.7. Specifically, Fig. 3.7a and 3.7b shows the sorbent micro-structure of a completely decomposed $CaCO_3$ up to 800 °C under vacuum condition for 40 min. On the other hand, Fig. 3.7c and 3.7d refer to non-isothermal calcination reaction up to 900 °C with 5 % of CO_2 in balance with N_2 at 1.3 bar for 5 h. A comparison between these pictures suggests that a significant sorbent micro-structure difference is straightforward. More specifically,

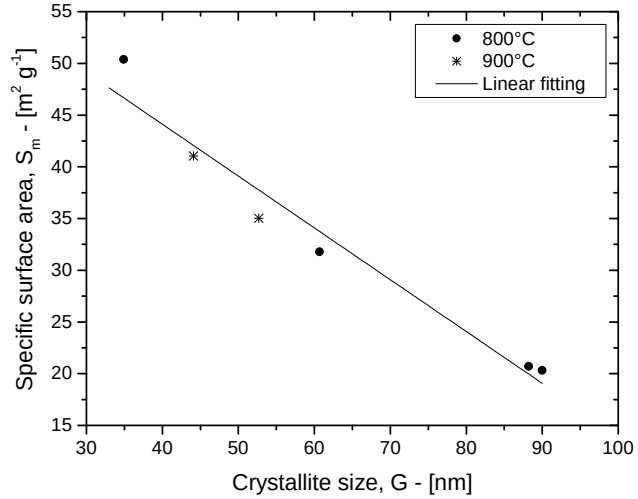

(a) *Surface area vs G.*

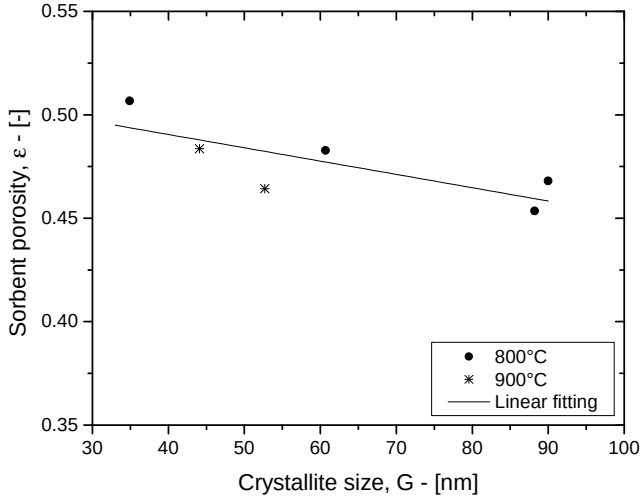

(b) *Porosity vs G.*

Figure 3.6: Linear correlations between the sorbent specific surface area and its crystallite size (G, and between the sorbent porosity and G.

sample produced under vacuum conditions shows a pore network made of cracks and slit-shaped pores, while the other one provides an internal pore structure that mainly consists of pseudo-spherical grains. Interestingly, the sample in Fig. 3.7a and 3.7b surely provides higher specific surface area and porosity values, and smaller crystallite size than those of sample in Fig. 3.7c and 3.7d, according to Tab. 3.1 and 3.2.

3.4 Conclusions

In this work three different techniques were used for the investigation of possible relationships between the CaO micro-textural properties (specific surface area and particle porosity) and the sorbent crystallite size, namely TGA, N_2-adsorption and XRD. By performing $CaCO_3$ calcinations in vacuum the CO_2 sintering effects on the final CaO sorbents were minimized, promoting the CO_2 removal from the reactor atmosphere. Therefore, high porosities (0.48–0.51) and specific surfaces ($41 - 50\,m^2\,g^{-1}$) were obtained, associated with

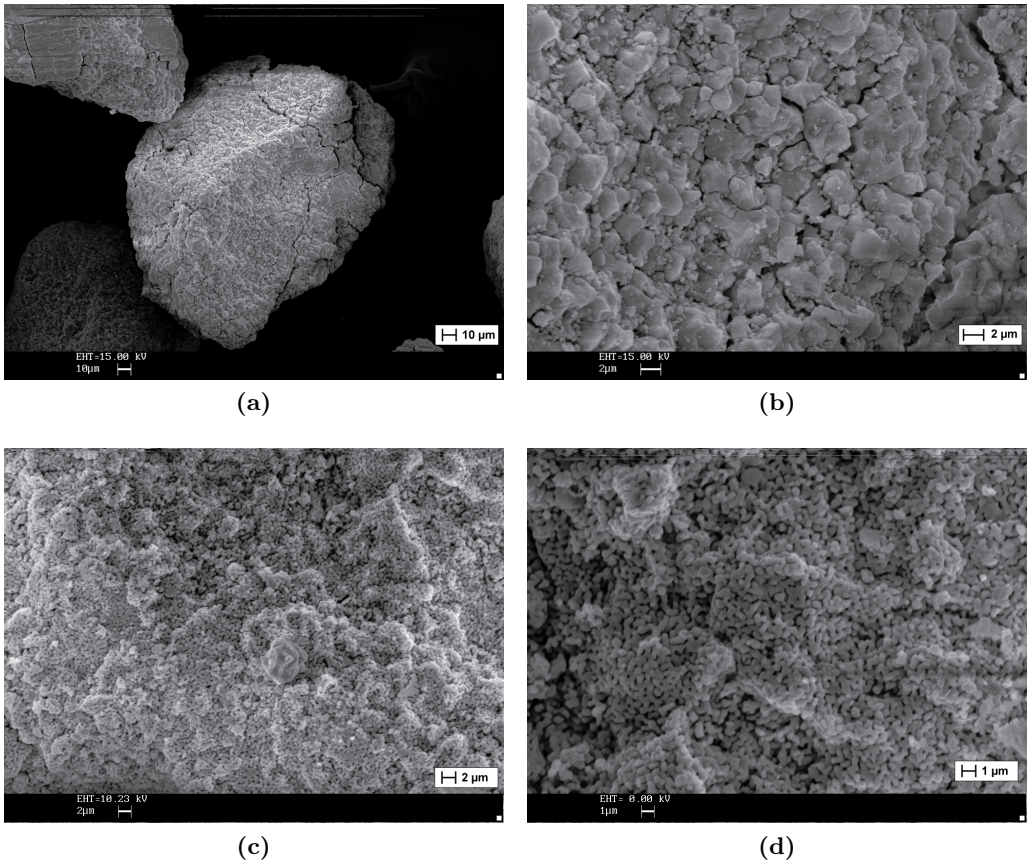

Figure 3.7: SEM images of a completely calcined calcium carbonate at 800 °C under vacuum conditions for 40 min (a) and (b); SEM images of a completely calcined $CaCO_3$ at 900 °C and 1.3 bar with 5 % of CO_2 for 5 h (c) and (d).

low crystallite sizes (40–50 nm).
The investigation of the crystallite growth kinetics through a grain growth model for solid state sintering (Brook, 1976; Rahaman, 2007; Zhu, Wu, and Wang, 2011) suggested a sintering mechanism controlled by lattice diffusion according to Brook (1976) and Rahaman (2007), in agreement with the results of Borgwardt (1989b). In addition, the exponent (obtained by means of a model fitting on the 800 °C experimental data) of the German and Munir model (German and Munir, 1976) suggested that the sorbent specific surface reduction is mainly due to grain boundary diffusion sintering mechanisms. These two results indicate that multiple sintering mechanisms simultaneously occur during the intermediate stage of CaO sintering at 800 °C.
According to Borgwardt (1989b), the Coble model (Coble, 1961b) was used to estimate the induction period on the porosity values profiles over time of CaO sorbent. However, this model located (by extrapolation) the beginning of the induction period after only 5 min of the heating step. This result is clearly unfeasible, because the $CaCO_3$ thermal decomposition initiates after about 20 min of heating at about 610 °C, suggesting that the material may never reach the theoretical porosity value during its decomposition at these operative conditions (800 °C in vacuum). Instead, sintering mechanisms may accelerate the porosity reduction since the early stages of the $CaCO_3$ calcination reaction probably because of the presence CO_2 inside the decomposing calcite particles despite vacuum conditions.
Linear correlations were obtained between the sorbent specific surface area/porosity and

the CS, regardless of the reactor temperature. This result is in good agreement with Biasin et al. (2015) who determined a linear correlation between the initial sorbent porosity and its crystallite size. In addition to this result, this work provided a linear correlation between the sorbent specific surface area and its crystallite size, meaning that the lower the crystallite size the higher the sorbent porosity and specific surface area. These results may enforce the hypothesis formulated by Biasin et al. (2015), who claimed that a low crystallite size in the initial uncarbonated CaO is a good indicator of the initial sorbent porosity, that determines the maximum CO_2 capture capacity during the CaO carbonation reaction. Moreover, this work revealed that a low crystallite size provides high specific surface area in the initial sorbent micro-structure, probably because of the high crystallite boundary length per unit of surface area (Biasin et al., 2015), that ensures high conversion rates during the CO_2 capture step.
Finally, a calcite decomposition under vacuum conditions (below 0.01 bar) at 800 °C for 40 min generate a poorly sintered sorbent micro-structure as clearly indicated by the SEM images, that shows a CaO pore network that consists of slit-shaped pores and particle cracks. This kind of pore configuration was never been observed by literature contributions, that usually show sorbent micro-structure mainly made of grains.
Work in progress to complete this experimental campaign, where the number of experimental points needs to be increased to enforce and empathize the micro-structural properties trends especially at 900 °C.

Chapter 4

Introduction to the Small Angle Scattering

Although a detailed description of the small angle scattering (SAS) theory is beyond the scope of this work of thesis, this chapter would provide the mathematical basics of the X-ray small angle scattering theory in terms of scattering amplitudes, intensity and absolute units. In addition, the main governing equations of the SAS fitting model used in this work of thesis will be provided and described, namely the "Unified fit" (Beaucage, 1995; Beaucage, 1996), with the aim to obtain the micro-textural properties of a porous material from the experimental scattering intensity profiles. Finally, last part of this chapter will provide the main equations to calculate the scattering length density and the linear adsorption coefficient of a general compound, and, particularly, of calcium oxide and calcium carbonate. These properties are necessary to reduce the scattering intensity profiles in terms of absolute units and to extract those sorbent properties that depends on the scatterers concentration, such as the sorbent porosity, the specific surface area, the pore number density, etc.

4.1 Introduction

When a X-ray photon interacts with the matter it can be scattered and/or absorbed. Specifically, a scattering event is a physical process that occurs when a electromagnetic radiation (like X-rays) deviates from its straight trajectory because of localized inhomogeneities (also named "scatteres") in the medium where the radiation is propagating.
According to Als-Nielsen and McMorrow, 2011, if the scattered wave wavelength (energy) is the same of the incident wave, the scattering event is named "elastic". Vice-versa, because a X-ray photon has a momentum $\hbar\mathbf{k}$ and an energy $\hbar\omega$, from a quantum mechanic point of view the energy may be transferred to an electron and the resulting scattered

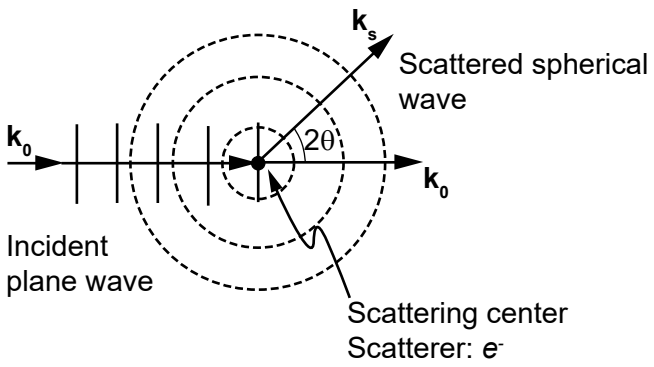

Figure 4.1: Scattering event of one electron.

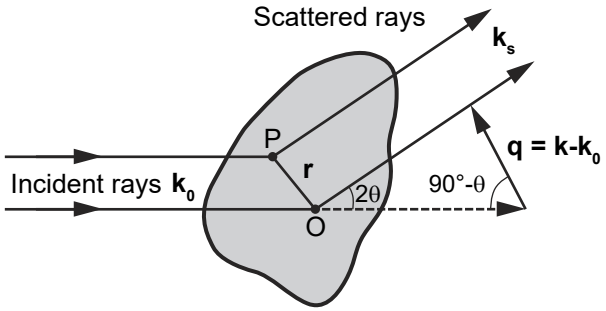

Figure 4.2: Scattering event by a single particle.

photon has a lower energy respect to the incident one. This process is known as "inelastic" scattering or Compton effect. However, despite this theoretical distinction, in this work scattering processes are considered to be only *elastic* and *coherent*.

The fundamental relation describing the diffraction of X-rays by crystalline materials is the well-known Bragg's equation

$$n\,\lambda = 2d\,\sin(\theta), \tag{4.1}$$

where n is an integer, λ is the X-ray wavelength, d is the inter-planar spacing of parallel lattice planes and 2θ is the diffraction angle, the angle between the incoming and outgoing X-ray beams. Eq. (4.1) shows how the angle of diffraction θ is inversely proportional to the separation of the diffracting lattice planes. In ordinary crystals the majority of the observed lattice spacings are of the same order of magnitude as the X-ray wavelengths generally employed, so that the angles θ are usually rather large (Guiner, Fournet, and Walker, 1955).

The study of small-angle X-ray diffraction was introduced when it became desirable to detect large lattice spacings, of the order of tens or hundreds of inter-atomic distances. If a sample has a non-periodic structure or if its lattice has been sufficiently perturbed, the diffraction patterns are not limited to spots or lines but contain more or less extended regions of scattering (Guiner, Fournet, and Walker, 1955).

The classical description of the X-ray scattering by an electron consists in a plane incident monochromatric wave with a wavevector $\mathbf{k_0}$ that interacts with the electron, which then radiates a spherical wave $\mathbf{k_s}$, as shown in Fig. 4.1. By considering a small angle scattering event of a particle, as represented in Fig. 4.2, the scattered X-rays by different electrons travel through the particle. Consequently X-rays scattered by different electrons arrive at the detector with differing phases. These phase differences must be taken into account when the amplitudes the scattered waves are added together to calculate the resultant scattered amplitude. Specifically, Fig. 2.13 is useful to calculate the phase difference between the waves from scatterers at points O and P displaced from O by the vector $\mathbf{r}$. The angle between the directions of these two beams is the scattering angle 2θ. Two scatterers, which are assumed to be small enough that they can be considered to be points, are located at O and P. According to this geometry, the difference in the distance traveled by the upper and lower rays is

$$\left|\hat{\mathbf{k}}_\mathbf{0} - \hat{\mathbf{k}}_\mathbf{s}\right| \cdot \mathbf{r}$$

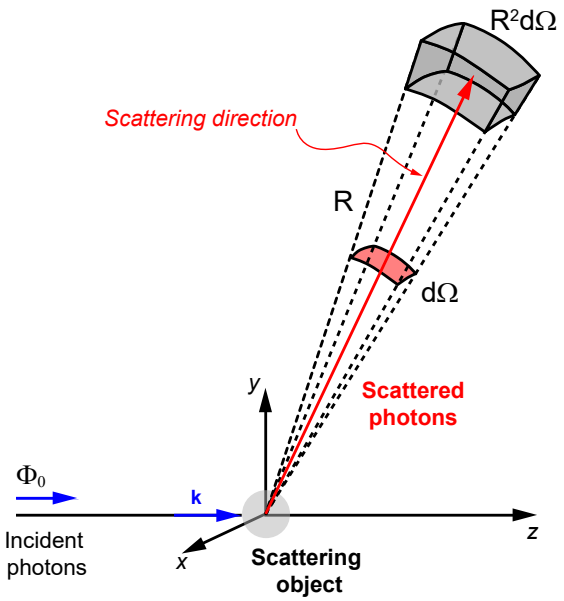

Figure 4.3: Schematic layout of a scattering experiment used to determined the differential scattering cross section.

where $\hat{\mathbf{k}}_\mathbf{0}$ and $\hat{\mathbf{k}}_\mathbf{s}$ are unit vectors associated to $\mathbf{k_0}$ and $\mathbf{k_s}$ wavevectors. The corresponding phase difference (in radians) of the phases of the two waves is

$$\Delta\phi(\mathbf{r}) = (\mathbf{k_0} - \mathbf{k_s}) \cdot \mathbf{r} = \mathbf{q} \cdot \mathbf{r}, \tag{4.2}$$

where $\mathbf{q}$ is known as the *scattering vector* defined as

$$\mathbf{q} = \mathbf{k_0} - \mathbf{k_s}. \tag{4.3}$$

By considering elastic scattering events, such that $|\mathbf{k_0}| = |\mathbf{k_s}| = |\mathbf{k}|$, the scattering vector modulus is

$$q = |\mathbf{q}| = 2\ |\mathbf{k}|\ \sin(\theta) = \frac{4\pi}{\lambda} \sin(\theta), \tag{4.4}$$

and $\mathbf{q}$ is the natural variable to describe an elastic scattering process and it is usually expressed in terms of Å^{-1}.

4.1.1 The scattering cross section

Assuming elastic scattering events (such that the electrons energy does not change during the scattering event), the number of X-ray photons per second are recorded by a detector that subtends the solid angle element $d\Omega$, as shown in Fig. 4.3 that represent a generic scattering experiment. The *differential (microscopic) scattering cross section* is defined as

$$\frac{d\sigma}{d\Omega} = \frac{\text{number of photons scattered per second into } d\Omega}{\Phi_0\, d\Omega} = \frac{I_{\text{scattered}}}{\Phi_0\, d\Omega}, \tag{4.5}$$

where Φ_0 is the incident beam flux (number of photons per unit of area per unit of time) and $I_{\text{scattered}}$ is the scattered intensity. According to the previous definition, the differential scattering cross section dimensions are [area]. Although the SI unit of a cross section

is m^2 Cohen et al., 2007, commonly the conventional unit is the *barn* [b], where 1 b is $1 \times 10^{-28}\,\mathrm{m}^2$.
According to the previous definition, the *total (microscopic) scattering cross section* is defined by

$$\sigma = \int \frac{d\sigma}{d\Omega}\, d\Omega = \frac{\text{total number of photons scattered per second}}{\Phi_0}. \tag{4.6}$$

If the detector is placed directly in the incident beam and the change in intensity due to the sample is measured, the the corresponding *absorption cross section* is defined by considering the number of adsorption events

$$\frac{d\sigma_a}{d\Omega} = \frac{\text{number of absorption events per second into } d\Omega}{\Phi_0\, d\Omega}, \tag{4.7}$$

and the total absorption cross section is

$$\sigma_a = \int \frac{d\sigma}{d\Omega}\, d\Omega = \frac{\text{total number of absorption events per second}}{\Phi_0}. \tag{4.8}$$

The number of adsorption events per unit of time, W_a is proportional to the intensity through the sample $I(z)$ and the number of atoms per unit of area $\rho_{\mathrm{at}}\, dz$ where ρ_{at} is the atomic number density and dz is the differential sample thickness. Here, the absorption cross section is the proportionality factor and W_a is calculated by means of

$$W_a = I(z)\, \sigma_a\, \rho_{\mathrm{at}}\, dz. \tag{4.9}$$

According to the Lambert-Beer's equation, the intensity through the sample thickness is

$$I(z) = I_0\, \exp\left(-\rho_{\mathrm{at}}\, \sigma_a\, z\right), \tag{4.10}$$

where I_0 is the incident intensity and $\rho_{\mathrm{at}}\, \sigma_a$ is by definition the linear absorption coefficient Thompson et al., 2001

$$\mu = \rho_{\mathrm{at}}\, \sigma_a. \tag{4.11}$$

4.1.2 The scattering cross section of one electron

Figs. 4.3 and 4.1 schematically represent a scatterng event, where the scattering object is a single free electron. Because the energy density of the incident beam (whose incident flux is Φ_0) is proportional to $|\mathbf{E}_{in}|^2$, where $\mathbf{E}_{in}$ is its electric field, the number density of photons is proportional to $|\mathbf{E}_{in}|^2 / \hbar\omega$ and the incident flux Φ_0 is the number density multiplied by the speed of light (in vacuum) c. Similarly, the intensity of the scattered beam is proportional to the number density of the radiated beam $|\mathbf{E}_{rad}|^2 / \hbar\omega$ (where $\mathbf{E}_{rad}$ is the radiated electric field) multiplied by the subtended area of the detector $R^2\, d\Omega$ and c (the notation and the formalism in describing an electromagnetic wave refers to § C). Following the definition of Eq. (4.5), the differential scattering cross section of one electron is

$$\frac{d\sigma}{d\Omega} = \frac{|\mathbf{E}_{rad}|^2\, R^2}{|\mathbf{E}_{in}|^2}. \tag{4.12}$$

The radiated field is proportional to the charge of the electron, $-e$, and to its acceleration $a_x(t')$ calculated at a time t' earlier than the observation time t due to finite speed c at

which the radiation propagates. Therefore, the radiated field is of the form

$$E_{\mathrm{rad}}(R,t) \propto \frac{-e}{R} a_x(t') \sin(\Xi), \tag{4.13}$$

where $t' = t - R/c$ and Ξ is the angle between the x-axis and the direction of propagation. The electron acceleration is evaluated from the the force on the electron divided by its mass, that yelds

$$a_x(t') = \frac{-e}{m} E_{\mathrm{in}}\, e^{i\,k\,R}$$

where $E_{\mathrm{in}} = E_0 e^{-i\omega t}$ is the electric field of the incident wave and ω is its angular frequency. By introducing the Thomson scattering length, or classical radius, of the electron,

$$r_0 = \frac{e^2}{4\pi\epsilon_0\, m_e\, c^2}, \tag{4.14}$$

Eq. 4.12 becomes

$$\frac{d\sigma}{d\Omega} = r_0^2\, P. \tag{4.15}$$

where P is the polarization factor for scattering and depends on the X-ray source:

$$P = \begin{cases} 1 & \text{synchrotron: vertical scattering plane,} \\ \cos^2(\Xi) & \text{synchrotron: horizontal scattering plane,} \\ \frac{1}{2}\left(1 + \cos^2(\Xi)\right) & \text{unpolarized source.} \end{cases} \tag{4.16}$$

4.2 The scattering amplitude and intensity

The scattering amplitude, $A(\mathbf{q})$, for a system of scatterers is the vector sum of the scattering amplitudes from the scatterers that make up the system (Glatter and Kratky, 1982). In order to account for differences of phase, the scattering amplitude is often expressed as a complex quantity. Therefore, the scattered intensity of a system is obtained from the product $A(\mathbf{q})\, A^*(\mathbf{q})$ where $A^*(\mathbf{q})$ is its complex conjugate (Brumberger, 1994). The scattering amplitude $A(\mathbf{q})$ from a system of n scatterers is the sum of the waves scattered by these scatterers, which are located at points $\mathbf{r_k}$ with $k = 1, \ldots, n$. However, it is convenient to introduce the relative amplitude $F(\mathbf{q})$ of a scatterers, expressed in terms of electron units

$$A(\mathbf{q}) = A_e\, F(\mathbf{q}), \tag{4.17}$$

where A_e is the scattering amplitude of one electron. Commonly, the relative scattering amplitude is called amplitude form factor (Brumberger, 1994). When n scatterers have amplitudes $f_j(\mathbf{q})$, the resultant amplitude form factor $F(\mathbf{q})$ for a system of n scatterers is obtained by adding the amplitudes of the waves from the individual scatterers with allowance for the differences in the phases:

$$F(\mathbf{q}) = \sum_{j=1}^{n} f_j(\mathbf{q})\, e^{i(\mathbf{q}\cdot\mathbf{r_j})}. \tag{4.18}$$

When the scatterers are electrons $f_j(\mathbf{q}) = 1$ for all j and Eq. (4.18) becomes

$$F(\mathbf{q}) = \sum_{j=1}^{n} e^{i(\mathbf{q}\cdot\mathbf{r_j})}. \tag{4.19}$$

By considering a continuous charge distribution $\rho_e(r)$, the sum in Eq. (4.19) is replaced by volume integrals, as

$$F(\mathbf{q}) = \int_V \rho_e(\mathbf{r})\, e^{i(\mathbf{q}\cdot\mathbf{r})}\, dV. \tag{4.20}$$

Therefore, the form factor depends on the morphology of the particle in terms of size and shape, by means of the integral over the scatterer volume V.
Therefore, the scattered intensity $I(\mathbf{q})$ is

$$I(\mathbf{q}) = A(\mathbf{q})\, A^*(\mathbf{q}) = |A(\mathbf{q})|^2 = A_e^2\, F(\mathbf{q})\, F^*(\mathbf{q}) = A_e^2\, |F(\mathbf{q})|^2\,, \tag{4.21}$$

where $|F(\mathbf{q})|^2$ for a continuous distribution of charge is

$$|F(\mathbf{q})|^2 = \int_{V_2}\int_{V_1} \rho(\mathbf{r_1})\, \rho(\mathbf{r_2})\, \cos\left[\mathbf{q}\cdot(\mathbf{r_1}-\mathbf{r_2})\right] dV_1\, dV_2, \tag{4.22}$$

where $\cos\left[\mathbf{q}\cdot(\mathbf{r_1}-\mathbf{r_2})\right]$ arises by taking into account the symmetric properties of the Fourier transform when either symmetric or antisymmetric functions are considered.
In SAS literature, the particle form factor is often defined as

$$P(\mathbf{q}) = |F(\mathbf{q})|^2\,,$$

that refers to the intensity and not to the amplitude (Als-Nielsen and McMorrow, 2011). Because the amplitude form factor $F(\mathbf{q})$ is a function of the scattering vector q, $F(\mathbf{q})$ depends on both the magnitude and direction of q. However, most of the samples investigated by the SAS technique are isotropic, their amplitude form factor depends only on the scattering vector modulus q. Therefore, the measured value of the relative scattering intensity $|F(\mathbf{q})|^2$ is the average $\langle|F(\mathbf{q})|^2\rangle$ of $|F(\mathbf{q})|^2$ over all orientations of q.
According to Guiner, Fournet, and Walker (1955), by assuming that all particle orientations are equally probable $\cos\left[\mathbf{q}\cdot(\mathbf{r_1}-\mathbf{r_2})\right]$ is replaced by function $\cos(\mathbf{q}\cdot\mathbf{r})$, where vector $\mathbf{r}$ ($\mathbf{r} = \mathbf{r_1}-\mathbf{r_2}$) with magnitude r ($r = |\mathbf{r_1}-\mathbf{r_2}|$) takes all orientation with equal probability. In addition, letting the angle between the angle between the two vectors $\mathbf{q}$ and $\mathbf{r}$ indicated as α the average phase function is

$$\left\langle e^{i\,\mathbf{q}\cdot\mathbf{r}}\right\rangle = \frac{\displaystyle\int_0^{2\pi}\int_0^{\pi} e^{i\,q\,r\,\cos(\alpha)}\sin(\alpha)\, d\alpha\, d\phi}{\displaystyle\int_0^{2\pi}\int_0^{\pi}\sin(\alpha)\, d\alpha\, d\phi} = \frac{\sin(q\,r)}{q\,r} = \langle\cos(\mathbf{q}\cdot\mathbf{r})\rangle\,, \tag{4.23}$$

and Eq. (4.22) becomes

$$|F(\mathbf{q})|^2 = \int_{V_2}\int_{V_1} \rho(\mathbf{r_1})\, \rho(\mathbf{r_2})\, \frac{\sin(q\,r)}{q\,r}\, dV_1\, dV_2. \tag{4.24}$$

4.2.1 Centrosymmetric particle

When a center of symmetry exists, Eq. (4.20) by accounting for Eq. (4.23) becomes

$$\langle F(q)\rangle = \int_V \rho_e(r)\,\frac{\sin(q\,r)}{q\,r}\,dV, \tag{4.25}$$

and considering the following definition,

$$\int_r^{r+dr} \rho_e(r)\,dV = 4\pi\,r^2\,\bar{\rho}_e(r)\,dr, \tag{4.26}$$

Eq. (4.25) becomes

$$\langle F(q)\rangle = \int_0^{\infty} 4\pi\,r^2\,\bar{\rho}_e(r)\,\frac{\sin(q\,r)}{q\,r}\,dr. \tag{4.27}$$

4.2.2 Spherically symmetric particle

A particular case of the scattering amplitude form factor is that of a spherically symmetric particle. In this case, the electronic density at any point depends only on the distance r of this point from the center of the particle and is denoted as $\rho_e(r)$[1]. Therefore, Eq. (4.27) becomes

$$\langle F(q)\rangle = \int_0^{\infty} \rho_e(r)\,\frac{\sin(q\,r)}{q\,r}\,4\pi\,r^2 dr, \tag{4.28}$$

by replacing $\bar{\rho}_e(r)$ with $\rho_e(r)$. For this particular case, it can be demonstrated that a rotation of the particle does not change the amplitude of the scattered radiation (Guiner, Fournet, and Walker, 1955)

$$\left\langle F^2(q)\right\rangle = \langle F(q)\rangle^2 = F^2(q).$$

Form factor of isolated particles

The form factor of an isolated sphere or radius R is obtained by solving Eq. (4.28) over the sphere volume. However, according to Brumberger (2013) it is convenient to express the single particle form factor amplitude as

$$\langle F(q)\rangle = V\,\Phi(q), \tag{4.29}$$

where $\Phi(q)$ is

$$\Phi(q) = \frac{1}{V}\int_0^{\infty} \rho_e(r)\,\frac{\sin(q\,r)}{q\,r}\,4\pi\,r^2 dr. \tag{4.30}$$

By considering spherical coordinates, Eq. (4.30) becomes

$$\Phi(q) = 3\,\frac{\sin(qR) - qR\,\cos(qR)}{(qR)^3} = \frac{3\,J_1(qR)}{qR}, \tag{4.31}$$

where $J_1(qR)$ is the Bessel function of the first kind. Figs. 4.4a and 4.4b show the reduced scattering form factor ($|\Phi(q)|^2$) of a spherical particle for two different choices of sphere radius. In addition, when $q = 0$, $|\Phi(q)|^2 = 1$.

[1]For this reason, $\rho_e(r) = \bar{\rho}_e(r)$ when scatterers are spherically symmetric.

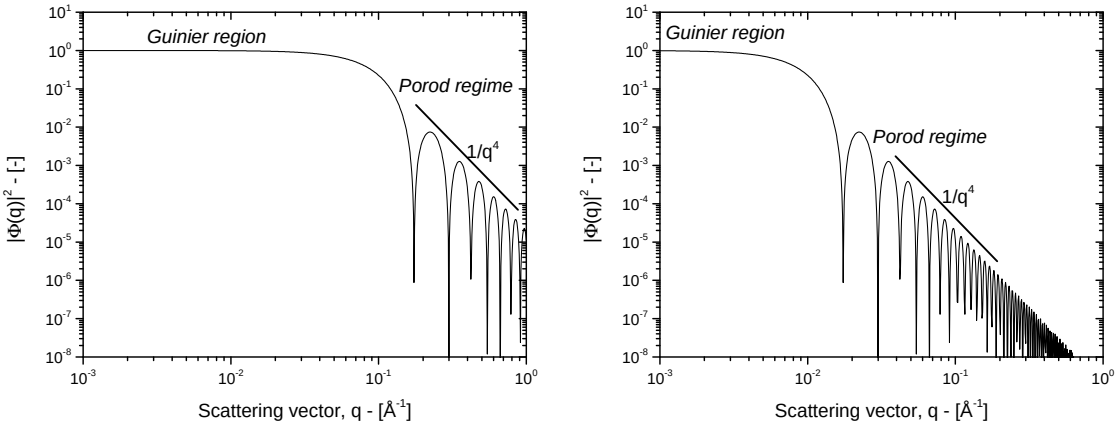

(a) $R_g = 20\,\text{Å}$ *(*$R \cong 25.8\,\text{Å}$*).* **(b)** $R_g = 200\,\text{Å}$ *(*$R \cong 258\,\text{Å}$*).*

Figure 4.4: Calculated reduced scattering form factor amplitudes for a sphere of different radii.

The Guinier regime

According to Glatter and Kratky (1982), in the long-wave limit, namely when $qR \to 0$, if Eq. (4.31) is expanded, it becomes

$$\Phi(q) = \frac{3}{(qR)^3}\left[qR - \frac{q^3R^3}{3!} + \frac{q^5R^5}{5!} - \ldots\right], \tag{4.32}$$

that simplifies to give

$$\Phi(q) \approx 1 - \frac{q^2R^2}{10}. \tag{4.33}$$

Therefore, by considering that $e^{-x} \approx 1 - x$, Eq. (4.30) in the long-wave limit becomes

$$|\Phi(q)|^2 \approx e^{-\frac{q^2R^2}{5}}. \tag{4.34}$$

When the long-wave approximation is verified the scattering intensity over the scattering vector q is used to determine the radius of the particle R (Glatter and Kratky, 1982). Specifically, the Gunier plot consists in plotting $\ln[I(q)]$ vs q^2 in order to obtain a straight line, whose slope $-R^2/5$ is used to determine the particle radius.
According to Als-Nielsen and McMorrow (2011), the Guinier analysis can be applied no only for the case of spheres but also to the SAS profiles of any dilute system containing scatterers or arbitrary shape. However, in this case the sphere radius is replaced by the radius of gyration.
The radius of gyration R_g is defined as the root-mean squared distance from the particle center of gravity. If the particle electron density is uniformly distributed with spherical symmetry, the squared radius of gyration is

$$R_g^2 = \frac{1}{V}\int_V r^2\,dV. \tag{4.35}$$

More generally, if the electron density is not uniformly distributed into the scatterer, the radius of gyration is obtained firstly evaluating (Als-Nielsen and McMorrow, 2011)

$$R_g^2 = \frac{\int_V \rho_e(\mathbf{r}) r^2 \, dV}{\int_V \rho_e(\mathbf{r}) \, dV}. \tag{4.36}$$

and then performing an orientational average.
For the case of uniform spheres

$$R_g^2 = \frac{3}{5} R^2, \tag{4.37}$$

such that Eq. (4.34) becomes

$$|\Phi(q)|^2 \approx e^{-\frac{q^2 R_g^2}{3}}, \tag{4.38}$$

that is commonly used to estimate the radius of gyration from the Guinier plot. Despite this equation was derived fro the case of spherical scatterers of uniform density, its validity is generally true (Als-Nielsen and McMorrow, 2011).
The radius of gyration represents the effective size of the scatterer whether the size and shape of the scattering particle. In addition, the Guinier analysis fro the R_g determination is independent of the absolute intensity and of any model (Als-Nielsen and McMorrow, 2011).

The Porod regime

Opposite to the Guinier analysis, the Porod regime is verified for the case of the short wavelength limit, namely when $qR \gg 1$ (Porod, 1951; Glatter and Kratky, 1982). Therefore, under such regime Eq. (4.31) becomes

$$\Phi(q) = \left[\frac{\sin(qR)}{q^3 R^3} - \frac{\cos(qR)}{q^2 R^2} \right] \approx 3 \left[-\frac{\cos(qR)}{q^2 R^2} \right], \tag{4.39}$$

and $|\Phi(q)|^2$ is

$$|\Phi(q)|^2 = 9 \, \frac{\langle [\cos(qR)]^2 \rangle}{q^4 R^4} = \frac{9}{2} \frac{1}{q^4 R^4}. \tag{4.40}$$

By considering that the relationship between the volume V and the surface S of a sphere is

$$V^2 = \left[\frac{4\pi}{3} R^3 \right]^2 = \frac{4\pi}{9} R^4 \, S$$

Eq. (4.40) changes into

$$|\Phi(q)|^2 = \frac{2\pi}{q^4} S, \tag{4.41}$$

that is the so-called Porod law. Therefore, in the short-wavelength limit the SAS intensity is proportional to the surface area of a sphere and inversely proportional to the fourth power of q. Usually, the Porod plot, namely $|\Phi(q)|^2 \, q^4$ vs q, is used to determine the q region where the Porod regime falls, whose slope is -4 (Figs. 4.4 and 4.5).

4.3 The scattering contrast

In general, scatterers with an electron density $\rho_e(\mathbf{r})$ are suspended in a scattering medium that has an uniform electron density $\rho_{e,0}$. Assuming that scatterer occupies a volume V_s and the total sample volume is V, that of the suspending medium is $V - V_s$. As consequence, the scattering amplitude form factor $F(\mathbf{q})$ of the sample is

$$F(\mathbf{q}) = \int_{V_s} \rho_e(\mathbf{r})\, e^{i\,q\cdot\mathbf{r}}\, dV + \rho_{e,0} \int_{V-V_s} e^{i\,q\cdot\mathbf{r}}\, dV, \tag{4.42}$$

that can be written as

$$F(\mathbf{q}) = F_s(\mathbf{q}) + F_M(\mathbf{q}),$$

where

$$F_s(\mathbf{q}) = \int_{V_s} [\rho_e(\mathbf{r}) - \rho_{e,0}]\; e^{i\,q\cdot\mathbf{r}}\, dV, \tag{4.43}$$

and

$$F_M(\mathbf{q}) = \rho_{e,0} \int_{V} e^{i\,q\cdot\mathbf{r}}\, dV. \tag{4.44}$$

By comparing Eq. (4.20) with Eq. (4.44), $F_M(\mathbf{q})$ is the amplitude of a scatterer with a uniform density with a characteristic scatterer size of the order of the medium size. This size normally is of the order of at least a tenth of a millimeter (Brumberger, 1994). On the other hand, scatterer sizes that can be studied by SAS are rarely greater than a few tenths of a micrometer, because equipment cannot be constructed that will allow intensity measurements at q values small enough to investigate larger scatterers. Therefore, for all the observable values of q, $F_M(\mathbf{q})$ can be expected to be negligible if compared with compared to $F_s(\mathbf{q})$ (Brumberger, 1994).
Consequently, when, instead of being in a vacuum, a scatterer is immersed in a medium of constant electron density $\rho_{e,0}$, the observable amplitude $F(\mathbf{q})$ can be obtained from Eq. (4.20) by replacing the electron density $\rho_e(\mathbf{r})$ of the scatterer with the effective electron density, that is

$$\rho_e(\mathbf{r}) - \rho_{e,0}.$$

Additionally, when the electron density $\rho_e(\mathbf{r})$ has a constant value $\rho_{e,1}$, the resulting observable amplitude $F_s(\mathbf{q})$ is

$$F_s(\mathbf{q}) \approx (\rho_{e,1} - \rho_{e,0}) \int_{V_s} e^{i\,q\cdot\mathbf{r}}\, dV, \tag{4.45}$$

such that $\langle |F_s(\mathbf{q})|^2 \rangle$ is proportional to $(\rho_{e,1} - \rho_{e,0})^2$, that is indicated as $\Delta\rho_e^2$ and defines the sample scattering contrast. Precisely, $\langle |F_s(\mathbf{q})|^2 \rangle$ is also proportional to the value that would be obtained when a scatterer of electron density $\rho_{e,0}$ is suspended in a medium of electron density $\rho_{e,1}$. Therefore, scattering experiments cannot distinguish between the two systems and this is often called the "two phase approximation" (Brumberger, 1994).

4.4 The absolute units

The SAS data provided by a detector are usually conveniently rescale to form the macroscopic scattering cross section $d\Sigma/d\Omega$ in terms of cm^{-1}, defined as

$$\frac{d\Sigma}{d\Omega} = \frac{d\sigma}{d\Omega}\,\frac{N}{V_{\mathrm{sample}}}, \tag{4.46}$$

where N/V_{sample} is the scatterers number density into the probing sample. This procedure requires the measurement of the scattering sample intensity $I(q)$ and of the empty beam transmission $I_0(\lambda)$, which is the incident beam intensity. Therefore, these intensities are linked to the absolute intensity, namely the macroscopic scattering cross section as

$$I(q) = I_0(\lambda)\,T(\lambda)\,e_s\,\frac{d\Sigma}{d\Omega}\,(q)\;\Omega \tag{4.47}$$

where $T(\lambda)$ is the measured sample transmission coefficient, e_s is the sample thickness and Ω is the solid angle subtended by the detector. Specifically, $I_0(\lambda)$ is given by

$$I_0(\lambda) = \Phi_0(\lambda)\,A_0,\,\eta, \tag{4.48}$$

where Φ_0 is the incident flux of photons on sample, A_0 is the illuminated area and η is the detector efficiency. Therefore, the scattering cross section is obtained through Eq. (4.47) once $I(q)$, $I_0(\lambda)$, $T(\lambda)$ and the other constants are noticed,

$$\frac{d\Sigma}{d\Omega}\,(q) = \frac{I(q)}{I_0(\lambda)\,T(\lambda)\,e_s}. \tag{4.49}$$

Finally, it is remarkable to notice that the macroscopic scattering cross section $d\Sigma/d\Omega$ is expressed in terms of scattering cross section per unit of sample volume.
However, in some cases it is more convenient to express the absolute intensity in terms of unit of sample mass (inside the illuminated volume) instead of unit of sample illuminated volume, for example when the sample holder has not common geometries or when sample is a granular material and it becomes difficult to correctly estimate the illuminated volume. Once the sample thickness is notice, the differential scattering cross section per unit of sample mass $d\Sigma_m/d\Omega$ is equal to $d\Sigma/d\Omega$ multiplied by the illuminated sample volume and divided by the sample mass,

$$\frac{d\Sigma_m\,(q)}{d\Omega} = \frac{I(q)}{I_0(\lambda)\,T(\lambda)\,e_{\mathrm{solid}}\,\rho_{\mathrm{solid}}}, \tag{4.50}$$

where e_{solid} is the solid sample thickness and ρ_{solid} is the material skeleton density.

4.4.1 Macroscopic cross section from a monodisperse system

For an infinitely diluted system made of a monodisperse collection of scatterers, the macroscopic scattering cross section is expresses as (Pedersen, 1997)

$$\frac{d\Sigma\,(q)}{d\Omega} = \frac{N}{V_{\mathrm{sample}}}\,\Delta\rho_e^2\,V^2\,P(q), \tag{4.51}$$

where N/V_{sample} is the scatterers number density, $\Delta\rho_e^2$ is the scattering contrast, V is the scatterer volume and $P(q)$ i the particle form factor (Pedersen, 1997), defined as

$$P(q) = |\Phi(q)|^2\,.$$

Additionally, by considering the scatterers volume fraction ϕ_v,

$$\phi_v = \frac{N}{V_{\text{sample}}} V,$$

Eq. 4.51 becomes

$$\frac{d\Sigma\,(q)}{d\Omega} = \phi_v\,\Delta\rho_e^2\,V\,P(q). \tag{4.52}$$

4.4.2 The Polydispersivity

The SAS analysis applied to polydispersed systems become significantly complicated than the case of monodispersed samples. However, according to (Pedersen, 1997) it is possible to use a local monodisperde approximation to include the polydispersivity effects on the SAS intensity profiles (Pedersen, 1994). This approach assumes that a particle of a certain size, is always surrounded by particles with the same size. Accordingly, the scattering is approximated by that of monodisperse sub-systems weighted by the size distribution, namely

$$\frac{d\Sigma\,(q)}{d\Omega} = \frac{N}{V_{\text{sample}}}\,\Delta\rho_e^2 \int_0^\infty f(R)\,V^2(R)\,P(q,R)\,dR, \tag{4.53}$$

where $f(R)$ is the normalized number size distribution $\int_0^\infty f(R)\,dR = 1$.
It should be noted, that the validity of Eq. (4.53) is restricted for those systems with small polydispersities and the detailed description for polydisperse systems refers to other literature contributions, like Kotlarchyk and Chen (1983), Brumberger (1994), or Pedersen (1997).
From a qualitative point of view, polydispersivity acts to smear out features in the SAXS profiles (Als-Nielsen and McMorrow, 2011). Fig. 4.5 shows the polydispersivity effects on a collection of spherical particles whose radius is 30 Å. Specifically, in this figure it is assumed that the spherical particles are normally distributed $\mathcal{N}(\mu, \sigma^2)$ where μ and σ^2 are the mean and the variance of the normal distribution $\mathcal{N}$ and three different cases of polydispersivity (i.e the dimensionless ratio σ/μ) were considered, namely 5 %, 10 % and 30 %. The dashed black like refers to the well-defined SAS profile from monodispersed spheres with radius 30 Å. However, a modest percentage polydispersivity, such as 5 % (continuous blue line) leads to to a rapid damping of the intensity oscillations. As the percentage polydispersivity increases, the smoothing effect on the SAS curve increases up to the total disappear of the characteristic oscillations.

4.4.3 The Porod invariant

The Porod invariant (Porod, 1951) is an important integral feature of the scattering intensity. Specifically, the Porod invariant Q is defined as (Glatter and Kratky, 1982)

$$Q = \int_0^\infty \frac{d\Sigma(q)}{d\Omega}\,q^2\,dq = 2\pi^2\Delta\rho_e^2\,\varepsilon\,(1-\varepsilon), \tag{4.54}$$

where ε is the scatterer volume fraction into the illuminated volume. This integral is extremely useful to estimate the particle volume fraction (i.e. in this work the porosity of pores) once the scattering intensity is expressed in terms of absolute units. Even if the integration integral is infinite, it can be demonstrated that the resulting value, the invariant Q, is limited (Porod, 1951; Guiner, Fournet, and Walker, 1955; Glatter and Kratky, 1982; Brumberger, 1994).

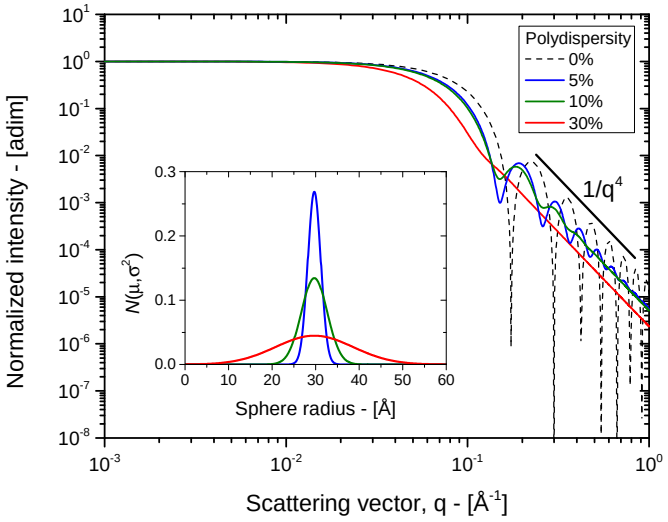

Figure 4.5: Effect of the polydispesivity percentage on the calculated SAS profiles for spherical particles. Dashed line refers to a monodispersed collection of spheres of radius 30 Å. Normal distributions centered on 30 Å are represented in the inset for different polydispesivity percentages (5 %, 10 % and 30 %).

4.5 The scattering structure factor: inter-particle interactions

The validity of the aforementioned equations is restricted to highly diluted systems. When the scatterers concentration increases inter-particle correlations may be accounted for by introducing a structure factor $S(q)$ (Als-Nielsen and McMorrow, 2011). The structure factor describes the interference of scattering from different particles and contains information on the interaction between the particles. For very dilute systems $S(q) = 1$ and the structure factor can be neglected (Pedersen, 1997).
Therefore, for a mono-disperse collection of (spherically symmetric) concentrated particles the scattering cross section of Eq. (4.52) becomes (Pedersen, 1997)

$$\frac{d\Sigma\,(q)}{d\Omega} = \phi_v\,\Delta\rho_e^2\,V\,P(q)\,S(q), \tag{4.55}$$

while for polydisperse systems Eq. (4.53) changes into

$$\frac{d\Sigma\,(q)}{d\Omega} = \frac{N}{V_{\text{sample}}}\,\Delta\rho_e^2\int_0^\infty f(R)\,V^2(R)\,P(q,R)\,S(q,R)\,dR. \tag{4.56}$$

Only in few cases the structure factor can be analytically calculated. Most of the available results have been obtained from liquid state theory for particles with spherical symmetry interacting with a spherically symmetric potential (Pedersen, 1994). The Ornstein-Zernike approach is a suitable way to describe inter-particle contributions. Specifically, the Ornstein-Zernike integral equation with an approximate closure relation that relates the interaction potential to the direct correlation function (D'Aguanno and Klein, 1991).
In this work, the Percus-Yevick approximation (Percus and Yevick, 1958) is used as a closure relationship that solves the Ornstein-Zernike integral equation. This closure assumes particles with a hard-sphere radius R_{HS} and a hard-sphere volume fraction η interacting with a hard-sphere potential. Therefore, the final formulation for $S(q)$ is calculated

accounting for the Percus-Yevick approximation (Kinning and Thomas, 1984) providing

$$S(q) = \frac{1}{1 + 24\eta \, \dfrac{G(q\,R_{HS})}{q\,R_{HS}}}, \tag{4.57}$$

where in Eq. (4.57) $G(q\,R_{HS})$ is

$$G(A) = \alpha \left[\frac{\sin(A) - A\,\cos(A)}{A^2}\right] + \beta \left[\frac{2A\,\sin(A) + (2 - A^2)\cos(A) - 2}{A^3}\right] + \\ + \gamma \left[\frac{6 - A^4\,\cos(A) + 4\,(3A^2 - 6)\cos(A) + (A^3 - 6A)\sin(A)}{A^5}\right], \tag{4.58}$$

and

$$\alpha = \frac{(1 + 2\eta)^2}{(1 - \eta^4}, \\ \beta = -6\eta \frac{(1 + \eta/2)^2}{(1 - \eta)^2}, \\ \gamma = \eta\,\frac{\alpha}{2}.$$

Beaucage et al. (1995) used a semi-empirical function based on Eq. (4.57) for $S(q)$ which describes correlations of particles or domains in terms of a radius of correlation, ζ (the corresponding R_{HS} in Eq. (4.57)), and a packing factor, κ,

$$S(q) = \frac{1}{1 + 3\kappa \, \dfrac{[\sin(q\,\zeta) - q\,\zeta\,\cos(q\,\zeta)]}{(q\,\zeta)^3}}, \tag{4.59}$$

where Eq. (4.59) is obtained from Eq. (4.57) by substituting η with κ and letting $\kappa \to 0$. The packing factor describes the degree of correlation ($0 < \kappa < 5.92$) and is equal to 8 times the hard-sphere volume fraction (Beaucage et al., 1995). The maximum value of κ, 5.92, is obtained by calculation of this ratio for hexagonal or cubic close-packed crystal structures. Moreover, weakly correlated particles are expected to display two size scales, ζ, the average Bragg-like spacing between domains and the radius of gyration, R_g, for the domains. In general $\zeta \geq R_g$ and corresponds well with the Bragg-spacing of $2\pi/q_{\max}$ where $q_{\max}$ is the value of q for the maximum peak intensity. The effects of ζ and κ values on the final structure factor profile is shown in Figs. 4.6a and 4.6b respectively.

4.6 The unified fit approach

In this work of thesis the analysis of the USAXS and SAXS intensity profiles (expressed in terms of absolute units on a sample mass basis) was performed using the IGOR Pro-based IRENA program (Ilavsky and Jemian, 2009). Specifically the "Unified fit" tool was used to fit the slit-smeared scattering intensity profiles. Such tool is based on the unified approach proposed by Beaucage (1995) and Beaucage (1996), that allows the description of the SAS profiles over a wide range of q by means of an arbitrary number of interrelated structural levels. This provides the model with a high flexibility in describing the SAS response of multiple-size-scale structures (Beaucage, 1995). Each level is characterized by a Guinier regime and a power law regime. A specific power law regime, namely the Porod regime, is identified when the local scattering intensity vs q slope in a double logarithmic plot is

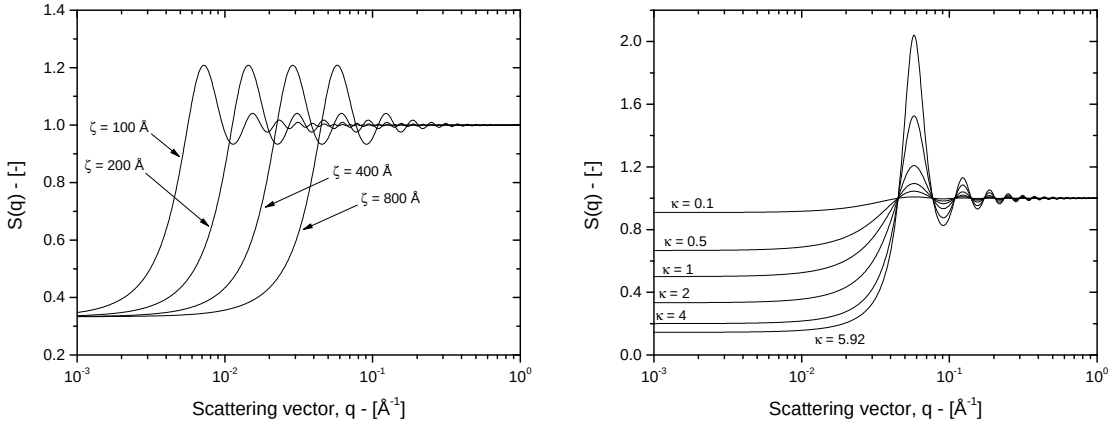

(a) *Varying* ζ, $\kappa = 2$. **(b)** *Varying* κ, $\zeta = 100\,$Å.

Figure 4.6: Parameters effects on the final structure factor $S(q)$ of Eq. 4.59.

-4 (Glatter and Kratky, 1982). Even though the model is derived assuming spherical and centrosymmetric particles (Beaucage, 1995), thanks to its formulation in terms of radius of gyration and free power-law exponents it can be applied to a broad range of scattering intensity profiles of different scatterer shapes, like spheres, rods, lamellae, cylinders etc. Beaucage (1995) and Beaucage (1996).

The unified fit approach proposed by Beaucage (1995) and Beaucage (1996) is expressed as a summation of terms, each representing a structural level, in addition to the background constant:

$$\frac{d\Sigma_m(q)}{d\Omega} \cong \sum_{i=1}^{n} \frac{d\Sigma_{m,i}(q)}{d\Omega} + B_{bkg,m} = \sum_{i=1}^{n} \left\{ G_i \exp\left(-\frac{q^2\, R_{g,i}^2}{3}\right) + \right.$$
$$\left. + B_i \exp\left(-\frac{q^2\, R_{g,i-1}^2}{3}\right) \left[\frac{\left(\operatorname{erf}\left(q\, R_{g,i}\right)/\sqrt{6}\right)^3}{q} \right]^{P_i} \right\} S_i(q) + B_{bkg,m}. \quad (4.60)$$

In Eq. (4.60) $i = 1$ refers to the smallest-size structural level (Ilavsky and Jemian, 2009), n is the number of the structural levels, G_i is the Guinier exponential prefactor of level i, $R_{g,i}$ is the radius of gyration of level i, B_i is the constant prefactor of the power law scattering profile of level i, P_i is the power law exponent, which assumes the value of 4 when the scattering profile falls in the Porod regime, $S_i(q)$ are the structure factors of each level i, and $B_{bkg,m}$ is the background constant (over q). $R_{g,i-1}$ defines the high-q power-low cut-off size of each level and it is usually equals to the radius of gyration of the previous level, as suggested by Beaucage (1995). Specifically, the cut-off radius of gyration of the first level was set to zero, because no smaller structural level influences the first level structures.

When the scatterers interactions are negligible (ideal case), the structure factor approaches to 1 (Lurio et al., 2000) and the unified model described by Eq. (4.60) is equivalent to the formulation proposed by Beaucage (1995). As the scatterer concentration increases, a structure factor may be required to account for the interferences in the scattering intensity profile (Glatter and Kratky, 1982; Lurio et al., 2000). Specifically, in this work a structure factor was taken into account, based on the hard sphere model (Ilavsky and Jemian, 2009), which includes two additional fitting parameters, namely the packing factor κ_i and the correlation distance ζ_i, according to Eq. (4.59).

All the fitting parameters (G_i, B_i, $R_{g,i}$, P_i, κ_i, ζ_i, with $i = 1, 2, \ldots, n$ and $B_{bkg,m}$) were estimated from the experimental scattering intensity profiles by a non-linear Levemberg-Marquardt least-squares fitting. The expressions of the differential scattering cross section obtained by fitting the experimental scattering intensity data by means of Eq. (4.60) were used to estimate the particle porosity and the specific surface area. Specifically, the particle (internal) porosity ε (defined as the volume of the pores inside the particles over the particle volume) was calculated by using the Porod invariant (Glatter and Kratky, 1982) for a two phase system (in this case pores and the solid matrix). The relationship between the Porod invariant Q (expressed in terms of sample volume) and the particle porosity is provided by the following equation:

$$Q = Q_v = \int_0^\infty \left(\frac{d\Sigma_v(q)}{d\Omega} - B_{bkg,v} \right) q^2 \, dq = 2\pi^2 \, \Delta\rho_e^2 \, \varepsilon \, (1 - \varepsilon), \tag{4.61}$$

where the Porod invariant was conveniently renamed as Q_v for the sake of clarity. In Eq. (4.61) $\Delta\rho_e^2$ is is the scattering contrast between voids and the solid matrix and in this work is equal to the scattering length density of the solid phase and $B_{bkg,v}$ is the background constant expressed per unit of sample volume. The differential scattering cross sections per unit of sample mass and of sample volume are related by the following equation:

$$\left(\frac{d\Sigma_m(q)}{d\Omega} - B_{bkg,m} \right) = \frac{1}{\rho_{\text{solid}}(1 - \varepsilon)} \left(\frac{d\Sigma_v(q)}{d\Omega} - B_{bkg,v} \right). \tag{4.62}$$

By substituting Eq. (4.62) into Eq. (4.61) the Porod invariant in terms of unit of sample mass Q_m can be defined and related directly to the particle porosity:

$$Q_m = \int_0^\infty \left(\frac{d\Sigma_m(q)}{d\Omega} - B_{bkg,m} \right) q^2 \, dq = \frac{2\pi^2 \, \Delta\rho_e^2 \, \varepsilon}{\rho_{\text{solid}}}. \tag{4.63}$$

The experimental differential scattering cross section per unit of sample mass was fitted by means of the Beaucage model represented in Eq. (4.60), therefore the scattering intensity profile is the result of the summation over the contributions $d\Sigma_{m,i}(q)/d\Omega$ of the n structural levels (in addition to the background constant). Thus, the Porod invariant can be computed as the summation of n integrals

$$Q_{m,i} = \int_0^\infty \frac{d\Sigma_{m,i}(q)}{d\Omega} \, q^2 \, dq,$$

related to the particle porosity by the following equation:

$$Q_{m,i} = \frac{2\pi^2 \, \Delta\rho_e^2}{\rho_{\text{solid}}} \varepsilon_i, \tag{4.64}$$

where ε_i is the contribution to the particle porosity of the structural level i and $\varepsilon = \sum_{i=1}^{n} \varepsilon_i$. Typically, the sample specific area of an ideal two-phase system with one structural level can be estimated in the Porod regime as the constant prefactor of the power law scattering profile divided by $2\pi\Delta\rho_e^2$ (Beaucage, 1995; Hu et al., 2011). Accordingly, in this work, the contribution to the specific surface (per unit of sample mass) of the structural level i is estimated in the Porod regime as

$$S_{m,i} = \frac{B_i}{2\pi \, \Delta\rho_e^2}. \tag{4.65}$$

Additionally, the total sample specific surface area per unit of sample mass is computed as the sum of the contributions of each structural level $S_m = \sum_{i=1}^{n} S_{m,i}$.

4.6.1 Pore size distributions

The sample pore size distributions (PSDs) were obtained following the method of Beaucage, Kammler, and Pratsinis (2004), that estimates the sample PSDs in terms of number distributions using the unified fit parameters. This methodology was applied to each structural level i (Ilavsky and Jemian, 2009). Assuming a log-normal distribution for a monomodal distribution of spheres (spherical pores), namely assuming that the sample pore radius (R) distribution for each structural level $f_i(R)$ is computed as

$$f_i(R) = \frac{1}{R\,\sigma_i\,\sqrt{2\pi}} \exp\left\{\frac{\left[\ln\left(R/m_i\right)\right]^2}{2\,\sigma_i^2}\right\} \tag{4.66}$$

where the two parameters of the log-normal distribution, namely the median m_i and the standard deviation σ_i of each structural level i were estimated by means of the unified fit parameters (the radius of gyration $R_{g,i}$, the Guinier regime prefactor G_i and the Porod's law constant P_i) calculated from the non-linear fitting of the experimental scattering intensity profiles. Specifically, the standard deviation of level i was calculated as follows (Beaucage, Kammler, and Pratsinis, 2004)

$$\sigma_i = \left[\frac{1}{12}\ln\left(\frac{B_i\,R_{g,i}^4}{1.62\,G_i}\right)\right]^{1/2}, \tag{4.67}$$

and the median value of level i as

$$m_i = \left[\frac{5}{3}\frac{R_{g,i}^2}{\exp\left(14\,\sigma_i^2\right)}\right]^{1/2}. \tag{4.68}$$

In order to obtain the volume distributions (per unit of particle volume) $f_{v,i}(R)$, the number distributions were multiplied by the sphere volume and by the ratio of the total number of spheres over the particle volume. Finally, the total pore size distribution $f_v(R)$ was calculated by summing the PSDs associated with the structural levels,
According to this approach, the number of pore distribution per unit of mass $f_{m,i}(R)$ of level i was calculated from the corresponding fractional numeral pore distribution according to

$$f_{m,i}(R) = \frac{\varepsilon_i}{\rho(1-\varepsilon_i)}\frac{f_i(R)}{\displaystyle\int_0^\infty f_i(R)\,\frac{4}{3}\pi\,R^3\,dR}. \tag{4.69}$$

Therefore, the total number of pore per unit of sample mass of each level was estimated by integrating Eq. (4.69) over the sample radius domain

$$N_{m,i} = \int_0^\infty f_{m,i}(R)\,dR. \tag{4.70}$$

where the total number of pores for each time-step was estimated by means of $N_m = \sum_{i=1}^{n} N_{m,i}$.
Finally, the mean pore radius $\langle R_{v,i}\rangle$ associated to each distribution $f_{v,i}$ was calculated from the standard deviation and the median values through the relationship $\langle R_{v,i}\rangle =$

$m_i \exp\left(\sigma_i^2/2\right)$ citepEvans2000 and the overall mean pore radius $\langle R_v \rangle$ associated with the total pore size distribution was numerically computed as

$$\langle R_{v,i} \rangle = \frac{\int_0^\infty f_v(R)\, R\, dR}{\int_0^\infty f_v(R)\, dR}. \tag{4.71}$$

4.7 The X-ray properties of matter

The scattering contrast was introduced and defined in § 4.3. This quantity is essential to correctly estimate those scatterer properties that depends on the absolute scattering intensities (like porosity, specific surface area and pore number density). In this work the scattering contrast is defined as

$$\Delta\rho_e^2 = \left(sld_1 - sld_0\right)^2, \tag{4.72}$$

where sld_i is the scattering length density of the specie i and, as previously mentioned, subscripts 1 and 2 refers to the scatterer matter and the medium (solvent) respectively. Before to provide the equations to calculate the scattering length density of compounds (§ 4.7.2) it is necessary to introduce the atomic form factor f_i from which the sld_i is calculated.

4.7.1 The Atomic Form Factor

According to Als-Nielsen and McMorrow, 2011, a volume of element $d\mathbf{r}$ at $\mathbf{r}$ contributes an amount of $-r_0\, \rho_e(\mathbf{r})\, dV$ to the scattered field with a phase factor of $\exp\left(i\mathbf{q}\cdot\mathbf{r}\right)$, where $\rho_e(\mathbf{r})$ is the local electron number density of the atom, such that the total scattering length of one atom is

$$-r_0\, f^0(\mathbf{q}) = -r_0 \int_V \rho_e(\mathbf{r}) e^{(i\mathbf{q}\cdot\mathbf{r})}\, dV \tag{4.73}$$

where $f^0(\mathbf{q})$ is defined as the *atomic form factor*. In the limit values of the scattering vector i.e. $q \to 0$ all the atom volume elements scatter in phase such that $f^0(\mathbf{q}=0) = Z$, that is the number of electrons in the atom. On the other hand, as q increases, different volume elements scatter out of phase and consequently $f^0(q \to \infty) = 0$.
Additionally, the atomic form factor is the Fourier transform of the electron number distribution in the atom volume (or in the sample volume) and the scattered intensity is the product of Eq. (4.73) and its complex conjugate. Actually, the atomic form factor (in units of $-r_0$) is a complex number that includes the dispersion corrections f' and f'', such that

$$f(\mathbf{q}, \hbar\omega) = f^0(\mathbf{q}) + f'(\hbar\omega) + i f''(\hbar\omega), \tag{4.74}$$

where the real and the imaginary parts of the dispersion corrections f' and f'' are functions of the X-ray energy $\hbar\omega$ (or equivalently frequency) and their behavior is dominated by the tightly bond inner-shell electron. The values of these two dispersion contributors assume their extremal values when the X-ray energy is equal to one of the absorption edge energies of the atom and this behavior is strictly element specific. For this reason they are also known as the resonant scattering terms. On the other hand, the Thomson term $f^0(\mathbf{q})$ only depends on the scattering vector $\mathbf{q}$, because the non-resonant scattering i produced by all atomic electrons, which have a spatial order of magnitude as the X-ray wavelength.
The atomic form factor values can be estimated from several sources, like Thompson et al.

(2001) or web-sites, like NIST (1997) (based on the literature contribution by Chantler (1995)). Additionally, according to Als-Nielsen and McMorrow (2011), several effort have been spent to calculate the atomic form factor of free atoms from their wavefunctions, like Cromer and Mann, 1968 or the tabulated values of in the International Tables for Crystallography Kopsky and Litvin, 2010. The well-known Kramers-Kronig relations are used to calculated of the dispersion corrections values (Als-Nielsen and McMorrow, 2011) of one atom, even if more accurate and realistic models are available in literature, such as Chantler (1995) or Henke, Gullikson, and Davis (1993).
Usually, the atomic form factor of an element is expressed in term of its real and imaginary part, indicated as f_1 and f_2 respectively.
In this work, the CaO-based solid sorbent were tested by means of the X-ray SAS technique. More specifically, porous calcium oxide (CaO) was investigated, whose solid precursor is calcium carbonate ($CaCO_3$). Therefore, the atomic form factor of their elements (Ca, C and O) were obtained from NIST (1997) database, that provides the real and the imaginary parts of the dispersion corrections f' and f'' over the beam energy for each element. These data were combined in order to provide the molecular form factor dispersion corrections of CaO and $CaCO_3$. The results in terms of f' and f'' vs the beam energy are represented in Fig. 4.7a for CaO and Fig. 4.7b for $CaCO_3$. These profiles are clearly highly non-linear and are characterized by a series of edges due to the K-shell of the elements their are made of, that generate discontinuities into the dispersion corrections f' and f''.

4.7.2 The Scattering Length Density

The atomic scattering length density, *sdl* is defined as

$$sdl = r_0 \, \rho_{\text{at}} \, f_1, \tag{4.75}$$

where f_1 is the real part of the atomic form factor and

$$\rho_{\text{at}} = \frac{\rho_i \, \text{Na}}{M_i}, \tag{4.76}$$

where ρ_i is the atomic (or molecular) mass density, Na is the Avogradro's number and M_i is the atomic (molecular) weight. Obviously, the product $r_0 \, f_1$ is the scattering length of one atom i (b_i).
Considering a molecule made of NA atoms ($\prod_{i=1}^{\text{NA}} A_{i,n_i}$, where A_i represents the i-th element) with number of atom i n_i and weight fractions w_i where $i = 1, \ldots, \text{NA}$, it can be demonstrated that the total scattering length of such molecule is

$$sld_{\text{molec}} = \frac{\rho_{\text{molec}} \, \text{Na}}{M_{\text{molec}}} \sum_{i=1}^{\text{NA}} n_i \, b_i = \rho_{\text{molec}} \sum_{i=1}^{\text{NA}} \frac{sld_i \, w_i}{\rho_i}. \tag{4.77}$$

Tanking into account a mixture of NC atom and/or molecules, whose molar and weight fractions are respectively x_j and w_j, with $j = 1, \ldots, \text{NC}$, the scattering length density of such system is

$$\begin{aligned} sld_{\text{mix}} &= \frac{\rho_{\text{mix}} \, \text{Na}}{M_{\text{mix}}} \sum_{j=1}^{\text{NC}} x_j \, sdl_j, \\ &= \rho_{\text{mix}} \sum_{j=1}^{\text{NC}} \frac{sdl_j \, w_j}{\rho_j}, \end{aligned} \tag{4.78}$$

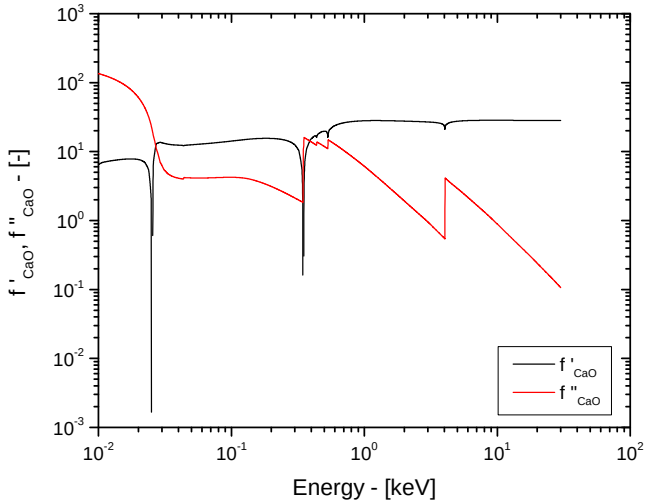

(a) *Calcium oxide.*

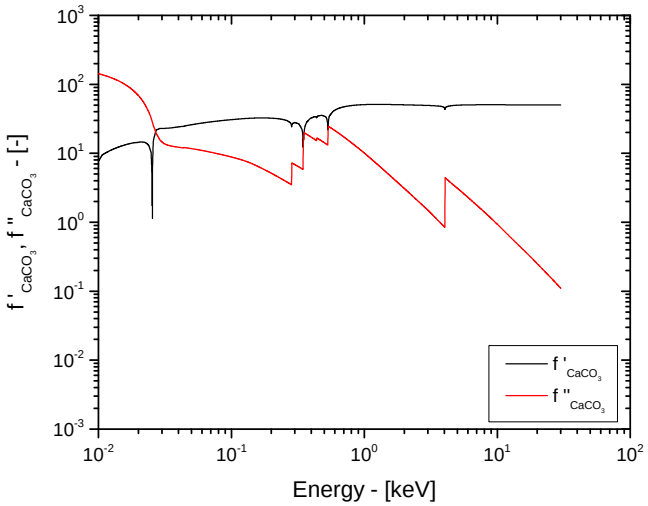

(b) *Calcium carbonate.*

Figure 4.7: Real and imaginary parts of the molecular form factor dispersion corrections f' and f'' over the beam energy for calcium oxide and calcium carbonate.The atomic form factors of each elements refer to NIST (1997).

and, more generally, by taking into account Eq. (4.77), Eq. (4.78) becomes

$$\begin{aligned} sld_{\text{mix}} &= \frac{\rho_{\text{mix}}\,\text{Na}}{M_{\text{mix}}} \sum_{j=1}^{\text{NC}} x_j \left(\sum_{i=1}^{\text{NA}} n_{i,j}\, b_{i,j} \right), \\ &= \rho_{\text{mix}} \sum_{j=1}^{\text{NC}} w_j \left(\sum_{i=1}^{\text{NA}} \frac{sdl_{i,j}\, w_{i,j}}{\rho_{i,j}} \right). \end{aligned} \tag{4.79}$$

4.7.3 The Linear Adsorption Coefficient

In a transmission experiment, the transmission coefficient T is defined from the the Lambert-Beer's equation, Eq. (4.10),

$$T = \frac{I(z)}{I_0} = e^{-\mu\, z}, \tag{4.80}$$

and this quantity is easily measured by estimating the beam intensity before and after the sample. Once the transmission coefficient T is known, the sample thickness z is estimated by means of Eq. (4.80) with a known linear absorption coefficient μ. Vice-versa, μ can be estimated is the sample thickness is known.
According to Eq. (4.11), the atomic linear absorption coefficient is estimated from the absorption scattering cross section and, according to the mixing formulas of the scattering length density, the linear absorption coefficient of a molecule made of NA atoms is

$$\mu_{\text{molec}} = \rho_{\text{molec}} \sum_{i=1}^{\text{NA}} \frac{\mu_i\, w_i}{\rho_i}, \tag{4.81}$$

while the linear absorption coefficient of a mixture of NC atom and/or molecules is

$$\begin{aligned} \mu_{\text{mix}} &= \rho_{\text{mix}} \sum_{j=1}^{\text{NC}} \frac{\mu_j\, w_j}{\rho_j}, \\ &= \rho_{\text{mix}} \sum_{j=1}^{\text{NC}} w_j \left(\sum_{i=1}^{\text{NA}} \frac{\mu_{i,j}\, w_{i,j}}{\rho_{i,j}} \right), \end{aligned} \tag{4.82}$$

where j refers to the j-th atom or molecule inside the mixture, whose weight fraction is w_j. Subscripts i, j into a generic properties $\cdot_{i,j}$ means the property $\cdot$ of atom i that is inside the molecule j.

Chapter 5

Analysis of textural properties of CaO-based CO_2 sorbents by ex-situ USAXS

This chapter deals with the small angle scattering experiments performed at the Advanced Photon Source (APS), a 3rd generation synchrotron light source at the Argonne National Laboratory (Argonne, Illinois). Small angle X-ray scattering technique has never been applied to the characterization of CaO based sorbents. For this reason, before to applied this technique by means of an in-situ approach, *ex-situ* small angle scattering measurements were performed to test the technique capabilities to investigate the highly porous CaO-based samples.
Specifically, ten different samples were produced using the thermo-gravimetric technique and then tested at the APS. Both partially and completely calcined sorbent were generated by considering short (40–50 min) and high (240–720 min) heating step periods and exploring two final $CaCO_3$ calcination reaction temperatures, namely 800 °C and 900 °C under vacuum conditions. In this way, significant different sorbent micro-structures were generated (because of the sintering processes that mainly contribute to affect the sorbent pore network after the reaction) with the aim to test the USAXS/SAXS capabilities to investigate this kind of materials. Additionally, partially CaO carbonated samples were investigated by stopping the carbonation reaction before and after the transition point. In this way, the $CaCO_3$ product layer effect on the sorbent micro-structure was investigate by means of the small angle scattering technique.

5.1 Introduction

Thus far, the micro-textural properties of CaO based CO_2 solid sorbents have been investigated using techniques, such as those based on the gas-adsorption and the mercury porosimetry, that can be used only ex-situ (Barker, 1973; Bhatia and Perlmutter, 1983a; Borgwardt, 1989b; Sun et al., 2007; Sun et al., 2008b; Sun et al., 2008a; Grasa et al., 2009; Zhu, Wu, and Wang, 2011). These techniques suffer from several important limitations that can affect the material property measurements: the sorbent properties are analysed at different operative conditions (i.e. 77 K for N_2 gas adsorption) respect to the process operative conditions (500–900 °C); the material needs to be stored under an inert atmosphere before the measurement in order to prevent the CaO hydration; the nascent calcium oxide micro-textural properties at the beginning of the calcination reaction can be hardly investigated (or they cannot be investigated at all), because the material needs to be cooled down and the micro-structural properties change during the cooling time. Additionally, the mercury porosimetry technique is limited by the instrument highest achievable pressure, that defines the minimum measurable (accessible to mercury) pore size as stated by

Table 5.1: Chemical and physical properties of calcium carbonate and calcium oxide (Haynes, 2014; Ilavsky and Jemian, 2009).

Property	$CaCO_3$	CaO
Molecular weight, M $\left[\mathrm{g\,mol^{-1}}\right]$	100.087	56.077
Density, ρ $\left[\mathrm{g\,m^{-3}}\right]$	2.71	3.34
Linear absorption coefficient, μ, $\left[\mathrm{cm^{-1}}\right]$	19.5	41.11
Contrast (18 keV), $\Delta\rho_e^2$ $\left[\mathrm{cm^{-4}}\right]$	526.34×10^{20}	803.17×10^{20}

Lowell (2004), according to the Washburn equation (Washburn, 1921). Finally, the probing gas accessibility in the gas-adsorption techniques may be limited by the complex and disordered structure of the sampling material, like distortions and constrictions (Nguyen and Bhatia, 2012).

An analytical technique capable to avoid such drawbacks is the X-ray Small-Angle Scattering (SAS). X-ray based SAS is a non-destructive and non-invasive technique that allows the micro-structural properties investigation of micro/nano-scale inhomogeneous materials, by means of differences in X-ray contrast (the electron density difference of the two phases) due to the scatteres (like pores, particles, micelles, polymers chains etc.). SAS can provide both qualitative and quantitative information about the micro-structural properties and morphology of the material in-homogeneities, namely pores in the case of porous materials. Specifically, the material porosity, specific surface area and mean pore radius, as well as pore size distributions (PSDs) are estimated (Chavez Panduro et al., 2012; Hu et al., 2011; Nguyen and Bhatia, 2012; Spalla, Lyonnard, and Testard, 2003; Lee et al., 2014; Beaucage, Kammler, and Pratsinis, 2004) from the measured scattering data, expressed in terms of scattering intensity profiles as a function of scattering vector modulus q defined as $q = (4\pi/\lambda)\sin(\theta/2)$, where λ is the wavelength of the incident X-ray beam and θ is the scattering angle (Glatter and Kratky, 1982). The lower limit of the q-range of an instrument is commonly used to roughly estimate the maximum diameter $d_{\max}$ of the scatterers by using the Bragg equation (Glatter and Kratky, 1982) according to Eq. (2.18).

X-Ray SAS is not affected by the aforementioned limitations of mercury porosimetry and of gas-adsorption based techniques. A very relevant advantage of X-Ray SAS is that it can be used both ex-situ and in-situ, without the need of extracting the material samples from the process operative conditions and avoiding the experimental issues related to the sample contamination/hydration (when exposed to the ambient conditions). X-Ray SAS in-situ time resolved measurements can be carried out by using a capillary flow cell wherein the samples to be tested are placed (Becker et al., 2010; Biasin et al., 2015; Biasin, Segre, and Strumendo, 2015; Chupas et al., 2008), thus allowing the sample microstructural evolution analysis also in high temperature operative conditions. Finally, SAS measurements can be coupled with WAXS (Wide Angle X-Ray Scattering) data providing simultaneously information about the sample microstructure and conversion (Becker et al., 2010; Benmore et al., 2016). However, while X-Ray SAS was already used to analyze porous materials (Chavez Panduro et al., 2012; Lee et al., 2014; Spalla, Lyonnard, and Testard, 2003), it was never used thus far to characterize CaO based CO_2 sorbents.

In this work the micro-textural properties (porosity, specific surface, pore radius, pore size distribution) of CaO based CO_2 sorbents are characterized ex-situ for the first time using synchrotron radiation X-ray SAS and the obtained results are validated by comparison with literature data obtained by traditional techniques (mercury porosimetry and gas-adsorption). Overall ten different samples were analyzed. Six of such samples were analysed after being calcined (thermally activated). Because the carbonation reaction

Table 5.2: Properties of the $CaCO_3$ samples calcined under vacuum conditions (below 0.01 bar).

Sample	Particle size [µm]	Final calcination temperature [°C]	Heating duration [min]	Conversion X_{CaCO_3} [%]	w_{CaO} [%]	w_{CaCO_3} [%]
A	150 ÷ 160 µm	800	40	100	100	0
B	150 ÷ 160 µm	800	32.6	59.8	45.1	54.9
C	150 ÷ 160 µm	800	720	100	100	0
D	150 ÷ 160 µm	900	50	100	100	0
E	150 ÷ 160 µm	900	240	100	100	0
F	70 ÷ 74 µm	800	40	100	100	0

performances are strongly influenced by the calcination reaction conditions, two calcination reaction temperatures (800 °C and 900 °C) were explored for the sorbent activation by considering both low and high sintering times in order to reduce or promote the sintering processes. Additionally, four samples were partially carbonated at different CaO conversions and tested in order to investigate the sorbent property evolution during the carbonation. SAS measurements were performed at the 9-ID-C beamline at the Advanced Photon Source (APS), Argonne National Laboratory. The beamline provides USAXS (Ultra Small Angle X-Ray Scattering), SAXS and WAXS measurements in an energy range between 10 and 24 keV, allowing a total measurable q-range (USAXS + SAXS) of about $0.0001 \div 1.0\,\text{Å}^{-1}$ (Ilavsky et al., 2009). This wide q-range allows to investigate porous materials whose pore size (pore diameter, d) varies from a minimum of about 1 nm up to a maximum of 10 µm (Ilavsky, 2010). In this way, both micro-pores (< 2 nm) and meso-pores ($2 < d < 50$ nm) can be investigated.

5.2 Experimental details

5.2.1 Materials

Commercial calcium carbonate by AppliChem (marble granular A6297) was used as calcium oxide solid sorbent precursor (Tab. 5.1). The 150÷160 µm fraction in particle diameter was used. Such particle size was chosen for two reasons: it allows to reduce or neglect the intra-particle diffusion effects during the carbonation reaction and ensures a good compactness within the capillary used for the SAS measurements. Additional details on sorbent precursor are described in § 2.7.

5.2.2 Sample preparation

In this work ten different samples were investigated using synchrotron radiation USAXS/SAXS techniques. Each sample differs as far as the micro-textural properties and the sample chemical composition was determined by means of thermo-gravimetric analysis (TGA). Specifically, the thermo-gravimetric analyzer DynTHERM MP-ST by RUBOTHERM GMBH was used to produce the CaO-based samples and the reactant conversion was determined by means of the experimental sample weight change over time.
Five samples consist of completely calcined/thermally activated $CaCO_3$, at different operative conditions in terms of reactor temperature and heating time. The carbonate activation was performed under non-isothermal conditions from ambient temperature up to the final calcination temperature of 800 °C or 900 °C, using a heating rate of $50\,°\text{C}\,\text{min}^{-1}$ and

Table 5.3: Properties of the partially carbonated CaO samples (reaction temperature of 650 °C, total pressure of 1.3 bar, CO_2 molar fraction of 10 %, particle size of 150 ÷ 160 µm).

Sample	Carbonation time [min]	Conversion, [%]	w_{CaO} [%]	w_{CaCO_3}
G	7.29	9.91	83.6	16.4
H	17.5	43.4	42.2	57.8
I	23.3	61.2	26.2	73.8
L	32.4	78.7	13.2	86.8

loading about 100 mg of $CaCO_3$ as sorbent precursor. After reaching the final calcination temperature, the temperature was kept constant until the end of the heating step and finally the samples were cooled down again at ambient temperature (cooling step). Calcinations were performed under vacuum conditions (below 0.01 bar) in order to reduce the CO_2 influence during the reaction and during the high temperature sintering processes. For the two completely calcined samples at 800 °C (sample A and C, Tab. 5.2) the duration of the heating step was about 40 min and 720 min respectively, in order to obtain a completely calcined $CaCO_3$ with limited sintering effects (sample A), and a second sorbent (sample C) where the additional time at high temperature with respect to sample A favored the pore network modification due to sintering. The sample A carbonate conversion over time is shown in Fig. 3.1a. A similar procedure was repeated for the samples calcined at 900 °C (sample D and E, Tab. 5.2) with duration of the heating step of about 50 min and 240 min respectively (Fig. 3.1b). A fifth completely calcined sample was produced at the same calcination reaction conditions of sample A, but using a smaller particle size, namely 70÷74 µm, in order to check the influence of a different particle size on the final sorbent micro-structural properties and the particle size effect on the SAS experimental response. Using the same experimental procedure of sample A, a partially calcined sample (sample B, Tab. 5.2) was obtained by stopping the reaction after 32.58 min from the beginning of the heating step, to investigate the micro-structural properties before the end of the calcination reaction.

Additionally, four samples were calcined using the same operative conditions as for sample A. Afterwards, the reactor temperature was decreased down to 650 °C and a gas mixture with 10 % (molar fraction) of CO_2 in balance with N_2 was fed to the reactor at 1.3 bar bar, with a total flowrate of 150 NmL min^{-1}. Under such isothermal conditions, the carbonation reaction took place and different CaO conversions were obtained by stopping the gas mixture feed and switching the furnace heater off. In this way, four partially carbonated samples with different CaO conversions were obtained, namely 9.91 %, 43.38 %, 61.19 % and 78.66 % (sample G, H, I and L respectively as listed in Tab. 5.3). In order to take into account the apparent mass changes due to the buoyancy effects in the TGA, each sample-run (in terms of weight change over time) was subtracted by the corresponding blank-run.

The reactant conversions during calcination and the carbonation were calculated using Eqs. (2.7) and 2.8.

After the reaction step, the reaction chamber was cooled down maintaining the material under a continuous flux of pure nitrogen at 1.3 bar, in order to purge the reactor from the remaining CO_2 and to maintain an inert atmosphere inside the reaction chamber. Once the material reached the ambient temperature, each sample was unloaded and sealed under vacuum into borosilicate glass capillaries (Kimbel Chase Melting Point capillary, 34505-99), whose external diameter ranges from 1.5 to 1.8 mm with a wall thickness of about 0.2 mm. This procedure was used to avoid the sorbent hydration, because of the high hygroscopic

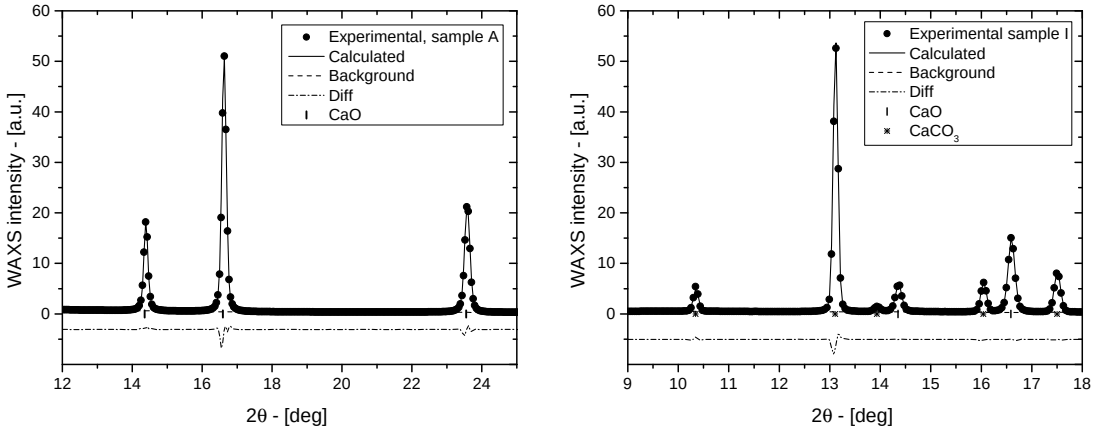

Figure 5.1: WAXS patterns of the completely calcined sample A (a) and of the partially carbonated (carbonate mass fraction of 0.7947) sample I (b). The experimental data (dots) and the calculated values (solid line) are compared. Each Bragg peak position for CaO and $CaCO_3$ are shown by markers.

nature of CaO at room temperature.

5.2.3 Ex-Situ SAXS-USAXS experiments

The produced samples were tested by SAS at the 9-ID-C of the Advanced Photon Source (APS), at Argonne National Laboratory (Argonne, Illinois). The measurements were carried out irradiating each sealed capillary with an incident monochromatric beam radiation of 18 keV and a corresponding wavelength of about 0.6888 Å. Each sample was probed using an illuminated area smaller than 1 mm high and 2 mm wide. During each test, three different detectors were used in order to record the data, namely the USAXS, SAXS and WAXS detectors (Ilavsky et al., 2013; Ilavsky et al., 2009). The combination of these three detectors provides a corresponding wide q-range of about $0.0004 \div 4.5\,\text{Å}^{-1}$. Before analyzing the produced samples, a test was performed on an empty capillary in order to obtain its scattering contribution, that was subtracted from the sample scattering responses. Three different samplings were performed for each sample by moving the illuminated area, because the packing of the powder inside each capillary could be not-homogeneous.

5.2.4 USAXS and SAXS data reduction in absolute intensity scale

The SAXS scattering profiles were reduced using the Nika program (Ilavsky, 2012), while USAXS data were reduced by means of Indra program (Ilavsky and Jemian, 2009). These two data-sets were finally merged with the Irena package (Ilavsky and Jemian, 2009), to obtain the whole scattering intensity vs q profiles of the USAXS and SAXS detectors. The scattering curves were then normalized in terms of absolute units (Zhang et al., 2010), namely in terms of the differential scattering cross section. The measured intensity profile $I(q)$ at the detector is related to the differential scattering cross section per unit volume of the illuminated sample and per unit of solid angle (Ω) $d\Sigma/d\Omega$ by Eq. 4.47 Ilavsky et al. (2009) and Long et al. (1991).
Because of the cylindrical geometry of the capillary and because the samples are granular materials, it is difficult to precisely estimate the illuminated sample volume. It is more convenient to express the absolute intensity in terms of unit of sample mass (inside the

Table 5.4: Chemical compositions of the partially calcined and of the partially carbonated samples estimated by means of the Rietveld analysis of the WAXS data diffraction patterns.

Sample	w_{CaO} [%]	w_{CaCO_3} [%]
B	43.4	56.7
G	84.4	15.6
H	41.2	58.8
I	20.5	79.5
L	10.5	89.5

illuminated volume) instead of unit of sample illuminated volume. Therefore, the solid phase thickness e_{solid} of each sample was estimated using the Lambert-Beer law from the measured sample transmission coefficient T and the linear absorption coefficient μ of each sample. The differential scattering cross section per unit of sample mass $d\Sigma_m/d\Omega$ is equal to $d\Sigma/d\Omega$ multiplied by the illuminated sample volume and divided by the sample mass, according to Eq. 4.50. Skeleton densities of pure CaO and $CaCO_3$ are listed in Tab. 5.1 (Haynes, 2014) and the chemical composition of each sample (Tab. 5.2 and Tab. 5.3) was calculated from the TGA data of reactant conversion.
By using the one-dimensional collimating geometry for the USAXS data collection, the measured scattering intensity profiles are affected by slit smearing. However, no desmearing procedure (Ilavsky et al., 2013; Lake, 1967; Pete R. Jemian, 1990) was necessary, because the slit smearing effects are numerically accounted for into the Irena packages (Ilavsky and Jemian, 2009). Therefore, all the scattering intensity profiles showed in this work refer to slit-smeared curves.

5.2.5 Calculation of the sorbent textural properties

The analysis of the USAXS and SAXS intensity profiles (expressed in terms of absolute units on a sample mass basis) was performed using the IGOR Pro-based IRENA program (Ilavsky and Jemian, 2009). Specifically the "Unified fit" tool was used to fit the slit-smeared scattering intensity profiles. Such tool is based on the unified approach proposed by Beaucage (1995) and Beaucage (1996), that allows the description of the SAS profiles over a wide range of q by means of an arbitrary number of interrelated structural levels. This provides the model with a high flexibility in describing the SAS response of multiple-size-scale structures (Beaucage, 1995). The small angle scattering data analysis by means of the "Unified fit" approach and the symbolism refer to § 4.6.

5.2.6 Analysis of WAXS data

Wide Angle X-ray Scattering (WAXS) data were collected in terms of scattering intensity over the scattering vector q. Each experimental scattering pattern was converted in terms of intensity versus two-theta values and analyzed by means of the Rietveld profile method using the General Structure Analysis System (GSAS) software (Larson and Dreele, 2000). A profile function based on a pseudo-Voigt and asymmetry function was used to refine the peak shape (Stephens, 1999), while a cosine Chebyshev function of 12 polynomial terms was used to fit the background contribution. Additionally, the instrumental contribution was taken into account by means of the profile refinement of LaB_6. In this work the WAXS diffraction patterns were used for the determination of the phase weight fractions in order to: a) check the data of sample chemical composition obtained by

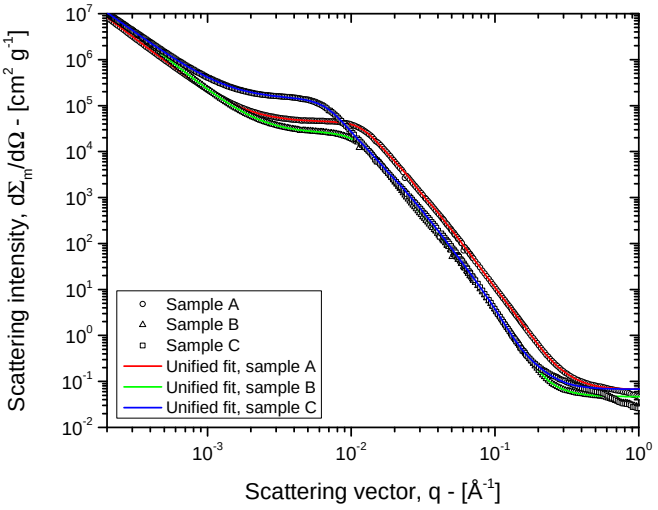

Figure 5.2: Experimental slit-smeared scattering intensities profiles in absolute units and unified fits of completed and partially calcined samples A, B, C. Slit length is $0.028\,028\,\text{Å}^{-1}$; for the un-reacted $CaCO_3$ the slit length is $0.024\,164\,\text{Å}^{-1}$ and the beam energy is 24 keV.

thermos-gravimetric analysis; b) to verify if any sample hydrated to form calcium hydroxide. Fig. 5.1 shows two typical WAXS profiles of the completely calcined sample A and of the partially carbonated sample I. From a comparison between the theoretical Bragg peaks and the experimental profiles, no hydration was detected in the ten samples. This result suggests that the storage method by means of a material sealing inside capillaries under vacuum condition could be an appropriate solution to prevent the sorbent hydration over long periods. Finally, the weight fractions of the partially calcined and of the partially carbonated samples computed by the Rietveld method are listed in Tab. 5.4 that reveals a good agreement with the estimated composition obtained from the TGA data (Tab. 5.2 and Tab. 5.3).

5.3 Results and Discussion

The experimental scattering intensity profiles of the ten samples showed in Figs.5.2, 5.3, 5.4 and 5.12 were used to compute the sample textural properties (radius of gyration, specific surface, porosity, pore size distribution) and to identify and/or verify trends of such properties over time and over $CaO/CaCO_3$ conversions. From the experimental scattering intensity profiles three regions can be identified (by looking at the Figs.5.2, 5.3, 5.4 and 5.12 from the right to the left). The first region is placed at high-q values and is characterized by an approximately flat scattering intensity profile due to the background contribution to the scattering experimental response. A second region can be located roughly between $1.5 \times 10^{-3}\,\text{Å}^{-1}$ and $3 \times 10^{-1}\,\text{Å}^{-1}$. In the first part of this second region, a plateau can be observed, defining a Guinier regime. A third region can be observed at lower-q values (approximately between $1 \times 10^{-4}\,\text{Å}^{-1}$ and $1.5 \times 10^{-3}\,\text{Å}^{-1}$) and is approximately described by a power-law profile. This region represents the experimental scattering response of large structures. Such large structures can be related to the scattering response of the sorbent particles (whose particle diameter is $150 \div 160\,\mu\text{m}$), and, more precisely, to the inter-particle voids. These large structure size can be roughly estimated by means of Eq. 2.18, obtaining a maximum scatterer size of about 6 µm. This value suggests that the inter-particle void scattering response is compatible with this low-q region. Additionally, this

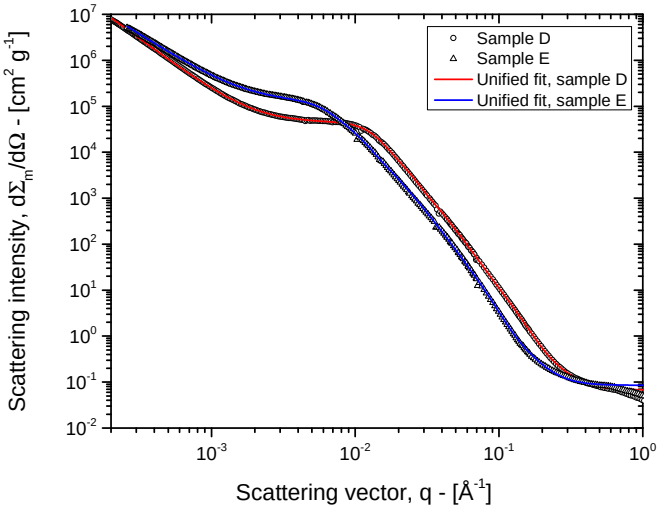

Figure 5.3: Experimental slit-smeared scattering intensities profiles in absolute units and unified fits of completely calcined samples D and E. Slit length is $0.028\,028\,\text{Å}^{-1}$; for the un-reacted $CaCO_3$ the slit length is $0.024\,164\,\text{Å}^{-1}$ and the beam energy is 24 keV.

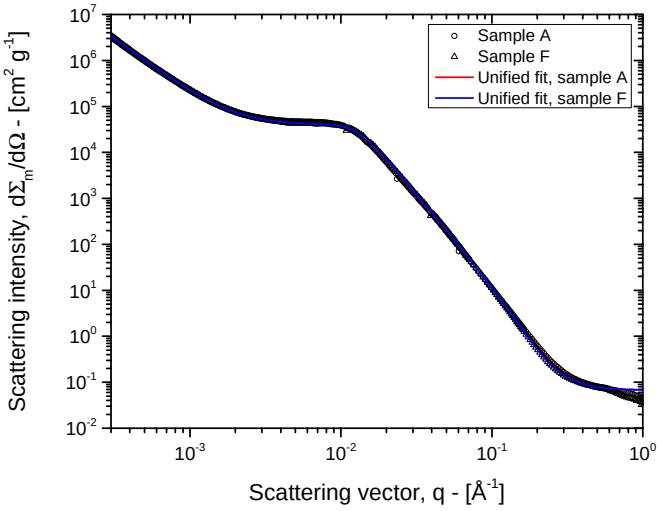

Figure 5.4: Experimental slit-smeared scattering intensities profiles in absolute units and unified fits of completely calcined samples A and F with different particle size. Slit length is $0.028\,028\,\text{Å}^{-1}$; for the un-reacted $CaCO_3$ the slit length is $0.024\,164\,\text{Å}^{-1}$ and the beam energy is 24 keV.

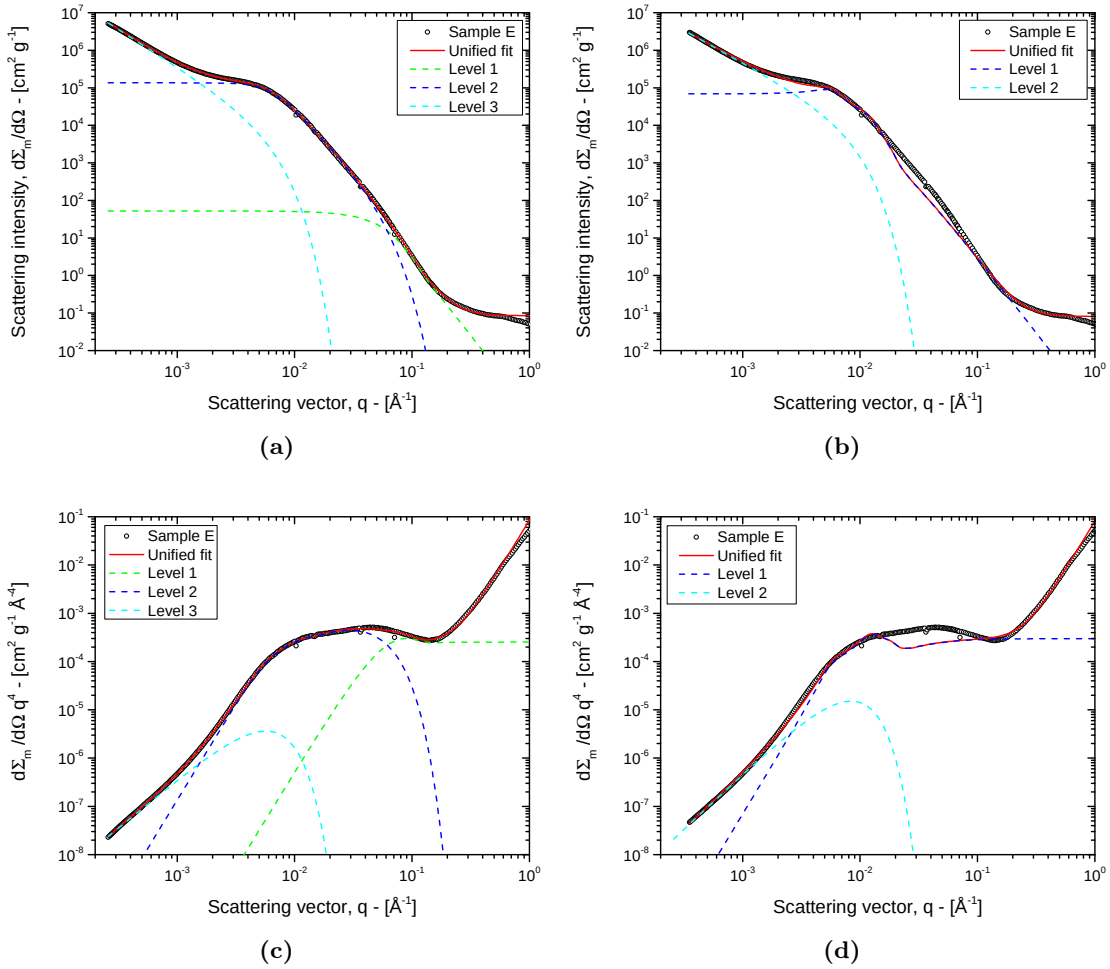

Figure 5.5: Fitting of the sample E scattering intensity profile using 2 and 3 levels in the unified fit model (4b and 4a respectively). The scattering intensity trends are emphasized in the Porod representation (4d and 4c).

region is influenced by multiple scattering effects, that distort the local scattering intensity profiles and the single scattering analysis cannot be correctly applied.

5.3.1 Model application: structural levels and structure factor

The analysis of the scattering intensity profiles revealed that the second region after the first Guinier plateau is characterized by a non-constant power-law slope, suggesting the presence of several structural levels that overlap in the second region. Specifically, both the highly-sintered samples (C and E) and the partially carbonated materials (samples H and I) scattering intensity profiles clearly reveal the existence of another structural level in the direction of high-q values near to the background region. This is illustrated in Figs. 5.5a and 5.5b where the non-linear fittings of sample E intensity profile using two and three structural levels of the unified fit model described by Eq. (4.60) are compared. Specifically, three levels are required in order to fit accurately the experimental scattering intensity profile of sample E, while two levels do not guarantee a reasonable fitting result. This can be more clearly appreciated in a double logarithm plot of $d\Sigma_m/d\Omega\, q^4$ versus the scattering vector q, usually called the Porod representation (Spalla, Lyonnard, and Testard, 2003). Such plot emphasizes the trends and slopes of the scattering intensity

profiles as shown in igs. 5.5c and 5.5d. For these reasons, three different structural levels (plus the background contribution) were considered in the unified fit approach to analyze the experimental scattering intensity profiles of the CO_2 sorbents, namely two levels 1 and 2 for the second region and one level 3 for low-q region.

The scattering intensity profile representation by means of three structural levels and specifically by two levels in the second region suggests that the sorbent pore network (internal porosity) is characterized by two different structures, namely by two distinct population of pores.

In the unified fit approach - Eq. (4.60) - P_1 and P_2 refer to the power-law exponents of the first and second levels, namely of the two populations that are approximately placed inside the q-range $1.5 \times 10^{-3}\,\text{Å}^{-1} \div 3 \times 10^{-1}\,\text{Å}^{-1}$. According to Porod (1951) these exponents assume the value of 4 (Porod's law) when the scattering response derives from a smooth and sharp interface , that in the case of CaO based CO_2 sorbents identifies the pore-solid interface of these two structures, namely the specific surface areas associated to the pore network. The power-law exponents P_1 and P_2 were initially included in the fitting parameters and the resulting numerical values of these two parameters ranged from 3.9 to 4.3. For this reason, these two exponents were set to be equal to 4 and the respective B_1 and B_2 constants become the Porod's law proportionally constants.

In the third level, namely in the region influenced by multiple scattering where no Guinier regime is observed, G_3 was set to zero. Additionally, because of the multiple scattering effects that distort the local power-law exponent slope, the power-law exponent P_3 was left as a free fitting parameter, because no physical meaningful information can be obtained by the use of the single scattering approach.

In order to take into account the interferences arising when scatterers are concentrated, the structure factor of Eq. 4.59 was taken into account in the profile fitting for the second level, except for the case of sample L (sample almost completely carbonated) and the unreacted $CaCO_3$ scattering intensity profiles. For these last two samples, the structure factor of the second level was set equal to one. Additionally, the structure factors for the first and third levels were always set equal to 1.

The scattering intensity profiles calculated by means of Eq. (4.60) are shown in Figs. 5.5a and 5.5b as continuous lines.

5.3.2 Calcined and sintered sorbents

Calcination conditions were selected in order to generate different pore structures in the final sorbents and to test the SAXS capabilities applied to the CO_2 capture sorbents characterization.

Three different sets of micro-structural parameters were obtained for each sample, namely the radius of gyration (directly obtained from the fitting results), the specific surface area by means of Eq. 4.65 and the sorbent porosity using Eq. (4.64). The specific surface areas and the porosities were calculated for the structural levels 1 and 2. The properties of each sample (averaged over three samplings) are listed in Tab. 5.5; S_m and ε indicate the sums of the specific surface areas and of the porosities over the structural levels 1 and 2. Specifically, each sorbent is characterized by two distinct populations of pores. The first population (associated to the first structural level) is characterized by a small radius of gyration (up to 30 Å) and a low pore fraction (up to 2 %) if compared with those of the second population. However, because of the high surface-to-volume ratio of the first population, its surface area contribution is comparable with that of the second population, as can be noticed from the specific surface values listed in Tab. 5.55 that range from a minimum of $4.34\,\text{m}^2\,\text{g}^{-1}$ (for the highly-sintered sorbents) to a maximum of $14.8\,\text{m}^2\,\text{g}^{-1}$ when the sintering effects are negligible. This result suggests that the small population

Table 5.5: Micro textural properties of the calcined samples. S_m, ε and N_m are the sum of the specific surface area, the internal porosity and of the pore number density of the two pores populations respectively.

Sample	$R_{g,1}$ [Å]	$R_{g,2}$ [Å]	$S_{m,1}$ $[m^2\,g^{-1}]$	$S_{m,2}$ $[m^2\,g^{-1}]$	S_m $[m^2\,g^{-1}]$	ε_1 [–]	ε_2 [–]	ε [–]	$N_{m,1} \times 10^{-16}$ $[g^{-1}]$	$N_{m,2} \times 10^{-16}$ $[g^{-1}]$	$N_m \times 10^{-16}$ $[g^{-1}]$
A	17.7	146	14.8	34.1	48.9	0.020	0.361	0.381	80.6	2.20	82.8
B	17.9	164	4.64	18.0	22.7	0.007	0.205	0.212	17.3	0.833	18.1
C	26.6	278	4.34	18.0	22.4	0.011	0.360	0.371	7.24	0.331	7.57
D	17.8	145	13.7	38.5	52.2	0.020	0.395	0.415	64.4	2.58	67.0
E	30.3	262	4.58	18.5	23.1	0.012	0.312	0.325	6.43	0.455	6.89
F	17.2	135	11.7	36.1	47.8	0.017	0.370	0.3870	56.1	2.54	58.6

Table 5.6: Textural properties of the calcined samples A, C and D obtained from N_2-adsorption analysis, using BET and BJH methods.

Sample	S_m (BET) $[m^2\,g^{-1}]$	ε (BJH) $[-]$	S_m (BJH) $[m^2\,g^{-1}]$	$\langle R_v \rangle$ (BJH) [Å]
A	50.4	0.507	57.0	132
C	20.7	0.454	23.6	204
D	41.0	0.484	46.3	126

could play a relevant role during the first instants of the CaO carbonation because of its significant surface area, while the second population contribution on the carbonation reaction kinetics is likely to be dominant at high CaO conversions and its high porosity values determine the maximum conversion.
Fig. 5.2 represents the scattering intensity profiles of the samples calcined at 800 °C (A, B and C). Specifically, the sample A scattering response is considered as a reference profile of a sample not strongly affected by the sintering processes. In fact, even though the surface reaction and the sintering phenomena are simultaneous processes during the calcination step (Borgwardt, 1989b), the short duration of the heating step for sample A suggests that the sintering effects are modest. This is confirmed by the sample A high porosity and specific area values listed in Tab. 5.6, namely 0.507 and $50.4\,m^2\,g^{-1}$. These values were estimated by means of N_2-adsorption measurements, using the BJH and BET methods respectively. The porosity of sample A is close to the theoretical value of 0.54 (Beruto, Barco, and Searcy, 1983; Grasa et al., 2009), confirming modest sintering effects on the final sorbent micro-structural properties. Instead, the sample C was highly sintered (compared to sample A) because the duration of the heating step was much longer and its experimental scattering response shows in the high-q values region a lower intensity with respect to sample A. This is confirmed by the sample C specific surface area values estimated by means of the BET and BJH techniques respectively, namely $20.7\,m^2\,g^{-1}$ and $23.6\,m^2\,g^{-1}$ that are less than half of the sample A surface area values listed in Tab. 5.6. The sorbent porosity variation is less pronounced and decreases down to 0.454 (Tab. 5.6), losing about 10 % of its initial pore volume (that of sample A). Additionally, the Guinier regime is shifted in the direction to low-q values, with a higher intensity than sample A. These differences in the scattering intensity profiles suggest that because of the sintering processes the sorbent pore size increased, as confirmed by the increase of the mean pore radius (estimated by means of the BJH technique listed in Tab. 5.6) from 132 Å to 204 Å. Finally, the evident non-constant slope in sample C high-q region confirms the presence of a smaller population, located near the background region. Fig. 5.3 shows the scattering intensity profiles of samples D and E obtained with a calcination final temperature of 900 °C. Also in this case, a profile evolution similar to that of samples A/C is observed, this trend is due to pores growth caused by sintering effects during the additional time at high temperature of sample E respect to sample D. The radius of gyration evolution of the two pore populations over time is showed in Fig. 5.6. Specifically, the weakly sintered samples (samples A and D) are characterized by a similar radius of gyration of both the two pore populations (about 17 Å for the first population and $135 \div 146$ Å for the second one), meaning that the sintering effects on the sorbent pore structure have a modest impact on the radius of gyration at short times. As sintering processes take place the radius of gyration increases as well as its growing rate with the sintering temperature, as shown by the 900 °C samples (D and E) in Fig. 5.6. It is remarkable to notice that the first population radius of gyration is placed near to the boundary value between the micro-pore and the meso-pore region. This result reveals the presence of a micro-pore fraction observed by Zhu, Wu, and Wang (2011)

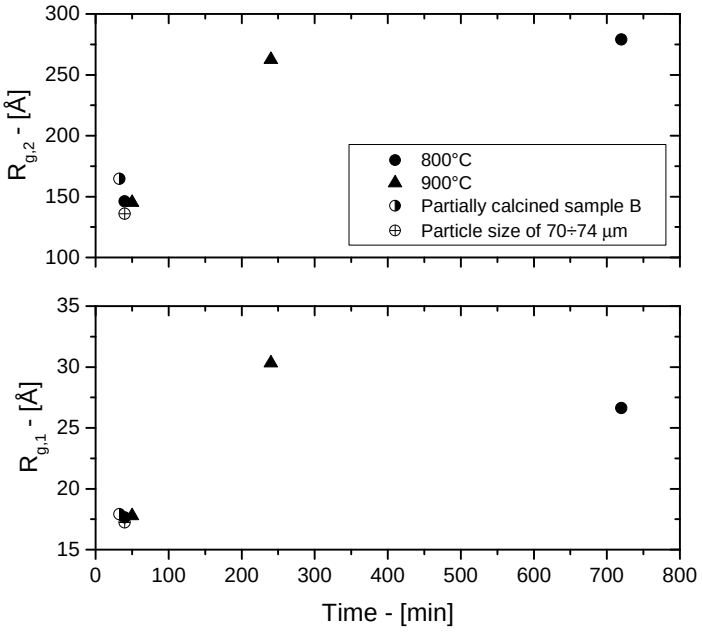

Figure 5.6: Radius of gyration evolution of the two pore populations over time (from the beginning of the heating step). Results are plotted on the bottom for the first population, on the top for the second population.

and Li, Liang, and Cai (2016) by means of N_2-adsorption. The reduction of the high-q region scattering intensity of sample C suggests a decrease of the sorbent specific surface area if compared with that of sample A, because the Porod's power-law proportionally constant is dictated by the high-q region intensity. A similar behavior can be noticed in the samples calcined at 900 °C (D and E) showed in Fig. 5.3. The specific surface areas of all samples are represented in Fig. 5.7, where also the total internal specific surface area (sum of the specific area of the two populations) of each sorbent is reported. Also in this case the similar starting point in terms of specific surface area of sample A and D at short times (between $49\,m^2\,g^{-1}$ and $52\,m^2\,g^{-1}$) confirm the modest sintering contribution during the calcination reaction under vacuum conditions. On the other hand, the specific surface areas of the samples C and E are significantly reduced due to sintering. Additionally, the reduction of the specific surface area from the fully calcined samples (A and D) to the sintered samples (C and E) is stronger for the first (level 1) population than for the second (level 2) population. Fig. 5.8 shows the evolution of the two population porosity over time. After that all the carbonate is calcined, the overall porosity is reduced over time (samples C and E) due to the sintering processes (Borgwardt, 1989b). For the samples calcined at 800 °C sintering affected only slightly the sorbent porosity whose decrease is about 0.01 in magnitude, meaning that only a small pore fraction disappeared. On the other hand, the sorbents calcined at 900 °C (samples D and E) show a higher sintering rate. It is noticeable (Table 5) that the contribution of the second population, in relative terms respect to the first population, to the porous matrix evolution over time is more significant at high temperature , in fact the increase from 800 °C to 900 °C of the variations of the microstructural properties, especially of the porosity, over time is more pronounced for the second population.
The pore number densities per unit of solid mass $N_{m,i}$ were computed from the pore radius

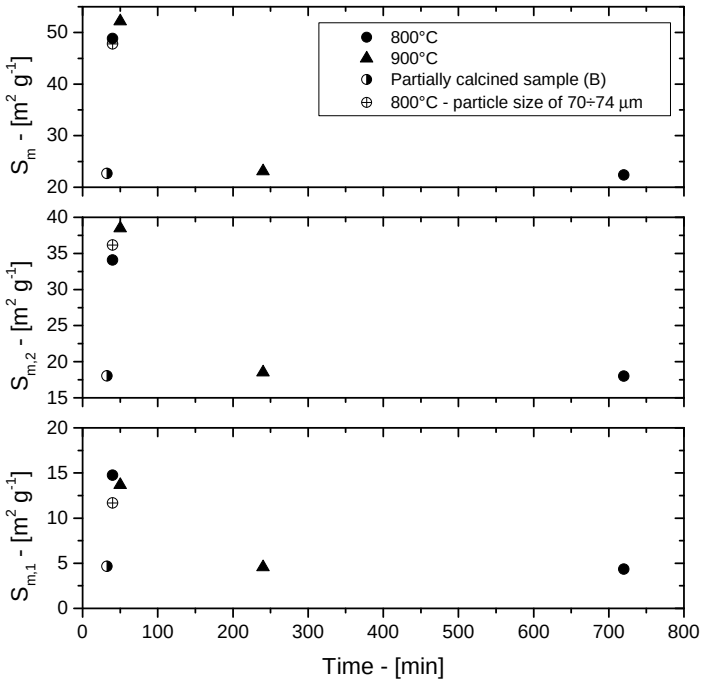

Figure 5.7: Evolution of the specific surface area of the two pore populations (bottom and middle figures for the first and second population respectively) and of the total sample internal specific surface area (top figure) over time (from the beginning of the heating step).

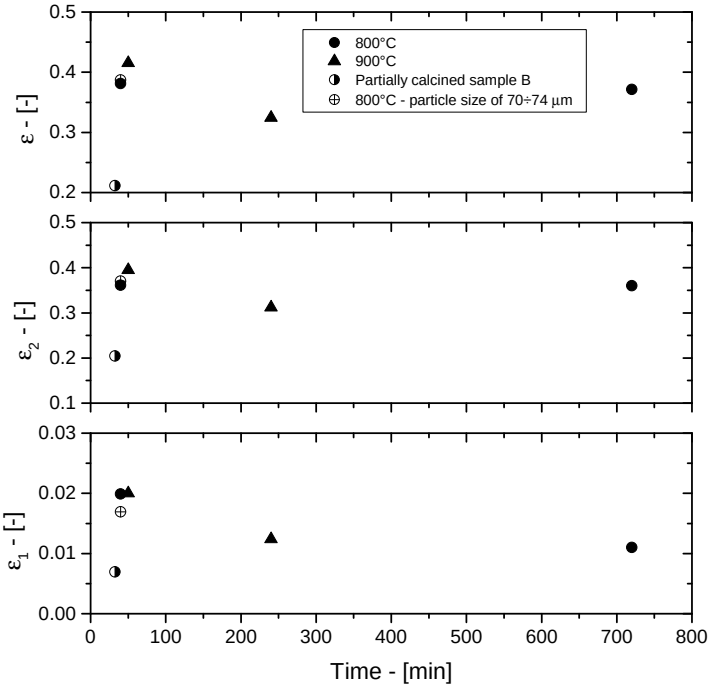

Figure 5.8: Evolution of the porosity of the two pore populations (bottom and middle figures for the first and second population respectively) and of the total sample internal porosity (top figure) over time (from the beginning of the heating step).

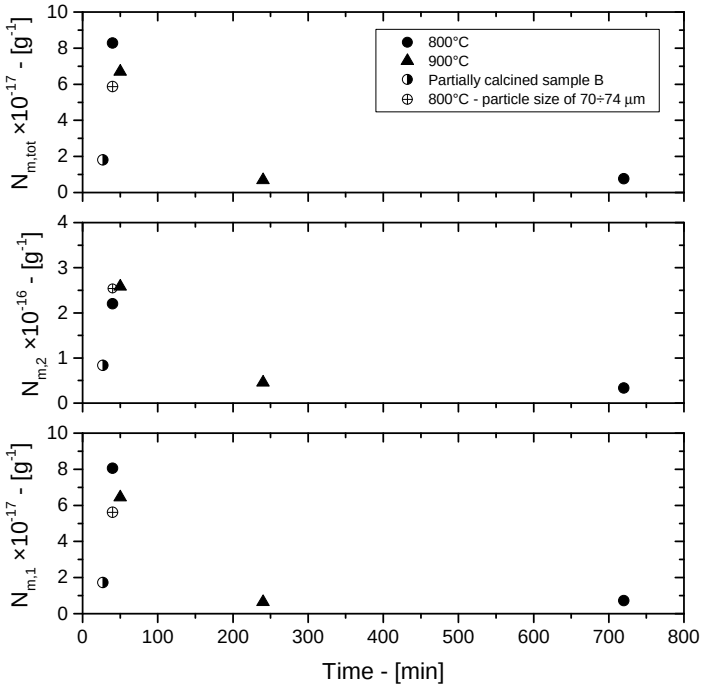

Figure 5.9: Evolution of the pore number density of the two pore populations (bottom and middle figures for the first and second population respectively) and of the total sample pore number density (top figure) over time (from the beginning of the heating step).

distributions for each structural level i as:

$$N_{m,i} = \frac{S_{m,i}}{\int_0^\infty f_i(R)\, 4\pi R^2\, dR}, \tag{5.1}$$

and their evolution over time is shown in Fig. 5.9. N_m represents the sum of the pore number densities of the two structural levels 1 and 2. For both populations, the pore number densities increase during the carbonate calcination and decrease during the sintering process after the calcination; this is partially in contrast with the observations of Zhu, Wu, and Wang (2011), who, referring to a calcium carbonate calcination in nitrogen at $750 - 800\,°C$, qualitatively stated that the micropore number slightly increases over time. It is noticeable that pore number density of the first population is significantly (more than one order of magnitude) higher than the second population, in agreement with high value of the first population specific surface. Because of the increase of the radius of gyration and the decrease of the pore number densities for both populations after the calcination it is likely that pore coalescence is the main process governing the sintering of samples A and D to samples C and E. The intensity profile of the partially calcined sample B indicates that this sample is characterized by a smaller internal porosity respect to the completely calcined sample A. In fact, both the high q power-law region and the Guinier regime lie below the sample A intensity profile. Such small porosity refers to those pores generated before the interruption of the calcination reaction. As a result, the sample B porosity and specific surface are expected to be smaller than those of sample A (Fig. 5.7 and 5.8). However, the presence of the Guinier regime at the same q values of sample A suggests a similar radius of gyration. This qualitative information that can be obtained from the scattering intensity profiles are confirmed by the quantitative values listed in Tab. 5.5. In

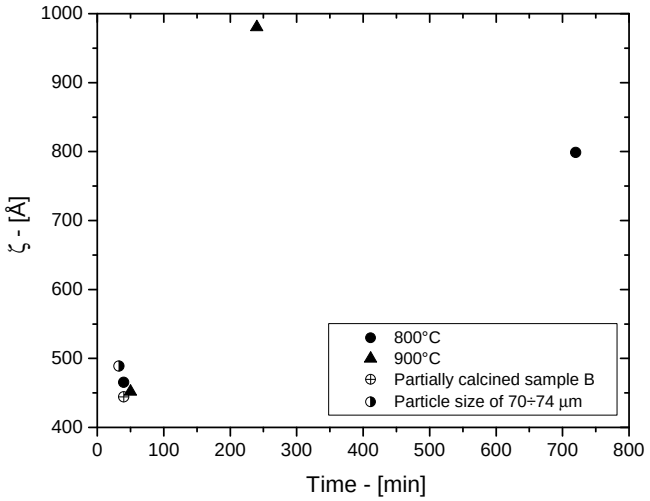

Figure 5.10: Correlation distance evolution over time (from the beginning of the heating step).

fact, the radius of gyration values of the partially calcined sample B (17.9 Å and 164 Å) are close to those of the completely calcined samples A and D, while its specific surface areas (on a sample mass basis) and porosities (expressed as pore volume over particle volume) are significantly lower than those of samples A and D. However, the unreacted $CaCO_3$ core is still non-porous, therefore the specific surfaces and the porosities of sample B must be rescaled on the fraction of sample mass and volume which actually reacted. More precisely, if sample B surface area is rescaled by the calcium oxide weight fraction (Tab. 5.2) the resulting value is $50.2\,m^2$ per gram of CaO, very close to those of samples A and D; similarly, the sample B porosity expressed per unit of reacted sample volume (pore volume plus CaO volume) is about 0.4 again close to the porosities of samples A and D. These observations suggest that the sample B reacted fraction morphology is very similar to the morphology of the completed calcined samples, namely that during the last part of the calcination the sorbent micro-textural properties do not change significantly.

The values of pore number densities of samples A and B (Tab. 5.5) can be used to compute the rates of pore formation during calcination (after rescaling sample B pore number density by the CaO mass fraction), at 800 °C in vacuum. As a rough estimate, it is obtained that pores of the first population form with a specific rate around $1.1 - 5.7 \times 10^{16}\,g^{-1}\,min^{-1}$ while pores of the second population form at a specific rate around $5.3 - 5.5 \times 10^{14}\,g^{-1}\,min^{-1}$.

Fig. 5.4 shows a comparison between the intensity profiles of sample F and of sample A. These two samples were generated following the same calcination procedure but using a different particle size, namely 70÷74 µm and 150÷160 µm respectively. The nice agreement of these two scattering intensity profiles suggests that no remarkable difference is to be expected as far as the micro-structural properties of these two samples. In fact, the comparison of the estimated properties listed in Tab. 5.5 shows that the particle size does not have a significant effect on the sorbent micro-textural properties. The USAXS/SAXS approach used in this work allows to estimate also the correlation distances ζ obtained as fitting parameter of the structure factor $S_2(q)$, accounting for the mesopore (level 2) scattering intensity profile interferences due when the scatterer volume concentration is high. Such parameter provides information about the average pore-to-pore distance of the mesopore population (Beaucage et al., 1995). Fig. 5.10 shows the correlation distance evolution of the calcined samples over time. Samples A, B and C are characterized by a

Table 5.7: Sphericity factors of the two pore populations and mean pore radius $\langle R_v \rangle$ calculated by the sample volume pore size distribution.

Sample	Ψ_1 [−]	Ψ_1 [−]	$\langle R_v \rangle$ [Å]
A	0.861	0.817	133
B	0.829	0.687	157
C	1.04	0.794	253
D	0.979	0.843	130
E	0.920	0.661	228
F	0.956	0.856	127
G	0.940	0.825	144
H	0.542	0.646	175
I	0.563	0.497	210
L	0.543	0.302	232

similar correlation distance, namely 460 Å, 497 Å and 441 Å respectively, suggesting that the average pore distance at the end of the calcination reaction under vacuum is approximately 45 nm. Additionally, the pore correlation distance of the partially calcined sample is similar to the correlation distance at the end of the calcination reaction (that of sample A); this observation suggests again that the sample B pore network texture in the reacted volume is similar to the final pore matrix of sample A. After the calcination reaction, the pore correlation distances increase over time and, specifically, up to 806 Å for the case of sample C (sintering temperature of 800 °C) and 963 Å for sample E (sintering temperature of 900 °C), as shown in Fig. 5.10; these trends, showing that the pore-to-pore distance increases over time and increasing the sintering temperature, confirm pore coalescence as the main process occurring during sintering.

Following Beaucage, Kammler, and Pratsinis (2004), the unified fit parameters were used to estimate the sample pore size distributions for the structural levels 1 and 2 by means of Eqs. (4.66), (4.67) and (4.68). Bimodal pore size distributions were obtained for each sample, as a consequence of the two overlapping structural levels used to fit the second region of the scattering intensity profiles. Specifically, the volume PSDs associated to levels 1 and 2 were merged in order to obtain the sample PSD. The calculated PSDs of sample A, C and D are compared in Fig. 5.11 with the corresponding N_2-adsorption PSDs obtained by means of the BJH method assuming cylindrical pore shape. A good agreement between the PSDs estimated by USAXS-SAXS and those obtained by the BJH method, especially for samples A and D, can be noticed. The parameters obtained through the unified fit of the scattering intensity profiles don't provide a direct information regarding the pore shape. For this reason, a sphericity factor Ψ_i is used in order to investigate the pore shape deviations from the spherical shape and, according to Wadell (1935), McCabe, Smith, and Harriott (2005), and Seader and Henley (2006), is defined as:

$$\Psi_i = \frac{3}{R_{\mathrm{sph},i}} \frac{\varepsilon_i}{S_{V,i}}, \tag{5.2}$$

where the subscript i refers to the structural level i (in this case level 1 or 2), $S_{V,i}$ is the specific surface area of pores belonging to level i per unit of particle volume and $R_{\mathrm{sph},i}$ is the pore radius assuming a spherical pore shape, that is equal to $(5/3)^{1/2}\, R_{g,i}$ (Glatter and Kratky, 1982). The sphericity factor is equal to 1 in the case of spherical pores and assumes lower values for shapes different from the spherical one, namely 0.846 for the

octahedron, 0.806 for the cube, 0.671 for a tetrahedron, and 0.874 for ideal cylinders. During the calcination reaction at 800 °C, the sphericity factor increases from 0.83 to 0.86 for the micropore population and from 0.69 to 0.82 for the mesopore population (Tab. 5.7). During the sintering step after the calcination reaction, the sphericity factor generally shows a decrease over time, in fact at 900 °C (after 4 hours of sintering) it decreases from 0.98 to 0.92 for micropores and from 0.84 to 0.66 for mesopores, and at 800 °C (after 12 h of sintering) decreases from 0.82 a 0.79 for mesopores; however, at 800 °C (after 12 hours of sintering) it increases from 0.86 to roughly 1 for micropores (Tab. 5.7). Generally, the trends seem to be an increase of the sphericity factor during the calcination reaction and a decrease of the sphericity factor during sintering ; after the calcination, however, such statements are to be taken as hypotheses, given the paucity of data available and the inaccuracy of these estimates of the sphericity factors above all for the micropore population (more affected by the experimental error, because of the smaller values of its textural properties). This is confirmed by sample F sphericity factors, which should be similar to those of sample A (samples A and F differ only in the particle size and were produced with the same calcination conditions); sample F sphericity factor for mesopores is 0.86 (0.82 for sample A), however it is 0.96 for micropores, not close to the sample A value (0.86).

Finally, a comparison was performed between the textural properties of samples A, C, D measured by USAXS/SAXS and by N_2-adsorption. In the USAXS-SAXS measurements, the sample mean pore radius was calculated as the first moment of the sample bimodal volume distribution and listed in Tab. 5.7. An excellent agreement can be observed between the mean pore radius of samples A, B and C, namely 133 Å, 253 Å and 130 Å (Tab. 5.7), with those estimated by N_2-adsorption with the BJH method, namely 132 Å, 204 Å and 126 Å (Tab. 5.6) respectively. A nice agreement between the results obtained by the two techniques (USAXS/SAXS and N_2-adsorption) was obtained also as far as the specific surface area, in fact the specific surface areas of samples A, C, and D measured by USAXS/SAXS are $48.9\,m^2\,g^{-1}$, $22.4\,m^2\,g^{-1}$ and $52.2\,m^2\,g^{-1}$ (Tab. 5.5) respectively, while the BET estimations are $50.4\,m^2\,g^{-1}$, $20.7\,m^2\,g^{-1}$ and $41.0\,m^2\,g^{-1}$ (Tab. 5.6). Finally, the agreement of the results obtained by the two techniques is confirmed in terms of the sample PSDs shown in Fig. 5.11. Instead, the porosity values estimated from the USAXS/SAXS scattering intensity profiles (Tab. 5.5) through Eq. (4.64) (Porod invariant), even though follow qualitatively the expected trends over time and respect to the calcination temperature (Fig. 5.8),are systematically lower respect to those computed by the BJH method (Tab. 5.6). Specifically, the discrepancy ranges from a minimum of 18 % lower than the BJH porosity value of sample D up to 28 % for the case of sample A. The porosity values computed in this work by the BJH method are aligned with the common porosity values of CaO sorbents derived from N_2 decomposition of calcium carbonate: 0.52 (Bhatia and Perlmutter, 1983a), 0.48 (Borgwardt, 1989b), 0.46 and 0.47 (Grasa et al., 2009), 0.53 and 0.47 (Rodriguez-Navarro et al., 2009). Additionally, Spalla, Lyonnard, and Testard (2003), Chavez Panduro et al. (2012), and Nguyen and Bhatia (2012)) demonstrated that the textural properties (particularly the pore volume) estimated by means of SAS are systematically higher than those estimated with the gas-adsorption technique, because of the SAS capability to detect the additional porosity associated with the isolated pores, that could be not accessible by the probing gas. In this work the mismatch between the porosity values estimated by USAXS-SAXS and by BJH analysis could be due to the multiple scattering corrections that are necessary to correctly calibrate the absolute intensity in the scattering intensity profiles and that may become less accurate when the the sorbent porosity is high, as in the case of the samples analyzed in this work.

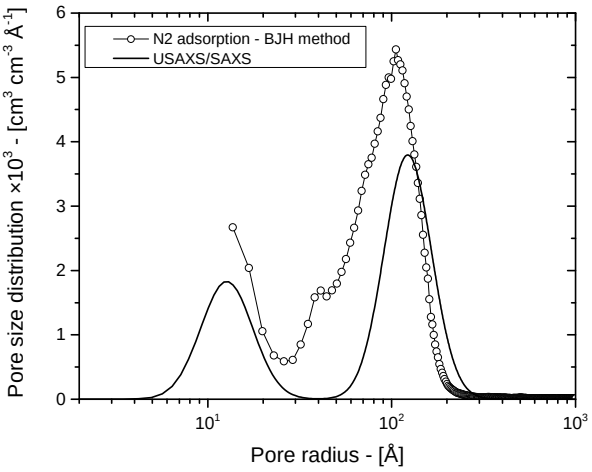

(a) *Sample A.*

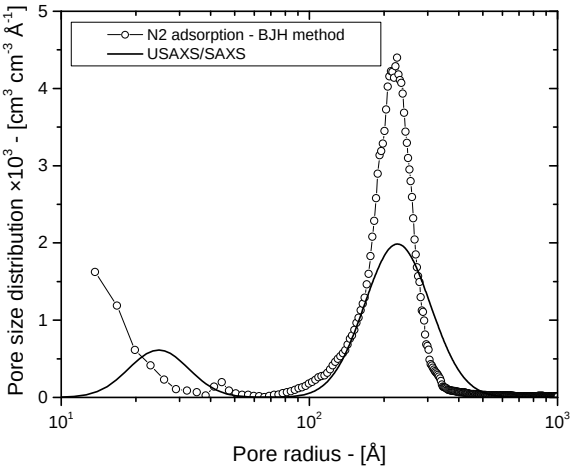

(b) *Sample C (highly sintered).*

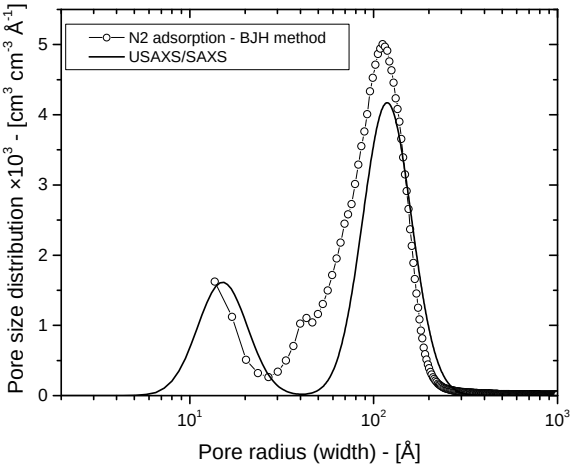

(c) *Sample D.*

Figure 5.11: Comparison between the volume pore size distributions obtained by means of the N_2-adsorption technique using the BJH method for cylindrical pore shape and by USAXS-SAXS.

Table 5.8: Micro textural properties of the carbonated samples.

Sample	$R_{g,1}$ [Å]	$R_{g,2}$ [Å]	$S_{m,1}$ $[m^2\,g^{-1}]$	$S_{m,2}$ $[m^2\,g^{-1}]$	S_m $[m^2\,g^{-1}]$	ε_1 [–]	ε_2 [–]	ε [–]	$N_{m,1} \times 10^{-16}$ $[g^{-1}]$	$N_{m,2} \times 10^{-16}$ $[g^{-1}]$	$N_m \times 10^{-16}$ $[g^{-1}]$
G	19.9	153	8.27	30.3	38.5	0.014	0.340	0.354	28.2	1.62	29.8
H	21.0	176	5.8	12.6	18.4	0.006	0.162	0.168	46.2	0.431	46.7
I	27.4	225	3.031	7.29	10.3	0.005	0.087	0.092	7.84	0.176	8.02
L	43.2	382	0.958	1.40	2.36	0.003	0.019	0.022	0.901	0.035	0.936

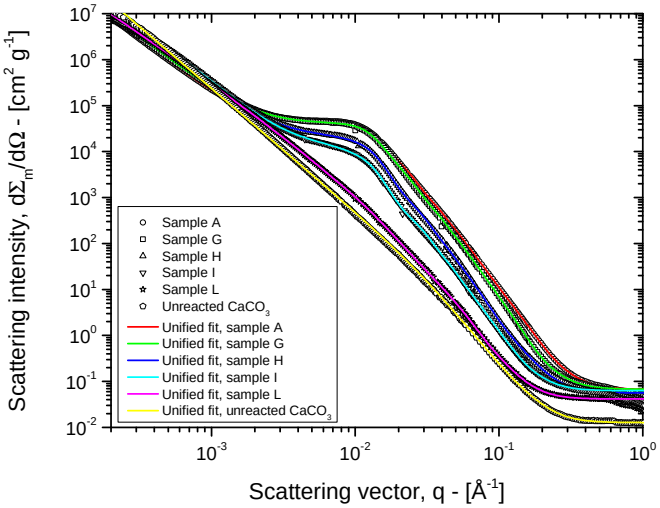

Figure 5.12: Experimental slit-smeared scattering intensities profiles in absolute units and unified fits of partially carbonated samples G, H, I, L (at different CaO conversion degrees) compared to sample A (sorbent before the carbonation beginning) and un-reacted (before the calcination) $CaCO_3$. Slit length is $0.028\,028\,\text{Å}^{-1}$; for the un-reacted $CaCO_3$ the slit length is $0.024\,164\,\text{Å}^{-1}$ and the beam energy is 24 keV.

5.3.3 Carbonated sorbents

For the investigation of the the sorbent micro-structural properties evolution during the carbonation reaction, four samples were calcined following the same procedure of sample A, namely a non-isothermal calcination reaction up to 800 °C under vacuum conditions for 40 min. After the calcination step, the temperature was decreased down to 650 °C and a mixture with 10 % of CO_2 in balance with nitrogen was fed at 1.3 bar. Isothermal CaO carbonation reactions were thus performed and four different carbonated samples were produced by stopping the gas flow and the furnace heating at different times during the carbonation. Specifically, in addition to sample A (which corresponds the unreacted CaO sorbent) four samples G, H, I, and L were produced at the following CaO conversions: 9.91 %, 43.38 %, 61.19 % and 78.66 % (Tab. 5.3le 3). Samples G, H and I where produced during the first chemically controlled regime. Instead, sample L was obtained immediately after to the sharp transition point between the chemically controlled step and the slow product layer controlled regime, in order to check the variation of the micro-structural properties after the transition point, that denotes a drastic change of the sorbent properties.

The slit-smeared scattering intensity profiles of the carbonated samples are shown in Fig. 5.12, where the scattering intensity of sample A (the uncarbonated CaO sorbent) is also included. Additionally, the uncalcined non-porous $CaCO_3$ (sorbent precursor) scattering profile is plotted as well, as a comparison with the USAXS-SAXS response of sample L. As the carbonation reaction takes place, the sorbent scattering intensity profile degenerates down to the smooth profile of sample L, which is similar to the scattering response of the non-porous $CaCO_3$ This suggests a gradual loss of the sorbent porosity due to the calcium carbonate product layer, that fills the sorbent pores up to the plugging of the majority of pores. Sample L scattering intensity profile is clearly different respect to the scattering intensity profiles of samples G, H, I, which this confirms the drastic change of sorbent microstructural properties after the transition point.

As indicated by the decrease of the high-q values intensity, the specific surface area of the two pore populations seems to be the first sorbent micro-structural property to

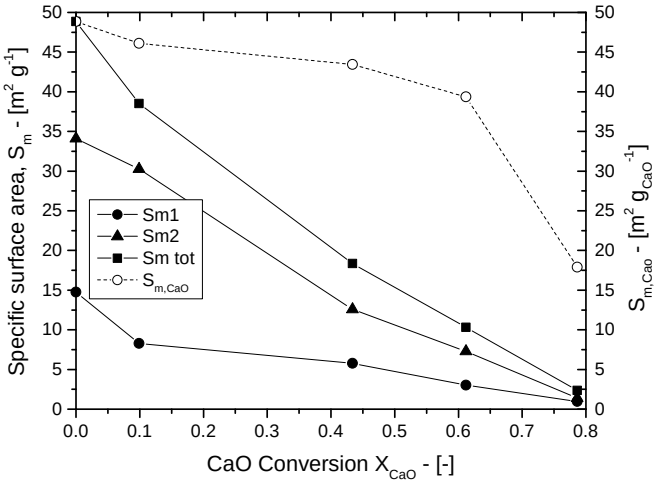

Figure 5.13: Evolution of the specific surface area of two pore populations and of the sample specific surface area over the CaO conversion during the carbonation reaction.

be affected by the carbonation reaction, as shown by the scattering intensity profile of sample G in Fig. 5.12. In the specific surface area evolution over the CaO carbonation conversion represented in Fig 5.13, it is remarkable that the decreasing rates of the two pore populations in the first instants of the carbonation reaction (below 10 %) are different. As shown in the inset of Fig. 5.14, also the porosity of the small population has a decreasing rate (in relative terms of percentage of porosity loss over CaO conversion) in the first part of the carbonation higher than the second population. These trends suggest that the small pore population has a more relevant contribution during the first instants of the carbonation reaction (below 10 % of conversion). This is confirmed by the pore number density trends over time (Fig. 5.14), in which for the micro-pore population a strong decrease of pore number density is evident in the first part of the carbonation. Additionally, the specific surface areas per g of unreacted CaO (Fig. 5.12) don't change significantly for most of the carbonation, with values between $45 - 49\,\mathrm{m^2\,g^{-1}}$ from the beginning of the reaction to a CaO conversion of 0.413, which might support an interpretation of a heterogeneous sorbent particle in which different regions react at different times.

The total internal porosity trend over the CaO conversion is mostly linear (Fig. 5.14), as expected according to Eq (2.5). However, as already noted for the calcined sorbents, the porosity values, computed by Eq. (4.64), are lower than expected likely because of the multiple scattering corrections.
With the increase of the CaO conversion, the Guinier regimes (Fig. 5.12) seem to be slightly shifted towards to the small-q region suggesting an increase of the pore radius of gyration. The calculated radius of gyration over the CaO conversion of the two pore populations is represented in Fig. 5.15 where it can be observed that the radius of gyration of both populations increase, above all in the last part of the carbonation, and that the increase seems stronger for the second population. These trends could be explained by a transfer of the contracting second population pores to the first population.

Additionally, it should be noticed that this critical point is associated with a loss of the majority of the sorbent porosity and specific surface area that converge to near to small values (Figs. 5.13 and 5.14). Specifically, at 78.66 % of CaO conversion the estimated sorbent surface area is $2.36\,\mathrm{m^2\,g^{-1}}$ and the corresponding particle porosity is 0.022, that confirm the abrupt change into the sorbent pore structure.

According to the relationship between the sorbent porosity and the CaO conversion in

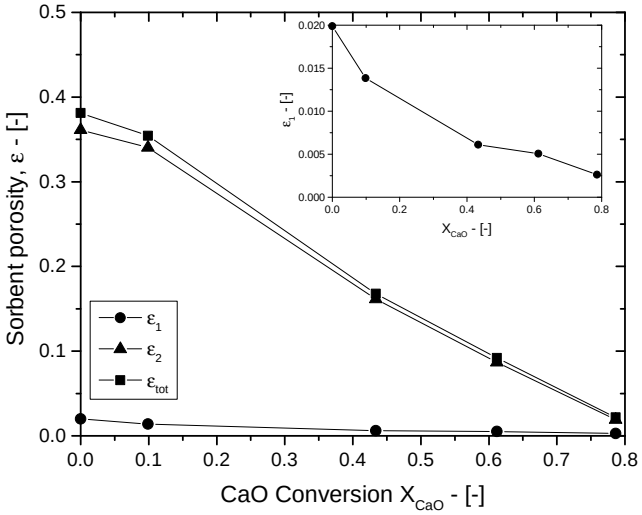

Figure 5.14: Evolution of the porosity of the two pore populations and of the total sample internal porosity over the CaO conversion during the carbonation reaction.

Eq (2.5), the final conversion is mainly due to the second population contribution because of its higher porosity values than those of the small pore population. Although the porosity of the first population has a modest contribution to the CaO conversion, its pore structure could play a relevant role in the reaction kinetics because of its significant surface area contribution.

The values of sample L micro-structural properties, listed in Tab. 5.8, suggest that the bulk porosity is almost completely plugged by $CaCO_3$ and only a low pore fraction is still available. This remaining pore structure is mainly due to the contribution of the larger pores. Additionally, because of the SAS capability to investigate isolated pores, the remaining porosity could be also associated to isolated pores. This remaining porosity can still contribute to the CaO conversion after the transition point , but with a very slow reaction rate because of the $CaCO_3$ product layer thickness and the low specific surface area still available. The unreacted $CaCO_3$ (sorbent precursor) intensity profile was fitted with only one structural level and the estimated porosity and specific surface area are about $6.7 \times 10^{-4}\,m^2\,g^{-1}$ and $1.15\,m^2\,g^{-1}$ respectively. The difference between these values and those of sample L (Tab. 5.8) confirms the residual pore structure after the transition point in the highly-carbonated sample.

The detailed information that the SAS technique is capable to provide and, specifically, its capability to the two populations of pores reveal that the transition point is characterized by a sudden and sharp change in the sorbent pore structure, namely an abrupt increase of radius of gyration and a loss of the porosity and surface area of the two populations of pores. This result suggest a different explanation respect the previous literature contributions that identified the transition only with the pore closure of small pores Bhatia and Perlmutter (1983a) and Sun et al. (2008a).

The correlation distance ζ was also analyzed for the carbonated samples as a function of the CaO conversion. The sample correlation distance remained almost constant during the carbonation reaction and specifically within $379 \div 449\,Å$. The constancy of the correlation distance for most of the CaO carbonation might support the interpretation of a heterogeneous sorbent particle in which different regions react at different times.

The sphericity factor was calculated according to Eq. (5.2) for both the two pore

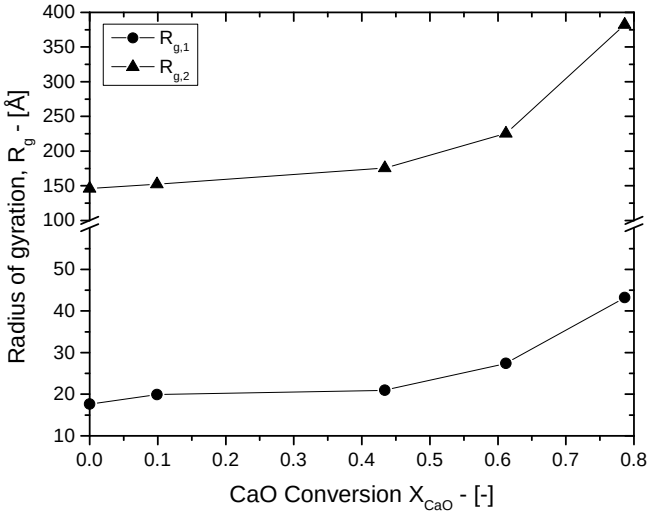

Figure 5.15: Evolution of the radius of gyration of the two pore populations over the CaO conversion during the carbonation reaction.

populations and their evolution over the carbonation reaction is showed in Fig. 5.17. Interestingly, this plot suggests that the overall effect of the carbonation reaction on the pore shape is to decrease the pore sphericity of the two populations. Specifically, it seems that for the micro-pore population after a first sphericity factor reduction, a rather constant region is observed for CaO conversions higher than 0.4 and the micro-pore sphericity factor assumes an average value of about 0.55. This behavior is not observed for the case of the second pore population (meso-pore population) whose sphericity factor evolution shows a decreasing trend down to a final value of 0.3.

5.4 Conclusions

In this work, X-ray synchrotron-based small angle scattering technique was applied for the first time to the micro-structure investigation of completely and partially calcited $CaCO_3$ and CaO carbonated samples for CO_2 capture applications. Small angle scattering data were collected at the beamline 9-ID-B, C of the Advanced Photon Source (APS) at the Argonne National Laboratory.
These measurements were capable to provide a detailed description of the material pore structure in terms of particle porosity, specific surface area, radius of gyration and pore size distribution. Specifically, the small angle scattering intensity profile analysis by means of the "Unified fit" approach (Beaucage, 1995; Beaucage, 1996) confirmed the bimodal distribution of the CaO samples, characterized by two distinct pore populations made of micro- and meso-pores respectively. Additionally, the USAXS/SAXS technique was capable to provide a quantitative and detailed description of the structure of each pore population in terms of porosity, specific surface area, radius of gyration. Such detailed description of the sorbent micro-structure could not be achieved by the traditional N_2-adsorption and mercury porosimetry techniques.

As far as the $CaCO_3$ calcined samples, the estimated micro-textural values of the specific surface areas and the pore radius are in quantitative agreement with the N_2-adsorption measurements results, namely with the BET and BJH methods, especially for the case of the average pore radius, where the agreement with the BJH results is excellent. Additionally, bimodal pore size distributions obtained from the scattering intensity data

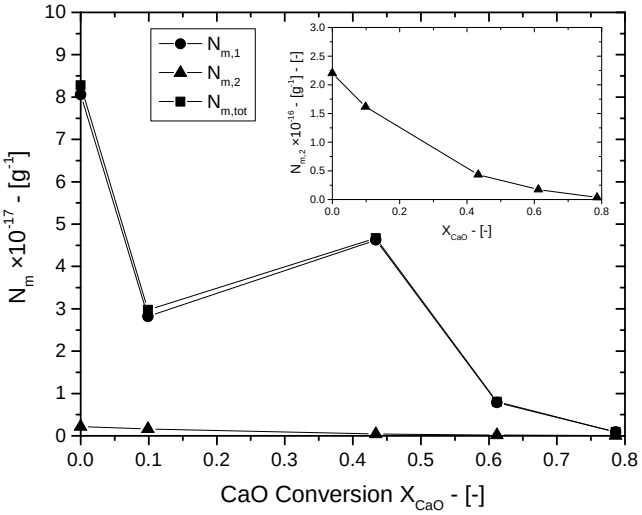

Figure 5.16: Evolution of the pore number density of the two pore populations and of the total sample pore number density over the CaO conversion during the carbonation reaction.

analysis (Beaucage, Kammler, and Pratsinis, 2004) are in good agreement with those obtained with the N_2-adsoption technique (the BJH method).

Although the micro-pore population exhibits significant low porosities values (from 0.01 to 0.02) respect to the meso-pore population ($0.21 \div 0.42$), its specific surface areas are comparable with those of the meso-pore population in terms of order of magnitude.
During the high temperature sintering step, the meso-pore population plays a relevant role in the sorbent micro-structure evolution over time respect to the micro-pore population, especially when temperature is increased from 800 °C to 900 °C and its evolution is more pronounced respect than the micro-pores. More specifically, these high specific surface areas (in relative terms) are surely due to high surface-to-volume ratio of the micro-pore population than the meso-pores, but especially by the significant higher pore number density values of the micro-pore fraction respect to the meso-pore one, that is about one order of magnitude higher than that of the meso-pores. In fact, the pore number per unit of sample mass of each population was estimated from the measured pore size distribution, providing the micro- and meso-pore number density evolution over time.

The analysis of the partially calcined sample suggest that its reacted volume morphology is similar to that of the completed calcined samples, meaning that its micro-structure does not change significantly during the last part of the thermal decomposition under vacuum conditions. This sample allowed a rough estimation of the pore generation rates during the $CaCO_3$ calcination reaction, namely $1.1 - 5.7 \times 10^{16}\,g^{-1}\,min^{-1}$ for the micro-pores and $5.3 - 5.5 \times 10^{14}\,g^{-1}\,min^{-1}$ for meso-pores. With the aim to obtain information about the pore shape, a pore sphericity factor was introduced to quantify the deviation from the spherical shape. Specifically, during the calcination reaction the micro- and meso-pore sphericity factors increase, showing a decreasing trend during the sintering step once the $CaCO_3$ calcination reaction is completed. Interestingly, micro-pores exhibit a higher initial spherical shape (about 0.8) respect to the meso-pore (0.7).

Correlation distances were provided by the structure factor second structural level of the "Unified fit" associated with the meso-pore population. This quantity is capable to provide an average estimation of the pore-to-pore distance (Beaucage et al., 1995), whose value is approximately 45 nm when low residence times are considered. This value was

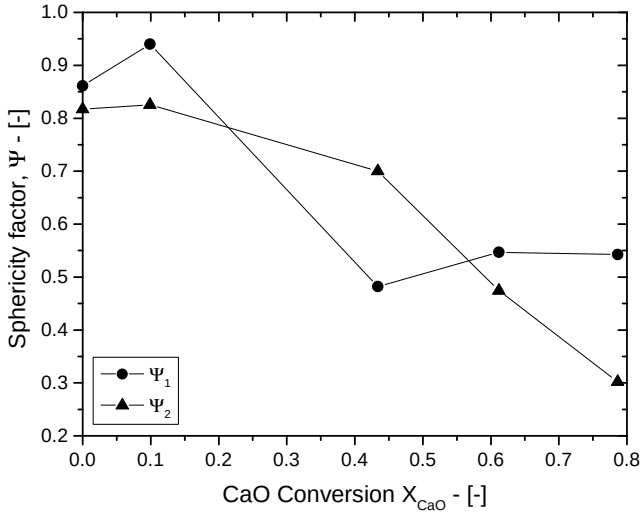

Figure 5.17: Evolution of the radius of gyration of the two pore populations over the CaO conversion during the carbonation reaction.

also confirmed by the partially calcined sample correlation distance, proving that its pore network is similar to those of the completely calcined samples. As the heating duration progresses, the meso-pore correlation distance increases up to about 81 nm (at 800 °C) and 96 nm (at 900 °C), suggesting that the pore coalescence process is the main mechanism of sintering (in vacuum conditions).

The analysis of the scattering intensity profiles of the partially carbonated samples pointed out a drastic change of the sorbent micro-textural properties after the transition point, where the majority of pores are plugged by the non-porous $CaCO_3$ product layer. The different slopes of the specific surface area reduction profiles over the CaO conversion suggests the more relevant contribution of the micro-pore population during the first instants of the reaction, associated with a strong decrease of the micro-pore number density trend. Additionally, the specific surface area per unit of unreacted calcium oxide is mostly constant during the carbonation reaction, ranging close to the initial sorbent specific surface area value. Finally, an unexpected increase of the pore radius of gyration (of both the two pore populations) was observed, especially after the transition point. This behavior was ascribed to a transfer of the contracting meso-porosity into the micro-pore population.

The overall maximum CaO conversion value was mainly associated with the meso-pore volume fraction because of the high porosity values of the meso-pore population respect to the micro-pore one. On the other hand, the high specific surface of the micro-pore population could play a significant role in the fast chemically-controlled regime of carbonation reaction rate, although its modest porosity value. The overall effect of the CaO carbonation reaction on the pore shape consists in a decreasing of the sphericity the two pore population, leading to a final value of 0.55 for micro-pores and 0.3 for meso-pores.

Finally, correlation distances seem to be quite constant during the CaO carbonation reaction and, specifically before the transition point, namely $38 \div 45$ nm. This result together with the constant specific surface area associated with the unreacted CaO and the interpretation of the meso-porosity migration into the micro-pore population suggest a heterogeneous pore micro-structure into the sorbent particle, where different region exhibit different reacting times.

These results are significant to demonstrate how small angle scattering technique can be successful applied for the investigation of the calcium based solid sorbents micro-structure

during the sorbent activation and CO_2 capture step, proving that both qualitative and quantitative micro-textural properties can be estimated from the scattering intensity profiles.

Part III

In-situ Characterization Techniques

Chapter 6

Micro-structure characterization of nascent CaO during the $CaCO_3$ decomposition by in-situ USAXS

The successful application of the ex-situ small angle scattering technique to the characterization of the CaO micro-structure led to the investigation of the nascent calcium oxide micro-textural properties during the calcite decompositions and sintering by means of *in-situ* time-resolved small angle scattering measurements at the same operative conditions, in terms of temperature and reactor atmosphere composition.

Small angle X-ray scattering technique was successful applied for the *first time* to the investigation of the nascent porosity of the decomposing calcite by means of in-situ measurements. Experiments were performed at the Advanced Photon Source (APS) at the Argonne National Laboratory (Argonne, Illinois).

This chapter deals with the sorbent micro-textural properties generation during the precursor activation, by exploring different reaction temperatures and atmosphere compositions (CO_2/N_2). Specifically two different sets of experiments were investigated: samples calcined below 800°C in pure nitrogen and those calcined at 800°C or 900°C varying the CO_2 content from a minimum of 1 % up to a maximum of 50 % in balance with N_2. Afterwards, an additional residence time (at the same operative conditions of the reaction step) was considered to allow sintering phenomena to affect the final sorbent micro-textural properties. These operative conditions were carefully selected to investigate the high temperature and time dependent phenomena, like pore generation and sintering mechanisms and their interactions between each others.

6.1 Introduction

Several literature contributors studied the sintering mechanisms effects of the sorbent micro-textural properties on completely calcined $CaCO_3$ sorbents. Borgwardt (1989b) investigated the sintering of nascent calcium oxide generated by means of a differential reactor under N_2 atmosphere at 700 °C, varying the sintering temperature (from 700 up to 1000 °C) and the residence time. High specific surface areas were obtained at700 °C, namely $104\,m^2\,g^{-1}$ meaning that sintering process do not significantly affect the CaO micro-structure at this temperature. Both the CaO specific surface area and porosity were reduced by means of sintering and this process was significantly accelerated by temperature. Afterwards, this study was extended including the CO_2 and H_2O effects (Borgwardt, 1989a). Specifically, the CO_2 presence in the calcination atmosphere accelerates the CaO micro-structure sintering acting as a sintering catalyst on both the surface area and porosity reduction (Borgwardt, 1989a). However, under such conditions the specific surface area decrease is significantly faster than the porosity loss. The CO_2 sintering catalytic effects

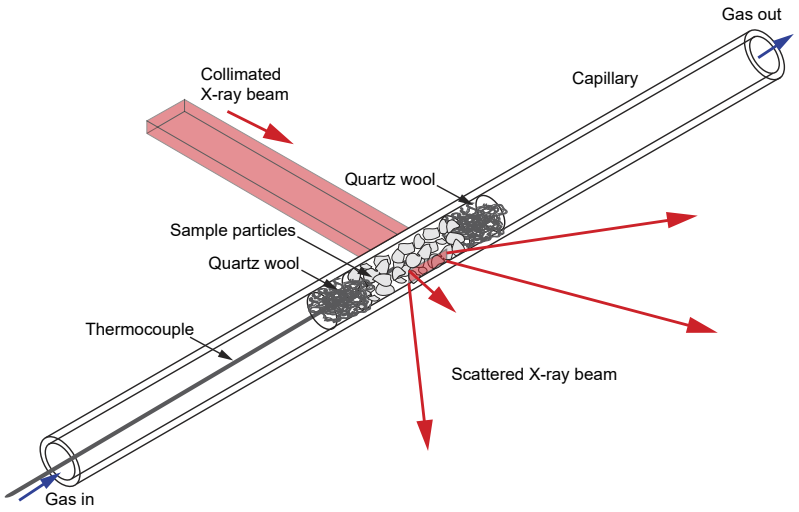

Figure 6.1: Schematic representation of the capillary-based set-up used for the in-situ SAS measurements.

were also observed by Ewing, Beruto, and Searcy (1979), Beruto, Barco, and Searcy (1984), and Mai and Edgar (1989), even though this last contributor used calcium oxide derived from the calcium hydroxide decomposition which sinter faster than the CaO derived from $CaCO_3$ (Borgwardt, 1989a). Fuertes et al. (1991) investigated both the CaO specific surface area and the pore size distribution (PSD) evolution during sintering under N_2 and CO_2 atmosphere in a temperature range $700 \div 900\,°C$ observing an increase of the sorbent mean pore radius with sintering time and temperature. Interestingly, the CaO pore radius evolution at different CO_2 concentrations ($0 \div 15\,\%$ in balance with N_2) accelerates and the pore radius profiles over the sintering step changes from concave (pure N_2) trends to convex ones. More recently Zhu, Wu, and Wang (2011) investigated the CaO nano grain micro-textural properties by means of different calcination reaction temperatures and sintering times investigating the sorbent crystallite size and PSDs effects on the CaO carbonation reaction kinetics.

Thus far, the sorbent micro-textural properties generation and evolution during the $CaCO_3$ calcination reaction have been debated by only few literature contributors and the investigation of these phenomena is still open. The pore generation, the surface evolution, the reaction kinetics, sintering phenomena and micro-structure interactions during the $CaCO_3$ thermal decomposition are only few examples.

Beruto (1976) investigated the kinetics decomposition of powder calcite under vacuum conditions in the temperature range between 450 °C and 750 °C, observing little changes in the particle shape and little sintering by means of scanning electron microscope (SEM) images. Conversely to $CaCO_3$ calcined in air or N_2, the calcite decomposed in-vacuo shows weak diffraction peaks indicating a poorly crystalline structure. Beruto (1976) associated this low crystalline material with a metastable form of CaO (that is converted in to a stable polycrystalline lime in the later stages of the reaction), chemically more reactive that the stable calcium oxide. Beruto and Searcy (1974), Beruto (1976), and Powell and Searcy (1982) observed the existence of an intermediate layer between the undecomposed $CaCO_3$ and the final CaO product composed by this metastable material, namely porous aggregated of small NaCl-type CaO crystals. Powell and Searcy (1982) stated that this intermediate layer was characterized by a uniform pore size different from the final CaO structure. The transformation of the intermediate CaO layer to the final CaO product was retained to occur by means of a collapse of the pore structure, generating the pore

Table 6.1: Chemical and physical properties of calcium carbonate and calcium oxide (Haynes, 2014; Ilavsky and Jemian, 2009).

Property	$CaCO_3$	CaO
Molecular weight, M $\left[\mathrm{g\,mol^{-1}}\right]$	100.087	56.077
Density, ρ $\left[\mathrm{g\,m^{-3}}\right]$	2.71	3.34
Linear absorption coefficient, μ, $\left[\mathrm{cm^{-1}}\right]$	19.5	41.11
Contrast (18 keV), $\Delta\rho_e^2$ $\left[\mathrm{cm^{-4}}\right]$	524.32×10^{20}	798.5×10^{20}

distribution (Beruto, Barco, and Searcy, 1983; Powell and Searcy, 1982).

Afterwards, Ewing, Beruto, and Searcy (1979) performed calcination under in-vacuo (below 0.1 torr) at 650 °C and demonstrated that CO_2 influences the surface sintering by changing the pores geometry with low significant effect on porosity. This change in the micro-structure morphology was associated with high CO_2 concentration gradients inside the decomposing calcite material with which the metastable calcium oxide reacts (Ewing, Beruto, and Searcy, 1979; Powell and Searcy, 1982). Additionally, metastable CaO crystals are highly CO_2 reactive and probably form a metastable solution of CO_2 (such as ${CO_3}^{2-}$ dissolved in CaO (Ewing, Beruto, and Searcy, 1979).

Ewing, Beruto, and Searcy (1979), Powell and Searcy (1982), and Beruto, Barco, and Searcy (1983) estimated significantly high maximum specific surface areas of CaO decomposed in vacuum, namely $92\,\mathrm{m^2\,g^{-1}}$, $127\,\mathrm{m^2\,g^{-1}}$ and $116\,\mathrm{m^2\,g^{-1}}$. These values are in excellent agreement with those estimated by Borgwardt (1989b) and Rodriguez-Navarro et al. (2009) by means calcite thermal decomposition in N_2 atmosphere: $104\,\mathrm{m^2\,g^{-1}}$ and $79.2\,\mathrm{m^2\,g^{-1}}$ (detected at a $CaCO_3$ mass conversion value of 11 %) respectively. According to Rodriguez-Navarro et al. (2009) three different classes of pores characterized the calcium oxide micro-structure: micro-pores between the nascent CaO nano-crystals (less than 2 nm in size), meso-pores placed between isolated crystals (up to $30 - 50$ nm in size) and macro-pores (more than 50 nm) located between CaO iso-oriented domains. This pore network texture agrees with that proposed by Borgwardt (1989b) who argued a CaO pore matrix composed by micro and macro pores during the initial stage of sintering. Micro-porosity progressively disappears during the intermediates stage increasing the macro pores number.

Therefore, in order to investigate the sorbent micro-structure generation and evolution during the calcination reaction it is essential to account for the sintering mechanism effects. Many researchers investigated the surface evolution during the $CaCO_3$ calcination reaction like Agnew et al. (2000), Bailliez and Nzihou (2004), Fierro, Adánez, and García-Labiano (2004), Glasson (1958), and Silcox, Kramlich, and Pershing (1989) observing increasing surface area profiles over time up to a maximum value (before the $CaCO_3$ complete conversion) and then decreasing to an asymptotic value due to sintering processes. These trends were modeled (Agnew et al., 2000; Bailliez and Nzihou, 2004; Fierro, Adánez, and García-Labiano, 2004; Mahuli et al., 1999; Mai and Edgar, 1989; Silcox, Kramlich, and Pershing, 1989) by means of a combination of structural kinetics models (i.e. the grain model) and semi-empirical correlations, such as those proposed by Nicholson (1965) or R. M. German and Munir (1976), in order to represent to man mechanisms: pore generation and surface reduction due to sintering. On the other hand, Ewing, Beruto, and Searcy (1979) and Powell and Searcy (1982) interestingly observed linear surface areas evolutions over the $CaCO_3$ reaction under vacuum conditions or significantly low CO_2 partial pressures ($0.1 \div 0.9$ torr). Such profiles deviated from the linearity when the CO_2 partial pressures were higher than 0.9 torr (Ewing, Beruto, and Searcy, 1979).

According to García-Labiano et al. (2002), the porosity evolution profile during the calcite decomposition should be linear over the calcination reaction conversion, as stated

by Eq.(2.3). By assuming an initial sorbent precursor ($CaCO_3$) porosity equal to zero, Eq.(2.3) predicts the well-known CaO theoretical porosity of 0.545. This linear trend was observed only by Beruto, Barco, and Searcy (1983) during the calcite decomposition at 686 °C under vacuum conditions.

The CaO micro-textural properties are completely determined by the sorbent pore size distribution that was observed to be characterized by a bimodal pore structure as investigated by (Li, Liang, and Cai, 2016; Li, Cai, and Huang, 2006; Maya, Chejne, and Bhatia, 2017a; Rodriguez-Navarro et al., 2009; Zhu, Wu, and Wang, 2011). Two pores populations have been identified placed in the micro and macro pore regions respectively (Zhu, Wu, and Wang, 2011). Specifically, the micro-pore population was observed to be located between the micro and macro pore threshold, approximately in the correspondence to a pore radius of about 20 Å (Li, Liang, and Cai, 2016; Zhu, Wu, and Wang, 2011). On the other hand, meso pores population have been detected in a pore radius range of $100 \div 500$ Å, depending on the $CaCO_3$ thermal activation conditions (Li, Liang, and Cai, 2016; Rodriguez-Navarro et al., 2009; Zhu, Wu, and Wang, 2011). More recently, Benedetti et al. (2017) observed bimodal populations on thermally activated $CaCO_3$ under vacuum conditions, confirming the bimodal nature of the CaO PDSs. Interestingly., the micro pores population was detected in the highly sintered CaO samples where the high temperature sintering phenomena strongly influenced the PSD (Benedetti et al., 2017; Li, Liang, and Cai, 2016; Rodriguez-Navarro et al., 2009; Zhu, Wu, and Wang, 2011).

The micro-textural properties of CaO based sorbents for CO_2 capture have been widely investigated by means of the traditional ex-situ techniques, namely the gas-adsorption and the mercury porosimetry (Barker, 1973; Beruto, Barco, and Searcy, 1983; Bhatia and Perlmutter, 1983a; Borgwardt, 1985; Borgwardt, 1989b; Ewing, Beruto, and Searcy, 1979; Fierro, Adánez, and García-Labiano, 2004; Fuertes et al., 1991; García-Labiano et al., 2002; Glasson, 1958; Grasa et al., 2009; Borgwardt, 1989a; Li, Liang, and Cai, 2016; Maya, Chejne, and Bhatia, 2017a; Maya, Chejne, and Bhatia, 2017b; Milne et al., 1990; Powell and Searcy, 1982; Rodriguez-Navarro et al., 2009; Silcox, Kramlich, and Pershing, 1989; Sun et al., 2007; Zhu, Wu, and Wang, 2011). Because of the ex-situ nature of these techniques several important limitations may arise that can affect the material property measurements:

1. the sorbent properties are analyzed at fairly different operative conditions (i.e. 77 K for N_2 gas adsorption) respect to the thermal activation conditions ($600 \div 900$ °C);

2. because of the high hygroscopic nature of calcium oxide the material needs to be stored under an inert atmosphere;

3. the micro-textural properties generation during the calcination reaction can be hardly investigated, because the reaction needs to be stopped by cooling and the micro-structural properties change during this last step.

Additionally, the mercury porosimetry technique is limited by the instrument highest achievable pressure, that defines the minimum measurable (accessible to mercury) pore size as stated by Lowell (2004), according to the Washburn equation (Washburn, 1921). Finally, the probing gas accessibility in the gas-adsorption techniques may be limited by the complex and disordered structure of the sampling material, like distortions and constrictions (Nguyen and Bhatia, 2012).

Recently, Benedetti et al. (2017) investigated the CaO micro-textural properties evolution during the calcination and carbonation reaction by means of the ex-situ Synchrotron Radiation (SR) X-ray Small Angle Scattering Technique (SAS) that is not affected by the aforementioned limitations of mercury porosimetry and of gas-adsorption based techniques.

Specifically, Ultra Small Angle X-ray Scattering (USAXS), Small Angle X-ray Scattering and Wide Angle Scattering (WAXS) techniques have been applied for the first time to the CaO-based CO_2-capture sorbent characterization. Sorbent micro-textural properties and chemical composition were estimated in terms of porosity, specific surface area, mean pore radius, PSD and sorbent weight fractions, in agreement with those obtained by means of the N_2-adsorption technique and TGA analysis.

SR X-ray based SAS is a non-destructive and non-invasive technique that allows the micro-structural properties investigation of micro/nano-scale inhomogeneous materials, by means of differences in X-ray contrast (the electron density difference of the two phases) due to the scatteres (like pores, particles, micelles, polymers chains etc.). SAS can provide both qualitative and quantitative information about the micro-structural properties and morphology of the material in-homogeneities, namely pores in the case of porous materials. Specifically, the material porosity, specific surface area and mean pore radius, as well as pore size distributions (PSDs) are estimated (Chavez Panduro et al., 2012; Hu et al., 2011; Nguyen and Bhatia, 2012; Spalla, Lyonnard, and Testard, 2003; Lee et al., 2014; Beaucage, Kammler, and Pratsinis, 2004) from the measured scattering data, expressed in terms of scattering intensity profiles as a function of scattering vector q. Here, the scattering vector is defined as $q = (4\pi/\lambda)\sin(\theta/2)$, where λ is the wavelength of the incident X-ray beam and θ is the scattering angle (Glatter and Kratky, 1982). The lower limit of the q-range of an instrument is commonly used to roughly estimate the maximum diameter $d_{\max}$ of the scatterers by using the Bragg equation (Glatter and Kratky, 1982) through Eq. (2.18).

The most relevant advantage of the X-Ray SAS technique is it possibility to be used both ex-situ and *in-situ*. Specifically, in this work *in-situ* time-resolved SR X-ray SAS measurements were carried out to investigate the micro-textural properties of nascent CaO *during* the thermal activation of calcite and their evolution during sintering time. By the use of a capillary flow-cell/furnace wherein the samples to be tested were placed, different calcination reaction conditions were explored in order to monitor the thermal activation and sintering steps, without the need of extracting the material samples from the process operative conditions and avoiding the experimental issues related to the sample contamination/hydration (when exposed to the ambient conditions). Calcination reactions were performed at relative low temperatures ($600 \div 700\,^{\circ}C$) in nitrogen atmosphere and at higher temperatures in the range between $800\,^{\circ}C$ and $900\,^{\circ}C$ varying the CO_2 atmosphere concentration from a minimum of 1 % to a maximum of 50 % in balance with N_2. Additionally, all experiment have been performed at atmospheric pressure.

SAS measurements were performed at the 9-ID-C beamline at the Advanced Photon Source (APS), Argonne National Laboratory. The beamline provides both ex-situ and in-situ USAXS, SAXS and WAXS measurements in an energy range between 10 and 24 keV, allowing a total measurable q-range (USAXS + SAXS) of about $0.0001 \div 1.0\,\text{Å}^{-1}$ (Ilavsky et al., 2009). This wide q-range permits to investigate porous materials whose pore diameter, d, varies from a minimum of about 1 nm up to a maximum of 10 µm (Ilavsky, 2010). These capabilities make the USAXS+SAXS technique the ideal one to investigate the bimodal nature of the CaO-based pore structure, namely capable to explore both micro-pores (<2 nm) and meso-pores ($2 < d < 50$ nm) region of the sorbent pore matrix, especially during the high temperature activation.

6.2 Experimental details

6.2.1 Materials

Commercial calcium carbonate by AppliChem (marble granular A6297) was used as calcium oxide solid sorbent precursor (Tab. 6.1). This $150 \div 160$ µm particle size was selected

Table 6.2: Summary of the experimental operative conditions. CO_2 contents are in balance with N_2.

Sample	Final temperature [°C]	CO_2 % vol. time [−]	Reaction time [min]	Sintering [min]	Slit length $\left[\text{Å}^{-1}\right]$
A	600	0	229	0	0.02502
B	620	0	95	0	0.02491
C	650	0	36	29	0.02411
D	680	0	36	34	0.02502
E	700	0	26	21	0.02502
F	800	1	9	63	0.02491
G	800	5	36	77	0.02491
H	800	10	56	66	0.02502
I	850	10	9	81	0.02491
J	900	10	9	81	0.02491
K	900	25	13	95	0.02491
L	900	50	27	140	0.02491

because it ensures a good compactness within the capillary used for the SAS measurements. Additional details on sorbent precursor are described in § 2.7.

6.2.2 In-Situ SR-SAXS, USAXS and WAXS experiments

In-situ time-resolved SR X-ray small and wide angle scattering measurements on $CaCO_3$ calcination reaction and CaO sintering were performed at the beamline 9-ID-C of the Advanced Photon Source (APS), at Argonne National Laboratory. The experiments consisted of measuring the X-ray scattering data from a $CaCO_3$ powder material during two high temperature steps, namely the thermal decomposition of calcite into porous calcium oxide and carbon dioxide (calcination reaction) followed by a calcium oxide sintering step. These calcination reaction tests were performed by means of a flow-cell/furnace (Chupas et al., 2008) designed for conducting in-situ synchrotron-based studies of materials under non-ambient conditions. The experimental set-up allowed to control the sample environment conditions in terms of temperature (in this work up to 900 °C) and atmosphere/gas-flow. Because the flow-cell/furnace is based on a capillary sample geometry, 1.1 mm internal diameter quartz capillaries (by Friedrich & Dimmock Inc, 0.2 mm wall thickness and 75 mm long) were used to load about 5 mg of sorbent precursor (powder $CaCO_3$), that filled 3–5 mm of the capillary, as schematically depicted in Fig. 6.1. Each sample was mounted on the flow cell system and linked to a set of pipes and fittings in order to flow the gas throughout the powder-based sample. Quartz wool was placed at the capillary extremities to fasten the powder on the capillary center in order to prevent any change of position during the experiments due to the gas-flow. Calcite thermal decompositions were carried out flowing nitrogen and carbon dioxide mixture throughout the sample. Pure nitrogen flows were fed from a N2 gas cylinder (whose pressure was conveniently reduced at 1 bar), while CO_2/N_2 mixture were made and flowed through a syringe pump (Teledyne Isco 1000D Syringe Pump). During each experiment, sample temperature was controlled by means of a K-type thermocouple, placed within the capillary in contact with the powder.

Measurements were carried out irradiating each the heating capillary with an incident monochromatic beam radiation of 24 keV and a corresponding wavelength of about

0.5166 Å. During each test, three different detectors were used in order to record the sample X-ray scattering data, namely the USAXS, SAXS and WAXS detectors (Ilavsky et al., 2013; Ilavsky et al., 2009). Each sample was probed using a specific illuminated area and an exposure time, namely 0.8×0.6 mm and 90 s for the USAXS detector and 0.8×0.2 mm and 20 s for the pinSAXS and WAXS ones. The combination of these three detectors provides a corresponding wide q-range of about $2 \times 10^{-4} \div 7$ Å^{-1}. Additionally, by considering the detectors movement time and the USAXS motor tuning step, the sampling frequency was approximately one each 4–5 min.

Before sample tests, blanks measurements were performed with empty capillaries in order to account for the scattering contribution of the experimental set-up, that was conveniently subtracted from the scattering response of each sample.

6.2.3 Calcination reactions and sintering tests

In this work, commercial calcium carbonate samples were thermally decomposed and then sintered varying the furnace temperature, the atmospheric gas composition and the residence time in order to generate different porous CaO samples. It is worth noting that during the calcite thermal decomposition two different simultaneous phenomena take place, namely the calcination reaction and sintering processes (Ewing, Beruto, and Searcy, 1979; Fuertes et al., 1991; Glasson, 1958; Borgwardt, 1989b; Milne et al., 1990; Rodriguez-Navarro et al., 2009; Zhu, Wu, and Wang, 2011). Therefore, in this work two different steps have been conveniently identified in order to describe the micro-textural CaO evolution during the experiments: the reaction (RT) and sintering time (ST). The former refers to time elapsed by the thermal decomposition of the $CaCO_3$ to achieve the complete conversion from the generation of the first CaO peak in the WAXS data. During this step both the calcination reaction and the high temperature sintering mechanisms contributes to affect and evolve the sorbent internal micro-structure. On the other hand, the latter step is an additional high temperature residence time (that was considered after the completion of the $CaCO_3$ decomposition), where only sintering processes contribute in the CaO micro-textural properties evolution. During this step temperature and atmospheric composition were the same of the calcination reaction.

Calcite thermal decompositions were performed in N_2 or CO_2/N_2 atmosphere at 1 bar of total pressure with a gas flow rate of about 10 NmL min^{-1}. In this work, the gas flow rate was used for two main reasons, namely to control the atmosphere composition and to facilitate the CO_2 removal from the reaction zone that may locally affects both the calcination reaction (Criado et al., 1995; Galan, Glasser, and Andrade, 2013; Gallagher and Johnson, 1976; García-Labiano et al., 2002; Khinast et al., 1996; Mahuli et al., 1999; Manovic et al., 2009; Taghl Darroudi and Alan W. Searcy, 1981; Valverde, Sanchez-Jimenez, and Perez-Maqueda, 2015; Wilburn et al., 1991; Zhong and Bjerle, 1993) and sintering processes kinetics (Alvfors and Svedberg, 1992; Beruto, Barco, and Searcy, 1984; Borgwardt, 1989a; Ewing, Beruto, and Searcy, 1979; Fuertes et al., 1991; Glasson, 1958; Mai and Edgar, 1989; Maya, Chejne, and Bhatia, 2017a; Maya, Chejne, and Bhatia, 2017b; Milne et al., 1990; Stanmore and Gilot, 2005).

The final calcination temperature was varied between 600 °C and 900 °C using a heating rate of 20 °C min^{-1}, while the atmosphere sample composition was ranged from pure N_2 to 50 % of CO_2 (on volumetric basis) in balance with N_2. Such operative conditions were conveniently chosen in order to slow-down the calcination reaction rate by means of temperature and atmosphere composition to obtain a reasonable number of sampling during the reaction and sintering step according to the detectors sampling frequency (one scan every 4–5 min). A summary of all the experiments performed in this work is listed in Tab. (6.2), where it is specify the final calcination temperature, the reaction and the

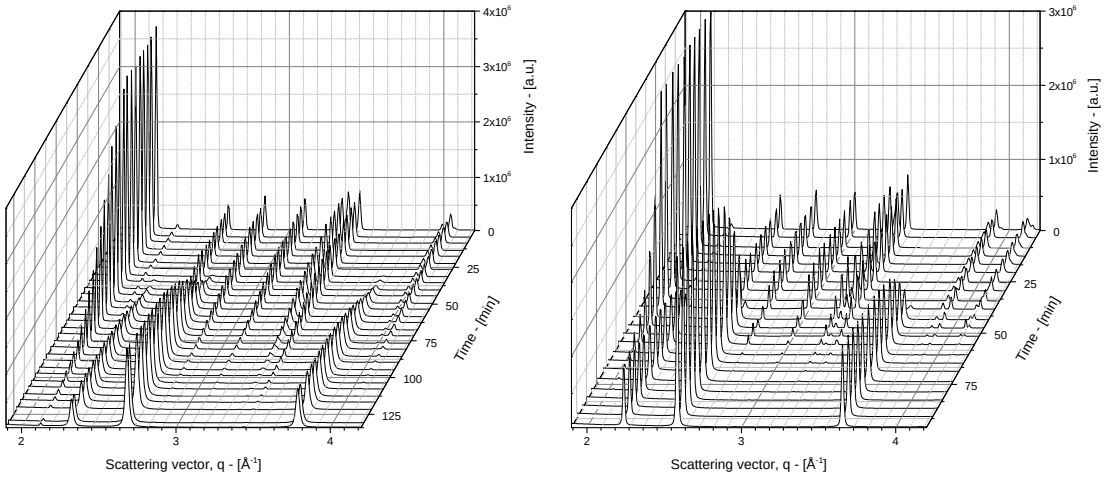

(a) **(b)**

Figure 6.2: Typical time-resolved WAXS patterns during two calcination reactions: (a) refers to sample B (reaction conditions: 620 °C in N_2) and (c) refers to sample H (800 °C and 10 % of CO_2 in balance with N_2). The decreasing peaks are those of $CaCO_3$ that is converting into CaO represented by the intensity increasing peaks.

sintering time of each sample. Two different set of experiments were performed depending on the selected operative conditions, namely calcination reactions in N_2 atmosphere performed in the temperature range between $600 \div 700$ °C (samples from A to E listed Tab. (6.2)) and calcination reaction in CO_2/N_2 atmosphere (from a minimum of 1 % to a maximum of 50 % of CO_2 in balance with N_2) in a higher temperature range of $800 \div 900$ °C (samples from F to L listed in Tab. (6.2)). Such operative conditions aimed to ease the investigation of sorbent pore network generation by slowing down the thermal decomposition rate, namely by means of relative low calcination temperatures (Borgwardt, 1985; Galan, Glasser, and Andrade, 2013; Gallagher and Johnson, 1973; Manovic et al., 2009; Stanmore and Gilot, 2005) and of the chemical reaction equilibrium, namely a CO_2 concentration close to that of the equilibrium (Barker, 1973; Borgwardt, 1989a; Criado et al., 1995; Manovic et al., 2009; Stanmore and Gilot, 2005; Taghl Darroudi and Alan W. Searcy, 1981; Valverde, Sanchez-Jimenez, and Perez-Maqueda, 2015). Therefore, by using these aforementioned operative conditions, the reaction time ranged from a minimum of 45 min to a maximum of 260 min. Once the calcination reaction was completed, a pure sintering step was followed maintaining the same operative conditions in terms of temperature and gas composition. Sintering steps ranged from a minimum of 30 min (at low temperatures, namely $600 \div 700$ °C in N_2) up to a maximum of 140 min min ca. (high temperatures of $800 \div 900$ °C with CO_2/N_2).

During the experiments, a one-dimensional (slit smeared) collimated USAXS detector was used to record absolute intensity calibrated scattering data (Ilavsky et al., 2009). On the other hand, a two-dimensional SAXS (pinhole collimated) and WAXS detectors were used to collect the sample scattering data in the small and wide angle regions.

6.2.4 WAXS data analysis for sample composition estimation

Time resolved Wide Angle X-ray Scattering (WAXS) data were collected in terms of scattering intensity over the scattering vector q by means of Nika program (Ilavsky et al., 2012). WAXS data patterns showed the CaO and $CaCO_3$ intensity peaks over the

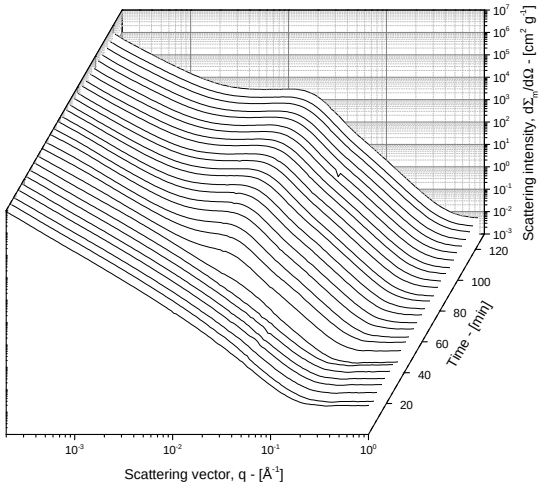

Figure 6.3: Typical experimental slit-smeared time resolved scattering intensities profiles in absolute units (per unit of sample mass) during the CaCO3 thermal activation at 620 °C in N_2 -(sample B). Slit-length is listed in Tab. 6.2.

scattering vector q allowing to provide the sample composition (CaO and $CaCO_3$ content) estimation for each time-step WAXS data, as shows in Fig. 6.2a and 6.2b. Solid sample compositions are essential to estimate the conversion over the reaction time profiles of the calcite decomposition. In fact, WAXS data could be easily converted in terms of intensity versus two-theta values and analyzed by means of the Rietveld profile method providing the sorbent chemical compositions. However, because of the WAXS detector low resolution, poorly discretized WAXS intensity patterns over q were recorded, such that each diffraction peak was described by less than 6–7 experimental points (in terms of intensity and scattering vector or, equivalently, two-theta angle). For this reason, in this work $CaCO_3$ weight fractions, $w_{CaCO_3}(t)$, were estimated by means of the ratio between the experimental $CaCO_3$ peaks areas of pure calcite and those of the partially calcined sorbent. Areas under the peaks were numerically computed from the WAXS experimental data using the trapezoidal rule. Afterwards, CaO weight fractions $w_{CaO}(t)$ were calculated as $1 - w_{CaCO_3}(t)$. Calcium carbonate weight fractions were used to calculate the reactant conversion $X_{CaCO_3}(t)$ over the reaction time according to Eq. (2.19).

6.2.5 USAXS and SAXS data reduction in absolute intensity scale

Time resolved USAXS data were reduced by means of Indra program (Ilavsky and Jemian, 2009) after the blank subtraction. The scattering curves were then normalized in terms of absolute units (Zhang et al., 2010), namely in terms of the differential scattering cross section over the scattering vector q. The measured intensity profile $I(q,t)$ over time at the detector is related to the differential scattering cross section per unit volume of the illuminated sample and per unit of solid angle (indicted with Ω) $d\Sigma/d\Omega$ by Eq. 4.47 Ilavsky et al. (2009) and Long et al. (1991).

Because of the cylindrical geometry of the capillary and because the samples are granular materials, it is difficult to precisely estimate the illuminated sample volume. More conveniently, the instantaneous absolute intensity was expressed in terms of unit of sample mass (inside the illuminated volume) instead of unit of sample illuminated volume. Therefore, the sample thickness e_s was replaced by the instantaneous solid phase thickness e_{solid} that was estimated using the Lambert-Beer law from the time-resolved measured sample transmission coefficient $T(t)$ and the linear absorption coefficient $\mu(t)$ calculated

for each time-step. For each time step the differential scattering cross section per unit of sample mass sample mass $d\Sigma_m/d\Omega$ is equal to $d\Sigma/d\Omega$ multiplied by the illuminated sample volume and divided by the sample mass, according to Eq. 4.50. The instantaneous linear absorption coefficients and sample densities were computed from those of pure species listed in Tab. 6.1 by means of the CaO and $CaCO_3$ weight fractions over the reaction time estimated from the WAXS data.

Time-resolved SAXS scattering profiles were reduced using the Nika program (Ilavsky et al., 2012) subtracting the blanks scattering profiles. These two data-sets (USAXS and SAXS profiles) were finally merged with the Irena package (Ilavsky and Jemian, 2009), to obtain the whole scattering intensity vs q profiles for each time-step of the USAXS and SAXS detectors. In this work the absolute calibration of SAXS data was not necessary because of the absolute calibrated USAXS data that provided to the SAXS profiles the proper intensity magnitude. A typical example of time-resolved USAXS+SAXS data expressed in terms of absolute units (per unit of mass) is showed in Fig. 6.3.

Because of the one-dimensional collimating geometry for the USAXS data collection, the measured scattering intensity profiles are affected by slit smearing. However, in this work no desmearing procedure (Ilavsky et al., 2013; Lake, 1967; Pete R. Jemian, 1990) was necessary, because the slit smearing effects are numerically accounted for into the Irena packages (Ilavsky and Jemian, 2009). Therefore, all the scattering intensity profiles showed in this work refer to slit-smeared curves in the USAXS region (approximately between $2 \times 10^{-4} \div 0.1\,\text{Å}^{-1}$).

6.2.6 Calculation of the sorbent textural properties

The analysis of the USAXS and SAXS time-resolved intensity profiles (expressed in terms of absolute units on a sample mass basis) was performed using the IGOR Pro-based IRENA program (Ilavsky and Jemian, 2009). In this work, the slit-smeared scattering intensity profiles were fit by means of the "Unified fit" tool that is based on the unified approach proposed by Beaucage (1995) and Beaucage (1996). This model allows the description of the SAS profiles over a wide range of q by means of an arbitrary number of interrelated structural levels, providing to the model a high flexibility in describing the SAS response of multiple-size-scale structures Beaucage (1995).
The analysis of the time-resolved small angle scattering data by means of the "Unified fit" approach refers to § 4.6 where Eq. 4.60 was applied for each time step of the collected USAXS/SAXS experimental data.

6.3 Results and Discussion

6.3.1 Calcination reaction kinetics from WAXS data analysis

Time-resolved WAXS data were used to estimate the sorbent weight fraction evolution during the calcination reaction, namely during the reaction time. Afterwards, the calcium carbonate conversion over the reaction time was estimated by means of Eq. (2.19) for each experimental time-step. Fig. 6.4a shows the $CaCO_3$ conversion reaction of those samples thermally activated under a reaction atmosphere of pure N_2. In order to obtain a suitable number of sampling during the $CaCO_3$ decomposition (compatible with the sampling frequency of the three detectors), the reaction temperatures were set to be lower than 700 °C to slow down the reaction kinetics. Such temperatures are 700 °C (sample A), 620 °C (sample B), 650 °C (sample C), 680 °C (sample D) and 700 °C (sample E). According to Fig. 6.4a, as the temperature reaction decreases the $CaCO_3$ decomposition rate decreases allowing satisfactory sampling number during the calcination reaction, as the cases of

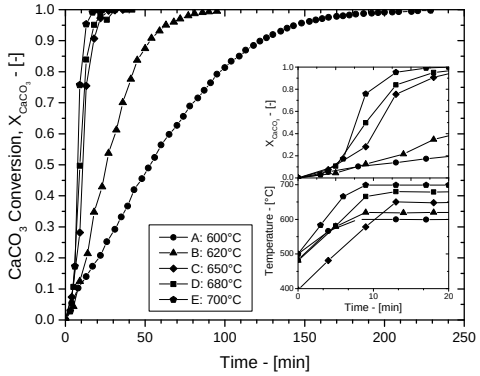

(a) *Samples A, B, C, D, E - calcinations in N_2.*

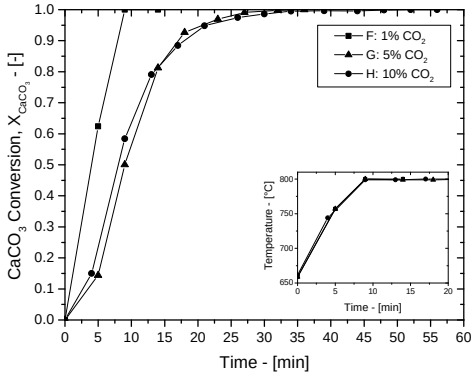

(b) *Samples F, G, H - calcinations at* 800 °C.

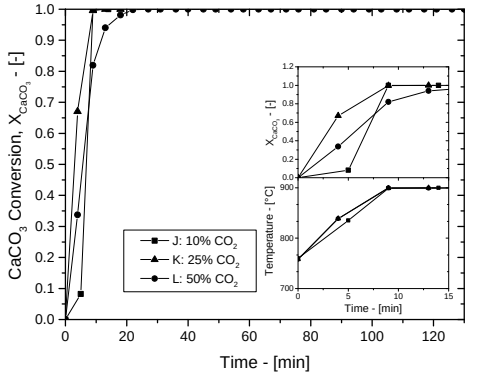

(c) *Samples J, K, L - calcinations at* 900 °C.

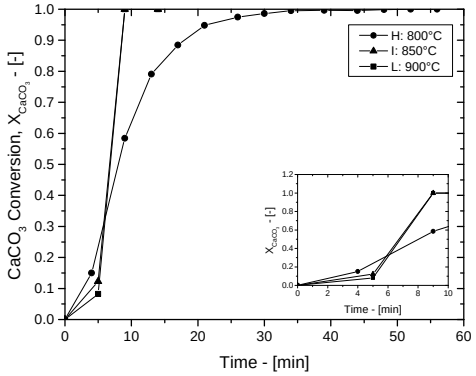

(d) *Samples H, I, J - calcinations with* 10 % *of CO_2 in balance with N_2.*

Figure 6.4: Calcium carbonate conversions profiles over time at different final calcination reaction temperatures and atmosphere compositions estimated from the WAXS data analysis: samples A, B, C, D and E were calcined under a reaction atmosphere of pure N_2 (a); three different atmosphere compositions were explored at 800 °C, namely 1 % (sample F), 5 % (sample G) and 10 % (sample H) of CO_2 in balance with N_2; the 900 °C calcination reaction were performed with 10 % (sample J), 25 % (sample K) and 50 % (sample L) of CO_2 in balance with N_2; last figure (d) compares the calcination temperature effect with a 10 % of CO_2 (in balance with N_2) atmosphere.

samples A and B conversion over time profiles. On the other hand, the 800 °C, 850 °C and 900 °C calcination reactions could not be adequately sampled by this instrumentation frequency because of their higher reaction rates. In these cases, the $CaCO_3$ decomposition rate was slowed down by means of adverse chemical reaction equilibrium conditions, namely performing the high temperatures calcination reactions in presence of CO_2 in the reaction atmosphere (García-Labiano et al., 2002; Khinast et al., 1996; Taghl Darroudi and Alan W. Searcy, 1981; Zhong and Bjerle, 1993). The 800 °C and 900 °C $CaCO_3$ conversion profiles are showed in Fig. 6.4b and Fig. 6.4c. However, as the reaction temperature increases the higher decomposition rates do not guarantee an adequate sampling number when the CO_2 content is not close enough to that of the equilibrium, as can be noticed from samples H, I and K in Fig. 6.4b and Fig. 6.4c, namely at 800 °C with 1 % of CO_2, 850 °C with 10 % of CO_2 and 900 °C with 10 % and 25 % of CO_2 in balance with N_2. In fact, in these cases the equilibrium CO2 partial pressures are approximately 0.21 bar (800 °C), 0.48 bar (850 °C) and 1.1 bar (900 °C), according to the thermodynamics data of Knacke, Kubaschewski, and

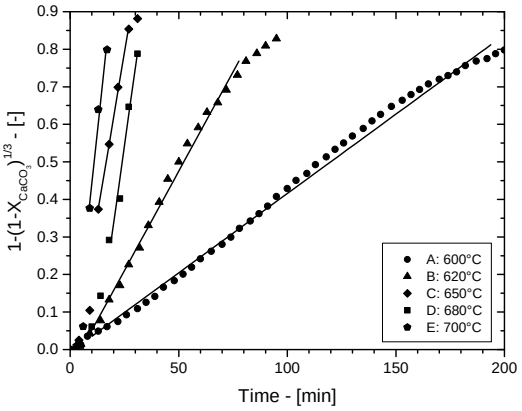

(a) *Grain model plot.*

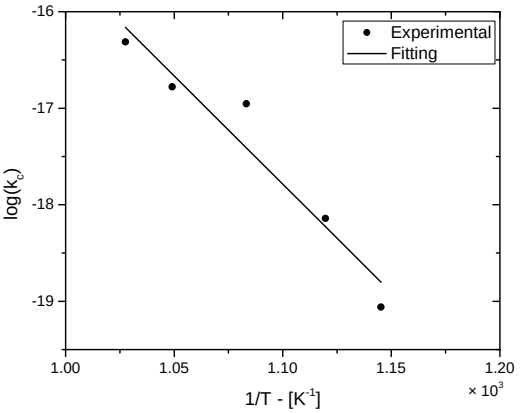

(b) *Arrhenius plot for N_2 $CaCO_3$ calcination reactions.*

Figure 6.5: Calcination reaction kinetics analysis considering the pure N_2 atmosphere calcined samples (A, B, C, D and E): the grain model representation (a) and the Arrhenius plot (b) are respectively represented.

Hesselmann (1991).

With the aim to estimate and verify the $CaCO_3$ calcination reaction activation energy, the pure nitrogen thermal activations were considered, namely those of samples from A to E. The poorly sampled conversion over times profiles of the 800 °C, 850 °C, and 900 °C did not allow the estimation of a reaction rate. Additionally, as can be noticed from the insets of Figure 3(a), the calcination reactions were performed under non-isothermal conditions before the heating resistances reached the set-point temperature. For this reason, the firsts 3/4 points were not considered in the kinetic parameter estimations, such that only isothermal data were considered. Despite the clear influence of the CO_2 pressure on the $CaCO_3$ decomposition rate, as shown by Fig. 6.4b and Fig. 6.4c, this effect is negligible or absent when $p_{CO_2} < 10^{-2} p_{CO_2}$, according to Darroudi$_{1981}$, where p_{CO_2} is the CO_2 partial pressure in the reaction atmosphere and p_{CO_2} is that of the equilibrium. This is the case of the N_2 calcined samples (A÷E) where p_{CO_2} is zero and, thus, fairly below the aforementioned threshold. This approach was originally proposed by Beruto and Searcy (1974) and then experimentally demonstrated by Taghl Darroudi and Alan W. Searcy (1981). Also Borgwardt (1985) neglected the CO_2 dependence of the calcination reaction rate by performing $CaCO_3$ decompositions in nitrogen atmospheres. Because the calcination reaction is a non-catalytic gas-solid reaction, as suitable structural model is necessary to describe the $CaCO_3$ conversion evolution over the reaction time. Several literature contributors used the grain model approach (J. Szekely and Sohn, 1976) to investigate the calcination reaction kinetics, as Fierro, Adánez, and García-Labiano (2004), García-Labiano et al. (2002), Mahuli et al. (1999), Milne et al. (1990), and Silcox, Kramlich, and Pershing (1989). This model assumes the initial solid reactant internal structure made of solid dense grains with a certain shape (Szekely and Evans, 1970).

The USAXS/SAXS data analysis of the undecomposed $CaCO_3$ reveals a certain internal structure as shown in Fig. 6.7a. Specifically, the estimated calcite specific surface area and porosity values are on average approximately $0.67\,m^2\,g^{-1}$ and 0.002 respectively with a corresponding radius of gyration of about 48 Å. This modest internal structure of calcite is additionally confirmed by the specific surface are value estimated by means of the $CaCO_3$ particle diameter (that ranges between 150÷160 µm), namely $0.0145\,m^2\,g^{-1}$ that is one order of magnitude lower than the USAXS/SAXS value. Under the assumption of spherical

$CaCO_3$ particles, this estimation was obtained by means of $3/(\rho_r\, r_0)$, where ρ_r is the $CaCO_3$ density (Tab. 6.1). However, these values are enough modest to approximate the initial $CaCO_3$ internal structure to that of non-porous materials. For this reason, according to J. Szekely and Sohn (1976) a specific case of grain model was considered, namely the shrinking unreacted core model of a non-porous reactant. By considering a chemically controlled regime, the reaction rate is

$$\frac{dX_{\mathrm{CaO}}}{dt} = k_c \frac{3}{r_0} \left(1 - X_{\mathrm{CaO}}\right)^{2/3}, \tag{6.1}$$

where k_c is the calcination reaction kinetics (expressed in $\mathrm{m\,s^{-1}}$). Once integrated with the initial condition $X_{\mathrm{CaO}}(t=0) = 0$ Eq. (6.1) becomes

$$t = 3\tau_{\mathrm{kin}} \left[1 - \left(1 - X_{\mathrm{CaO}}\right)^{1/3}\right], \tag{6.2}$$

where τ_{kin} is defined as $r_0/(3k_c)$. Eq. (6.2) sates that when the reaction is under kinetic control a plot of $\left[1 - \left(1 - X_{\mathrm{CaO}}\right)^{1/3}\right]$ vs t (grain model representation) should be a straight line (J. Szekely and Sohn, 1976), with a slope of $3\tau_{\mathrm{kin}}$. Fig. 6.5 shows how the N_2 reaction atmosphere calcination reactions conversions agree with the chemically reaction kinetic controlled shrinking unreacted core model. Specifically, after a short induction period (that shows a lower slope), the linear trends the profiles suggest that the calcination reaction is controlled by the reaction kinetics. The lower slope of the induction period could be related to the non-isothermal reaction conditions, where the temperature is still increasing up to the selected set-point, as shown by the insets of Fig. 6.4a. Additionally, the last part of the conversion vs time profiles seems to deviate from the chemically controlled regime and such data were not used for the kinetic constant estimation. The experimental conversion profiles data were fitted using Eq. (6.2) by means of a least squares linear fitting as shows by the continuous lines depicted in Fig. 6.4a. The resulting slopes were used to estimate the kinetic constant for each calcination reaction temperature. An Arrhenius plot of the estimated kinetic constants shows a linear diminishing trend over the inverse of the absolute temperature, as represented in Fig. 6.4b from which the pre-exponential and the activation energy parameters were computed by means of a least squares linear fitting. Specifically, a pre-exponential coefficient of $963.8\,\mathrm{m\,s^{-1}}$ and an activation energy of $186.36\,\mathrm{kJ\,mol^{-1}}$ were calculated. This result is in good agreement with those determined by Gallagher and Johnson (1973) where an activation energy of $208.1\,\mathrm{kJ\,mol^{-1}}$ was estimated; Powell and Searcy (1980) who measured about $209.3\,\mathrm{kJ\,mol^{-1}}$; Borgwardt (1985), who estimated an activation energy of about $205\,\mathrm{kJ\,mol^{-1}}$; Criado et al. (1995) where a value of $187\,\mathrm{kJ\,mol^{-1}}$ was determined. On the other hand, Silcox, Kramlich, and Pershing (1989) and Milne et al. (1990) estimated significantly lower values, namely $33.4\,\mathrm{kJ\,mol^{-1}}$ and $91.3\,\mathrm{kJ\,mol^{-1}}$ respectively.

Finally, it is remarkable to notice how the CO_2 partial pressure in the reaction atmosphere show two main effects on the conversion over time profiles: it slow down the $CaCO_3$ calcination reaction rate and it delays the beginning of the thermal decomposition. In fact, the first CaO peak in the WAXS data was observed in a time rage between $26 \div 31$ min for the case of the N_2 calcined samples (A$\div$E). This values increases with temperature, namely 36 min and 41 min for the 800 °C and 900 °C calcination reactions respectively.

6.3.2 USAXS/SAXS data: profiles and trends

Time-resolved experimental scattering intensity profiles of the different calcined samples (listed Table 2) were used to compute the sample textural properties (radius of gyration,

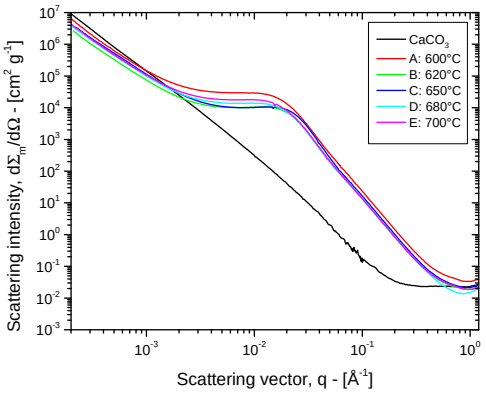

(a) *Samples from A, B, C, D and E - N_2.*

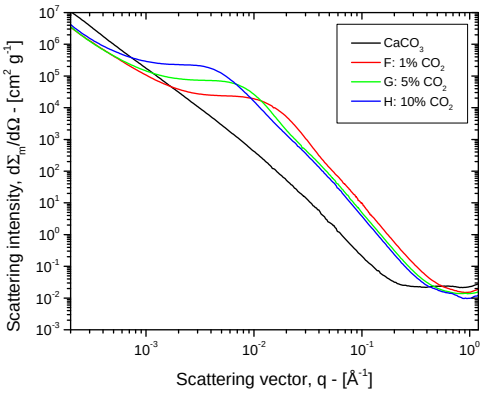

(b) *Samples F, G and H* - 800 °C.

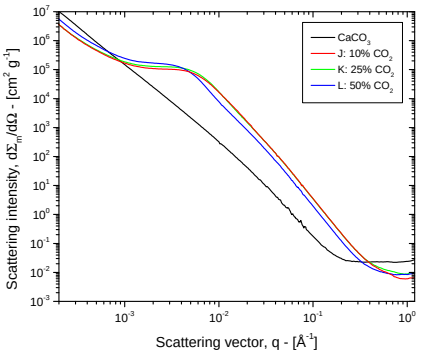

(c) *Samples J, K and L* - 900 °C.

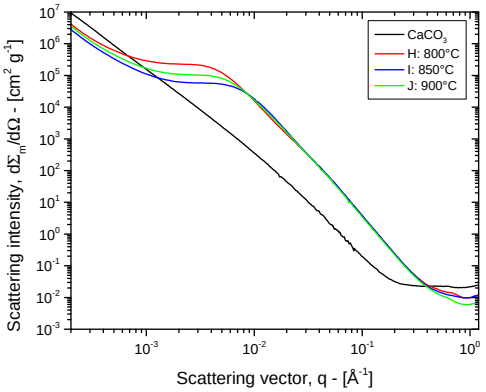

(d) *Samples H, I and J - 10 % of CO_2.*

Figure 6.6: Experimental slit-smeared scattering intensities profiles of completely calcined $CaCO_3$ measured at different operative reaction conditions and compared with the undecomposed calcite (black lines): (a) calcination reactions performed in N_2 at different final calcination reaction temperatures (600÷700 °C), namely samples A, B, C, D, and E; (b) refers to calcination reactions performed at 800 °C using three different atmosphere mixture, 1 % of CO_2 (sample F), 5 % of CO_2 (sample G) and 10 % of CO_2 sample (H); (c) refers to completely decomposed calcite obtained at 900 °C and 10 % of CO_2 (sample J), 25 % of CO2 (sample K) and 50 % of CO_2 (sample L); (d) refers to calcination reactions performed in atmospheres of 10 % of CO_2 in balance with N_2 exploring three different final temperatures, namely 800 °C (sample F), 850 °C (sample I) and 900 °C (sample J). Slit-lengths are listed in Tab. 6.2.

specific surface, porosity, PSD and pore number density) generation and evolution during the $CaCO_3$ thermal activation (reaction time) and during the CaO high temperature sintering (sintering time) step. The sorbent micro-textural properties trends over time (reaction and sintering) and over $CaCO_3$ conversions were identified and verified.

As can be observed form the experimental scattering intensity profiles showed in Fig. 6.6 three different regions can be identified (by looking at the Fig. 6.6 profiles from the right to the left). The first region is placed at high-q values and is characterized by a flat-like scattering intensity profile due to the background contribution to the scattering experimental response. A second region can be located roughly between $1.5 \times 10^{-3}\,\text{Å}^{-1}$ and $6 \times 10^{-1}\,\text{Å}^{-1}$. In the first part of this second region, a plateau can be observed, defining a Guinier regime, that is followed (in the direction of high-q values) by a decreasing trend of the scattering intensity down to the background region. A third region can be observed at lower-q values (approximately between $1 \times 10^{-4}\,\text{Å}^{-1}$ and $1.5 \times 10^{-3}\,\text{Å}^{-1}$) and is approximately described by a power-law profile. On the other hand, the experimental scattering responses of the undecomposed $CaCO_3$ seems to be not provided by a second region and Guinier regimes are not observed, as shown by the experimental $CaCO_3$ scattering profiles (black lines) of Fig. 6.6.

The last region represents the experimental scattering response of large structures, that are associated with the scattering response of the sorbent particles (whose particle diameter is $150 \div 160\,\mu\text{m}$), and, more precisely, to the inter-particle voids that they generate. These large structures size can be roughly estimated by means of Eq. (2.18), obtaining a maximum scatterer size of about $6\,\mu\text{m}$. This value suggests that the inter-particle void scattering response is compatible with this low-q region. Additionally, this region is influenced by multiple scattering effects that distort the local scattering intensity profile and the single scattering analysis cannot be correctly applied. For this reason none structural information can be obtained from this region under this assumption.

6.3.3 Unified fit application to USAXS/SAXS data: structural levels and structure factor

Powder-based calcium carbonate is the starting material of each experiment, whose scattering intensity profile is depicted in Fig. 6.7a. As previously mentioned, only two region are shown by the $CaCO_3$ scattering profile respect to those of the calcined samples (Fig. 6.6 and Fig. 6.10).

Specifically, the $CaCO_3$ scattering intensity trends are empathized by the Porod representation (Spalla, Lyonnard, and Testard, 2003), where the experimental scattering intensity profile $d\Sigma_m/d\Omega$ multiplied by q^4 is plotted in a double logarithm scale over the scattering vector q, as shown in Fig. 6.7b.The $CaCO_3$ scattering intensity profiles were fitted by means of the unified fit using two structural levels. The first level models the high-q region while the second one the low-q profile (affected by the multiple scattering effects) as shown in Figs. 6.7a and 6.7b. This number of levels used to fit the $CaCO_3$ scattering profiles is additionally confirmed by the agreement between the experimental intensity derivative and that of the unified fit, as depicted in Fig. 6.7c.

On the other hand, the analysis of the time-resolved scattering intensity profiles during and after the $CaCO_3$ thermal activation by means of the unified fit revealed that the second region after the first Guinier plateau is characterized by a non-constant power-law slope, suggesting the presence of additional structural levels that overlap in the direction of the high-q values. This behavior is observed both in the completely calcined samples intensity profiles (showed in Fig. 6.6) and in those measured after the sintering period (Fig. 6.10). Additionally, this non-constant power law slope of the scattering intensity is emphasized by considering the Porod representation of the experimental scattering intensity profiles

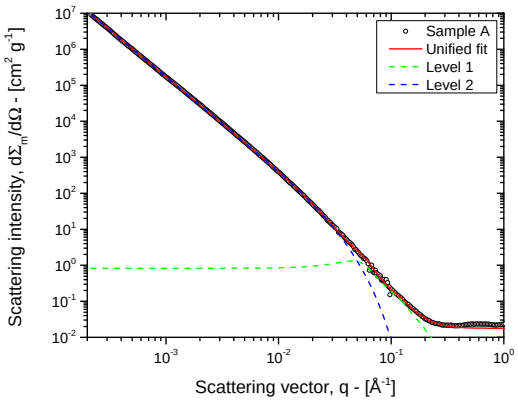

(a) $d\Sigma_m/d\Omega$ *vs* q.

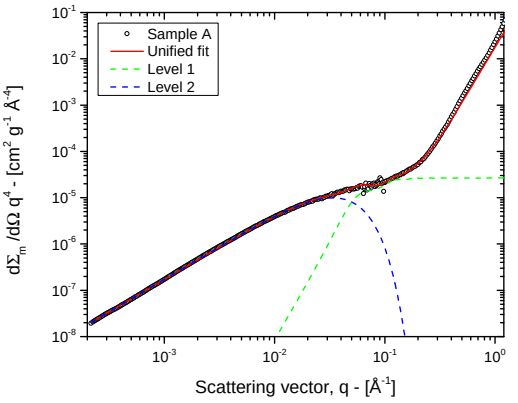

(b) $d\Sigma_m/d\Omega\, q^4$ *vs* q.

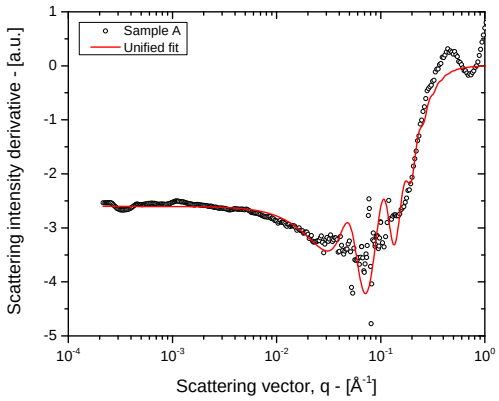

(c) *Scattering intensity derivative over* q.

Figure 6.7: Experimental slit-smeared scattering intensity profile (a) of the undecomposed $CaCO_3$ at room temperature and the unified fit result by means of two structural levels. The Porod plot (b) emphasizes the experimental intensity and the predicted profile trends. The scattering intensity derivative is compared with that of the unified fit (c). Slit-length is listed in Tab. 6.2.

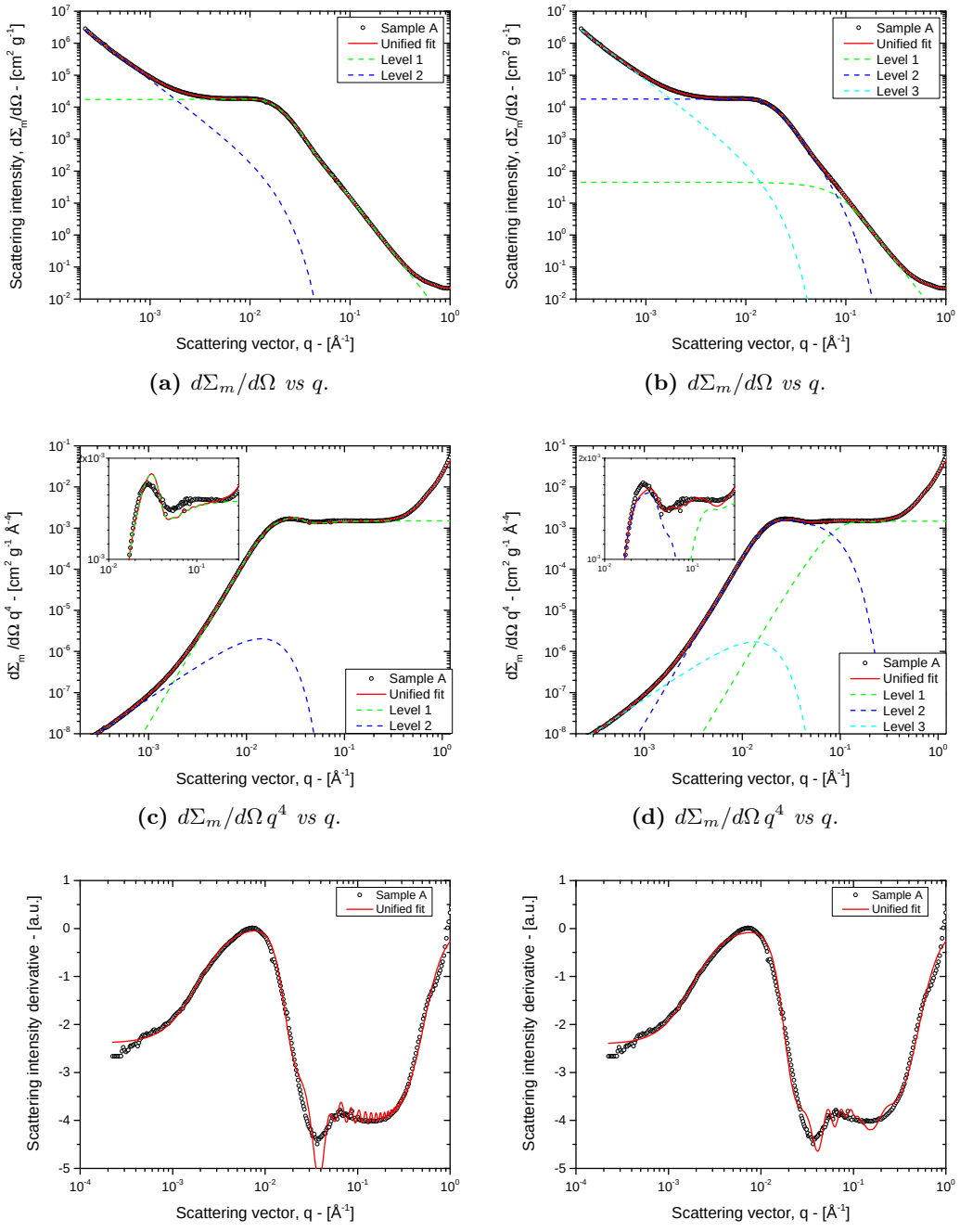

(a) $d\Sigma_m/d\Omega$ *vs* q. **(b)** $d\Sigma_m/d\Omega$ *vs* q.

(c) $d\Sigma_m/d\Omega\, q^4$ *vs* q. **(d)** $d\Sigma_m/d\Omega\, q^4$ *vs* q.

(e) *Scattering intensity derivative over* q. **(f)** *Scattering intensity derivative over* q.

Figure 6.8: Comparison between the experimental slit-smeared scattering intensity profile of the completely calcined sample A (600 °C in N_2) and the unified fit model by means of two (a) and three (b) structural levels. These levels are also represented in the Porod plots (c) and (d) and compared with the experimental data. A final comparison is proposed between the experimental scattering intensity derivative and with those of the model with two (e) and three (f) levels. Slit-lengths are listed in Tab. 6.2.

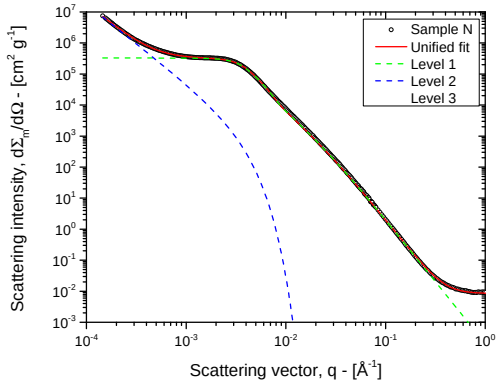

(a) $d\Sigma_m/d\Omega$ *vs* q.

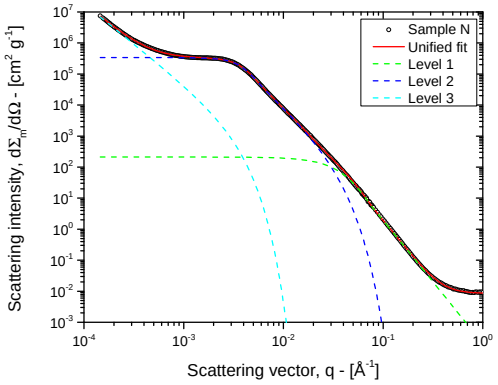

(b) $d\Sigma_m/d\Omega$ *vs* q.

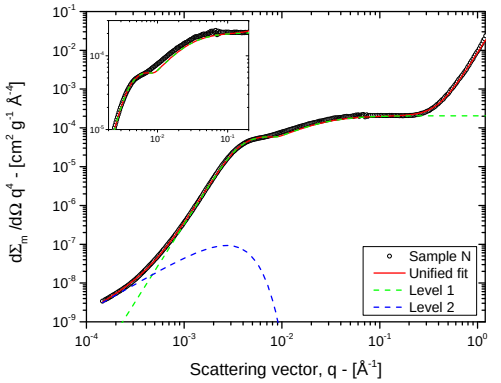

(c) $d\Sigma_m/d\Omega\, q^4$ *vs* q.

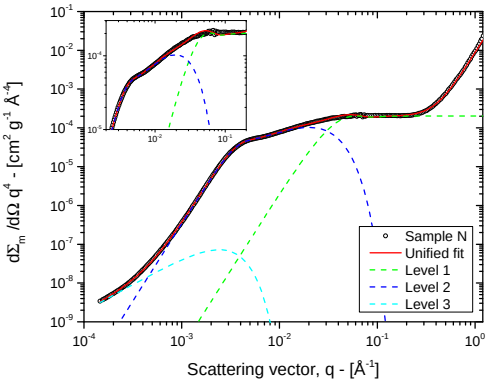

(d) $d\Sigma_m/d\Omega\, q^4$ *vs* q.

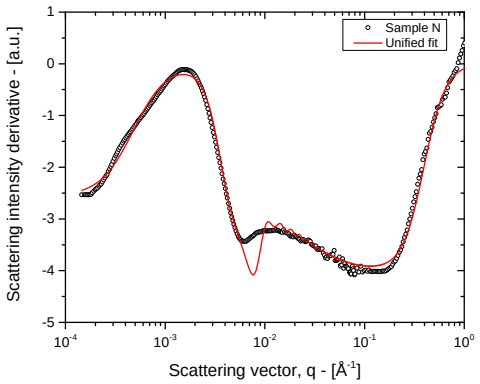

(e) *Scattering intensity derivative over* q.

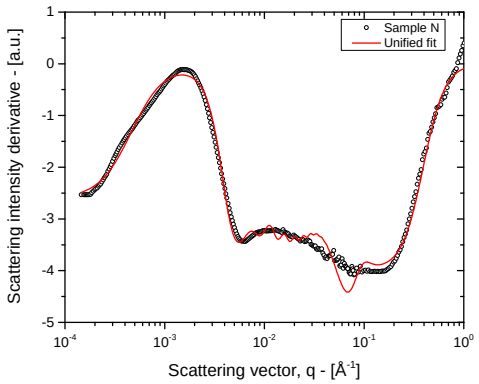

(f) *Scattering intensity derivative over* q.

Figure 6.9: Comparison between the experimental slit-smeared scattering intensity profile of the completely calcined sample L (900 °C with 50 % of CO_2 in balance with N_2) and the unified fit model by means of two (a) and three (b) structural levels. The number of levels comparison is also represented in the Porod plots (c) and (d) and compared with the experimental data. A final comparison is proposed between the experimental scattering intensity derivative and with those of the model with two (e) and three (f) levels. Slit-lengths are listed in Tab. 6.2.

showed in Fig. 6.8b and Fig. 6.9b. Moreover, the experimental scattering derivative is particularly useful to appreciate the non-constant trend after the Gunier regime (towards high-q values), as shows in Fig. 6.8e and Fig. 6.9e where the global maxima are associated with the Guinier regime plateau. Because of the experimental noise (especially in the overlapping region of USAXS and SAXS profiles), a smoothing filer was necessary to achieve reasonable scattering intensity derivative profiles and a Savitzky-Golay filter was used.

As previously observed by Benedetti et al. (2017), the highly-sintered samples (Fig. 6.10) clearly reveal the existence of another structural level in the direction of high-q values near to the background region.
Specifically, three levels are required in order to accurately fit the experimental scattering intensity profile of samples during and after the calcination reaction, while two levels do not guarantee a reasonable fitting result. This is showed in Fig. 6.8 and Fig. 6.9 where two limiting cases of completely calcined $CaCO_3$ (in terms of operative conditions) were considered, namely a calcination reaction performed at 600 °C in N_2 (sample A) and one performed at 900 °C with 50 % of CO_2 in balance with N_2 (sample L). The comparisons between the model predictions with two or three levels and the experimental scattering profiles are shown in Figs. 6.8a and 6.8b and Figs. 6.9a and 6.9b respectively. The Porod representations are significantly useful to discriminate between two and three levels, as represented in Figs. 6.8c and 6.8d and Figs. 6.9c and 6.9d. Specifically, the insets of the Porod plot empathize how the tree structural levels lead to a better representation of the second region, while a two levels approach does not guarantee the best fit result. Finally, the scattering intensity derivatives of the experimental profiles and of unified fit model are represented in Figs. 6.8e and 6.8f and Figs. 6.9e and 6.9f. The derivative comparison suggests how the tree structural levels case can better represent the scattering intensity over q trends than the two-levels approach can do. The comparison between the two and the three levels approach was additionally monitored by means of the chi-squared values, defined as the sum of the squared difference between the experimental and the predicted values divided by the proper squared variance (Bevington and Robinson, 2003). In both the two cases chi-squared values were significantly reduced for the case of the three-levels approach.

Therefore, the scattering intensity profile representation by means of three structural levels and specifically by two levels in the second region suggests that the sorbent pore network (internal porosity) is characterized by two different structures, namely by two distinct population of pores, as previously noticed by Li, Liang, and Cai (2016), Li, Cai, and Huang (2006), Maya, Chejne, and Bhatia (2017a), Rodriguez-Navarro et al. (2009), and Zhu, Wu, and Wang (2011) and, more recently by Benedetti et al. (2017) by means of the USAXS/SAXS technique. On the other hand, the undecomposed $CaCO_3$ representation through two levels (namely only one for the single scattering region) reveals a calcite structure made of a single scatters population.

According to Eq. (4.60), in the unified fit approach P_1 and P_2 are the power-law exponents of the first and second levels, namely of the two populations that are approximately placed inside the q-range $2 \times 10^{-3} \div 3 \times 10^{-1}$ Å^{-1}. The Porod's analysis (Porod, 1951) associated to these exponents the value of 4 (Porod's law) when the scattering response derives from a smooth and sharp interface (Hu et al., 2011). In this work, such interface is the pore-solid interface of the CaO sorbent, namely the specific surface area associated with the pore network. In order to verify the Porod's exponents values of the two populations a non-linear fitting of the unified fit model over the experimental scattering intensity profiles was performed to estimate P_1 and P_2. The resulting numerical values of these two parameters ranged from 3.85 to 4.10 on average. Additionally, it is remarkable to notice how the experimental scattering intensity derivatives values are quite constant in the q-range $2 \times 10^{-2} \div 2 \times 10^{-1}$ Å^{-1} and assume approximately the value of -4. Such value

Table 6.3: Sorbent micro-textural properties at the end of the calcination reaction.

Sample	$R_{g,1}$ [Å]	$R_{g,2}$ [Å]	$S_{m,1}$ [$m^2\,g^{-1}$]	$S_{m,2}$ [$m^2\,g^{-1}$]	S_m [$m^2\,g^{-1}$]	ε_1 [–]	ε_2 [–]	ε [–]	ϕ [–]
A	22	102	46.9	67.6	114.5	0.072	0.443	0.515	0.054
B	23	89	45.9	61.5	107.4	0.073	0.363	0.436	0.196
C	23	83	54.8	73.8	128.7	0.091	0.428	0.519	0.048
D	23	106	44.2	63.9	108.0	0.071	0.459	0.530	0.029
E	21	99	45.8	65.7	111.5	0.065	0.461	0.527	0.034
F	24	118	31.1	43.1	74.2	0.053	0.355	0.408	0.251
G	25	217	16.6	22.4	39.0	0.031	0.389	0.420	0.230
H	24	357	12.4	16.6	29.0	0.022	0.468	0.490	0.101
I	24	163	16.2	22.1	38.2	0.029	0.254	0.283	0.481
J	24	181	19.3	27.0	46.3	0.033	0.333	0.366	0.329
K	67	290	11.8	19.3	31.1	0.061	0.339	0.400	0.267
L	50	520	7.0	9.7	16.7	0.028	0.350	0.378	0.307

enforces the Porod's law assumption in the power-law regions of the two pore populations. For these reasons, these two exponentials were set to be 4 and the corresponding B_1 and B_2 constants become the Porod's law proportionally constants.

In the third level G_3 was set to zero because no Guinier regime was observed. Additionally, because this third region is affected by multiple scattering effects that distort the local trends, the power-law exponent P_3 was left as a free fitting parameter because none physical meaningful information can be obtained by means of the single scattering approach.

As the calcination reaction progresses the pores concentration increases up to arise scattering interferences. Therefore, in order to take into account this phenomenon, the structure factor $S(q,t)$ of Eq. (4.59) was taken into account in the profile fitting for the second level. The structure factor was not necessary for the case of the unreacted $CaCO_3$ scattering intensity profile and during the first instants of the calcination reaction, where the sorbent porosity was almost modest. In these cases $S(q,t)$ was set equal to one. Additionally, the structure factors associated with the first and third levels were always set equal to 1.

6.3.4 Sorbent textural properties generation

Samples calcined in nitrogen atmosphere

As previously mentioned, the calcination reaction conditions were carefully chosen in order to investigate the sorbent pore network generation and evolution during the calcite thermal decomposition. Low final calcination temperatures were imposed, namely 600 °C, 620 °C, 650 °C, 680 °C and 700 °C, compared with the typical higher calcination reactions temperatures that ranges between 800 °C and 900 °C (Barker, 1973; Bhatia and Perlmutter, 1983a; Biasin et al., 2015; Borgwardt, 1989b; Rodriguez-Navarro et al., 2009; Silcox, Kramlich, and Pershing, 1989; Zhu, Wu, and Wang, 2011) in order to maximize the sampling rate, according to the detector sampling frequency (4/5 min). The number of detector scans during a typical calcination test can be observed in Figure 10 (a) and (b), where the USAXS/SAXS intensity profiles of sample A and B are depicted as parametric curves of the reaction time. These two pictures describes the evolution of the

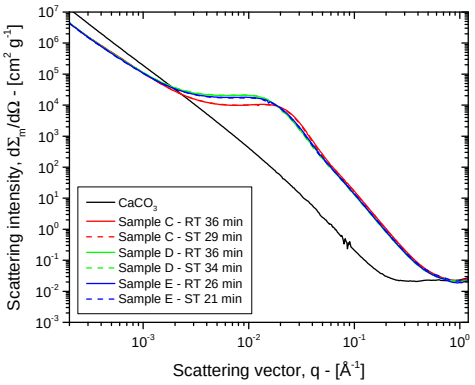

(a) *Samples C, D and E - N2.*.

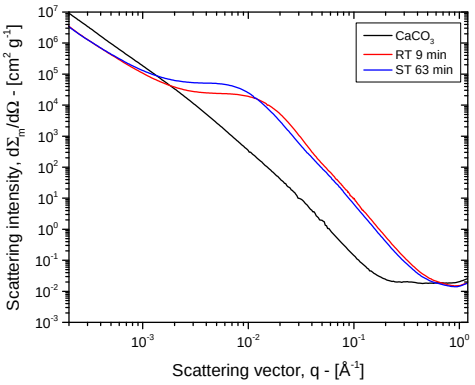

(b) *Sample F* - 800 °C, 1 % CO_2.

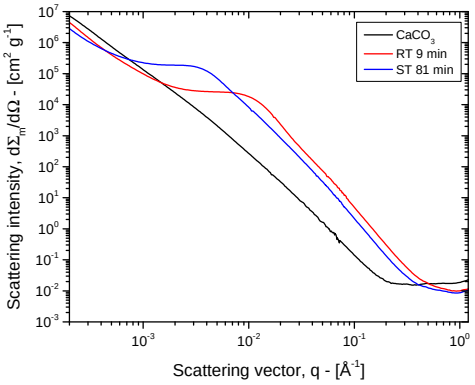

(c) *Sample I* - 850 °C, 10 % CO_2.

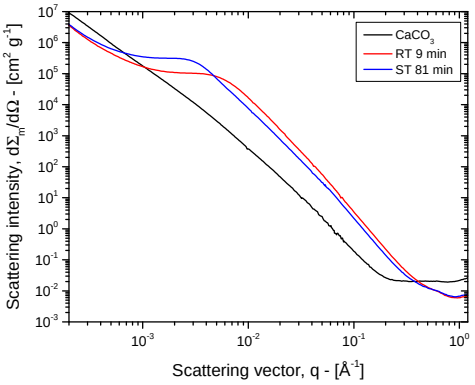

(d) *Sample J* - 900 °C, 10 % CO_2.

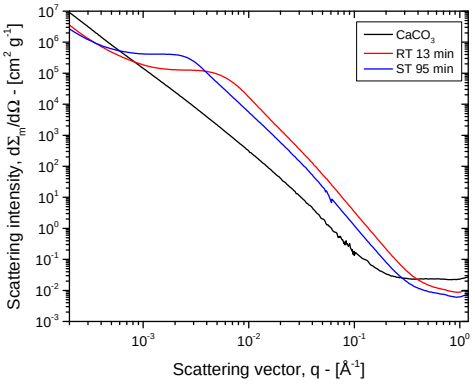

(e) *Sample K* - 900 °C, 25 % CO_2.

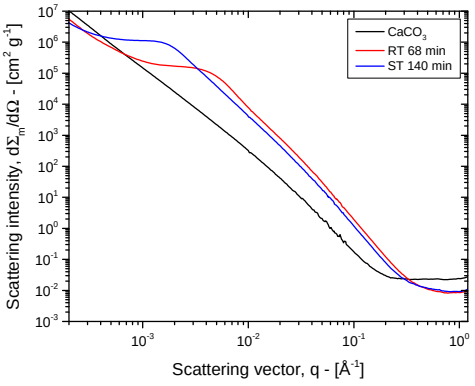

(f) *Sample L* - 900 °C, 50 % CO_2.

Figure 6.10: Comparison between the experimental slit smeared scattering intensity profiles of completely calcined $CaCO_3$ (measured when the reaction stopped) and those after a period of sintering, (a) refers to samples C, D and E, (b) sample F, (c) sample I, (d) sample J, (e) sample K, (f) sample L. Reaction time (RT) defines the duration of the calcination reaction, while sintering time (ST) indicates the additional time after the end of the reaction. Slit-lengths are listed in Tab. 6.2.

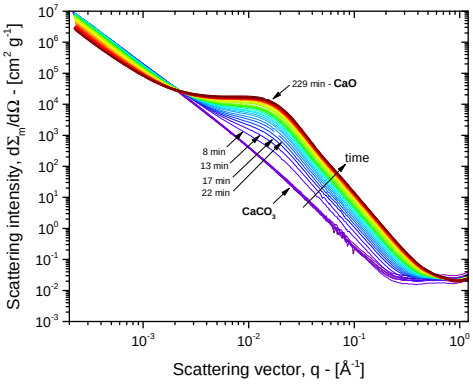

(a) *Sample A* - 600 °C, N_2.

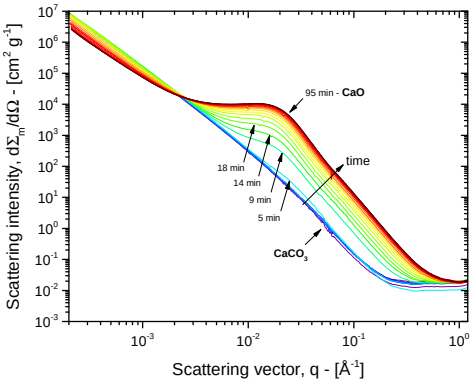

(b) *Sample B* - 620 °C, N_2

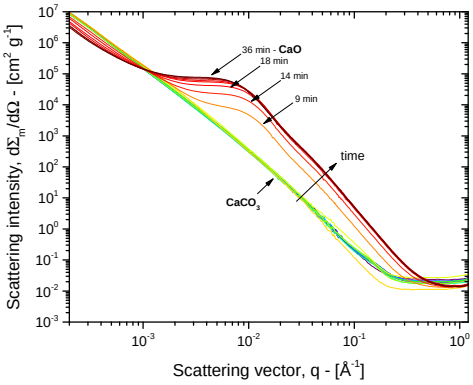

(c) *Sample G* - 800 °C, 5 % CO_2.

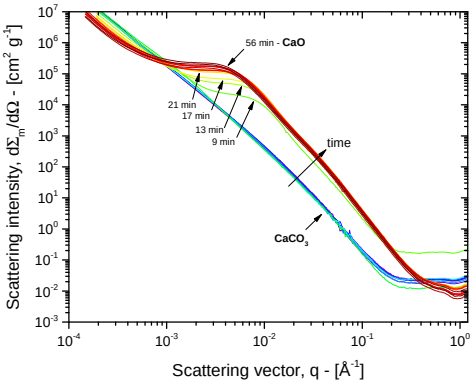

(d) *Sample H* - 800 °C, 10 % CO_2.

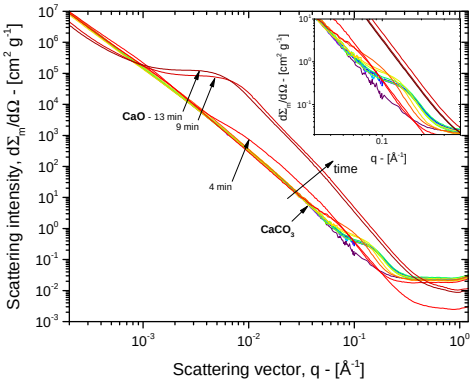

(e) *Sample K* - 900 °C, 25 % CO_2.

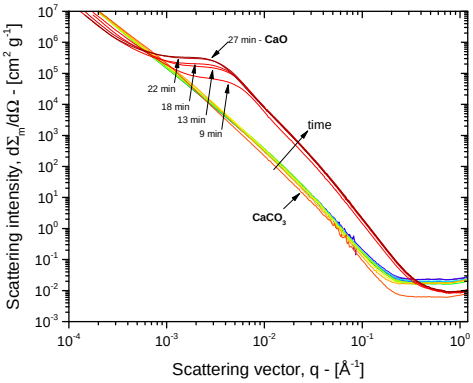

(f) *Sample L* - 900 °C, 50 % CO_2.

Figure 6.11: Experimental slit smeared scattering intensity profiles evolution during the calcination reaction of samples A (a), B (b), G (c), H (d), K (e) and L (f). Time labels indicate the first instants of the calcination reaction, namely the reaction time step where the sorbent pore network is generating. Slit-lengths are listed in Tab. 6.2.

Table 6.4: Sorbent micro-textural properties at the end of the calcination reaction (cont.).

	Ψ_1		Ψ_1		$\langle R_v \rangle$	$N_{m,1} \times 10^{-18}$	$N_{m,2} \times 10^{-17}$	$N_m \times 10^{-18}$	ζ
	$X_{CaCO_3} = 0$	$X_{CaCO_3} = 1$	$X_{CaCO_3} = 0$	$X_{CaCO_3} = 1$	[Å]	[g^{-1}]	[g^{-1}]	[g^{-1}]	[Å]
A	0.39	1.01	0.36	0.93	85	3.3	1.27	3.43	310
B	0.42	0.88	0.41	0.82	75	2.56	1.2	2.68	268
C	0.40	1.04	0.35	1.01	71	3.36	1.79	3.54	239
D	0.43	1.04	0.44	1.00	90	2.94	1.13	3.05	369
E	0.43	1.03	0.27	1.05	86	3.8	1.29	3.93	333
F	0.41	0.84	0.21	0.82	101	1.46	0.49	1.51	489
G	0.59	0.87	0.18	0.96	201	0.68	0.08	0.69	653
H	0.36	1.00	0.55	1.08	327	0.63	0.03	0.63	1226
I	0.37	0.71	-	0.68	142	0.58	0.11	0.59	486
J	0.38	0.78	0.27	0.75	156	0.85	0.14	0.86	533
K	0.59	0.90	0.33	0.70	236	0.06	0.04	0.07	964
L	0.44	0.90	0.55	0.77	449	0.06	0.01	0.06	1431

Table 6.5: Sorbent maximum micro-textural properties during the $CaCO_3$ thermal decomposition.

Sample	$R_{g,1}$ [Å]	$R_{g,2}$ [Å]	$S_{m,1}$ $[m^2\,g^{-1}]$	$S_{m,2}$ $[m^2\,g^{-1}]$	S_m $[m^2\,g^{-1}]$	ε_1 [–]	ε_2 [–]	ε [–]	$\langle R_v \rangle$ [Å]	$N_{m,1} \times 10^{-18}$ $[g^{-1}]$	$N_{m,2} \times 10^{-17}$ $[g^{-1}]$	$N_m \times 10^{-18}$ $[g^{-1}]$
A	17	120	49.5	69.9	119.4	0.076	0.445	0.516	109	3.58	1.33	3.71
B	70	110	45.9	61.5	107.4	0.073	0.363	0.436	93	2.56	1.2	2.68
C	52	89	56.2	74.4	130.7	0.093	0.428	0.519	74	3.9	1.83	4.06
D	83	136	44.2	63.9	108.0	0.071	0.459	0.53	114	2.94	1.13	3.05
E	59	152	45.8	65.7	111.5	0.073	0.461	0.527	109	3.8	1.29	3.93
F	244	408	31.1	43.1	74.2	0.053	0.355	0.408	186	1.46	0.49	1.51
G	26	217	17.7	24.2	41.8	0.032	0.396	0.427	201	0.81	0.09	0.82
H	133	357	13.9	19.0	32.9	0.024	0.468	0.49	327	0.79	0.05	0.79
I	139	163	16.2	22.1	38.2	0.029	0.254	0.283	142	0.58	0.11	0.59
L	148	326	19.3	27.0	46.3	0.033	0.333	0.366	195	0.85	0.14	0.86
M	67	410	15.6	21.6	37.2	0.075	0.339	0.409	236	0.1	0.06	0.1
N	155	678	7.4	10.6	18.0	0.03	0.361	0.391	449	0.06	0.01	0.06

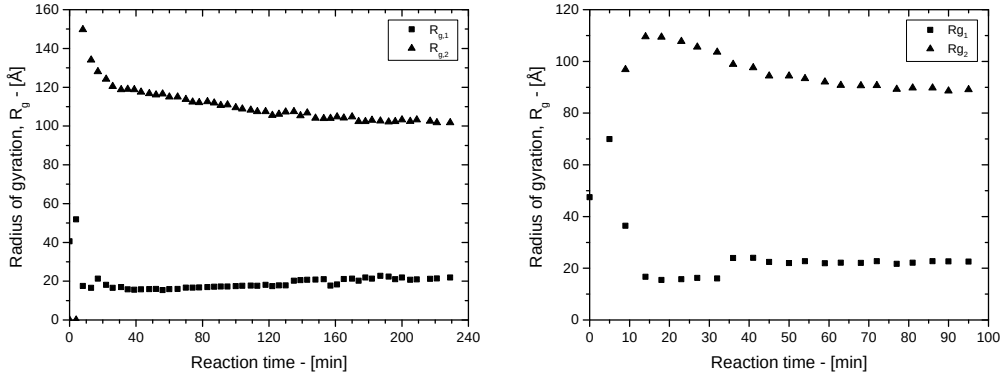

(a) *Sample A* - 600 °C, N_2. **(b)** *Sample B* - 620 °C, N_2.

Figure 6.12: Radius of gyration evolution of the two pore populations over the reaction time for sample A (a) and B (b).

scattering intensity pattern of the sorbent internal pore structure starting from the initial undecomposed calcite up to the completely calcined CaCO3. Figs. 6.11a and 6.11b suggest that the pore network generation during the first instants of the calcination reaction seems to be a gradual process as the calcination reaction progresses, as shown by the firsts USAXS/SAXS intensity profiles of the decomposing calcite. The first sample A WAXS peak of CaO appeared after 35 min (4 min of reaction time) from the beginning of the heating step at a reaction temperature of 483 °C and the first USAXS/SAXS response (the first sign of the generating internal structure) after 39 min (8 min of RT), as shown in Fig. 6.11a. For the case of sample B the first WAXS CaO peak was observed after 32 min (5 min of RT) from the beginning of the heating step at a temperature of 579 °C and corresponded with the first USAXS/SAXS response, as can be observed in Fig. 6.11b. On the other hand, the first WAXS CaO peaks for samples C, D and E were observed at 27 min (4 min of RT) and 481 °C, 26 min (5 min of RT) and 497 °C, 31 min (5 min of RT) and 583 min respectively. The first USAXS/SAXS responses were respectively detected at 32 min (9 min of RT) and 578 °C, 31 min (10 min of RT) and 579 °C, 31 min (5 min of RT) and 583 °C. These data suggest that for the case of calcined $CaCO_3$ samples in N_2 atmosphere the calcite decomposition begins at about 480 °C after 30 min ca. from the beginning of the heating step. At this time-step the internal structure of the calcining $CaCO_3$ is generated providing the scattering intensity responses represented in Fig. 6.3 and Figs. 6.11a and 6.11b. The completely decomposed $CaCO_3$ scattering intensity profiles (in N_2 atmosphere) are represented in Fig. 6.6a, showing a similar profile in shape and magnitude. This suggests a similar internal micro-structure generated during the N_2 atmosphere thermal decomposition, namely similar micro-textural properties.

Radius of gyration evolution The unified fit approach provides the sample micro-textural properties over time in terms of radius of gyration, specific surface area and porosity. The final sorbent micro-textural properties of the completely calcined $CaCO_3$ are listed in Tabs. 6.3 and 6.4 and were estimated from the USAXS/SAXS profiles measured in the correspondence of the time-step when the $CaCO_3$ conversion becomes one. However, in addition to the calcination reaction others high temperature phenomena (like sintering) contribute to affect and reduce the sorbent micro-textural properties values. For this reason, maximum values of the sorbent properties are observed during the reaction (as listed in Tabs. 6.5) and only in few cases coincide with those measured at the end of the calcination reaction.

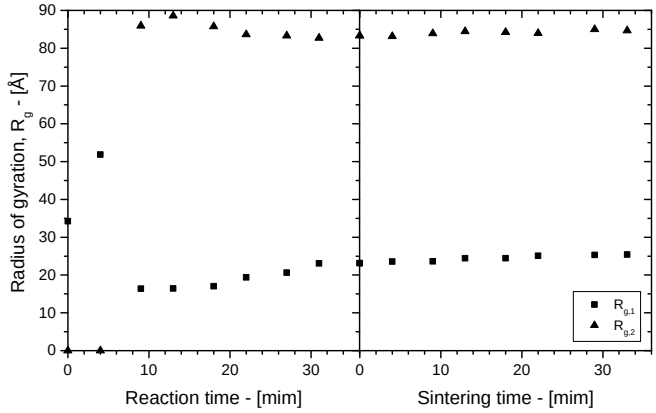

(a) *Sample C* - 650 °C, N_2.

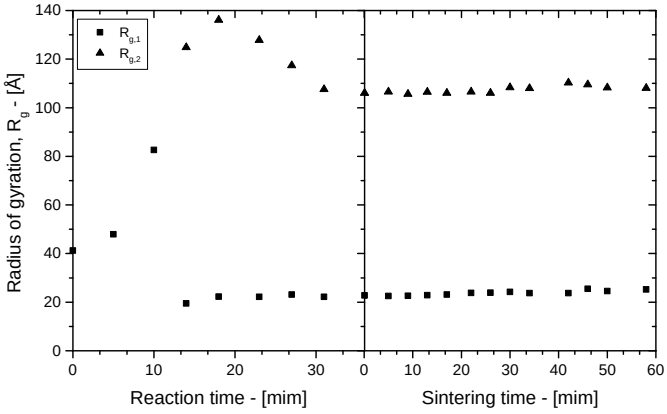

(b) *Sample D* - 680 °C, N_2.

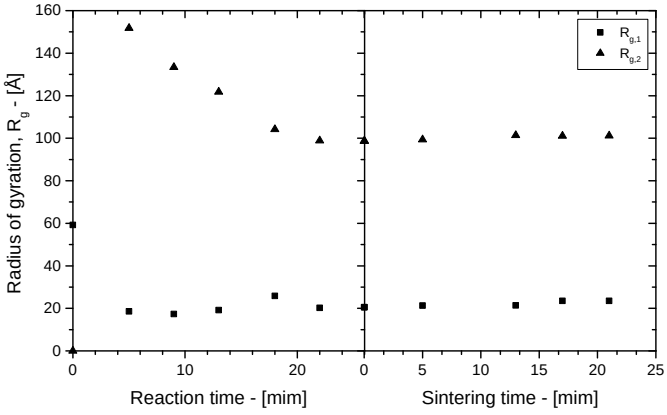

(c) *Sample E* - 700 °C, N_2.

Figure 6.13: Radius of gyration evolution of the two pore populations over the reaction and sintering time for samples C (a), D (b) and E (c).

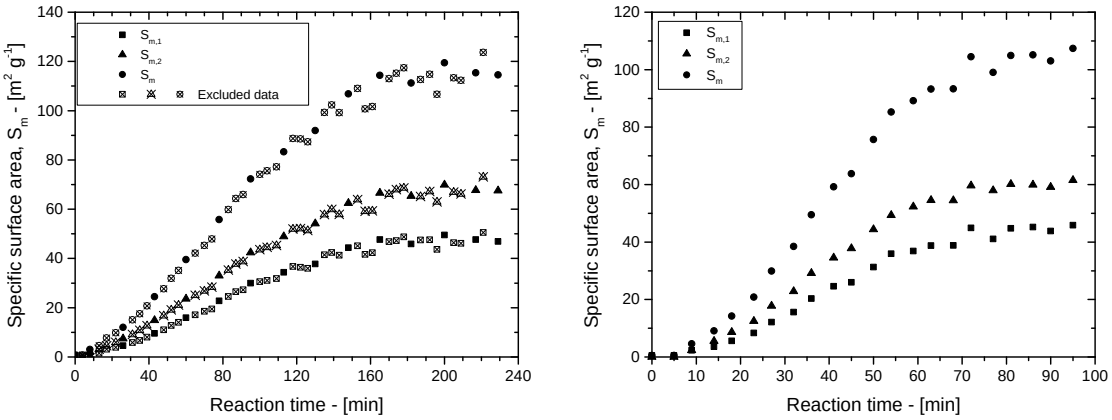

(a) *Sample A* - 600 °C, N_2. **(b)** *Sample B* - 620 °C, N_2.

Figure 6.14: Evolution of the specific surface area of the two pore populations (squares and triangles) and of the total sample internal specific surface area (dots) over the reaction and sintering time for samples A (a) and B (b). Crossed symbols showed in sample A specific surface area evolution (a) refer to the collected data by the untuned detector scans.

Each sorbent is characterized by two distinct populations of pores, namely a micro-pore population associated with the first unified fit structural level and a meso-pore one associated with the second structural level. Two radii of gyration are associated with the two pore populations that provide an estimation of their respective sizes. Specifically, the radius of gyration evolution of the two pore populations over the reaction are represented in Figs. 6.12 and 6.13. Interestingly, during the first instants of the calcination only one structural level (plus an additional one to represent the low-q region of the large structure affected by the multiple scattering effects) was necessary to fit the scattering intensity profile. This means that the decomposing $CaCO_3$ is characterized by only one pore population at the beginning of the calcination reaction. Such pore population is characterized by an initial radius of gyration that ranges between 35 Å and 60 Å. As the calcination reaction progresses, $R_{g,1}$ increases up to the generation of two distinct population of pores. In fact, after a first increase of $R_{g,1}$, its value suddenly decreases down to a lower value, namely at about 20–23 Å. Afterwards, the radius of gyration of the first population remains quite constant during the rest of the calcination reaction, showing a minimal increase with the reaction time, as shown by the $R_{g,1}$ profiles represented in Fig. 6.12 and 6.13. On the other hand, the meso-pore radius of gyration $R_{g,2}$ seems to arise from the highest value of $R_{g,1}$ reaching then its maximum value at a reaction time of about 10÷15 min. Conveniently, $R_{g,2}$ was set to be zero at the beginning of the calcination reaction as shown in Figs. 6.12 and 6.13. This behavior suggests that the initial structure of the nascent CaO is probably characterized by meso-pore structures of about 35–60 Å in size and an absent or a negligible micro-pore population. Afterwards, the nascent pore network shows two distinct pore populations, namely a quite-constant micro-pore population and a meso-pore one, that decreases in magnitude after its maximum value as the reaction progresses, reaching then a constant value (20–23 Å). This trend can be specifically appreciated by samples A and B radius of gyration profiles showed in Figs. 6.12a and 6.12b. It is remarkable to notice that on average, the final radii of gyration are about 22 Å and 96 Å for the micro and macro pore populations respectively.

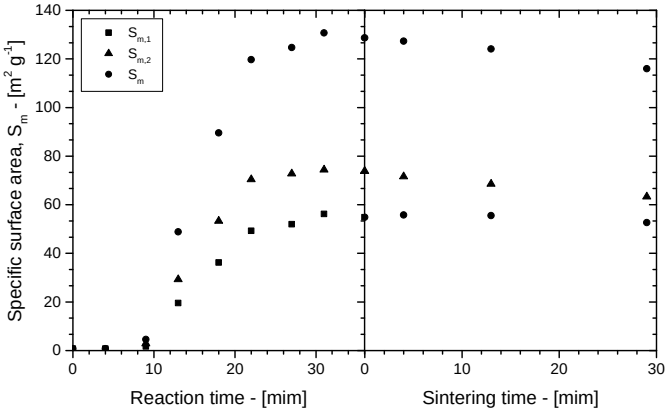

(a) *Sample C* - 650 °C, N_2.

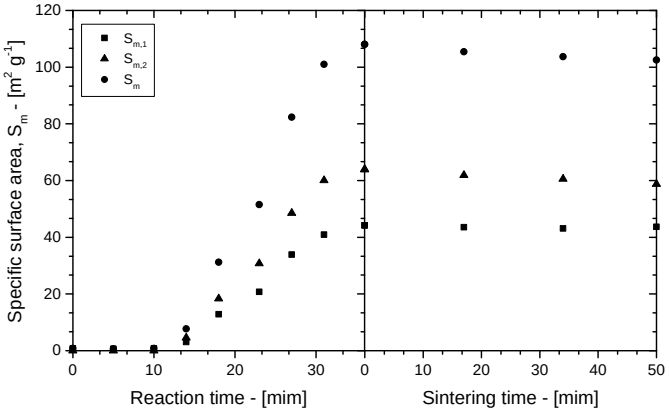

(b) *Sample D* - 680 °C, N_2.

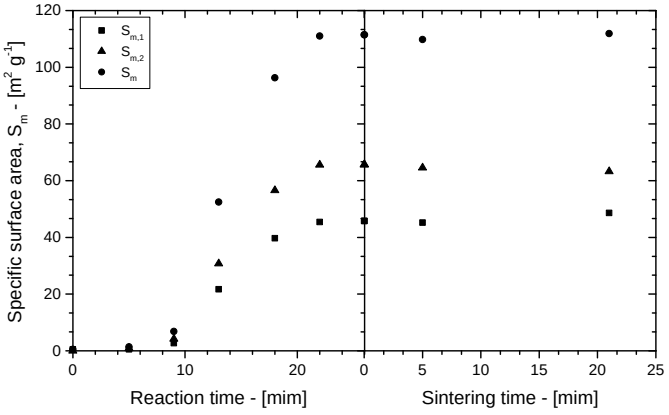

(c) *Sample E* - 700 °C, N_2.

Figure 6.15: Evolution of the specific surface area of the two pore populations (squares and triangles) and of the total sample internal specific surface area (dots) over the reaction and sintering time for samples C (a) and D (b) and E (c).

Specific surface area evolution According to Eq. (4.65), the specific surface areas of the two pore populations per unit of sorbent mass were calculated for each sample time-step, as well as the total sorbent internal specific surface area over the reaction time. The specific surface area evolution over time of the N_2 calcined samples are showed in Figs. 6.14 and 6.15. Specifically, the specific surface area profiles represented in Fig. 6.14a show two/three crossed markers between two dark markers. These crossed points were calculated from those USAXS/SAXS profiles measured by the untuned USAXS detector. In fact, due to the high temperature reactions conditions the USAXS motor controlled loses its tuning reducing the scattering intensity magnitude. This phenomenon generates apparent local decreases in those properties strictly related to the absolute scale of the scattering intensity (the sample differential scattering cross section), namely the sample specific surface area and porosity, as shown in Fig. 6.14a and Fig. 6.18a. After every tuning process (on average one every three/four scans) the USAXS detector was able to provide the correct differential scattering cross section magnitude and thus the true absolute sample specific surface area and porosity. For this reason, those properties estimated from the untuned data were neglected. Unfortunately, this increase the sampling frequency as shown in Fig. 6.14a and Fig. 6.18a from one every 5 min to one every 10–15 min. For the sake of clarity, the untuned properties were showed only for the case of sample A and those of the other samples were conveniently omitted. Finally, it should be noted that the radius of gyration estimation from the scattering intensity profiles do not depend by the absolute scattering intensity magnitude, according to Eq. (4.60), because it only depends on the scattering intensity local slope (that of the Guinier regime).

As the calcination reaction progresses, the total specific surface area profiles over the reaction time show the well know profile, namely an initial increase of the sample specific surface area, followed by a decrease down to an asymptotic value, according to Glasson (1958), Silcox, Kramlich, and Pershing (1989), and Mai and Edgar (1989) for the calcium oxide derived from calcium hydroxide, Mahuli et al. (1999) and Fierro, Adánez, and García-Labiano (2004). The transition between the these two steps shows a maximum value in the surface area evolution during the $CaCO_3$ thermal activation. This behavior is the result of two main phenomena, namely the calcination reaction itself that contributes to generate and increase the sorbent specific surface area and of the sintering processes whose time scale are similar to that of the calcite thermal decomposition (García-Labiano et al., 2002; Mai and Edgar, 1989; Silcox, Kramlich, and Pershing, 1989). Once the calcination reaction is completed the final total samples specific surface area are significantly high, namely $114.5\,m^2\,g^{-1}$ (sample A), $107.4\,m^2\,g^{-1}$ (sample B), $128.7\,m^2\,g^{-1}$ (sample C), $108\,m^2\,g^{-1}$ (sample D) and $111.5\,m^2\,g^{-1}$ (sample E) as listed in Tab. 6.3. These values are significantly higher than those estimated by Glasson (1958) $43.2\,m^2\,g^{-1}$, Barker (1973) $25\,m^2\,g^{-1}$, Bhatia and Perlmutter (1983a) $8\div15.5\,m^2\,g^{-1}$, Zhu, Wu, and Wang (2011) who measured less than $16\,m^2\,g^{-1}$. Borgwardt (1985) obtained higher specific surface areas in the rage between $79\,m^2\,g^{-1}$ and $90\,m^2\,g^{-1}$ by means of calcination reactions performed in the temperature range similar to those of samples A$\div$E, namely 600$\div$650 °C. Afterwards, Borgwardt (1989b) estimated an higher CaO specific surface area value of $104\,m^2\,g^{-1}$ by means of a calcination reaction performed at 700 °C in nitrogen atmosphere. Milne et al. (1990) measured values of less than $80\,m^2\,g^{-1}$, close to those of Gullett and Bruce (1987) and Rodriguez-Navarro et al. (2009). The CaO specific surface values estimated in this work are significantly similar to those determined by Ewing, Beruto, and Searcy (1979) by means of calcite powder decomposition in vacuum at 650 °C, namely $92\,m^2\,g^{-1}$. More interestingly, the sample C (calcined at 650 °C in N_2) final specific surface area of $128.67\,m^2\,g^{-1}$ (Tab. 6.3) is in excellent agreement with that estimated by Powell and Searcy (1982), namely $127\,m^2\,g^{-1}$ through a single crystal calcination reaction at 650 °C under vacuum condition. Additionally, the sample A, B, D and E values are in agreement

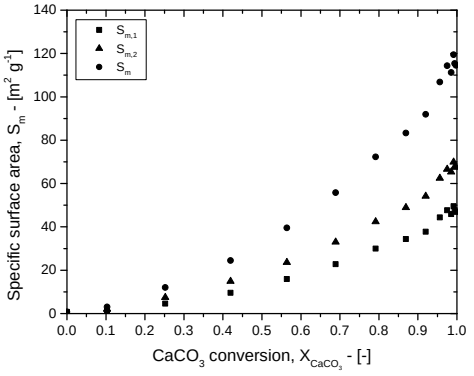

(a) *Sample A* - 600 °C, N_2 - S_m *vs* $X_{\mathrm{CaCO_3}}$.

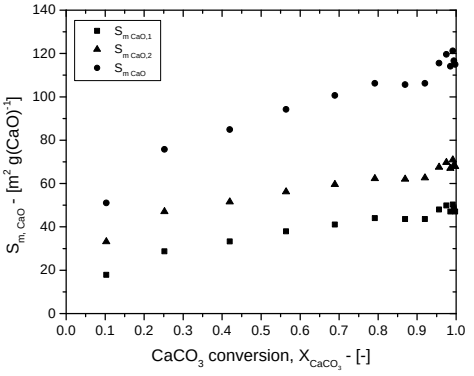

(b) *Sample A* - 600 °C, N_2 - $S_{m,\mathrm{CaO}}$ *vs* $X_{\mathrm{CaCO_3}}$.

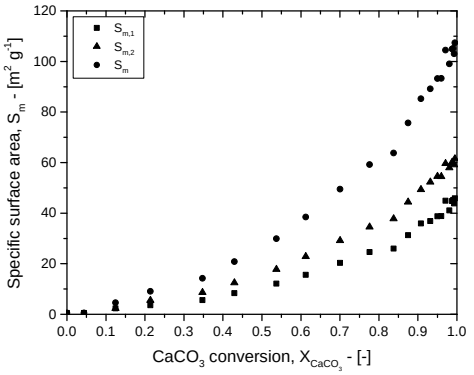

(c) *Sample B* - 620 °C, N_2 - S_m *vs* $X_{\mathrm{CaCO_3}}$.

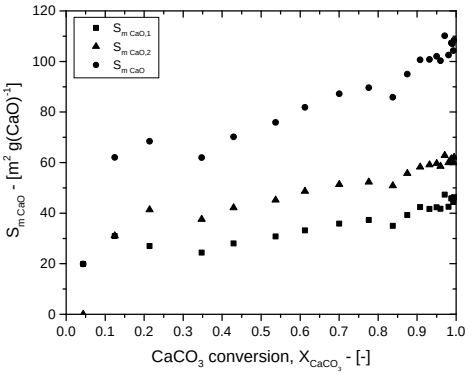

(d) *Sample B* - 620 °C, N_2 - $S_{m,\mathrm{CaO}}$ *vs* $X_{\mathrm{CaCO_3}}$.

Figure 6.16: Evolution of the specific surface area of two pore populations (squares and triangles) and of the total specific surface area (dots) over the $CaCO_3$ conversion for sample A and B: (a) and (b) shows the specific surface area evolution per unit of sample mass; (c) and (d) the specific surface area per unit of CaO mass.

with the Powell and Searcy (1982) observations, namely final specific surface areas in the range of $110 \div 127\,\mathrm{m^2\,g^{-1}}$ between 600 °C and 700 °C. The specific surface areas values of samples A, C and D becomes higher if their maximum values are considered (Tab. 6.5): $119.4\,\mathrm{m^2\,g^{-1}}$, $130.7\,\mathrm{m^2\,g^{-1}}$ and $108\,\mathrm{m^2\,g^{-1}}$ respectively. Ewing, Beruto, and Searcy (1979) demonstrated the presence of a metastable nascent CaO highly CO_2 reactive in the decomposing $CaCO_3$. Accordingly, lower specific surface area values are due to the high internal/local CO_2 concentration gradients (probably caused by large sample size) that may promote the CaO specific surface area reduction.

The final specific surface areas of the two pore populations listed in Tab. 6.3 shows similar values despite the different final calcination temperatures, namely within the ranges of $44 \div 55\,\mathrm{m^2\,g^{-1}}$ and $61 \div 75\,\mathrm{m^2\,g^{-1}}$.respectively. This observation is in agreement with the similar (in magnitude and shape) USAXS/SAXS final scattering intensity responses of the calcined samples in N_2 atmosphere, as showed in Fig. 6.6a.

Figs. 6.16a and 6.16c and Figs. 6.17a, 6.17c and 6.16 show the samples A, B, C, D and E specific surface area profiles over the calcium carbonate conversion during the reaction step. In all these cases the specific surface area evolution during the $CaCO_3$ decomposition shows an increasing trend that clearly deviates from the linearity. This is in agreement with the Ewing, Beruto, and Searcy (1979) investigation, who observed a linear specific surface area evolution over the CaO molar fraction (and thus the $CaCO_3$ conversion for calcination

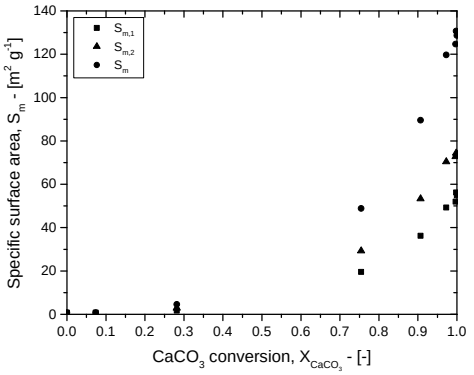

(a) *Sample C* - 650 °C, N_2 - S_m *vs* $X_{\mathrm{CaCO_3}}$.

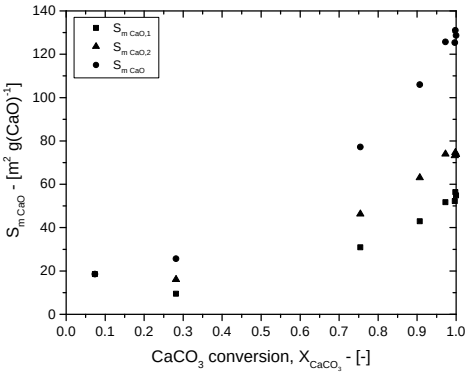

(b) *Sample C* - 650 °C, N_2 - $S_{m,\mathrm{CaO}}$ *vs* $X_{\mathrm{CaCO_3}}$.

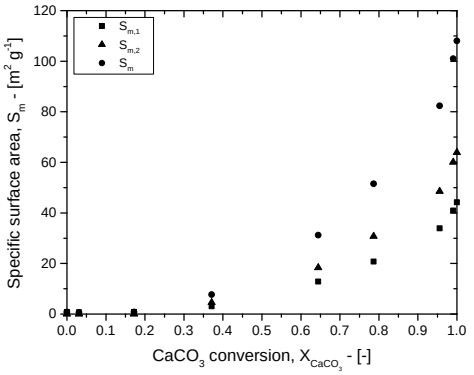

(c) *Sample D* - 680 °C, N_2 - S_m *vs* $X_{\mathrm{CaCO_3}}$.

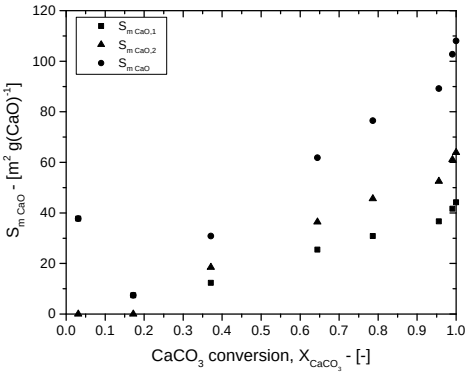

(d) *Sample D* - 680 °C, N_2 - $S_{m,\mathrm{CaO}}$ *vs* $X_{\mathrm{CaCO_3}}$.

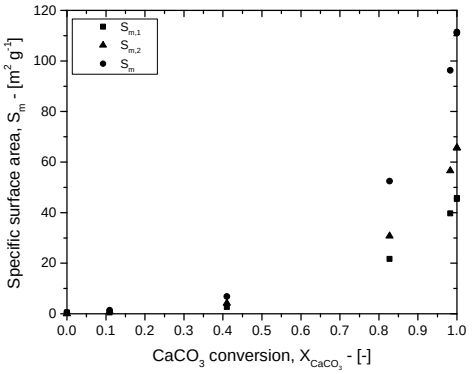

(e) *Sample E* - 700 °C, N_2 - S_m *vs* $X_{\mathrm{CaCO_3}}$.

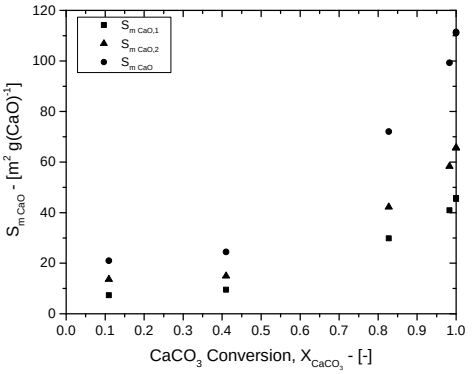

(f) *Sample E* - 700 °C, N_2 - $S_{m,\mathrm{CaO}}$ *vs* $X_{\mathrm{CaCO_3}}$.

Figure 6.17: . Evolution of the specific surface area of two pore populations (squares and triangles) and of the total specific surface area (dots) over the calcination reaction for sample C, D, E and F: (a), (c) and (e) show the specific surface area evolution per unit of sample mass; (b), (d) and (f) the specific surface area per unit of CaO mass.

reactions performed at 650 °C in-vacuo. Additionally, Ewing, Beruto, and Searcy (1979) proved that this linear trend holds for calcite decomposition performed at less than 0.9 torr of CO_2 in the reaction atmosphere. At higher CO_2 pressures Ewing, Beruto, and Searcy (1979) observed that the sorbent surface areas vary erratically from run to run with profiles lower than those obtained from vacuum calcination reactions, showing lower final CaO surface values when the calcination reaction stopped. Contrary to this observation, in this work non-linear and well-defined profiles of the surface area vs X_{CaCO_3} are observed in Figs. 6.16a and 6.16c and Figs. 6.17a, 6.17c and 6.16. Additionally, these profiles achieve high specific surface area values at the end of the calcination reaction, comparable with those obtained through CaCO3 decomposition in-vacuo. According to the Ewing, Beruto, and Searcy (1979) investigation, this behavior is ascribe to the CO_2 concentration gradients that are generated during the calcite thermal decomposition. In fact, Ewing, Beruto, and Searcy (1979) argued that low CO_2 pressures seem to influence the nascent CaO morphology (verified by means of SEM images of partially calcined samples) increasing the initial dimensions of pores. This is in agreement with the $R_{g,2}$ maxima showed in Figs. 6.12 and 6.13 at the beginning of the calcination reaction, namely at reaction times of about $10 \div 15$ min. This increase of the second population radius of gyration means an increase of its overall pore size, that exhibit a lower surface-to-volume ratio, with a consequent decrease of the associated specific surface area.

The sample specific surface areas were rescaled in order to obtain the sorbent internal surface area per unit of calcium oxide mass, $S_{m,CaO}$, converted by the calcination reaction. Because of the zero values of the CaO mass at the beginning of the reaction (RT$= 0$), the first $S_{m,CaO}$ value was neglected in order to avoid any indeterminate form. The $S_{m,CaO}$ profiles over the $CaCO_3$ conversion are depicted in Figs. 6.16b and 6.16d for the case of samples A and B, showing a quite linear profile over X_{CaCO_3}. On the other hand, the $S_{m,CaO}$ profiles over X_{CaCO_3} of samples C, D and E showed in Figure 16 (b), (d) and (f) seem to be almost similar to the vs evolution represented in Figs. 6.17b, 6.17d and 6.17f.

In this work, the maximum CaO specific surface area values per unit of sample mass (listed in Tab. 6.5) were obtained at end of the calcination reaction as shown in Figs. 6.16a and 6.16c and Figs. 6.17a, 6.17c and 6.16. This result is in contrast with that obtained by Rodriguez-Navarro et al. (2009) who observed a maximum surface area ($79.2\,m^2\,g^{-1}$) at a $CaCO_3$ conversion value of about 0.11 at 750 °C in nitrogen.

Particle porosity evolution The sorbent particle porosities were estimated by means of Eq. (4.64), that provided two different values, according to the two structural levels of the unified fit approach. In this way, the porosity evolution over the reaction time was obtained for each sample, as showed in Figs. 6.18 and 6.19. Even for the case of porosity, Fig. 6.18a shows those values obtained from the untuned USAXS detector measurements, that were excluded because not with the real absolute scale. The sample A and B porosity evolution over time are represented by increasing profiles that reach its maximum value at the end of the reaction time, as shown by Figs. 6.18a and 6.18b. The same trends can be observed in Fig 6.19 for the case of sample C, D and E respectively. The final calcination reaction porosities are listed in Tab, 6.3, whose values are respectively 0.515, 0.436, 0.519, 0.530 and 0.527. These porosities are significantly close to the maximum CaO porosity, namely 0.545, meaning that sintering phenomena during the reaction time are quite modest for temperatures below 700 °C. In fact, the maximum porosity values achieved by each sample coincide with those estimated when the calcination reaction stopped, except for the case of sample A, whose maximum porosity is slightly different, namely 0.516. As can be observed from Figs. 6.18 and 6.19 and from the tabulated porosity values in Tab, 6.3, the meso-pore population contributes to the majority of the sample porosity, showing values of about 0.4 at the end of the calcite decomposition. This value is in good agreement with

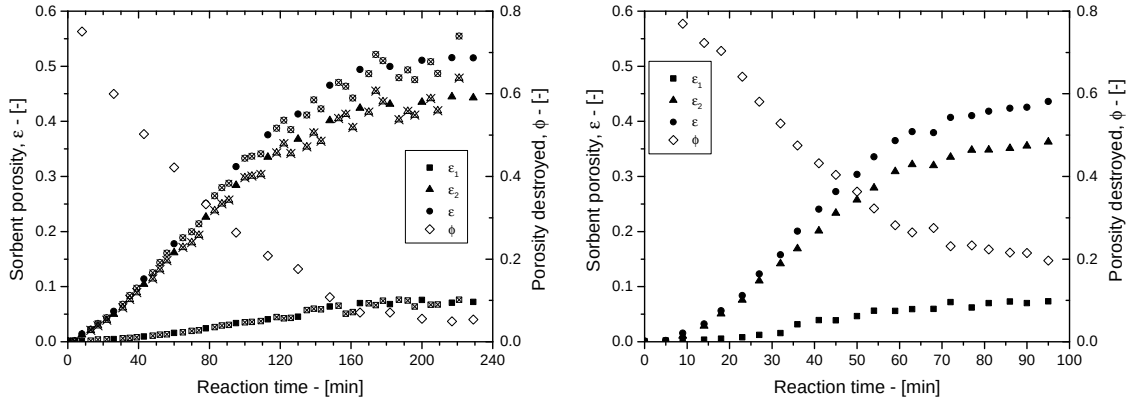

(a) *Sample A* - 600 °C, N_2. **(b)** *Sample B* - 620 °C, N_2.

Figure 6.18: Porosity evolution of the two pore populations (squares and triangles) and of the total sample internal porosity (dots) over the reaction time for sample A (a) and (b). The right-side axis refers to the total fraction of pore destroyed during the reaction time (diamond symbols). Open markers showed in sample A porosity evolution (a) refer to the collected data by the untuned detector scans.

the meso-porosities values measured by Beruto, Barco, and Searcy (1983), namely in the range of $0.41 \div 0.44$. On the other hand, the micro-pore population is characterized by a remarkable lower volume of pores, namely a final value less than 0.1, namely in the range of $0.065 \div 0.09$. However, in contrast to this result, the micro-pore population is characterized by a considerable specific surface area ($44 \div 55\,\mathrm{m^2\,g^{-1}}$), that is comparable with that of the meso-pore population ($63 \div 74\,\mathrm{m^2\,g^{-1}}$), because of its high surface-to-volume ratio.

Because of the gas-solid non-catalytic nature of the calcination reaction, the sorbent porosity evolution during the thermal decomposition should be linear over the $CaCO_3$ conversion, as stated by Eq. (2.5), according to Bhatia and Perlmutter (1981), García-Labiano et al. (2002), and Mahuli et al. (1999). This trend is in agreement with the results of Beruto, Barco, and Searcy (1983), who observed a linear evolution of the sample total porosity over the $CaCO_3$ decomposed fraction. However, in this work, different porosity evolution profiles were observed, as shown in Fig 6.20, where the ideal linear porosity trend, $\varepsilon_{\mathrm{ID}}$, was represented by a continuous line, calculated through Eq. (2.5) by assuming a zero porosity value of the initial calcite. Interestingly, these figures show how the sorbent porosity evolution deviates from the ideal profile of Eq. (2.5) since the beginning of the reaction. Although this deviation becomes gradually important, especially during the of the second half of the reaction, the final sample porosity is significant close to the theoretical value, as shown in Fig 6.20. Additionally, the deviation from the ideal porosity values seems to be more important as the calcination temperature increases as shown by the sample C, D and E porosity profiles vs $X_{\mathrm{CaCO_3}}$ depicted in Figs. 6.20c, 6.20d and 6.20e. At the light of these porosity trends, a different relationship between ε and $X_{\mathrm{CaCO_3}}$ was considered. Indeed, Ramachandran and Smith (1977) modified Eq. (2.5) by considering the faction of pore removed (or destroyed) by sintering, ϕ,

$$\begin{aligned} \varepsilon &= \left[\varepsilon_0^{\mathrm{CaCO_3}} + (1 - Z_{\mathrm{calc}})(1 - \varepsilon_0^{\mathrm{CaCO_3}})\, X_{\mathrm{CaCO_3}}\right](1 - \phi) \\ &= \varepsilon_{\mathrm{ID}}\,(1 - \phi)\,, \end{aligned} \tag{6.3}$$

where, here, the linear porosity evolution over the $CaCO_3$ conversion is indicated with $\varepsilon_{\mathrm{ID}}$, namely the ideal linear porosity trend during the calcination reaction. According

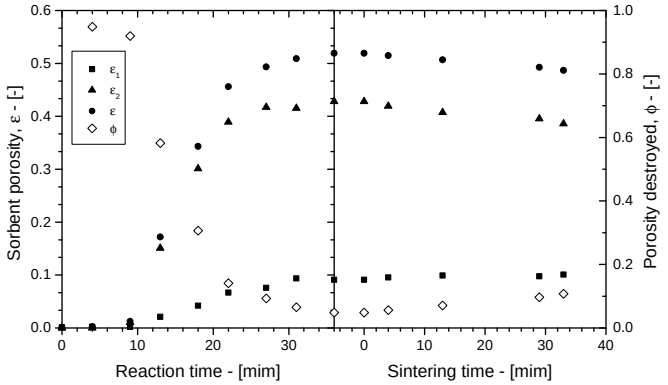

(a) *Sample C* - 650 °C, N_2.

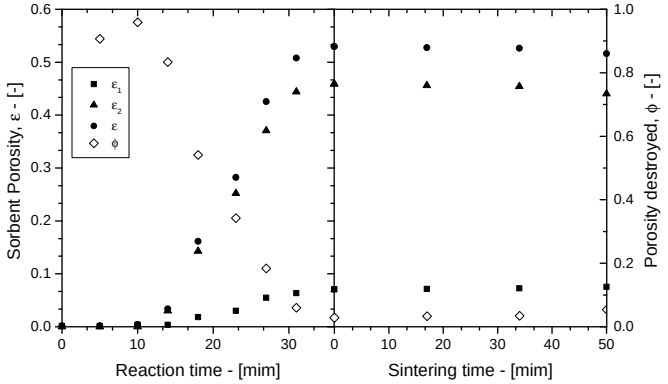

(b) *Sample D* - 680 °C, N_2.

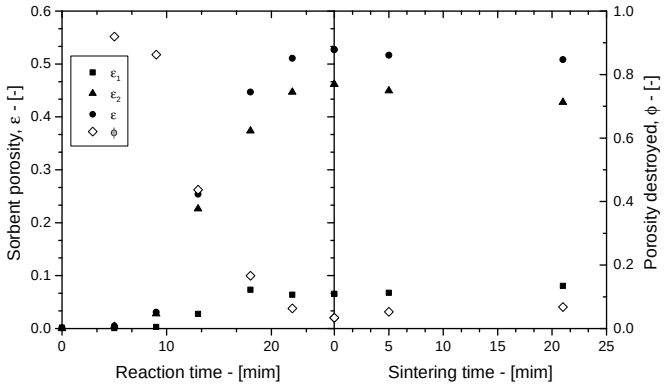

(c) *Sample E* - 700 °C, N_2.

Figure 6.19: Porosity evolution of the two pore populations (squares and triangles) and of the total sample internal porosity (dots) over the reaction and sintering time for samples C (a), D (b) and E (c). The right-side axis refers to the total fraction of pore destroyed during the reaction and sintering time (diamond symbols). Open markers showed in sample A porosity evolution (a) refer to the collected data by the untuned detector scans.

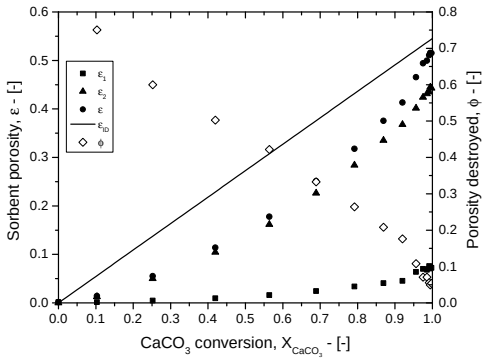

(a) *Sample A* - 600 °C, N_2.

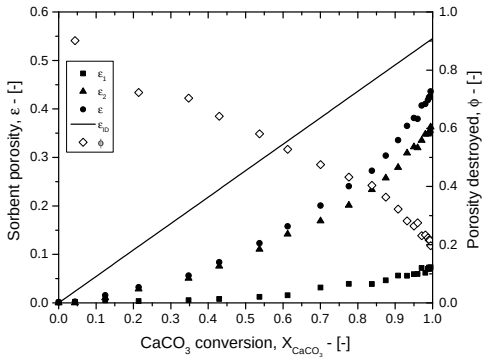

(b) *Sample B* - 620 °C, N_2.

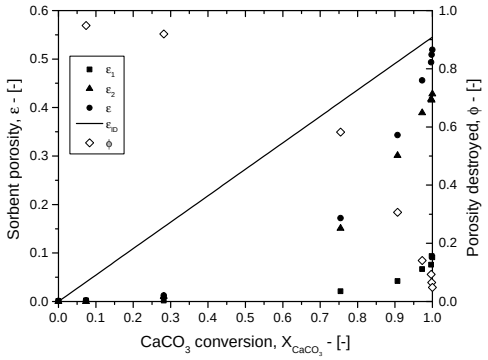

(c) *Sample C* - 650 °C, N_2.

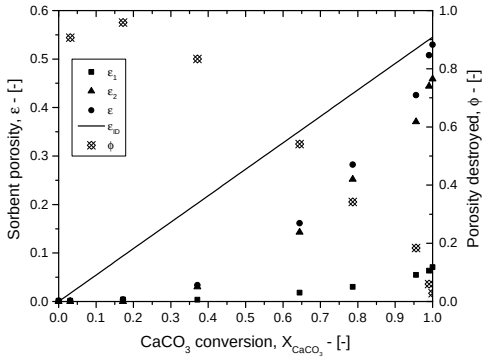

(d) *Sample D* - 680 °C, N_2.

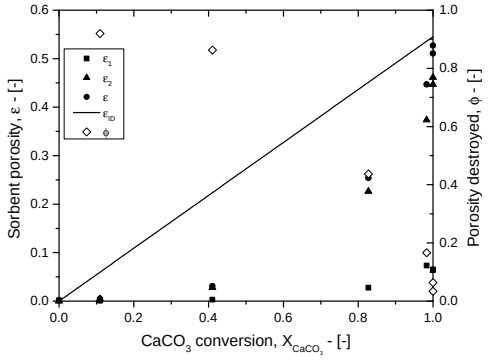

(e) *Sample E* - 700 °C, N_2.

Figure 6.20: Evolution of the sorbent internal porosity of the two pore populations (squares and triangles) and of the total sorbent internal porosity (dots) over the calcination reaction conversion for the thermally activated runs in N_2, namely samples A, B, C, D and E. Solid lines represent the ideal linear total sample porosity evolution during the reaction, predicted by means of the difference between molar volumes of calcite and of CaO. The right-side of each plot refers to the total fraction of pore destroyed evolution during the calcination reaction.

to Ramachandran and Smith (1977) and Bhatia and Gupta (1992) the fraction of pore destroyed by sintering was modeled as a first order rate process, governed by an Arrhenius-type equation, namely $\dot{\phi} = k_{\phi}\,(1-\phi)$, that monotonically increases as time progresses up to the asymptotic value one. Despite Ramachandran and Smith (1977) applied Eq. (6.3) with the aim to account for the sintering effects on porosity during the gas-solid reactions, in this work sintering seems to be not responsible of the porosity deviation from the ideal value. In fact, sintering effects are irreversible phenomena that reduce the sample porosity. Contrarily, in this work the final sorbent void fraction is significantly close to the theoretical value, as showed in Fig 6.20, even though the actual sample porosity values are quite distant from the theoretical ones. Additionally, by solving Eq. (6.3) for ϕ, the experimental sample fraction of pores destroyed was calculated by means of

$$\phi = 1 - \frac{\varepsilon}{\varepsilon_{\mathrm{ID}}}, \tag{6.4}$$

and then plotted in Figs. 6.18 and 6.19 as functions of time. Interestingly, ϕ exhibits decreasing trend profiles over the reaction time, in contrast with the first-order rate process proposed by Ramachandran and Smith (1977) to account for the sintering phenomena, namely a monotonic increasing function with time. This result seems to confirm that sintering phenomena are not the main responsible of the porosity deviation evolution during the calcination reaction, as confirmed by the ϕ vs $X_{\mathrm{CaCO_3}}$ profiles depicted in Fig. 6.20, that shows a decreasing profiles down to asymptotic values as the carbonation reaction progresses. The final value of ϕ for each sample is listed in Tab. 6.3, where the total pore volume reduction when the calcination reaction stopped ranges between from a minimum of 0.029 (sample D) up to a maximum value of 0.196 for the case of sample B, that showed the lowest total sample porosity among the calcined samples in nitrogen atmosphere. Therefore, the decreasing trends of the fraction of pore removed over time and the low calcination reaction temperatures indicate that another phenomenon different from sintering could explain the pore deviation from the theoretical one. According to Ewing, Beruto, and Searcy (1979) the high CO_2 concentration gradients generated by the $CaCO_3$ decomposition may interact with the nascent CaO layer through mechanisms of CO_2 chemisorption (Fukuda and Tanabe, 1973), as suggested by Beruto, Barco, and Searcy (1984). This process changes the morphology of the nascent porosity (Ewing, Beruto, and Searcy, 1979) making the deviation of the specific surface area vs $X_{\mathrm{CaCO_3}}$ profile from the linearity. According to Ewing, Beruto, and Searcy (1979) the CO2 interaction with the nascent CaO do not significantly promote sintering phenomena because the low reaction temperature. However, this change in pore geometry generates a sorbent porosity that deviated from the theoretical one. Once the CO_2 concentration decreases, the reversible desorption mechanisms restore the sorbent porosity, that approach to the final theoretical values compatible with the modest sintering effects that aim to reduce the overall sample porosity.

Sphericity factor evolution As previously mentioned, the use of the radius of gyration into the unified fit approach provides to the model shape independent features, allowing the scatterers intensity description by means of only one dimensional parameter. This formulation is very convenient during the model fitting over the scattering profiles because it avoids any a priori assumption on the scatterers shape and it reduces the number of the fitting parameters. However, if the radius of gyration approach simplify the unified fit model, this approach does not provide any information about the scatterers (pores in this work) shape. In fact, in some cases the sphere-shape assumption could not be valid as shown by Beaucage (1995). For this reason, a sphericity factor Ψ_i is introduced in order

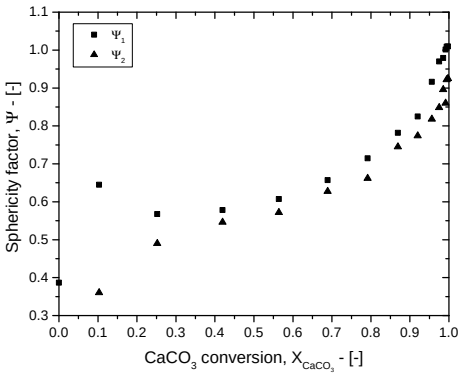

(a) *Sample A* - 600 °C, N_2.

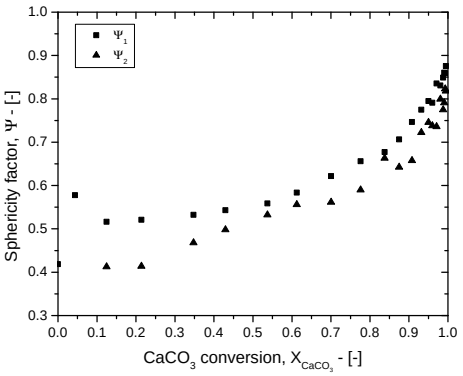

(b) *Sample B* - 620 °C, N_2.

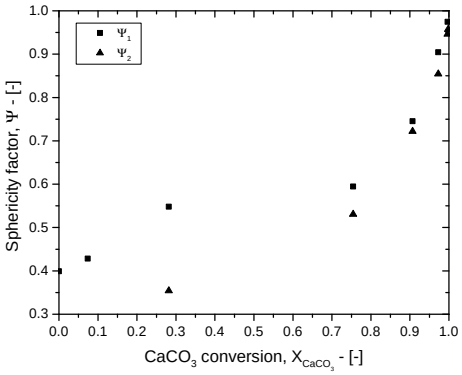

(c) *Sample C* - 650 °C, N_2.

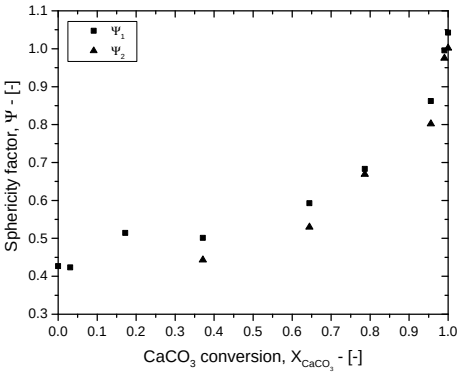

(d) *Sample D* - 680 °C, N_2.

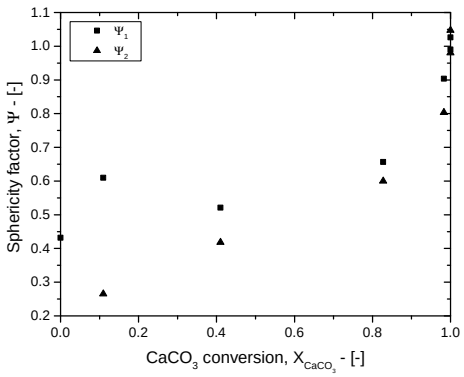

(e) *Sample E* - 700 °C, N_2.

Figure 6.21: Sphericity factor evolution of the two pore population (squares and triangles) over the $CaCO_3$ conversion for samples A (a), B (b), C (c), D (d) and E (e).

to investigate the pore shape difference from that of spheres and its evolution over time, according to Eq. 5.2.

The sphericity parameter could provide useful information about the sorbent pore shape, this parameter is equal to 1 in the case of spherical pores and it assumes lower values for shapes fairly different from the sphere one, i.e. 0.846 for the octahedron, 0.806 for the cube, 0.671 for a tetrahedron, but also 0.794 and 0.874 for ideal cones and cylinders.

Following this approach, two sphericity factors were calculated according to the two pore populations, as showed in Fig. 6.21. It is remarkable to notice how the initial value the micro-pore population sphericity factor is about 0.4, meaning that the initial pore geometry is fairly from the sphere shape. This is in agreement with the investigations of Powell and Searcy (1982), Beruto, Barco, and Searcy (1983), and Rodriguez-Navarro et al. (2009) who observed rod-shaped CaO aggregates in the early stages of the calcination reaction compatible with these low sphericity factor value. As the calcination reaction progresses Ψ_1 sharply increases up to values of $0.6 \div 0.7$ and then slightly increases laying in this range of values up to X_{CaCO_3} values close to 0.8. Again, this is consistent with the FESEM images of Rodriguez-Navarro et al. (2009) who showed a process of coalescence of the rod-shaped CaO particles. The meso-pore population seems to be generated with a sphericity factor similar to that of the micro-pore population and specifically in the range of $0.3 \div 0.4$. Even in this case, Ψ_2 increases up to $0.6 \div 0.7$ fairly close to Ψ_1 values. When the $CaCO_3$ conversion is high, namely more than 0.8, the two populations sphericity factors rapidly approaches to one, suggesting a pore shape evolution towards spherical shapes near to the end of the calcination reaction. Additionally, except for the case of sample B, whose final sphericity factors approaches to 0.9 as showed in Fig. 6.21b, the sphericity factors profiles seem to be slightly influenced by the calcination reaction temperature, showing almost the same trend, as depicted in Fig. 6.21.

Another important observation close to the pore shape investigation, is the specific surface area per unit of sample volume profiles over the respective sample porosities, as shown in Fig. 6.22a and 6.22b for the cases of sample A and B. Both the meso-pore population and the total surface areas shows linear trend over the meso-pore and total porosity respectively. Precisely, these trends seem to be slightly concave suggesting a modest change in the surface-to-pore ratio during the reaction, probably due to a pore-shape evolution during the calcination reaction. On the other hand the micro-pore population specific surface area shows a pronounced concave positive correlation over ε_1, as emphasized by the insets of Fig. 6.22a, 6.22c and 6.22e. Finally, the pore surface-to-volume ratio of the two pore populations, indicated as $R_{S/V,1}$ and $R_{S/V,2}$, were plotted over the respective radius of gyration, as depicted in Fig. 6.22b, 6.22d and 6.22f. Interestingly, positive correlations are observed, suggesting that the surface-to-volume ratio seems to be directly proportional to the pore size (namely the radius of gyration) during the whole calcination reaction.

At the light of these observations, the internal micro-structure of the decomposing $CaCO_3$ in nitrogen atmosphere at temperature below 800 °C seems to be slightly affected by the sintering phenomena, this is consistent with Borgwardt (1989b) who did not observed any sintering effect in completely calcined samples obtained at these calcination reaction conditions. Interestingly, the deviation from the linearity evolution over the $CaCO_3$ conversion of the porosity and the specific surface area are probably related to the CO_2 concentration gradients inside the decomposing $CaCO_3$ particles, according to Beruto (1976), Ewing, Beruto, and Searcy (1979), and Powell and Searcy (1982), which demonstrated the existence of a metastable CaO intermediate layer by means of in vacuo calcination reactions. This intermediate layer (made of normal NaCl-type CaO particles) is highly CO_2 reactive even at carbon dioxide pressures below those predicted from the chemical equilibrium. Ewing, Beruto, and Searcy (1979) showed that the reaction of the metastable CaO layer with the releasing CO_2 of the decomposing particle causes changes

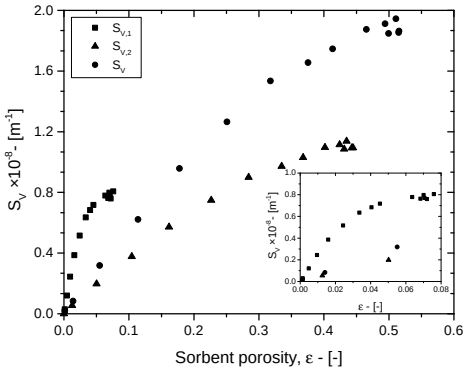

(a) *Sample A* - 600 °C, N_2 - S_V *vs* ε.

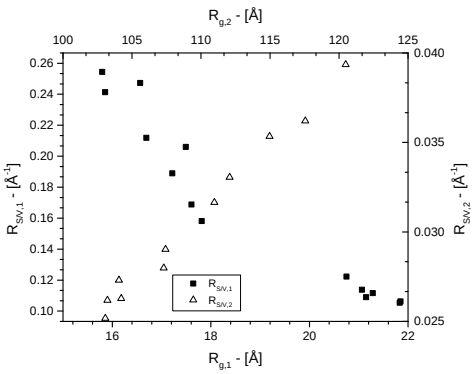

(b) *Sample A* - 600 °C, N_2 - $R_{S/V}$ *vs* R_g.

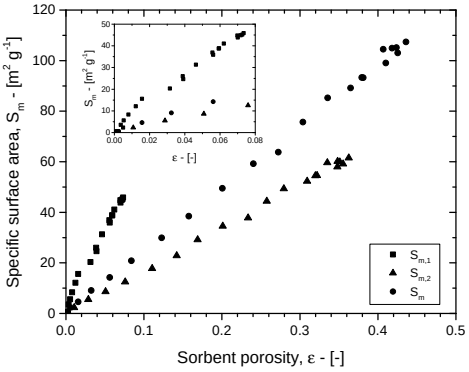

(c) *Sample B* - 620 °C, N_2 - S_V *vs* ε.

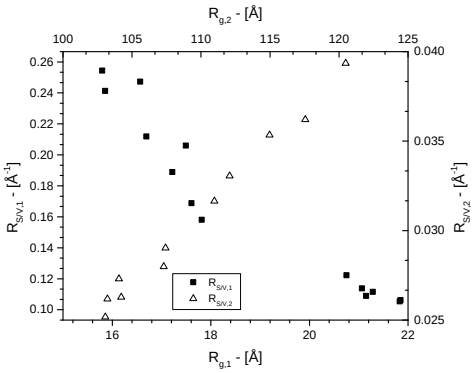

(d) *Sample B* - 620 °C, N_2 - $R_{S/V}$ *vs* R_g.

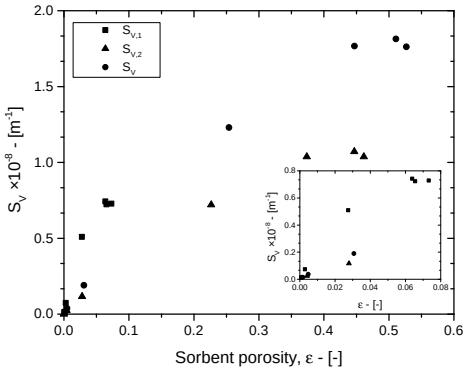

(e) *Sample E* - 700 °C, N_2 - S_V *vs* ε.

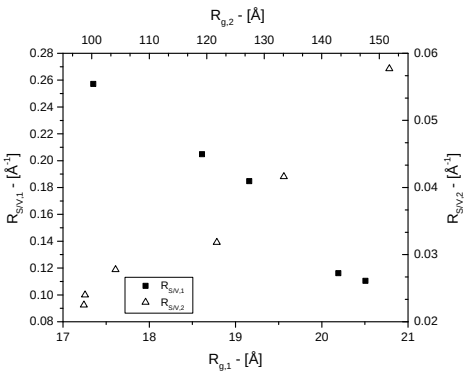

(f) *Sample E* - 700 °C, N_2 - $R_{S/V}$ *vs* R_g.

Figure 6.22: First column refers to the specific surface areas per unit of sample volume of the two pore populations (squares and triangles) and of the total specific surface area per unit of sample volume (dots) over their porosities values. The second one refers to the surface-to-pore volume ratio of the two pore populations correlated with their respective radii of gyration.

in the geometry of the nascent porosity but does not promote sintering. This is in good agreement with radius of gyration profiles evolution over the reaction time, as previously discussed and showed in Fig. 6.12 and 6.13, especially for the case of the meso-pore radius of gyration $R_{g,2}$ that shows a maximum value over the reaction time. These changes in the pore shape reduce both the sorbent surface and porosity, leading to a deviation from the theoretical values, as showed in Figs. 6.16, 6.17 and Fig 6.20. Although the deviation from the linear evolution of the sorbent specific surface area was observed by Ewing, Beruto, and Searcy (1979), in this work non-linear and well-defined (monotonically increasing) profiles were observed, as shown in Figs. 6.16, 6.17, that is in contrast with the results of Ewing, Beruto, and Searcy (1979) where none profile was recognized. Additionally, the pore shape changes could be the main responsible of the non-ideal evolution of the sorbent porosity observed during the calcite thermal decomposing (Fig 6.20). Furthermore, this result is supported by the decreasing magnitude of the experimental fraction of pore destroyed, instead of an increasing trend typical of the sintering phenomena (Figs. 6.18, 6.19 and Fig. 6.20). According to Powell and Searcy (1982), Beruto, Barco, and Searcy (1983), and Rodriguez-Navarro et al. (2009) who observed needle- or rod-shaped CaO aggregates, the initial pore shape of nascent CaO could compatible with these geometries, as showed by the initial low pore sphericity values close to 0.3÷0.4. However, when the internal sorbent CO_2 concentrations decrease due to the end of the calcination reaction, the whole sorbent pore structure evolves increasing the sphericity factor of the two pore population up to values around one (Fig. 6.21). Because of the negligible sintering effects due to the low calcination temperatures, both the specific surface area and the porosity values fall close to the theoretical ones, namely fairly close to $127\,m^2\,g^{-1}$ (Powell and Searcy, 1982) and 0.545.

Evolution of the pore size distributions Following the approach proposed by Beaucage, Kammler, and Pratsinis (2004), the pore size distributions of each sample (under the assumption of spherical pore shape) were estimated by means of Eqs. (4.66), (4.67) and (4.68), as shown in Fig. 6.23. Time-resolved unified parameters were used to calculate the sorbent PSD generation and evolution during the reaction time. For the case of calcined samples in nitrogen atmosphere (samples A÷E) the initial micro-structure is characterized by a mono-modal distribution, as can be observed in the insets of Fig. 6.23. This result is a direct consequence of two structural levels (one for the multiple scattering region) used in the unified fit approach to fit the initial USAXS/SAXS scattering intensity profiles during the first minutes of the calcination reaction, namely up to 5–8 min of reaction time as shown in Figs. 6.11a and 6.11b. As consequence, the initial $CaCO_3$ structure shows a slightly distribute structure as confirmed by the PSD calculated at the RT of 0 min. Once the calcite decomposition is initiated, the nascent CaO micro-structure is characterized by a pore matrix mono-modally distributed, as suggested by the PSDs of sample B at 5 min in Fig. 6.11b, sample C at 4 min Fig. 6.11c and sample D PSDs at the reaction times of 5 min and 10 min depicted in Fig. 6.11d. For the cases of samples A and E, an initial mono-modal PSD of nascent CaO was not observed, probably because of the detector sampling frequency that did not record the early instants of the reaction. As the reaction time progresses, the internal sample pore matrix seems to decompose into two distinct pore populations: one placed in the limit of the micro-pore population (20 Å) and the second one in the meso-pore range. However, the initial mono-modal PSDs show a broad pore size domain that spans from 15–20 Å up to 100 Å, suggesting that the micro-pore fraction of nascent calcium oxide could be significantly low in size/volume. Consequently, its scattering response might not be sufficiently intense to be recorded by the USAXS/SAXS detectors. Actually, its number of pore per unit of mass is significantly higher than that of the meso-pore population, as represented by in Figs. 6.24a and 6.24b and in Fig. 6.25a. These values were calculated

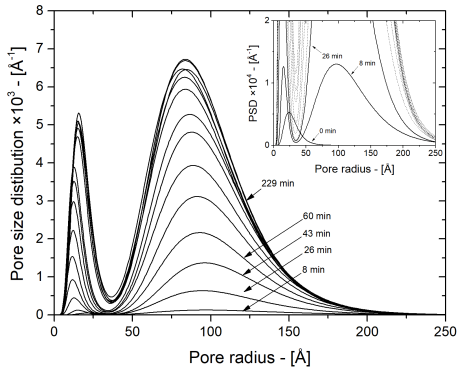

(a) *Sample A* - 600 °C, N_2.

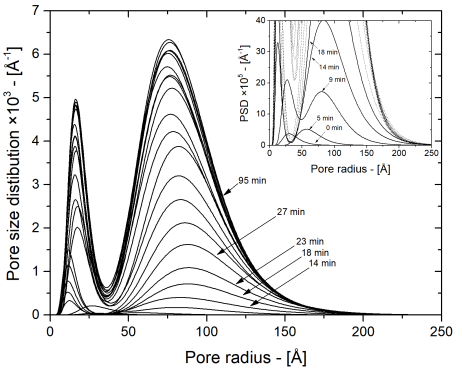

(b) *Sample B* - 620 °C, N_2.

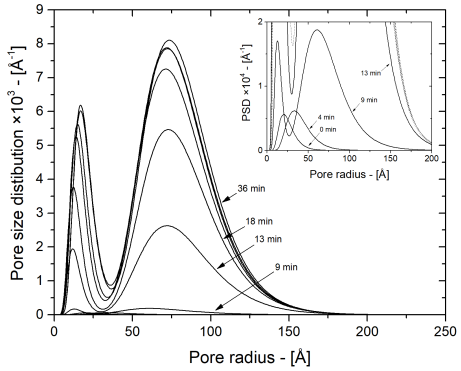

(c) *Sample C* - 650 °C, N_2.

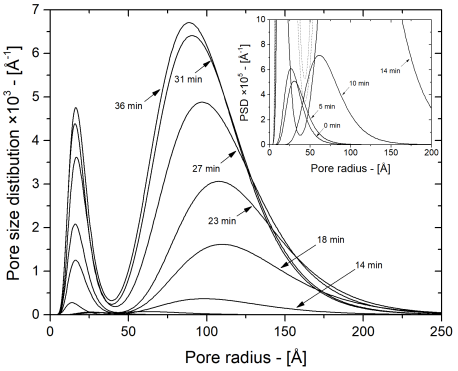

(d) *Sample D* - 680 °C, N_2.

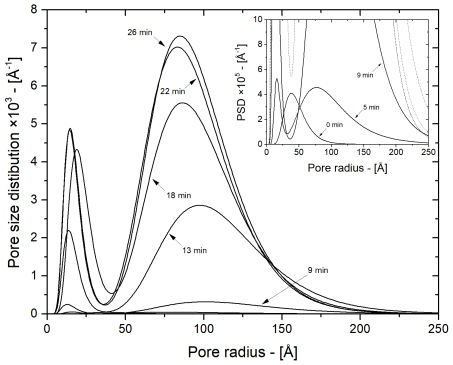

(e) *Sample E* - 700 °C, N_2.

Figure 6.23: Pore size distributions generation and evolution during calcination reaction (reaction time step) in nitrogen atmosphere at different final temperature: samples A (a), B (b), C (c), D (d) and E (e).

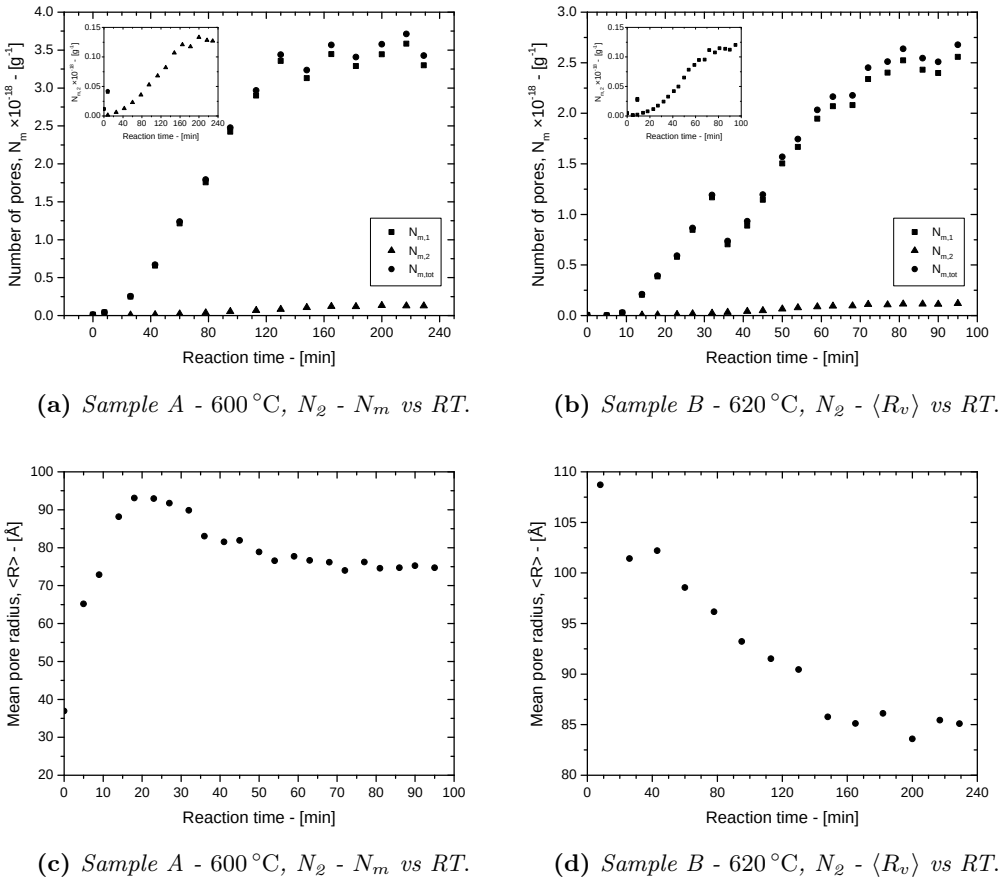

(a) *Sample A* - 600 °C, N_2 - N_m *vs RT.*

(b) *Sample B* - 620 °C, N_2 - $\langle R_v \rangle$ *vs RT.*

(c) *Sample A* - 600 °C, N_2 - N_m *vs RT.*

(d) *Sample B* - 620 °C, N_2 - $\langle R_v \rangle$ *vs RT.*

Figure 6.24: Evolution of the number of pores per unit of sorbent mass of the two pore populations (squares and triangles) and of the total number of pores per unit of sorbent mass (dots) during the calcination reaction, namely the reaction time for samples A (a) and B (b). Mean pore radius evolution over the reaction time for samples A (c) and B (d).

by means of Eqs. (4.69) and (4.70) from the volumetric PSDs of each population of pores, which show that the number of micro-pores (roughly $1 \times 10^{18}\,\mathrm{g}^{-1}$) is about one order of magnitude than the meso-pore number ($1 \times 10^{17}\,\mathrm{g}^{-1}$), as showed in Tab. 6.4 where are listed the final number of pores per unit of sample mass of the two pore population and of the overall pore network. Figs. 6.24a and 6.24b show the number of pore per unit of sample mass evolution of samples A and B over the reaction time. These profiles shows increasing trends with the RT similar to those of Figs. 6.14a and 6.14b and Figs. 6.18a and 6.18b of the specific surface area and porosity respectively. It should be noted that the discontinuity of the micro-pore number per unit of solid mass of sample B depicted in Fig. 6.24b is a direct consequence of the $R_{g,1}$ profile evolution showed in Fig.'6.12b, that exhibits a similar behavior. This is probably due to some experimental noise in the USAXS experimental data in the region of the USAXS and SAXS connection. In particular, the merging procedure of two scattering profile could increase the local experimental noise of this region, where the micro-pore SAS parameters are estimated. On the other hand, the number of pores evolution over time at higher calcination temperature is characterized by an initial increase of the pore number up to a maximum value (listed in Tab. 6.5) and then followed by a slow decrease of the pores number, as shown in Fig. 6.25a. Specifically, this behavior is observed in both the two pore populations. These trends confirm that two main (simultaneous) processes occur during the calcination reaction (performed in nitrogen

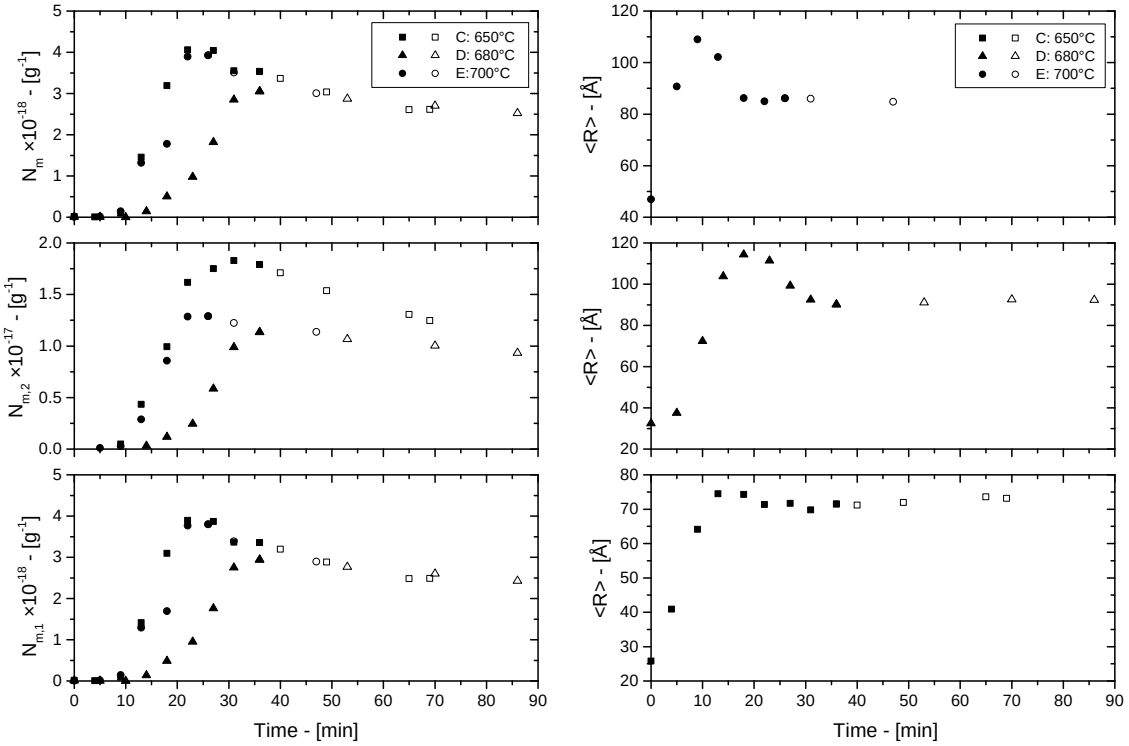

(a) *Samples C, D and E - N_m vs time.* **(b)** *Samples C, D and E - $\langle R_v \rangle$ vs time.*

Figure 6.25: Evolution of the number of pores per unit of sorbent mass of the two pore populations and of the total number of pores per unit of sorbent mass during the calcination reaction, namely the reaction time for samples C, D and E (a). On the right size, the respective mean pore radius evolution over the reaction time. Black markers refer to the reaction time, while the empty ones refer to sintering time.

atmosphere and at temperatures below 700 °C): a pore generation process followed by a pore reduction one. The first is predominant since the beginning of the calcination reaction and during the majority of the reaction time (up to conversion values of about 0.8). The latter process becomes more significant in the last instants of the reaction when the $CaCO_3$ conversion is approaching to one, namely higher than 0.8, especially for the cases of samples C, D and E. This final evolution of the number of pores profiles of samples C, D and E enforces the idea that sintering could be important in the late stages of the calcination reaction. On the other hand, because of the low calcination reaction temperatures, samples A and B number of pores profiles do not exhibit a decreasing section probably due to the low (or negligible) sintering kinetics. Finally, Eq. (4.71) was used to calculate the overall mean pore radius of the two volume pore distributions. According to the radius of gyration evolution represented in Figs. 6.12 and 6.13, the sample mean pore radius increases in the early stages of the calcination reaction up to a maximum value and then decreases down to a quite constant value as shown in Figs. 6.24c and 6.24d and Fig. 6.25b. Again, this evolution seems to be in good agreement with the metastable nascent CaO layer that interact with the CO_2 released during the reaction changing the nascent pores geometry. Interestingly, the maximum values of the mean pore radius (Tab. 6.5) occur in the early stages of the reaction as represented in Fig. 6.24c. Opposite to this behavior, it is remarkable to notice how the maximum number of pores is reached later, approximately close to the end of the calcite decomposition, as shown in Figs. 6.24a and 6.24b. Additionally,

Table 6.6: Sorbent micro-textural properties estimated at the end of the sintering step.

Sample	$R_{g,1}$ [Å]	$R_{g,2}$ [Å]	$S_{m,1}$ [$m^2\,g^{-1}$]	$S_{m,2}$ [$m^2\,g^{-1}$]	S_m [$m^2\,g^{-1}$]	ε_1 [–]	ε_2 [–]	ε [–]	ϕ [–]
C	25	85	54.1	61.2	115.2	0.101	0.386	0.487	0.108
D	25	109	43.7	58.8	102.5	0.076	0.44	0.516	0.054
E	24	101	48.6	63.3	111.9	0.081	0.428	0.508	0.068
F	26	178	21.7	28.5	50.2	0.041	0.365	0.405	0.257
G	25	309	11.6	15.8	27.5	0.021	0.366	0.387	0.29
H	51	467	9.9	13.5	23.4	0.02	0.451	0.470	0.137
I	23	450	7.0	9.5	16.5	0.012	0.295	0.307	0.437
J	50	532	7.6	9.1	16.7	0.028	0.332	0.361	0.339
K	107	665	5.9	8.3	14.1	0.025	0.363	0.388	0.289
L	114	1002	4.0	5.8	9.9	0.031	0.342	0.374	0.315

Table 6.7: Sorbent micro-textural properties estimated at the end of the sintering step (cont.).

Sample	Ψ_1 [–]	Ψ_1 [–]	$\langle R_v \rangle$ [Å]	$N_{m,1} \times 10^{-18}$ [g^{-1}]	$N_{m,2} \times 10^{-17}$ [g^{-1}]	$N_m \times 10^{-18}$ [g^{-1}]	ζ [Å]
C	0.99	1.01	73	2.49	1.25	2.61	238
D	1.01	1.00	92	2.43	0.93	2.52	351
E	1.00	0.95	85	2.89	1.14	3.01	323
F	0.85	0.84	154	0.85	0.15	0.86	683
G	0.82	0.85	275	0.46	0.03	0.46	1197
H	0.97	0.96	405	0.40	0.01	0.40	1595
I	0.74	0.69	389	0.30	0.01	0.30	1317
J	0.82	0.74	452	0.07	0.01	0.07	1564
K	0.89	0.77	550	0.04	0.004	0.05	1858
L	0.80	0.65	796	0.01	0.001	0.01	2866

the maximum mean pore radius is observed in sample A and B as depicted inFigs. 6.24c and 6.24d but none maximum values of N_m is noticed from Figs. 6.24a and 6.24b.

Samples calcined in presence of CO_2

In order to explore higher calcination reaction temperatures than 700 °C, the CO_2 presence in the reaction atmosphere was necessary to slow down the calcite decomposition rates and to obtain a reasonable number of samplings during and after the reaction, according to the detectors sampling frequency (one every 4–5 min). Three temperatures were explored, namely 800 °C, 850 °C and 900 °C using different carbon dioxide pressures in the reaction atmosphere. Despite the CO_2 partial pressures close to those of equilibrium, high calcination reaction rated were observed especially when the CO_2 concentration was relative low, as for the cases of samples F, I, J, where the calcination reaction step was almost completely lost, as shown by the $CaCO_3$ conversion vs time profiles of these samples reported in Figs. 6.4b, 6.4c and 6.4d. The first effect of the CO_2presence during the reaction consisted in the delaying the beginning of the reaction, namely the first CaO peak detected by the WAXS analysis: from 35–32 min (and a corresponding temperature that ranges from 481 °C to 583 °C) from the beginning of the heating step for the case of the

calcined sample in nitrogen up to 41 min at a reaction temperature of about 744÷757 °C. More specifically, although the different reaction temperatures and CO_2 concentrations, the first CaO peaks were observed at these time and temperatures, except for the cases of samples K and L, where the $CaCO_3$ decomposition initiated at about 45 min from the beginning of the heating step and a corresponding temperature of 839 °C.

Fig. 6.6 shows the final USAXS/SAXS profiles of the calcined samples in the presence of the CO_2 atmosphere. Specifically, from a qualitative point of view the USAXS/SAXS profiles the 800 °C calcined samples, showed in Fig. 6.6b, exhibit a shifting of Guinier regime (belonging to the second region of the SAS profile) towards to lower q-values with the CO_2 increase in the reaction atmosphere. This suggests a progressive increase of the final mean pore radius with the increase of the CO_2 content. Additionally, the power-law region intensity of the 1 % CO_2 calcined sample F is higher in magnitude than those of samples G and H, suggesting a greater specific surface area respect to the other sample calcined in 5 % and 10 % of CO_2. Fig. 6.6c compares the USAXS/SAXS profiles of the 900 °C calcined samples, where the Guinier regime slightly shifts towards to the low q-region suggests a modest increase of the pore radius with the CO_2 content. The higher magnitude of the sample J (10 % of CO_2) power-law region respect to that of samples K and L, indicates a relative larger sample J specific surface area compared with those of the others 900 °C calcined samples. The same CO_2 effects are observed for the cases of the 900 °C calcined samples, as shown in Fig. 6.6c. Finally, the calcination temperature influence on the SAS profiles for the 10 % CO_2 calcined samples (H, I, J) consists in a Guinier regime shifting towards to the low q-values, namely a significant increase of the mean pore radius, as shown in Fig. 6.6d. On the other hand, the similar power-law region indicated a non-significant variation of the sorbent specific surface area with the increase of the temperature.

The USAXS profiles evolutions over the reaction time are shown in Figs. 6.11c, 6.11d, 6.11e and 6.11f concerning the samples G, H, K and L respectively, conveniently chosen as examples. Interestingly, in two cases (samples G and K) an evident micro-structure was observed before the beginning of the calcination reaction as showed in Figs. 6.11c and 6.11d, and empathized in their insets, suggesting the presence of a generating scattering structure in the high-q region. Especially for the case of sample K (900 °C, 25 % of CO_2) a SAS response can be clearly appreciated at high-q values close to the background region. For these samples, two structural levels (plus another one for the low-q region) were necessary to fit the USAXS/SAXS profiles before the beginning of the calcination reaction. However, when the calcination reaction initiated, the SAS response of this structure completely disappeared (probably covered by the scattering response of nascent CaO), leaving the usual USAXS/SAXS profiles of the calcining $CaCO_3$. We speculate that this behavior could be probably due to some impurities (like carbonates different from $CaCO_3$) in the starting material that decomposes at a lower temperature. Because of the low content, the WAXS analysis did not detect their scattering responses.

Opposite to the calcined samples in nitrogen atmosphere, in this case the micro-structure development of the decomposing $CaCO_3$ seems to happen in a more sudden way, as shows by the scattering intensity curves in Figs. 6.11c, 6.11d, 6.11e and 6.11f. In fact, 9 min of reaction time seems to be enough to almost reach the final micro-textural internal structure, namely the a similar scattering profile of the completely calcined $CaCO_3$. This behavior is probably due to the high calcination temperature, however the sudden micro-structure development was also observed in those samples calcined at CO_2 pressures close to the chemical equilibrium, namely samples H, K and L represented in Figs. 6.11d, 6.11e and 6.11f respectively.

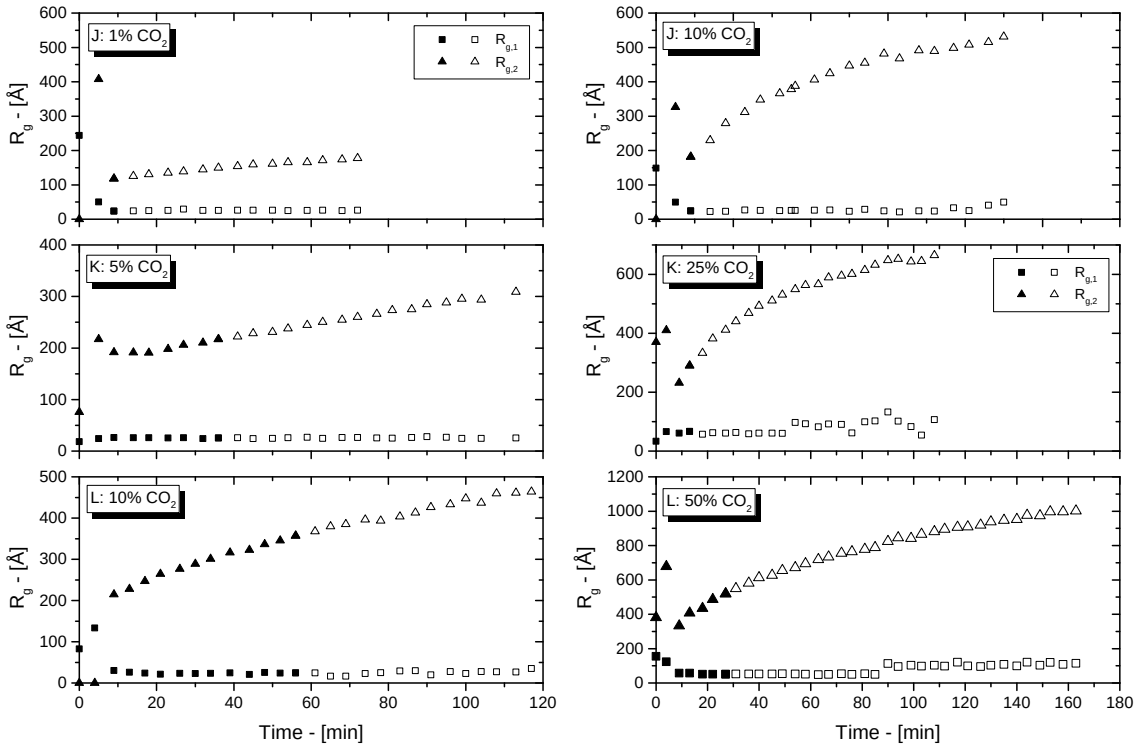

(a) *Samples F, G, and H* - 800 °C. **(b)** *Samples J, K, and L* - 900 °C.

Figure 6.26: Radius of gyration evolution of the two pore populations over time of samples calcined at 800 °C (a) and 900 °C (b). Solid markers refer to the reaction time and open ones refer to sintering time.

Radius of gyration evolution Despite the high reaction temperature and the presence of the CO_2 in the reaction atmosphere which are the favoring conditions for sintering processes Borgwardt (1985) and Borgwardt (1989a), two structural levels were necessary to fit the SAS profiles of samples F÷L, as shown in Fig. 6.9 for the case of sample L, meaning that the CaO micro-structure is still characterized by two pore populations. According to the unified fit model of Eq. (4.60) two radius of gyration were obtained from the experimental scattering profiles fitting. Their evolution over time (reaction and sintering times) are showed in Fig. 6.26, where radius of gyration profiles evolution of the calcined samples at 800 °C and 900 °C are depicted in Figs. 6.26a and 6.26b respectively. Samples calcined at 800 °C and 900 °C shows an initial radius of gyration significantly higher to those of samples calcined in N_2. Specifically, the initial radius of gyration associated with the micro-pore population ranges from a minimum of 82 Å (sample H) up to a maximum of 243 Å (sample F), except for the case of sample G, where the first micro-structure developed before the beginning of the calcination reaction, showed in Fig. 6.11c, reveals an initial $R_{g,1}$ of about 18 Å. On the other hand, the 900 °C calcined samples show $R_{g,1}$ values of 148 Å for sample J and 154 Å for sample L, while sample K shows an initial $R_{g,1}$ of 33 Å due to the scattering micro-structure developed before the calcination reaction, as represented in Fig. 6.11e. Despite the modest experimental USAXS and SAXS samplings during the RT, the radius of gyration profiles show a similar evolution of that of the N_2 calcined samples, namely an initial increase of $R_{g,1}$, followed by a pore structure splitting in two populations (Fig. 6.11). After the micro-structure separation, the meso-pore radius of gyration seems to reach a maximum value (as for the case of N_2 calcined samples) and

then decreases down to lower size. Specifically, the maximum $R_{g,2}$ values at 800 °C are listed in Tab. 6.5, namely 409 Å, 217 Å and 357 Å, which then decreased down to 118 Å, 217 Å and 357 Å final values respectively (Tab. 6.3). On the other hand, 326 Å, 410 Å and 678 Å are the maximum radii of gyration values of the second pore population for samples J, K and L (Tab. 6.5) and the respective final values are namely 182 Å, 290 Å and 520 Å, as listed in Tab. 6.6. Even for the case of the CO_2 calcined samples, the maximum value of the radii of gyration observed in the early stages of the reactions is in good agreement with the investigations of Beruto (1976) and Ewing, Beruto, and Searcy (1979), who observed a pore geometry change due to the CO_2 effect on the nascent metastable CaO. In this case, this process seems to be accelerated both by temperature and by the CO_2 presence in the reaction atmosphere, according to the 900 °C $R_{g,2}$ maximum values that increases with the CO_2 partial pressure. Additionally, because of the favorable sintering condition the meso-pore population final radius of gyration increases both with temperature and with the CO_2 content, according to Fuertes et al. (1991). Opposite to this observation the $R_{g,2}$ profile over time represented in Fig. 6.33 of samples calcined with 10 % of CO_2 (in balance with N_2). In this case, the final $R_{g,2}$ (at the end of the calcination reaction) values are 357 Å (sample H, 800 °C), 163 Å (sample I, 850 °C) and 182 Å (sample J, 900 °C). In fact, as the CO_2 pressure is close to that of the equilibrium the decomposition rate decreases, giving sufficient time to the sintering phenomena to modify the sorbent micro-structure. As previously mentioned, accordingly to the thermo-chemical data of Knacke, Kubaschewski, and Hesselmann (1991) the difference between the CO_2 reactor partial pressure and that predicted by chemical equilibrium for samples H, I and J are 0.11 bar, 0.38 bar and 0.9 bar respectively, suggesting a modest reaction rate, as that of sample H showed in Fig. 6.4c. This explains the high reaction time of sample H, 56 min, respect of those of samples I and J, namely 9 min.

After the first instants of the reaction where the radius of gyration of the pore structure is almost unstable, the micro-pore radius of gyration profile settles down to a quite constant value over the reaction time,namely about 20÷26 Å, as shown in Fig. 6.26 and Fig. 6.33a. Interestingly, these values are in agreement with those of nitrogen calcined samples (A÷E). However, the high temperature and CO_2 pressure calcined samples, show values twice times higher than the previous results, namely 67 Å for sample K (900 °C, 25 % of CO_2) and 51 Å for sample L (900 °C, 50 % of CO_2).

Specific surface area evolution The specific surface area profiles over time of the calcined samples in the presence of CO_2 are showed in Fig. 6.28 and Fig. 6.33b. The profile evolution of these samples is similar to those of the N_2 calcined samples showed in Figure 13 and Figure 14. Due to the more intense sintering effects, their magnitude is significantly less respect to samples A÷E. According to Glasson (1958), Silcox, Kramlich, and Pershing (1989), Mai and Edgar (1989), Mahuli et al. (1999), and Fierro, Adánez, and García-Labiano (2004) these trends are the results of two main processes that simultaneously occur during the $CaCO_3$ thermal decomposition: the micro-structure generation and sintering. The latter phenomenon irreversibly reduces the sorbent internal surface area, and, more specifically, affects the sorbent micro-textural properties. Because of the similar time-scales of these two phenomena, the instantaneous sample specific surface area is the result of these processes. Specifically, the pore generation is the dominant mechanism during the early stages of the reaction, where the sample specific surface area increases with the reaction time, as shown in Fig. 6.28 and Fig. 6.33b. After this point, sintering effects control the late steps of the reaction time, reducing the sorbent surface area, providing a maximum specific surface area value to the profile evolution. It is remarkable to notice how this kind of evolution is observed both in the micro-pore and in meso-pore specific surface area profiles and, specifically, how these profiles evolves at the same time-steps (the

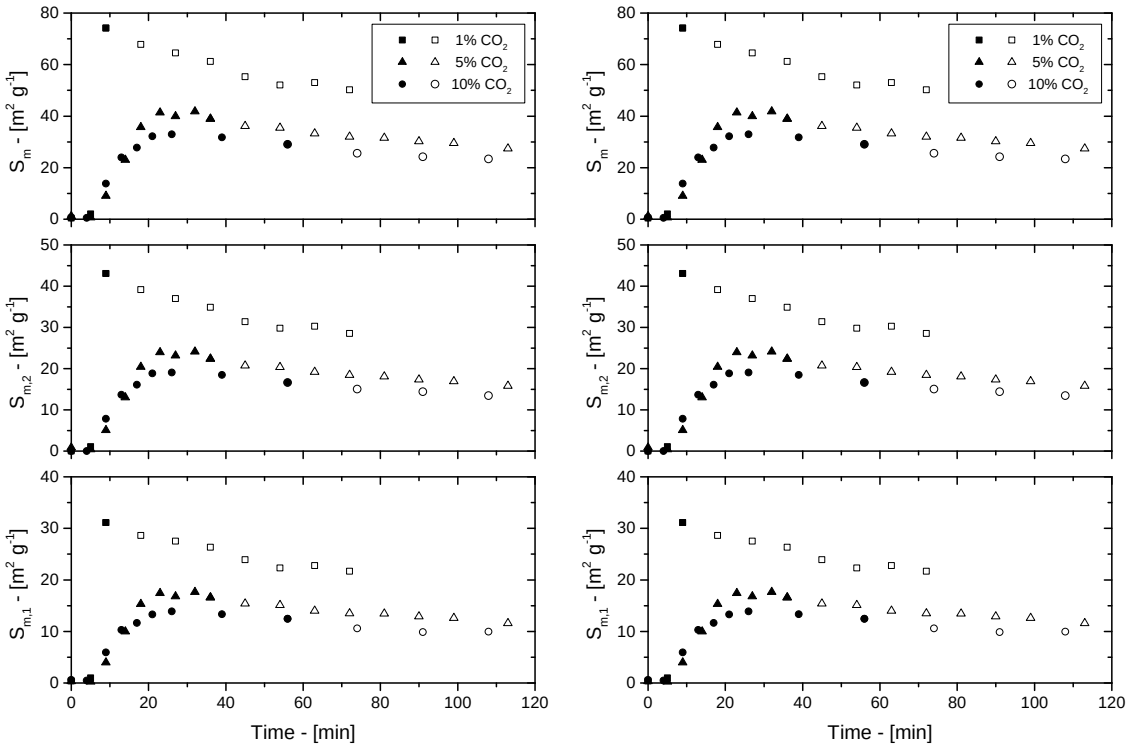

(a) *Samples F, G, and H* - 800 °C. **(b)** *Samples J, K, and L* - 900 °C.

Figure 6.27: Evolution of the specific surface area of the two pore populations and of the total specific surface area over time of calcined samples at 800 °C (a) and 900 °C (b). Solid markers refer to the reaction time and open ones refer to sintering time.

maximum values of each sample are reached at the same times). This suggests that the two simultaneous processes (namely pore generation and sintering) affect the whole sorbent internal micro-structure at the same rate. This suggests that in this work, pore generation and sintering phenomena affect the generating CaO structure with mechanism of pore-scale independent. However, because of the high surface-to-volume ratio of the micro-pore population, sintering phenomena should be more intense respect to those acting on the meso-pore one. This suggests that the meso-pore sintering mechanisms seem to control the other sintering processes of the micro-pore population, which should be more intense because of the higher micro-pore density, Fig 6.40 and Fig. 6.42, and of the high surface-to-volume ratio.

The final total specific surface area values at 800 °C (Tab. 6.3) are $74.2\,m^2\,g^{-1}$ (sample F), $39.0\,m^2\,g^{-1}$ (sample G) and $29.0\,m^2\,g^{-1}$ (sample H) and their respective maximum values are respectively $74.2\,m^2\,g^{-1}$ (this value coincides with the final value), $41.8\,m^2\,g^{-1}$ and $32.9\,m^2\,g^{-1}$ (Tab. 6.5). These values indicated how the CO_2 content accelerates the sintering phenomena effects of the sorbent micro-textural properties. Additionally, these maximum values are significantly lower if compared with the N_2 calcined samples specific surface area. This suggests that sintering phenomena are important since the beginning of the reaction, especially in the presence of CO_2 that acts as a sintering catalyzer Beruto, Barco, and Searcy (1984) and Borgwardt (1989a). Specifically, this processes is more appreciated for the cases of the 900 °C calcined samples, where the final (namely when the calcination reaction is complete) specific surface areas (Tab. 6.3) are $46.3\,m^2\,g^{-1}$ (sample J), $31.1\,m^2\,g^{-1}$ (sample K) and $16.7\,m^2\,g^{-1}$ (sample L) and the respective maximum values

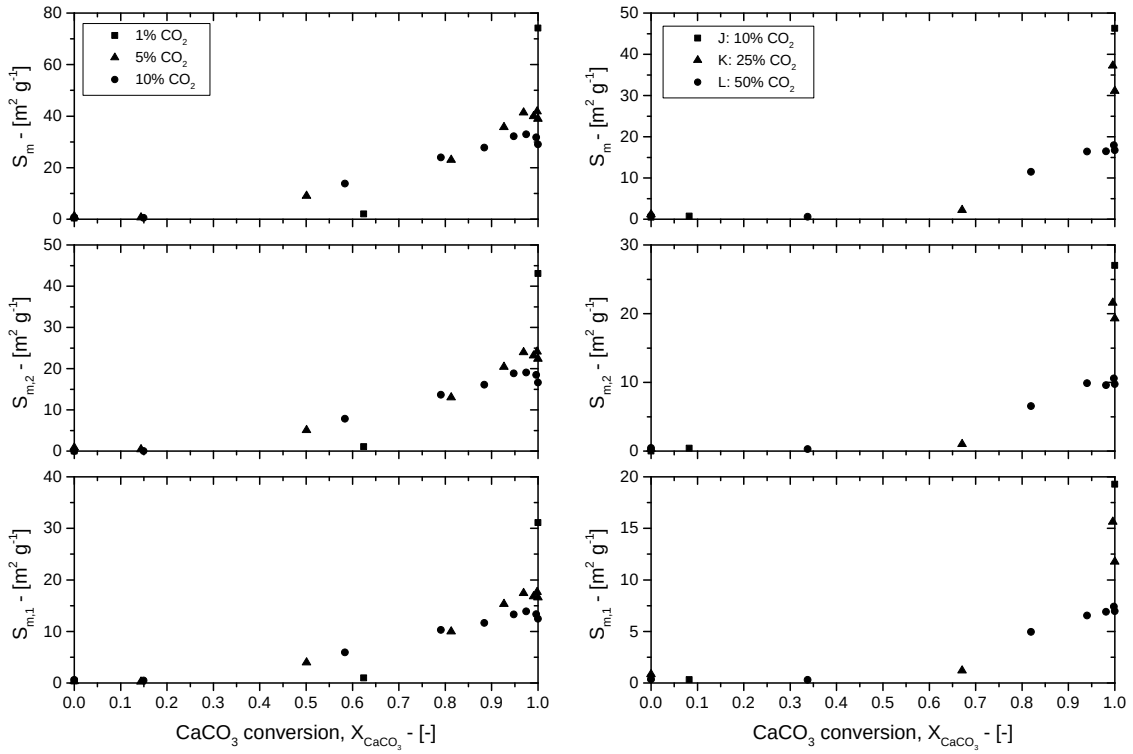

(a) *Samples F, G, and H* - 800 °C. **(b)** *Samples J, K, and L* - 900 °C.

Figure 6.28: Evolution of the specific surface area of the two pore populations and of the total specific surface area over the $CaCO_3$ conversion for the calcined samples at 800 °C (a) and 900 °C (b).

are 46.3 $m^2\,g^{-1}$ (the same of the final surface area value), 37.2 $m^2\,g^{-1}$ and 18.0 $m^2\,g^{-1}$. Interestingly, at 800 °C an increase of the CO_2 content by ten times leads to a reduction of the final total specific surface area of about 2.5 times. The same reduction factor is observed both for the micro-pore (from 31.1 $m^2\,g^{-1}$ to 12.4 $m^2\,g^{-1}$) and for the meso-pore population (from 43.1 $m^2\,g^{-1}$ to 16.6 $m^2\,g^{-1}$). At 900 °C, a CO_2 increase of five times (from 10 % to 50 %) determined a total specific surface area reduction of about 2.8 times and the same effect on the micro-pore (from 19.3 $m^2\,g^{-1}$ to 7.0 $m^2\,g^{-1}$) and meso-pore (from 27.0 $m^2\,g^{-1}$ to 9.7 $m^2\,g^{-1}$) surface area. As previously mentioned, because sintering is not only influenced by temperature and CO_2 content but also by time, sample H shows the lower final specific surface area among the calcined samples with 10 % of CO_2, namely a final total specific surface area of 29.0 $m^2\,g^{-1}$ at 800 °C, 38.2 $m^2\,g^{-1}$ at 850 °C and 46.1 $m^2\,g^{-1}$ at 900 °C, as shown in Fig. 6.33b.

The specific surface area profiles over the $CaCO_3$ molar conversion do not show linear trends, as represented in Fig. 6.28 and Fig. 6.34a. However, well-defined profiles can be appreciated in Fig. 6.28 and Fig. 6.34a as in the cases of the N_2 calcined samples. This result is in contrast with the investigation of Ewing, Beruto, and Searcy (1979), where none defined profile was observed in the specific surface area over the CaO mole fraction (namely the $CaCO_3$ conversion) in the presence of CO_2. Interestingly, these trends depicted in Fig. 6.28 and Fig. 6.34a are similar to those estimated for the cases of the N_2 calcined samples showed in Figs. 6.16a and 6.16c and Fig. 6.34b, namely convex increasing functions with the reaction time. However, for the calcined samples in the presence of CO_2, this evolution seems to be characterized by two different slopes: an initial slightly

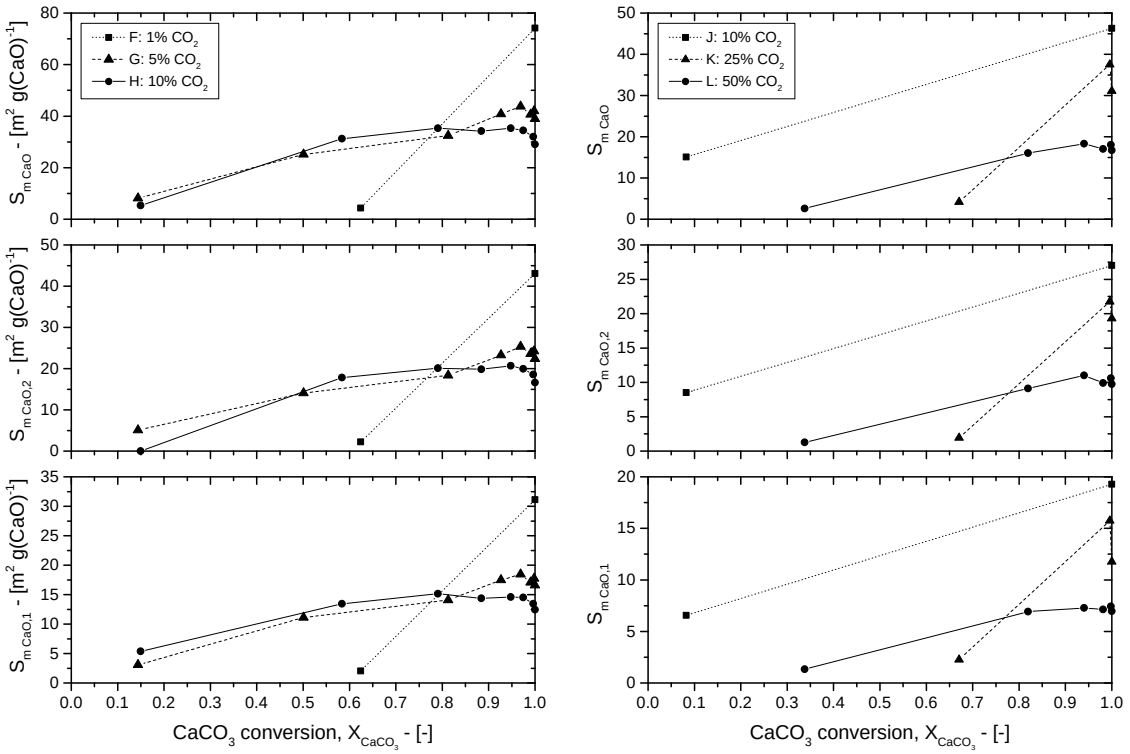

(a) *Samples F, G, and H* - 800 °C. **(b)** *Samples J, K, and L* - 900 °C.

Figure 6.29: Evolution of the specific surface area per unit of CaO mass of the two pore populations and of the total specific surface area per unit of CaO mass of the calcined samples at 800 °C (a) and 900 °C (b).

increasing profile followed by a change of slope in the second half of the $CaCO_3$ decomposition, as shown in Fig. 6.28 and Fig. 6.34a. This evolution is emphasized by the 900 °C calcined samples showed in Fig. 6.28b. These trends are useful to investigate the specific surface generation, especially during the early stages of the reaction: after a first sort of "induction" period up to about 0.5÷0.6 $CaCO_3$ conversion where the sample surface area is below $20\,m^2\,g^{-1}$, the majority of the surface is generated during the late stages of the reaction. Only when the reaction is near to the competition sintering processes becomes the dominant phenomena and affect the sorbent internal micro-structure by reducing the specific surface area. This induction period, observed in Fig. 6.27, is in good agreement with the observations of Ewing, Beruto, and Searcy (1979), where the specific surface area associated with the nascent metastable CaO layer is reduced by the high CO_2 pressure gradients established during the early steps of the calcination reaction. Additionally, the CO_2 presence in the reaction atmosphere accelerates and increases in magnitude the sintering phenomena effects, according to Beruto, Barco, and Searcy (1984). Such CO_2 pressure gradients established inside the $CaCO_3$ particle are probably generated by the intra-particle diffusional effects that prevent the CO_2 release outside the particle produced by the reaction front. This process is clearly limited by the CO_2 content in the reaction atmosphere, as for the cases of samples F÷L.

On the other hand, if the sample specific surface area per unit of CaO mass over the calcium carbonate conversion is considered, as shown in Fig. 6.29, the surface evolution reveals an initial increasing trend followed by a second decreasing profile, as for the cases of samples G and H in Fig. 6.29a and sample L in Fig. 6.29b. The other samples (F, J

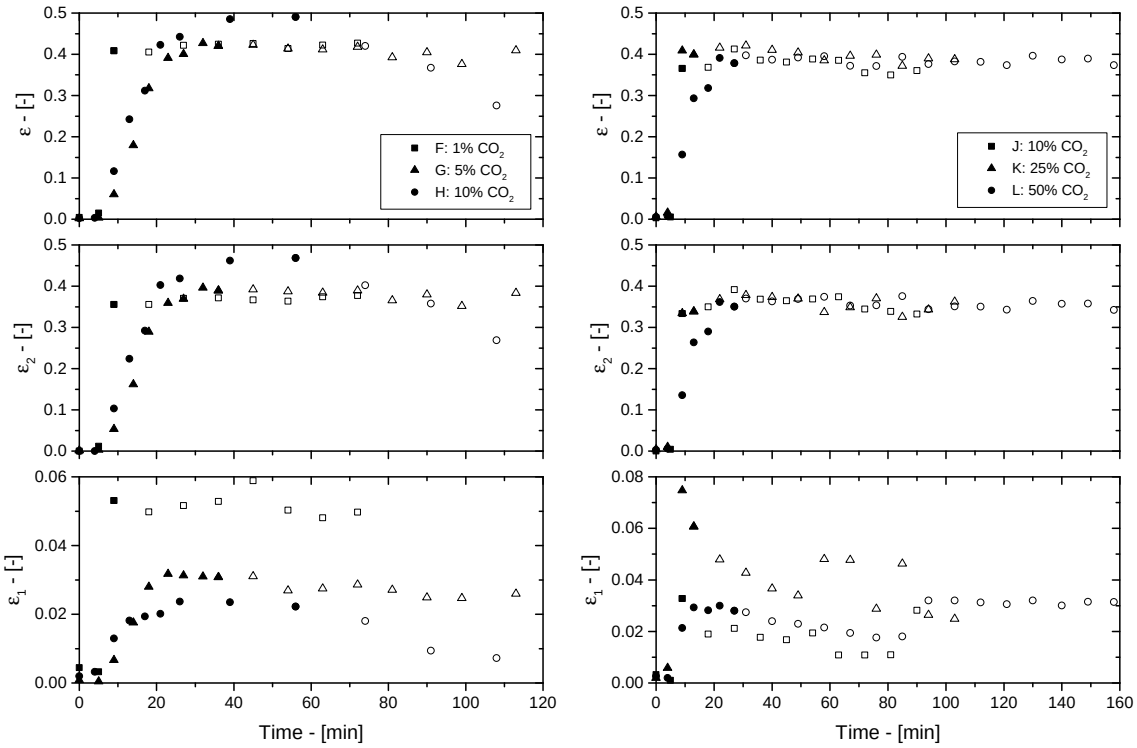

(a) *Samples F, G, and H* - 800 °C. **(b)** *Samples J, K, and L* - 900 °C.

Figure 6.30: Evolution of the internal porosity of the two pore populations and of the total internal porosity over time of samples calcined at 800 °C (a) and 900 °C (b). Solid markers refer to the reaction time and open ones refer to sintering time.

and K) did not allowed a good discretization in the early stages of the reaction, because of their high reaction rates and none well-definite trends can be observed. These profiles suggest how the specific surface area increases even during the first instant of the reaction, where the specific surface area per unit of sample mass over time and over the $CaCO_3$ conversion show an initial induction period where the sample surface area seems to remain at low values. On the other hand, the change in trend showed in Fig. 6.29 at about 0.5–0.6 of calcium carbonate conversion emphasizes the sintering effects on the CaO surface area. Interestingly, the increase of temperature and CO_2 concentration in the reaction atmosphere (that has catalytic sintering effects) accelerated the sintering phenomena by reducing the final specific surface area. However, such phenomena mainly occur during the late stage of the reaction, when the specific surface area is almost developed.

Particle porosity evolution Considering the porosity profiles evolution for the calcined samples in presence of CO_2 and, specifically, their magnitude, it is remarkable to notice how the final total porosity values are close to those estimated for the N_2 calcined samples, although their specific surface areas are significantly lower compared with sample A÷E. Despite the higher temperature and the CO_2 content in the reaction atmosphere at 800 °C the final sample porosities are 0.408 (sample F), 0.420 (sample G) and 0.490 (sample H), as listed in Tab. 6.3. Interestingly, these values slightly increases with the CO_2 content and the meso-porosities values show a similar behavior, namely 0.355, 0.389 and 0.468 respectively. On the other hand, the micro-pore volume fraction seems to decrease in magnitude: 0.053, 0.031 and 0.022 respectively. These values suggest that at 800 °C the

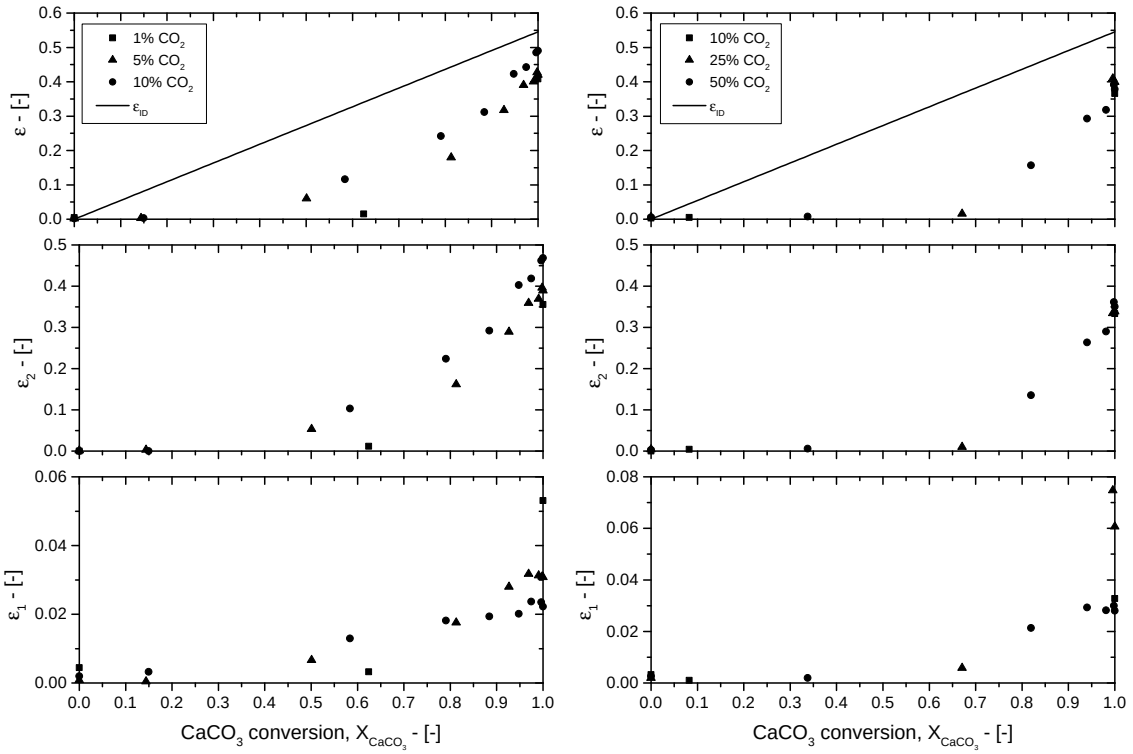

(a) *Samples F, G, and H* - 800 °C. **(b)** *Samples J, K, and L* - 900 °C.

Figure 6.31: Evolution of the internal porosity of the two pore populations and of the total internal porosity over the CaCO3 conversion of samples calcined at 800 °C (a) and 800 °C (b). Solid lines represent the theoretical porosity profile.

increase of the CO_2 content into the reaction atmosphere leads to an increase of the meso-porosity with a decrease of the micro-pore volume fraction. This behavior seems to hold at 900 °C as well, where the final total porosity values are 0.366 for sample J, 0.400 for sample K and 0.378 for sample L and the corresponding meso-porosities are 0.333, 0.339 and 0.350, as listed in Tab. 6.3. On the other hand, the micro-pore volume fractions do not properly show a decreasing trends except for the case of samples J, K and L: 0.033, 0.061 and 0.028 respectively. Contrary to the previous samples, the 850 °C calcined $CaCO_3$ (sample I) shows the minimum porosity values achieved in this work, namely a total pore volume fraction of 0.283 made by 0.254 of meso-pores and 0.029 of micro-pores (Tab. 6.3). The reason of this discrepancy could be probably related to the probing illuminated volume position, namely a packed bed region where the produced CO_2 by the $CaCO_3$ decomposition is locally not completely purged off, favoring the sintering effects on the micro-textural properties, as confirmed by the low specific surface values.

The experimental non-linear profiles of the porosity over the $CaCO_3$ conversion are also observed for the cases of the calcined samples in the presence of CO_2 in the reaction atmosphere, as shown in Fig. 6.31 and Fig. 6.35b. Specifically, the deviation between the experimental and the theoretical porosity values increases from 800 °C to 900 °C calcined samples. After a first initial induction period, the majority of the sorbent porosity of both the two pore populations is generated at high $CaCO_3$ conversion values, namely at X_{CaCO_3} values higher than 0.6–0.5, as shows in Fig. 6.31 and Fig. 6.35b. These trends are in agreement with the corresponding specific surface areas over the calcium carbonate conversion profiles showed in Fig. 6.28, where the majority of the surface area is generated

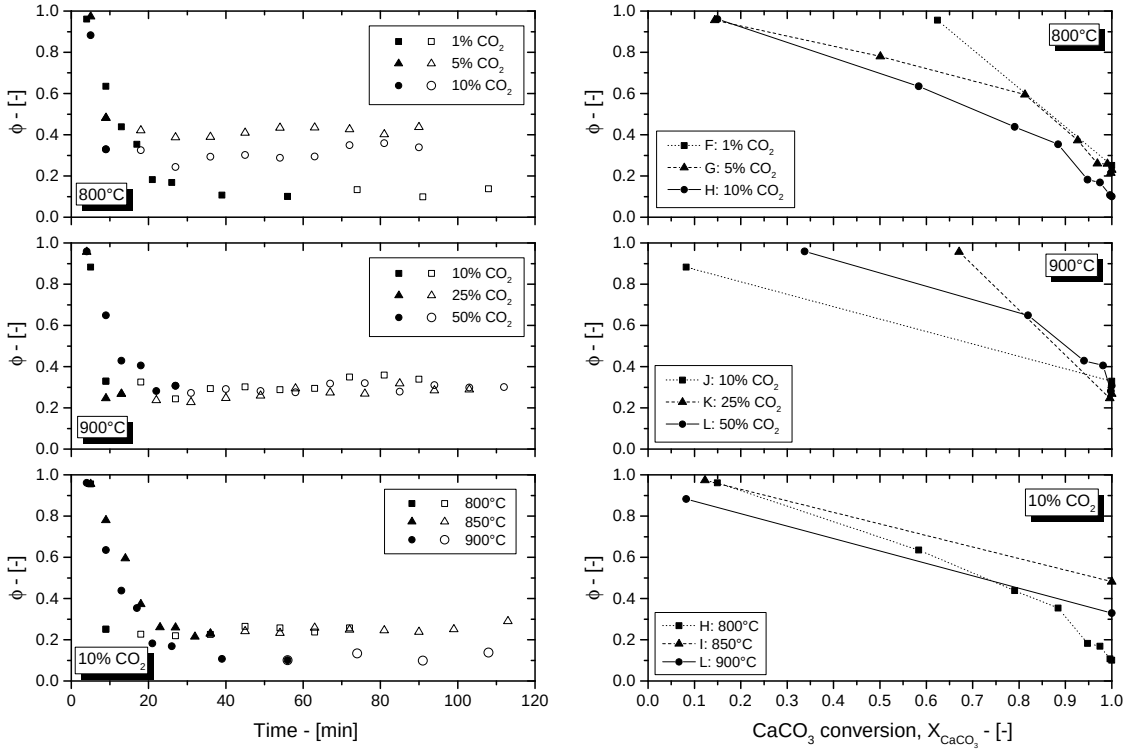

(a) ϕ *vs time.* **(b)** ϕ *vs* $X_{\mathrm{CaCO_3}}$.

Figure 6.32: Evolution of the fraction of pore destroyed over time (a) and over the $CaCO_3$ conversion (b) of samples calcined in CO_2 atmosphere. Black markers refer to the reaction time and open ones refer to sintering time. The first and the second row refer to calcined samples at 800 °C and 900 °C respectively. The third one refers to calcination reactions performed under reaction atmospheres of 10 % of CO_2 in balance with N_2 (samples H, I, J).

in the correspondence of 0.5–0.6 $CaCO_3$ conversion.

Such profiles are probably related to the CO_2 mass transfer effects inside the decomposing $CaCO_3$ particle. In fact, during the early stages of the reaction the high CO_2 amounts released by the reaction affects the first CaO layers by favoring the sintering effects. As the $CaCO_3$ conversion increases, the intra-particle CO_2 concentration gradients decrease allowing the development of the sorbent micro-textural properties. Again, this effect is probably due to the intra-particle diffusive effects that establish CO_2 concentration gradients inside the particle.

Accordingly, Fig. 6.32 shows the fraction of pore destroyed over time and $CaCO_3$ conversion, calculated by means of Eq. 6.4. Specifically the ϕ over time and over $X_{\mathrm{CaCO_3}}$ profiles show decreasing trends down to asymptotic values (as for the case of the N_2 calcined samples) when the calcination reaction is completed. The final fraction of pore removed decreases with the increase of the CO_2 pressure at 800 °C (Tab. 6.3), namely are 0.251 (sample F), 0.23 (sample G) and 0.101 (sample H), according to the respective increasing porosity values. At 900 °C the final ϕ values seems to be quite constant, namely 0.329 (sample J), 0.267 (sample K) and 0.307 (sample L). For the case of the calcined samples with 10 % of CO_2 the 800 °C and 850 °C samples show a higher fraction of pore destroyed than that of the 900 °C calcined sample J, as shown in Figs. 6.32a and 6.32a, where the highest ϕ value is that of the sample I (850 °C), namely 0.481.

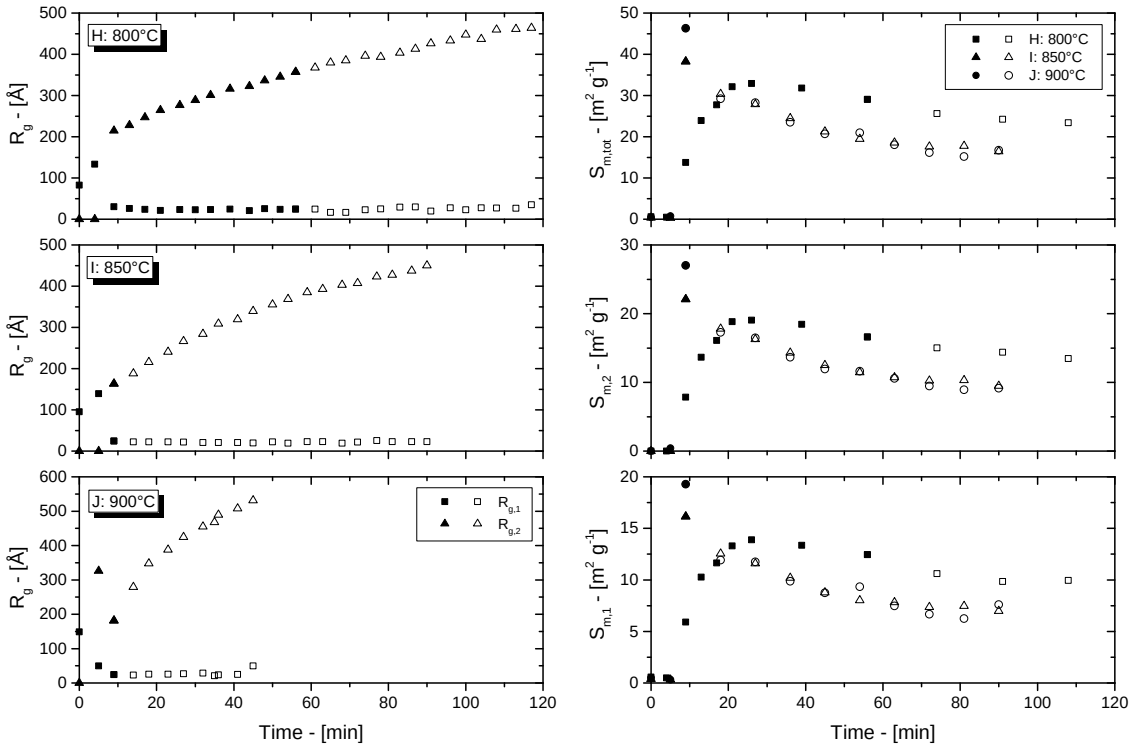

(a) *R_g vs time.* **(b)** *S_m vs X_{CaCO_3}.*

Figure 6.33: Radius of gyration of the two pore populations evolution over time (a) and specific surface evolution of the two pores populations and of the total specific surface area (b) over time of samples calcined under a reaction atmosphere with 10 % of CO_2 in balance with N_2. Black markers refer to the reaction time and open ones refer to sintering time.

Sphericity factor evolution According to the N_2 calcined samples the initial sphericity factor of the micro-pore population is about 0.4, as depicted in Fig. 6.36, evaluated through Eq. (5.2). However, the initial meso-pore population sphericity factor is about 0.2–0.3, contrary to the N_2 calcined samples where the initial Ψ_2 value is about 0.6–0.7.This result suggests that the increase of the calcination temperature and the CO_2 content increase the meso-pore sphericity value leaving the micro-porosity shape almost unvaried. At 800 °C, as the reaction progresses, the sphericity factor of the two pore population approaches to the unity, as shows in Fig. 6.36a. The increase of the CO_2 content in the reaction atmosphere leads to an increase of the pore sphericity factor, whose value approaches to one when the calcination reaction is completed. On the other hand, at 900 °C the final sphericity factors associated with the meso-pore population is lower, namely final values that approach to final values of about 0.7, while the final micro-pore sphericity factors are slightly higher, namely about 0.8–0.9 (Tab. 6.3). According to Fig. 6.36c, both the final sphericity values of the two populations are about 0.7, meaning that both the two pore populations are quite distant from the pore sphericity, as the case of the 900 °C calcined samples.

In the presence of CO_2 the specific surface area per unit of volume of the first pore population is still positive correlated with its pore volume fraction , showing a quite linear trend over , as depicted in Fig. 6.37. On the other hand the meso-pore specific surface area per unit of sample volume shows a different correlation over the meso-pore porosity, namely a positive correlation at low porosity values (up to 0.2–0.3) followed by a negative correlation when approached to high values, namely 0.4–0.5, as shown in Fig. 6.37.

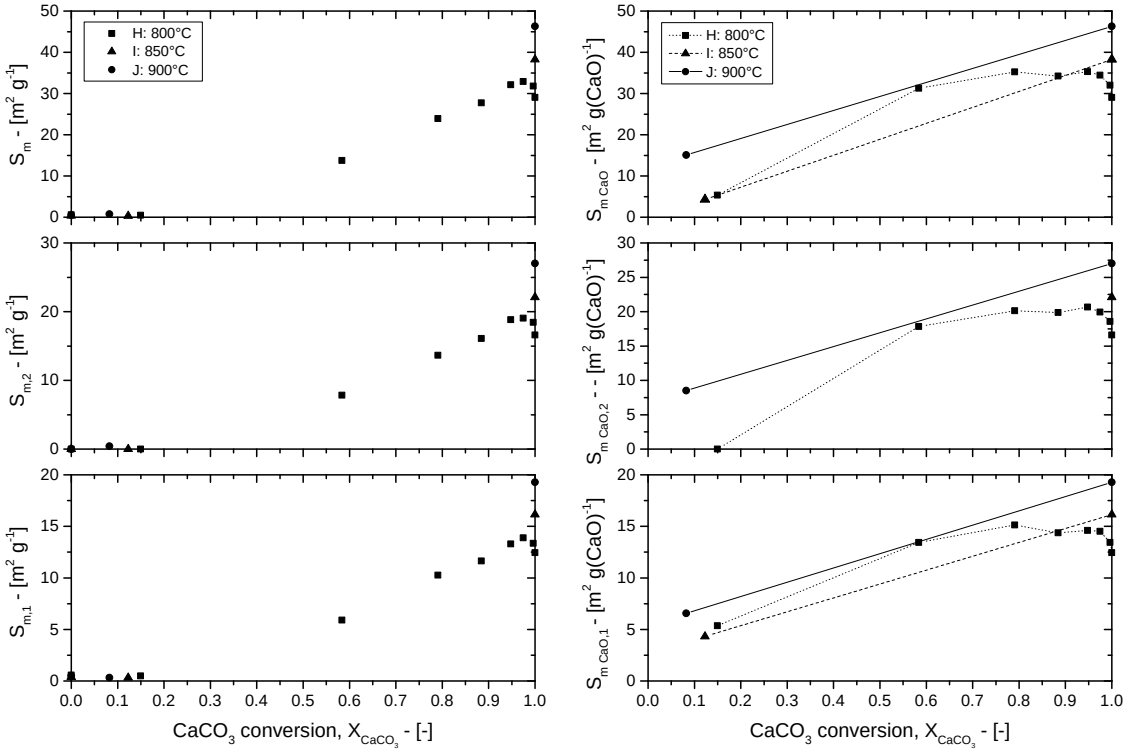

(a) S_m *vs* $X_{\mathrm{CaCO_3}}$. **(b)** $S_{m,\mathrm{CaO}}$ *vs* $X_{\mathrm{CaCO_3}}$.

Figure 6.34: Evolution of the specific surface area per unit of sample mass (a) and per unit of CaO mass over the $CaCO_3$ conversion of the two pore populations and of the total surface area for samples calcined under a reaction atmosphere with 10 % of CO_2 in balance with N_2.

However, as the CO_2 pressure into the reaction atmosphere increases, these trends changes showing a positive correlation up to 0.4–0.5 values. Additionally, the calcination temperature contributes in changing the specific surface per unit of volume correlation over the meso-porosity, as shown in Fig. 6.37a, where the increase of temperature evolves the non linear correlation towards linear trends.

Fig. 6.38 shows the surface-to-pore ratio correlations over the micro- and meso-porosity values. The surface-to-pore ratio of the micro-pore population, $R_{S/V,1}$ seems to change its trend with the increase of temperature and CO_2 content, namely from a porosity correlation observed for the case of the N_2 calcined samples to a negative correlation, that becomes more pronounced when at 900 °C with 50 % of CO_2 as showed by Fig. 6.38d. This evolution seems to gradually occur when the CO_2 content increases, as shown in Figs. 6.38a and 6.38b for the 800 °C calcined samples and the $R_{S/V,1}$ vs $R_{g,1}$ correlation definitely becomes negative when both temperature and pressure are high, as for the case of sample L (900 °C, 25 % of CO_2).

Pore size distributions By considering, the PSDs of the calcined sample in the presence of CO_2 (Fig. 6.39), the initial PSD estimated during the early steps of the calcination reaction, namely below than 5 min, show broader meso-pore distributions if compared with those estimated for the N_2 calcined samples, as shown in the insets of Fig. 6.39b, 6.39c and 6.39d. In fact, if the initial PSD for the N_2 calcined samples range from few angstroms up to 100–120 Å, at 800 °C the initials PSD covered a pore size domain up to 300 Å. The

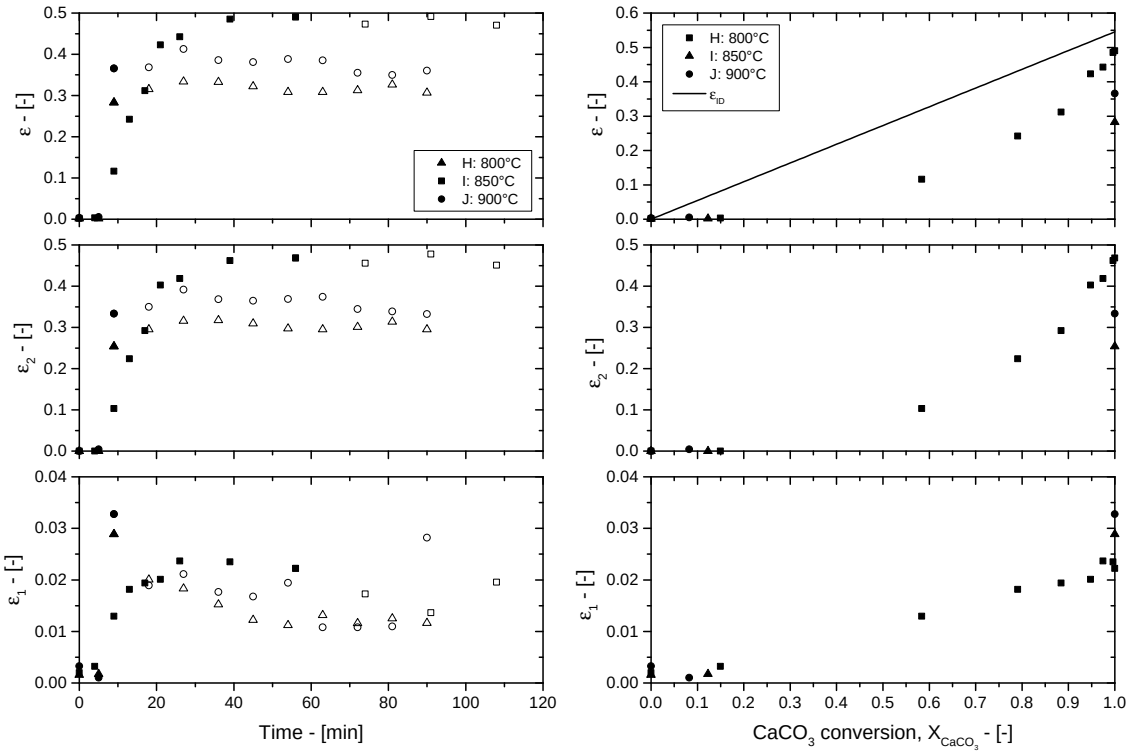

(a) *ε vs time.* **(b)** *ε vs* $X_{\mathrm{CaCO_3}}$.

Figure 6.35: Evolution of sample internal porosity of the two pore populations and of the total sample porosity over time (a) and over the $CaCO_3$ conversion (b) for samples calcined under a reaction atmosphere with 10 % of CO_2 in balance with N_2.. Black and open markers refer to reaction and sintering time respectively. Solid line represent the ideal porosity evolution over the $CaCO_3$ conversion.

same effect is noticed in the final PDSs, where at 800 °C the increase of the CO_2 content in the reaction atmosphere leads to a broadening of the meso-pore distribution as shown by Fig. 6.39a, 6.39b and 6.39c. The meso-pore populations of sample F roughly spans from 50 Å to 250 Å, from 80 Å to 450 Å ca. for sample G and from 80 Å to 750 Å for the case of sample H. This PSD broadening of the meso-pore population is also observed in a more intense way for the 900 °C calcined sample, where the final meso-pore distribution of sample L ranges from 100 Å up to 1200 Å, as depicted in Fig. 6.39f. This is consistent with the radius of gyration evolutions represented in Fig. 6.26 and Fig. 6.33a, namely an increase with time, temperature and CO_2 content. On the other hand, the micro-pore population seems to be slightly influenced by temperature and pressure changes, whose distribution ranges from few angstrom up to 50 Å.

Eq. (4.70) was used to estimated the number of pores per unit of sample mass of the two populations over time. The results are represented in Fig. 6.40 and Fig. 6.42a. As for the case of the N_2 calcined samples (A÷E), the number of pore evolution of the micro- and meso-pore population shows an initial increase of the pore number, followed by a reduction. It is remarkable to notice how the CO_2 concentration significantly reduce the sorbent number of pores both at 800 °C and at 900 °C, as shows in Figs. 6.40a and 6.40b respectively and the micro-pore number remain still higher (roughly on order of magnitude) than those of the meso-pore. Additionally, opposite to samples A÷E the final (when the calcination reaction stops) number of pore is significantly reduce (almost one order of

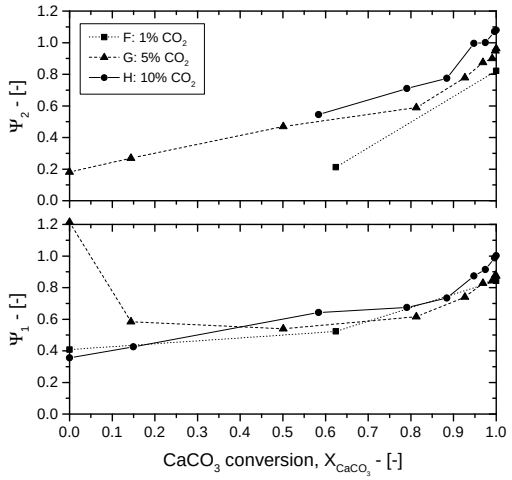

(a) *Samples F, G, and H* - 800 °C.

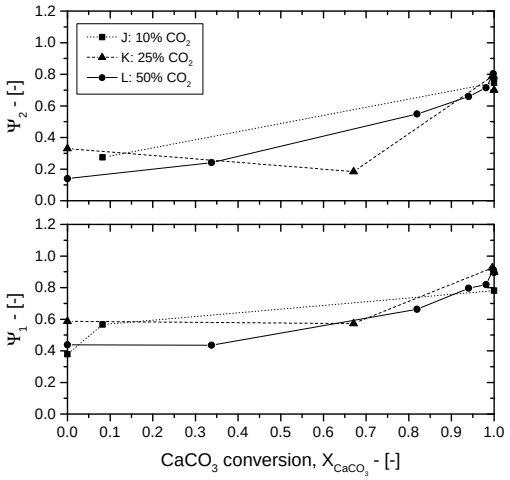

(b) *Samples J, K, and L* - 900 °C.

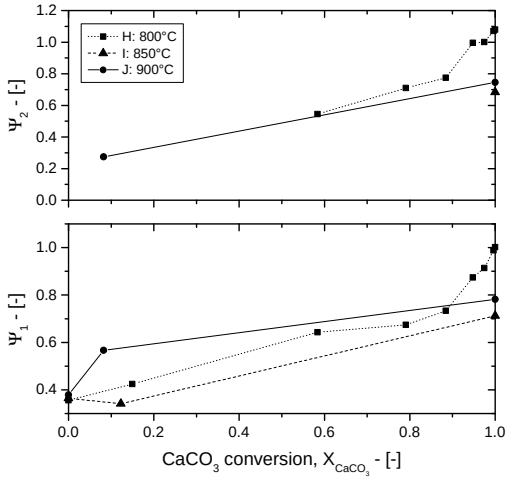

(c) *Samples H, I, J* - 10 % CO_2.

Figure 6.36: Sphericity factor evolution of the two pore populations (squares and triangles) over the CaCO3 conversion of samples calcined at 800 °C (a) and at 900 °C (b), and samples calcined under a reaction atmosphere with 10 % of CO_2 in balance with N_2.

magnitude): from an average value of about $3 \times 10^{18}\,g^{-1}$ down to an average value of $6 \times 10^{17}\,g^{-1}$. Specifically, at 800 °C the increase of the CO_2 content leads to a significant decrease of the final meso-pore number, namely $0.49 \times 10^{18}\,g^{-1}$ (1 % of CO_2, sample F), $0.08 \times 10^{18}\,g^{-1}$ (5 % of CO_2, sample G) and $0.03 \times 10^{18}\,g^{-1}$ (10 % of CO_2, sample H), as listed in (Tab. 6.3). In addition, the micro-pore population also decreases in number with the CO_2 content: $1.46 \times 10^{18}\,g^{-1}$ (1 % of CO_2, sample F), $0.68 \times 10^{18}\,g^{-1}$ (5 % of CO_2, sample G) and $0.63 \times 10^{18}\,g^{-1}$ (10 % of CO_2, sample H). The increase of the reaction temperature from 800 °C to 900 °C leads to a significantly decrease of the pores number per unit of sample mass and the final total pores number per unit of mass respectively approaches to $0.86 \times 10^{18}\,g^{-1}$ (sample J), $0.07 \times 10^{18}\,g^{-1}$ (sample K) and $0.06 \times 10^{18}\,g^{-1}$ (sample L).

Interestingly, the number of pores per unit of mass of the calcined samples with 10 % of CO_2 reveal an increase of the final meso-pores number with the temperature, as shown by the final values of samples H (800 °C) and J (900 °C), namely $0.08 \times 10^{17}\,g^{-1}$ and

$0.11 \times 10^{17}\,g^{-1}$ respectively, as listed in Tab. 6.3. A similar behavior is observed by the micro-pore population, that exhibits an increasing number of pores with the increase of the CO_2 in the reaction atmosphere, namely. $0.68 \times 10^{18}\,g^{-1}$ (800 °C, sample H) and $0.58 \times 10^{18}\,g^{-1}$ (900 °C, sample J), as listed in Tab. 6.3. More interestingly, despite its modest porosity values (0.029 and 0.254), the 850 °C calcined sample I exhibits high meso-pore numbers per unit of sample mass, namely $0.11 \times 10^{17}\,g^{-1}$ compared with $0.03 \times 10^{17}\,g^{-1}$ of the respective 800 °C sample H and a micro-pore number of pores of $0.58 \times 10^{18}\,g^{-1}$ in agreement with the sample H and sample J values (Tab. 6.3).

6.3.5 Sorbent sintering

Calcium oxide sintering in nitrogen atmosphere

Once the calcination reaction was completed, namely at the end of the reaction time (RT), an additional time was considered in order to allow the sorbent micro-structure evolution by means of only the sintering phenomena, namely the sintering time (ST). For the N_2 calcined sample, the sintering step was considered only for samples C, D and E, whose calcination temperatures are 650 °C, 680 °C and 700 °C. For the low temperature calcined samples, namely sample A (SI600°C) and B (620 °C), a sintering time was not considered because of these low temperatures that did not permit a sorbent micro-structural evolution over a reasonable period. According to Tab. 6.2, sintering times for the N_2 calcined sample varies from a minimum of 21 min to a maximum of 34 min. A comparison of the USAXS/SAXS of samples C, D and E profiles measured at the end of the reaction and sintering time are shown in Fig. 6.10a. From a qualitative point of view, this picture suggests a non-significant evolution of the samples internal micro-structure due to sintering phenomena, as indicated by the similar SAS profiles, except for the case of sample C, that shows a lower Guinier regime. On the other hand, the sintering effects on the SAS profiles of the completely calcined samples in the presence of CO_2 consist in shifting the Guinier regime towards the low-q regions and in a decrease in magnitude of the power-law region as depicted in Fig. 6.10. Specifically, this effect is empathized by the increase of the CO_2 content in the reaction atmosphere and becomes more important with the increase of temperature, as showed in Figs. 6.10d, 6.10e and 6.10f for the 900 °C calcined samples.

As expected by the low sintering temperatures, the radius of gyration of the two pore populations is quite constant during sintering time for the N_2 calcined samples, as shown in Figs. 6.15a, 6.15b and 6.15c. Specifically, the micro-pore population estimated at the end of the sintering time is 25 Å (sample C), 25 Å (sample D) and 24 Å (sample E) as listed in Tab. 6.6, that are similar to those calculated at the end of the reaction time, namely 23 Å, 23 Å and 21 Å respectively (Tab. 6.3). Similarly, the final meso-pore radius of gyration values at the end of the sintering time are 85 Å (sample C), 109 Å (sample D) and 101 Å (sample E), which are significantly closer to the radii of gyration determined at the end of the calcination reaction: 83 Å, 106 Å and 99 Å respectively. These results are confirmed by the overall mean pore radius evolution calculated from the sample PSDs during the sintering time by means of Eq. (4.71), as shown in Fig. 6.25b, namely 71 Å (sample C), 90 Å (sample D) and 86 Å (sample E) estimated at the end of the calcination reaction and 73 Å (sample C), 92 Å (sample D) and 95 Å (sample E) at the end of the sintering time.

According to the sample specific surface area over time profiles showed in Fig. 6.15, the maximum value is observed near to the end of the reaction time, namely when the calcination reaction is complete. Afterwards, a slow decrease is observed during the sintering time leading to a loss of the sorbent specific surface area. Interestingly, the highest reduction of the sorbent specific surface area (for the case of the N_2 calcined samples) was observed for the 650 °C calcined sample C that exhibits the greater final surface area at the

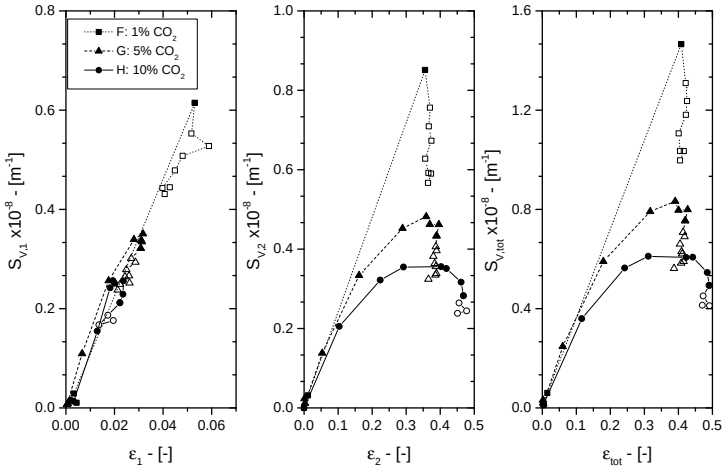

(a) *Samples F, G, and H* - 800 °C.

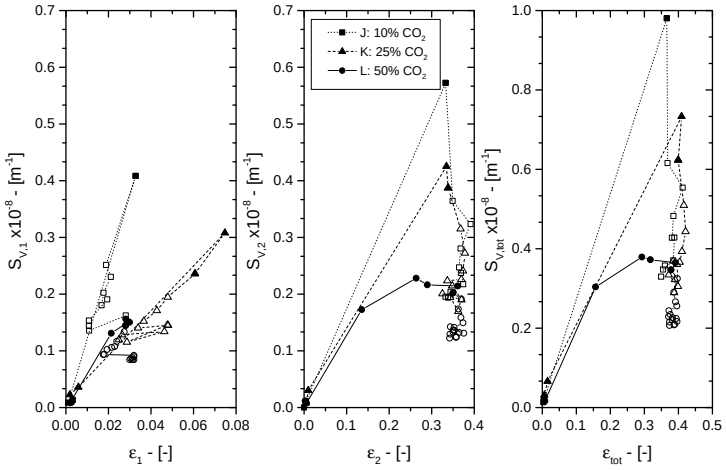

(b) *Samples J, K, and L* - 900 °C.

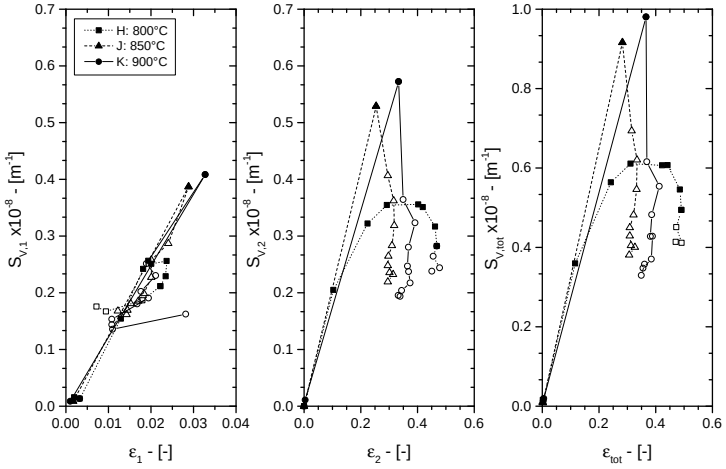

(c) *Samples H, I, J* - 10 % CO_2.

Figure 6.37: Specific surface area per unit of sample volume of the two pore populations (squares and triangles) and of the total specific surface area per unit of volume (dots) over the respective internal porosity values. Black and open markers refer to reaction and sintering time respectively.

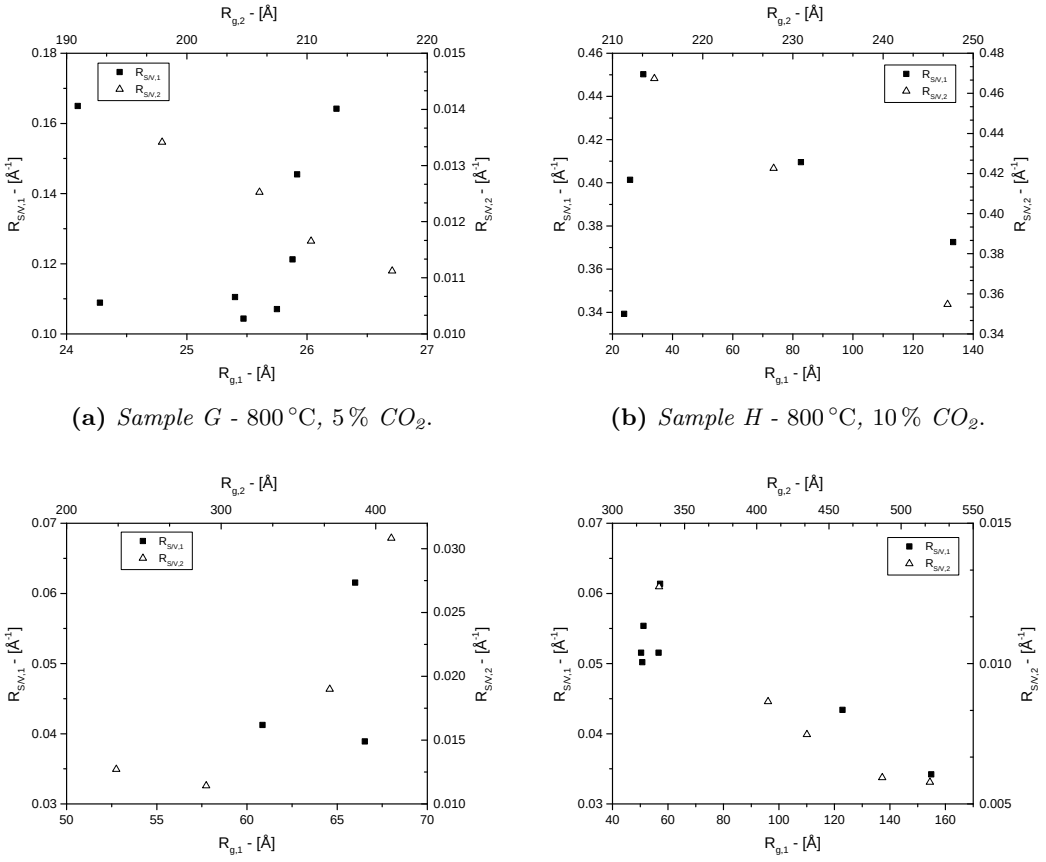

(a) *Sample G* - 800 °C, 5 % CO_2. **(b)** *Sample H* - 800 °C, 10 % CO_2.

(c) *Sample K* - 900 °C, 25 % CO_2. **(d)** *Sample L* - 900 °C, 50 % CO_2.

Figure 6.38: Surface-to-pore volume ratio of the two pore populations correlated with their respective radii of gyration for samples calcined at 800 °C with 5 % (a) and 10 % (b) of CO_2 and at 900 °C with 25 % (c) and 50 % (d) of CO_2 in balance with N_2.

end of the reaction time, namely from 128.7 $m^2\,g^{-1}$ (Tab. 6.3) to 115.2 $m^2\,g^{-1}$ (Tab. 6.6). On the other hand, the surface area reduction of sample D and E is more modest, namely 108.0 $m^2\,g^{-1}$ and 111.5 $m^2\,g^{-1}$ once the calcination reaction was completed (Tab. 6.3) and 102.5 $m^2\,g^{-1}$ and 111.9 $m^2\,g^{-1}$ (Tab. 6.6) estimated at the end of the sintering time. Additionally, according to the micro and meso-pore specific surface areas of Tab. 6.3 and Tab. 6.6, at these low temperatures (650÷700 °C) sintering phenomena seems to mostly affect the meso-pore specific surface areas, while the micro-pore ones remain quite constant. Precisely, the final specific surface area inherently to the reaction and sintering times are 73.8 $m^2\,g^{-1}$ (sample C), 63.9 $m^2\,g^{-1}$ (sample D) and 65.7 $m^2\,g^{-1}$ (sample E) and 54.1 $m^2\,g^{-1}$ (sample C), 43.7 $m^2\,g^{-1}$ (sample D) and 48.6 $m^2\,g^{-1}$ (sample E), as listed in Tab. 6.3 and Tab. 6.6.

Even in the case of the porosity values profiles over time shows a decrease of the sorbent porosity after the maximum value placed near to the end of the reaction time. Additionally, the highest decrease is observed for the case of sample C (650 °C, N_2), namely a final total internal porosity that ranges from 0.519 (Tab. 6.3) to 0.487 (Tab. 6.6). For the case of samples D and E the total sample porosities estimated at the end of the reaction and sintering times are 0.530 (sample D) and 0.527 (sample E) and 0.516 (sample D) and 0.508 (sample E), as listed in Tab. 6.3 and Tab. 6.6.

During the sintering time, the micro-pore volume fraction is quite constant during this

stage, namely a final total porosity values of 0.091 (sample C), 0.071 (sample D) and 0.065 (sample E) estimated at the end of the calcination reaction and 0.101 (sample C), 0.076 (sample D) and 0.081 (sample E) estimated at the end of sintering time. This result is in agreement with the specific surface area evolution during the sintering time. During the sintering time, the meso-porosity values is the main responsible of the total sample porosity evolution. In fact, during this step, the sample porosities vary from 0.428 (sample C), 0.459 (sample D) and 0.461 (sample E) to 0.386 (sample C), 0.440 (sample D) and 0.428 (sample E), as listed in Tab. 6.3 and Tab. 6.6.

More interestingly, the total fraction of pore destroyed during sintering time shows a slightly increase as depicted in Fig. 6.19. Specifically, the final ϕ values estimated at the end of the sintering time are 0.108 (sample C), 0.054 (sample D) and 0.068 (sample E), which are slightly higher than those estimated at the end of the calcination reaction: 0.048 (sample C), 0.029 (sample D) and 0.034 (sample E). Opposite to the ϕ evolution over the reaction time, during the sintering step the fraction of pore removed exhibits an increasing trend over time, in agreement with Ramachandran and Smith (1977).

According to Eq. 5.2, sintering effects slightly affected the sphericity factors of the two pores populations, assuming values close to one. Specifically, sintering phenomena seems to slightly reduce the pore sphericity, especially for the case of sample E, where the meso-pore population value changes from 1.047 to 0.945, as can be observed in Tab. 6.4 and Tab. 6.7.

These surface and porosity profiles over the sintering time indicate that sintering processes are in the initial stage, namely a evident decrease of the sorbent specific surface area coupled with a modest porosity evolution, according to Kang and Jung (2004), Rahaman (2007), and Maya, Chejne, and Bhatia (2017a). Additionally, neck growth during the early stages of the densifying mechanisms are in agreement with the constant radius of gyration and a slightly decrease of the sorbent sphericity factors.

Fig. 6.25a shows the number of pore per unit of sample mass evolution of the two pore population over the sintering time. After the maximum number of pore, that occurs nearly close to the end of the thermal decomposition, a decrease of the pore number is observed in both the pore populations. Specifically, the total number of pores destroyed are $0.93 \times 10^{18}\,\mathrm{g}^{-1}$ (sample C), $0.53 \times 10^{18}\,\mathrm{g}^{-1}$ (sample D) and 0.92×10^{18} (sample E). Interestingly, samples C and D show the major micro-pore number variation during the entire sintering step, namely $0.87 \times 10^{18}\,\mathrm{g}^{-1}$ and $0.91 \times 10^{18}\,\mathrm{g}^{-1}$. Additionally, these samples exhibit the highest total specific surface areas ($128.7\,\mathrm{m}^2\,\mathrm{g}^{-1}$ and $111.5\,\mathrm{m}^2\,\mathrm{g}^{-1}$ respectively), suggesting that the micro-pore fraction largely contributes in the development of the surface area.

Fig. 6.43a shows the samples C, D and E PSDs before and after sintering time. As previously noted, on volume basis the micro-pore distribution is slightly affected by the sintering step, showing almost the same profile, as depicted in the inset of Fig. 6.43a. On the other hand, the micro-pore population shows a PSD (on volume basis) that modestly broadens towards higher pore radii, as depicted in Fig. 6.43a.

On the basis of these observations, in this work modest sintering phenomena were observed at temperatures below 800°C, in contrast with Borgwardt (1989a) stated that at 700 °C CaO does not sinter. These effects are the decrease of the pore number, the specific surface area of the two pore populations and of the sorbent meso-porosity, while the radius of gyration of the two pore populations remain quite constant, as well as the overall mean pore radius.

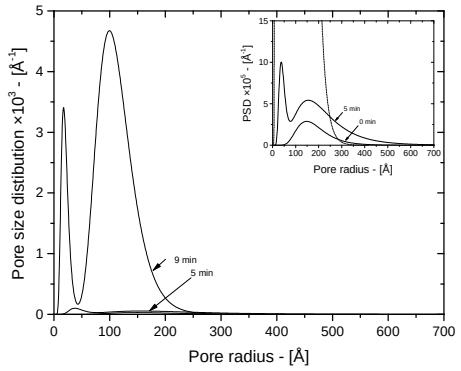

(a) *Sample F* - 800 °C, 1 % CO_2.

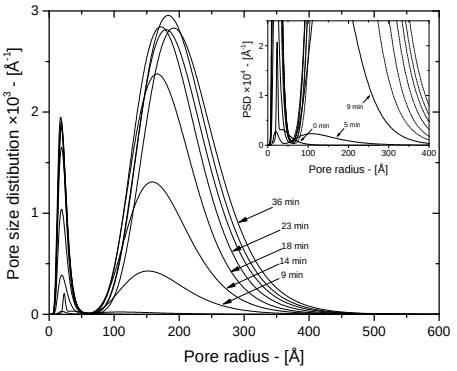

(b) *Sample G* - 800 °C, 5 % CO_2.

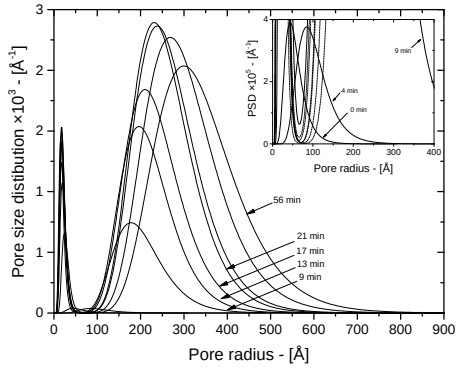

(c) *Sample H* - 800 °C, 10 % CO_2.

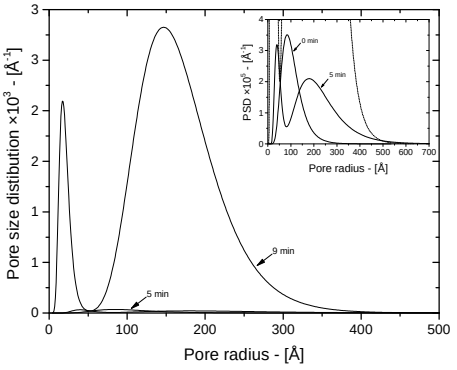

(d) *Sample J* - 900 °C, 10 % CO_2.

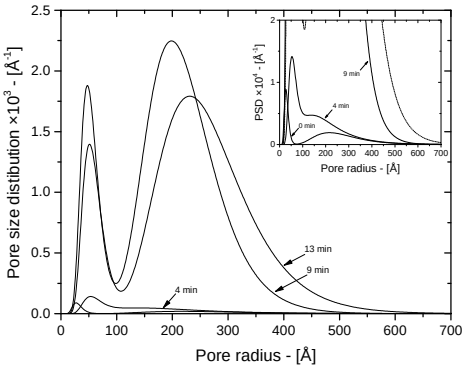

(e) *Sample K* - 900 °C, 25 % CO_2.

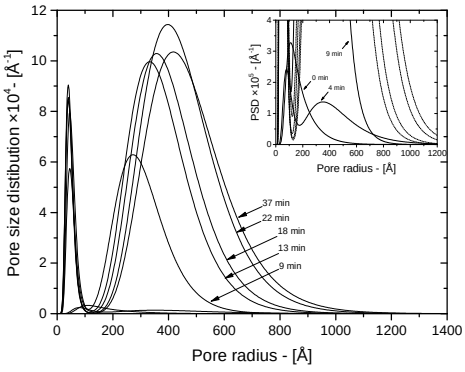

(f) *Sample L* - 900 °C, 50 % CO_2.

Figure 6.39: Pore size distributions generation and evolution during calcination reactions (reaction time step) performed with the presence of CO_2 in the reaction atmosphere: at 800 °C with 1 % (a), 5 % (b) and 10 % (c) of CO_2; at 850 °C with 10 % of CO_2 (d); at 900 °C with 10 % (e), 25 % (f) and 50 % (g) of CO_2. Time labels indicate the first stages of the reaction time and the last time-step.

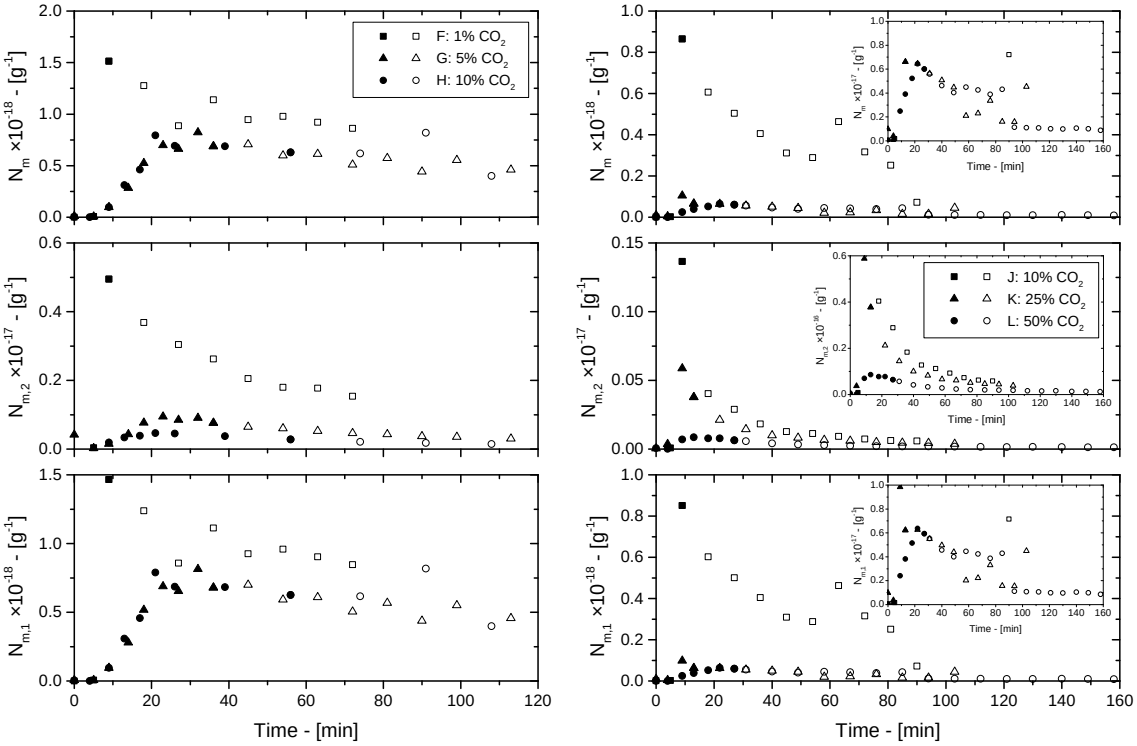

(a) *Samples F, G, and H* - 800 °C. **(b)** *Samples J, K, and L* - 900 °C.

Figure 6.40: Evolution of the number of pores per unit of mass of the two pore populations and of the total number of pores per unit of mass over time of samples calcined at 800 °C (a) and 900 °C (b). Black and open markers refer to reaction and sintering time respectively.

Calcium oxide sintering in presence of CO_2

According to Fuertes et al. (1991), as sintering processes and modifies the micro-textural properties, the sorbent main pore radius of gyration increases with time and the presence of CO_2 in the reaction atmosphere accelerates this effect. This is represented in Fig. 6.26, where the radii of gyration profiles over time are represented. The CO_2 effect on the sorbent micro-structure case an overall increase of the radius of gyration since during the reaction time. Once the reaction is completed, sintering processes continue to increase the mean pore radius even for the case of the micro-pore population. Specifically, opposite to the N_2 calcined samples the micro-pore population radius of gyration increases with time and the growth rate accelerates with temperature and the CO_2 content. In fact, on average at 800 °C the micro-pore radius of gyration estimated at the end of the reaction time is about 25 Å (Tab. 6.6) and the final micro-pore radii of gyration after a sintering time of about 63÷77 min are: 26 Å (1 % of CO_2, sample F), 25 Å (5 % of CO_2, sample G) and 51 Å (10 % of CO_2, sample H). At 900 °C, the micro-pore radius of gyration evolution during the sintering time is more intense, namely from 24 Å to 50 Å (10 % of CO_2, sample J), from 67 Å to 107 Å (25 % of CO_2, sample K) and from 50 Å to 114 Å (50 % of CO_2, sample L), as listed in Tab. 6.3 and Tab. 6.6. Interestingly, at 800 °C the micro-pore radius of gyration shifts towards to higher values only when the CO_2 content is high (more than 5 %) and, on the other hand, at 900 °C pore growth is substantially higher when the CO_2 is greater than 10 %. Accordingly, the meso-pore radius evolution between the initial and final during sintering time at 800 °C are 98 Å and 180 Å (1 % of CO_2, sample F), 118 Å and 309 Å (5 % of CO_2, sample G), 217 Å and 467 Å (10 % of CO_2, sample H). At 900 °C the

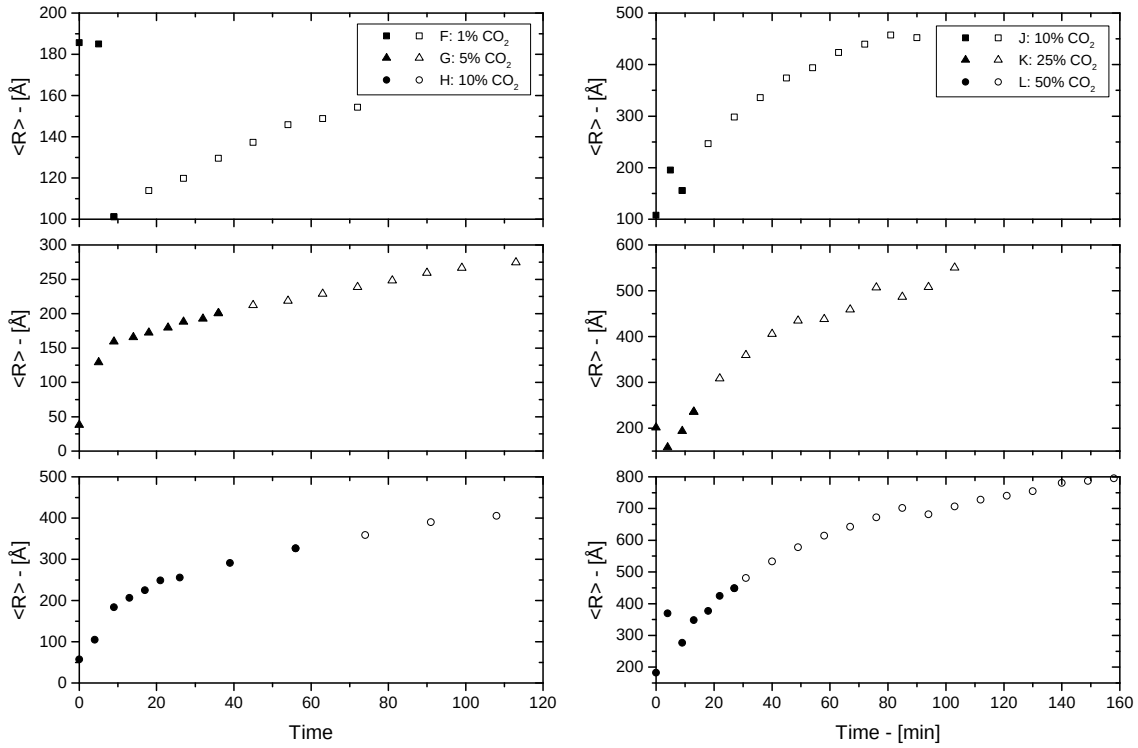

(a) *Samples F, G, and H* - 800 °C. **(b)** *Samples J, K, and L* - 900 °C.

Figure 6.41: Mean pore radius evolution over time of samples calcined at 800 °C (a) and 900 °C (b). Black and open markers refer to reaction and sintering time respectively.

meso-pore radius of gyration evolutions are: from 182 Å to 532 Å (10 % of CO_2, sample J), from 290 Å to 665 Å (25 % of CO_2, sample K), from 520 Å to 1002 Å (50 % of CO_2, sample L). These trends are represented in Fig. 6.26a for the 800 °C samples and Fig. 6.26b for the 900 °C ones, while Fig. 6.33a compares the radii of gyration profiles for those samples calcined with 10 % of CO_2. It is remarkable to notice how the combination of temperature and CO_2 accelerates the pore radius growth during sintering time: the meso-pore radius of gyration exceeds the value of 500 Å at 900 °C, while 63 min and 81 min are not enough to reach this value for the case of sample H (800 °C) and I (850 °C). Finally, it is remarkable to observe the micro-pore population radius of gyration is quite constant during the reaction time, while it evolves during the sintering time. This observation is strictly true except for samples K and L, where both the high temperature and CO_2 pressure contribute to affect the micro-pore population.

Fig. 6.27a and 6.27b show the surface reduction profiles over sintering time (open markers) of the 800 °C and 900 °C calcined samples respectively. The investigation over the CO_2 content in the reaction atmosphere emphasizes the CO_2-catalytic effect on the reduction not only during the sintering time but also during the reaction step, and, specifically during the lasts stages of the reaction. This behavior is observed in Fig. 6.27, where solid and open markers refers to the reaction and sintering time respectively. In order to quantify the sintering effect of the CaO specific surface area a comparison between the initial and final surface area during the sintering time was conveniently considered. Specifically, at 800 °C the major sintering effects are observed at CO_2 contents below 1 %, with a surface reduction (during sintering time) of 24 $m^2\,g^{-1}$ (from 74.2 $m^2\,g^{-1}$ to 50.2 $m^2\,g^{-1}$) for sample F,

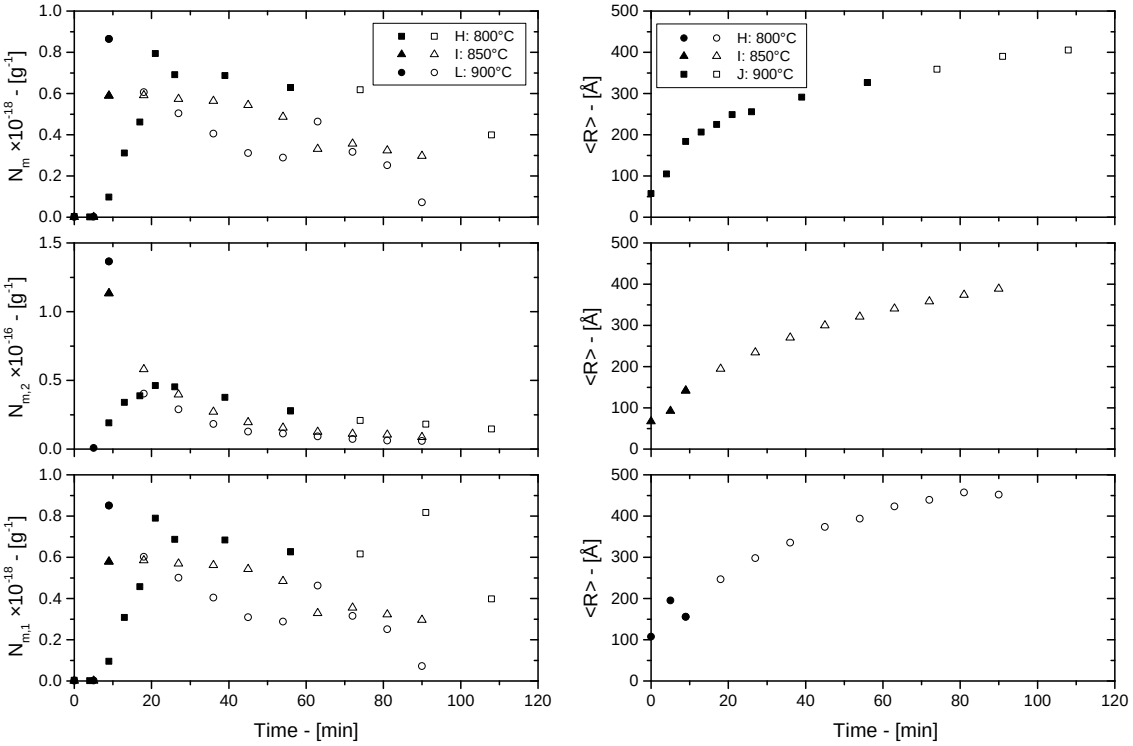

(a) N_m *vs time.* **(b)** $\langle R_v \rangle$ *vs time.*

Figure 6.42: Evolution of the number of pores per unit of mass of the two pore populations and of the total number of pores per unit of mass over time (a) and mean pore radius evolution over time (b) of samples calcined under a reaction atmosphere of 10 % of CO_2 in balance with N_2. Black and open markers refer to reaction and sintering time respectively.

11.5 $m^2\,g^{-1}$ (from 39 $m^2\,g^{-1}$ to 27.5 $m^2\,g^{-1}$) for sample G and 19.1 $m^2\,g^{-1}$ (from 29 $m^2\,g^{-1}$ to 9.9 $m^2\,g^{-1}$) for sample H. This result is related to the sorbent specific surface area value at the end of the reaction, where the presence of the CO_2 reduce the CaO surface generation, as shown in Fig. 6.27. According to this results, at 900 °C the total specific surface reduction is 29.6 $m^2\,g^{-1}$ (from 46.3 $m^2\,g^{-1}$ to 16.7 $m^2\,g^{-1}$) for sample J, that is the maximum surface area reduction observed at this temperature, 16.9 $m^2\,g^{-1}$ (from 31.1 $m^2\,g^{-1}$ to 14.1 $m^2\,g^{-1}$) for sample K and 6.8 $m^2\,g^{-1}$ from 16.7 $m^2\,g^{-1}$ to 9.9 $m^2\,g^{-1}$) for the case of sample L. Additionally, it is remarkable to notice in Fig. 6.27 how the specific surface area profiles over sintering time of samples G, H and L seem to approach the asymptotic values, that is approximately around $20 \div 30$ $m^2\,g^{-1}$ at 800 °C and roughly at 10 $m^2\,g^{-1}$ at 900 °C in terms of total sorbent specific surface area. Interestingly, these asymptotic values are in agreement with those estimated by Mai and Edgar (1989) by means of CaO derived from calcium hydroxide. Specifically, the asymptotic specific surface area values of the two pore populations are quite similar and roughly around $13 \div 16$ $m^2\,g^{-1}$ (meso-pores) and $9 \div 12$ $m^2\,g^{-1}$ (micro-pores) at 800 °C; 5.9 $m^2\,g^{-1}$ and 4.0 $m^2\,g^{-1}$ for the case of 900 °C calcined samples. Interestingly, the 850 °C calcined sample I shows similar asymptotic specific surface area values to the corresponding sample H calcined at 800 °C, as shown in Fig. 6.33b, namely a final total specific surface area of 16.4 $m^2\,g^{-1}$ (Tab. 6.6), whose corresponding micro- and meso pore values are 7.0 $m^2\,g^{-1}$ and 9.5 $m^2\,g^{-1}$ respectively.

Once the reaction is completed, the porosity evolution during the sintering time shows

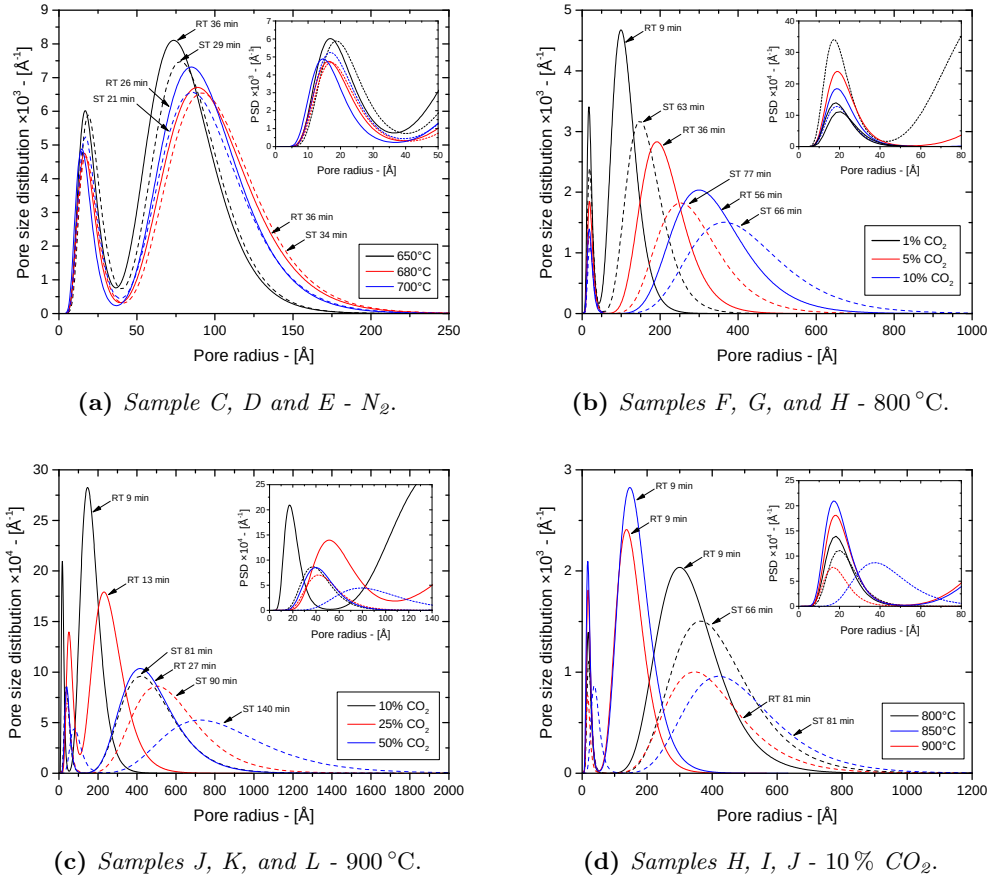

(a) *Sample C, D and E - N_2.*

(b) *Samples F, G, and H* - 800 °C.

(c) *Samples J, K, and L* - 900 °C.

(d) *Samples H, I, J* - 10 % *CO_2.*

Figure 6.43: Comparison of the sorbent pore size distribution estimated at the end of the reaction (RT) and sintering time (ST) for samples calcined in N_2 (a), in presence of CO_2 at 800 °C (b) and at 900 °C (c), with a reaction atmosphere with 10 % of CO_2 in balance with N_2 (d).

quite constant trends as shown in Fig. 6.30 and Fig. 6.35a. Actually, a slight porosity reduction is observed at 800 °C that becomes more important with the increase of the CO_2 content in the reactor atmosphere, namely from 0.408 to 0.405 (1 % of CO_2, sample F), from 0.420 to 0.387 (5 % of CO_2, sample G) and from 0.490 to 0.470 (10 % of CO_2, sample H), as listed in Tab. 6.3 and Tab. 6.6. This modest sorbent internal porosity reduction is confirmed at 900 °C, namely from 0.366 to 0.361 (10 % of CO_2, sample J), from 0.400 to 0.388 (25 % of CO_2, sample K) and from 0.378 to 0.374 (50 % of CO_2, sample L) as listed in Tab. 6.3 and Tab. 6.6. According to these trends, the fraction of pore destroyed slightly increase with the sintering time, as shown in Fig. 6.32a. Specifically, more than one fourth of the total sample porosity is destroyed at 900 °C (Tab. 6.6), in agreement with samples F and G values. It is remarkable to notice, how the pore fraction destroyed at 800 °C with 10 % of CO_2 is about half of this value, namely 0.137 (sample F, Tab. 6.6). Opposite to this observation, at 850 °C with the same amount of carbon dioxide ϕ is more than three times intense 0.437, as listed in Tab. 6.6. This value decreases at 900 °C for the case of sample J, whose pore fraction destroyed is 0.339.

This slightly decrease of the sorbent porosity coupled with a significant reduction of the specific surface area suggests that sintering processes are governed by surface diffusion, according to Beruto, Barco, and Searcy (1984). On the other hand, this micro-structure evolution was observed by Borgwardt (1989a) and Borgwardt (1989b), who explained this

behavior through a neck growth mechanism, that occurs during the early stages of sintering German (2014).

Although the meso-porosity profiles over sintering time are quite constant, as shown in Fig. 6.30 and Fig. 6.35a, the porosity associated with the micro-pore population seems to be substantially reduced by means of the sintering phenomena. Specifically, the micro-pores reduction is more intense with the increase of temperature and CO_2 content, namely 23 %, 31 % and 12 % relative to samples F, G and H respectively. The micro-porosity reduction is in agreement with the number of micro-pores per unit of sample mass trends represented in Fig. 6.40a. Despite the quite constant meso-porosity over sintering time profiles, even the specific number of meso-pores decreases with time, especially for the case of sample F. This suggests that in both the two pore population sintering processes contribute in reducing the number of pores. However, the quite constant meso-porosity values could probably due to a fraction of micro-pores that moves to the meso-pore population by means of coalescence mechanisms (like Oswald ripening). Similar behaviors are observed for the case of 900 °C calcined samples, where the micro-porosity decrease during the sintering step is shown in Fig. 6.30b. Specifically, the relative micro-porosity evolution are about 14 % and 59 % for the case of samples J and L. The increase of sample L micro-porosity (from 0.028 to 0.031) is probably due to the fitting process of the experimental scattering intensity profiles. In fact, as previously mentioned, the micro-pore population structural level is placed between the SAXS and USAXS regions, where respective experimental profiles overlaps, generating some noise in the final scattering curve. However, both the number of pores of the two population decrease over the sintering time, as for the case of the 800 °C samples. However, at this temperature and high CO_2 content, the total number of pores are almost one order of magnitude lower than those of samples F, G and H, as shown in Fig. 6.40. This difference in pore number is not only merely due to the sintering phenomena. In fact, according to Tab. 6.3, these operative conditions seems to directly generate (during the reaction step) a micro-structure with a more modest pore number, respect to the other samples.

By a comparison between the initial and final sphericity factors of the two pore populations, Eq. (5.2), during the sintering step (Tab. 6.3 and Tab. 6.6), the pore shape is not significantly affected by sintering phenomena with the presence of CO_2. For the case of the 800 °C calcined samples, the two pore populations sphericity factors lies around the value 0.8 (sample F and G) and 0.9 (sample H). Accordingly to the sphericity values estimated at the end of the reaction time (Tab. 6.4), at higher temperatures and CO_2 pressures, the sphericity factors slightly decreases to 0.7 and 0.8 values, remaining quite constant over the sintering step (Tab. 6.7).

Open markers in Fig. 6.37 represent the correlation between the sorbent specific surface area (per unit of total volume) and its porosity during sintering time. Once the calcination reaction is completed sintering processes affect the meso-pore population specific surface area (and the total one) but preserving its porosity, as shown by the vertical distribution of the empty markers in Fig. 6.37. These trends confirm the early stages of the sintering processes (and, precisely the first stage) despite the operative conditions (temperature and CO_2 pressure) should favor both the surface and porosity reduction. Opposite to this observation, the micro-pore population shows a negative correlation over the micro-porosity suggesting a decrease of both the specific surface area and porosity during the sintering time, as shown in Fig. 6.37. Interestingly, this observation seems to indicate that in the early stage of sintering also the micro-porosity as affected by the sintering mechanisms and the induction period is strictly related to the meso-pore population, that contributed to the majority of the sorbent porosity.

Finally, the comparisons between the initial and final PSD during the sintering time are shown in Fig. 6.43. Specifically, at 800 °C the overall effect of sintering on the final PSD

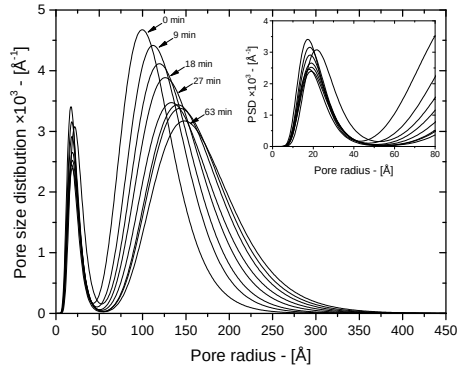

(a) *Sample F* - 800 °C, 1 % CO_2.

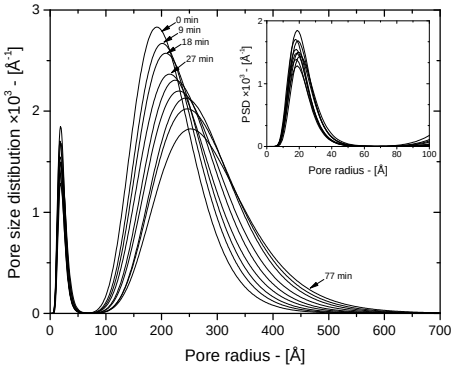

(b) *Sample G* - 800 °C, 5 % CO_2.

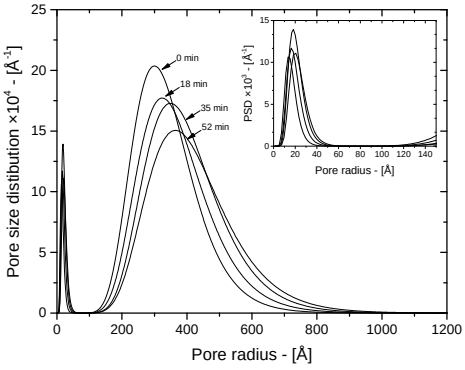

(c) *Sample H* - 800 °C, 10 % CO_2

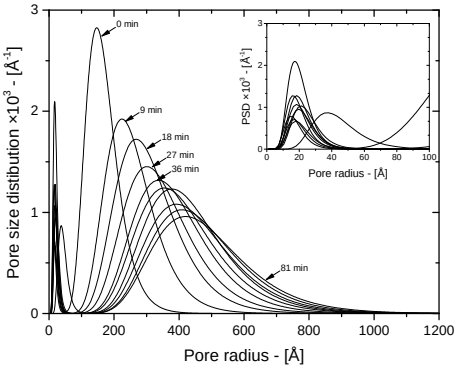

(d) *Sample J* - 900 °C, 10 % CO_2.

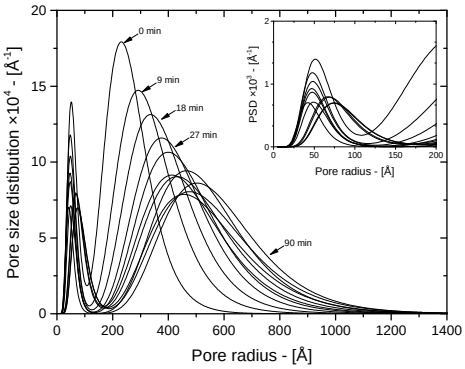

(e) *Sample K* - 900 °C, 25 % CO_2.

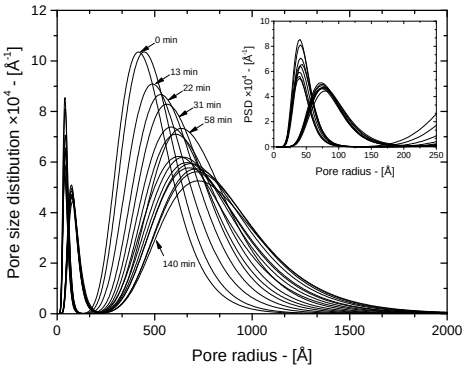

(f) *Sample L* - 900 °C, 50 % CO_2.

Figure 6.44: Pore size distributions evolution during the sintering step in the presence of CO_2 at different sintering temperatures, namely800 °C with 1 % (a), 5 % (b) and 10 % (c) of CO_2; 900 °C with 10 % (d), 25 % (e) and 50 % (f) of CO_2. Time labels indicate the first stages of the sintering steps and the last time-step.

(roughly after one hour of sintering time) consists in shifting and broadening of the meso-pore population distribution towards to higher pore radius, as shown in Fig. 6.43b. The detailed evolution of the PSD over the sintering time is represented in Figs. 6.43a, 6.43b and 6.43c for the case of samples F, G and H respectively, where the first time steps are indicated. This overall effect on the meso-porosity distribution is more intense at higher temperature and CO_2 pressures, as shown in Fig. 6.43c for the 900 °C calcined samples and Fig. 6.43d for the case of samples calcined with 10 % of CO_2 pressure. According to Figs. 6.44d, 6.44e and 6.44f the PSD evolution over sintering time for samples calcined at 900 °C (samples J, K and L) is considerable during the early stage of the sintering step, where the PSD broadening and shifting is more appreciable.

During the last steps of the sintering step, the sample PSDs evolution by means of sintering becomes less intense showing quite similar distributions. Opposite to these observations, at 800 °C the sintering effects on the micro-pore distribution mainly consists in a decrease of the micro-pore peaks, with a slightly shifts toward to higher pore values, as shown in the insets of Fig. 6.43b and Fig. 6.44a, 6.44b and 6.44c. This result is consistent with the quite constant micro-pore radius of gyration evolution as represented in Fig. 6.26a. At higher CO_2 pressures and temperatures, namely at 900 °C as for the case of samples J, K and L, the micro-pore population is broadened and shifted towards to higher pore radius as shown in the inset of Fig. 6.43c. On the other hand, the micro-pore population distribution shows an evolution similar to that of the 800 °C calcined samples except in the late stages of the sintering step, where a micro-pore distribution shift towards to higher pore sized is observed , as shown in the insets of Figs. 6.44d, 6.44e and 6.44f.

6.3.6 Meso-pore correlation distance during the $CaCO_3$ calcination and CaO sintering

During the $CaCO_3$ thermal decomposition, as pores increase in size and number density a structure factor $S(q,t)$ was necessary to account for the correlation interferences in the resulting sample scattering intensity profiles (§ 4.5). Specifically, in order to obtain the best-fit results a structure factor was necessary to be applied at the second-structural level of the "Unified fit", namely to the scattering intensity profile associated with the meso-pore population. According to Eq. (4.59), two additional fitting parameters were required to account for the meso-pore scattering intensity correlation interferences using the approach proposed by Beaucage et al. (1995). As previously mentioned in § 4.5, correlation distance ζ provides the average Bragg-like spacing between scatterers (Beaucage et al., 1995), pores in this work. This additional information provided by the SAS analysis is unique and none other analytical technique is capable to provide this kind of data, namely the average estimation of the meso-pore distance. More specifically, the evolution of the meso-pore correlation distances during the calcite decomposition and sintering steps are showed in Fig. 6.45.

Interestingly, by considering those samples calcined below 800 °C in N_2 atmosphere (A÷E), their correlation distance ζ is quite constant over the reaction and sintering steps, as shown in Fig. 6.45a. Furthermore, the meso-pore correlation distances of samples A÷E are fairly similar between each others, raging between 239 Å and 369 Å, as listed in Tab. 6.4. In addition, sintering phenomena did not affect the meso-pore distance, whose values are almost the same of those estimated at the end of the $CaCO_3$ calcination reaction (samples C, D and E) as listed in Tab. 6.7. This suggests how sintering effects seem to be negligible at these conditions, namely below 800 °C in pure nitrogen.

On the contrary, meso-pore correlation distances significantly increase during the calcite thermal activation and sintering at high temperatures (800–900 °C) and in presence of CO_2, as shown in Figs. 6.45b, 6.45c and 6.45d. More specifically, at 800 °C the initial

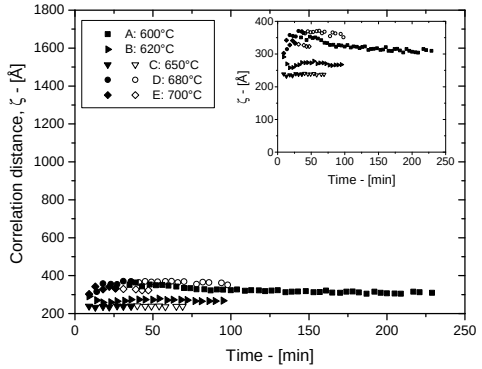

(a) *Samples A, B, C, D and E - calcinations in N_2 below* 800 °C

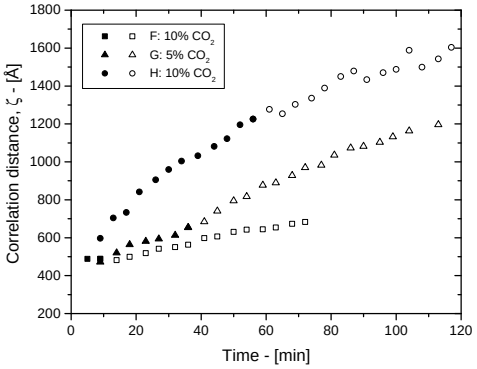

(b) *Samples F, G, and H* - 800 °C.

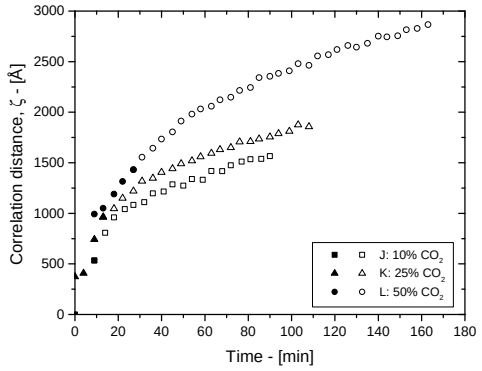

(c) *Samples J, K, and L* - 900 °C.

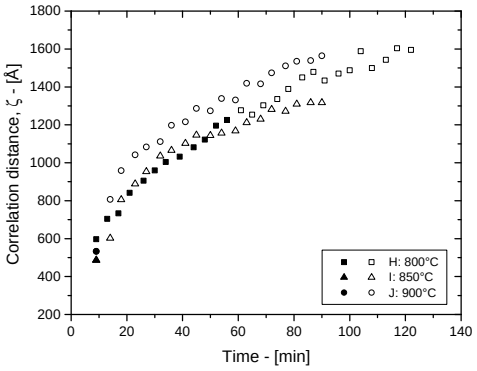

(d) *Samples H, I, J* - 10 % CO_2.

Figure 6.45: Evolution of the correlation distance over the reaction and sintering time associated with the second pore-population (meso-pore) according to the second structural level of the unified fit model. Different correlation distance profiles were obtained depending of experimental operative conditions, namely reactor temperatures that range from 600 °C to 700 °C in N_2 atmosphere (a), 800 °C (b), 900 °C (c) with the presence of CO_2 in the reaction atmosphere, and calcination reactions with 10 °C of CO_2 (d).

meso-pore correlation distances (during the $CaCO_3$ calcination) are higher that those of samples A÷E calcined and sintered at low temperature (in relative terms) and in nitrogen, about 489 Å (sample F, 1 % of CO_2), 472 Å (sample G, 5 % of CO_2) and 597 Å (sample H, 10 % of CO_2), suggesting that one of the CO_2 effects on the sorbent micro-structure is the increase of the average meso-pore distance. This is confirmed by the corresponding values estimated once the calcite decomposition is complete, that are 653 Å for sample G and 1226 Å for sample H (sample F excluded because of its low experimental points number), as listed in Tab. 6.4. Samples calcined at 900 °C exhibit higher final ζ values, which range between 533–1431 Å (the former refers to sample K), according to Tab. 6.4.
Open markers in Figs. 6.45b, 6.45c and 6.45d show how sintering processes affect the sorbent micro-structure by significantly increase the average meso-pore distance. For samples sintered at 800 °C the correlation meso-pore distance increased up to 1595 Å (sample H), while at 900 °C approached up to 2866 Å (sample J), as listed in Tab. 6.7. Therefore, the increase of temperature and CO_2 content in the reaction atmosphere accelerate the high temperature sintering mechanisms that affect the sorbent micro structure (porosity,specific surface area, pore number density, etc.), promoting the increase of the average meso-pore

distance.
Finally, Fig. 6.45c represents the correlation distances evolution for those samples calcines in presence of 10 % of CO_2 and varying the reactor temperature. Interestingly, a good agreement was obtained between the ζ evolution profiles of these samples (H, I and J), whose values range from about 350 Å, up to 1600 Å ca.

6.4 Conclusions

In this work, time-resolved X-ray synchrotron-based small angle scattering technique was applied for the first time to the investigation of the nascent CaO micro-structure during calcite thermal decomposition, namely the $CaCO_3$ calcination reaction, by means of an *in-situ* approach. Small angle scattering data were collected at the beamline 9-ID-B, C of the Advanced Photon Source (APS) at the Argonne National Laboratory.

Calcination reaction experiments were performed varying the reaction conditions in terms of temperature and CO_2 content in the reactor atmosphere and considering an additional residence time (at the same operative conditions) in order to allow sintering processes to affect the sorbent micro-structure. Two different sets of experiment were considered depending on the calcite thermal decomposition conditions, namely below 800°C in pure nitrogen (exploring a temperature range of 600÷700 °C) and at 800–900 °C varying the CO_2 content in the reactor atmosphere (from a minimum of 1 % up to a maximum of 50 °C in balance with N_2).

These measurements were capable to provide a detailed description of the sorbent micro-structure during pore generation and sintering processes, providing the instantaneous sample composition, porosity, specific surface area, radius of gyration, pore number density and pore size distribution. More specifically, time-resolved small angle scattering profiles were analyzed by means of the "Unified fit" approach (Beaucage, 1995; Beaucage, 1996) that is capable to provide a quantitative and detailed description of each pore population by means of an arbitrary number of structural levels.

During the early stages of the calcite decomposition, the nascent CaO micro-structure is characterized by one population of pores, that increases in size up to a pore network split into two different populations of pores: a micro-pore and a meso-pore population. The micro-pore radius of gyration suddenly drops down to a quite constant value (about 20 Å) over the reaction and sintering steps, whereas the meso-pore radius of gyration increases up to a maximum value and then approaches to an asymptotic one, that increases with time if sintering effects are significant. Samples calcined below 800 °C in nitrogen atmosphere exhibit similar meso-pore radius of gyration values, ranging between 83 Å and 106 Å and suggesting modest sintering effects of the final sorbent micro-structure, as confirmed by the high final specific surface areas and particle porosities significant close to the theoretical value (54 %). Specifically, the 650 °C calcined sample in pure nitrogen provided a final total specific surface area of 128.7 $m^2\,g^{-1}$, in excellent agreement with that obtained by Ewing, Beruto, and Searcy (1979), by means of vacuum calcination conditions of single crystal-based $CaCO_3$, namely 127 $m^2\,g^{-1}$. These specific surface areas are provided both by meso- and micro-pores. Actually, micro-pore population exhibits high and comparable surface areas with those of meso-pores even though their micro-pore volume fraction is significantly lower respect to the meso-porosity, namely at least one order of magnitude lower. However, the high pore number density associated with the micro-pore population (roughly $10^{18}\,g^{-1}$) in addition to its high surface-to-volume ratio makes its specific surface area comparable with that of the meso-porosity, that exhibits a pore number density of about one order of magnitude lower ($10^{17}\,g^{-1}$ ca.).

The micro-structure of nascent CaO seems to be distributed since the beginning of the calcite decomposition, in contrast with Powell and Searcy (1982) who suggested the development of the CaO micro-structure through an uniform intermediate pore layer.

Interestingly, in-situ USAXS/SAXS measurements allowed the investigation of the high temperature and time dependent phenomena, as pore generation and sintering, which can be hardly investigated by means of ex-situ based techniques. In fact, by considering samples calcined below 800 °C in nitrogen, even though the modest sintering effects of the final sorbent micro-structure, both the specific surface area and particle porosity profiles exhibit non-linear trends over the calcite conversion. More specifically, the porosity profiles deviated from the theoretical ones during almost the whole reaction period, approaching fairly close to the theoretical values once the calcination reaction is complete. This behavior was ascribed to reversible CO_2 interaction phenomena (like adsorption) with the nascent metastable CaO, because of the high amount of CO_2 released by the particle itself due to the reaction, according to Ewing, Beruto, and Searcy (1979). Accordingly, the specific surface area and porosity profiles shows increasing profiles over the reaction time reaching their maxima nearly when the $CaCO_3$ is completely decomposed. On the contrary, the maximum value of the meso-pore radius of gyration was achieved before the reaction was completed and a similar trend was observed by the pore number density of the two pore populations. Precisely, these profiles suggest that two different and competitive mechanisms occur during the calcite decomposition, namely a pore generation phenomena and a pore consumption process. The former seems to control the early steps of the calcination reaction, while the latter the late stages of the calcite decomposition. These behaviors were observed even for the case of samples calcined at high temperature and in presence of CO_2.

At low temperatures (600÷700 °C) and in atmosphere of pure nitrogen, the initial pore sphericity factors associated with the two pore populations are 0.4 and 0.6–0.7 respectively, and approaches up to one when the calcite decomposition is complete. On the other hand, at higher temperatures and in presence of CO_2 the initial meso-pore sphericity factor is slightly lower, namely in the range of 0.2÷0.4. Sintering seems to slightly reduce the pore sphericity factors of the two populations to 0.7–0.8.

Correlation distances were provided by the structure factor associated with the second structural level of the "Unified fit" approach, namely the scattering intensity response of the meso-pore population. This quantity provided an average estimation of the pore-to-pore distance (Beaucage et al., 1995), that is almost constant (during the reaction and sintering steps) for samples calcined below 800 °C in N_2, namely in the range of 239÷369 Å. With the increase of temperature and CO_2 content in the reactor atmosphere, the meso-pore correlation distance increases during the reaction up to final values of more than 1400 Å. Interestingly, once the reaction is complete, sintering processes continue to increase the average meso-pore distance up to more than 2800 Å.

Finally, an activation energy of 44.5 kcal mol^{-1} was estimated from the N_2-calcined samples conversion profiles (obtained from the WAXS data analysis), that is in excellent agreement with that estimated by Borgwardt (1985), namely 48 kcal mol^{-1}.

Chapter 7

Sorbent Micro-textural Characterization During the CaO-CO_2 Reaction by in-situ USAXS Measurements

Ex-situ SAS measurements on partially carbonated samples were capable to provide detailed information about the sorbent micro-structure evolution during the chemically controlled kinetic regime and after the transition point to the product layer diffusion controlled step.
Therefore, in this chapter X-ray small angle scattering technique was applied for the first time to the investigation of the sorbent micro-structure evolution during the CaO carbonation reaction by means of an *in-situ* approach. Different sorbent micro-structures were produced varying the final calcination temperature and atmosphere composition (CO_2/N_2) in order to consider samples with different degree of sintering effects on the final sorbent micro-structure. Specifically, calcite decompositions were performed below 800 °C in pure nitrogen to produce sorbent with negligible sintering effects, whereas temperature and CO_2 content were increase up to 900 °C and 50 % to promote sintering phenomena. Afterwards, these different samples were carbonated at 550 °C with 0.4 % of CO_2 in order to quantify the sorbent micro-textural properties on the carbonation reaction performances. Experiments were performed at the Advanced Photon Source (APS) at the Argonne National Laboratory (Argonne, Illinois).

7.1 Introduction

The separation of CO_2 streams by means of calcium oxide is based on the reversible chemical reaction of Eq. (2.1), where fresh porous calcium oxide is obtained from a previous activation step, namely the calcite thermal decomposition, usually performed in the temperature range of 700÷900 °C. Fresh calcined $CaCO_3$ is a very high reactive solid during the carbonation reaction, whose initial conversion rate could be less than $0.28\,s^{-1}$, as recently demonstrated by Biasin et al. (2015) by means of in-situ synchrotron radiation-based XRD measurements. Specifically, the CaO-CO_2 reaction kinetics consists of two different steps: a fast chemically controlled regime, followed by a slower step limited by the diffusion of carbon dioxide into the product layer of $CaCO_3$ (Barker, 1973; Bhatia and Perlmutter, 1983a; Mess, Sarofim, and Longwell, 1999; Abanades and Alvarez, 2003; Alvarez and Abanades, 2005; Sun et al., 2008a). The transition between these two stages occurs sharply and has been related to a critical thickness of the product layer, stopping the CaO carbonation reaction before the complete conversion (Barker, 1973; Mess, Sarofim, and Longwell, 1999; Alvarez and Abanades, 2005).

Currently, it is accepted that the chemisorption of carbon dioxide in porous CaO particle occurs as a non-catalytic gas-solid reaction (Bhatia and Perlmutter, 1983a; Sun et al., 2008a; Grasa et al., 2009), where the initial porous CaO sorbent undergoes to a series of micro-structural changes as the reaction progresses. More specifically, because of the different molar volumes between the reactant calcium oxide ($16.9\,cm^3\,mol^{-1}$) and the product calcium carbonate ($36.9\,cm^3\,mol^{-1}$), the formation and growth of the non-porous product layer fills and plugs the sorbent pore matrix, making the diffusion of the gaseous CO_2 into the sorbent particle more difficult. Several literature contributors (Bhatia and Perlmutter, 1983a; Abanades and Alvarez, 2003; Alvarez and Abanades, 2005; Sun et al., 2008a; Grasa et al., 2009) investigated the $CaCO_3$ pore filling by means of the experimental sorbent pore size distributions (obtained through the gas-adsorption and mercury porosimetry techniques) and scanning electron microscopy (SEM). Bhatia and Perlmutter (1983a) ascribed the transition from the two regimes to the closure of small pores approximately below 100 nm in size. On the other hand, Sun et al. (2008a) proposed that the consumption of pores below 250 nm in size make the transition from the fast stage to the slow one, by means of a random pore model based on discrete pore size distribution measurements.
According to Alvarez and Abanades (2005), Benedetti and Strumendo (2015), Grasa et al. (2009), and Sun et al. (2008a) the sorbent pore size distribution plays a crucial role in the description of the CaO-CO_2 reaction kinetics. Furthermore, with a detailed knowledge of the initial sorbent PSD it is possible to accurately describe the whole carbonation reaction profile over the reaction time, as suggested by Benedetti and Strumendo (2015) and by Sun et al. (2008a), who applied structural models for non-catalytic gas-solid reactions (Bhatia, 1985; Sotirchos and Yu, 1985) to the CaO carbonation reaction kinetics.
This strong influence of the sorbent micro-structural properties on the carbonation reaction makes the sorbent characterization an essential step for the investigation of the carbonation reaction performances, namely the carbonation kinetics and maximum CO_2 uptake.
Although several important efforts have been made to develop detailed structural models to describe both the CaO carbonation, as those of Benedetti and Strumendo (2015) and Sun et al. (2008a) with modified random pore models or, more recently, as that of Li, Sun, and Cai (2012) who proposed a rate equation-based model, the sorbent micro-structural evolution during the reaction is still poorly investigate by means of experimental measurements. Specifically, the evolution of micro-textural properties during the CaO carbonation reaction has been investigated by means of the ex-situ techniques, namely those based on the gas-adsorption and the mercury porosimetry (Barker, 1973; Bhatia and Perlmutter, 1983a; Alvarez and Abanades, 2005; Grasa et al., 2009; Sun et al., 2008a). One of the main drawback of these techniques consists in their incapability to be applied in-situ, namely at the sample operative conditions of the CaO carbonation reaction, where the sorbent micro-structure is evolving due to the reaction.
X-ray Small-Angle Scattering (SAS) is a non-destructive and non-invasive technique that allows the micro-structural properties investigation of micro/nano-scale inhomogeneous materials, by means of differences in X-ray contrast (the electron density difference of the two phases) due to the scatteres (like pores, particles, micelles, polymers chains etc.). SAS can provide both qualitative and quantitative information about the micro-structural properties and morphology of the material in-homogeneities, namely pores in the case of porous materials. Specifically, the material porosity, specific surface area and mean pore radius, as well as pore size distributions (PSDs) are estimated (Chavez Panduro et al., 2012; Nguyen and Bhatia, 2012; Spalla, Lyonnard, and Testard, 2003; Beaucage, Kammler, and Pratsinis, 2004; Lee et al., 2014) from the measured scattering data, expressed in terms of scattering intensity profiles as a function of scattering vector modulus q.
The most relevant advantage of the X-Ray SAS technique is its possibility to be used *both*

ex-situ and in-situ.

In this work, the micro-textural properties of the CaO as solid sorbent were investigated for the *first time* by means of an in-situ approach using synchrotron radiation X-ray SAS technique. Specifically, different calcination operative conditions were explored in terms of temperature (650÷900 °C) and atmosphere composition (CO_2/N_2) in order to produce different CaO solid sorbent micro-structures by promoting or minimizing the sintering effects on the final pore network. Afterwards, these different sorbents were carbonated at 550 °C with 0.4 % of CO_2 in balance with N_2, in order to investigate the influence of sorbent micro-structure on the CaO carbonation reaction performances. SAS measurements were performed at the 9-ID-C beamline at the Advanced Photon Source (APS), Argonne National Laboratory. The beamline provides USAXS (Ultra Small Angle X-Ray Scattering), SAXS and WAXS measurements in an energy range between 10 and 24 keV, allowing a total measurable q-range (USAXS + SAXS) of about $0.0001 \div 1.0\,\text{Å}^{-1}$ (Ilavsky et al., 2009). This wide q-range allows to investigate porous materials whose pore size (pore diameter, d) varies from a minimum of about 1 nm up to a maximum of 10 µm (Ilavsky, 2010). In this way, both micro-pores (<2 nm) and meso-pores ($2 < d < 50$ nm) can be investigated.

7.2 Experimental details

7.2.1 Materials

Commercial calcium carbonate by AppliChem (marble granular A6297) was used as calcium oxide solid sorbent precursor (Tab. 6.1). This 150÷160 µm particle size was selected because it ensures a good compactness within the capillary used for the SAS measurements. Additional details on sorbent precursor are described in § 2.7.

7.2.2 In-Situ SR-SAXS, USAXS and WAXS experiments

In-situ time-resolved X-ray SR-based small and wide angle scattering measurements were performed during the CaO carbonation reaction at the beamline 9-ID-C of the Advanced Photon Source (APS), at Argonne National Laboratory.
The experiments consisted of investigating the CaO micro-textural properties during the CO_2 capture step, using completely calcined $CaCO_3$ samples obtained from a preliminary precursor ($CaCO_3$) thermal decomposition.
The experiments were performed by means of a flow-cell/furnace (Chupas et al., 2008) designed for conducting in-situ synchrotron-based studies of materials under non-ambient conditions, where samples were continuously illuminated by an X-ray beam. The experimental set-up allowed to control the sample environment conditions in terms of temperature (in this work up to 900 °C) and atmosphere/gas-flow.
About 5 mg of sample (powder-based $CaCO_3$) was loaded into a 1.1 mm internal diameter quartz capillaries (by Friedrich & Dimmock Inc, 0.2 mm wall thickness and 75 mm long), that filled about 3–5 mm of the capillary. Each sample was mounted on the flow cell system and linked to a set of pipes and fittings in order to flow the gas throughout the powder-based sample. Quartz wool was placed at the capillary extremities to fasten the powder on the capillary center in order to prevent any change of position during the experiments due to the gas-flow.
Both sorbent thermal activations and the CaO carbonation reactions were carried out flowing nitrogen and carbon dioxide mixtures throughout the sample. Pure nitrogen flows were fed from a N_2 gas cylinder (whose pressure was conveniently reduced at 1 bar), while CO_2/N2 mixtures were made and flowed through a syringe pump (Teledyne Isco 1000D Syringe Pump). During each experiment, sample temperature was controlled by means of

a K-type thermocouple, placed within the capillary in contact with the powder.
Measurements were carried out irradiating each the heating capillary with an incident monochromatric beam radiation of 24 keV with a wavelength of about 0.5166 Å. During each test, three different detectors were used in order to record the sample X-ray scattering data, namely the USAXS, SAXS and WAXS detectors (Ilavsky et al., 2013; Ilavsky et al., 2009). Each sample was probed using a specific illuminated area and an exposure time, namely 0.8×0.6 mm and 90 s for the USAXS detector and 0.8×0.2 mm and 20 s for the pin-SAXS and WAXS ones. The combination of these three detectors provides a corresponding wide q-range of about $2 \times 10^{-4} \div 7\,\text{Å}^{-1}$. Additionally, by considering the detectors movement time and the USAXS motor tuning step, the sampling frequency was approximately one each 4–5 min.
Before sample tests, blanks measurements were performed with empty capillaries in order to account for the scattering contribution of the experimental set-up, that was conveniently subtracted from the scattering response of each sample.

7.2.3 CaO samples preparation and carbonation tests

Typically, calcium carbonate is used as a sorbent precursor for CaO sorbents generation by means of thermal decompositions, where the initial non-porous $CaCO_3$ decomposes to porous CaO and CO_2. Because of the different molar volumes between the sorbent precursor and CaO (from $39.9\,\text{cm}^3\,\text{mol}^{-1}$ to $16.9\,\text{cm}^3\,\text{mol}^{-1}$) and the CO_2 release, the produced calcium oxide particles becomes porous, whose theoretical void fraction is up to 54 %.
In this study, commercial calcium carbonate samples were thermally decomposed and then sintered varying the furnace temperature, the atmospheric gas composition and the residence time in order to generate different porous CaO samples.
Calcite thermal decompositions were performed in N_2 or CO_2/N_2 atmosphere at 1 bar of total pressure with a gas flow rate of about $10\,\text{NmL}\,\text{min}^{-1}$. In this work, the gas flow rate was used for two main reasons, namely to control the atmosphere composition and to facilitate the CO_2 removal from the reaction zone that may locally affect both the calcination reaction (Criado et al., 1995; Galan, Glasser, and Andrade, 2013; Gallagher and Johnson, 1976; García-Labiano et al., 2002; Khinast et al., 1996; Mahuli et al., 1999; Manovic et al., 2009; Taghl Darroudi and Alan W. Searcy, 1981; Valverde, Sanchez-Jimenez, and Perez-Maqueda, 2015; Wilburn et al., 1991; Zhong and Bjerle, 1993) and sintering processes kinetics (Glasson, 1958; Alvfors and Svedberg, 1992; Beruto, Barco, and Searcy, 1984; Borgwardt, 1989a; Ewing, Beruto, and Searcy, 1979; Fuertes et al., 1991; Maya, Chejne, and Bhatia, 2017b; Milne et al., 1990).
The final calcination temperature was varied between 600 °C and 900 °C using a heating rate of $20\,^\circ\text{C}\,\text{min}^{-1}$, while the atmosphere sample composition was ranged from pure N_2 to 50 % of CO_2 (on volumetric basis) in balance with N_2. More specifically, non-isothermal calcination reactions were performed in nitrogen atmosphere by exploring three final temperatures: 650 °C, 680 °C and 700 °C. On the other hand, three samples were calcined at 800 °C with 1 %, 5 % and 10 % of CO_2 in balance with nitrogen and other three at 900 °C with 10 %, 25 % and 50 % of CO_2. Once the calcite decomposition was completed, an additional isothermal heating step (15÷160 min) was considered to allow sintering mechanisms to affects the sorbent micro-structure in terms of porosity, specific surface area and mean pore radius.
After the precursor activation, each sample was cooled down to 550 °C keeping flowing the sample with N_2. Afterward, the CaO carbonation step was carried out isothermally with 0.5 % of CO_2 in balance with nitrogen at 1 bar. This atmosphere was maintained constant with gas flow rate of about $10\,\text{NmL}\,\text{min}^{-1}$ controlled by the syringe pump for a minimum of 70 min up to a maximum of 180 min.

Table 7.1: Summary of the experimental operative conditions. CO_2 contents are in balance with N_2.

Sample	T_{calc} [°C]	Calcination CO_2 % vol. [−]	Calcination time [min]	Sintering time [min]	T_{carb} [°C]	Carbonation CO_2 % vol. [−]	Slit length $\left[\text{Å}^{-1}\right]$
A	650	0	36	33	550	0.4	0.024111
B	680	0	30	17	550	0.4	0.025020
C	700	0	26	60	550	0.4	0.025020
D	800	1	9	109	550	0.4	0.024906
E	800	5	36	133	550	0.4	0.024906
F	800	10	56	129	550	0.4	0.025020
G	900	10	9	122	550	0.4	0.024906
H	900	25	13	133	550	0.4	0.024906
I	900	50	136	141	550	0.4	0.024906
J	680	0	31	15	500	0.1	0.025020
K	650	0	91	160	500	0.5	0.025020
L	680	0	26	19	500	0.5	0.025020

A summary of all the experiments performed in this work is listed in Tab. 7.1, where both calcination and carbonation reaction conditions are specified for each sample.
On the other hand, three samples were carbonated at 500 °C with 0.1 % of CO_2 (sample J) and with 0.5 % of CO_2 (samples K and L) as listed in Tab. 7.1.
The aforementioned operative conditions were conveniently chosen in order to slow-down the reaction rates by means of temperature and atmosphere composition to obtain a reasonable number of sampling during the experiments according to the detectors sampling frequency (one scan every 4–5 min).
During the experiments, a one-dimensional (slit smeared) collimated USAXS detector was used to record absolute intensity calibrated scattering data (Ilavsky et al., 2009). On the other hand, a two-dimensional SAXS (pinhole collimated) and WAXS detectors were used to collect the sample scattering data in the small and wide angle regions.

7.2.4 WAXS data analysis for sample composition estimation

Time resolved Wide Angle X-ray Scattering (WAXS) data were collected in terms of scattering intensity over the scattering vector q by means of Nika program (Ilavsky, 2012). WAXS data patterns showed the CaO and $CaCO_3$ intensity peaks over the scattering vector q allowing to provide the sample composition (CaO and $CaCO_3$ content) estimation for each time-step as shows in Fig. 7.1. Solid sample compositions are essential to estimate the conversion over the reaction time profiles of the CaO carbonation reaction. In fact, WAXS data could be easily converted in terms of intensity versus two-theta values and analyzed by means of the Rietveld profile method providing the sorbent chemical compositions. However, because of the WAXS detector low resolution, poorly discretized WAXS intensity patterns over q were recorded, such that each diffraction peak was described by less than 6–7 experimental points (in terms of intensity and scattering vector or, equivalently, two-theta angle). For this reason, in this work CaO weight fractions over the reaction time, $w_{CaO}(t)$, were estimated by means of the ratio between the experimental CaO peak areas of pure fresh sorbent and those of the partially carbonated sorbent. Areas under the peaks were numerically computed from the WAXS experimental data using the trapezoidal rule.

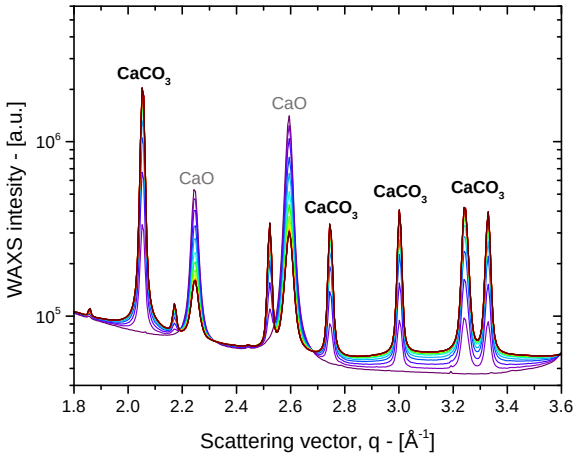

Figure 7.1: Typical time-resolved WAXS pattern during a CaO carbonation reaction at 550 °C with 0.4 % of CO_2 in balance with N_2 (sample A).

Afterwards, $CaCO_3$ weight fractions $w_{CaCO_3}(t)$ were calculated as $1 - w_{CaO}(t)$. Calcium oxide weight fractions were used to calculate the sorbent conversion X_{CaO} over the reaction time according to Eq. (2.20).

7.2.5 USAXS and SAXS data reduction in absolute intensity scale and sorbent textural properties calculation

Time resolved USAXS data were reduced by means of Indra program (Ilavsky and Jemian, 2009) after the blank subtraction. The scattering curves were then normalized in terms of absolute units (Zhang et al., 2010), namely in terms of the differential scattering cross section over the scattering vector q. The measured intensity profile $I(q,t)$ over time at the detector is related to the differential scattering cross section per unit volume of the illuminated sample and per unit of solid angle (indicted with Ω) $d\Sigma/d\Omega$ by Eq. 4.47 Ilavsky et al. (2009) and Long et al. (1991).

Because of the cylindrical geometry of the capillary and because the samples are granular materials, it is difficult to precisely estimate the illuminated sample volume. More conveniently, the instantaneous absolute intensity was expressed in terms of unit of sample mass (inside the illuminated volume) instead of unit of sample illuminated volume. Therefore, the sample thickness e_s was replaced by the instantaneous solid phase thickness e_{solid} that was estimated using the Lambert-Beer law from the time-resolved measured sample transmission coefficient $T(t)$ and the linear absorption coefficient $\mu(t)$ calculated for each time-step. For each time step the differential scattering cross section per unit of sample mass sample mass $d\Sigma_m/d\Omega$ is equal to $d\Sigma/d\Omega$ multiplied by the illuminated sample volume and divided by the sample mass, according to Eq. 4.50. The instantaneous linear absorption coefficients and sample densities were computed from those of pure species listed in Tab. 6.1 by means of the CaO and $CaCO_3$ weight fractions over the reaction time estimated from the WAXS data.

Time-resolved SAXS scattering profiles were reduced using the Nika program (Ilavsky et al., 2012) subtracting the blanks scattering profiles. These two data-sets (USAXS and SAXS profiles) were finally merged with the Irena package (Ilavsky and Jemian, 2009), to obtain the whole scattering intensity vs q profiles for each time-step of the USAXS and SAXS detectors. In this work the absolute calibration of SAXS data was not necessary because of the absolute calibrated USAXS data that provided to the SAXS profiles

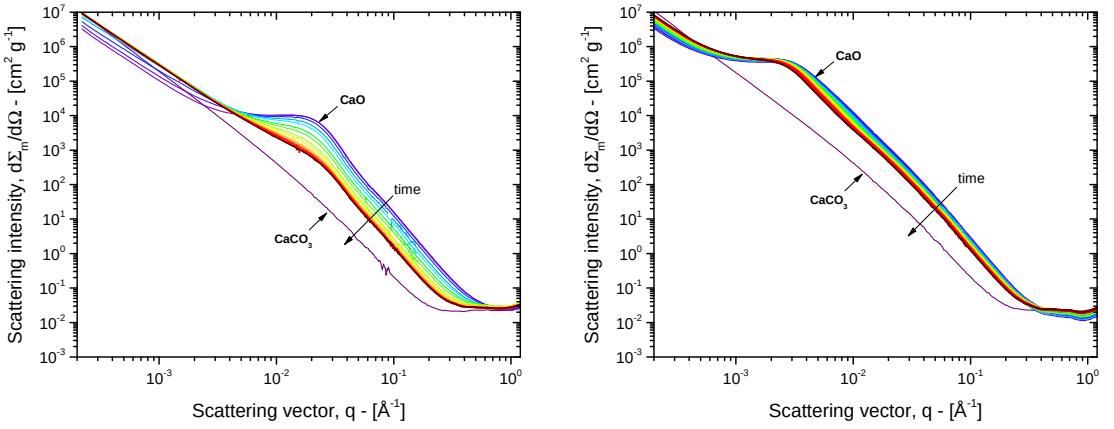

(a) *Sample A* - 650 °C N_2. **(b)** *Sample A* - 800 °C 10 % *of* CO_2.

Figure 7.2: Experimental slit smeared scattering intensity profiles evolution during the CaO carbonation reaction of samples A (a) and F (b), whose sorbent precursors were obtained by means of calcination reactions at 650 °C in N_2 and 800 °C with 10 % of CO_2 in balance with N_2. Slit-lengths are listed in Tab. 7.1.

the proper intensity magnitude. A typical example of time-resolved USAXS+SAXS data expressed in terms of absolute units (per unit of mass) is showed in Fig. 7.2.

Because of the one-dimensional collimating geometry for the USAXS data collection, the measured scattering intensity profiles are affected by slit smearing. However, in this work no desmearing procedure (Ilavsky et al., 2013; Lake, 1967; Pete R. Jemian, 1990) was necessary, because the slit smearing effects are numerically accounted for into the Irena packages (Ilavsky and Jemian, 2009). Therefore, all the scattering intensity profiles showed in this work refer to slit-smeared curves in the USAXS region (approximately between $2 \times 10^{-4} \div 0.1\,\text{Å}^{-1}$).

The analysis of the USAXS and SAXS time-resolved intensity profiles (expressed in terms of absolute units on a sample mass basis) was performed using the IGOR Pro-based IRENA program (Ilavsky and Jemian, 2009). In this work, the slit-smeared scattering intensity profiles were fit by means of the "Unified fit" tool that is based on the unified approach proposed by Beaucage (1995) and Beaucage (1996). This model allows the description of the SAS profiles over a wide range of q by means of an arbitrary number of interrelated structural levels, providing to the model a high flexibility in describing the SAS response of multiple-size-scale structures (Beaucage, 1995). According to Beaucage (1995), each level is described by a Guinier and a power law regime. Specifically, a Porod regime is a particular power law case that arises when the local scattering intensity vs q slope in a double logarithmic plot is -4 (Glatter and Kratky, 1982).
The analysis of the time-resolved small angle scattering data by means of the "Unified fit" approach refers to § 4.6 where Eq. 4.60 was applied for each time step of the collected USAXS/SAXS experimental data.

7.3 Results and Discussion

7.3.1 USAXS/SAXS data: profiles and trends

Time-resolved experimental scattering intensity profiles of samples (listed Tab. 7.1) were used to compute the sample textural properties (radius of gyration, specific surface,

porosity, PSD and pore number density) evolution during the CaO carbonation reaction step. The sorbent micro-textural properties trends over time and over CaO conversions were identified and verified.

As can be observed form the experimental scattering intensity profiles showed in Figs. 7.2a and 7.2b (for the cases of sample A and F), three different regions can be identified (by looking at the profiles from the right to the left). The first region is placed at high-q values and is characterized by a flat-like scattering intensity profile due to the background contribution to the scattering experimental response. A second region can be located roughly between 1.5×10^{-3} Å^{-1} and 6×10^{-1} Å^{-1}. In the first part of this second region, a plateau can be observed, defining a Guinier regime, that is followed (in the direction of high-q values) by a decreasing trend of the scattering intensity down to the background region. A third region can be observed at lower-q values (approximately between 1×10^{-4} Å^{-1} and 1.5×10^{-3} Å^{-1}) and is approximately described by a power-law profile.

On the other hand, the experimental scattering responses of the undecomposed $CaCO_3$ seems to be not provided by a second region and Guinier regimes are not observed, as shown by the experimental $CaCO_3$ scattering profiles (black lines) of Figs. 7.2a and 7.2b.

The last region represents the experimental scattering response of large structures, that are associated with the scattering response of the sorbent particles (whose particle diameter is 150÷160 µm), and, more precisely, to the inter-particle voids that they generate. These large structures size can be roughly estimated by means of Eq. (2.18).

obtaining a maximum scatterer size of about 6 µm. This value suggests that the inter-particle void scattering response is compatible with this low-q region. Additionally, this region is influenced by multiple scattering effects that distort the local scattering intensity profile and the single scattering analysis cannot be correctly applied. For this reason none structural information can be obtained from this region under this assumption.

7.3.2 Unified fit application to USAXS/SAXS data: structural levels and structure factor

Sorbent precursor powder-based calcium carbonate is the staring material of each experiment, whose scattering intensity profile is showed in Figs. 7.2a and 7.2b. As previously mentioned, only two region are shown by the $CaCO_3$ scattering profile respect to those of the completely calcined samples (Fig. 7.2). On the other hand, the analysis of the time-resolved scattering intensity profiles during the CaO carbonation reaction by means of the unified fit revealed that the second region (after the first Guinier plateau) is characterized by a non-constant power-law slope, suggesting the presence of additional structural levels that overlap in the direction of the high-q values. This is represented in Figs. 7.3a, 7.3c and 7.3e where the experimental scattering response of sample C, F and I is showed and compared with their respective unified fit profile results and theirs local levels. This behavior is observed both in the completely calcined samples intensity profiles (before the carbonation) and in those of the partially carbonated samples, specifically at the transition point, as shown in Figs. 7.3a, 7.3c and 7.3e. Additionally, this non-constant power law slope of the scattering intensity is emphasized by considering the Porod representation of the experimental scattering intensity profiles showed in Figs. 7.3b, 7.3d and 7.3f.
Specifically, three levels are required in order to accurately fit the experimental scattering intensity profile of samples before and during the the CaO carbonation reaction, while two levels do not guarantee a reasonable fitting result, according to Benedetti et al. (2017).

Therefore, the scattering intensity profile representation by means of three structural levels and specifically by two levels in the second region suggests that the sorbent pore network (internal porosity) is characterized by two different structures, namely by two distinct populations of pores, as previously noticed by Li, Liang, and Cai (2016), Li, Cai,

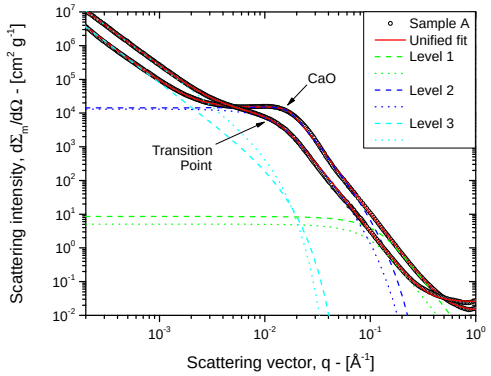

(a) *Sample C - $d\Sigma_m/d\Omega$ vs q.*

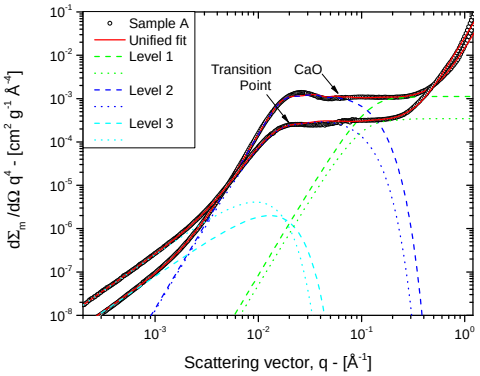

(b) *Sample C - $d\Sigma_m/d\Omega\, q^4$ vs q.*

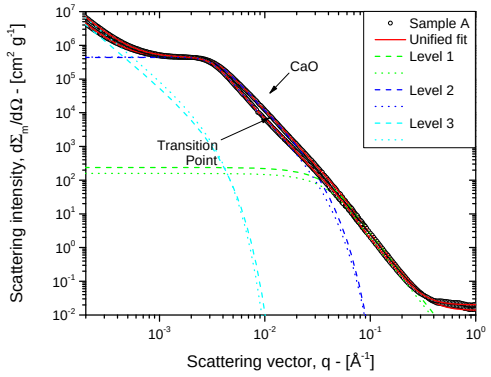

(c) *Sample F - $d\Sigma_m/d\Omega$ vs q.*

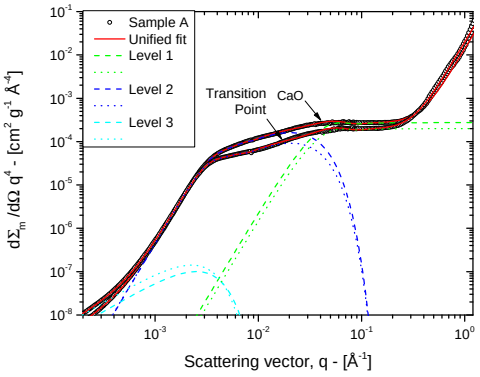

(d) *Sample F - $d\Sigma_m/d\Omega\, q^4$ vs q.*

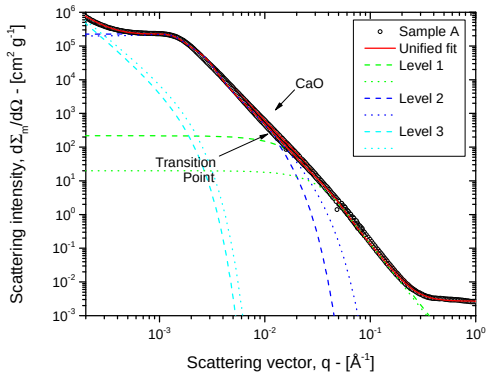

(e) *Sample I - $d\Sigma_m/d\Omega$ vs q.*

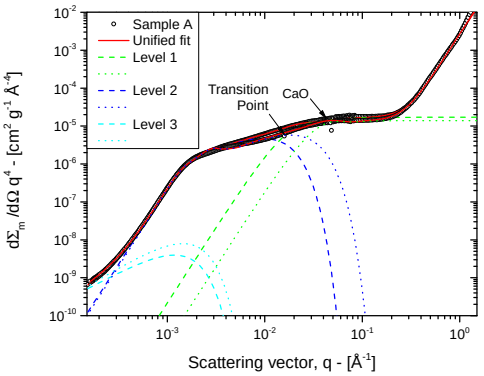

(f) *Sample I - $d\Sigma_m/d\Omega\, q^4$ vs q.*

Figure 7.3: Comparison between the experimental slit smeared scattering intensity profiles and fitting results by means of the unified fit approach with local levels between the scattering response fresh CaO and at the transitions point of the CaO carbonation reaction for sample C (a), sample F (c) and sample I (d). The scattering intensity trends are emphasized in the Porod representation (b, d and e). Slit-lengths are listed in Tab. 7.1.

and Huang (2006), Maya, Chejne, and Bhatia (2017a), Rodriguez-Navarro et al. (2009), and Zhu, Wu, and Wang (2011) and, more recently by Benedetti et al. (2017) by means of the USAXS/SAXS technique. On the other hand, the undecomposed $CaCO_3$ representation through two levels (namely only one for the single scattering region) reveals a calcite structure made of a single scatters population.

According to Eq. (4.60), in the unified fit approach P_1 and P_2 are the power-law exponents of the first and second levels, namely of the two populations that are approximately placed inside the q-range $2 \times 10^{-3} \div 3 \times 10^{-1}$ Å^{-1}. The Porod's analysis (Porod, 1951) associated to these exponents the value of 4 (Porod's law) when the scattering response derives from a smooth and sharp interface (Hu et al., 2011). In this work, such interface is the pore-solid interface of the CaO sorbent, namely the specific surface area associated with the pore network. In order to verify the Porod's exponents values of the two populations a non-linear fitting of the unified fit model over the experimental scattering intensity profiles was performed to estimate P_1 and P_2. The resulting numerical values of these two parameters ranged from 3.85 to 4.10 on average. Therefore, these two exponentials were set to be 4 and the corresponding B_1 and B_2 constants become the Porod's law proportionally constants.
In the third level G_3 was set to zero because no Guinier regime was observed. Additionally, because this third region is affected by multiple scattering effects that distort the local trends, the power-law exponent P_3 was left as a free fitting parameter because none physical meaningful information can be obtained by means of the single scattering approach.

As the CaO carbonation reaction progresses the pores concentration increases up to arise scattering interferences. Therefore, in order to take into account this phenomenon, the structure factor $S(q,t)$ of Eq. (4.59) was taken into account in the profile fitting for the second level. The structure factor was not necessary for the case of the first structural level associated with the first smaller in size pore population. In this cases $S(q,t)$ was set equal to 1.

Despite the initial uncarboanted sorbent scattering intensity profiles of samples J, K and L are characterized by three structural levels, their scattering profiles gradually evolves up to provide scattering intensity profiles for which four different structural levels are necessary to obtain the best fit results. This behavior is showed in Fig. 7.4a for the uncarbonated CaO sorbent of sample K and Fig. 7.4b when the carbonation reaction reached the transition point between the kinetic regimes. Specifically, the Porod plots empathized the different trends of the scattering intensity profiles, especially in the second region profile, as shown in Figs. 7.4c and 7.4d. Moreover, the experimental scattering derivatives are particularly useful to appreciate the non-constant trend after the Gunier regime (towards high-q values), as shows in Fig. 7.4e and 7.4f where maxima confirm the different pore structures, especially in the correspondence of the transition point. Because of the experimental noise (especially in the overlapping region of USAXS and SAXS profiles), a smoothing filer was necessary to achieve reasonable scattering intensity derivative profiles and a Savitzky-Golay filter (Savitzky and Golay, 1964) was used.

7.3.3 Sorbent textural properties evolution

The main focus of this work is to investigate the influences of the sorbent micro-textural properties on the CaO carbonation reaction performances in terms of reaction kinetics and maximum CO_2 capture capacity. For this reason, different sorbent micro-structures were generated varying the $CaCO_3$ calcination reaction conditions in terms of final temperature, atmosphere composition (N2/CO2 content) and residence time at high temperature (Tab. 7.1). Before the carbonation reaction, each fresh CaO sample scattering

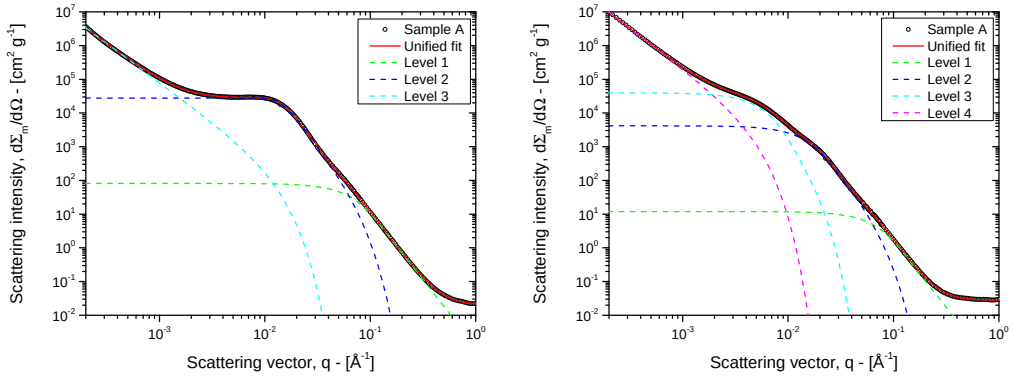

(a) $d\Sigma_m/d\Omega$ *vs* q. **(b)** $d\Sigma_m/d\Omega$ *vs* q.

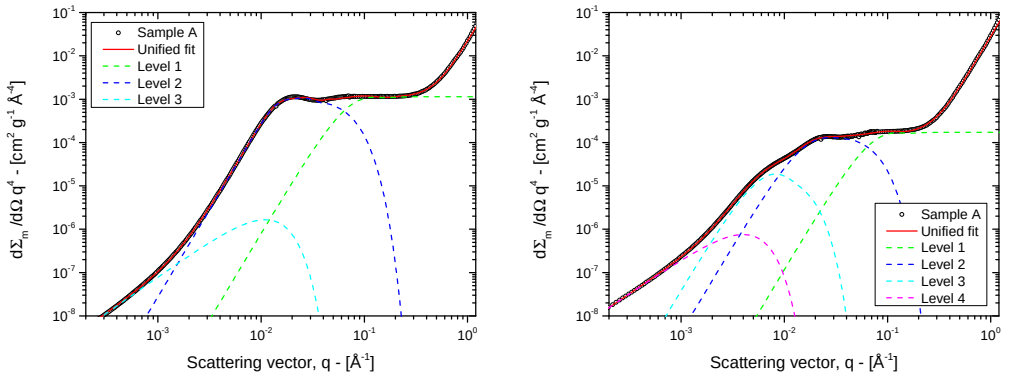

(c) $d\Sigma_m/d\Omega\, q^4$ *vs* q. **(d)** $d\Sigma_m/d\Omega\, q^4$ *vs* q.

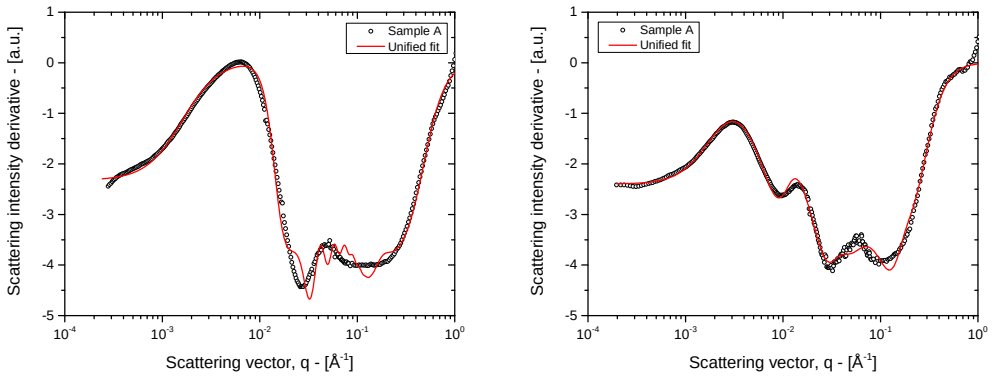

(e) *Scattering intensity derivative over* q. **(f)** *Scattering intensity derivative over* q.

Figure 7.4: Experimental slit-smeared scattering intensity profiles and unified results with local levels of the fresh CaO sorbent (a) and at the transition point (b) of sample K. These levels are also represented in the Porod plots (c) and (d) and compared with the experimental data. A final comparison is proposed between the experimental scattering intensity derivatives and with those of the model with three (e) and four (f) levels. Slit-lengths are listed in Tab. 7.1.

Table 7.2: Initial sorbent micro-textural properties of uncarbonated CaO samples.

Sample	$R_{g,1}$ [Å]	$R_{g,2}$ [Å]	$S_{m,1}$ [$m^2\,g^{-1}$]	$S_{m,2}$ [$m^2\,g^{-1}$]	S_m [$m^2\,g^{-1}$]	ε_1 [–]	ε_2 [–]	ε [–]	$N_{m,1} \times 10^{-16}$ [g^{-1}]	$N_{m,2} \times 10^{-16}$ [g^{-1}]	$N_m \times 10^{-16}$ [g^{-1}]	$\langle R_v \rangle$ [Å]
A	25	85	54.1	61.1	115.2	0.101	0.386	0.487	248.68	12.47	261.14	73
B	22	88	56.9	74.2	131.1	0.088	0.434	0.522	396.29	17.14	413.43	74
C	16	106	38.4	53.4	91.8	0.039	0.408	0.447	522.02	8.50	530.52	93
D	23	200	18.3	25.2	43.5	0.030	0.379	0.408	92.76	1.08	93.84	180
E	21	319	11.2	16.1	27.3	0.018	0.405	0.423	63.24	0.30	63.54	292
F	41	500	10.2	15.3	25.5	0.033	0.523	0.556	18.90	0.17	19.06	429
G	26	542	7.1	9.9	17.1	0.014	0.403	0.417	26.67	0.07	26.74	450
H	97	652	5.8	9.0	14.8	0.039	0.348	0.388	1.61	0.04	1.65	497
I	109	1048	0.6	0.9	1.5	0.005	0.061	0.065	0.686	0.001	0.688	861
J	22	94	51.6	68.6	120.2	0.077	0.437	0.514	195.24	6.42	201.67	80
K	26	126	39.1	52.2	91.4	0.074	0.471	0.546	313.80	12.63	326.43	109
l	24	97	50.9	65.5	116.4	0.085	0.445	0.530	379.43	14.08	393.51	83

intensity profile was analyzed by means of the unified fit approach of Eq. 4.60 providing its micro-textural properties, as listed in Tab. 7.2.

Specifically, the initial micro-structure of these samples is characterized by two different populations of pores, according to the structural level number used in the unified fit approach. Samples calcined below 800 °C in N_2 (A÷C and J÷L) provide the highest textural properties than the other samples showing high total specific surface areas (from 91.4 $m^2\,g^{-1}$ to 131.1 $m^2\,g^{-1}$) and porosities (up to 0.546). Furthermore, it is noticeable how the micro-pore population exhibits a comparable specific surface area with that of the meso-pore population, despite the significant low porosity (0.04÷0.1) if compared with that of the meso-pores that mainly contribute to the overall pore volume fraction. This behavior is ascribed to the high surface-to-volume ratio of the micro-pores and, more specifically, to the high specific micro-pore number (per unit of mass) that is almost one order of magnitude greater than the meso-pore number per unit of mass, namely ranging from $195.2 \times 10^{16}\,g^{-1}$ to $522.0 \times 10^{16}\,g^{-1}$ respect to $6.4 \div 17.1 \times 10^{16}\,g^{-1}$ (Tab. 7.2). Precisely, the specific pore number per unit of mass was estimated from the sorbent pore size distributions (Fig. 7.5) according to Eqs. (4.69) and (4.70).

Moreover, according to Tab. 7.2 these samples are characterized by small radii of gyration if compared with samples calcined at higher temperature and in presence of CO_2. The smaller radius of gyration, $R_{g,1}$, ranges from 16 Å up to 26 Å meaning that the first pore population is placed between the micro- and meso-pore ranges. On the other hand, the second population radius of gyration ($R_{g,2}$) is placed in the meso-pore region, ranging from 85 Å to 126 Å. As previously mentioned, according to Beaucage, Kammler, and Pratsinis (2004) the unified fit parameters that result from the experimental intensity profile analysis are used to estimate the sample pore size distribution under the assumption of spherical pore shape, as represented in Fig. 7.5a, showing bimodal distribution according to the two populations of pores. Although the different final calcination temperatures (650 °C, 680 °C and 700 °C), the final sorbent PSDs are fairly similar, because of negligible sintering effects in the final sorbent pore network (Borgwardt, 1985; Borgwardt, 1989b).

As far as samples calcined at high temperature and in presence of CO_2 in the reactor atmosphere (samples D÷I), these are characterized by a lower micro-textural properties if compared with those of the N_2 calcined samples, because of the sintering effects on the CaO micro-structure promoted by the presence of CO_2 in the atmosphere (Beruto, Barco, and Searcy, 1984; Borgwardt, 1989b; Fuertes et al., 1991; Borgwardt, 1989a; Maya, Chejne, and Bhatia, 2017b; Sun et al., 2007; Zhu, Wu, and Wang, 2011). More specifically, samples calcined at 800 °C (D, E and F) exhibit specific surface areas at least two times lower than those of the N_2 calcined samples, ranging from 25.5 $m^2\,g^{-1}$ to 43.5 $m^2\,g^{-1}$ (Tab. 7.2). Although this evident reduction in the total specific surface area, the sorbent porosity is still high (0.41÷0.56) where the meso-pore population provides the majority of the pore volume. The lower specific surface areas (respect to samples calcined below 800 °C) are explained by an increase of the meso-pore radius of gyration that ranges from 200 Å to 500 Å and by a significant decrease of the specific pore number of the two pore populations, namely $18.9 \div 92.8 \times 10^{16}\,g^{-1}$ for micro-pores and $0.2 \div 1.1 \times 10^{16}\,g^{-1}$ for meso-pores. On the other hand, the micro-pore population radius of gyration is quite similar to that of samples calcined below 800 °C in nitrogen and increases up to 41 Å when the 10 % of CO_2 in the reactor atmosphere is considered. Even in this case, the low micro-pore radius combined with a high specific pore number provide a micro-pore specific surface area fairly similar to that of the meso-pores, that ranges from 10.2 $m^2\,g^{-1}$ to 18.3 $m^2\,g^{-1}$ respect to 15.3÷25.2 $m^2\,g^{-1}$ of the meso-pore population. However, because of the high pore volume fraction of meso-pores, the overall mean pore radius increases up to 450 °C as listed in Tab. 7.2.

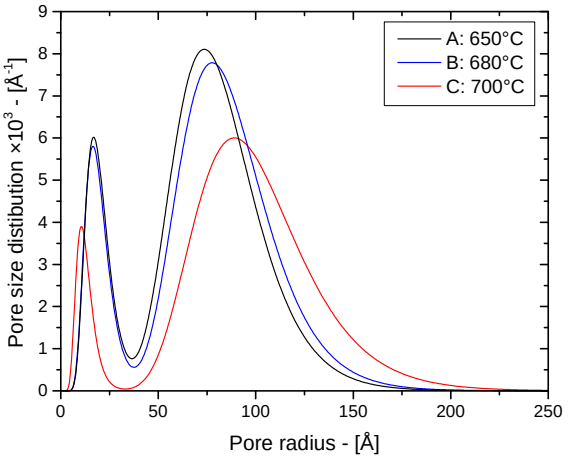

(a) *Samples A, B and C.*

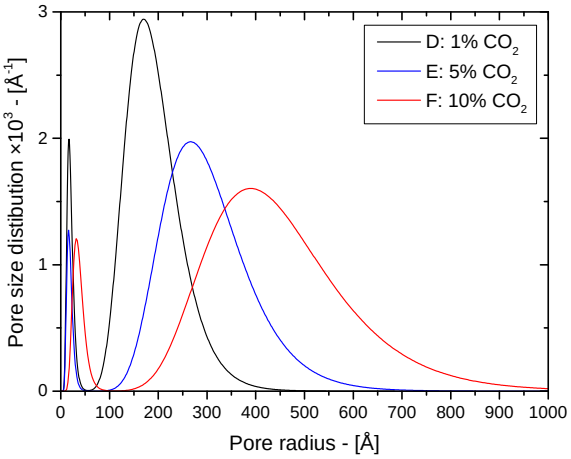

(b) *Samples E, F and G.*

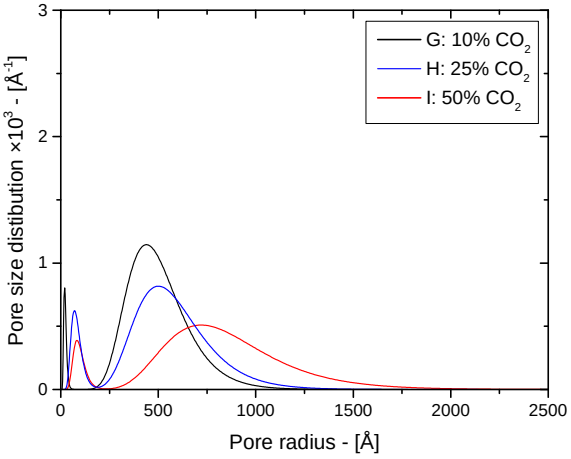

(c) *Samples I, J and K.*

Figure 7.5: Comparison between the initial sorbent pore size distributions of different uncarbonated CaO samples obtained through different calcination reaction conditions, namely at temperatures below 700 °C in N_2 (a), at 800 °C (b) and at 900 °C (c) with different CO_2 contents in balance with N_2.

Samples G, H and I were thermally activated at 900 °C by considering high CO_2 contents in the reactor, namely 10 %, 25 % and 50 %, and considering a sintering step that ranges from 109 min to 133 min (Tab. 7.1). The resulting sorbent micro-structure is significantly affected by the high temperature sintering mechanisms (Beruto, Barco, and Searcy, 1984; Borgwardt, 1989a; Maya, Chejne, and Bhatia, 2017b). Specifically, according to the micro-textural properties listed in Tab. 7.2, the material specific surface area is quite reduced respect to the low sintered samples, ranging from a minimum of $1.5\,m^2\,g^{-1}$ to a maximum value of $17.1\,m^2\,g^{-1}$. These values are associated with sample porosities that are 0.42 and 0.39 for the case of samples G and H, but decrease down to 0.07 for sample I calcined at 900 °C with 50 % of CO_2, where sintering phenomena largely contributed to affect the sorbent pore structure. These trends are consistent with the micro- and meso-pore number per unit of sample that is reduced down to four and three order of magnitude respectively if compared with those of samples calcined below 800 °C (Tab. 7.2). In addition, high mean pore radii are observed for this sample set, that increase up to 861 Å for the case of sample I, whose micro-pore and meso-pore radii of gyration grew up to 109 Å and 1048 Å respectively during the reaction.
As a result, the PSDs of the 800 °C and 900 °C samples are quite different from those of samples calcined below 800 °C, as shown in Fig. 7.5. Specifically, sintering mechanisms (accelerated by the presence of CO_2) shift the porosity distribution in the direction of the high pore radius and this effect is further emphasized by the increase of the CO_2 content during the calcite thermal decomposition. Additionally, it is remarkable to notice how sintering phenomena effects on the sorbent micro-structure significantly increase with temperature and CO_2 from 800 °C and 900 °C as shown in Figs. 7.5b and 7.5c.

Afterwards, these highly different sorbents (A÷I) pore networks were isothermally carbonated at 550 °C with 0.4 % of CO_2 in balance with N_2. Because of the non-catalytic gas-solid nature of the CaO carbonation reaction, the initial sorbent micro-structure strongly influence the reaction kinetics itself and significant different conversion over time profiles were obtained as shown in Fig. 7.6, although the same carbonation reaction conditions. As previously mentioned, the calcium oxide conversion profiles were obtained from the WAXS data analysis collected during the experiments. Different initial sorbent micro-structures provided different behaviors during the reaction, in terms of induction period (Bhatia and Perlmutter, 1983a), reaction rate (dX_{CaO}/dt), transition point (from the fast and chemically kinetic regime to the slow and product layer diffusion controlled one) and maximum CO_2 uptake, as shown in Fig. 7.6.
Specifically, according to several literature contributors (Barker, 1973; Abanades and Alvarez, 2003; Bhatia and Perlmutter, 1983a; Grasa et al., 2009; Stanmore and Gilot, 2005; Sun et al., 2008a; Grasa et al., 2009; Biasin et al., 2015) the transition point ($X_{CaO,TP}$) is usually associated with the change in slope of the CaO conversion over time profile from the fast to the slow stage of the reaction. Although this transition occurs quite suddenly at a given level of conversion (Abanades and Alvarez, 2003), a general procedure to determine such conversion position has never been proposed. Therefore, because of its relevance in the investigation of the CaO carbonation reaction (especially for in-situ tests), in this work the transition point was associated with the minimum value of the CaO over time conversion second derivative, as shown in Fig. 7.7. This method allowed to definitely identify that point where the conversion over time profile changes its slope. This is particularly useful when the transition between the two kinetics regimes is not evident, as for the cases of the high sintered samples (D÷I) that provided smoother transitions (Figs. 7.6b and 7.6c) respect to those materials calcined below 800 °C in N_2 showed in Fig. 7.6a. Specifically, before the numerical differentiation of the conversion over time profiles a 3rd degree Savitzky-Golay filter (Savitzky and Golay, 1964) was used to reduce the experimental noise of data. Afterwards, the first and second derivatives of the conversion

profiles were computed by means of the numerical procedure of Savitzky and Golay (1964).

As previously mentioned, samples calcined below 800 °C in nitrogen provided similar PSDs as shown in Fig. 7.5a. Additionally, the initial micro-textural properties of these samples are almost similar, as listed in Tab. 7.2. Therefore, similar CaO conversion over time profiles were obtained (Fig. 7.6a), that slightly differ from each others only in the induction period. Nevertheless, the slope of the kinetic regime, the transition points (0.50, 0.57 and 0.56 for sample A, B and C respectively, as listed in Tab. 7.3) and the maximum CaO conversion (about 0.65) are almost the same.

On the other hand, the highly sintered samples provided different conversion profiles that exhibit a smoother transition point, a slow reactivity (in terms of chemically controlled regime slope) and a lower transition point. Interestingly, even though the 800 °C calcined samples provide high porosity values (comparable to those of samples A, B and C) and, thus, a higher maximum theoretical conversions, their transition points occurred at 0.43 (sample D), 0.23 (sample E) and 0.16 (sample F) that are quite lower than those of samples A, B and C.

According to Tab. 7.3, the more the CO_2 content during the $CaCO_3$ thermal activation and sintering steps (and, thus, the more sintering effects on the fresh CaO sorbent), the less the transition point conversion during the CaO carbonation reaction. This behavior is observed both in 800 °C calcined samples and in the 900 °C ones, whose transition conversion values are 0.12 (sample G), 0.09 (sample H) and 0.05 (sample I).

Additionally, the product layer diffusion controlled step of these samples is characterized by a (slow) still increasing trend, as shown in Figs. 7.6b and 7.6c, opposite to the samples A, B and C profiles, whose slow regime is almost flat, as emphasized by the first derivative trend in Fig. 7.7.

Fig. 7.8 shows the pore population radii of gyration evolution over time, where the meso pore-radius of gyration increases with time as the carbonation reaction progresses. More specifically, the meso-pore radius of gyration increases up to an asymptotic value, that is achieved in the correspondence of the transition point, as shown in Fig. 7.8a for the case of sample B and C, ranging from an initial value of 88 Å and 106 Å (Tab. 7.2) up to 155 Å and 147 Å respectively (Tab. 7.3). Even though the sample A meso-pore radius of gyration seems to be quite constant, its magnitude slightly increases during the CaO carbonation reaction, namely from an initial value of 85 Å to 105 Å when the transition point is reached. On the other hand, the micro-pore radius of gyration is quite constant over the reaction, ranging around an average value of about 20 Å.

Fig. 7.8b, shows the radius of gyration evolution for those samples calcined at 800 °C that exhibit an increase of the meso-pore radius of gyration with time, even though the growth rate is less intense respect to the former cases. This is clearly in agreement with the carbonation kinetics of samples D÷E showed in Fig. 7.6b. Interestingly, consistent with samples calcined in nitrogen below 800 °C, the most relevant increase of the meso-pore radius of gyration is observed for the case of sample D, calcined at 800 °C with 1 % of CO_2, namely from an initial value of 200 Å up to the transition point value of 270 Å, whereas sample E and F show an increase of 59 Å and 36 Å for their respective initial values (Tabs. 7.2 and 7.3). In addition, it is remarkable to notice that sample D shows the lowest sintering effects on the final sorbent micro-structure respect to those activated in presence of higher CO_2 contents, according to the sample micro-textural properties of Tab. 7.2.

The meso-pore radius of gyration increase becomes less intense when highly sintered sorbents are carbonated, as for the cases of samples G÷H, namely those calcined at 900 °C in presence of high CO_2 contents. In fact, Fig. 7.8c shows a modest meso-pore population radius of gyration as the reaction progresses. This behaviour is ascribed to the highly sintered pore structure, that provides a low sorbent reactivity, as shown in Fig. 7.8c. Although some experimental noise in the data (especially for sample I) their meso-pore

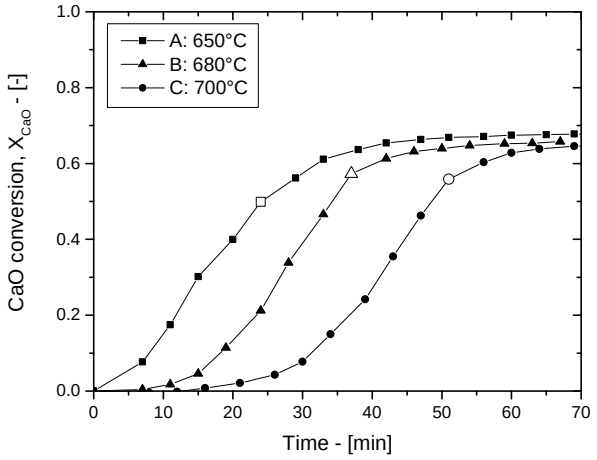

(a) *Samples A, B and C.*

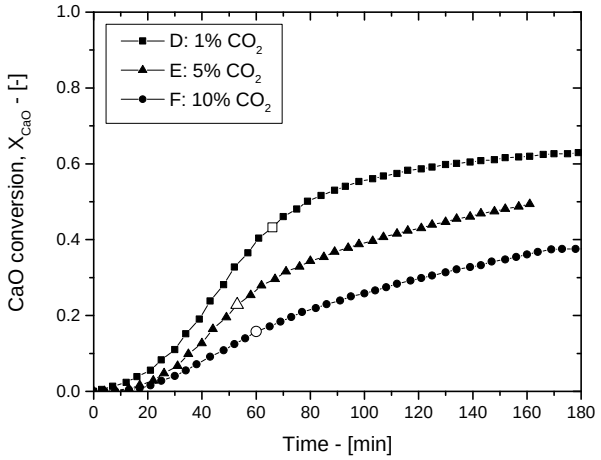

(b) *Samples E, F and G.*

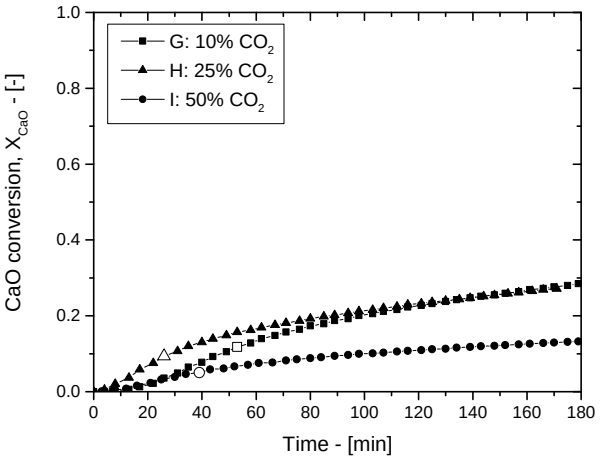

(c) *Samples I, J and K.*

Figure 7.6: Calcium oxide conversion profiles for isothermal carbonations at 550 °C with 0.4 % of CO_2 in balance with N_2. Legends refer to calcination operative conditions (temperature and CO_2 content), while empty markers highlight the reaction kinetics transition point.

Table 7.3: Sorbent micro-textural properties estimated at the transition point.

Sample	$R_{g,1}$	$R_{g,2}$	$S_{m,1}$	$S_{m,2}$	S_m	ε_1	ε_2	ε	$N_{m,1}$ $\times 10^{-16}$	$N_{m,2}$ $\times 10^{-16}$	N_m $\times 10^{-16}$	$\langle R_v \rangle$	time	$X_{\mathrm{CaO},TP}$
	[Å]	[Å]	$[\mathrm{m^2\,g^{-1}}]$	$[\mathrm{m^2\,g^{-1}}]$	$[\mathrm{m^2\,g^{-1}}]$	[–]	[–]	[–]	$[\mathrm{g^{-1}}]$	$[\mathrm{g^{-1}}]$	$[\mathrm{g^{-1}}]$	[Å]	[min]	[–]
A	17	105	15.5	23.6	39.1	0.016	0.131	0.148	101.50	2.39	103.89	88	24	0.50
B	19	155	10.8	15.7	26.5	0.012	0.098	0.110	53.92	0.72	54.64	122	37	0.57
C	18	147	11.3	14.6	25.8	0.012	0.111	0.122	69.89	0.96	70.85	118	51	0.56
D	25	270	6.0	8.3	14.2	0.009	0.159	0.168	19.23	0.14	19.37	251	66	0.43
E	24	378	7.8	10.3	18.0	0.012	0.304	0.317	31.03	0.11	31.14	358	53	0.23
F	50	536	7.3	9.7	17.0	0.027	0.396	0.424	6.89	0.06	6.95	601	60	0.16
G	30	557	5.4	7.2	12.6	0.011	0.332	0.343	13.91	0.04	13.95	534	53	0.12
H	101	650	5.5	8.6	14.1	0.037	0.343	0.260	1.48	0.03	1.52	546	26	0.09
I	116	929	0.5	0.7	1.2	0.002	0.059	0.061	0.27	0.00	0.27	932	39	0.05
J	20	98	27.9	37.6	65.5	0.033	0.243	0.277	171.79	4.67	176.46	87	8	0.36
L	20	126	6.2	8.8	17.8	0.008	0.056	0.107	26.49	0.76	27.27	181	77	0.62
K	27	103	9.8	11.6	22.2	0.015	0.064	0.092	25.46	1.16	26.63	106	30	0.55

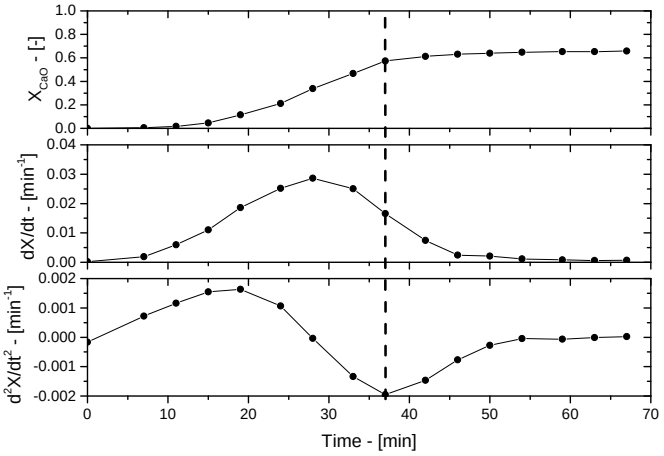

Figure 7.7: Method for the transition point determination by means of the first and second derivative of the CaO conversion over time profile for sample B.

radius of gyration is almost constant over time (up to the transition point), namely in the ranges of 542÷557 Å (sample G), 652÷650 Å (sample H) and 928÷1048 Å (sample I), as listed in Tabs. 7.2 and 7.3.

Finally, the micro-pore radius of gyrations is quite constant during the reactions, except for the highly sintered sorbents where a slight increase is observed (up to 9 Å for the case of sample F).

Consistent to the aforementioned behaviors, as the reaction progresses the sorbent PSDs are shifted in the direction of the high pore radius, as shown in Fig. 7.9 where the PSDs evolution of samples A, F and I are represented. Interestingly, the micro-pore population of sample A, seems to decrease in size and to be shifted towards smaller pore radii. This is partially confirmed by the slight decrease of sample A micro-pore radius of gyration, as shown in Fig. 7.9a, namely from 25 Å to 17 Å. The increase of the mean sorbent pore radius is additionally confirmed by the average pore radius estimate from the sorbent PSDs. Specifically. for samples calcined below 800 °C in nitrogen, the overall pore radius increases from 73 Å to 88 Å (sample A), from 74 Å to 122 Å (sample B) and from 93 Å to 118 Å (sample C) as listed in Tabs. 7.2 and 7.3.
The PSD shift in the direction of high pore radii is particularly appreciated for the case of sample F showed in Fig. 7.9b, whose mean pore radius increases from 180 Å to 251 Å. On the other hand, the PSD is slightly affected by the CaO carbonation reaction, remaining almost unchanged as shown in Fig. 7.9b. Although the highest increase in the meso-pore radius of gyration is observed for the case of sample D, the most significant increase of the mean pore radius (estimated from the volumetric pore size distribution) is achieved by sample F, namely from an initial value of 429 Å up to 601 Å.

Opposite to these observations, several structural kinetics models describing the CaO carbonation behaviors assume decreasing pore radius over the reaction, due to the product layer ($CaCO_3$) deposition up to the pore closure, such as those proposed by Bhatia and Perlmutter (1983a) and Bhatia and Perlmutter (1983b). Additionally, Alvarez and Abanades (2005) proposed a method to estimate the critical product layer thickness from the sorbent PSD assuming a progressive pore radius decrease as the carbonation reaction progresses. Based on this assumption, the predicted PSDs of carbonated samples are shifted in the direction of small pore radii, clearly in conflict with the aforementioned observations of this work. However, one of the main difference respect to this work consists in initial CaO PSDs characterized by only one pore population roughly placed around

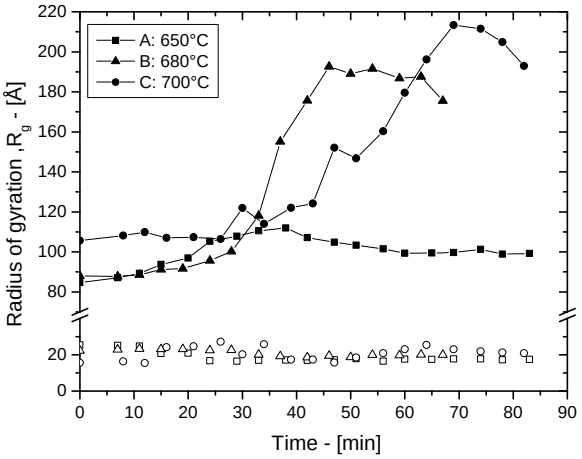

(a) *Samples A, B and C.*

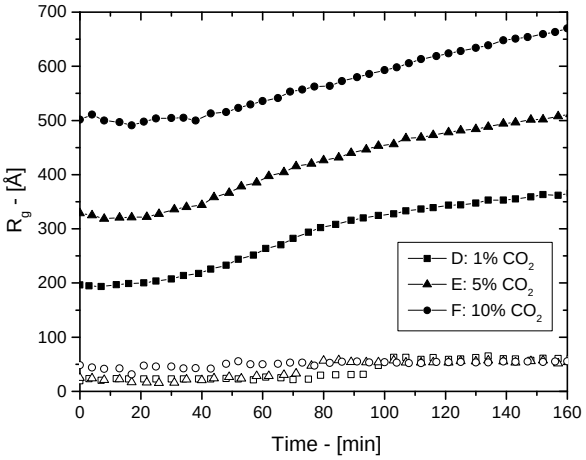

(b) *Samples D, E and F.*

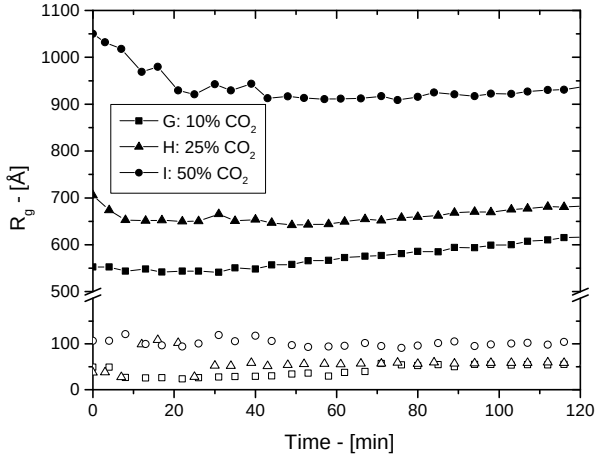

(c) *Samples G, H and I.*

Figure 7.8: Radius of gyration evolution of the two pore populations over the time for samples calcined below 800 °C in nitrogen (a), at 800 °C (b) and 900 °C (c) with different CO_2 contents. Empty markers refer to the micro-pore radius of gyration ($R_{g,1}$) almost constant during the reaction.

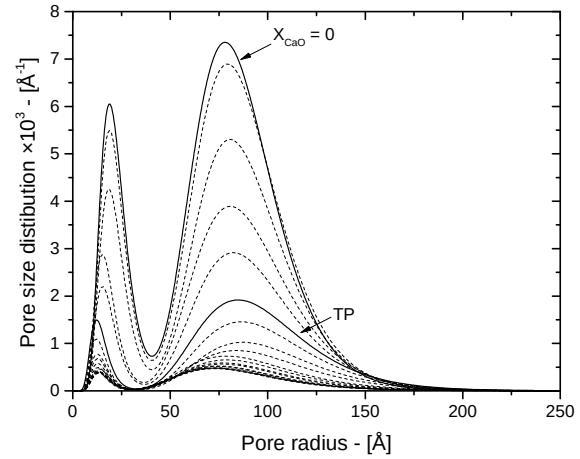

(a) *Sample A.*

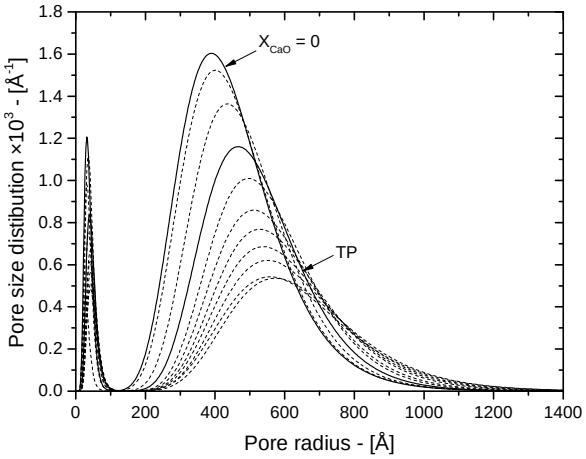

(b) *Sample F.*

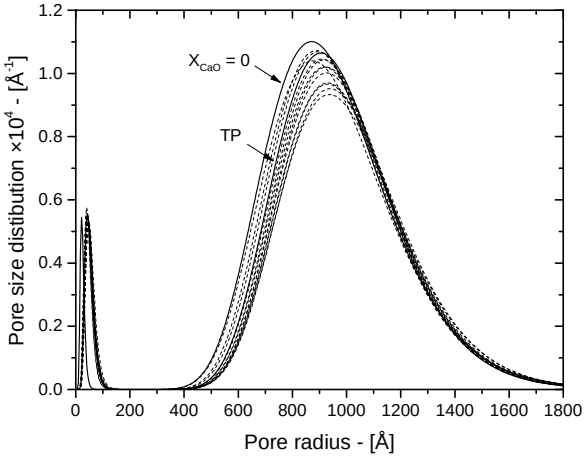

(c) *Sample I.*

Figure 7.9: Evolution of the sorbent pore size distribution during the carbonation reaction for sample A (a), sample F (b) and sample I (c). Solid lines represent the initial PSDs and those estimated at the transition point. Dashed lines the PSDs evolution before and after the transition between the two kinetic regimes.

200÷600 nm (Alvarez and Abanades, 2005). Based on the aforementioned observations, the micro-pore population is retained to play an important role during the reaction: the contracting meso-pores may be transferred into the smaller population, shifting the second population in the direction of the high pore radii. This interpretation could explain the increase of the mean pore radius during the reaction, even though the different molar volumes between calcium oxide and calcium carbonate reduce and plug the sorbent pore network.

Fig. 7.10 shows the radius of gyration evolution of samples J, K and L over the carbonation reaction. The initial CaO sorbents of these samples were obtained through calcination reactions in pure nitrogen at 650 °C (sample K) and 680 °C (samples J and L). Afterwards, CaO carbonation reactions were performed at 500 °C with 0.5 % (samples K and L) and 0.1 % (sample J) of CO_2 in balance with N_2, according to Tab. 7.1. Interestingly, these carbonation experiments show a third radius of gyration in the correspondence or after the transition point. This is in agreement with the aforementioned observations in the scattering intensity profiles of sample K showed in Fig. 7.4b, where a fourth structural level was necessary to obtain the best-fit result using the "Unified fit" approach. Even though the initial pore structure is characterized by two populations of pores, the carbonation reaction seems to generate a third population of meso-pores with a higher pore radius, as shown in Fig. 7.10a, 7.10b and 7.10c. More specifically, sample K exhibits an increasing meso-pore radius of gyration up to a meso-pore split into two different populations, which provides quite constant pore radius values after the transition point. This phenomenon is ascribed to a segregation process that occurs during the carbonation reaction, where different pore regions react at different times inside the sorbent particle. Specifically, a meso-pore fraction (the third one) is affected by the carbonation reaction and increases its pore radius (up to 250÷300 Å), according to the radius of gyration trends depicted in Fig. 7.8. On the other hand, the second meso-pore population, probably located in the center of the sorbent particle, remains quite unchanged because of the $CaCO_3$ product layer that plugs the outer meso-pores, limiting the CO_2 diffusion into the sorbent particle and, thus, the carbonation of the inner sorbent pore matrix, that exhibits a constant pore radius of gyration quite similar to that of the initial sorbent meso-pore value. This pore segregation is consistent with the remaining porosity observed in Fig. 7.9 by the final sorbent pore size distributions. However, this remaining porosity fraction is always below 0.1, associated with a specific surface area about less than 5 $m^2\,g^{-1}$, meaning that the majority of the sorbent porosity and surface areas have been consumed by the CaO carbonation reaction. Additionally, this is in agreement with the SAS capability to investigate the isolated pore structures respect to the gas adsorption techniques, that are limited to the gas probing accessibility to achieve the sorbent pore network beyond the porosity plugged by the product layer.

With the aim to investigate the influence of the initial sorbent pore network on the CaO carbonation reaction performances, the maximum conversion time derivative and the transition point conversion were plotted over the initial radii gyration of samples carbonated at the same operative conditions (550 °C with 0.4 % of CO_2), namely samples from A to I, as shown in Figs. 7.11a and 7.11b. More specifically these two plots indicate that the meso-pore radius of gyration has the most relevant effect of the CaO carbonation reaction, where the smaller the intial meso-pore radius of gyration (and thus the meso-pore size) the higher the maximum reaction rate and the conversion transition point between the two kinetic reaction regimes. Conversely, the initial micro-pore radius does not provide a clear influence on the reaction as for the case of the meso-pore population size, as shown in the insets of Figs. 7.11a and 7.11b. Additionally, the maximum value of the carbonation reaction rate was obtained from the conversion over time first derivative, that is always placed in the fast and chemically controlled step, as shown in Fig. 7.7.

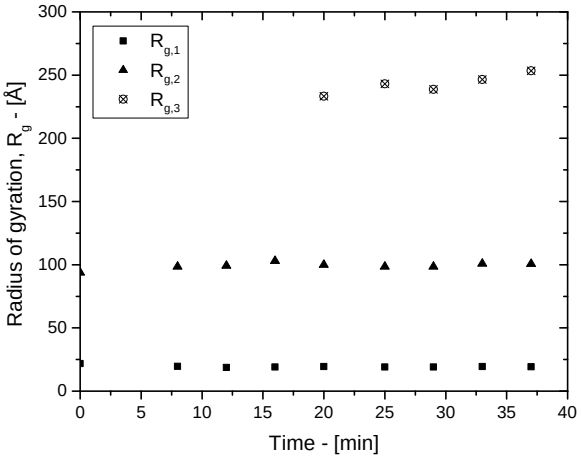

(a) *Sample J.*

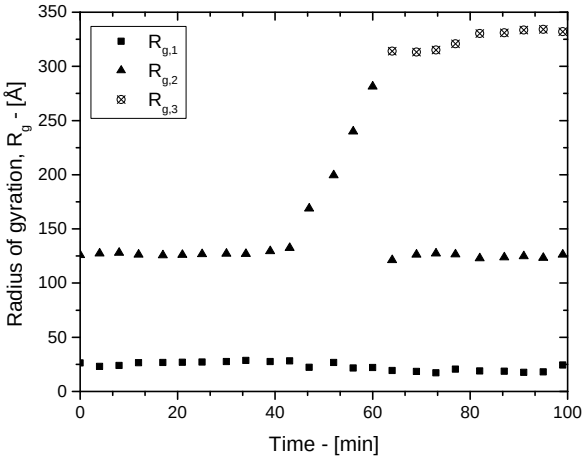

(b) *Sample K.*

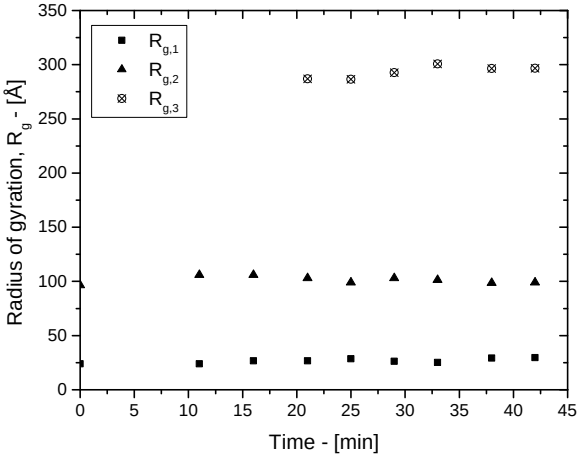

(c) *Sample L.*

Figure 7.10: Evolution of the pore radii of gyration over time during the CaO carbonation reaction for sample J, sample K and sample L. Empty and crossed markers refers to a third pore population.

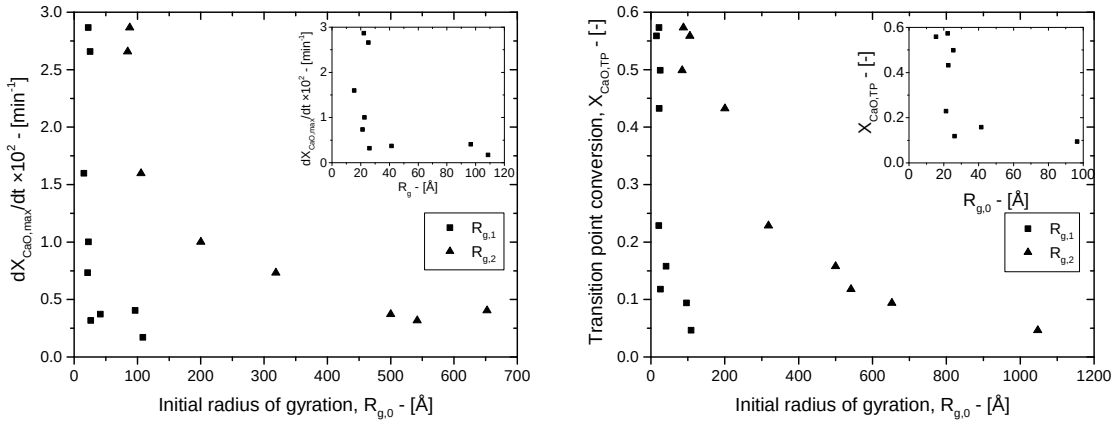

(a) $dX_{\mathrm{CaO},max}/dt$ *vs* $R_{g,1}$ *and* $R_{g,2}$.

(b) $X_{\mathrm{CaO},TP}$ *vs* $R_{g,1}$ *and* $R_{g,2}$.

Figure 7.11: Influence of the sorbent radius of gyration of the two pore populations on the maximum reaction rate (a) and on the transition point value (b).

The evolution of the sorbent specific surface area for samples calcined below 800 °C in pure nitrogen (A, B and C) is shown in Fig. 7.12. After a first induction period (in agreement with that of the conversion over time profiles in Fig. 7.6), a sharp decrease of the sorbent specific surface area is observed, where almost the overall sorbent surface area is consumed. This first region is clearly associated with the fast and chemically kinetic regime of the CaO carbonation reaction, where the formation and growth of the calcium carbonate solid product fill the pore structure consuming the available surface area. Afterwards, the decreasing trend profile of the specific surface area sharply change once the sorbent specific surface area approaches to small values. This change in slope occurs in the correspondence of the transition point between the two kinetic regimes. Specifically, the relative sorbent surface area reduction ($\Delta S_m/S_{m,0}$) between the initial value and the transition point is about 66 % for sample A, 80 % for sample B and 72 % for sample C, according to the sorbent specific surface area values listed in Tabs. 7.2 and 7.3. A comparison between the micro-pore specific surface area evolution and that of the meso-pores, showed Fig. 7.12, does not suggest substantial differences in the specific surface area decreasing trends of the two pore populations. This suggests that micro- and meso-pores show almost the same (high) reactivity when samples are calcined below 800 °C in pure nitrogen. Accordingly, the relative percentage reduction in the micro-pore specific surface area is 71 %, 81 % and 71 % for samples A, B and C respectively; whereas the meso-pore specific surface area reduction is about 61 % (sample A), 79 % (sample B) and 73 % (sample C). These relative decreasing values show how both the two pore population specific surface areas are reduced almost with the same magnitude.

The decreasing profiles of the sorbent specific surface area for samples calcined at 800 °C and 900 °C in presence of CO_2 (Fig. 7.13) exhibit smoother trends if compared with those of Figure 12. More specifically, the specific surface area consumption becomes less intense with the increase of the sintering effects on the initial sorbent micro-structure, namely with the increase of the CO_2 content in the atmosphere during the sorbent precursor activation. In fact, the specific surface area profile over time of sample D is fairly similar to those of samples A, B and C, because of the non-significant sintering effects on the initial pore structure, that exhibits a CaO specific surface area of 43.5 $m^2\,g^{-1}$ (Tab. 7.1). On the other hand, samples E and F show slightly decreasing profiles, that approach to an asymptotic value of about 10 $m^2\,g^{-1}$ (probably associated with the isolated pore structures). For these

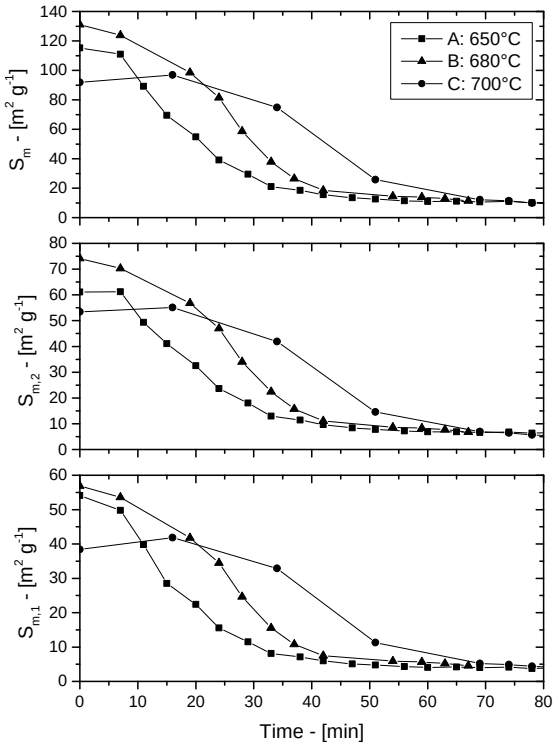

Figure 7.12: Evolution of the specific surface area of two pore populations and of the sample specific surface area over time for samples calcined in pure nitrogen below 800 °C (A, B and C). Legend refers to the final calcination temperature.

samples, the sorbent consumption is significantly intense (respect to samples A, B and C) showing a pore surface reduction of 67 %, 34 % and 33 % for samples D, E and F respectively (Tabs. 7.2 and 7.3). On the other hand, the surface reduction trends for sorbent produced at 900 °C with high CO_2 contents in the reaction atmosphere show more modest specific surface reductions, namely 26 % for sample G, 5 % for sample H and 23 % for the case of sample I (Tabs. 7.2 and 7.3). This low sorbent specific surface area reduction is clearly associated with the low sorbent reactivity due to the highly sintering pore structure in the initial CaO sorbents, providing relative small initial specific surface areas, namely below $17.1\,m^2\,g^{-1}$.
Even for these samples (D÷G) the specific surface area consumptions associated with the two pore populations are fairly similar to the total sorbents specific surface area reductions. This behavior suggests that the specific surface area of both the two pore populations are consumed with the same magnitude by the CaO carbonation reaction, as for the cases of samples A, B and C.

Fig. 7.14 shows the sorbent specific surface area evolution during the CaO carbonation reaction. Interestingly, linear trends are observed for the cases of samples calcined below 800 °C in nitrogen. These profiles slightly deviate from the linearity when sintered samples are considered, namely those calcined at 800 °C and 900 °C in presence of CO_2 (D÷I). The deviation from the linear trends can be further appreciated in Figs. 7.15a, 7.15c and 7.15d, where the specific surface area of the two pore populations and that of the sorbent are plotted over the CaO conversion for the case of sample A, F and G. Specifically, a linear fitting was performed on the two pore populations surface areas and on that of the total sorbent for samples calcined below 800 °C in nitrogen and then carbonated at 550 °C with 0.4 % of CO_2, namely samples A, B and C (Tab. 7.1), as shown in Fig. 7.15a. Linear

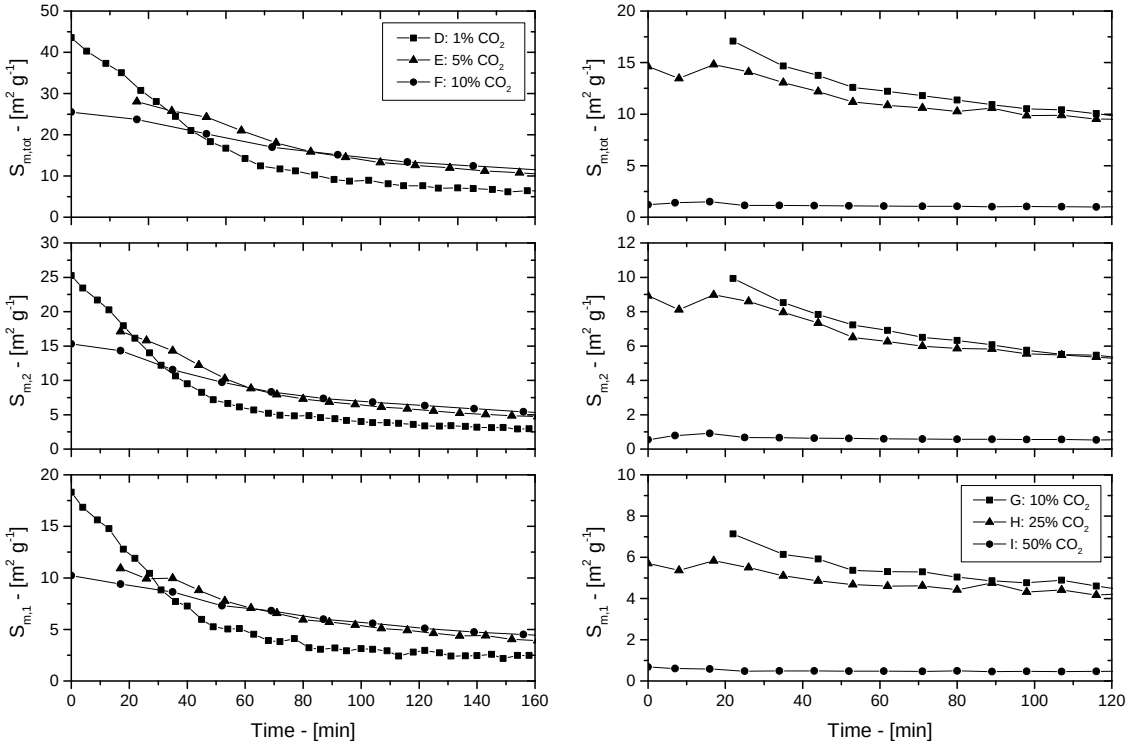

(a) *Samples D, E and F.* **(b)** *Samples G, H and I.*

Figure 7.13: Evolution of the specific surface area of two pore populations and of the sample specific surface area over time for samples calcined at 800 °C (a) and at 900 °C (b) varying the CO_2 content in the reactor atmosphere.

fittings provide that the linear decreasing trend of the normalized sorbent specific surface area (S_m/S_m^0) over the CaO carbonation reaction can be expressed as:

$$\frac{S_m}{S_m^0} = 1 - 1.36\, X_{\mathrm{CaO}}, \tag{7.1}$$

where the linear slope was obtained as the average value of those of samples A, B and C. Additionally, Tab. 7.4 provides the average linear slopes for the first and second population specific surface area reductions associated with these samples, where it is remarkable to notice how the decreasing rates of the micro- and meso-pore specific surface areas occur with the same magnitude. Similar results were obtained for the case of samples J, K and L calcined below 800 °C in nitrogen and then carbonated at 500 °C with 0.1/0.5 % of CO_2 (Tab. 7.1), as listed in Tab. 7.4. Specifically, the average slope of the specific surface area decrease is fairly similar to that of samples A÷C, namely −1.40. The slight difference between these values could be ascribed to the different carbonation reaction conditions in terms of temperature and CO_2 content in the reaction atmosphere. Even for these samples, the two populations average decreasing trends show a similar slope, namely −1.45 for micro-pores and −1.42 for meso-pores, suggesting that both micro- and meso-pore surface areas are consumed with the same rate.

Opposite to the aforementioned linear behaviors, the specific surface area decrease of the sintered samples (E÷I) is non-linear, as can be appreciated in Fig. 7.15c for sample F and Fig. 7.15d for sample G. Interestingly, the best fit results of these profiles were obtained by means of a second degree polynomial, whose initial slopes (at $X_{\mathrm{CaO}} = 0$) are

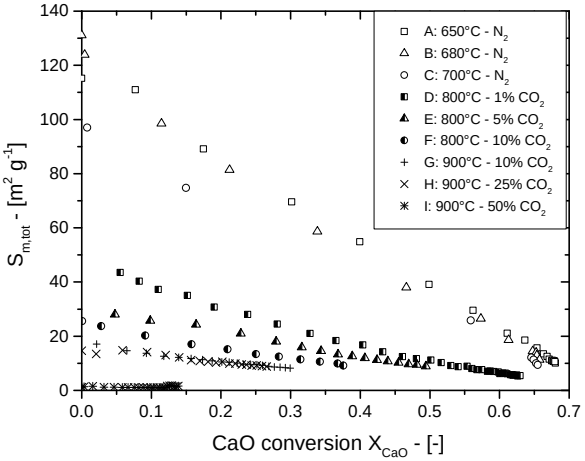

Figure 7.14: Evolution of the sorbent specific surface area over the CaO conversion during the carbonation reaction for samples carbonated at 550 °C with 0.4 % of CO_2 in balance with N_2. Legend refers to the sorbent thermal activation conditions in terms of final calcination temperature and atmosphere composition.

Table 7.4: Linear slopes per unit of initial specific surface area (samples A÷C and J÷L) and normalized slopes for samples D÷I evaluated before the carbonation reaction ($X_{\mathrm{CaO}} = 0$) and in the correspondence of the transition point ($X_{\mathrm{CaO},TP}$).

Sample	$dS_{m,1}/dt\ \left(S^0_{m,1}\right)^{-1}$		$dS_{m,2}/dt\ \left(S^0_{m,2}\right)^{-1}$		$dS_m/dt\ \left(S^0_m\right)^{-1}$	
	$X_{\mathrm{CaO}} = 0$	$X_{\mathrm{CaO},TP}$	$X_{\mathrm{CaO}} = 0$	$X_{\mathrm{CaO},TP}$	$X_{\mathrm{CaO}} = 0$	$X_{\mathrm{CaO},TP}$
A÷C	-1.36	–	-1.36	–	-1.36	–
D÷F	-1.76	-1.08	-2.39	-0.84	-2.14	-1.07
G÷I	-2.26	-1.25	-4.04	-1.08	-3.3	-1.14
J÷L	-1.45	–	-1.42	–	-1.4	–

listed in Tab. 7.4. According to this profile evolutions, Tab. 7.4 summarizes the initial and final slopes averaged on those of samples D÷F (calcined at 800 °C) and G÷I (calcined at 900 °C). Even though the initial significant slopes (from -2.14 to -3.30) associated with the total sorbent decreasing specific surface area, the final transition values (-1.07 and -1.14) are smaller if compared with those of samples A÷C and J÷L. The micro- and meso-pore slopes confirm these trends, where the micro-pore surface reduction is slower than that of the meso-pores at the beginning of the reaction. An opposite behavior is observed in the correspondence of the transition point, where the micro-pore reduction is slightly higher than that of the meso-pore population (Table 5).
Empty markers in Figs. 7.15a, 7.15c and 7.15d refer to the specific surface area per unit of CaO mass evolution over the CaO conversion. Specifically, this trend is highly non-linear, in contrast with the specific surface area trends over the CaO conversion. Interestingly, for the case of sample A÷C the CaO specific surface of the two populations (and thus of the sorbent) is almost constant during the chemically controlled regime, whereas a sharp drop down to low values is noticed when the slow product layer diffusion controlled step takes place, as shown in Fig. 7.15a. However, by considering samples calcined at 800 °C (sample F) and 900 °C (sample G) with CO_2, the CaO specific surface area is quite constant during the reaction as shown in Figs. 7.15b and 7.15c. Precisely, these trends slightly decrease during the reaction and none sudden decrease is noticed for the case of sample F and G.

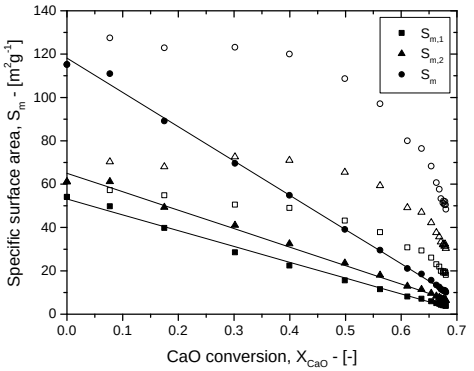

(a) S_m *vs* X_{CaO} *- Sample A.*

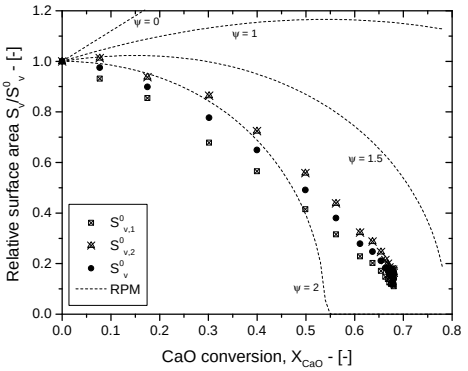

(b) S_v/S_v^0 *vs* X_{CaO} *- Sample A.*

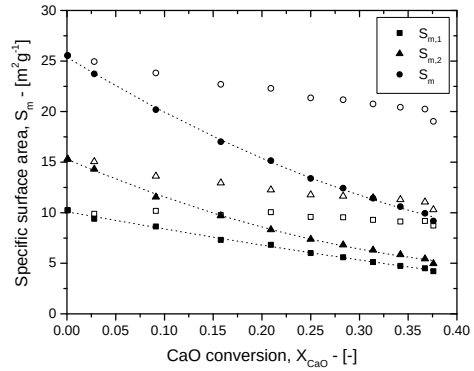

(c) S_m *vs* X_{CaO} *- Sample F.*

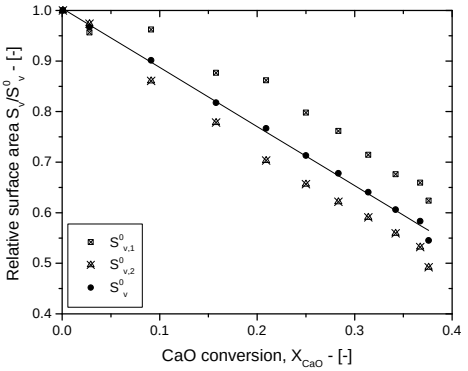

(d) S_v/S_v^0 *vs* X_{CaO} *- Sample F.*

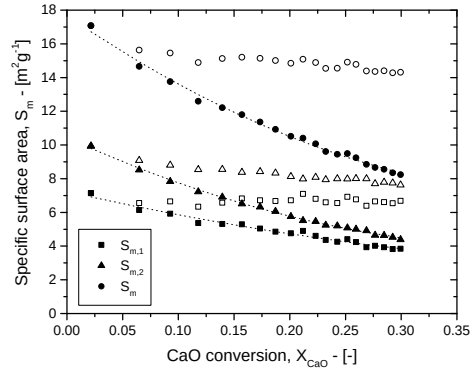

(e) S_m *vs* X_{CaO} *- Sample G.*

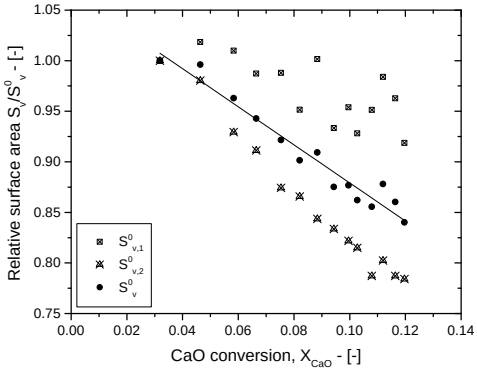

(f) S_v/S_v^0 *vs* X_{CaO} *- Sample G.*

Figure 7.15: Specific surface area evolution of the two pore populations and of the total sorbent over the CaO carbonation reaction for samples A (a), F (c) and G (e). Empty markers refer to the specific surface area per unit of CaO mass; solid lines refer to linear fitting, dotted lines to parabolic fittings. Evolution of the relative surface area per unit of sorbent volume (S_v/S_v^0) of the two pore populations (empty and crossed markers) and of the total sorbent (solid markers) over the CaO conversion for samples A (b), F (d) and G (f). Solid lines represent the linear fittings.

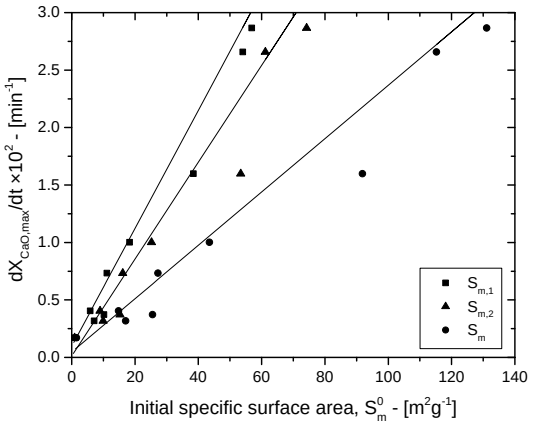

Figure 7.16: Maximum conversion time derivative as a function of the initial sorbent specific surface areas for samples A to I. Solid lines refer to linear fittings.

Although the reduced specific surface areas per unit of sample mass (S_m/S_m^0) shows a linear trend over the CaO conversion for samples calcined below 800 °C in pure nitrogen, the reduced specific surface area per unit of sample volume (precisely, the particle volume) over the CaO conversion exhibits a non-linear decreasing profile, as shown in Fig. 7.15b. This trend was compared with the random pore model (RPM) prediction proposed by Bhatia and Perlmutter (1983a):

$$\frac{S_v}{S_v^0} = [1 + (Z_{\text{carb}} - 1)\, X_{\text{CaO}}]\, \sqrt{1 - \psi \log [1 + (Z_{\text{carb}} - 1)\, X_{\text{CaO}}]}, \tag{7.2}$$

where ψ is a structural factor that depends on the initial porosity, specific surface area per unit of volume and mean pore length under the assumption of thin cylindrical pore shape (Bhatia and Perlmutter, 1980). Even though the structural parameter ψ was varied from 0 up to 2, the predicted profile did not match the experimental data as shown in Fig. 7.15b. The reasons of this mismatch could be ascribed to the several model assumptions, namely (1) pore shape is assumed to be cylindrical (Bhatia and Perlmutter, 1980); (2) the model does not account for pore closure, instead of RPM proposed by Bhatia (1985) and Sotirchos and Yu (1985); (3) pore segregation into the particle is not taken into account. All these assumptions are retained to be the main causes of the model incapability to represent the relative sorbent specific surface area decrease.

As far as the reduced sorbent specific surface area per unit of sample volume over the CaO conversion of 800 °C and 900 °C calcined samples, an interesting linear trend was observed as depicted in Fig. 7.15d for sample F and Fig. 7.15f for sample G. Despite data are somehow scattered, also the reduced specific surface area per unit of volume of the two pore populations seem to be linear. These linear profiles are obviously not considered by Eq. (7.2) unless in those particular cases where ψ and Z_{carb} are zero, that is clearly unreal for the case of the CaO carbonation reaction.

The maximum conversion rates estimated from the first CaO conversion derivative are plotted in Fig. 7.16 as a function of the initial specific surface area of the two pore populations and the total sorbent specific surface area. Interestingly, the resulting profiles exhibit linear trends defined by the following equations

$$\left.\frac{dX_{\text{CaO}}}{dt}\right|_{\text{max}} = \begin{cases} 2.32 \times 10^{-4}\, S_m^0 + 4.53 \times 10^{-4}\, \text{s}^{-1} \\ 5.13 \times 10^{-4}\, S_{m,1}^0 + 9.87 \times 10^{-4}\, \text{s}^{-1} \\ 4.22 \times 10^{-4}\, S_{m,2}^0 + 9.15 \times 10^{-4}\, \text{s}^{-1} \end{cases} \tag{7.3}$$

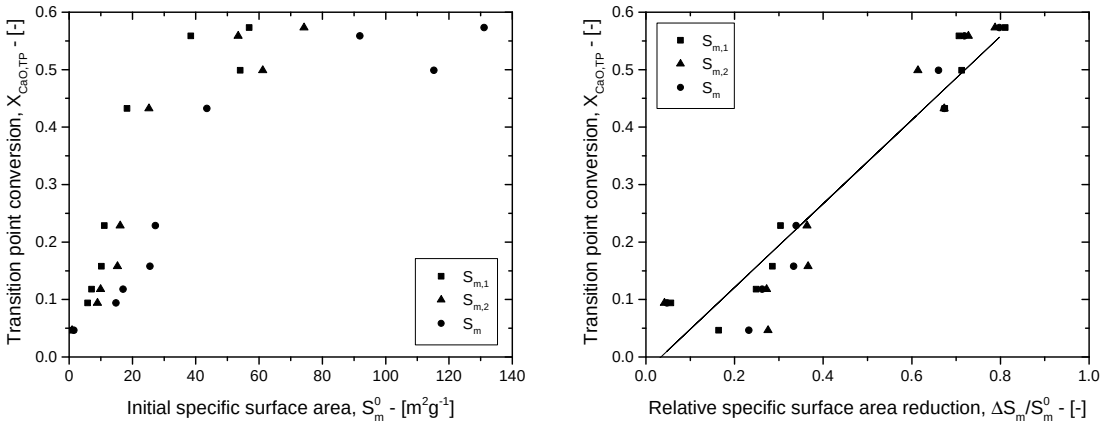

(a) **(b)**

Figure 7.17: Correlations between the CaO conversion at the transition point over the initial sorbent specific surface areas (a) and the surface area relative reduction (b) between the initial values and those in the correspondence of the transition point for samples A÷I. Linear fitting (solid line) refers to the total sorbent specific surface area reduction.

proving that the increase of the initial specific surface area makes the CaO sorbent particle more reactive towards the CO_2 reactant. More specifically, linear trends in Fig. 7.16 suggest how the micro-pore specific surface area provide a more impact on the maximum CaO conversion rate respect to the initial meso-pore specific surface area, according to the more pronounced slope of the micro-pore population ($5.13 \times 10^{-4}\,\mathrm{m^{-2}\,s^{-1}}$) respect to that of meso-pores ($4.22 \times 10^{-4}\,\mathrm{m^{-2}\,s^{-1}}$).

Fig. 7.17a shows the CaO conversion evaluated at the transition point as a function of the initial sorbent specific surface areas. These trends seem to suggest how a high initial CaO specific surface are provides a higher transition point in terms of CaO conversation, even though a well definite trend cannot be appreciated unless for low values of the initial specific surface area, where a linear trend seem to hold well. However, if the CaO transition conversion is plotted as a function of the relative sorbent specific surface reduction, a linear trend is observed as shown in Fig. 7.17, even though data are somehow scattered. Specifically, the linear fitting between the CaO transition conversion and the relative sorbent specific surface area reduction provides the following relationship

$$X_{\mathrm{CaO},TP} = 0.698\frac{\Delta S_m}{S_m^0} - 1.2 \times 10^{-4}, \tag{7.4}$$

suggesting that the higher the sorbent specific surface area reduction the higher the CaO transition conversion between the two kinetic regimes.

Fig. 7.18 shows the sorbent porosity evolution over the CaO carbonation reaction conversion for samples calcined below 800 °C in pure nitrogen (A, B and C). Consistent with the specific surface area evolution showed in Fig. 7.12, after a first induction period the majority of the sorbent void fraction is consumed during the first chemically controlled step, according to the CaO conversion over time profiles in Fig. 7.6a. When the reaction kinetic moves into the product layer diffusion controlled step, the porosity decreasing profiles show a sharp change in slope where almost the sample porosity is completely consumed by the $CaCO_3$ product layer, stopping the reaction before the complete conversion. Similar trends were observed for the cases of samples D÷F and G÷I, in agreement with the specific surface areas evolution during the reaction as showed in Fig. 7.12.

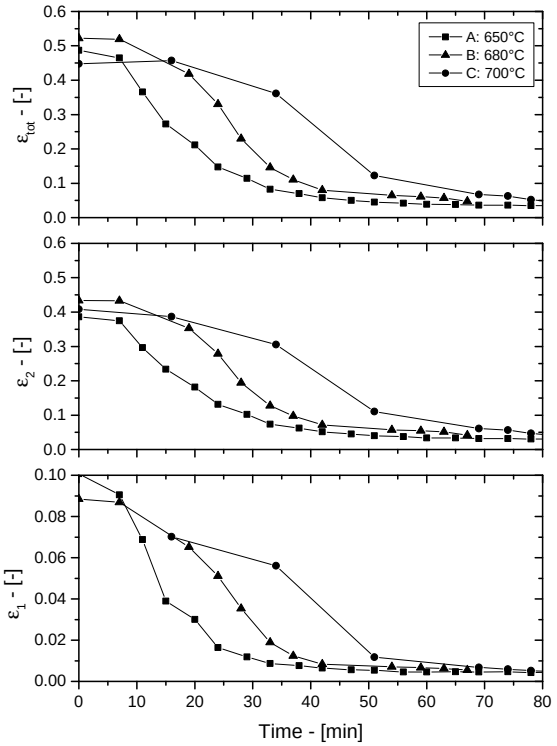

Figure 7.18: Evolution of the sorbent porosity of the two pore populations and of the sample porosity over time for samples calcined in pure nitrogen below 800 °C (A, B and C). Legend refers to the final calcination temperature.

According to Eq. 2.5, namely the relationship between the sorbent CaO conversion and its porosity, the final CaO conversion is mainly due to the second population contribution because of its high porosity value respect to the micro-pore population, according to sample values listed in Tab. 7.2. Additionally the linear sorbent porosity evolution over the CaO carbonation reaction, stated by Eq. 2.5, was verified in Fig. 7.19, where linear trends are showed for samples carbonated at 550 °C with 0.5 % of CO_2.

Fig. 7.20 shows the reduced specific surface area evolution over the reduced sorbent porosity (normalized by their respective initial values). More specifically, well defined linear profiles were observed especially for the case of low sintered samples, namely those calcined below 800 °C in nitrogen showed in Fig. 7.22a. These trends are in agreement with those showed in Fig. 7.15 because of the linear relationship between the sorbent porosity and the CaO conversion, as stated by Eq. 2.5. More specifically, Fig. 7.20a verifies these trends, were the reduced surface area over the CaO conversion slopes (listed in Tab. 7.4) are actually the ratio of $(Z_{\text{carb}} - 1)(1 - \varepsilon_0)/\varepsilon_0$ and Eq. (7.1) slope, namely -1.36, is the average value of such ratio of samples A, B and C. On the other hand, non-linear trends showed in Figs. 7.20b and 7.20c are consistent with those depicted in Figs. 7.15c and 7.15e, namely specific surface area profiles over the CaO conversion and, thus, the sorbent porosity during the CaO carbonation reaction that exhibit a different trends respect to those samples calcined at low temperatures (in relative terms) and in nitrogen. This suggests how the sorbent micro-structure is used in a different ways by the CaO carbonation reaction when sintered samples (those calcined at 800 °C and 900 °C in presence of CO_2) are considered respect to those where sintering effects are negligible (samples A, B and C).

Fig. 7.21 shows the initial sorbent porosity influence on the maximum CaO conversion derivative and even though well-defined profiles are not observed as for the case of the

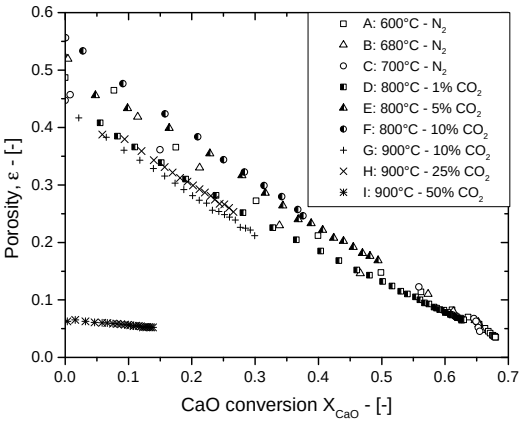

Figure 7.19: Linear sorbent porosity profiles evolution over the CaO conversion during the carbonation reactions. Legend specifies the precursor calcination reaction conditions.

initial sorbent specific surface area (Fig. 7.16), these data suggest how a high sorbent porosity provides high initial conversion rates during the chemically controlled kinetic regime. However, this apparent trend is retained to be associated to the fact that a highly porous CaO sorbent is provided by a significant specific surface area, as listed in Tab. 7.2. A similar behavior is observed in Fig. 7.22a where the transition CaO conversion is plotted as a function of the initial sorbent porosity. However, these data do not exhibit a defined trend, despite they suggest the higher the initial porosity the greater the transition point conversion. However, by considering the CaO conversion at the transition point as a function of the relative porosity reduction $\Delta\varepsilon/\varepsilon_0$, a positive and linear trend is observed, as showed in Fig. 7.22b, whose linear fitting provides the following relationship

$$X_{\mathrm{CaO},TP} = 0.7\,\frac{\Delta\varepsilon}{\varepsilon_0} + 0.02, \tag{7.5}$$

even though data are somehow slightly scattered. Accordingly, it is remarkable to notice how the sorbent porosity is mainly exploited by the CaO carbonation reaction when sintering effects are modests on the final solid sorbent micro-structure. Specifically, the relative porosity reduction for samples A, B and C are 70 %, 79 % and 73 %, according to porosities values listed in Tabs. 7.2 and 7.3, that decrease down to 59 %, 25 % and 54 % for those samples calcined at 800 °C (D, E and F) and even more for samples calcined at 900 °C: 18 % (sample G), 2 % (sample H) and 7 % (sample I).

Figs. 7.23a and 7.23b show the pore number per unit of sample mass associated with the two pore populations over time. These trends are in agreement with those of the sorbent specific surface area and of the porosity, as shown in Fig. 7.12, Fig. 7.13a and in Fig. 7.18 respectively. Specifically, as the carbonation reaction progresses the specific pore number per unit of sample mass is reduced down to a low constant value. Even though the reduction trends are quite similar for samples calcined below 800 °C in nitrogen (as shown in Fig. 7.23a), as the CO_2 content increases during the activation step, and, thus sintering effects on the final sorbent micro-structure, the rate of pore consumption during the CaO carbonation reaction decreases (Fig. 7.23b).

Interestingly, according to Tabs. 7.2 and 7.3 the relative meso-pore number (per unit of sample mass) consumption (between the initial time and in correspondence of the transition point) is mostly higher than that of the micro-pores. Specifically, samples calcined below 800 °C in nitrogen provide a relative meso-pore number consumption of 81 % (sample A), 96 % (sample B) and 89 % (sample C), while the micro-pore relative reductions are 59 %

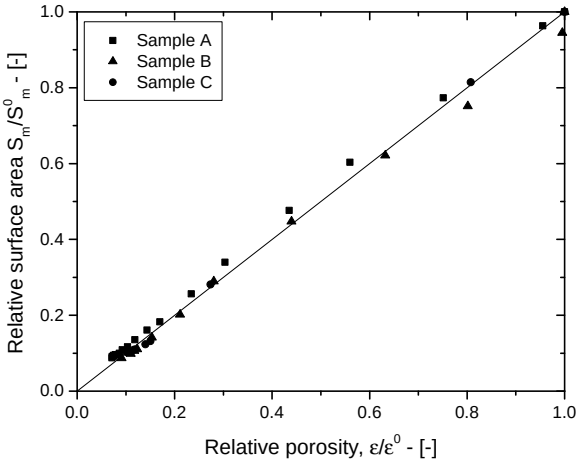

(a) *Samples A, B and C - N_2 calcinations.*

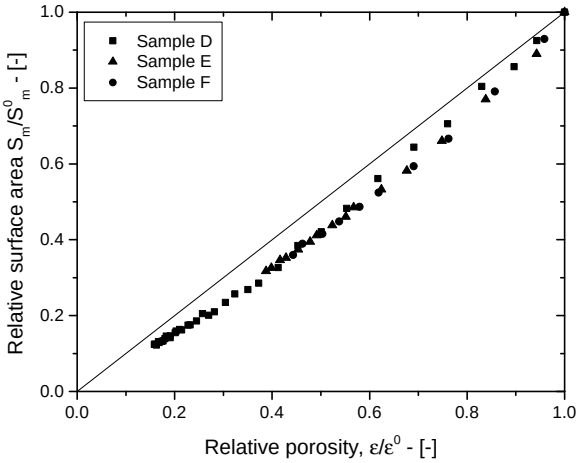

(b) *Samples D, E and F -* 800 °C *calcinations.*

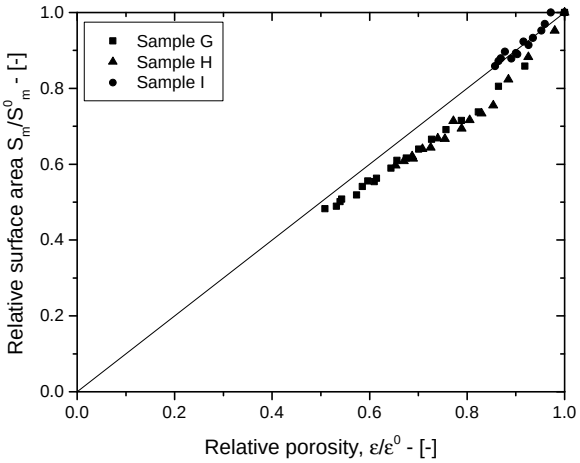

(c) *Samples G, H and I -* 900 °C *calcinations.*

Figure 7.20: Relative specific surface area evolution over the sample relative porosity during the CaO carbonation reaction for samples calcined below 800 °C in N_2 (a), for samples calcined at 800 °C (b) and samples calcined at 900 °C in presence of CO_2.

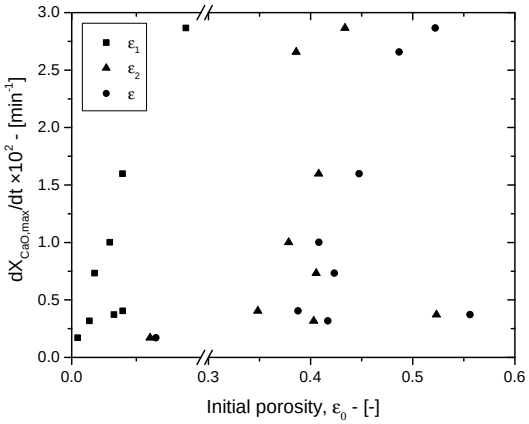

Figure 7.21: Maximum conversion over time derivative as a function of the initial sorbent porosities.

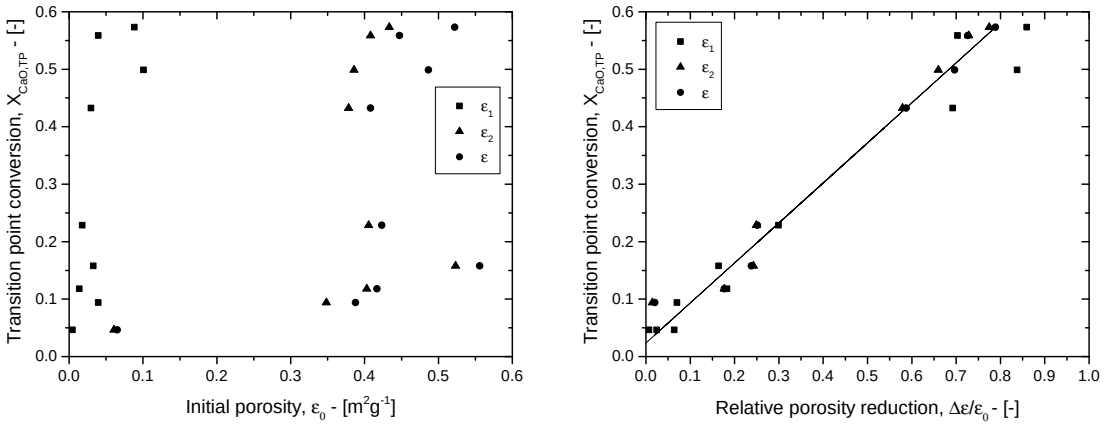

(a) $X_{\mathrm{CaO},TP}$ *vs* ε_0. **(b)** $X_{\mathrm{CaO},TP}$ *vs* $\Delta\varepsilon/\varepsilon_0$.

Figure 7.22: Correlations between the CaO transition point conversion over the sorbent initial porosities (a) and over the relative sorbent porosity reduction (b).

(sample A), 86 % (sample B) and 87 % (sample C). Similar behaviors were observed for the 800 °C calcined samples that provide relative meso-pore number density reductions of 87 % (sample D), 65 % (sample E) and 90 % (sample F) and lower relative micro-pore consumptions of 79 % (sampled), 50 % (sample E) and 85 % (sample F). Samples calcined at 900 °C exhibit similar trends, even though pore matrix is less exploited by the carbonation reaction, showing meso-pore number density reductions of 47 % for sample G and 10 % for sample H, with associated micro-pore reductions of 48 % and 8 % respectively. On the contrary, sample I shows a different behavior because its meso-pore consumption is about 5 %, while the relative micro-pore reduction is significantly higher, namely 61 %.

More specifically, the decreasing trends of the pore number density over the CaO conversion are shown in Fig. 7.24. Considering sample A trends in Fig. 7.24a, the relative meso-pore number per unit of mass shows a quite linear decreasing profile during the reaction. On the other hand, the micro-pore profile seems to exhibit a different trend, even though data seems to be somehow scattered, namely a first decreasing trend down to the transition point (at 0.5 of CaO conversion), followed by a sharp change in slope after this point. This sudden change of the relative micro-pore number per unit of sample mass was

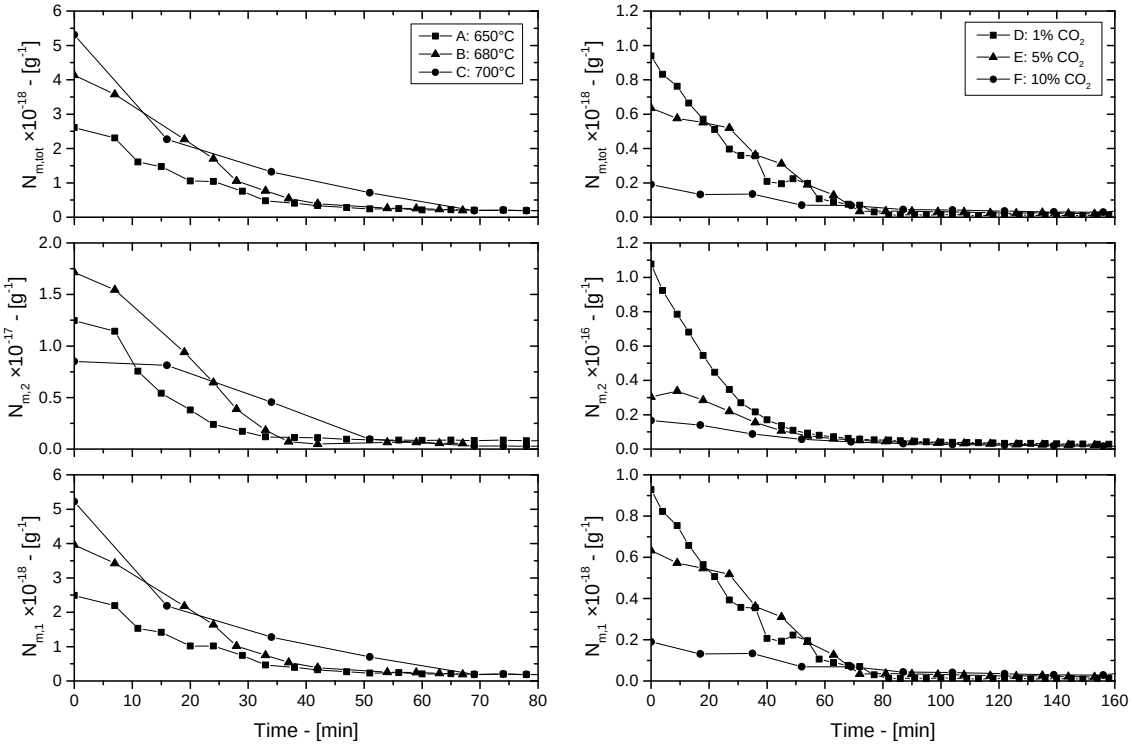

(a) *Samples A, B and C - N_2 calcinations.* **(b)** *Samples D, E and F - 800 °C calcinations.*

Figure 7.23: Evolution of the sorbent pore number per unit of mass of the two pore populations and of the sorbent over time for samples calcined in pure nitrogen below 800 °C (A, B and C) and at 800 °C in presence of CO_2 (b). Legends refer to the calcination reaction conditions.

observed also for the cases of samples calcined at 800 °C and 900 °C, as shown in Figs. 7.24b and 7.24c for sample F and G respectively. However, in these two cases the decreasing profiles after the transition point (0.16 for sample F and 0.12 for sample G) occurs with a lower slope respect to that of sample A. On the other hand, the relative meso-pore number per unit of mass profiles show smoother decreasing trends if compared with that of sample A, suggesting a less intense pore consumption respect to a poorly sintered micro-structure, as such of the calcined samples below 800 °C in nitrogen.

Fig. 7.25 shows the decreasing profiles of the sorbent specific surface area and porosity (in relative terms) over the relative total number of pores per unit of sample for the case of sample A and G. The former is showed in Fig. 7.25a where both the relative porosity and specific surface area reductions exhibit fairly similar behaviors over the pore number reduction (per unit of sample mass). More specifically, the transition between the two regimes occurs after the consumption of the majority of porosity and specific surface area, namely below 0.3–0.4 values. The transition is associated with a change in trends of the decreasing profiles, after that the two profiles seem to be quite linear. These trends are also observed or the case of sample G, where the different slopes in the decreasing profiles are more emphasized, as showed in Fig. 7.25b. Additionally, in this case the relative specific surface area and porosity reductions seem to occur following linear trends over the relative sorbent pore number per unit of sample mass, changing their slopes in the correspondence of the transition point.

In order to quantify the influence of the initial pore number per unit of sample mass

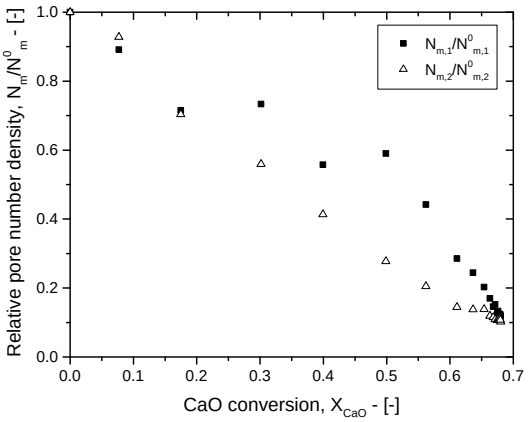

(a) *Sample A - Calcination at* 650 °C *in* N_2.

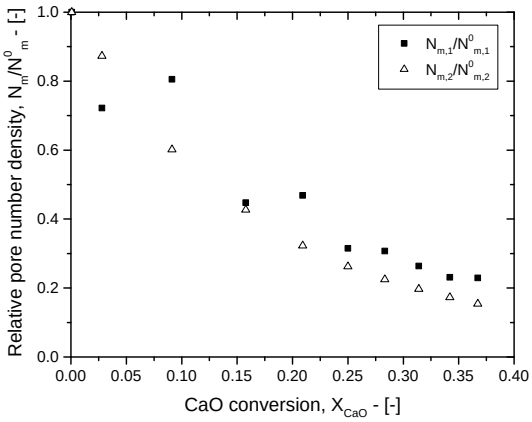

(b) *Sample F - Calcination at* 800 °C *with* 10 % *of* CO_2.

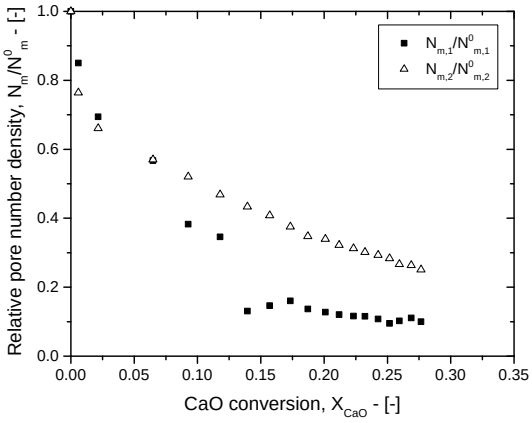

(c) *Sample G - calcination at* 900 °C *with* 10 % *of* CO_2.

Figure 7.24: Evolution of the pore number per unit of sample mass of the two pore populations over the CaO conversion for sample A (a), sample F (b) and sample G (c).

of the two pore populations on the CaO carbonation reaction performances, the maximum conversion derivative is plotted over N^0_m as shown in Fig. 7.26a. Interestingly, positive correlation is observed suggesting that the higher the micro- and meso-pore number concentration, the higher the initial conversion rate. In addition, a similar trend is showed by considering the CaO conversion at the transition point over the initial pore number per unit of mass, as shown in Fig. 7.26b, where the meso-pore number density influence seems to be more significant respect to the micro-pore number per unit of mass.

As the carbonation reaction progresses the overall effect on the pore shape consists in a reduction of their sphericity, whose initial pore sphericity factors is approximately one, namely a pore shape fairly close to the spherical shape, as shown in Fig. 7.27 for the case of samples calcined below 800 °C in pure nitrogen, where sintering phenomena effects are quite negligible on the initial sorbent micro-structure. Specifically, the final meso-pore sphericity factor approaches to 0.4÷0.3 values, while the micro-pore population sphericity factor is reduced down to quite higher values than the meso-pore one, namely 0.48÷0.58. Similar trends are observed for the cases of samples calcined at 800 °C and 900 °C, even though the final sphericity factor of the two pore populations stop in the rage between 0.6 and 0.8, because of the lower reactive behavior of their respective micro-structures respect

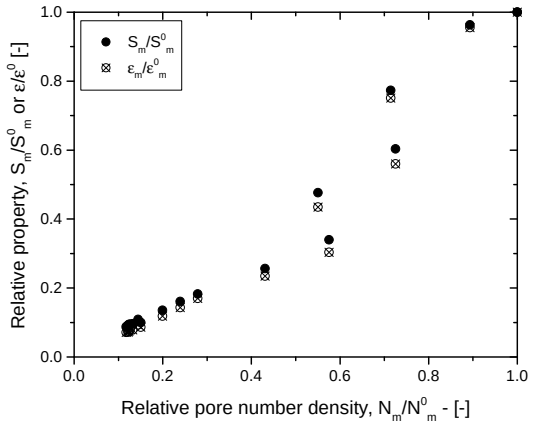

(a) *Sample A - Calcination at* 650 °C *in* N_2.

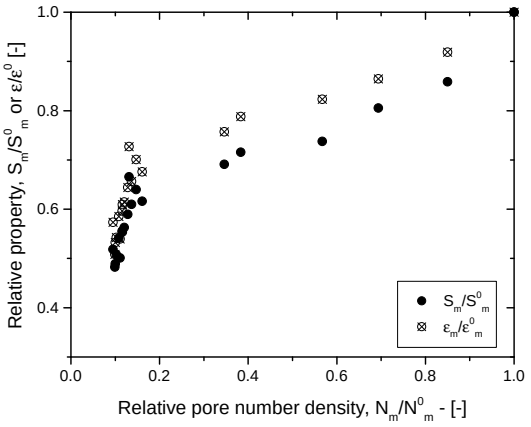

(b) *Sample G - Calcination at* 900 °C *with* 10 % *of* CO_2.

Figure 7.25: Reduced sample specific surface area and porosity over the reduced pore number density per unit of sample mass for sample A (a) and sample G (b).

to those samples were sintering effects are quite negligible.

Finally, meso-pore correlation distances were provided by the structure factor $S_2(q,t)$ associated with the meso-pore population scattering intensity profiles (Beaucage et al., 1995). According to Beaucage et al. (1995) the correlation distance (over the CaO conversion) provides the average meso-porosity pore-to-pore distance as the carbonation reaction progresses, as shown in Fig. 7.28. Specifically, samples calcined below 800 °C in nitrogen (A, B and C) exhibit quite constant correlation distances during the carbonation reaction, that range from a minimum of 218 Å to 368 Å, as shown in Fig. 7.28a, suggesting that the average-pore pore distance remains quite unvaried as the carbonation reaction progresses. On the other hand, samples calcined in presence of CO_2 (D÷I), whose internal micro-structure is affected my sintering phenomena, show a slight increasing correlation distance during the CaO carbonation reaction, as depicted in Figs. 7.28b and 7.28c for the cases of samples calcined at 800 °C and 900 °C respectively. Specifically, the meso-pore correlation distance of sample D increased up to 1242 Å starting from the initial value of 655 Å, while samples E and F exhibit a more modest evolution: from 1180 Å to 1461 Å (sample E) and from 1584 Å to 1868 Å (sample F). Similar trends were observed for the 900 °C calcined samples, where meso-pore correlation distance increased from the initial value of 1581 Å to 1825 Å for sample G and from 1765 Å to 2092 Å for the case of sample H. Sample I correlation distance is almost constant during the reaction, ranging from 3989 Å to 4106 Å, as shown in the Fig. 7.28c inset, probably because the low final CaO conversion (less that 20 %), that slightly affects the sorbent internal pore network. This behavior suggests that one of the main effects of the carbonation reaction on the sorbent micro-structure consists in increasing the meso-pore average distance, when the initial sorbent pore matrix is highly affected by sintering effects.

7.4 Conclusions

In this work, time-resolved X-ray synchrotron based small angle scattering technique was applied for the first time to the investigation of the CaO sorbent micro-structure evolution during the carbonation reaction by means of an in-situ approach. Small angle

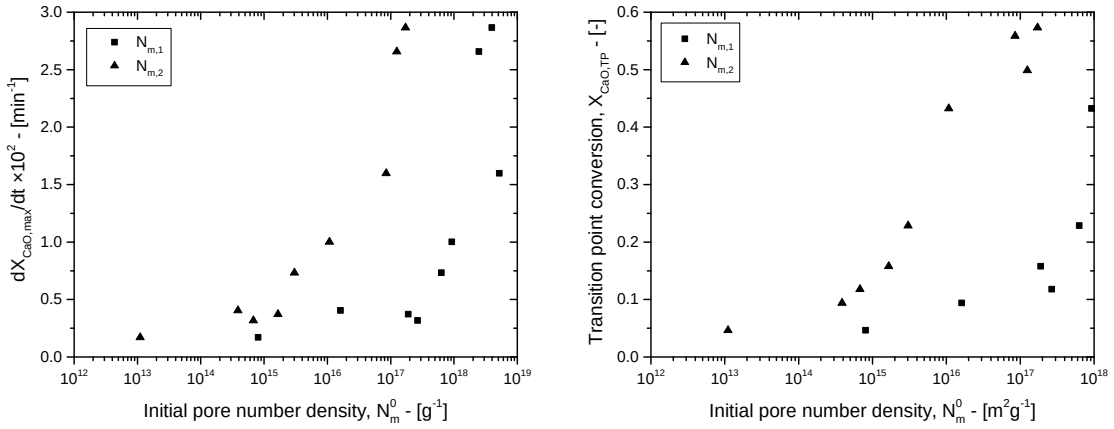

(a) $dX_{\mathrm{CaO},max}$ *vs* N_m^0. **(b)** $X_{\mathrm{CaO},TP}$ *vs* N_m^0.

Figure 7.26: Influence of the initial number of pore per unit of sample mass of the two pore populations on the maximum conversion time derivative (a) and on CaO conversion at the transition point (b).

scattering data were collected at the beamline 9-ID-B, C of the Advanced Photon Source (APS) at the Argonne National Laboratory.

Several different $CaCO_3$ calcination reaction conditions were explored varying the final heating step temperature and atmosphere composition in order to obtain different final CaO sorbent micro-textural properties. Specifically, three samples were calcined in pure nitrogen varying the final reactor temperature from 650 °C to 700 °C, in order to minimize sintering effects on the final sorbent pore network. On the other hand, with the aim to promote sintering processes, temperature was increased up to 800 °C and 900 °C exploring two different sets of atmosphere compositions, namely from 1 % to 10 % at 800 °C and from 10 % to 50 % at 900 °C in balance with N_2.

Afterwards, samples were carbonated at 550 °C with 0.4 % of CO_2 in balance with N_2 in order to test the micro-structure influence of the CaO carbonation reaction performances, in terms of reaction kinetics and maximum CO_2 capture capacity. More specifically, instead on the maximum final CaO conversion, the transition point CaO conversion was considered, namely such conversion value observed in correspondence of the transition between the chemically controlled regime and the product layer diffusion controlled one, because in some cases the final CaO conversion was still increasing. Such CaO conversion values were obtained by considering the minimum values of the second derivative CaO conversion over time profiles obtained from the WAXS data analysis.

As expected, different CaO micro-structures provided fairly different CaO conversion over time profiles, especially when the sorbent pore matrix is significantly affected by sintering effects, namely those samples calcined at high temperature and in presence of CO_2. Specifically, these samples show a less reactivity to carbonation with respect to those exhibiting negligible sintering phenomena, even though CaO carbonation reactions were performed at the same conditions in terms of temperature and atmosphere composition.

Time-resolved small angle scattering profiles were analyzed by means of the "Unified fit" approach (Beaucage, 1995; Beaucage, 1996), that is capable to provide a quantitative and detailed description of each pore population by means of an arbitrary number of structural levels.

As the carbonation reaction progresses, the meso-pore radius of gyration increases up to generate a third pore population or an asymptotic value in correspondence of the transition

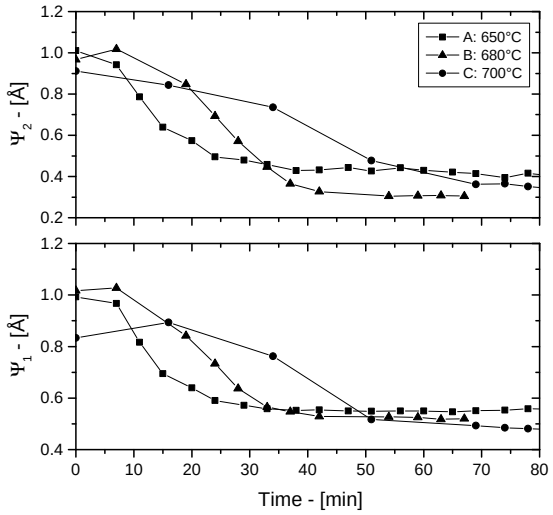

Figure 7.27: Sphericity factor evolution of the two pore populations over the calcium oxide conversion during the carbonation reaction for sample A (calcined at 650 °C in N_2).

point, except for the highly sintered sorbents. This phenomenon is likely due to small pore consumption, that shifts the sorbent pore size distributions (PSDs) to higher pore radii values, up to segregate a small amount of pores (below 5 %) probably located in the inner core of the sorbent particle, where the calcite product layer plugs the outer particle porosity preventing the CO_2 diffusion into the inner part of the sorbent. Furthermore, the increase of the meso-pore radius of gyration was ascribed to a transfer of the contracting meso-porosity into the micro-pore population. On the other hand, the micro-pore radius of gyration is mostly constant during the CaO carbonation reaction.
Additionally, a negative correlation was pointed out between the initial meso-pore radius of the different calcined samples and the maximum conversion time derivative of the CaO carbonation reaction, located in the chemically controlled regime. A similar trend was obtained for the transition point CaO conversion, suggesting that the higher the initial meso-pore radius of gyration the higher the initial reaction rate and the transition point.
Linear specific surface area decreasing profiles over the CaO conversion were observed for samples calcined below 800 °C in nitrogen, where sintering phenomena are negligible. Such trend deviated from the linearity when the specific surface areas are expressed in terms of per unit of particle volume (instead of sample mass) and the random pore model fails to represent such profiles even though its dimensionless parameter ψ was varied from 0 to 2. An opposite behavior was observed for the cases of samples calcined at 800 °C and 900 °C in presence of CO_2, which provided non-linear (pseudo-quadratic) specific surface area per unit of sample mass profiles over the CaO conversion. On the other hand, if rescaled in terms per unit of sample volume, well-defined linear trends were observed.

The increase of the sorbent specific surface area makes the particle more reactive as confirmed by the well-define linear trend between the maximum carbonation rate the sorbent initial specific surface area, where the relative micro-pore trend exhibits a relative higher slope if compared with the meso-pore trends, suggesting a more impact on the micro-pore specific surface area on the reaction conversion rate respect to the meso-pore population. A similar trend was observed for the CaO conversion at the transition point, whose profile is more emphasized if the relative surface area reduction is considered. Therefore, a significant sorbent specific surface area means both a higher conversion rate and a higher CaO conversion transition point. More specifically, two linear correlations were provided

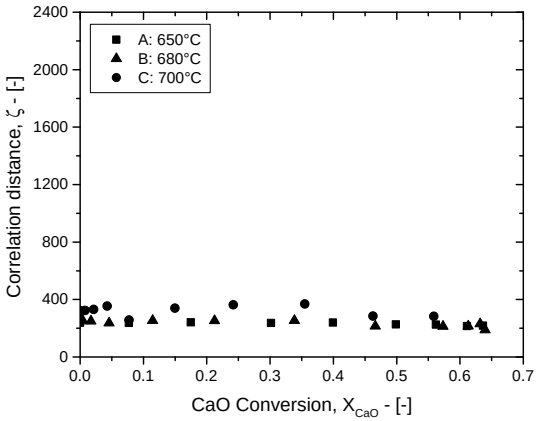

(a) *Samples A, B and C - N_2 calcinations.*

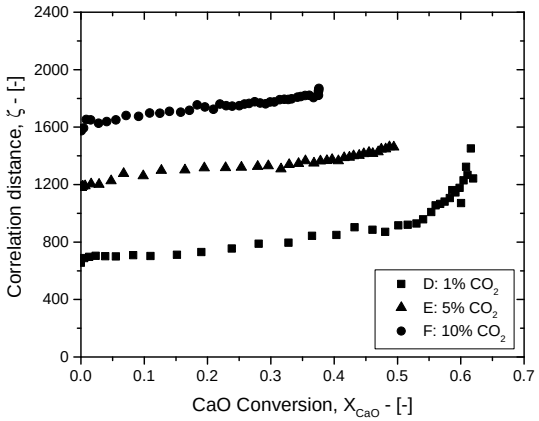

(b) *Samples D, E and F - 800 °C calcinations.*

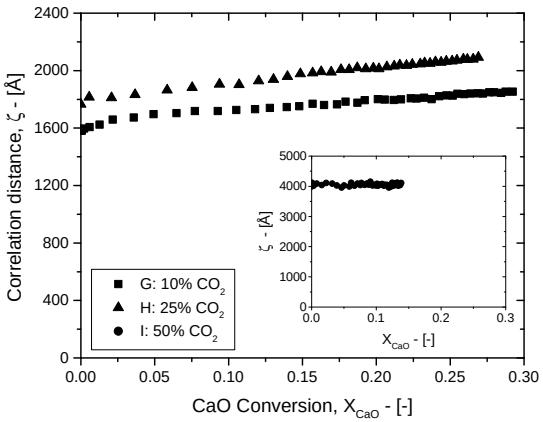

(c) *Samples G, H and I - 900 °C calcinations.*

Figure 7.28: Evolution of the meso-pore correlation distance over the CaO conversion for samples calcined below 800 °C in N_2 (a), for samples calcined at 800 °C (b) and samples calcined at 900 °C in presence of CO_2.

by fitting the experimental data concerning calcination reactions performed at 550 °C with 0.4 % of CO_2. According to the linear trend between the specific surface area and the CaO conversion, a similar profile was observed as for the case of the sorbent specific surface area over the sorbent porosity evolution, because of the well-known linear trend between the sorbent porosity and the CaO conversion. Such trends deviated from the linearity when sintered samples are considered.

The maximum conversion rate data do not show a well-defined trend over the initial sorbent porosity, even though a positive correlation is showed with the sorbent micro- and meso-porosity values. Similarly, the transition CaO conversion over the initial sorbent porosity do not provided a well-defined trend. However, a positive linear profile is observed if the transition CaO conversion is plotted over the relative porosity reduction (between the initial and the transition point value), in agreement with the sorbent porosity over the sample porosity linear profile.

With the increase of sintering effects on the sorbent pore matrix, both the consumed relative porosity and specific surface area decrease, namely from 70÷73 % of relative porosity reduction for samples were sintering effects are negligible (calcined below 800 °C in nitrogen), down to 2÷18 % when sintering phenomena strongly affects the sorbent pore network

(those calcined at 900 °C with 10÷50 % of CO_2 in balance with N_2); from 66÷80 % down to 4÷26 % for the relative specific surface area reduction respectively. Accordingly, the relative pore number density consumption decreases for the case of highly sintered samples where the meso-pore number density reduction is higher than that of the micro-pores, even though the micro-pore number per unit of sample mass is about one order of magnitude higher than that of the meso-porosity.

The sorbent specific surface area and porosity reduction over the pore number density reduction showed quite linear trends which change slope at the transition point from the chemically controlled regime to the product layer controlled one. This change in slope is more emphasized when highly sintered samples are considered.
In addition, the initial pore number per unit of sample mass seems to be positive correlated with the maximum conversion rate and the transition CaO conversion.
Furthermore, the carbonation reaction effect on the pore shape consists in a decrease of the sphericity factors of the two pore populations from initial values close to one, down to 0.3÷0.4 for meso-pores ad 0.48÷0.58 for meso-pores.

Finally, the meso-pore correlation distance is quite constant during the CaO carbonation reaction for those samples where sintering effects are negligible (calcined below 800 °C in N_2) and slightly increases during the reaction for the case of the highly sintered samples.

Part IV

Modeling

Chapter 8

CFD Analysis of the CaO-CO_2 Reaction in a Thermo-Gravimetric Apparatus

Thermo-gravimetric analysis (TGA) is a useful technique to study the kinetics of gas-solid reactions and specifically it has been widely used to investigate the carbonation reaction between carbon dioxide and calcium oxide based solid sorbents, which is the basis of a promising CCS technology. Typical conversion rates of the carbonation reaction initial fast stage measured by TGA are lower than about $0.06\,s^{-1}$.
However, TGA results can be significantly affected by the external mass transfer when a fast gas-solid reaction, such as the carbonation reaction, is considered, namely, when the intrinsic conversion rates are higher than $0.2\,s^{-1}$. In this case the conversion measurement using the thermo-gravimetric analysis may lead to inaccurate results (apparent reaction rate) if the mass transfer of the gaseous reactant is not properly accounted for. In this work a non-stationary computational fluid dynamics (CFD) study of the carbonation reaction was performed considering a horizontal TGA type, using the CFD commercial code ANSYS FLUENT® 15.0, neglecting inter-particle and intra-particle mass diffusion. A surface reaction model was assumed at the crucible surface and the conversion-time profiles were calculated varying the reactant gas flow rate.

8.1 Introduction

Human activities have changed the energy budget of the Earth by introducing in the atmosphere greenhouse gases (GHGs) such as carbon dioxide. The Intergovernmental Panel on Climate Change provides a scientific demonstration of the climate change due to the GHGs emissions and, more specifically, of the carbon dioxide (Stocker, 2013). The carbon dioxide capture and storage (CCS) is one of the mitigation strategies for the atmospheric GHG reduction. Specifically, the CO_2 separation with solid sorbents is a promising technology that can be integrated with existing CO_2 emitting plants. It is based on the CO_2 carbonation reaction with calcium oxide, a fast non-catalytic gas-solid reaction that uses inexpensive solid reactants.
According to Bhatia and Perlmutter (1983a), the conversion-time curves of the carbonation reaction are characterized by an initial fast chemically controlled regime followed by a slow product layer diffusion controlled stage.
The thermo-gravimetric analysis (TGA) is a widely used technique for studying the kinetics of the carbonation reaction (Barker, 1973). Typical conversion rates of the carbonation reaction initial fast stage measured by TGA are lower than about $0.06\,s^{-1}$ (Sun et al., 2008b).

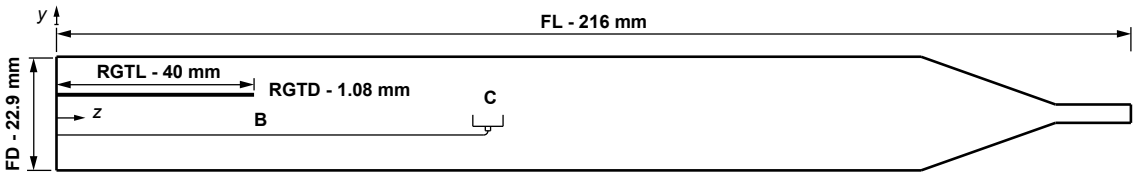

Figure 8.1: Geometry of the TA SDT Q600, where FD is the furnace diameter, FL is the furnace length, RTGL is the reactive gas tube length, RTGD is the reactive gas tube diameter, B is the beam of the balance and C is the crucible.

However, the conversion measurements of a fast gas-solid reaction, such as the carbonation, using the TGA may lead to inaccurate results if the mass transfer of the gaseous reactant is not carefully accounted for (Song et al., 2006). Recently, (Biasin et al., 2015), using synchrotron radiation in-situ XRD to investigate the carbonation reaction, measured initial conversion rates of about $0.28\,\mathrm{s}^{-1}$ significantly higher than the values previously obtained through TGA, and suggested that such difference could be due to the external mass diffusion affecting the thermo-gravimetric data. However, several authors, who performed TGA measurements of the carbonation reaction, claimed that their results are not limited by the external mass diffusion (Sun et al., 2008b), being independent from the gas flow rate (Grasa et al., 2009). Therefore, in this work a computational fluid dynamics (CFD) study is performed on a TGA apparatus, to investigate the effect of external mass diffusion on the carbonation reaction conversion measurements by TGA. The CFD commercial code ANSYS FLUENT® 15.0 is used to perform the numerical simulations. The velocity field around and inside the crucible where the reaction occurs as well as the reactant concentration profiles are analyzed, in order to evaluate the effect of these variables on the reaction rate measurements. In this work, inter-particle and intra-particle mass transfer resistances are neglected: typically, the assumption of negligible inter-particle diffusion is experimentally satisfied by using small amounts of sample mass, while the assumption of negligible intra-particle diffusion is realized by using small particle size (less than $53 \div 63\,\mu\mathrm{m}$) and high carbon dioxide partial pressure (Sun et al., 2008b).

8.2 TGA equipment

The apparatus selected for the CFD simulations of this work is the TA SDT Q600. It is a horizontal thermo-balance which is composed by several components: a balance, a heating system, a tubular furnace, a unit for the temperature measurement and a recording

Table 8.1: Gas flow regime inside the TGA furnace and the reactive gas tube at 650 °C and 1 atm. $\dot{V}_0$ is the normal flowrate and $\dot{V}$ is the effective flowrate.

Flow rate		Furnace			Reactive gas tube		
$\dot{V}_0$ $[\mathrm{Nm^3\,min^{-1}}]$	$\dot{V}$ $[\mathrm{m^3\,s^{-1}}]$	$\bar{v}_F$ $[\mathrm{m\,s^{-1}}]$	$Re_{\mathrm{N_2}}$ $[-]$	$Re_{\mathrm{CO_2}}$ $[-]$	$\bar{v}_{\mathrm{RGT}}$ $[\mathrm{m\,s^{-1}}]$	$Re_{\mathrm{N_2}}$ $[-]$	$Re_{\mathrm{CO_2}}$ $[-]$
25	1.41×10^{-6}	0.003 43	0.737	1.21	1.53	15.6	24.5
50	2.82×10^{-6}	0.006 86	1.47	2.41	3.07	31.2	49.0
100	5.63×10^{-6}	0.0137	2.95	4.82	6.15	62.4	98.0
200	1.13×10^{-5}	0.0274	5.89	9.64	12.3	125	196
300	1.69×10^{-5}	0.0412	8.84	14.5	18.5	187	294
400	2.25×10^{-5}	0.0549	11.8	19.3	24.6	249	392

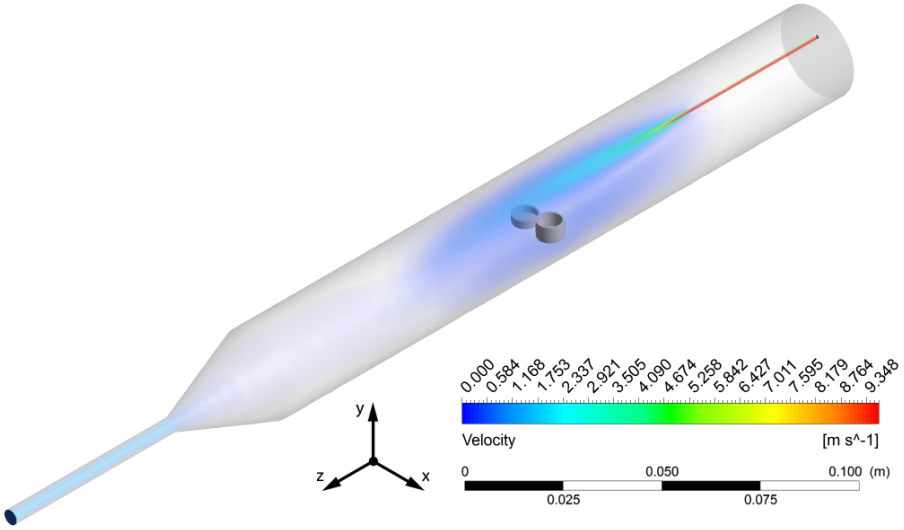

Figure 8.2: Three-dimensional representation of the velocity field (650 °C, 1 atm, inlet gas is CO_2 and flowrate equal to 100 $Nm^3\,min^{-1}$).

system. Fig. 8.1 shows the geometry of the furnace where two crucibles are located. The reaction atmosphere is fed from the reactive gas tube (at the left of Fig. 8.1) connected to the inert or reactive gas lines. Downstream of the crucibles the reaction chamber tapers until reaches the purge gas zone, where exhaust gases leave the reaction chamber.

8.2.1 Meshing

The computational domain was meshed with a hybrid mesh. Close to the furnace walls a structured mesh was imposed, whereas an unstructured mesh was used for the other parts of the domain. Specifically, tetrahedron cells were chosen and mesh refining was performed in the proximity of the sudden expansion and close to the two crucibles. The cell maximum and minimum size were set to 6 mm mm and to 0.3 mm, respectively. In this way, about 800 000 computational cells and 2 000 000 nodes were obtained.

8.3 Operative conditions

In the simulated carbonation thermo-gravimetric experiment, a small amount (5 mg) of sorbent sample (CaO) was loaded in one of the two crucibles (the crucible internal diameter is 5.5 mm). Such sample amount is small enough that inter-particle mass diffusion can be neglected (Sun et al., 2008b). The simulated experiment is operated at 1 bar and at isothermal conditions (650 °C), which in a real TGA experiment are typically reached by heating the furnace in nitrogen. Therefore, in the first instants of the simulations nitrogen is fed at 650 °C.
Afterwards, a gas switch is performed from the inert atmosphere to the reactive gas which consists of pure carbon dioxide. TGA results are commonly expressed in dimensionless form through the CaO fractional conversion as a function of time.

8.4 Carbonation reaction rates

The aim of the work is to investigate the influence of the external mass diffusion on the initial fast stage (controlled by the surface chemical reaction) of the carbonation. The

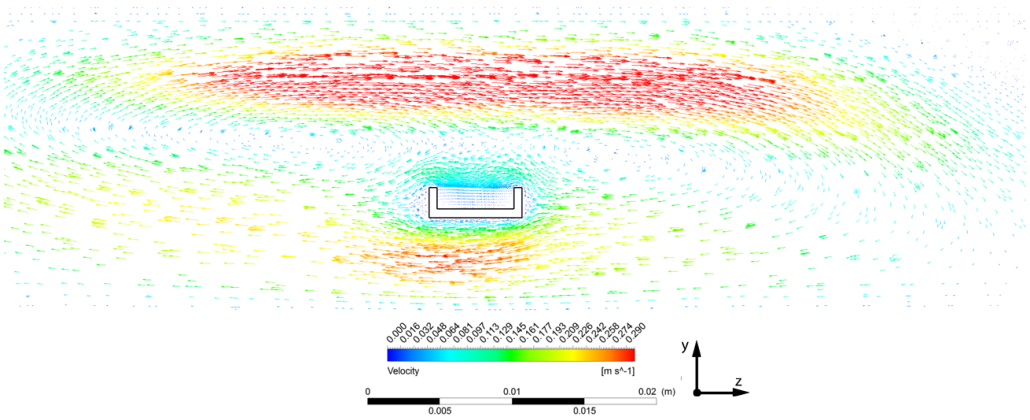

Figure 8.3: Predicted velocity field around and inside the crucible where reaction occurs (650 °C, 1 atm, inlet gas is CO_2 and flowrate equal to 100 $Nm^3\,min^{-1}$).

second carbonation stage is slow and controlled by the product-layer diffusion (Bhatia and Perlmutter, 1983a) and, therefore, is neglected in this work, because in this stage the external mass diffusion has no effect on the carbonation kinetics. Consequently, in this CFD study a simple reaction rate model is assumed, neglecting the product-layer diffusion, the abrupt transition between the first and second stage, and the pore closure. Additionally, the effect of the CO_2 equilibrium concentration on the reaction rate was neglected as well, because of the low temperature (650 °C). The functional form used to express the conversion rate is based on the work of Sun et al. (2008b), who demonstrated with experimental results that at low CO_2 partial pressures the carbonation reaction is first order, but when the CO_2 partial pressure is higher than 10 kPa the reaction rate is zeroth order. Therefore, when the CO_2 partial pressure is higher than 10 kPa, the CaO conversion (X) rate is expressed as

$$\frac{dX}{dt} = k_0\, M_{\mathrm{CaO}}\, S_0\, (1 - X) = k_0'\, (1 - X)\ , \tag{8.1}$$

where k_0 is the zeroth order intrinsic rate constant, S_0 is the initial specific surface area and M_{CaO} is the CaO molecular weight, which can grouped in the constant k_0'. This constant can be estimated from the data of Biasin et al. (2015), obtained with a technique alternative to TGA (in-situ synchrotron radiation XRD) and not affected by external mass diffusion. They measured an average initial dX/dt equal to 0.28 s^{-1} and from this value k_0' was estimated.
Following Sun et al. (2008b), below a partial pressure of 10 kPa, the reaction order switches to first order, and, accordingly, the conversion rate is expressed as

$$\frac{dX}{dt} = k_1'\, C_{\mathrm{CO_2}}\, (1 - X)\ , \tag{8.2}$$

where $k_0' = k_1'\, C^*_{\mathrm{CO_2}}$ and $C^*_{\mathrm{CO_2}}$ is the concentration value when the CO_2 partial pressure is equal to 10 kPa and $C_{\mathrm{CO_2}}$ is the CO_2 concentration at the crucible surface. Because the inter-particle diffusion resistances are negligible, the reaction is assumed to occur at the crucible surface, where the CaO moles are expressed in terms of surface density (CaO moles loaded per unit of crucible internal bottom surface).

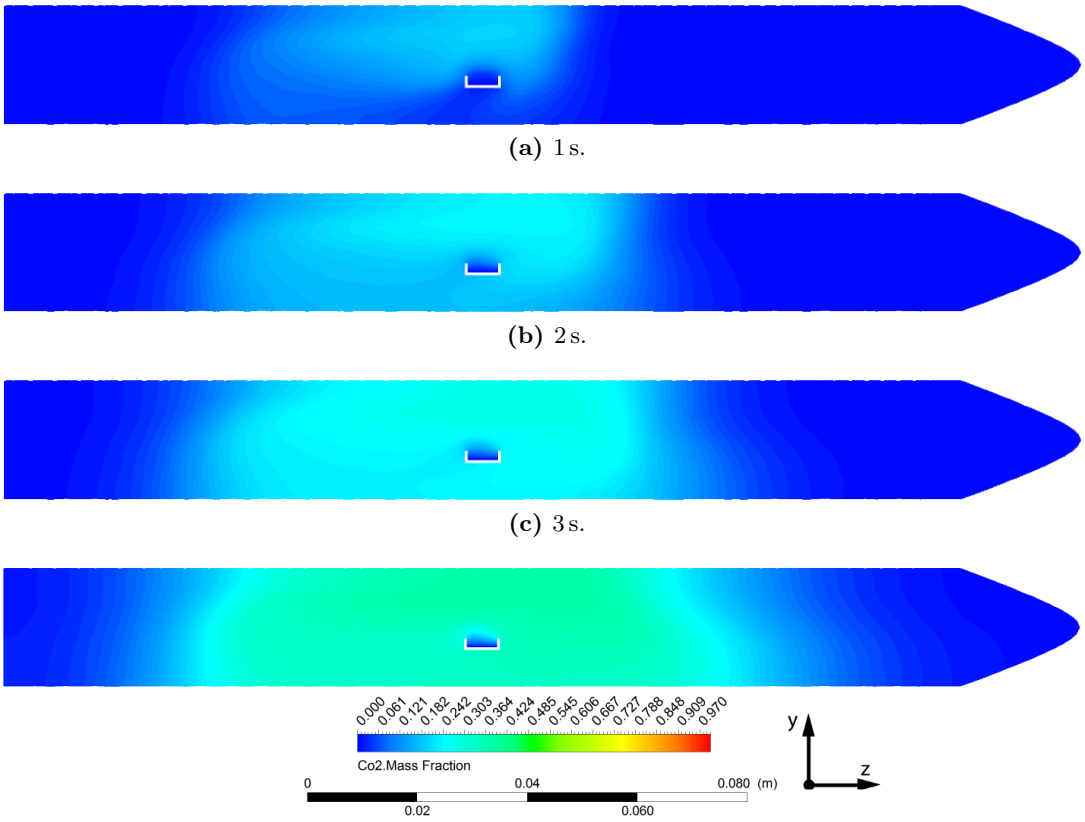

(a) 1 s.

(b) 2 s.

(c) 3 s.

(d) 5 s.

Figure 8.4: Contours of the CO_2 mass fraction in the first seconds of the simulations (650 °C, 1 atm, inlet gas is CO_2 and flowrate equal to 100 $Nm^3\,min^{-1}$).

8.5 TGA gas flow regime

The numerical simulations were performed with gas flow rates that range from 25 to 400 $Nm^3\,min^{-1}$. The gas fed is initially pure N_2, which is afterwards switched to pure CO_2. Based on these operative conditions, the Reynolds number was calculated both for the furnace and the reactive gas tube. The definition of the Reynolds number employed for cylindrical pipes is

$$Re_{i,j} = \frac{\rho_i \, \bar{v}_j \, d_j}{\mu_i},$$

where i refers to N_2 or CO_2, j to the reactive gas tube or to the furnace, ρ_i is the density of species i, $\bar{v}_j$ is the average gas velocity inside j, d_j is the diameter, μ_i is the viscosity of the gaseous species i. The results are listed in Tab 8.1, which shows that the gas flow regime is laminar ($Re_{i,j} \leq 2100$) both in the furnace and in the reactive gas tube.

8.6 Results

The output of the CFD simulations consist of the velocity field and the CO_2 concentration field inside the TGA (TA SDT Q600), and the conversion-time curves.

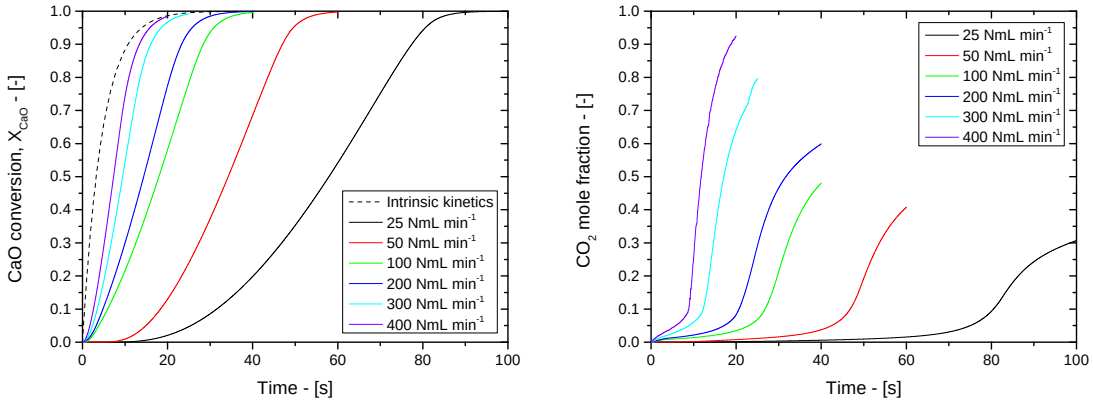

(a) *Conversion vs time curves.* **(b)** *CO_2 mole fraction vs time.*

Figure 8.5: Simulation results of the conversion-time curves and of the (surface averaged) CO_2 mole fraction at the reaction surface (650 °C,5 atm, inlet gas is CO_2).

8.6.1 Velocity field

Fig. 8.2 shows the three-dimensional velocity field inside the furnace (for 100 $Nm^3\,min^{-1}$). A detailed view of the velocity field around and inside the reaction crucible (the crucible where the CaO sample is loaded and the reaction occurs) is shown in Fig. 8.3. Since the effective cross section of the furnace is reduced due to the presence of the two crucibles, the flow accelerates and the velocity increases above the crucibles, as shown in Fig. 8.3. The gas velocity is considerably small (much smaller than in the bulk) inside the crucible.

8.6.2 Carbon dioxide concentration field

When the gas flow is switched from N_2 to CO_2, an axial carbon dioxide profile is established due to CO_2 convection and diffusion. Fig. 8.4 shows the CO_2 reactant front at the first instants after the gas switch. The surface of the crucible is progressively reached by CO_2 whose concentration gradually increases, as represented in Figure 5b.

8.6.3 Surface reaction

The carbonation reaction occurs at the surface of the smaller crucible according to Eqs. (8.1) and (8.2). The results of the numerical simulations, in terms of conversion vs time, are reported in Fig. 8.5a which shows the apparent reaction rates computed from the CFD output, compared to the solution of Eq. (8.1) that represents the intrinsic reaction rate when the reaction surface is exposed to the bulk concentration value. This trend of the apparent reaction rate is clearly due to the CO_2 mole fraction profile at the reaction surface (Fig. fig:CO2VsTimeCdf).
The CO_2 mole fraction vs time curve is the result of the balance between the incoming CO_2 from the bulk flow and the reactant consumption due to the carbonation. This CO_2 mole fraction profile cannot be predicted without a CFD simulation and the assumption of constant CO_2 concentration at the reaction surface (equal to the bulk concentration) is clearly inaccurate for the initial fast regime of the CaO carbonation.
The simulation results provide an apparent reaction rate that depends significantly on the external mass transfer. Specifically, the conversion-time curve based on the intrinsic reaction rate has an initial slope of 0.28 s^{-1} whereas for flowrates of $25 \div 400\,Nm^3\,min^{-1}$ the apparent conversion rate has a maximum slope of about 0.096 s^{-1}. It is noteworthy

that such value of apparent conversion rate is quantitatively in agreement with the typical values obtained experimentally from TGA measurements (Sun et al., 2008b).

8.7 Conclusions

In this work, CFD simulations of a typical CaO carbonation experiment in a horizontal TGA (TA SDT Q600) were performed to investigate the influence of the external mass transfer on the conversion data obtained through TGA.
Several results were obtained from the CFD simulations. The first is that the gas velocity field inside the TGA furnace, especially around and inside the crucible, is complex and the velocity inside the crucible is very low compared to the bulk velocity. Consequently, when the gas flow switches from the inert gas (N_2) to the reactant (CO_2), at the reaction surface the CO_2 concentration gradually increases up to reaching the bulk concentration, but most of the reaction occurs with a reactant concentration significantly lower than the bulk concentration. Finally, the apparent conversion-time curve (computed as output of the CFD simulations) are significantly different from the curves obtained from the intrinsic reaction rate due to the non-stationary local carbon dioxide concentration profiles. Specifically, the intrinsic conversion rates are about $3 \div 13$ times higher the apparent conversion rates (computed from the CFD simulations), thus demonstrating that TGA measurements of the carbonation reaction are strongly affected by the external mass transfer. It is noteworthy that the values of the computed apparent conversion rate are quantitatively in agreement with the typical values obtained experimentally in TGA measurements of the carbonation reaction.

Chapter 9

Application of a Random Pore Model with Distributed Pore Closure to the Carbonation Reaction

In this chapter a random pore model accounting for a *continuous* sorbent pore size distribution (PSD) was developed and applied to the carbonation reaction, including the reaction rate dependence on the equilibrium carbon dioxide partial pressure and the reaction order switch (from zeroth to first order). Such model is predictive once the intrinsic rate constant, the product-layer diffusivity and the initial pore size distribution are known. The simulation results include the conversion versus time curves, as well as the evolution of the pore size distribution and of the pore and reaction surfaces over time, and are compared with experimental data of conversion over time, obtained through a high-pressure thermo-gravimetric analyzer, at a carbon dioxide pressure of 5 bar. The simulation results show that the presented model is capable to predict accurately the whole conversion-time curves, particularly at short times, both in the fast and in the product-layer diffusion regimes, and to represent the abrupt transition due to the pore closure.

9.1 Introduction

The Global Warming is the direct consequence of the emissions of GHGs (Green House Gases) due to the human activities. According to Stocker (2013) anthropogenic emissions are mostly related to large stationary sources, which mainly involve fossil fuel combustion in power plants, oil refineries and large industrial facilities. The most important anthropogenic GHG is carbon dioxide and, considering the total emissions of CO_2 per year (for large stationary sources), 78 % are produced in the power generation industry and 20 % from gas processing.

A promising technology for the carbon dioxide capture is based on the carbonation reaction, represented by Eq. (2.1), using CaO based solid sorbents as a regenerable material to sequester CO_2 from combustion flue gases (Shimizu et al., 1999). However, the carbonation reaction kinetics is complex: after a fast chemically controlled initial reaction stage, a second slower reaction stage controlled by the diffusion in the product layer ($CaCO_3$) takes place (Barker, 1973). It has also been observed that the transition between the fast and slow regimes is abrupt (Grasa et al., 2009). Several kinetic models have been proposed to describe the CaO carbonation kinetics (Stendardo and Foscolo, 2009). However, most of them are not capable to predict correctly the conversion vs time curves and especially the sudden transition between the two regimes (Bhatia and Perlmutter, 1983a). Such sharp transition has been related to the smaller pore closure (Bhatia and Perlmutter, 1983b), therefore an accurate prediction of the CaO carbonation kinetics requires a structural model capable to represent the pore size distribution evolution over time.

In this work the Random Pore Model (RPM) independently developed by Bhatia (1985) and Sotirchos and Yu (1985) was selected and applied to the carbonation reaction. This model represents the evolution of the continuous pore size distribution of a porous network. In the carbonation reaction, as CaO is consumed a product layer of $CaCO_3$ is produced and interposes between the CaO solid reactant and the gas phase (CO_2). Because the molar volume of the product layer is larger than the reactant molar volume, each pore of the particle shrinks and eventually closes. Consequently, this reaction is characterized by incomplete conversion because of the pore closure.
In this work, the RPM developed by Bhatia (1985) and Sotirchos and Yu (1985) is modified in order to account for the CO_2 equilibrium concentration and for the reaction rate switch from zeroth to first order (Sun et al., 2008b). A similar modeling approach was proposed by Sun et al. (2008a), however they used a discretized (rather than a continuous) pore size distribution. Differently than in Sun et al. (2008a), in this work the carbonation kinetics is simulated at short times, in order to emphasize the details of the conversion vs time curve and to check the predicted result accuracy; additionally, the time evolution of the pore size distribution and of the reaction surface during the CaO carbonation are predicted as well.

9.2 Pore size distribution of the CaO based sorbents

CaO sorbents were used in this work to perform carbonation tests in a thermo-gravimetric analyzer. Porous CaO samples were obtained from commercial $CaCO_3$ ($150 \div 160\,\mu m$, § 2.7) and calcined at 800 °C in pure N_2. The pore size distribution of the CaO samples was obtained by N_2 adsorption (BJH). The RPM of Bhatia (1985) and Sotirchos and Yu (1985) requires to determine the initial pore size distribution of the porous solid reactant (CaO). In this work a log-normal distribution is used to represent the differential pore size distribution. Defining r_0 as the initial pore radius (in Å), the log-normal pore size distribution is expressed (Evans, Hastings, and Peacock, 2000) as:

$$\varepsilon_{\text{diff}}(r_0) = \frac{\varepsilon_0}{\sqrt{2\pi}\,\sigma_{N_0}\,r_0} \exp\left\{-\frac{\left[\ln(r_0) - \mu_{N_0}\right]^2}{2\,\sigma_{N_0}^2}\right\}, \tag{9.1}$$

where μ_{N_0} and σ_{N_0} are respectively the mean and the standard deviation of the normal distribution of the random variable $\ln(r_0)$; ε_0 is the initial total porosity of the sample, namely the total overlapped void fraction, according to Bhatia and Perlmutter (1980). According to Evans, Hastings, and Peacock (2000), the mean M_0 (in Å) of the log-normal distribution is related to the normal distribution parameters by:

$$M_0 = \exp\left(\mu_{N_0} + \frac{\sigma_{N_0}^2}{2}\right). \tag{9.2}$$

The pore length distribution $l(r_0)$ is obtained from the non overlapped pore size distribution dividing by $\pi\,r_0^2$.
By fitting the experimental data of N_2 adsorption through the log-normal pore size distribution the following values of the distribution parameters were computed:ε_0 is 0.499, μ_{N_0} 5.641 and σ_{N_0} 0.306.

9.3 The continuous random pore model applied to the carbonation reaction

The carbonation reaction is modeled in the RPM developed by Bhatia (1985) and Sotirchos and Yu (1985) for a first order irreversible reaction. In each pore, two different surfaces are identified: a reaction surface that moves inward and a pore surface that moves outward as reaction progresses. This model distinguishes the overlapped configuration from the non-overlapped one, linking the two geometries with the Avrami's equation, according to Bhatia and Perlmutter (1980). However, the carbonation reaction is reversible and, as demonstrated by Sun et al. (2008b), its reaction order switches from 0 to 1 depending on the CO_2 partial pressure. The carbonation reaction being reversible, the effect of the CO_2 partial pressure is expressed in terms of driving force with respect to the equilibrium, namely as $\left(p_{CO_2} - p_{CO_2}\right)$. Consequently, the RPM proposed Bhatia (1985) and Sotirchos and Yu (1985) requires to be modified to account for the reaction order switch and the equilibrium condition. Following this approach the carbonation reaction modeling is initially split into two cases, namely the first order, and the zeroth order reaction.

9.3.1 First order reaction

Assuming a first order reversible reaction, the surface reaction rate is expressed through:

$$\frac{\partial r_s}{\partial t} = k_s^{(1)}\, C_{CO_2}^{s^*}, \tag{9.3}$$

where r_s is the reaction surface radius, and $k_s^{(1)}$ is the first order rate constant. $C_{CO_2}^{s^*}$ is defined as $C_{CO_2}^{s} - C_{CO_2,\,\mathrm{eq.}}$, $C_{CO_2}^{s}$ being the concentration of CO_2 at the reaction front, and $C_{CO_2,\,\mathrm{eq.}}$ is the CO_2 equilibrium concentration which is evaluated following Baker (1962). The CO_2 concentration profile inside the solid product layer is calculated assuming pseudo-steady-state diffusion of CO_2 through the product layer (Bhatia, 1985), namely by solving the following diffusion equation for cylindrical pores:

$$\frac{\partial}{\partial r}\left(r\frac{\partial C_{CO_2}^{*}}{\partial r}\right) = 0 \qquad \text{for } r_p \le r \le r_s \tag{9.4}$$

where r is the radial coordinate of each cylindrical pore, $C_{CO_2}^{*}$ is defined as $(C_{CO_2} - C_{CO_2,\,\mathrm{eq.}})$ and r_p is the pore radius. The boundary conditions of Eq. (9.4) are

$$\begin{aligned} C_{CO_2}^{*} &= C_{CO_2}^{p^*} = C_{CO_2,\,\mathrm{bulk}}^{*} \qquad \text{at } r = r_p \\ -D_{pl}\frac{\partial C_{CO_2}^{p^*}}{\partial r} &= k_s^{(1)}\frac{\rho_s}{M_{CaO}} C_{CO_2}^{s^*} \qquad \text{at } r = r_s, \end{aligned} \tag{9.5}$$

where $C_{CO_2}^{p^*}$ refers to refers to the pore interface, D_{pl} is the CO_2 molecular diffusivity in the product layer, ρ_s is the mass skeleton density of the solid reactant and M_{CaO} is the CaO molecular weight. Eq. (9.4), once integrated with the boundary conditions Eq. (9.5), provides

$$C_{CO_2}^{*}(r) = \frac{C_{CO_2,\,\mathrm{bulk}}^{*}}{1 + \dfrac{k_s^{(1)}\,\rho_s}{M_{CaO}\,D_{pl}} r_s\, \ln\left(\dfrac{r}{r_p}\right)} \qquad \text{for } r_p \le r \le r_s. \tag{9.6}$$

Substituting Eq. (9.6) into Eq. (9.3) at $r = r_s$ $\left(C^*_{\mathrm{CO_2}}(r_s) = C^{s^*}_{\mathrm{CO_2}}\right)$:

$$\frac{\partial r_s}{\partial t} = \frac{k_s^{(1)}\, C^*_{\mathrm{CO_2,\,bulk}}}{1 + \dfrac{k_s^{(1)}\,\rho_s}{M_{\mathrm{CaO}}\, D_{pl}} r_s\, \ln\left(\dfrac{r}{r_p}\right)}. \tag{9.7}$$

9.3.2 Zero order reaction

According to Sun et al. (2008b), the carbonation reaction switches to zeroth order when $C^s_{\mathrm{CO_2}} = C_{\mathrm{CO_2},e}$, where $C_{\mathrm{CO_2},e}$ is the concentration corresponding to 10 kPa. In this case the reaction rate is expressed by

$$\frac{\partial r_s}{\partial t} = k_s^{(0)}, \tag{9.8}$$

where $k_s^{(0)}$ is the zeroth order rate constant. The rate constant $k_s^{(0)}$ is related to the first order rate constant $k_s^{(1)}$ by $C_{\mathrm{CO_2},e}$ through the relation:

$$k_s^{(0)} = k_s^{(1)}\, C_{\mathrm{CO_2},e}.$$

In this case, the boundary conditions of the pseudo-steady-state CO_2 diffusion equation are:

$$\begin{aligned} &C^*_{\mathrm{CO_2}} = C^{p^*}_{\mathrm{CO_2}} = C^*_{\mathrm{CO_2,\,bulk}} \qquad \text{at } r = r_p \\ &-D_{pl}\frac{\partial C^{p^*}_{\mathrm{CO_2}}}{\partial r} = k_s^{(0)}\frac{\rho_s}{M_{\mathrm{CaO}}} \qquad \text{at } r = r_s, \end{aligned} \tag{9.9}$$

Eq. (9.4), once integrated with Eq. (9.8), results results in the following equation

$$C^*_{\mathrm{CO_2}}(r) = C^*_{\mathrm{CO_2,\,bulk}} - \frac{k_s^{(0)}\,\rho_s}{M_{\mathrm{CaO}}\, D_{pl}} r_s\, \ln\left(\frac{r}{r_p}\right) \qquad \text{for } r_p \le r \le r_s. \tag{9.10}$$

9.3.3 Governing equations

The previous equations Eqs. (9.7)–(9.8) for r_s and Eqs. (9.6)–(9.10) for the CO_2 concentration at the reaction interface are solved with the rate of change of the pore radius (Bhatia, 1985),

$$\frac{\partial r_p}{\partial t} = -\frac{(Z_{\mathrm{carb}} - 1)\,(1 - X)\; r_s}{[1 + (Z_{\mathrm{carb}-1})\, X]\; r_p}\left(\frac{\partial r_s}{\partial t}\right), \tag{9.11}$$

and with the conversion equation (Bhatia, 1985):

$$X = 1 - \frac{\exp\left[-\displaystyle\int_0^\infty \pi r_s^2(r_0, t) l(r_0)\, dr_0\right]}{1 - \varepsilon_0}, \tag{9.12}$$

where Z_{carb} is the ratio of the $CaCO_3$ over the CaO molar volume (Appendix B), X is the initial total porosity and X is the CaO conversion (also indicated as X_{CaO}).

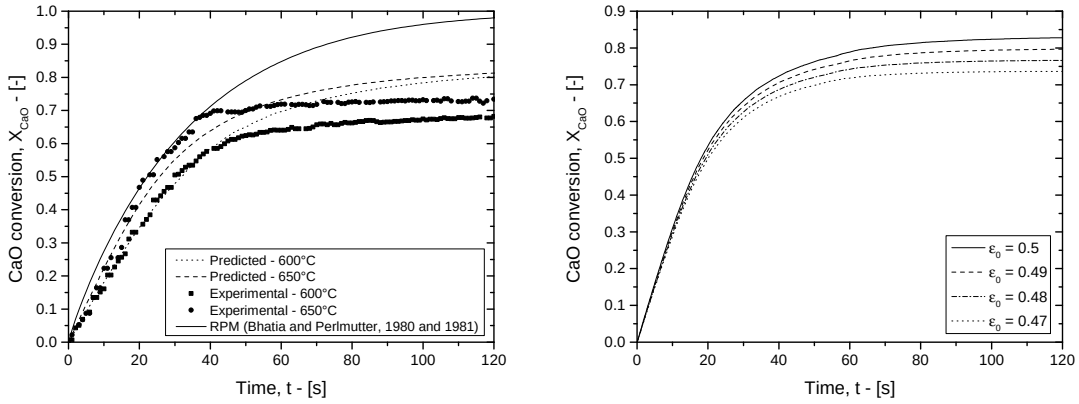

(a) *Comparison of the modified RPM results with experimental data.*

(b) *Effects of ε_0 on the conversion-time profiles..*

Figure 9.1: Comparison of the modified RMP predictions with experimental data and the initial porosity effects on the model predictions. Simulated and experimental data refer to 5 bar of pure CO_2.

9.3.4 Numerical Approach

The pore length distribution is discretized in nr computational grid points following the NUMOL procedure (Schiesser, 1991). Consequently, Eqs. (9.7)-(9.8) and Eq. (9.11) are evaluated in each grid point. Such approach allows to build a set of $2 \times nr$ ODEs.

9.4 Results and discussion

In order compare the simulation results with experimental data, TGA carbonation tests were performed using a DynTHERM MP-ST TGA by RUBOTERM GMBH. $150 \div 160\,\mu m$ particles and 5 bar of CO_2 were used to minimize intra-particle diffusion.
The modified random pore model proposed in this work is *predictive* (no adjustable parameters) given the initial continuous pore size distribution and the kinetic parameters (pre-exponential factor and activation energy) of the reaction rate constant and of the product layer diffusivity. As previously mentioned, the pore size distribution was measured by N_2-adsorption technique, while the parameters of the product layer diffusivity, namely

$$D_{pl} = 0.27 \exp\left(-\frac{E_{a,D}}{RT}\right),$$

where $E_{a,D}$ is $215\,kJ\,mol^{-1}$, R is the universal gas constant, T is in K and D_{pl} is in $m\,s^{-1}$, were taken from Sun et al. (2008a) and the parameters of the reaction rate constant were obtained by fitting the experimental conversion vs time curves at short times.
Fig. 9.1a shows the comparison between the experimental data (carbonation temperatures equal to 600 °C and 650 °C) and the simulation results. It is noteworthy that the modified RPM is capable to represent the whole conversion-time curve of the carbonation reaction including the sharp transition between the two regimes, even for short reaction times. Previous carbonation reaction models (except for Sun et al. (2008a)) were not capable to predict simultaneously both the regimes and the sharp regime transition (an example is shown in Fig. 9.1a for the model of Bhatia, S.K. and Perlmutter (1981) considering the temperature at 650 °C). Sun et al. (2008a) proposed an advanced carbonation reaction

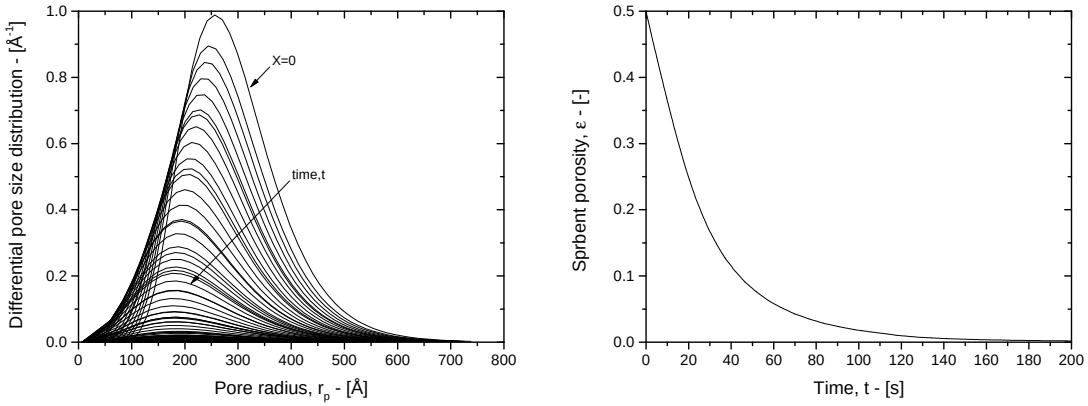

(a) *Predicted PSDs over time.* **(b)** *Predicted porosity over time.*

Figure 9.2: Predicted differential pore size distribution (Å^{-1}) and particle porosity evolution over time (5 bar of pure CO_2 and 650 °C).

model, however, they obtained a reasonable agreement with experimental data only on a large time scale (namely 2.000 s).
Fig. 9.1a shows that the final experimental conversion is overestimated by the simulation results. However, it is noticeable that the final predicted CaO conversion is rather sensitive to the initial porosity. In fact, Fig. 9.1b shows a parametric study in which, varying the initial particle porosity within a small range (from 0.47 to 0.5) the corresponding final conversions change significantly (from 73.7 % to 83.1 %). The N_2-adsorption data of the initial CaO samples provided a particle porosity of 0.499. The accuracy of such value, considering the high sensitivity of the conversion simulation results on the initial porosity, requires to be checked with alternative measurement techniques. Additionally, the output of the proposed model include the prediction of several structural properties. Fig. 9.2a shows the differential pore size evolution as carbonation reaction occurs and the particle porosity is completely lost (Fig. 9.2b) due to the pore closure after $2 \div 3$ min. Figs. 9.3a and 9.3b show the trends of the total pore and reaction surface vs the CaO conversion; the predicted pore specific surface area reaches a value of less than 10 % (of the initial specific surface) at the end of the carbonation.
These results were confirmed with a N_2-adsorption test on the reacted samples, which provided an experimental particle porosity of 0.015 and a reduced specific surface area ($S_p/S_{p,0}$) of 0.095.

9.5 Conclusions

In this work, a modified RPM was presented, based on the structural models of Bhatia (1985) and Sotirchos and Yu (1985), to represent the kinetics of the carbonation reaction, including the reaction order switch from first to zeroth and the CO_2 equilibrium concentration. The model is predictive (no adjustable parameters) given the continuous pore size distribution and the kinetic parameters of the reaction rate constant and of the product-layer diffusivity. The simulation results show that the proposed model is capable to predict the whole conversion-time curve of the carbonation reaction, particularly at short reaction times, including the sudden transition between the first fast regime and the second product layer diffusion controlled slow regime, and the pore closure due to the product layer deposition inside pores as reaction progresses. However, the final predicted conversion is

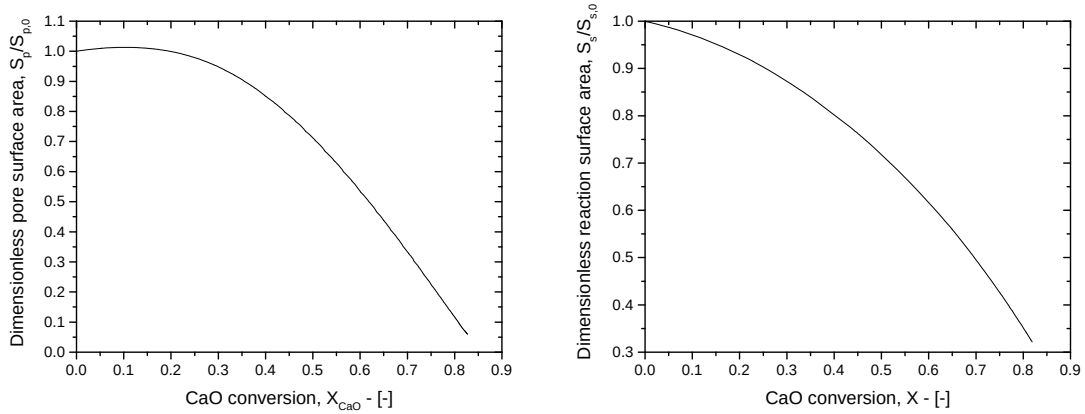

(a) *Pore surface.* **(b)** *Reaction surface.*

Figure 9.3: Prediction of the total pore and reaction surface evolution with conversion (5 bar of pure CO_2 and 650 °C).

highly sensitive to the initial porosity and an accurate experimental estimate of the porosity is required. Finally, the output of the proposed model include the prediction of several structural properties, namely the pore size distribution and the reaction surface evolution over time.

Conclusions

The carbon dioxide capture with calcium based solid sorbents is a promising technology to reduce the CO_2 emissions from fossil fuel combustion power plants (Metz et al., 2005), that is a post-combustion CO_2-capture process commonly named "Ca-looping cycle" included in the Carbon Capture and Storage (CCS) technologies (Blamey et al., 2010; Fennel and Anthony, 2015). This process is considered part of a mitigation strategy of the unequivocal global scale climate change (Stocker, 2013) and is based on the CO_2 carbonation reaction. Among the several CO_2 capture materials, calcium oxide is one of the most promising and attractive solid sorbent (Blamey et al., 2010; Shimizu et al., 1999), that is generated from the thermal activation of the non-porous precursor calcium carbonate.

This work of thesis deals with the micro-textural properties characterization of calcium oxide micro-structure that strongly influence the CaO carbonation reaction performances in terms of reaction kinetics and maximum CO_2 capture capacity. Such properties are generated during the high temperature calcium carbonate decomposition where the CO_2 release and the different molar volume between the solid reactant and solid product generate the sorbent pore network, defining the final sorbent micro-structural properties in terms of sorbent porosity, specific surface area, mean pore radius and average crystallite size. Both the $CaCO_3$ calcination and CaO carbonation reactions are non-catalytic gas-solid reactions where the solid reactant micro-structure interacts with the reaction kinetics itself (Bhatia and Perlmutter, 1983a; García-Labiano et al., 2002).
For these reasons, the CaO carbonation reaction and the $CaCO_3$ thermal decomposition have been widely investigated in literature, however, the material micro-structure evolution and the high temperature and time dependent phenomena like pore generation, sintering mechanisms, crystallite evolution and pore closure are still poorly studied and unknown and the investigation of these phenomena is still open.

This research project initiated with the investigation of the mutual relationship between the sorbent micro-textural properties and its average crystallite size, by considering completely calcined calcium carbonate sorbents produced under vacuum conditions (below 0.01 bar) and varying the heating step duration in order to promote sintering effects on the final pore matrix. Three different techniques were used for the investigation of possible relationships between the CaO micro-textural properties (specific surface area and particle porosity) and the sorbent crystallite size, namely TGA, N_2-adsorption and XRD. During thermal decompositions, sintering effects were minimized using vacuum conditions promoting the CO_2 removal from the reactor atmosphere. Therefore, high porosities (0.48–0.51) and specific surfaces (41–50 $m^2\,g^{-1}$) were obtained, associated with low crystallite sizes (40–50 nm), when short heating periods were considered, namely 40 min at 800 °C and 50 min at 900 °C respectively. Linear correlations were obtained between the sorbent specific surface area/porosity and the crystallite size, regardless of the reactor temperature. Particularly, a well defined linear correlation between the sorbent specific surface area and its crystallite size suggests that the lower the crystallite size the higher the sorbent porosity and specific surface area. These results are in agreement with the hypothesis formulated by Biasin et al. (2015), who claimed that a low crystallite size in the initial uncarbonated CaO is a good indicator of the initial sorbent porosity and specific surface area. Finally, SEM images of a completely calcined calcium carbonate under vacuum conditions at 800 °C

showed a poorly sintered micro-structure, that mainly consists of slit-shaped pores and particle cracks. Such pore network configuration has never been observed by literature contributors, who usually provided pore matrices mainly made of cylindrical-shaped pores and grains.

Although the traditional ex-situ techniques (such as N_2-adsorption and XRD) are actually widely used to characterize the sorbent micro-structure (Barker, 1973; Sun et al., 2007; Zhu, Wu, and Wang, 2011), the high temperature and time dependent phenomena that occur during sorbent activation and CO_2 capture steps cannot be easily investigated by means of ex-situ approaches. For this reason, *in-situ* X-ray small angle scattering (SAS) technique was applied for the first time to the investigation of the sorbent micro-textural properties at the same operative conditions of the calcite thermal activation and CaO carbonation reaction in terms of temperature and atmosphere compositions.

However, because this was the *first time* that SAS technique was applied to highly porous materials, like CaO for the CO_2 capture, ex-situ X-ray small angle scattering was firstly applied at the APS (Argonne National Laboratory) to investigate completely and partially calcined sorbent precursor ($CaCO_3$) and CaO carbonated samples in order to test the SAS capability to characterize this kind of porous and powder-based samples. The successful results of this experimental campaign provided a detailed description of the sorbent micro-structure, that confirmed the bimodal distribution of the CaO samples, characterized by two distinct pore populations made of micro- and meso-pores respectively. Additionally, the USAXS/SAXS technique was capable to provide a quantitative and detailed description of the structure of each pore population in terms of porosity, specific surface area, radius of gyration (Beaucage, 1995; Spalla, Lyonnard, and Testard, 2003; Chavez Panduro et al., 2012). Specifically, the specific surface areas and the pore radius are in quantitative agreement with the N_2-adsorption measurements results, namely with the BET and BJH methods, especially for the case of the average pore radius, where the agreement with the BJH results is excellent.

Although the micro-pore population exhibits low porosities values (from 0.01 to 0.02) respect to the meso-pore population (from 0.21 to 0.42), its specific surface areas are comparable with those of the meso-pore population in terms of order of magnitude. More specifically, these high specific surface areas (in relative terms) are due to high surface-to-volume ratio of the micro-pore population than the meso-pores, but especially by the significant higher pore number density values of the micro-pore fraction (roughly $10^{17}\,g^{-1}$) respect to the meso-pore one (about $10^{16}\,g^{-1}$), that is about one order of magnitude higher than that of the meso-pores. Interestingly, the partially calcined sample micro-structure suggests that its reacted volume morphology is fairly similar to that of the completed calcined samples. Sphericity factors (Wadell, 1935) were introduced to quantify the pore deviation from the spherical shape. During the $CaCO_3$ calcination reaction the micro- and meso-pore sphericity factors increase up to values close to 1 and, then, show a decreasing trend during sintering step once the $CaCO_3$ calcination reaction is completed. Interestingly, micro-pores exhibit a higher initial sphericity factor (about 0.8) respect to the meso-pore (0.7).

Correlation distances provide an average estimation of the pore-to-pore distance (Beaucage et al., 1995) of the meso-pore population whose value is approximately 45 nm when low residence times are considered. As the heating step duration progresses, the meso-pore correlation distance increases up to about 81 nm (at 800 °C) and 96 nm (at 900 °C), suggesting that the pore coalescence process is the main mechanism of sintering (in vacuum conditions).

The analysis of the scattering intensity profiles of the partially carbonated samples (at 650 °C with 10 % of CO_2 in balance with N_2) pointed out a drastic change of the sorbent micro-textural properties after the transition point (between the chemically controlled and

the product layer diffusion controlled steps), where the majority of pores are plugged by the non-porous $CaCO_3$ product layer. Additionally, the specific surface area per unit of unreacted calcium oxide is mostly constant during the carbonation reaction, ranging close to the initial sorbent specific surface area value. Finally, an unexpected increase of the pore radius of gyration (of both the two pore populations) was observed, especially after the transition point. This behavior was ascribed to a transfer of the contracting meso-porosity into the micro-pore population.
The overall maximum CaO conversion value was mainly associated with the meso-pore volume fraction because of the high porosity values of the meso-pore population respect to the micro-pore one. On the other hand, the high specific surface of the micro-pore population could play a significant role in the fast chemically-controlled regime of carbonation reaction rate, despite its modest porosity value.
The overall effect of the CaO carbonation reaction on the pore shape consists in a decreasing of the sphericity the two pore populations, leading to a final value of 0.55 for micro-pores and 0.3 for meso-pores. Finally, correlation distances seem to be quite constant during the CaO carbonation reaction, namely $38 \div 45$ nm, by considering a calcium oxide sorbent produced under vacuum conditions (at 800 °C).

In-situ time resolved USAXS, SAXS and WAXS measurements provided both micro-structure and reaction kinetics information *during* the calcite decomposition and the CaO carbonation reaction.

Specifically, an activation energy of 44.5 kcal mol^{-1} was estimated from the N_2-calcined samples conversion profiles (obtained from the WAXS data analysis), that is in excellent agreement with that obtained by Borgwardt (1985), namely 48 kcal mol^{-1}.
During the early stages of the calcite decomposition, the nascent CaO micro-structure is characterized by one population of pores, that increases in size up to a pore network split into two different population of pores: a micro-pore and a meso-pore population. The micro-pore radius of gyration suddenly drops down to a quite constant value (about 20 Å) over the reaction and sintering steps, whereas the meso-pore radius of gyration increases up to a maximum value and then approaches to an asymptotic one. Its final values strongly depends on the calcination reaction conditions and ranges from 83 Å to 102 Å when samples with low or negligible sintering effects are considered and increases up to 520 Å when the operative conditions favor sintering phenomena (Borgwardt, 1989b; Borgwardt, 1989a).
High specific surface areas were obtained for samples calcined below 800 °C in nitrogen atmosphere, namely 128.7 m^2 g^{-1} when calcite decompositions at 650 °C in N_2 were considered, in excellent agreement with that obtained by Ewing, Beruto, and Searcy (1979), by means of vacuum calcination conditions of single crystal-based $CaCO_3$, namely 127 m^2 g^{-1}.
Moreover, in addition to sintering phenomena other high temperature processes occur during the calcite decomposition, namely the CO_2 interactions with the nascent porous CaO (Beruto, 1976; Ewing, Beruto, and Searcy, 1979). In fact, the porosity trend over the $CaCO_3$ conversion does not follow the ideal linear trend during the reaction and approaches fairly close to the theoretical value (54 % for low-sintered samples) only when $CaCO_3$ decomposition is complete. In addition, the measured consumed pore fraction reveals a decreasing trend during calcination instead of an increasing one, indicating that sintering does not explain the measured porosity and specific surface profiles over $CaCO_3$ conversion. The pore number density profiles over time indicate a pore generation process during the early stages of the reaction, followed by a pore consumption one in the late stages. Finally, the meso-pore correlation distances for N_2-calcined samples are about $250 \div 350$ Å, and increase up to 3000 Å ca. in presence of CO_2.

The in-situ results of the CaO carbonation reaction reveal an increase of the meso-pore radius of gyration as the reaction progresses up to generate a third pore population or an asymptotic value in correspondence of the transition point, except for the highly sintered

sorbents. This phenomenon is likely due to small pore consumption, that shifts the sorbent pore size distributions (PSDs) to higher pore radii values, up to segregate a small amount of pores (below 5 %) probably located in the inner core of the sorbent particle, where the calcite product layer plugs the outer particle porosity preventing the CO_2 diffusion into the inner part of the sorbent.
Linear specific surface area profiles over the CaO conversion were measured, that slightly deviate from the linearity for those samples calcined at high temperatures (800–900 °C) and in presence of CO_2 in the reaction atmosphere.
In addition, a comparison between the initial sorbent micro-structural properties and those estimated in the correspondence of the transition point (between the chemically controlled and the product layer diffusion controlled regime) confirms how the sorbent micro-structure is mostly utilized by the CaO carbonation reaction when the initial sorbent pore network is poorly sintered. Precisely, relative porosity reductions of 70÷79 % were observed for samples calcined below 800 °C with N_2, associated with specific surface area and pore number density reductions of 66÷80 % and 60÷87 % respectively, that decrease down to 2÷18 % for the porosity and 4÷26 % concerning the specific surface area for samples calcined at 900 °C varying the CO_2 content from 10 % up to 50 %, even though the relative pore consumption is still high, namely from a minimum of 8 % up to 68 percent. These results confirm how highly sintered pore networks are less reactive respect to those of samples calcined at low temperature and inert atmospheres, where sintering phenomena are negligible.
Specifically, an inverse correlation between the maximum reaction rate (located in the chemically controlled regime) and the meso-pore radius of gyration was observed, while a well-defined linear trend is showed between the maximum CaO conversion derivative and the initial specific surface area. Interestingly, a positive correlation was identified between the maximum reaction rate and the pore number per unit of sample mass.
Additionally, the CaO conversion in the correspondence of the transition point is higher when the initial sorbent micro-structure exhibits low initial radii of gyration (of the two pore populations) and high specific surface areas.

Structural kinetic models can be used to predict the whole CaO conversion over time profile (Sun et al., 2008a) during the CaO carbonation. The continuous RPM with a distributed pore closure is capable to represent the sorbent internal micro-structure evolution by a distributed collection of thin and overlapping capillary (Bhatia, 1985). A good agreement was observed between the experimental CaO conversion over time profile with those predicted by a model random pore model. However, a good agreement was achieved with the experimental data (N_2-adsorption results) only for the final sorbent micro-textural properties and it fails in predicting the micro-structure evolution during the reaction, as showed by the different trends of the sorbent specific surface area and by the PSD evolution during the reaction.
Over the past two decades, thermo-gravimetric analysis has been widely used for the investigation of gas-solid reactions kinetics, and, specifically, for the CaO-CO_2 reaction (Barker, 1973; Grasa et al., 2009; Sun et al., 2008b; Alonso et al., 2014). However, thermo-gravimetric measurements of the CaO carbonation reaction kinetics are affected by external mass transfer diffusion limitations (Schulze et al., 2017) as suggested by the CFD study on a thermo-gravimetric analyzer. Therefore, apparent reaction kinetics may be potentially measured when fast gas-solid reactions are investigated (as the CaO carbonation reaction) if the external mass transfer is not correctly accounted for.

Concerning the future developments of this work of thesis, the proposed random pore model should be improved by considering the bimodal nature of the initial sorbent pore network and the transition of the contracting meso-pore into the micro-pore population,

in order to correctly predict the sorbent micro-textural properties evolution during the CaO carbonation reaction. Furthermore, despite several structural kinetic models have been proposed to describe both the calcite decomposition kinetics and the micro-structure generation, CO_2 interaction phenomena with nascent CaO in addition to sintering mechanisms should be taken in to account, in order to accurately describe the behavior of the generating sorbent pore network.

Finally, the results of this research project showed how the in-situ X-ray small angle scattering is a promising technique for the investigation of the sorbent micro-structure during the sorbent activation/regeneration and CO_2 capture steps at the same reaction operative conditions. This study could open new perspectives in the investigation of other natural solid sorbents and in the development of new synthetic and stabilized sorbents for the CO_2 capture.

Recently, Ca-based Al_2O_3-stabilized and templated sorbents have been investigated by means of in-situ USAXS, SAXS, WAXS measurements at the Advanced Photon Source. Work in progress on data analysis.

Appendix A

Chemical Equilibrium for Heterogeneous Reactions

A.1 The equilibrium constant

According to Sandler (2017) and Smith, Van Ness, and Abbott (2005) the equilibrium criteria for a single reaction can be written as

$$\prod_{i=1}^{\mathrm{nc}} a_i^{\nu_i} = K_{\mathrm{eq.}}(T), \tag{A.1}$$

where a_i is the activity coefficient of specie i for $i = 1, \ldots, \mathrm{nc}$, ν_i is the stoichiometric coefficient of specie i and $K_{\mathrm{eq.}}(T)$ is the equilibrium constant of the reaction, defined as

$$K_{\mathrm{eq.}}(T) = \exp\left(-\frac{\Delta G_R^0(T)}{RT}\right), \tag{A.2}$$

where $\Delta G_R^0(T)$ is the standard Gibbs free energy change of reaction:

$$\Delta G_R^0(T) = \sum_{i=1}^{\mathrm{nc}} \nu_i \, \mu_i^0, \tag{A.3}$$

where $\mu_i^0 = \mu_i^{\mathrm{pure}}(P^{\mathrm{ref.}})$.
By considering the standard conditions (1 bar and 25 °C) as reference state, $\mu_i^0(T) = \Delta G_i^0(T)$, where

$$\Delta G_i^0(T) = \Delta H_i^0(T) + T\, S_i^0, \tag{A.4}$$

where $\Delta H_i^0(T)$ and S_i^0 are the standard enthalpy and entropy of the specie i. These standard potentials are calculated from the respective standard values of formations of the nc species (namely $\Delta H_{f,i}^0(T^0)$ and $S_{f,i}^0(T^0)$), and Eq. (A.4) becomes

$$\Delta G_i^0(T) = \Delta H_{f,i}^0(T^0) + \int_{T^0}^{T} c_{p,i}(T')\, dT' + T\left[S_{f,i}^0(T^0) + \int_{T^0}^{T} \frac{c_{p,i}(T')}{T'}\, dT'\right], \tag{A.5}$$

where $c_{p,i}(T)$ is the gas heat capacity of specie i at constant pressure.
Last term for the chemical equilibrium calculation is the activity coefficient a_i of the specie i, defined as

$$a_i(T, P) = \frac{f_i(T, P, \mathbf{x_i})}{f_i^{\mathrm{pure}}(T, P^{\mathrm{ref.}})}, \tag{A.6}$$

Table A.1: Thermochemical data of selected chemical species, reference: Knacke, Kubaschewski, and Hesselmann (1991). Standard enthalpy and entropy of formation (T^0 is 25 °C) are expressed in kJ mol^{-1} and J K^{-1} mol^{-1}. Heat capacity are in J K^{-1} mol^{-1}.

Specie	Phase	$\Delta H^0_{f,i}(T^0)$	$S^0_{f,i}(T^0)$	A	$B \times 10^3$	$C \times 10^{-6}$	$D \times 10^6$
$CaCO_3$	S	−1208.356	93.052	104.516	21.924	−2.594	0
CaO	S	−635.089	38.212	50.417	4.184	−0.849	0
$Ca(OH)_2$	S	−986.089	83.387	101.788	17.987	−1.736	0
CO_2	G	−393.521	213.794	51.128	4.368	−1.469	0
H_2O	G	−241.856	188.824	34.376	7.841	−0.423	0

where $f_i(T, P, \mathbf{x_i})$ is the fugacity of specie i in mixture ($\mathbf{x_i}$ is the composition vector of the nc species involved in the reaction) and f_i^{pure} the fugacity of specie i in its standard state (Sandler, 2017).

A.2 Chemical equilibrium for the calcium oxide carbonation reaction

In order to calculate the equilibrium constant of reaction for Eq. (2.1), the following assumptions are taken into account

- the gas-phase mixture (CO_2 and and inert specie, usually N_2 or Ar) is ideal;
- each gaseous specie is ideal;
- the solid species activity coefficient are 1.

Therefore, Eq. (A.1) becomes

$$\frac{p_{CO_2}}{1\,\text{bar}} = K_{\text{eq.}}(T), \tag{A.7}$$

where $p_{CO_2} = y_{CO_2} P$ is the CO_2 partial pressure and 1 bar is the fugacity reference state for a pure gas.
With the aim to estimate the chemical equilibrium constant, a temperature dependence correlation is required. According to Knacke, Kubaschewski, and Hesselmann (1991), the specific heat capacity over the absolute temperature of the specie i is expressed as

$$c_{p,i}(T) = A + B\,T + C\,T^{-1} + D \cdot T^2, \tag{A.8}$$

where A, B, C and D are constants together with $\Delta H^0_{f,i}(T^0)$ and $S^0_{f,i}(T^0)$ are listed in Tab. A.1.

A.3 Others chemical equilibrium models

The CO_2 equilibrium partial pressure prediction is an important parameter in order to select the correct operative reaction conditions both for the calcification and the carbonation reaction and for the investigation of the reaction kinetics. For these reasons, several literature contributors proposed the equilibrium models to predict the carbon dioxide equilibrium partial pressure. Baker (1962) provided the following equation,

$$\log\left(p_{CO_2,\,eq.}\right) = 7.079 - \frac{38000}{4.574\,T}, \tag{A.9}$$

Table A.2: Summary of the different model prediction for the CO_2 equilibrium partial pressure of the calcination and carbonation reactions.

Reference	Pressure	Temperature	$T(1\,\text{atm})$
Knacke, Kubaschewski, and Hesselmann (1991)	bar	K	897.8 °C
García-Labiano et al. (2002)	Pa	K	895.1 °C
Silcox, Kramlich, and Pershing (1989)	atm	K	896.8 °C
Criado (1977)	kPa	K	903.2 °C
Baker (1962)	atm	K	900.4 °C

where $p_{CO_2,\,eq.}$ is the equilibrium partial pressure expressed in atm and T is the absolute temperature (in K).
Criado (1977) proposed the following equilibrium model,

$$p_{CO_2,\,eq.} = 1.87 \times 10^9 \exp\left(-\frac{19677}{T}\right), \tag{A.10}$$

where in this equation the equilibrium carbon dioxide partial pressure is expressed in kPa and T in K.
Silcox, Kramlich, and Pershing (1989) used the following relationship in modeling the thermal decomposition kinetics of $CaCO_3$,

$$p_{CO_2,\,eq.} = \exp\left[17.74 - 0.001\,08\,T + 0.332\,\ln(T) - \frac{22020}{T}\right], \tag{A.11}$$

where $p_{CO_2,\,eq.}$ is in atm and T in K.
García-Labiano et al. (2002) by means on the thermochemical data of Barin (1993) obtained

$$p_{CO_2,\,eq.} = 4.137 \times 10^{12} \exp\left(-\frac{20474}{T}\right), \tag{A.12}$$

where $p_{CO_2,\,eq.}$ is expressed in Pa and T in K.
Finally, a summary of the aforementioned chemical equilibrium models is proposed in Tab. (A.2).

Appendix B

The Z Parameter for the CaO carbonation reaction

The carbonation reaction is a non-catalytic gas-solid reaction where the solid phases (reactant and/or products) undergoes to a series of micro-structural modification, namely progressive loss of the sorbent porosity up to the pore closure. Therefore, Eq. (2.5) is a useful relationship to account for the sorbent porosity evolution during the CaO carbonation reaction. In order to derive such equation, the following assumption are taken into account:

1. the initial solid reactant consists in pure and solid calcium oxide;
2. the initial reactant is porous with a porosity value of ε_0;
3. sintering phenomena are not involved.

B.1 Stoichiometry of the carbonation reaction

According to the stoichiometry of the chemical equation Eq. (2.1), the mole number evolution of the CaO and $CaCO_3$ during the carbonation reaction is

$$\begin{aligned} n_A &= n_A^0 - \xi, \\ n_B &= n_B^0 + \xi, \end{aligned} \tag{B.1}$$

where for the sake of clarity the solid reactant CaO and the solid product $CaCO_3$ are conveniently named A and B respectively. In this way, n_A and n_B represent the number of moles of species A and B, n_A^0 and n_B^0 are the initial number of moles of A and B (that is zero for B according to the aforementioned assumptions) and ξ is the extent of reaction or reaction coordinate. Clearly, the stoichiometric coefficient of CaO and $CaCO_3$ are 1 and -1, according to Eq. (2.1).
Instead of the extent of reaction ξ, a more convenient parameter is considered, namely the CaO reaction conversion defined as

$$X_A = 1 - \frac{n_A}{n_A^0}, \tag{B.2}$$

such that Eq. (B.1) becomes

$$\begin{aligned} n_A &= n_A^0 \left(1 - X_A\right), \\ n_B &= n_A^0 X_A. \end{aligned} \tag{B.3}$$

B.2 Volumetric properties of solid species

The molar density of the chemical species A and B is defined as

$$\tilde{\rho}_i = \frac{\hat{\rho}_i}{M_i}, \quad i = A,\, B \tag{B.4}$$

where $\tilde{\rho}_i$ and $\hat{\rho}_i$ are the molar and the mass densities of specie i and M_i its respective molecular weight. These properties are listed in Tab. 2.1 for the case of CaO and $CaCO_3$. According to the aforementioned assumptions, the sorbent internal particle porosity as a function of the CaO conversion, $\varepsilon(X_A)$, is conveniently derived from the pore to solid volume ratio, namely

$$\frac{\varepsilon(X_A)}{1-\varepsilon(X_A)} = \frac{V^0_{\text{pores}} - \left[V_{\text{solid}}(X_A) - V^0_{\text{solid}}\right]}{V_{\text{solid}}(X_A)}, \tag{B.5}$$

where V^0_{pores} is the sorbent volume occupied by pores, $V_{\text{solid}}(X_A)$ is the total solid volume estimated at the conversion value of A, X_A, and V^0_{solid} is the initial solid volume, namely the initial CaO volume. By considering Eqs. (B.3) and (B.4) in Eq. (B.5), after some arrangements it becomes

$$\begin{aligned}
\frac{\varepsilon(X_A)}{1-\varepsilon(X_A)} &= \frac{V^0_{\text{solid}}}{V_{\text{solid}}(X_A)}\left(\frac{V^0_{\text{pores}}}{V^0_{\text{solid}}}+1\right)-1 \\
&= \frac{\dfrac{1}{\tilde{\rho}_A}}{\dfrac{1-X_A}{\tilde{\rho}_A}+\dfrac{X_A}{\tilde{\rho}_B}}\left(\frac{\varepsilon_0}{1-\varepsilon_0}+1\right)-1 \\
&= \frac{1}{1+X_A\left(\dfrac{\tilde{\rho}_A}{\tilde{\rho}_B}-1\right)}\,\frac{1}{1-\varepsilon_0}-1,
\end{aligned} \tag{B.6}$$

and solving Eq. (B.6) for $\varepsilon(X_A)$ gives

$$\varepsilon(X_A) = \varepsilon_0 - \left(\frac{\tilde{\rho}_A}{\tilde{\rho}_B}-1\right)(1-\varepsilon_0)\,X_A, \tag{B.7}$$

where, if compared with Eq. (2.5), the ratio between the two molar volumes is the Z parameter for the carbonation reaction, namely Z_{carb}:

$$Z_{\text{carb}} = \frac{\tilde{\rho}_A}{\tilde{\rho}_B} = \frac{\tilde{\rho}_{\text{CaO}}}{\tilde{\rho}_{\text{CaCO}_3}} = \frac{\hat{\rho}_{\text{CaO}}}{M_{\text{CaO}}}\frac{M_{\text{CaCO}_3}}{\hat{\rho}_{\text{CaCO}_3}}. \tag{B.8}$$

Using the CaO and $CaCO_3$ properties listed in Tab. 2.1, Z_{carb} is about 2.2 (precisely 2.1997).

B.3 The Z parameter for the calcination reaction

In absence of sintering phenomena, during the carbonation reaction the different molar volume between the solid reactant ($CaCO_3$) the product (CaO) generate the final pore network, that provide to the material the final micro-textural properties. According to the aforementioned demonstration, Eq. (B.7) becomes

$$\varepsilon(X_B) = \varepsilon_0 - (Z_{\text{calc}}-1)\,(1-\varepsilon_0)\,X_B, \tag{B.9}$$

where X_B is the fractional conversion of B ($CaCO_3$), ε_0 is the initial porosity of the solid reactant and Z_{calc} is

$$Z_{\text{calc}} = \frac{\tilde{\rho}_B}{\tilde{\rho}_A} = \frac{\tilde{\rho}_{\text{CaCO}_3}}{\tilde{\rho}_{\text{CaO}}} = \frac{1}{Z_{\text{carb}}}, \tag{B.10}$$

whose value is 0.4546. Because $Z_{\text{calc}} < 1$, Eq. (B.9) is conveniently rearranged as

$$\varepsilon(X_B) = \varepsilon_0 + (1 - Z_{\text{calc}})\,(1 - \varepsilon_0)\,X_B, \tag{B.11}$$

where $(1 - Z_{\text{calc}})$ is greater than 1.
Finally, these equations are consistent with the Bhatia and Perlmutter (1983b) approach, in which an unified approach was proposed in order to model the non-catalytic gas-solid reactions both for the case where porosity is consumed, $Z > 1$ (as the CaO carbonation reaction), and for reactions where porosity is generated, namely $Z < 1$ (such the $CaCO_3$ calcination reaction).

Appendix C

An Electromagnetic wave: the X-ray radiation

An X-ray is an electromagnetic wave with a wavelength in the order of magnitude of 1 Å, where both the electric **E** and the magnetic **H** fields oscillate and propagates at the speed of the light though vacuum. When the oscillations of the two fields are perpendicular to each other and perpendicular to the direction of propagation, the wave is called "transverse", as shown in Fig. C.1, where the direction of the electric field is given by the polarization unit vector $\hat{\varepsilon}$.
Considering for simplicity only the electric field **E**, Fig. C.2a shows the direction of the beam that is taken to be along the positive direction of the z-axis at a given instance of time. The propagation of the wave though the space is characterized by a wavelength λ or by the wavenumber k that is defined as

$$k = \frac{2\pi}{\lambda}. \tag{C.1}$$

From a mathematical point of view, the electric field amplitude is expressed as a sine wave (in this case a plane wave)

$$E(z) = E_0 \sin(kz),$$

that can be equivalently expressed in the complex form

$$E(z) = E_0 \, e^{ikz}.$$

Fig. C.2b shows the temporal variation of the electric field at a given point of the space, where the wave is characterized by a period T that is linked to the frequency f and the

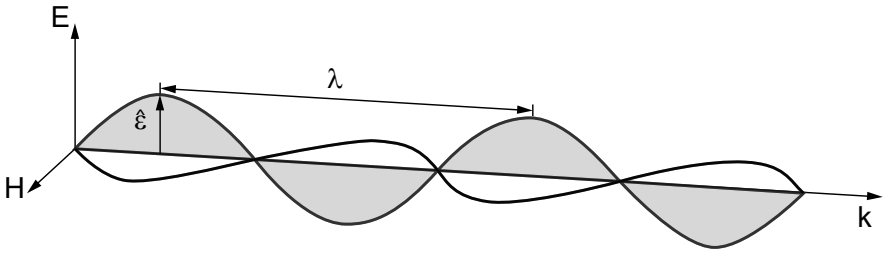

Figure C.1: A X-ray transverse electromagnetic wave representation, where **E** and **H** are respectively the electric and the magnetic fields. The two fields are perpendicular to each other and the direction of propagation is **k**. The polarization unit vector $\hat{\varepsilon}$ provides the direction of the electric field.

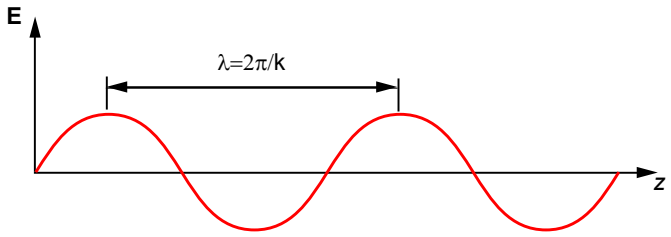

(a) *Spatial variation of* **E** *described by the wavelength* λ *or by the wavenumber modulus* k.

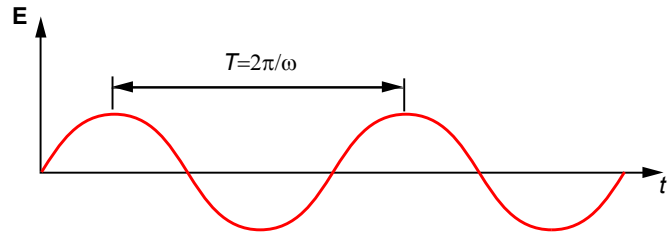

(b) *Temporal variation of* **E** *described by the period* T *or by the cyclic frequency* ω.

Figure C.2: Representation of an electromagnetic wave, where only the electric field is taken into account.

angular frequency ω by the following relationships

$$T = \frac{1}{f} = \frac{2\pi}{\omega}. \tag{C.2}$$

The spatial and the temporal properties of the electromagnetic wavelength are linked though the velocity of propagation (that is the speed of light[1] if the considered medium is vacuum):

$$f = \frac{v}{\lambda}, \tag{C.3}$$

where v is the speed of light though a certain medium.
The spatial and temporal variation of wave propagation along the z direction is taken into account by the expression

$$E(z,t) = E_0\, e^{i(kz-\omega t)},$$

in terms of wave amplitude. By taking into account the electric field polarization along the direction of the unit vector $\hat{\varepsilon}$ in the $3d$ space, the electric field is represented by the following equation

$$\mathbf{E}(\mathbf{r},t) = \hat{\varepsilon}\, E_0\, e^{i(\mathbf{k}\cdot\mathbf{r}-\omega t)}, \tag{C.4}$$

where k is the wavevector ans states the direction of propagation of the electromagnetic wave, whose magnitude is defined by Eq. (C.1). As shown in Fig. C.1, $\hat{\varepsilon}\cdot\mathbf{k} = 0$ and $\mathbf{k}\cdot\mathbf{E} = \mathbf{k}\cdot\mathbf{H} = 0$ by definition of the transverse wave.

[1]The speed of light through vacuum is approximately $3\times10^8\,\mathrm{m\,s^{-1}}$ Cohen et al., 2007.

C.1 Energy of the X-ray Radiation

From a quantum mechanical point of view, a monochromatic wave is considered a beam of quantized photons, with an energy $\mathcal{E}$ equals to $\hbar\omega$ and a momentum of $\hbar\,\mathbf{k}$, where $\hbar$ is the reduced Planck constant defined as

$$\hbar = \frac{h}{2\pi},$$

where h is the Planck constant, that is approximately Cohen et al., 2007.

$$h = 6.626\,070 \times 10^{-34}\,\mathrm{J\,s} = 4.135\,668 \times 10^{-15}\,\mathrm{eV\,s}.$$

A useful numerical relation between the X-ray wave energy $\mathcal{E}$ in keV and its wavelength λ (expressed in Å) is

$$\mathcal{E} = \frac{hc}{\lambda} \cong \frac{12.398}{\lambda}. \tag{C.5}$$

C.2 Euler's Formula

Every complex number $z = x + iy$ can be expressed in terms of complex exponential function

$$z = \rho\, e^{i\,\theta} \tag{C.6}$$

where ρ is the magnitude of z

$$\rho = |z| = \sqrt{x^2 + y^2}$$

and θ is the argument of z.
By considering the following expansion series

$$\begin{aligned} e^t &= 1 + t + \frac{t^2}{2!} + \frac{t^3}{3!} + \dots \\ \cos(t) &= 1 - \frac{t^2}{2!} + \frac{t^4}{4!} - \frac{t^6}{6!} + \dots \\ \sin(t) &= t - \frac{t^3}{3!} + \frac{t^5}{5!} - \frac{t^7}{67!} + \dots \end{aligned}$$

$e^{i\,\theta}$ can be expanded in terms of,

$$\begin{aligned} e^{i\,\theta} &= 1 + i\,\theta + \frac{(i\,\theta)^2}{2!} + \frac{(i\,\theta)^3}{3!} + \dots \\ &= \left(1 - \frac{\theta^2}{2!} + \frac{\theta^4}{4!} - \frac{\theta^6}{6!} + \dots\right) + i\,\left(\theta - \frac{\theta^3}{3!} + \frac{\theta^5}{5!} - \frac{\theta^7}{67!} + \dots\right) \\ &= \cos(\theta) + i\,\sin(\theta). \end{aligned}$$

that verifies the Euler's formula:

$$\rho e^{i\,\theta} = \rho\,\cos(\theta) + i\,\rho\,\sin(\theta). \tag{C.7}$$

Finally, it should be noting that the n-th power of z is

$$z^n = \left(\rho\, e^{i\,\theta}\right)^n = \rho^n\, e^{i\,n\,\theta},$$

while the complex conjugate of Eq. (C.6) is

$$z^* = x - i\,y = e^{i\,\theta}. \tag{C.8}$$

Bibliography

Abanades, J. Carlos and Diego Alvarez (2003). "Conversion limits in the reaction of CO_2 with lime". In: *Energy and Fuels* 17.2, pp. 308–315.

Agnew, J. et al. (2000). "Simultaneous calcination and sintering of calcium based sorbents under a combustion atmosphere". In: *Fuel* 79.12, pp. 1515–1523. ISSN: 00162361.

Alonso, M. et al. (2014). "Undesired effects in the determination of CO_2 carrying capacities of CaO during TG testing". In: *Fuel* 127, pp. 52–61.

Als-Nielsen, J. and D. McMorrow (2011). *Elements of Modern X-ray Physics*. Wiley.

Alvarez, Diego and J. Carlos Abanades (2005). "Determination of the Critical Product Layer Thickness in the Reaction of CaO with CO_2". In: *Industrial & Engineering Chemistry Research* 44.15, pp. 5608–5615.

Alvarez, Diego, J. Carlos Abanades, and J Carlos Abanades (2005). "Reaction of CaO with CO_2". In: *Industrial and Engineering Chemistry Research* 44.15, pp. 5608–5615.

Alvfors, Per and Gunnar Svedberg (1992). "Modelling of the simultaneous calcination, sintering and sulphation of limestone and dolomite". In: *Chemical Engineering Science* 47.8, pp. 1903–1912.

Arias, B. et al. (2013). "Demonstration of steady state CO_2 capture in a 1.7 MW h calcium looping pilot". In: *International Journal of Greenhouse Gas Control* 18, pp. 237–245.

Bailliez, S. and A. Nzihou (2004). "The kinetics of surface area reduction during isothermal sintering of hydroxyapatite adsorbent". In: *Chemical Engineering Journal* 98.1-2, pp. 141–152.

Baker, E. H. (1962). "The calcium oxide-carbon dioxide system in the pressure range 1-300 atmospheres". In: *J. Chem. Soc.* (0), pp. 464–470.

Barin, I. (1993). *Thermochemical data of pure substances*. Thermochemical Data of Pure Substances v. 1. VCH.

Barker, Ronald (1973). "The reversibility of the reaction $CaCO_3 \rightleftharpoons CaO + CO_2$". In: *Journal of Applied Chemistry and Biotechnology* 23.10, pp. 733–742. ISSN: 03759210.

Barrett, Elliott P., Leslie G. Joyner, and Paul P. Halenda (1951). "The Determination of Pore Volume and Area Distributions in Porous Substances. I. Computations from Nitrogen Isotherms". In: *Journal of the American Chemical Society* 73.1, pp. 373–380.

Beaucage, G. (1995). "Approximations Leading to a Unified Exponential/Power-Law Approach to Small-Angle Scattering". In: *Journal of Applied Crystallography* 28.6, pp. 717–728.

— (1996). "Small-Angle Scattering from Polymeric Mass Fractals of Arbitrary Mass-Fractal Dimension". In: *Journal of Applied Crystallography* 29.2, pp. 134–146.

Beaucage, G., H. K. Kammler, and S. E. Pratsinis (2004). "Particle size distributions from small-angle scattering using global scattering functions". In: *Journal of Applied Crystallography* 37.4, pp. 523–535.

Beaucage, G. et al. (1995). "Multiple Size Scale Structures in Silica—Siloxane Composites Studied by Small-Angle Scattering". In: *Hybrid Organic-Inorganic Composites*. ACS Symposium Series. Chap. 9, pp. 97–111.

Becker, J. et al. (2010). "Experimental setup for in situ X-ray SAXS/WAXS/PDF studies of the formation and growth of nanoparticles in near-and supercritical fluids". In: *Journal of Applied Crystallography* 43.4.

Benedetti, A. and M. Strumendo (2015). "Application of a random pore model with distributed pore closure to the carbonation reaction". In: *Chemical Engineering Transactions* 43, pp. 1153–1158. ISSN: 22839216.

Benedetti, A. et al. (2017). "Analysis of textural properties of CaO-based CO_2 sorbents by ex-situ USAXS". In: *Chemical Engineering Journal*.

Benmore, C.J. et al. (2016). "A SAXS-WAXS study of the endothermic transitions in amorphous or supercooled liquid itraconazole". In: *Thermochimica Acta* 644.

Beruto Dario Searcy, Alan W. (1976). "Calcium oxides of high reactivity". In: *Nature* 263.5574, pp. 221–222.

Beruto, D., L. Barco, and Alan W. Searcy (1984). "CO_2-Catalyzed Surface Area and Porosity Changes in High-Surface-Area CaO Aggregates". In: *Journal of the American Ceramic Society* 67.7, pp. 512–516.

Beruto, Dario, Luigi Barco, and Alan W. Searcy (1983). "Rearrangement of Porous CaO Aggregates During Calcite Decomposition in Vacuum". In: *Journal of the American Ceramic Society* 66.12, pp. 893–896.

Beruto, Dario and Alan W. Searcy (1974). "Use of the Langmuir method for kinetic studies of decomposition reactions: calcite ($CaCO_3$)". In: *Journal of the Chemical Society, Faraday Transactions 1: Physical Chemistry in Condensed Phases* 70, p. 2145.

Beruto, Dario et al. (1980). "Characterization of the porous CaO particles formed by decomposition of $CaCO_3$ and $Ca(OH)_2$ in vacuum". In: *Journal of the American Ceramic Society* 63.7-8, pp. 439–443.

Bevington, P R and D K Robinson (2003). *Data reduction and error analysis for the physical sciences*. McGraw-Hill Higher Education. McGraw-Hill. ISBN: 9780072472271.

Bhatia, S K (1985). "Analysis of distributed pore closure in gas-solid reactions". In: *AIChE Journal* 31.4, pp. 642–648.

Bhatia, S. K. and J. S. Gupta (1992). "Mathematical Modelling of Gas-Solid Reactions: Effect of Pore Structure". In: *Reviews in Chemical Engineering* 8.3-4, pp. 177–258.

Bhatia, S. K. and D. D. Perlmutter (1981). "A random pore model for fluid-solid reactions: II. Diffusion and transport effects". In: *AIChE Journal* 27.2, pp. 247–254.

— (1983a). "Effect of the product layer on the kinetics of the CO_2-lime reaction". In: *AIChE Journal* 29.1, pp. 79–86.

— (1983b). "Unified treatment of structural effects in fluid-solid reactions". In: *AIChE Journal* 29.2, pp. 281–289.

Bhatia, Suresh K and D D Perlmutter (1980). "A random pore model for fluid-solid reactions: I. Isothermal, kinetic control". In: *AIChE J.* 26.3, pp. 379–386.

Bhatia, S.K. and Perlmutter, D.D. (1981). "A random pore model for fluid-solid reactions: II Diffusion and Transport Effects". In: *AIChE Journal* 27.2, pp. 247–254.

Biasin, A, C U Segre, and M Strumendo (2015). "$CaCO_3$ Crystallite Evolution during CaO Carbonation: Critical Crystallite Size and Rate Constant Measurement by In-Situ Synchrotron Radiation X-ray Powder Diffraction". In: *Crystal Growth & Design* 15.11, pp. 5188–5201.

Biasin, A. et al. (2015). "Investigation of CaO-CO_2 reaction kinetics by in-situ XRD using synchrotron radiation". In: *Chemical Engineering Science* 127, pp. 13–24.

Blamey, J. et al. (2010). "The calcium looping cycle for large-scale CO_2 capture". In: *Progress in Energy and Combustion Science* 36.2, pp. 260–279.

Borgwardt, R H (1985). "Calcination kinetics and surface area of dispersed limestone particles". In: *AIChE Journal* 31.1, pp. 103–111.

Borgwardt, Robert H (1989a). "Calcium Oxide Sintering in Atmospheres Containing Water and Carbon Dioxide". In: *Ind. Eng. Chem. Res.* 28.1961, pp. 493–500.

— (1989b). "Sintering of nascent calcium oxide". In: *Chemical Engineering Science* 44.1, pp. 53–60.

Borgwardt, Robert H., Nancy F. Roache, and Kevin R. Bruce (1986). "Method for Variation of Grain Size in Studies of Gas-Solid Reactions Involving CaO". In: *Ind. Eng. Chem. Fundam* 25, pp. 165–169.

Brook, RJ (1976). "Controlled grain growth". In: *Treatise on materials science and technology* 9, pp. 331–364.

Brumberger, H. (1994). *Modern Aspects of Small-Angle Scattering*. Nato Science Series C: Springer Netherlands.

Brumberger, Harry (2013). *Modern aspects of small-angle scattering*. Vol. 451. Springer Science & Business Media.

Brunauer, Stephen, P. H. Emmett, and Edward Teller (1938). "Adsorption of Gases in Multimolecular Layers". In: *Journal of the American Chemical Society* 60.2, pp. 309–319.

Chantler, CT (1995). "Theoretical form factor, attenuation, and scattering tabulation for $Z = 1$–92 from $E = 1$–10 eV to $E = 0.4$–1.0 MeV". In: *Journal of Physical and Chemical Reference Data* 24.1, pp. 71–643.

Chavez Panduro, Elvia Anabela et al. (2012). "Small-angle X-ray scattering analysis of porous powders of $CaCO_3$". In: *Journal of Applied Crystallography* 45.5, pp. 881–889.

Chupas, P.J. et al. (2008). "A versatile sample-environment cell for non-ambient X-ray scattering experiments". In: *Journal of Applied Crystallography* 41.4.

Coble, R. L. (1961a). "Sintering crystalline solids. I. intermediate and final state diffusion models". In: *Journal of Applied Physics* 32.5, pp. 787–792.

— (1961b). "Sintering crystalline solids. II. experimental test of diffusion models in powder compacts". In: *Journal of Applied Physics* 32.5, pp. 793–799.

Cohen, E.R. et al. (2007). *Quantities, Units and Symbols in Physical Chemistry*. Royal Society of Chemistry.

Criado, J.M. (1977). "Influence of the pressure on the shape of DTA and DTG curves of reversible reactions of thermal decomposition of solids". In: *Thermochimica Acta* 19 (1).

Criado, Jose M. et al. (1995). "The effect of the CO_2 pressure on the thermal decomposition kinetics of calcium carbonate". In: *Thermochimica Acta* 254, pp. 121–127.

Cromer, Don T and Joseph B Mann (1968). "X-ray scattering factors computed from numerical Hartree–Fock wave functions". In: *Acta Crystallographica Section A: Crystal Physics, Diffraction, Theoretical and General Crystallography* 24.2, pp. 321–324.

D'Aguanno, Bruno and Rudolph Klein (1991). "Structural effects of polydispersity in charged colloidal dispersions". In: *ournal of the Chemical Society, Faraday Transactions* 87 (3), pp. 379–390.

De Jonghe, Lutgard C. and Mohamed N. Rahaman (2003). "Sintering of Ceramics". In: *Handbook of Advanced Ceramics: Materials, Applications, Processing and Properties*. Vol. 1-2. CRC press, pp. 187–264.

Dean, C. C. et al. (2011). "The calcium looping cycle for CO_2 capture from power generation, cement manufacture and hydrogen production". In: *Chemical Engineering Research and Design* 89.6, pp. 836–855.

Dinnebier, Robert E and Simon JL Billinge (2008). *Powder diffraction: theory and practice*. Royal Society of Chemistry.

Evans, M, N Hastings, and B Peacock (2000). *Statistical Distributions*. Vol. 2. 4. Wiley-Interscience, p. 221.

Evans, R. and U. Marini Bettolo Marconi (1985). "The role of wetting films in capillary condensation and rise: Influence of long-range forces". In: *Chemical Physics Letters* 114.4, pp. 415 –422.

Ewing, J., D. Beruto, and Alan W. Searcy (1979). "The Nature of CaO Produced by Calcite Powder Decomposition in Vacuum and in CO_2". In: *Journal of the American Ceramic Society* 62.11-12, pp. 580–584.

Falamaki, Cavus, Mahdi Shafiee Afarani, and Alireza Aghaie (2004). "Initial sintering stage pore growth mechanism applied to the manufacture of ceramic membrane supports". In: *Journal of the European Ceramic Society* 24.8, pp. 2285–2292.

Feng, Bo, Hui An, and Eddie Tan (2007). "Screening of CO_2 adsorbing materials for zero emission power generation systems". In: *Energy and Fuels*. Vol. 21. 2, pp. 426–434.

Fennel, Paul and Ben Anthony (2015). *Calcium and Chemical Looping Technology for Power Generation and Carbon Dioxide (CO2) Capture*. Vol. 1. Elsevier, p. 466.

Fennell, P S et al. (2007). "Regeneration of sintered limestone sorbents for the sequestration of CO_2 from combustion and other systems". In: *Journal of the Energy Institute* 80.2, pp. 116–119.

Fierro, V., J. Adánez, and F. García-Labiano (2004). "Effect of pore geometry on the sintering of Ca-based sorbents during calcination at high temperatures". In: *Fuel* 83.13, pp. 1733–1742.

Florin, Nicholas H. and Andrew T. Harris (2008). "Enhanced hydrogen production from biomass with in situ carbon dioxide capture using calcium oxide sorbents". In: *Chemical Engineering Science* 63.2, pp. 287–316.

Fuertes, A B et al. (1991). "Surface area and pore size changes during sintering of calcium oxide particles". In: *Chemical Engineering Communications* 109.1, pp. 73–88.

Fukuda, Yasuo and Kozo Tanabe (1973). "Infrared study of carbon dioxide adsorbed on magnesium and calcium oxides". In: *Bulletin of the Chemical Society of Japan* 46.6, pp. 1616–1619.

Galan, Isabel, Fredrik P. Glasser, and Carmen Andrade (2013). "Calcium carbonate decomposition". In: *Journal of Thermal Analysis and Calorimetry* 111.2, pp. 1197–1202.

Gallagher, P.K. and D.W. Johnson (1973). "The effects of sample size and heating rate on the kinetics of the thermal decomposition of $CaCO_3$". In: *Thermochimica Acta* 6.1, pp. 67–83.

Gallagher, P.K. K. and D.W. W. Johnson (1976). "Kinetics of the thermal decomposition of $CaCO_3$ in CO_2 and some observations on the kinetic compensation effect". In: *Thermochimica Acta* 14.3, pp. 255–261.

García-Labiano, F. et al. (2002). "Calcination of calcium-based sorbents at pressure in a broad range of CO_2 concentrations". In: *Chemical Engineering Science* 57.13, pp. 2381–2393.

German, R. M. and Z. A. Munir (1976). "Surface Area Reduction During Isothermal Sintering". In: *Journal of the American Ceramic Society* 59.9-10, pp. 379–383.

German, Randall (2014). *Sintering: From Empirical Observations to Scientific Principles*. Butterworth-Heinemann, pp. 1–536.

Glasson, D. R. (1958). "Reactivity of lime and related oxides. Production of calcium oxide". In: *Journal of Applied Chemistry* 8.12, pp. 793–797.

Glatter, O and O Kratky (1982). *Small Angle X-ray Scattering*. Academic Press.

Grasa, Gemma et al. (2009). "Application of the random pore model to the carbonation cyclic reaction". In: *AIChE Journal* 55.5, pp. 1246–1255.

Grasa, Gemma S. and J. Carlos Abanades (2006). "CO_2 Capture Capacity of CaO in Long Series of Carbonation/Calcination Cycles". In: *Industrial & Engineering Chemistry Research* 45.26, pp. 8846–8851.

Grasa, Gemma S. et al. (2008). "Reactivity of highly cycled particles of CaO in a carbonation/calcination loop". In: *Chemical Engineering Journal* 137.3, pp. 561 –567.

Gregg, SJ and Kenneth SW Sing (1983). "Adsorption, surface area, and porosity". In: *Academic Press, New York*.

Guiner, A, Gérard Fournet, and CB Walker (1955). *Small angle scattering of X-rays*. J. Wiley & Sons, New York.

Gullett, B. K. and K. R. Bruce (1987). "Pore distribution changes of calcium-based sorbents reacting with sulfur dioxide". In: *AIChE Journal* 33.10, pp. 1719–1726.

Halsey, George (1948). "Physical Adsorption on Non-Uniform Surfaces". In: *The Journal of Chemical Physics* 16.10, p. 931.

Harkins, William D. and George Jura (1944). "Surfaces of Solids. XII. An Absolute Method for the Determination of the Area of a Finely Divided Crystalline Solid". In: *Journal of the American Chemical Society* 66.8, pp. 1362–1366.

Harrison, Douglas P (2008). "Sorption-enhanced hydrogen production: A review". In: *Industrial & Engineering Chemistry Research* 47, pp. 6486–6501.

Haynes, W.M. (2014). *CRC Handbook of Chemistry and Physics, 95th Edition, 2014-2015*. Vol. 54. CRC press, p. 2704.

Henke, B.L., E.M. Gullikson, and J.C. Davis (1993). "X-Ray Interactions: Photoabsorption, Scattering, Transmission, and Reflection at $E = 50$–$30\,000$ eV, $Z = 1$–92". In: *Atomic Data and Nuclear Data Tables* 54.2, pp. 181–342.

Hu, Naiping et al. (2011). "Characterization of porous materials using combined small-angle X-ray and neutron scattering techniques". In: *Journal of Membrane Science* 379.1-2, pp. 138–145.

Ilavsky, J (2010). "Characterization of Complex Thermal Barrier Deposits Pore Microstructures by a Combination of Imaging, Scattering, and Intrusion Techniques". In: *Journal of thermal spray technology* 19.1-2, pp. 178–189.

Ilavsky, J. et al. (2013). "Ultra-Small-Angle X-ray Scattering Instrument at the Advanced Photon Source: History, Recent Development, and Current Status". In: *Metallurgical and Materials Transactions A* 44, pp. 68–76.

Ilavsky, Jan (2012). "Nika: Software for two-dimensional data reduction". In: *Journal of Applied Crystallography* 45.2, pp. 324–328.

Ilavsky, Jan and Peter R. Jemian (2009). "Irena: tool suite for modeling and analysis of small-angle scattering". In: *Journal of Applied Crystallography* 42.2, pp. 347–353.

Ilavsky, Jan et al. (2009). "Ultra-small-angle X-ray scattering at the Advanced Photon Source". In: *Journal of Applied Crystallography* 42.3, pp. 469–479.

Ilavsky, Jan et al. (2012). "High-energy ultra-small-angle X-ray scattering instrument at the Advanced Photon Source". In: *Journal of Applied Crystallography* 45.6, pp. 1318–1320.

IPCC (2014). *Climate Change 2014 Synthesis Report*. Tech. rep. Intergovernmental Panel on Climate Change, Geneva (Switzerland). Working Group III, pp. 1–112.

J. Szekely, J. W. Evans and H. Y. Sohn (1976). *Gas-Solid Reactions*. Ed. by Academic Press. Academic Press.

Kang, Suk Joong L and Yang Il Jung (2004). "Sintering kinetics at final stage sintering: Model calculation and map construction". In: *Acta Materialia* 52.15, pp. 4573–4578.

Khinast, J. et al. (1996). "Decomposition of limestone: The influence of CO_2 and particle size on the reaction rate". In: *Chemical Engineering Science* 51.4, pp. 623–634.

Kinning, David J. and Edwin L. Thomas (1984). "Hard-sphere interactions between spherical domains in diblock copolymers". In: *Macromolecules* 17.9, pp. 1712–1718.

Knacke, O., O. Kubaschewski, and K˙ Hesselmann (1991). *Thermochemical properties of inorganic substances*. Thermochemical Properties of Inorganic Substances v. 1. Springer-Verlag. ISBN: 9783540540144.

Kopsky, Vojtech and Daniel B Litvin (2010). *International tables for crystallography*. John Wiley.

Kotlarchyk, Michael and Sow-Hsin Chen (1983). "Analysis of small angle neutron scattering spectra from polydisperse interacting colloids". In: *The Journal of Chemical Physics* 79.5, pp. 2461–2469.

Kyaw, Kyaw et al. (1998). "Study of Carbonation of CaO for High Temperature Thermal Energy Storage". In: *Journal of Chemical Engineering of Japan* 31.2, pp. 281–284.

Lake, JA (1967). "An iterative method of slit-correcting small angle X-ray data". In: *Acta crystallographica* 23.1947, p. 191.

Larson, Allen C. and Robert B. Von Dreele (2000). "General Structure Analysis System (GSAS)". In: *Los Alamos National Laboratory Report LAUR*, pp. 86–748.

Lastoskie, C, K E Gubbins, and N Quirke (1993). "Pore size distribution analysis of microporous carbons: A density functional theory approach". In: *Journal of Physical Chemistry* 97.18, pp. 4786–4796.

Lee, Deuk Ki (2004). "An apparent kinetic model for the carbonation of calcium oxide by carbon dioxide". In: *Chemical Engineering Journal* 100, pp. 71 –77.

Lee, Sungwon et al. (2014). "Dehydration effect on the pore size, porosity, and fractal parameters of shale rocks: Ultrasmall-angle X-ray scattering study". In: *Energy and Fuels* 28.11, pp. 6772–6779.

Li, Z. S., P. T. Liang, and N. S. Cai (2016). "A rate equation theory for the pore size distribution of calcined CaCO3 in calcium looping". In: *Faraday Discussions* 192.0, pp. 197–216.

Li, Zhen Shan, Ning Sheng Cai, and Yu Yu Huang (2006). "Effect of preparation temperature on cyclic CO_2 capture and multiple carbonation-calcination cycles for a new Ca-based CO_2 sorbent". In: *Industrial and Engineering Chemistry Research* 45.6, pp. 1911–1917.

Li, Zhenshan, Hongming Sun, and Ningsheng Cai (2012). "Rate Equation Theory for the Carbonation Reaction of CaO with CO_2". In: *Energy & Fuels* 26.7, pp. 4607–4616.

Lippens, B C, B G Linsen, and J H Boer de (1964). "Studies on Pore Systems in Catalysts VIII. The Adsorption of Krypton and Nitrogen on Graphitized Carbon". In: *Journal of Catalysis* 3, pp. 32–37.

Lippens, B.C, B.G Linsen, and J.H.de Boer (1964). "Studies on pore systems in catalysts I. The adsorption of nitrogen; apparatus and calculation". In: *Journal of Catalysis* 3.1, pp. 32–37.

Liu, Wen et al. (2012). "An investigation of the kinetics of CO_2 uptake by a synthetic calcium based sorbent". In: *Chemical Engineering Science* 69.1, pp. 644 –658.

Long, G. G. et al. (1991). "High-resolution small-angle X-ray scattering camera for anomalous scattering". In: *Journal of Applied Crystallography* 24.pt 1, pp. 30–37.

Lowell, Seymour (2004). *Characterization of porous solids and powders: surface area, pore size and density*. Vol. 16. Springer.

Lurio, L B et al. (2000). "Absence of scaling for the intermediate scattering function of a hard-sphere suspension: static and dynamic X-ray scattering from concentrated polystyrene latex spheres." In: *Physical review letters* 84.4, pp. 785–8.

MacKenzie, A. et al. (2007). "Economics of CO_2 Capture Using the Calcium Cycle with a Pressurized Fluidized Bed Combustor". In: *Energy & Fuels* 21.2, pp. 920–926.

Mahuli, Suhas K. et al. (1999). "Combined calcination, sintering and sulfation model for $CaCO_3$-SO_2 reaction". In: *AIChE Journal* 45.2, pp. 367–382.

Mai, M. C. and T. F. Edgar (1989). "Surface area evolution of calcium hydroxide during calcination and sintering". In: *AIChE Journal* 35.1, pp. 30–36. ISSN: 15475905.

Manovic, Vasilije et al. (2009). "Influence of calcination conditions on carrying capacity of CaO-based sorbent in CO_2 looping cycles". In: *Fuel* 88.10, pp. 1893–1900.

Maya, Juan C., Farid Chejne, and Suresh K. Bhatia (2017a). "Novel model for the sintering of ceramics with bimodal pore size distributions: Application to the sintering of lime". In: *AIChE Journal* 63, pp. 893–902.

— (2017b). "On the modeling of the CO_2-catalyzed sintering of calcium oxide". In: *AIChE Journal* 63.8, pp. 3286–3296. ISSN: 1547-5905.

McCabe, Warren L., Julian C. Smith, and Peter Harriott (2005). *Unit Operations of Chemical Engineering*. McGraw-Hill New York, pp. 151–176.

Mess, D, a F Sarofim, and J P Longwell (1999). "Product layer diffusion during the reaction of calcium oxide with carbon dioxide". In: *Energy & Fuels* 13.5, pp. 999–1005.

Metz, Bert et al. (2005). *IPCC Special Report on Carbon Dioxide Capture and Storage*. Tech. rep. Intergovernmental Panel on Climate Change, Geneva (Switzerland). Working Group III, pp. 1–431.

Milne, Corey R et al. (1990). "Calcination and sintering models for application to high-temperature, short-time sulfation of calcium-based sorbents". In: *Industrial & Engineering Chemistry Research* 29.2, pp. 139–149.

Morales, J.M. Criado; J. (1978). "Determination of equilibrium constants of solid thermal decomposition reactions by thermogravimetry". In: *Thermochimica Acta* 23 (2).

Muller, C R et al. (2009). "Investigation of the Enhanced Water Gas Shift Reaction Using Natural and Synthetic Sorbents for the Capture of CO_2". In: *Industrial & Engineering Chemistry Research* 48.23, pp. 10284–10291.

Nguyen, Thanh X. and Suresh K. Bhatia (2012). "Characterization of accessible and inaccessible pores in microporous carbons by a combination of adsorption and small angle neutron scattering". In: *Carbon* 50.8, pp. 3045–3054.

Nicholson, D (1965). "Variation of surface area during the thermal decomposition of solids". In: *Trans. Faraday Soc.* 61.0, pp. 990–998.

NIST (1997). *X-Ray Form Factor, Attenuation, and Scattering Tables*. URL: `http://physics.nist.gov/PhysRefData/FFast/html/form.html`.

Pedersen, J. S. (1994). "Determination of size distribution from small-angle scattering data for systems with effective hard-sphere interactions". In: *Journal of Applied Crystallography* 27.4, pp. 595–608.

Pedersen, Jan Skov (1997). "Analysis of small-angle scattering data from colloids and polymer solutions: modeling and least-squares fitting". In: *Advances in Colloid and Interface Science* 70.Supplement C, pp. 171 –210. ISSN: 0001-8686.

Percus, Jerome K and George J Yevick (1958). "Analysis of classical statistical mechanics by means of collective coordinates". In: *Physical Review* 110.1, p. 1.

Pete R. Jemian (1990). "PhD thesis". PhD thesis. Northwestern University (Evanston, IL).

Porod, G. (1951). "Die Rontgenkleinwinkelstreuung von dichtgepackten kolloiden Systemen - I. Teil". In: *Kolloid-Zeitschrift* 124.2, pp. 83–114.

Powell, Elizabeth K. and Alan W. Searcy (1980). "The rate and activation enthalpy of decomposition of $CaCO_3$". In: *Metallurgical Transactions B* 11.3, pp. 427–432.

— (1982). "Surface Areas and Morphologies of CaO Produced by Decomposition of Large $CaCO_3$ Crystals in Vacuum". In: *Journal of the American Ceramic Society* 65.3, pp. 42–44.

Rahaman, Mohamed N . (2007). *Solid state and viscous sintering*. CRC press, pp. 45–104. ISBN: 978-0-8493-7286-5.

Ramachandran, P. A. and J. M. Smith (1977). "Effect of sintering and porosity changes on rates of gas-solid reactions". In: *The Chemical Engineering Journal* 14.2, pp. 137–146.

Ramkumar, Shwetha and Liang Shih Fan (2010). "Thermodynamic and experimental analyses of the three-stage calcium looping process". In: *Industrial and Engineering Chemistry Research* 49.16, pp. 7563–7573.

Renner, Terry (2007). *Quantities, Units and Symbols in Physical Chemistry*. Ed. by E Richard Cohen et al. The Royal Society of Chemistry.

Rodriguez-Navarro, Carlos et al. (2009). "Thermal decomposition of calcite: Mechanisms of formation and textural evolution of CaO nanocrystals". In: *American Mineralogist* 94.4, pp. 578–593.

Sandler, S.I. (2017). *Chemical, Biochemical, and Engineering Thermodynamics*. Wiley.

Savitzky, Abraham and Marcel JE Golay (1964). "Smoothing and differentiation of data by simplified least squares procedures". In: *Analytical chemistry* 36.8, pp. 1627–1639.

Schiesser, W.E. (1991). *The Numerical Method of Lines: Integration of Partial Differential Equations*. Academic Press.

Schulze, S. et al. (2017). "Heat and mass transfer within thermogravimetric analyser: From simulation to improved estimation of kinetic data for char gasification". In: *Fuel* 187, pp. 338–348.

Seader, D and Ernest J Henley (2006). "Separation Process Principles". In: *America* 1, pp. 778–871.

Seaton, N.a., J.P.R.B. Walton, and N. Quirke (1989). "A new analysis method for the determination of the pore size distribution of porous carbons from nitrogen adsorption measurements". In: *Carbon* 27.6, pp. 853–861.

Shimizu, T. et al. (1999). "A Twin Fluid-Bed Reactor for Removal of CO_2 from Combustion Processes". In: *Chemical Engineering Research and Design* 77.1, pp. 62–68.

Silcox, Geoffrey D, John C Kramlich, and David W Pershing (1989). "A mathematical model for the flash calcination of dispersed calcium carbonate and calcium hydroxide particles". In: *Industrial & Engineering Chemistry Research* 28.2, pp. 155–160.

Sing, K S W et al. (1985). "Reporting physisorption data for gas/solid systems". In: *Pure and Applied Chemistry* 57.4, pp. 603–619.

Smith, J.M., H.C. Van Ness, and M. Abbott (2005). *Introduction to Chemical Engineering Thermodynamics*. CHEMICAL ENGINEERING SERIES. McGraw-Hill Education.

Solomon, Susan (2007). *Climate change 2007, The physical science basis: Working group I contribution to the fourth assessment report of the IPCC*. Vol. 4. Cambridge University Press.

Song, Qiang et al. (2006). "Influence of Diffusion on Thermogravimetric Analysis of Carbon Black Oxidation". In: *Energy & Fuels* 20.5, pp. 1895–1900.

Sotirchos, Stratis V. and Huei Chung Yu (1985). "Mathematical modelling of gas-solid reactions with solid product". In: *Chemical Engineering Science* 40.11, pp. 2039–2052.

— (1988). "Overlapping grain models for gas-solid reactions with solid product". In: *Industrial & Engineering Chemistry Research* 27.5, pp. 836–845.

Spalla, O., S. Lyonnard, and F. Testard (2003). "Analysis of the small-angle intensity scattered by a porous and granular medium". In: *Journal of Applied Crystallography* 36.2, pp. 338–347.

Stanmore, B. R. and P. Gilot (2005). "Review-calcination and carbonation of limestone during thermal cycling for CO2 sequestration". In: *Fuel Processing Technology* 86.16, pp. 1707–1743.

Stendardo, Stefano and Pier Ugo Foscolo (2009). "Carbon dioxide capture with dolomite: A model for gas–solid reaction within the grains of a particulate sorbent". In: *Chemical Engineering Science* 64.10, pp. 2343 –2352.

Stephens, Peter W. (1999). "Phenomenological model of anisotropic peak broadening in powder diffraction". In: *Journal of Applied Crystallography* 32.2, pp. 281–289.

Stocker, Thomas (2013). *Climate change 2013: The physical science basis*. Cambridge University Press.

Suk-Joong L.Kang (2005). "Sintering Densification,Grain Growth,and Microstructure". In: *Elsevier Butterworth-Heinemann Linacre House*, pp. 9–18.

Sun, P. et al. (2007). "The effect of CaO sintering on cyclic CO_2 capture in energy systems". In: *AIChE Journal* 53.9, pp. 2432–2442.

Sun, Ping et al. (2008a). "A discrete-pore-size-distribution-based gas–solid model and its application to the reaction". In: *Chemical Engineering Science* 63.1, pp. 57–70.

— (2008b). "Determination of intrinsic rate constants of the CaO–CO_2 reaction". In: *Chemical Engineering Science* 63.1, pp. 47 –56.

Szekely, J and JW Evans (1970). "A structural model for gas-solid reactions with a moving boundary". In: *Chemical Engineering Science* 25.6, pp. 1091–1107.

Szekely, J. and JW Evans (1971). "Studies in gas-solid reactions: Part I. A structural model for the reaction of porous oxides with a reducing gas". In: *Metallurgical Transactions* 2.6, pp. 1691–1698.

Taghl Darroudi and Alan W. Searcy (1981). "Effect of CO_2 Pressure on the Rate of Decomposition of Calcite". In: *J. Phys. Chem* 7901.85, pp. 3971–3974.

Thompson, A.C. et al. (2001). *X-ray Data Booklet*. Lawrence Berkeley Laboratory.

Valverde, J. M., P. E. Sanchez-Jimenez, and L. A. Perez-Maqueda (2015). "Limestone calcination nearby equilibrium: Kinetics, CaO crystal structure, sintering and reactivity". In: *Journal of Physical Chemistry C* 119.4, pp. 1623–1641.

Wadell, Hakon (1935). "Volume, Shape, and Roundness of Quartz Particles". In: *The Journal of Geology* 43.3, pp. 250–280.

Washburn, Edward W. (1921). "Note on a Method of Determining the Distribution of Pore Sizes in a Porous Material". In: *Proceedings of the National Academy of Sciences* 7.4, pp. 115–116.

Wilburn, F. W. et al. (1991). "The effect of procedural variables on TG, DTG and DTA curves of calcium carbonate". In: *Journal of Thermal Analysis* 37.9, pp. 2003–2019. ISSN: 0368-4466.

Yu, Y.S. et al. (2012). "Modeling of the carbonation behavior of a calcium based sorbent for CO_2 capture". In: *International Journal of Greenhouse Gas Control* 10.0, pp. 510 –519.

Zhang, Fan et al. (2010). "Glassy carbon as an absolute intensity calibration standard for small-angle scattering". In: *Metallurgical and Materials Transactions A: Physical Metallurgy and Materials Science* 41.5, pp. 1151–1158.

Zheng, Jingmin and James S. Reed (1989). "Effects of Particle Packing Characteristics on Solid-State Sintering". In: *Journal of the American Ceramic Society* 72.5, pp. 810–817.

Zhong, Q. and I. Bjerle (1993). "Calcination kinetics of limestone and the microstructure of nascent CaO". In: *Thermochimica Acta* 223.C, pp. 109–120.

Zhu, Yanqing, Sufang Wu, and Xieqing Wang (2011). "Nano CaO grain characteristics and growth model under calcination". In: *Chemical Engineering Journal* 175, pp. 512–518.